MCEER
EARTHQUAKE ENGINEERING TO EXTREME EVENTS

ISSN 1520-295X

# Hybrid Simulation of the Seismic Response of a Steel Moment Frame Building Structure through Collapse

by
Maikol Del Carpio Ramos, Gilberto Mosqueda
and Dimitrios G. Lignos

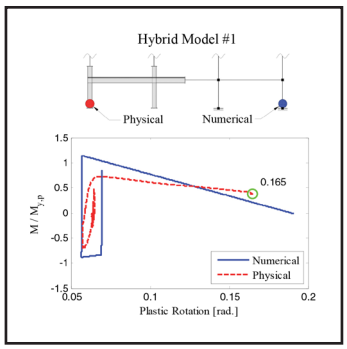


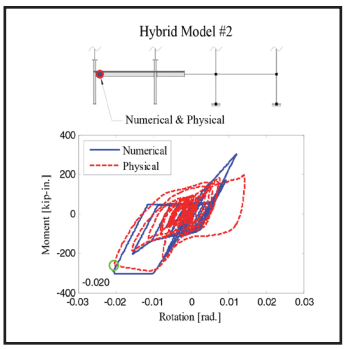


Technical Report MCEER-14-0003

October 30, 2014

This research was conducted at the University at Buffalo, State University of New York and was supported primarily by the George E. Brown, Jr. Network for Earthquake Engineering Simulation (NEES) Program of the National Science Foundation, NEESR award number CMMI-0748111.

# NOTICE

This report was prepared by the University at Buffalo, State University of New York as a result of research supported primarily by the George E. Brown, Jr. Network for Earthquake Engineering Simulation (NEES) Program of the National Science Foundation, NEESR award number CMMI-0748111, with additional support from the NEES equipment at the University at Buffalo. Neither MCEER, associates of MCEER, its sponsors, the University at Buffalo, State University of New York, the National Science Foundation, nor any person acting on their behalf:

a. makes any warranty, express or implied, with respect to the use of any information, apparatus, method, or process disclosed in this report or that such use may not infringe upon privately owned rights; or

b. assumes any liabilities of whatsoever kind with respect to the use of, or the damage resulting from the use of, any information, apparatus, method, or process disclosed in this report.

Any opinions, findings, and conclusions or recommendations expressed in this publication are those of the author(s) and do not necessarily reflect the views of MCEER, the National Science Foundation, or other sponsors.

# Hybrid Simulation of the Seismic Response of a Steel Moment Frame Building Structure through Collapse

by

Maikol Del Carpio Ramos,[1] Gilberto Mosqueda,[2] and Dimitrios G. Lignos [3]

Publication Date: October 30, 2014
Submittal Date: March 1, 2014

Technical Report MCEER-14-0003

NSF Grant CMMI-0748111

1 Ph.D. Candidate, Department of Civil, Structural and Environmental Engineering, University at Buffalo, State University of New York
2 Associate Professor, Department of Structural Engineering, University of California at San Diego
3 Assistant Professor, Department of Civil Engineering and Applied Mechanics, McGill University

MCEER
University at Buffalo, State University of New York
212 Ketter Hall, Buffalo, NY 14260
E-mail: *mceer@buffalo.edu*; WWW Site: *http://mceer.buffalo.edu*

# PREFACE

MCEER is a national center of excellence dedicated to the discovery and development of new knowledge, tools and technologies that equip communities to become more disaster resilient in the face of earthquakes and other extreme events. MCEER accomplishes this through a system of multidisciplinary, multi-hazard research, education and outreach initiatives.

Headquartered at the University at Buffalo, State University of New York, MCEER was originally established by the National Science Foundation (NSF) in 1986, as the first National Center for Earthquake Engineering Research (NCEER). In 1998, it became known as the Multidisciplinary Center for Earthquake Engineering Research (MCEER), from which the current name, MCEER, evolved.

Comprising a consortium of researchers and industry partners from numerous disciplines and institutions throughout the United States, MCEER's mission has expanded from its original focus on earthquake engineering to one which addresses the technical and socioeconomic impacts of a variety of hazards, both natural and man-made, on critical infrastructure, facilities, and society.

MCEER investigators derive support from the State of New York, National Science Foundation, Federal Highway Administration, National Institute of Standards and Technology, Department of Homeland Security/Federal Emergency Management Agency, other state governments, academic institutions, foreign governments and private industry.

*This report presents two series of hybrid simulations examining the seismic response of a four-story steel moment frame building structure in an effort to realistically capture system-level behavior through collapse. In the first series of tests, a half-scale 1½-bay by 1½-story physical sub-structure of a special moment resisting frame is considered, while in the second series the physical sub-structure corresponds to the gravity framing system with a similar-sized specimen. An objective of this work is to demonstrate the efficacy of hybrid simulation with substructuring as a cost-effective alternative to earthquake simulators for large-scale system-level testing of structural frame subassemblies. More specifically, the performance of a newly-developed substructuring technique and integration method for hybrid simulation are evaluated since these can be greatly challenged when employed with large and complex numerical sub-structures exhibiting large levels of nonlinear response. The test method was found to be reliable and to provide significant insight into experimental behavior of structural subassemblies under realistic seismic loading.*

# ABSTRACT

The overarching objective of this study is to advance knowledge on the collapse assessment of frame structures under earthquake loading through the development and implementation of an experimental framework for improved large-scale system-level testing. In particular, hybrid simulation with substructuring was investigated as a cost-effective alternative for large-scale testing of structural subassemblies. Through the use of substructuring techniques in hybrid simulation, only key subassemblies of a frame structure can be physically tested in a laboratory, while the rest of the frame is simulated in a computer model to capture the complete system behavior. Considerable efforts were made to implement the substructuring hybrid testing approach to examine frame structures through collapse. Such efforts included evaluating the performance of integration methods and substructuring techniques for hybrid simulation, which can be greatly challenged when employed with large and complex numerical sub-structures exhibiting large levels of nonlinear response. After examining these concerns, the experimental framework was implemented to examine the seismic response of two half-scale subassemblies of a moment and a gravity frame from the onset of damage through collapse. The physical subassemblies spanned one and one-half bays by one and one-half stories of the frame structures. These tests were conducted in response to the need for large-scale system-level testing for collapse assessment since only a few experimental programs in the past have subjected test specimens to large levels of loading near collapse.

The experimental test setup was designed to impose lateral (seismic) as well as vertical (gravity) forces on the physical sub-structures. Lateral loading on the physical subassemblies was applied through displacement-controlled actuators commanded by the hybrid simulation algorithm. The physical sub-structures included the composite floor slab and additional dead load at the first elevated story level. The axial forces on the columns at the second story, due to gravity loads from upper stories as well as seismic-induced variations from overturning forces, are applied through force-controlled actuators. The hybrid simulations were conducted at the Network for Earthquake Engineering Simulation (NEES) equipment site at the State University of New York at Buffalo (UB).

# ACKNOWLEDGEMENTS

This work was primarily supported by the National Science Foundation (NSF) under grant CMMI-0748111, with additional support from the NEES equipment at the University at Buffalo (also supported by NSF). This support is gratefully acknowledged. Any opinions, findings, conclusions or recommendations expressed in this report are those of the authors and do not necessarily reflect the views of the National Science Foundation.

The authors thank Dr. Judi Liu, Associate Professor at Purdue University, for sharing the experimental data on steel simple connections.

# TABLE OF CONTENTS

# TABLE OF CONTENTS (CONT'D)

# TABLE OF CONTENTS (CONT'D)

# TABLE OF CONTENTS (CONT'D)

# LIST OF FIGURES

# LIST OF FIGURES (CONT'D)

# LIST OF FIGURES (CONT'D)

# LIST OF FIGURES (CONT'D)

# LIST OF FIGURES (CONT'D)

# LIST OF FIGURES (CONT'D)

# LIST OF FIGURES (CONT'D)

# LIST OF FIGURES (CONT'D)

# LIST OF TABLES

# LIST OF TABLES (CONT'D)

# SECTION 1
# INTRODUCTION

## 1.1 Motivation

Over the last decade, several research projects have focused on the development of analytical tools for collapse assessment of structural systems subjected to seismic excitations (Elwood and Moehle, 2003, Sivaselvan and Reinhorn, 2006, Haselton and Deierlein, 2006, Huang and Foutch, 2009, Lignos and Krawinkler, 2012). Although a wealth of knowledge has been gained from these studies, there are only a limited number of experimental tests examining the behavior of structures at the system level (e.g., Nakashima *et al.*, 2006, Suita *et al.*, 2008). Such experimental data is essential to fully validate and improve the analytical tools that generally rely on empirical and mechanical component-level models to capture the global system behavior.

In addition, secondary systems such as frames designed as part of the gravity-force-resisting system (or simply "gravity frames") are commonly ignored in seismic performance assessment of structures that typically consider only the seismic-force-resisting system. The simple connections used in gravity frames are designed to carry gravity loads only and consequently assumed to provide minimal lateral resistance to the structure. However, cyclic testing of these connections (e.g., Liu and Astaneh-Asl, 2000b, and others) has shown some inherent moment capacity with increasing strength and stiffness at large deformations. Despite this, limited research has been conducted to assess the influence of the gravity-force-resisting system on the seismic response of structures near collapse.

In view of this lack of experimental data for collapse assessment, an experimental framework was developed and implemented at the Network for Earthquake Engineering Simulation (NEES) equipment site at the State University of New York at Buffalo (UB) to address the gaps in knowledge identified above, namely, (a) the need for large-scale system-level testing of structures to collapse, and (b) assessment of the contribution of gravity frames to the collapse capacity of structures. The test specimens consisted of one and one half bay by one and one half story subassemblies of a special steel moment and gravity-resisting frames. In contrast to the large number of traditional quasi-static tests (e.g., SAC Joint Venture [www.sacsteel.org]) conducted on cruciform or T-shaped subassemblies of beams and columns with idealized boundary conditions to prescribed cyclic loading protocols (component-level tests), the

larger subassemblies in this experimental program were subjected to more realistic loading conditions via hybrid simulation using similar laboratory equipment.

## 1.2 Research Objectives and Scope

The overarching objective of this research project is to advance knowledge on collapse assessment of structures through the development and implementation of a cost-effective experimental framework for improved large-scale system-level testing of frame structures to simulated dynamic earthquake loading. Through the use of substructuring in hybrid simulation, large-scale subassemblies of a steel moment frame building are tested as a cost-effective alternative to large-scale earthquake simulator testing. The experimental program developed in this research project represents an improvement to the traditional cyclic tests on cruciform or T-shaped subassemblies of beams and columns with idealized boundary conditions. The larger subassemblies tested here allow for the observation of component behavior, including their connections and interactions with neighboring members for improved system-level simulations. These tests were conducted in response to the need for large-scale testing for collapse assessment since only a few experimental programs in the past have subjected test specimens to levels of loading near collapse with realistic boundary conditions. This data is needed to better understand the behavior of structures near collapse at the system level.

Several challenges were encountered during the implementation of the hybrid testing method to examine frame structures through collapse. A major challenge included the stability of the numerical integration method to solve the equations of motion during a hybrid simulation. The available integrators, either explicit or implicit with fixed number of iterations, are greatly challenged when employed with large and complex numerical sub-structures experiencing significant levels of yielding. Another major challenge was related to the performance of the substructuring technique for multi-story frame structures with simplified boundary conditions to reduce the number of actuators needed to control the boundary degrees of freedom of the physical sub-structure at the interface with the numerical sub-structure. These two aspects formed the basis for some of the studies presented in this report to advance the state of practice of hybrid simulation for collapse assessment.

The objective of the experimental program is to obtain realistic experimental data to better understand the seismic behavior of steel moment frame building structures from the onset of damage through collapse. The data is also used to assess and improve the capabilities of analytical models to trace the response of structures near collapse.

The objectives of this research are summarized as follows:

- Evaluate the accuracy and stability of different integration methods used in hybrid simulation for tracing structural response through collapse.
- Assess the accuracy of a newly-developed substructuring technique with simplified boundary conditions to evaluate the response of frame structures through collapse.
- Design and conduct an experimental program to evaluate the seismic behavior of two half-scale subassemblies of a moment and gravity frame via hybrid simulation from the onset of damage through collapse.
- Assess the seismic performance of a steel moment and gravity frame subassemblies using the results of the experimental program.
- Assess and improve the capabilities of analytical models to trace the response of a steel moment frame system through collapse using the experimental data obtained from the hybrid simulations.
- Assess the influence of the gravity-force-resisting system on the response of the steel moment frame building structure using a seismic fragility framework.

## 1.3 Report Outline

This report is organized in nine sections, a list of references and two appendices. Section 1 presents the motivation as well as objectives and scope of the research studies presented in this report. Section 2 presents a review of literature focusing on experimental programs examining the behavior of different structural systems near collapse, and analytical studies and testing of gravity framing systems. Section 3 presents an evaluation of integration methods for hybrid simulation preceded by a brief introduction to hybrid simulation. Preliminary aspects of the experimental program developed in this research project are discussed in Section 4 including objectives and scope, a description of the prototype structure and the reduced-scale hybrid models, and the selection of the ground motion and testing protocol. Section 5 presents the design and construction of the physical sub-structures. Section 6 describes the development of the numerical sub-structures as well as the substructuring algorithm. An extensive evaluation of the substructuring technique is presented in this section. Section 7 presents the test results of the two series of hybrid simulations together with an assessment of the analytical tools employed to simulate the response of these systems through collapse. The collapse performance of the steel moment frame building structure was further evaluated in Section 8 using the methodology proposed in FEMA P695 (FEMA, 2009). A summary and conclusions of the experimental and numerical studies presented in this report are provided

in Section 9 followed by a list of references. A complete set of drawings of the two physical test specimens are included in Appendix A and Appendix B.

# SECTION 2
# REVIEW OF LITERATURE

## 2.1 Overview

This section presents a review of past research conducted in support of collapse assessment of structural systems subjected to seismic excitations as well as past studies on frames designed only for gravity loads. In Section 2.2, a brief description and major conclusions of studies relevant to this research project are presented which highlight the need for more experimental data for collapse assessment of structures. Section 2.3 presents a summary of past experimental studies examining the behavior of different structural systems through collapse. The experimental framework developed in this research project builds on many of these studies including Lignos and Krawinkler (2012), Hashemi *et al.* (2013), Liu and Astaneh-Asl (2000b), Wang *et al.* (2011), Cortes-Delgado (2013) and Schellenberg *et al.* (2009). From this review, it is clear that there are only a limited number of large-scale experimental tests examining the system-level response of realistic structures through collapse. These experiments are essential for a better understanding of collapse and to assist in the development and improvement of analytical tools for collapse predictions. This is followed by a summary of past studies on gravity framing systems presented in Section 2.4, including experimental tests on simple beam-column connections typically used in gravity frames.

## 2.2 Collapse Studies on Structural Systems under Seismic Excitations

Over the last few decades, several research projects have focused on developing methodologies for collapse assessment of structural systems. Villaverde (2007) presents a comprehensive review of these methods as well as past experimental work of specimens tested to collapse. From this review, Villaverde concluded that assessing the collapse capacity of structures subjected to seismic excitations is a complicated task that cannot be achieved through simplified methodologies such as those based on single-DOF models or nonlinear static analysis. Accurate analytical predictions of the collapse capacity are possible only through detailed dynamic finite-element analysis. However, Villaverde also pointed out that there is a need for experiments of more realistic specimens all the way to collapse.

Advances in nonlinear simulation techniques in recent years have permitted explicit simulation of different deterioration modes influencing the collapse response of structures. Lignos and Krawinkler

(2012) presented a review of literature of available hysteretic models that incorporate component deterioration. They also assembled a database of test results of steel and reinforced concrete frame components in order to understand the deterioration of structural components and evaluate the capability of analytical tools to simulate all important modes of deterioration. The database assisted in the development of relationships (regression equations) for modeling deterioration of plastic-hinge regions of steel components. The steel database also helped to judge the adequacy of existing deterioration models and to improve the hysteretic model developed by Ibarra *et al.* (2005). After a review of literature on collapse tests, Lignos and Krawinkler concluded that there are only a few experimental studies in which the structural system was tested through collapse. These tests are needed to demonstrate that predictions of collapse are indeed feasible. In view of this, they conducted two collapse tests of moment frame structures described in the next section.

Prior to Lignos and Krawinkler, Haselton and Deierlein (2006) used a database of 255 experimental tests of reinforced concrete columns to also develop relationships to predict modeling parameters of the hysteretic model of Ibarra *et al.* for reinforced concrete beam-column elements. The models were shown to capture the inelastic flexural response at large deformations associated with collapse of reinforced concrete frame building structures.

A Lagrangian approach for structural collapse simulation was proposed by Sivaselvan and Reinhorn (2006). In contrast to the widely-used displacement-based formulation used in conjunction with an incremental iterative scheme for nonlinear problems, the Lagrangian method provides a generalized formulation which separates modeling of components from the numerical solution, which can be potentially used for analysis of structural collapse. The advantages of the Lagrangian approach include allowing for larger time steps as compared to the conventional incremental iterative approach where the tangent matrix may not be positive definite and the Newton iterations may not be globally convergent limiting the size of the time step. Phenomenological models of components to simulate collapse can be incorporated without having to implement model-specific incremental state determination algorithms. The Lagrangian formulation presented by Sivaselvan and Reinhorn accounts for both material and geometric nonlinearities.

## 2.3 Experimental Studies of Collapse Assessment

Kato *et al.* (1973) conducted one of the first series of collapse tests using the simplified single-DOF model shown in Figure 2-1 in which the test specimen consisted of a steel column with a concentrated

mass at the top tested through collapse in a shake table. Numerical predictions carried out including P-Delta effects to reproduce the experimental test results were in good agreement.

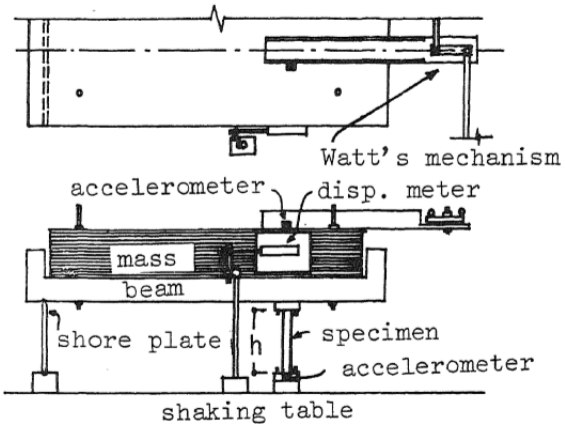


**Figure 2-1 Experimental test setup used for collapse tests by Kato *et al.* (1973)**

Vian and Bruneau (2001, 2003) carried out a series of shake table tests to assess P-delta effects on the response of fifteen collapsing single-DOF structures. Figure 2-2 shows the experimental tests setup and the test specimen consisting of a four-column steel frame structure. It was concluded in this study that the stability factor, defined as the ratio of axial force to the lateral stiffness of the structure times its height, is the most important parameter influencing the collapse behavior of the structures. The experimental program of Vian and Bruneau was complemented by Kanvinde (2003) with nineteen similar shake table tests. Kanvinde subsequently carried out analytical simulations using OpenSees which closely reproduced the shake table test results.

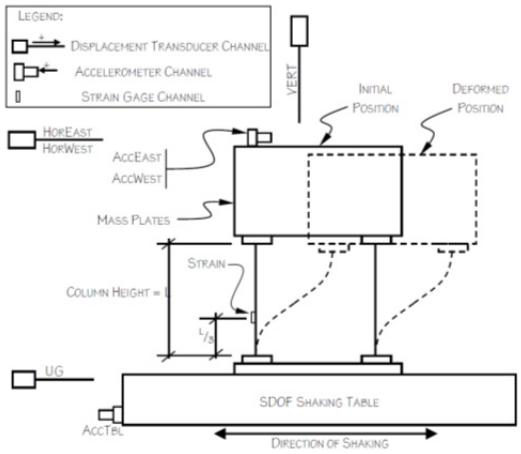


**Figure 2-2 Experimental test setup used for collapse tests by Vian and Bruneau (2001)**

Elwood and Moehle (2003, 2005) examined the behavior of shear-critical reinforced concrete columns subjected to seismic excitations leading to gravity load collapse. Two full-scale specimens consisting of a three-column reinforced concrete frame structure shown in Figure 2-3 were tested on a shake table. Analytical models traced the drift response of the physical specimens up to shear failure. However, the response at large deformation after shear failure was not captured.

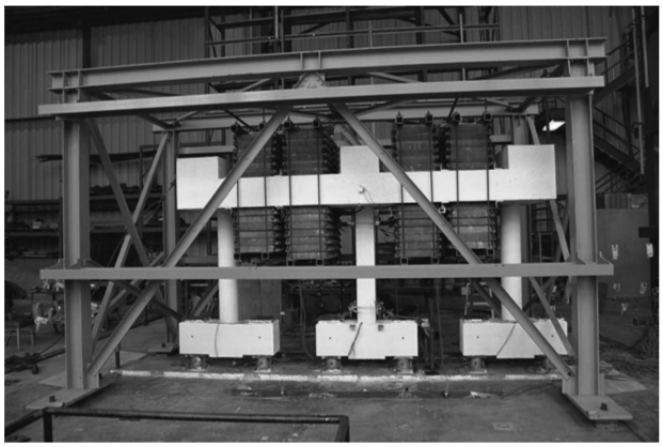

**Figure 2-3 Full-scale specimen for gravity load collapse tests (Elwood and Moehle, 2003)**

Nakashima *et al.* (2006) tested a full-scale model of a steel moment frame building with the objective of obtaining realistic information about the damage and strength deterioration and to examine the capability of analytical models commonly used in seismic design to trace the inelastic behavior to collapse. The steel moment frame model shown in Figure 2-4 was tested quasi-statically using a cyclic loading protocol. It was reported that the numerical models were able to accurately duplicate the cyclic behavior up to a drift ratio of 0.04. After that, the numerical models did not trace the response of the structure where serious strength deterioration occurred due to fracture of beams and anchor bolts and column local buckling.

**Figure 2-4 Overview of full-scale steel moment frame model tested by Nakashima *et al.* (2006)**

Rodgers and Mahin (2006) investigated experimentally and analytically the effects of various types of hysteretic responses of beam-column connections on the global seismic response of a steel moment frame system. Thirty two shake table tests were performed on the 1/3-scale model shown in Figure 2-5 as part of the experimental studies at the University of California at Berkeley. It was concluded in these studies that severe strength loss due to a combination of connection fracture, undesirable post-fracture hysteretic behavior and strong seismic excitations can lead to adverse consequences including collapse.

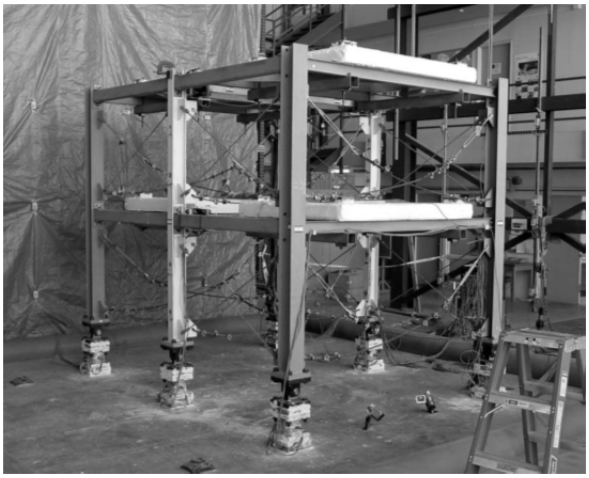

**Figure 2-5 One-third-scale test specimen used by Rodgers and Mahin (2006)**

Shirai *et al.* (2006) and Matsumori *et al.* (2006) reported a shake table test of a full-scale six-story reinforced concrete wall-frame structure at the E-Defense testing facility in Miki, Japan to simulate its collapse response. In this unprecedented experimental program, the reinforced concrete building shown in Figure 2-6 was designed and constructed according to Japanese standards of 1970s practice and was subjected to three-dimensional earthquake loading. The objective of this test was to collect data on the

collapse process of a realistic building structure subjected to severe earthquake loading. Based on this test, several analytical studies such as Kim *et al.* (2012) were undertaken to look into several aspects associated with numerical modeling.

**Figure 2-6 Full-scale six-story reinforced concrete structure tested at E-Defense (Kim *et al.*, 2012)**

Schellenberg and Mahin (2006) studied the ability of correctly accounting for second-order effects in hybrid simulation of structural collapse. In this study, the numerical simulations were carried out in the OpenSees platform and integrated with the laboratory hardware for the hybrid simulation through OpenFresco (2008). This new approach was validated with a hybrid test of a portal frame. They demonstrated that hybrid simulation of the seismic response of structures up to collapse is viable.

As mentioned earlier, Lignos and Krawinkler (2012) executed in 2007 collapse tests on two 1/8-scale aluminum frame models representative of moment frames to validate the capabilities of analytical modeling for collapse prediction. Figure 2-7 shows the aluminum frame structure connected to a mass simulator, both mounted on the shake table at the University at Buffalo. It was concluded in this study that relatively simple analytical models can predict the collapse capacity with a satisfactory level of accuracy as long as all important modes of deterioration are adequately represented in the analytical models.

**Figure 2-7 Overview of collapse shake table tests by Lignos and Krawinkler (2012)**

A comprehensive experimental program of a full-scale four-story steel moment frame building designed according to Japanese standards and shown in Figure 2-8 was conducted at the E-Defense shake table. The steel building was subjected to increasing intensities of the three components of the JR Takatori earthquake record to evaluate the seismic performance of the building under design-level ground motion to safety margin against collapse. This experimental program has motivated numerous studies to assess and improve the capabilities of analytical tools for collapse prediction.

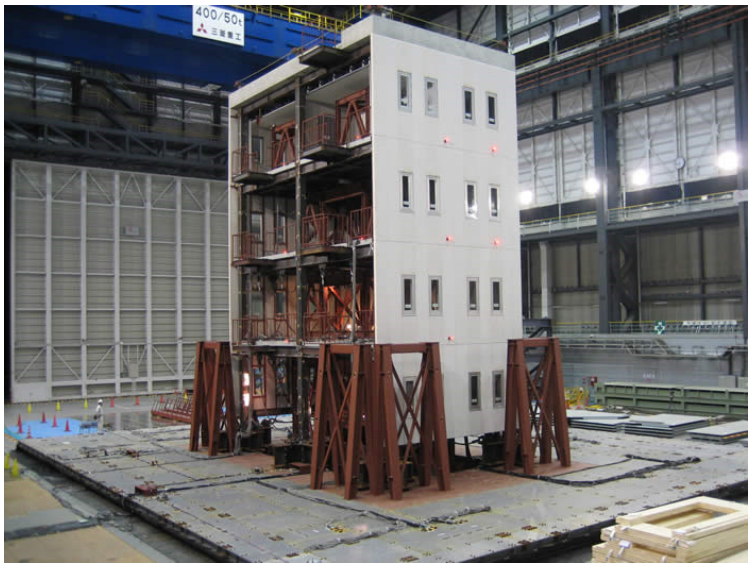

**Figure 2-8 Collapse test of a full-scale four-story steel building at E-Defense (picture courtesy of Hyogo Earthquake Engineering Research Center)**

Wang *et al.* (2011) performed a geographically distributed online hybrid simulation of the seismic response of a two-dimensional half-scale moment-resisting frame system to collapse. The prototype structure was based on the full-scale building structure designed according to Japanese standards of practice and tested to collapse at the E-Defense shake table laboratory in Japan (Suita *et al.*, 2008) which provided a benchmark for comparison. The distributed hybrid simulation included two bare steel physical sub-structures located in two laboratories at Kyoto University (KU) in Japan and at University at Buffalo (UB) in the U.S. as shown in Figure 2-9. The objective of the test was to investigate the implementation of a flexible test scheme with innovative substructuring techniques for hybrid simulation and the capability of the distributed hybrid test framework to capture the realistic collapse behavior of a structure. It was concluded that although the hybrid tests included several simplifications such as unidirectional loading and boundary condition assumptions, a similar response and collapse mechanism was observed in the distributed hybrid test. Prior to this test, Wang *et al.* (2008) conducted similar collapse tests where only the plastic-hinge regions at the base of the columns of the same prototype building structure were experimentally tested via distributed hybrid simulation.

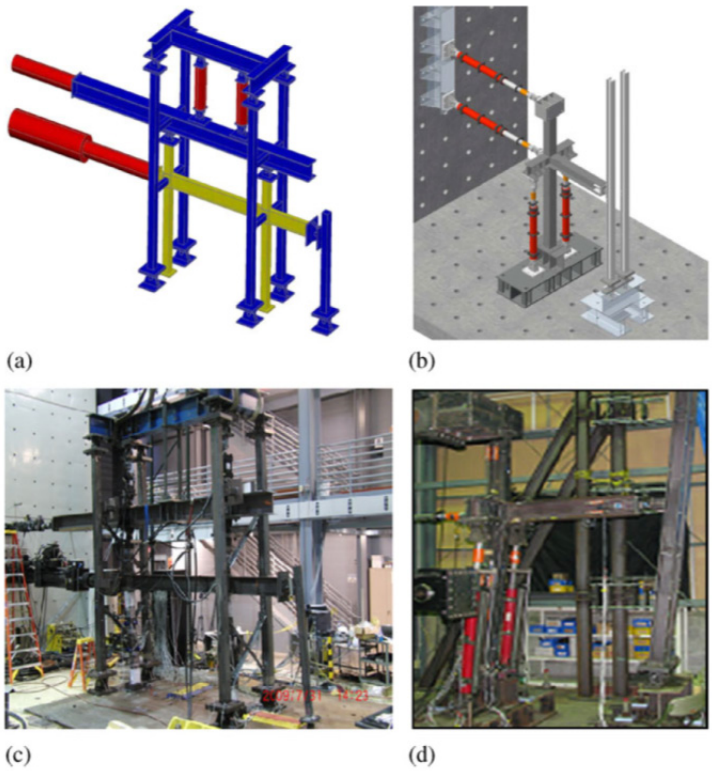


**Figure 2-9 Distributed collapse hybrid simulation: (a) test setup at UB, (b) test setup at KU, (c) photograph of test setup at UB and (d) photo of test setup at KU (Wang *et al.*, 2011)**

Mahmoud *et al.* (2013) tested via hybrid simulation three full-scale steel subassemblies of beams and columns with semi-rigid connections as shown in Figure 2-10 at the NEES equipment site at University of Illinois. This experimental program, although not conducted particularly for collapse assessment, is relevant to this research project for providing a methodology for assessing the system-level response of large-scale steel frames with semi-rigid connections.

**Figure 2-10 Experimental test setup at the NEES equipment site at University of Illinois (Mahmoud, 2011)**

Hashemi (2013) conducted a series of hybrid simulations at the NEES Equipment site at University at Buffalo as part of a research project that focused on the development of substructuring techniques to evaluate multi-story frame structures through collapse via hybrid simulation. The substructuring technique presented by Hashemi is a refinement of the work of Wang *et al.* (2011). The prototype structure is a 1/8-scale aluminum frame tested previously by Lignos and Krawinkler (2012) on a shake table to increasing ground motion intensities to collapse. These tests were reproduced by Hashemi for two hybrid models subjected to the same ground motion intensities used in the shake table tests and the substructuring technique. Figure 2-11 presents one of the hybrid models. The seismic response of the four-story aluminum moment frame model to collapse was examined with physical sub-structures and highly detailed numerical sub-structure models.

From the foregoing summary of experimental studies, it is evident that there are only a few experimental system-level tests carried out to understand the behavior of structures to collapse, especially of structures constructed to U.S. standards of practice. Limitations of the testing facilities in the U.S. have motivated several studies to turn to alternative large-scale testing methods such as hybrid simulation. While the hybrid test approach cannot match the realism of full-scale earthquake simulator testing, it can provide a

cost-effective method for evaluating the seismic performance of buildings at large scales with the capabilities available in many laboratories.

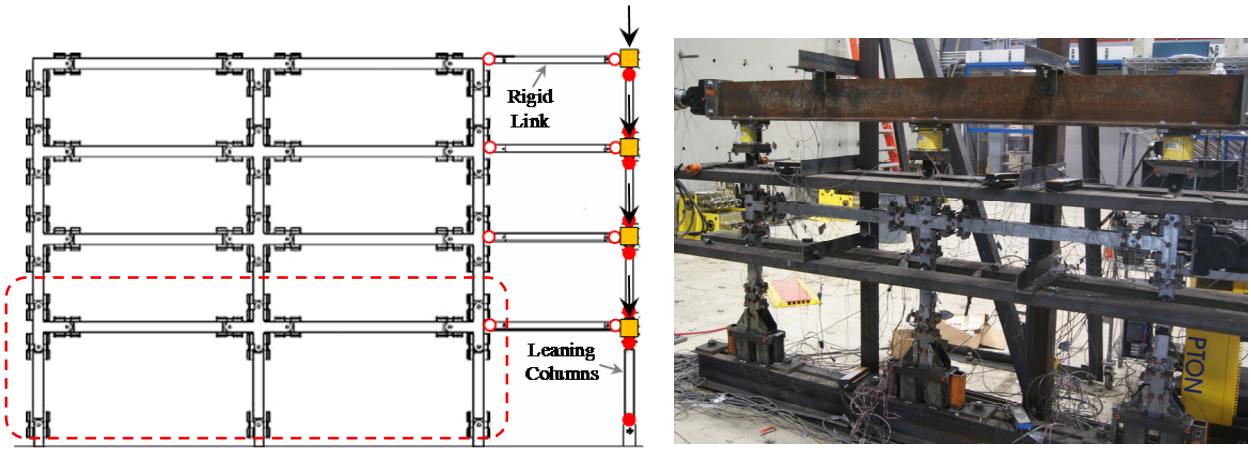


(a) Hybrid (physical and numerical) model (b) Physical sub-structure

**Figure 2-11 Hybrid simulation of frame structure with substructuring technique (adapted from Hashemi, 2013)**

## 2.4 Studies on Gravity Frames

Simple steel connections typically used in gravity frames are defined in AISC (2005) as a connection having a rotational stiffness less than $2EI/L$ (where $E$ is the modulus of elasticity, $I$ is the moment of inertia and $L$ is the length of the member). Although these simple connections are commonly idealized as pinned for the purpose of structural analysis, cyclic testing has demonstrated some inherent moment capacity. However, unlike fully-restrained connections (rotational stiffness greater than $20EI/L$) or partially-restrained connections (rotational stiffness ranging between $2EI/L$ and $20EI/L$), there is only a limited number of experimental tests examining the behavior of simple connections. This section presents a summary of previous tests on simple steel connections together with the most salient analytical studies examining the influence of the gravity frames on the global response of building structures.

Astaneh-Asl *et al.* (1989) conducted a series of tests on simple connections commonly used in engineering practice in the U.S. Figure 2-12 shows the experimental test setup where five full-scale beam-column subassemblies with shear-tab connection details were subjected to monotonic loading. The test specimens did not include the concrete floor slab. Considerable shear and bearing yielding of the shear-tab plate prior to failure was reported (failure was defined as fracture of net area of plate). In this study,

limit states were identified for shear-tab connections, namely, plate yielding, fracture of net section of plate, bolt fracture, weld fracture, and bearing failure of bolt holes. As a result of this experimental program, a design procedure for shear-tab plate connections was recommended.

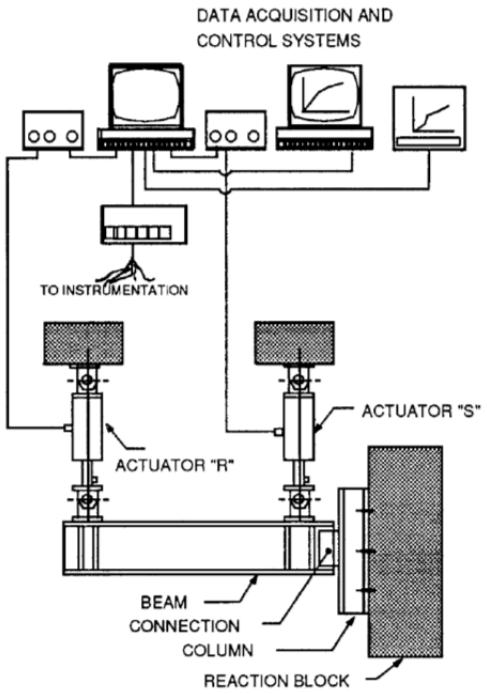


**Figure 2-12 Experimental test setup used by Astaneh-Asl *et al.* (1989)**

In a study of the seismic behavior of ductile steel moment frame structures by Gupta and Krawinkler (2000), the contribution of the gravity-force-resisting system (or simply gravity frames) was examined through a series of nonlinear static (pushover) as well as response history dynamic analyses conducted on the SAC building model structures (Gupta and Krawinkler, 1999). A simplified model of the gravity frames was used in this study where the inelastic moment-rotation response of the simple connections was simulated using a bilinear model without degradation. Based on judgment and limited experimental data (i.e., Astaneh-Asl *et al.*, 1989, and Leon *et al.*, 1998), the positive and negative yield moment of the bilinear model was set to 40% and 20% of the plastic moment of the bare beam section. It was concluded that the contribution of the gravity frames is a function of the number of gravity frames, the orientation of the gravity columns, the support boundary conditions of the columns and the simple beam-column connections. However, the contribution of the gravity columns was more pronounced than that of the simple connections.

As part of the SAC Joint Venture Steel Project (www.sacsteel.org), Liu and Astaneh-Asl (2000b) conducted a comprehensive series of cyclic tests on sixteen full-scale cruciform subassemblies of beams and columns with different simple connection details using the experimental test setup shown in Figure 2-13. Eight of those specimens are commonly used in current design practice in the U.S. For the remaining eight specimens, improved simple connections, not necessarily used in current practice, were developed. By far, this is the most extensive experimental study examining the behavior of simple connections in gravity frames. A detailed summary of some of these tests is presented in Section 6. As a result of this experimental program, guidelines were developed to predict moment-rotation relationships for simple connections.

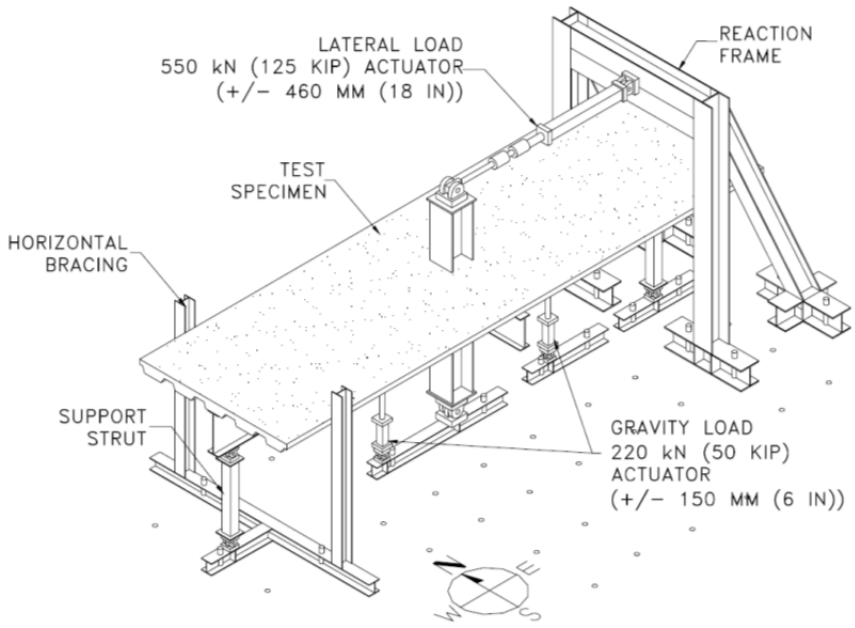


**Figure 2-13 Experimental test setup of Liu and Astaneh-Asl (2000a)**

Foutch and Yun (2002) conducted studies on the influence of the gravity framing system. A nine-story and a twenty-story steel moment frame building structures were designed as part of this study. The gravity frames were modeled similar to Gupta and Krawinkler. However, deterioration was included in the bilinear models by simulating a drop in strength at given rotations. The yield strength values of the bilinear model as well as rotation values at drop in strength were based on the experimental work of Liu and Astaneh-Asl (2000b). Foutch and Yun arrived at similar findings of Gupta and Krawinkler (2000) including a significant contribution of the gravity framing system and that most of the contribution was due to the flexural response of the continuous gravity columns.

Ji *et al.* (2009) investigated analytically the effects of continuous gravity columns on the seismic response of a three-story concentrically braced steel frame structure. To this end, the response of beam-column connections of gravity frames was not included. Pinned and fixed support conditions were assumed for the gravity columns. It was shown in this study that gravity columns contribute to the mitigation of drift concentration. Similar observations were reported by Tagawa *et al.* (2010) for U.S. steel moment-resisting frame structures.

Crocker and Chambers (2004) carried out a series of cyclic tests on T-shaped subassemblies to derive the rotation capacity of shear-tab connection details with a single line of bolts. To this end, maximum deformation demands on bolts in response to rotation demands were derived. Three full-scale test specimens were constructed with three, four and six bolts. The test specimens did not include the floor slab. The test data assisted in the development of equations to estimate the connection rotation capacity.

Marosi *et al.* (2011) conducted cyclic tests of eight shear-tab connections to address connection details with single, double and triple lines of bolts utilized in elements subjected to tension as a result of transferring lateral forces to seismic-resisting frames or catenary action that occurs in floor beams when a column is removed. The specimens did not include the floor slab. The test results showed that the multi-row connections reached strength levels consistent with typical predicted failure modes while maintaining similar levels of rotational ductility compared to the commonly used shear-tab connections with a single row of bolts.

Although the focus of this research project is on steel frame structures, it is important to point out that reinforced concrete gravity frames have been also studied experimentally. Some of these studies include the work of Bracci *et al.* (1992a, 1992b), Aycardi *et al.* (1992), El-Attar *et al.* (1991), and Calvi *et al.* (2002). Based on a series of shake table tests conducted at the University at Buffalo, Bracci *et al.* concluded that reinforced concrete frames designed only for gravity loads have some inherent strength for resisting seismic forces.

In summary, only a few experimental tests have been conducted on the simple connections that are not part of the seismic-force-resisting system commonly used for gravity framing in engineering practice in the U.S. Most of the test specimens did not include the concrete floor slab. The most extensive experimental program was conducted by Liu and Astaneh-Asl (2000b). Other tests of less relevance include the work of Sherman and Ghorbanpoor (2002), Abolmaali *et al.* (2003) and Gong (2010). Sherman and Ghorbanpoor (2002) tested shear-tab connections with extended shear-tab plates to avoid

costly details such as coping or flange reductions of framing beams. Abolmaali *et al.* tested double web angle steel connections and Gong tested shear-tab connections of a wide-flange beam to flexible wall supports such as HSS column sections.

## 2.5 Summary

The review of literature presented in this section as well as in others (Villaverde, 2007, Lignos and Krawinkler, 2012) have identified that there are only a limited number of large-scale experimental tests examining the system-level response of realistic structures in which the test specimens were loaded up to collapse. These experiments are key for a better understanding of collapse and essential to assist in the development and improvement of analytical tools for collapse predictions. More realistic collapse predictions involve the inclusion of the gravity framing system especially since previous research have shown an important contribution of the gravity frames in the seismic response of building structures.

# SECTION 3
# EVALUATION OF INTEGRATION METHODS FOR HYBRID SIMULATION

## 3.1 Introduction

Hybrid simulation, rooted in the pseudo-dynamic testing method (Takanashi, 1975, Takanashi and Nakashima, 1987, Mahin *et al.*, 1989, Shing *et al.*, 1996), provides a cost-effective solution for large-scale testing of structures subjected to seismic excitations by partitioning the structure into numerical and physical models. Typically, the physical sub-structures are portions of the structure difficult to model numerically and numerical sub-structures represent structural components with more predictable behavior. More recent applications of hybrid simulation have focused on large and complex structural systems, often including highly nonlinear behavior through collapse in the numerical models that challenges the capabilities of integration algorithms suitable for hybrid simulation (Wang *et al.*, 2011, Hashemi, 2013).

Several integration methods have been proposed and developed to solve the nonlinear equations of motion during a hybrid simulation (Schellenberg *et al.*, 2009, Chen and Ricles, 2008, Ahmadizadeh and Mosqueda, 2008, Nakashima *et al.* 1990, and Shing *et al.*, 1991). Although the accuracy and stability properties of the integration methods used in purely numerical simulations can be established for linear systems, they cannot be guaranteed for nonlinear systems. Furthermore, experimental errors in hybrid tests significantly affect the stability and accuracy properties of the integration methods.

On the other hand, numerical simulation of structural collapse is a highly nonlinear problem that requires the use of sophisticated integration methods together with small time steps for convergence, accuracy and stability of the results. However, the use of small time steps is typically avoided in hybrid simulation since it requires a large number of data communication procedures between the numerical and physical sub-structures, a time consuming process that introduces experimental errors into the numerical integration algorithms and increases the sensitivity of the system to delay errors. Experience has shown that the selection of the integration method and time step is crucial in collapse hybrid simulation.

This section examines the performance of integration methods for hybrid simulation for large and complex structural systems in the context of structural collapse due to seismic excitations. The section

presents a brief description of the integration methods followed by two study cases. The first case study presents a numerical evaluation using energy balance errors as a measure of accuracy, while the second case study presents twelve hybrid simulations conducted to evaluate the performance of these integration methods. Although the conclusions drawn from these cases studies cannot be generalized, they provide insight for the selection of integration algorithms for hybrid simulation of similar structural systems.

## 3.2 Integration Methods for Hybrid Simulation

In hybrid simulation, the nonlinear equations of motion shown in Equation 3-1 (discretized at the time instant $t_{i+1}$) are expressed for the hybrid (physical and numerical) model and solved for the displacement ($\mathbf{U}_{i+1}$), velocity ($\dot{\mathbf{U}}_{i+1}$), and acceleration ($\ddot{\mathbf{U}}_{i+1}$) vectors using time-stepping integration algorithms.

$$\mathbf{M}\ddot{\mathbf{U}}_{i+1} + \mathbf{C}\dot{\mathbf{U}}_{i+1} + \mathbf{P_r}(\mathbf{U}_{i+1}) = \mathbf{P}_{i+1} \tag{3-1}$$

While the mass matrix $\mathbf{M}$, damping matrix $\mathbf{C}$, and external force vector $\mathbf{P}_{i+1}$ are typically part of the numerical simulation, the resisting force vector $\mathbf{P_r}$ is composed of forces from both physical and numerical models.

Both explicit and implicit integration algorithms have been applied to solve the equations of motion in hybrid simulation. Explicit methods compute the response of the structure at the end of the current time step ($\mathbf{U}_{i+1}$, $\dot{\mathbf{U}}_{i+1}$, $\ddot{\mathbf{U}}_{i+1}$) based on the state of the structure at the beginning of the step ($\mathbf{U}_i$, $\dot{\mathbf{U}}_i$, $\ddot{\mathbf{U}}_i$). This is an attractive property for hybrid testing because the actuators are commanded a target displacement without knowledge of the specimen properties at the target. However, explicit integration methods are either unstable or cannot be applied at all when employed with structural systems presenting a singular mass matrix as a result of having massless DOF (Schellenberg *et al.* 2009). This can be a challenge when modeling frame structures in detail including panel zones and beams with concentrated plasticity.

On the other hand, implicit methods require knowledge of the structural response at the target displacement in order to compute the response, with iterations required to satisfy both the imposed kinematic conditions and the equilibrium conditions at the end of the time step. Iterations provide some challenges in the implementation of implicit integration methods in a hybrid simulation with physical sub-structures. Physical sub-structures could be erroneously and undesirably damaged in iterative schemes when the predicted (trial) displacements overshoot the target displacements, after which the physical sub-structure has to be unloaded to the corrected target displacement. Furthermore, implicit

methods require a tangent stiffness matrix which can be difficult to obtain from physical models (Mosqueda and Ahmadizadeh, 2011). Another feature of implicit integration methods incompatible with hybrid simulation is the non-uniform displacement increments produced during the equilibrium iterations typically performed using the Newton-Raphson algorithm. The displacement increments decrease rapidly with each iteration due to the quadratic convergence property of the Newton-Raphson algorithm. In a hybrid simulation where the same time interval is typically allocated to the actuator to apply each displacement increment, uniform displacement increments are preferred since these produce a continuous movement of the actuators instead of a jerky oscillatory movement that could be observed with rapidly decreasing displacement increments. Despite these difficulties, implicit integration methods have been successfully applied to hybrid simulations in the past to gain the benefits of improved stability and accuracy characteristics over explicit integration algorithms with larger integration time steps.

Another earlier approach to overcome the stability limitations associated with explicit methods was proposed by Dermitzakis and Mahin (1985). A combined implicit-explicit integration algorithm (Hughes and Liu, 1978) was applied for integration of the equation of motion by dividing the degrees of freedom (DOF) of a structure into one sub-structure containing physical DOFs and another containing analytical DOFs. An explicit method was used for the physical sub-structure and an implicit method was used for the analytical sub-structure. The division allowed for the application of unconditionally stable implicit algorithms to the analytical sub-structure.

Nakashima *et al.* (1990) used a predictor-corrector integration scheme (Hughes *et al.* 1979) in their implementation of the operator-splitting method for pseudo-dynamic testing. The numerical procedure is similar to the implicit-explicit formulation described above but only the stiffness matrix is divided into linear and nonlinear sub-structures. The advantage of using the operator-splitting predictor-corrector method is that unconditional stability is guaranteed for nonlinear structures of the softening type. The predictor-corrector formulation is non-iterative; hence, this method can be applied with the same simplicity of explicit methods.

From the foregoing discussion, two integration methods were selected for evaluation, namely, a modified version of the implicit Newmark method presented by Schellenberg *et al.* (2009) and the operator-splitting method developed by Nakashima *et al.* (1990), both with their corresponding versions with algorithmic damping as presented in Schellenberg *et al.* (2009). These two methods are some of the most widely used for hybrid simulation and include one with and one without iterations. Explicit integration methods were excluded from this evaluation since, as previously mentioned, they cannot be applied to the

structural systems analyzed in this study with a singular mass matrix. A brief description of the implementation of the integration methods is provided below.

### 3.2.1 Implicit Newmark Method (INM)

The implicit form of the Newmark method (Newmark, 1959), originally developed for purely numerical simulations, is the most popular integration method in structural dynamics. This section presents first this method similar to Schellenberg *et al.* (2009). The following section presents the modified version of the implicit Newmark method for hybrid simulation.

The equations of motion previously presented in Equation 3-1 can be written in residual form:

$$\mathbf{F}(\mathbf{U}_{i+1}) = \mathbf{M}\ddot{\mathbf{U}}_{i+1} + \mathbf{C}\dot{\mathbf{U}}_{i+1} + \mathbf{P_r}(\mathbf{U}_{i+1}) - \mathbf{P}_{i+1} = \mathbf{0} \tag{3-2}$$

The above system of nonlinear equations is solved using the iterative Newton-Raphson procedure:

$$\mathbf{J}(\mathbf{U}_{i+1}^{(k)})\cdot\Delta\mathbf{U}^{(k)} = -\mathbf{F}(\mathbf{U}_{i+1}^{(k)}) \tag{3-3}$$

In the above system of linear equations, $\mathbf{J}(\mathbf{U}_{i+1}^{(k)})$ is the Jacobian matrix (also known as iteration matrix) of the system of equations, $\Delta\mathbf{U}^{(k)}$ is the displacement increment vector, and $-\mathbf{F}(\mathbf{U}_{i+1}^{(k)})$ is the negative residual vector, both evaluated at iteration $k$. In structural dynamics, the Jacobian matrix and the negative residual vector are known as the effective stiffness matrix and the effective force vector (or unbalanced force vector), respectively.

$$\mathbf{K}_{\mathbf{eff}}^{(k)}\cdot\Delta\mathbf{U}^{(k)} = \mathbf{P}_{\mathbf{eff}}^{(k)} \tag{3-4}$$

The above expression can be evaluated using the equations of Newmark presented below, where $\gamma$ and $\beta$ define the variation of acceleration over a time step and determine the stability and accuracy of the integration method.

$$\mathbf{U}_{i+1} = \mathbf{U}_i + \Delta t\dot{\mathbf{U}}_i + \frac{\Delta t^2}{2}[(1-2\beta)\ddot{\mathbf{U}}_i + 2\beta\ddot{\mathbf{U}}_{i+1}] \tag{3-5}$$

$$\dot{\mathbf{U}}_{i+1} = \dot{\mathbf{U}}_i + \Delta t[(1-\gamma)\ddot{\mathbf{U}}_i + \gamma\ddot{\mathbf{U}}_{i+1}] \tag{3-6}$$

However, since the solution is advanced from time instant $i$ to time instant $i$+1 by solving for displacement increments as seen in Equation 3-4, the equations of Newmark need to be reformulated as follows:

$$\dot{\mathbf{U}}_{i+1} = \frac{\gamma}{\Delta t\,\beta}(\mathbf{U}_{i+1} - \mathbf{U}_i) - (\frac{\gamma}{\beta} - 1)\dot{\mathbf{U}}_i - \Delta t(\frac{\gamma}{2\beta} - 1)\ddot{\mathbf{U}}_i \tag{3-7}$$

$$\ddot{\mathbf{U}}_{i+1} = \frac{1}{\Delta t^2\beta}(\mathbf{U}_{i+1} - \mathbf{U}_i) - \frac{1}{\Delta t\,\beta}\dot{\mathbf{U}}_i - (\frac{1}{2\beta} - 1)\ddot{\mathbf{U}}_i \tag{3-8}$$

Expressions for the effective stiffness matrix and the effective force vector can be obtained by substituting the above Newmark equations into the residual form of the equations of motion presented in Equation 3-2.

$$\mathbf{K}_{\mathbf{eff}}^{(k)} = c_3\mathbf{M} + c_2\mathbf{C} + c_1\mathbf{K}_{\mathbf{t}}(\mathbf{U}_{i+1}^{(k)}) \tag{3-9}$$

$$\mathbf{P}_{\mathbf{eff}}^{(k)} = -\mathbf{M}\ddot{\mathbf{U}}_{i+1}^{(k)} - \mathbf{C}\dot{\mathbf{U}}_{i+1}^{(k)} - \mathbf{P}_{\mathbf{r}}(\mathbf{U}_{i+1}^{(k)}) + \mathbf{P}_{i+1} \tag{3-10}$$

where $c_1 = 1$, $c_2 = \gamma/(\Delta t\,\beta)$, and $c_3 = 1/(\Delta t^2\beta)$. The implicit Newmark integration method is a predictor-multi-corrector method. In the predictor phase, Equation 3-11 through Equation 3-13 (predictors) are used to calculate initial values of displacement, velocity and acceleration vectors to start the Newton-Raphson equilibrium iterations.

$$\mathbf{U}_{i+1}^{(k=1)} = \mathbf{U}_i \tag{3-11}$$

$$\dot{\mathbf{U}}_{i+1}^{(k=1)} = -(\frac{\gamma}{\beta} - 1)\dot{\mathbf{U}}_i - \Delta t(\frac{\gamma}{2\beta} - 1)\ddot{\mathbf{U}}_i \tag{3-12}$$

$$\ddot{\mathbf{U}}_{i+1}^{(k=1)} = -\frac{1}{\Delta t\,\beta}\dot{\mathbf{U}}_i - (\frac{1}{2\beta} - 1)\ddot{\mathbf{U}}_i \tag{3-13}$$

After Equation 3-4 is solved for the displacement increment vector, the initial (predicted) displacement, velocity and acceleration vectors are corrected subsequently using Equation 3-14 through Equation 3-16 until convergence is achieved.

$$\mathbf{U}_{i+1}^{(k+1)} = \mathbf{U}_{i+1}^{(k)} + c_1\Delta\mathbf{U}^{(k)} \tag{3-14}$$

$$\dot{\mathbf{U}}_{i+1}^{(k+1)} = \dot{\mathbf{U}}_{i+1}^{(k)} + c_2\Delta\mathbf{U}^{(k)} \tag{3-15}$$

$$\ddot{\mathbf{U}}_{i+1}^{(k+1)} = \ddot{\mathbf{U}}_{i+1}^{(k)} + c_3 \Delta \mathbf{U}^{(k)} \tag{3-16}$$

Convergence can be measured using several criteria with a list of tests provided by Schellenberg *et al.* (2009). The implicit Newmark method is stable if:

$$\frac{\Delta t}{T_n} \leq \frac{(\gamma - 0.5)\xi + \sqrt{0.5\gamma - \beta + (\gamma - 0.5)^2 \xi^2}}{(\gamma - 2\beta)\pi} \tag{3-17}$$

where $\Delta t$ is the size of the time step and $T_n$ is the shortest natural period of the structure. The method is unconditionally stable for values of $\gamma$ and $\beta$ of 0.50 and 0.25, respectively, for linear systems. The rate of convergence of the Newton-Raphson algorithm is quadratic. However, the algorithm is very expensive since it requires evaluation of the Jacobian and its inverse at each iteration step.

### 3.2.2 Modified Implicit Newmark Method for Hybrid Simulation (INM-HS)

Schellenberg *et al.* (2009) presented a version of the implicit Newmark method modified for hybrid simulation. This modified version overcomes the abovementioned problems of implicit integration methods by performing a constant number of iterations per integration step. Therefore, the iterative process is terminated after the specified number of constant iterations is completed. Consequently, the convergence test that terminates the analysis in case of non-convergence is eliminated in this approach. However, convergence criteria parameters can still be calculated to provide a measure of convergence. This approach is illustrated in Figure 3-1. As seen in the figure, the trial displacements (denoted as $\overline{\mathbf{U}}_{i+1}^{(2)}$, $\overline{\mathbf{U}}_{i+1}^{(3)}$, and $\overline{\mathbf{U}}_{i+1}^{(k+1)}$ in Figure 3-1) produced at each iteration are not directly used to update the state of the model (or to generate displacement commands to the physical sub-structure in a hybrid simulation) but instead these displacements are reduced using interpolation functions.

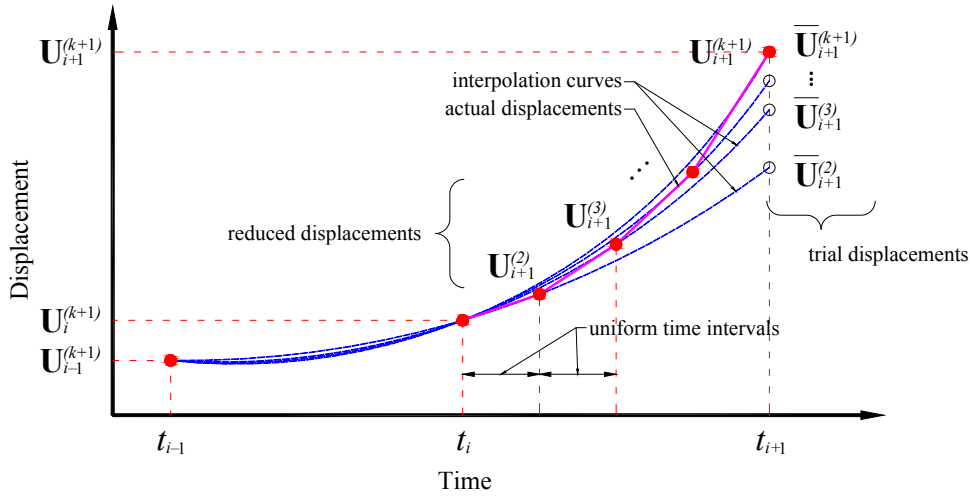


**Figure 3-1 Illustration of the modified implicit Newmark method for hybrid simulation (adapted from Zhong, 2005)**

The reduced displacements are interpolated between previous converged solutions ($\mathbf{U}_i$, $\mathbf{U}_{i-1}$, etc.) and the current trial displacement at time $i+1$ using Lagrange polynomials. Therefore, the corrector equations previously provided in Equation 3-14 through Equation 6-16 are re-written as follows:

$$\mathbf{U}_{i+1}^{(k+1)} = \mathbf{U}_{i+1}^{(k)} + c_1 \Delta \mathbf{U}_{scaled}^{(k)} \tag{3-18}$$

$$\dot{\mathbf{U}}_{i+1}^{(k+1)} = \dot{\mathbf{U}}_{i+1}^{(k)} + c_2 \Delta \mathbf{U}_{scaled}^{(k)} \tag{3-19}$$

$$\ddot{\mathbf{U}}_{i+1}^{(k+1)} = \ddot{\mathbf{U}}_{i+1}^{(k)} + c_3 \Delta \mathbf{U}_{scaled}^{(k)} \tag{3-20}$$

The scaled displacement increments shown above are calculated using the following expression provided by Schellenberg *et al.* (2009).

$$\Delta \mathbf{U}_{scaled}^{(k)}(x) = -\mathbf{U}_{i+1}^{(k-1)} + \sum_{j=i+1-n}^{i+1} \mathbf{U}_j \, L_{n,j}(x) \tag{3-21}$$

where $\mathbf{U}_{i+1}^{(k-1)}$ are the trial displacement at the previous iterations, $\mathbf{U}_j$ are the committed displacement at the previous time steps and the trial displacement of the current iteration, $L_{n,j}(x)$ are the Lagrange functions of order $n$, and $x = k/k_{max}$ is the location of the interpolation ($k_{max}$ is the maximum number of iterations performed at each integration step).

The resulting integration method produces uniform and monotonic displacements increments and therefore is compatible with hybrid simulation. More details of this integration method can be found in the original document (Schellenberg *et al.*, 2009). This approach was first introduced by Dorka and Heiland (1991) and Shing *et al.* (1991) with later refinements by Zhong (2005).

### 3.2.3 Implicit Generalized-Alpha Method for Hybrid Simulation (IGα-HS)

The family of alpha-methods refers to those integration methods that introduce high-frequency numerical dissipation to damp out spurious high-frequency response. This high-frequency algorithmic damping is a desirable characteristic of an integration method in a hybrid simulation since it damps out high-frequency response due to experimental errors. The implicit generalized-alpha method developed by Chung and Hulbert (1993) introduces this desired characteristic that is missing in the implicit Newmark method. Chung and Hulbert reported that the high-frequency numerical dissipation improves the convergence of iterative integration methods and that the overshoot phenomenon is no longer exhibited.

In this section, the presentation of Schellenberg *et al.* (2009) of the implicit generalized-alpha method with the modification for constant number of iterations is adopted here and briefly presented.

To introduce algorithmic damping, the weighted equations of motion are formulated between time steps $t_i$ and $t_{i+1}$ using the weighing parameters $\alpha_m$ and $\alpha_f$.

$$\mathbf{M}\ddot{\mathbf{U}}_{i+\alpha_m} + \mathbf{C}\dot{\mathbf{U}}_{i+\alpha_f} + \mathbf{P}_{\mathbf{r},i+\alpha_f} = \mathbf{P}_{i+\alpha_f} \tag{3-22}$$

The acceleration and velocity between time steps are written using the weighting parameters as follows:

$$\ddot{\mathbf{U}}_{i+\alpha_m} = (1-\alpha_m)\ddot{\mathbf{U}}_i + \alpha_m\ddot{\mathbf{U}}_{i+1} \tag{3-23}$$

$$\dot{\mathbf{U}}_{i+\alpha_f} = (1-\alpha_f)\dot{\mathbf{U}}_i + \alpha_f\dot{\mathbf{U}}_{i+1} \tag{3-24}$$

The internal resisting force and external force vectors are expressed using the generalized trapezoidal rule:

$$\mathbf{P}_{\mathbf{r},i+\alpha_f} = (1-\alpha_f)\mathbf{P}_{\mathbf{r}}(\mathbf{U}_i) + \alpha_f\mathbf{P}_{\mathbf{r}}(\mathbf{U}_{i+1}) \tag{3-25}$$

$$\mathbf{P}_{i+\alpha_f} = (1-\alpha_f)\mathbf{P}_i + \alpha_f\mathbf{P}_{i+1} \tag{3-26}$$

Substitution of Equation 3-23 through Equation 3-26 into the weighted equation of motion presented in Equation 3-22 yields a systems of nonlinear equations that can be written in residual form as follows:

$$\begin{aligned}\mathbf{F}(\mathbf{U}_{i+1}) = (1-\alpha_m)\mathbf{M}\ddot{\mathbf{U}}_i + \alpha_m\mathbf{M}\ddot{\mathbf{U}}_{i+1} + (1-\alpha_f)\mathbf{C}\dot{\mathbf{U}}_i + \alpha_f\mathbf{C}\dot{\mathbf{U}}_{i+1} \\ +[(1-\alpha_f)\mathbf{P_r}(\mathbf{U}_i) + \alpha_f\mathbf{P_r}(\mathbf{U}_{i+1})] - [(1-\alpha_f)\mathbf{P}_i + \alpha_f\mathbf{P}_{i+1}] = \mathbf{0}\end{aligned} \tag{3-27}$$

Similar to the implicit Newmark method (Section 3.2.1), the iterative Newton-Raphson procedure is used to solve the above system of nonlinear equations:

$$\mathbf{J}(\mathbf{U}_{i+1}^{(k)})\cdot\Delta\mathbf{U}^{(k)} = -\mathbf{F}(\mathbf{U}_{i+1}^{(k)}) \tag{3-28}$$

As mentioned earlier in Section 3.2.1, the Jacobian matrix of the system of equations $\mathbf{J}(\mathbf{U}_{i+1}^{(k)})$ and the negative residual vector $-\mathbf{F}(\mathbf{U}_{i+1}^{(k)})$ are known in structural dynamics as the effective stiffness matrix and the effective force vector (or unbalanced force vector), respectively.

$$\mathbf{K}_{\mathbf{eff}}^{(k)}\cdot\Delta\mathbf{U}^{(k)} = \mathbf{P}_{\mathbf{eff}}^{(k)} \tag{3-29}$$

Substituting the Newmark equations previously presented in Section 3.2.1, namely, Equation 3-8 and Equation 3-9, into Equation 3-27 yields expressions for the effective stiffness matrix and effective unbalanced force vector:

$$\mathbf{K}_{\mathbf{eff}}^{(k)} = \alpha_m c_3\mathbf{M} + \alpha_f c_2\mathbf{C} + \alpha_f c_1\mathbf{K_t}(\mathbf{U}_{i+1}^{(k)}) \tag{3-30}$$

$$\mathbf{P}_{\mathbf{eff}}^{(k)} = \mathbf{P}_{i+1} - \mathbf{M}[(1-\alpha_m)\ddot{\mathbf{U}}_i + \alpha_m\ddot{\mathbf{U}}_{i+1}] - \mathbf{C}[(1-\alpha_f)\dot{\mathbf{U}}_i + \alpha_f\dot{\mathbf{U}}_{i+1}] - \mathbf{P}_{\mathbf{r},i+\alpha_f}(\mathbf{U}_{i+1}^{(k)}) \tag{3-31}$$

where $c_1 = 1$, $c_2 = \gamma/(\Delta t\,\beta)$, and $c_3 = 1/(\Delta t^2\beta)$. This predictor-multi-corrector method uses Equation 3-32 through Equation 3-34 to calculate the initial values of the displacement, velocity and acceleration vectors in the prediction phase.

$$\mathbf{U}_{i+1}^{(k=1)} = \mathbf{U}_i \tag{3-32}$$

$$\dot{\mathbf{U}}_{i+1}^{(k=1)} = -(\frac{\gamma}{\beta} - 1)\dot{\mathbf{U}}_i - \Delta t(\frac{\gamma}{2\beta} - 1)\ddot{\mathbf{U}}_i \tag{3-33}$$

$$\ddot{\mathbf{U}}_{i+1}^{(k=1)} = -\frac{1}{\Delta t\,\beta}\dot{\mathbf{U}}_i - (\frac{1}{2\beta} - 1)\ddot{\mathbf{U}}_i \tag{3-34}$$

After solving Equation 3-28 for the displacement increments, such increments are scaled using Equation 3-21 previously presented in Section 3.2.2 and the correctors are written as follows:

$$\mathbf{U}_{i+1}^{(k+1)} = \mathbf{U}_{i+1}^{(k)} + c_1 \Delta \mathbf{U}_{scaled}^{(k)} \tag{3-35}$$

$$\dot{\mathbf{U}}_{i+1}^{(k+1)} = \dot{\mathbf{U}}_{i+1}^{(k)} + c_2 \Delta \mathbf{U}_{scaled}^{(k)} \tag{3-36}$$

$$\ddot{\mathbf{U}}_{i+1}^{(k+1)} = \ddot{\mathbf{U}}_{i+1}^{(k)} + c_3 \Delta \mathbf{U}_{scaled}^{(k)} \tag{3-36}$$

The iterations are repeated until the specified fixed number of iterations is reached. This generalized alpha method controls the amount of algorithmic damping with one parameter ($\rho$). Chung and Hulbert (1993) derived the following relationship to maximize high-frequency dissipation:

$$\alpha_m = \frac{2-\rho}{1+\rho} \in [2.0,\ 0.5] \tag{3-38}$$

$$\alpha_f = \frac{1}{1+\rho} \in [1.0,\ 0.5] \tag{3-39}$$

$$\beta = \frac{1}{(1+\rho)^2} \in [1.0,\ 0.25] \tag{3-40}$$

$$\gamma = 0.5 + \alpha_m - \alpha_f \in [1.5,\ 0.5] \tag{3-41}$$

### 3.2.4 Operator-Splitting Method (OS)

The operator-splitting method presented by Nakashima *et al.* (1990) comprises 2 phases, namely, a predictor and a corrector phase. In the predictor phase, the Newmark equations (Equation 3-42 and Equation 3-43) are used to predict the displacements ($\widetilde{\mathbf{U}}_{i+1}$) and velocities ($\widetilde{\dot{\mathbf{U}}}_{i+1}$) at time step $i$+1 using the displacements, velocities and acceleration at the previous time step ($\mathbf{U}_i$, $\dot{\mathbf{U}}_i$, $\ddot{\mathbf{U}}_i$).

$$\mathbf{U}_{i+1} = \mathbf{U}_i + \Delta t\dot{\mathbf{U}}_i + \frac{\Delta t^2}{2}(1-2\beta)\ddot{\mathbf{U}}_i + \Delta t^2\beta\ddot{\mathbf{U}}_{i+1} = \widetilde{\mathbf{U}}_{i+1} + \Delta t^2\beta\ddot{\mathbf{U}}_{i+1} \tag{3-42}$$

$$\dot{\mathbf{U}}_{i+1} = \dot{\mathbf{U}}_i + \Delta t(1-\gamma)\ddot{\mathbf{U}}_i + \Delta t\gamma\ddot{\mathbf{U}}_{i+1} = \widetilde{\dot{\mathbf{U}}}_{i+1} + \Delta t\gamma\ddot{\mathbf{U}}_{i+1} \tag{3-43}$$

In the operator-splitting method, the vector of internal resisting forces at time step $i$+1 is approximated as follows:

$$\mathbf{P_r}(\mathbf{U}_{i+1}) \cong \mathbf{K_i}\mathbf{U}_{i+1} - \mathbf{K_i}\widetilde{\mathbf{U}}_{i+1} + \mathbf{P_r}(\widetilde{\mathbf{U}}_{i+1}) \tag{3-44}$$

This approximation is based on the assumption that the difference between the elastic and nonlinear forces at the predictor displacements $\widetilde{\mathbf{U}}_{i+1}$ is approximately equal to the difference between the elastic and the nonlinear resisting forces at the new displacements $\mathbf{U}_{i+1}$ as illustrated in Figure 3-2.

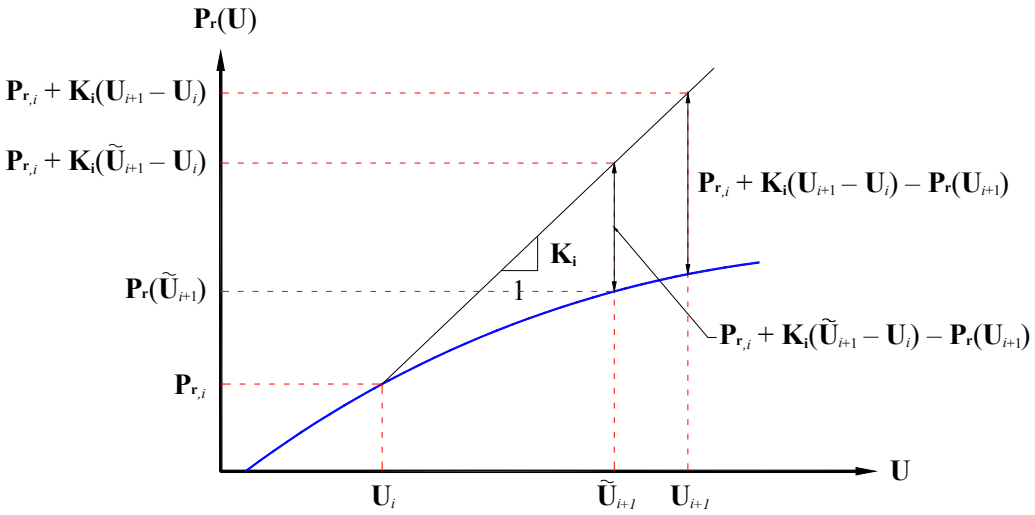


**Figure 3-2 Approximation of nonlinear resisting forces in OS method (after Schellenberg *et al.*, 2009)**

Substituting the predictor equations (Equation 3-42 and Equation 3-43) and Equation 3-44 of the approximate internal resisting force vector into the equation of motion (Equation 3-1) yields:

$$\mathbf{K_{eff}} \cdot \Delta\mathbf{U} = \mathbf{P_{eff}} \tag{3-45}$$

In the previous equation, $\Delta\mathbf{U}$ is the displacement increment vector between the predicted and new displacements. The effective stiffness matrix and the effective force vector are given by the following expressions:

$$\mathbf{K_{eff}} = c_3\mathbf{M} + c_2\mathbf{C} + c_1\mathbf{K_1} \tag{3-46}$$

$$\mathbf{P_{eff}} = \mathbf{P}_{i+1} - \mathbf{C}\widetilde{\mathbf{U}}_{i+1} - \mathbf{P_r}(\widetilde{\mathbf{U}}_{i+1}) \tag{3-47}$$

where $c_1 = 1$, $c_2 = \gamma/(\Delta t\,\beta)$, and $c_3 = 1/(\Delta t^2\beta)$. Once Equation 3-45 is solved for the displacement increment vector, the response quantities such as displacements, velocities and accelerations are corrected with Equation 3-48 through Equation 3-50:

$$\mathbf{U}_{i+1} = \tilde{\mathbf{U}}_{i+1} + c_1\Delta\mathbf{U} \tag{3-48}$$

$$\dot{\mathbf{U}}_{i+1} = \tilde{\dot{\mathbf{U}}}_{i+1} + c_2\Delta\mathbf{U} \tag{3-49}$$

$$\ddot{\mathbf{U}}_{i+1} = c_3\Delta\mathbf{U} \tag{3-50}$$

The operator-splitting integration method presents many advantages from a hybrid simulation point of view. Given that the method is a predictor-one-corrector, only one force acquisition from the physical sub-structure is necessary per integration step. The OS method was originally developed by Nakashima *et al.* (1990) using the initial stiffness matrix throughout the full length of the simulation. This represents an advantage since the tangent stiffness matrix of the physical sub-structure is not typically available in a hybrid simulation.

### 3.2.5 Generalized Alpha-OS Method (Gα-OS)

Schellenberg *et al.* (2009) presented the generalized alpha-OS integration method that is a combination of the operator-splitting method presented in the previous section and the generalized alpha methods developed by Chung and Hulbert (1993).

Similar to the implicit generalized alpha method, the derivation of the method starts by writing the weighting equations of motion that are repeated here for convenience.

$$\mathbf{M}\ddot{\mathbf{U}}_{i+\alpha_m} + \mathbf{C}\dot{\mathbf{U}}_{i+\alpha_f} + \mathbf{P}_{\mathbf{r},i+\alpha_f} = \mathbf{P}_{i+\alpha_f} \tag{3-51}$$

$$\mathbf{U}_{i+1} = \mathbf{U}_i + \Delta t\dot{\mathbf{U}}_i + \frac{\Delta t^2}{2}(1-2\beta)\ddot{\mathbf{U}}_i + \Delta t^2\beta\ddot{\mathbf{U}}_{i+1} = \tilde{\mathbf{U}}_{i+1} + \Delta t^2\beta\ddot{\mathbf{U}}_{i+1} \tag{3-52}$$

$$\dot{\mathbf{U}}_{i+1} = \dot{\mathbf{U}}_i + \Delta t(1-\gamma)\ddot{\mathbf{U}}_i + \Delta t\gamma\ddot{\mathbf{U}}_{i+1} = \tilde{\dot{\mathbf{U}}}_{i+1} + \Delta t\gamma\ddot{\mathbf{U}}_{i+1} \tag{3-53}$$

The nonlinear internal resisting force vector on the left hand side of the equation is approximated as follows:

$$\mathbf{P}_{\mathbf{r},i+\alpha_f} \cong \mathbf{K_i}\mathbf{U}_{i+\alpha_f} - (\mathbf{K_i}\tilde{\mathbf{U}}_{i+\alpha_f} - \tilde{\mathbf{P}}_{\mathbf{r},i+\alpha_f}) \tag{3-54}$$

Substituting the approximate resisting force vector given by Equation 3-54 into the weighted equation of motion in Equation 3-51 yields the following equation:

$$\mathbf{M}\ddot{\mathbf{U}}_{i+\alpha_m} + \mathbf{C}\dot{\mathbf{U}}_{i+\alpha_f} + \mathbf{K_i}(\mathbf{U}_{i+\alpha_f} - \widetilde{\mathbf{U}}_{i+\alpha_f}) + \widetilde{\mathbf{P}}_{\mathbf{r},i+\alpha_f} = \mathbf{P}_{i+\alpha_f} \tag{3-55}$$

In the above equation, the acceleration, velocities, and displacement in between time steps are expressed by the following weighted equations:

$$\ddot{\mathbf{U}}_{i+\alpha_m} = (1-\alpha_m)\ddot{\mathbf{U}}_i + \alpha_m\ddot{\mathbf{U}}_{i+1} \tag{3-56}$$

$$\dot{\mathbf{U}}_{i+\alpha_f} = (1-\alpha_f)\dot{\mathbf{U}}_i + \alpha_f\dot{\mathbf{U}}_{i+1} \tag{3-57}$$

$$\mathbf{U}_{i+\alpha_f} = (1-\alpha_f)\mathbf{U}_i + \alpha_f\mathbf{U}_{i+1} \tag{3-58}$$

$$\widetilde{\mathbf{U}}_{i+\alpha_f} = (1-\alpha_f)\widetilde{\mathbf{U}}_i + \alpha_f\widetilde{\mathbf{U}}_{i+1} \tag{3-59}$$

Similar to the implicit generalized alpha method previously presented, the resisting forces at the predictor displacements and the external forces are expressed as follows:

$$\widetilde{\mathbf{P}}_{\mathbf{r},i+\alpha_f} = (1-\alpha_f)\mathbf{P_r}(\widetilde{\mathbf{U}}_i) + \alpha_f\,\mathbf{P_r}(\widetilde{\mathbf{U}}_{i+1}) \tag{3-60}$$

$$\mathbf{P}_{i+\alpha_f} = (1-\alpha_f)\mathbf{P}_i + \alpha_f\,\mathbf{P}_{i+1} \tag{3-61}$$

The velocities and accelerations at $t_{i+1}$ are expressed in terms of the predictor displacement.

$$\dot{\mathbf{U}}_{i+1} = \frac{\gamma}{\Delta t\,\beta}(\mathbf{U}_{i+1} - \widetilde{\mathbf{U}}_{i+1}) + \dot{\mathbf{U}}_1 + \Delta t(1-\gamma)\ddot{\mathbf{U}}_i \tag{3-62}$$

$$\ddot{\mathbf{U}}_{i+1} = \frac{1}{\Delta t^2\beta}(\mathbf{U}_{i+1} - \widetilde{\mathbf{U}}_{i+1}) \tag{3-63}$$

The substituting of Equation 3-62 and Equation 3-63 into Equation 3-55 produces the system of linear equations that need to be solved for the displacement increments between the predicted and new displacements:

$$\mathbf{K_{eff}}\cdot\Delta\mathbf{U} = \mathbf{P_{eff}} \tag{3-64}$$

In the above system of equations, the effective stiffness matrix and the effective force vector take the following form:

$$\mathbf{K_{eff}} = \alpha_m c_3 \mathbf{M} + \alpha_f c_2 \mathbf{C} + \alpha_f c_1 \mathbf{K_i} \tag{3-65}$$

$$\begin{aligned}\mathbf{P_{eff}} = \mathbf{P}_{i+\alpha_f} - \mathbf{M}(1-\alpha_m)\ddot{\mathbf{U}}_i - \mathbf{C}[(1-\alpha_f)\dot{\mathbf{U}}_i + \alpha_f \widetilde{\dot{\mathbf{U}}}_{i+1}] \\ -[\widetilde{\mathbf{P}}_{\mathbf{r},i+\alpha_f} + \mathbf{K_i}(1-\alpha_f)(\mathbf{U}_i - \widetilde{\mathbf{U}}_i)]\end{aligned} \tag{3-66}$$

where $c_1 = 1$, $c_2 = \gamma/(\Delta t\,\beta)$, and $c_3 = 1/(\Delta t^2 \beta)$. Once Equation 3-64 is solved for the displacement increments, the response quantities such as displacements, velocities and accelerations are corrected with Equation 3-67 through Equation 3-69:

$$\mathbf{U}_{i+1} = \widetilde{\mathbf{U}}_{i+1} + c_1 \Delta \mathbf{U} \tag{3-67}$$

$$\dot{\mathbf{U}}_{i+1} = \widetilde{\dot{\mathbf{U}}}_{i+1} + c_2 \Delta \mathbf{U} \tag{3-68}$$

$$\ddot{\mathbf{U}}_{i+1} = c_3 \Delta \mathbf{U} \tag{3-69}$$

Similar to the implicit generalized alpha method, the generalized alpha OS method adjusts the amount of algorithmic damping with one parameter ($\rho$) using Equation 3-38 through Equation 3-41.

## 3.3 Case Study I: Numerical Evaluation of Integration Methods

The accuracy and stability properties of the integration methods described in Section 3.2 are numerically evaluated in this section by means of energy balance calculations. To this end, a numerical model of the two-dimensional (2D) steel moment-resisting frame shown in Figure 3-3(a) was developed in Matlab (MathWorks, 2011) where the different integration methods and energy balance calculations were implemented. A concentrated plasticity approach was adopted to model the inelastic response of the 2D frame. The beams and columns of the 2D frame consisted of two nonlinear rotational spring elements attached at the ends of a linear elastic frame element. The smooth hysteretic model developed by Sivaselvan and Reinhorn (2000) and shown in Figure 3-3(b) was assigned to the nonlinear rotational spring elements to reproduce the cyclic response of the plastic hinges. The centerline model of the frame structure does not account for joint deformation. Geometric nonlinearities were included in the model using a simplified P-Delta formulation. Rayleigh damping was used with a damping ratio of 0.5% anchored at the first two natural frequencies. Rigid diaphragms were assigned to all three story levels. All columns are axially rigid. The hysteretic model assigned to the rotational spring elements did not account

for axial force and bending moment (P-M) interaction. The first three natural periods of vibration of the 2D frame model are 0.85, 0.30, and 0.15 sec., respectively.

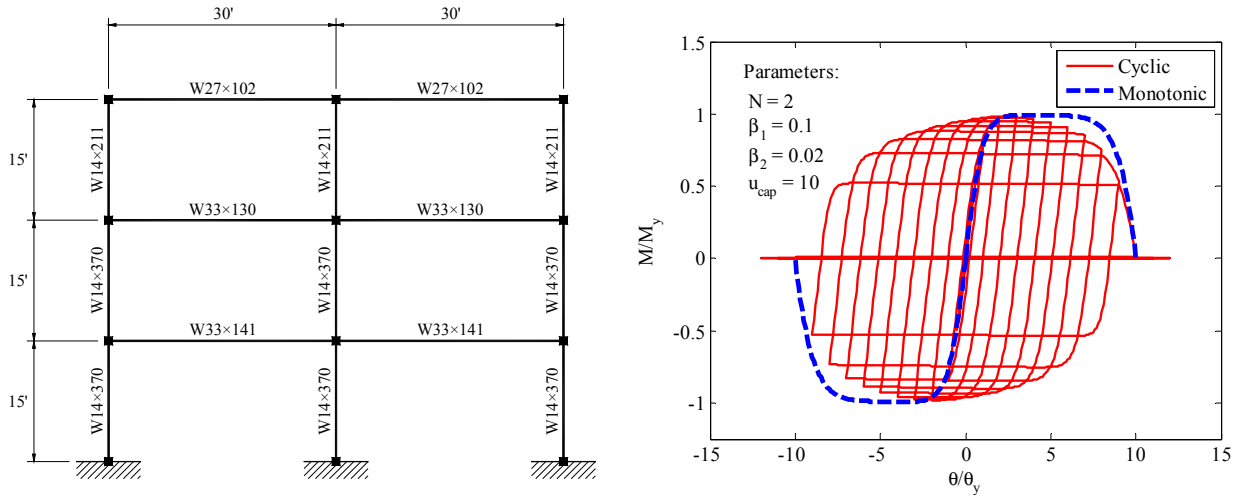


(a) 2D frame structure

(b) Sivaselvan-Reinhorn smooth hysteretic model

**Figure 3-3 Numerical model of the 2D frame structure and smooth hysteretic model**

The numerical model of the 2D frame was subjected to the Canoga Park earthquake record scaled by a factor 3.0 to produce a highly nonlinear response of the structure and consequently challenge the performance of the integration methods. Figure 3-4 shows an example of the level of inelastic response experienced by two plastic hinges at a girder located at the first story.

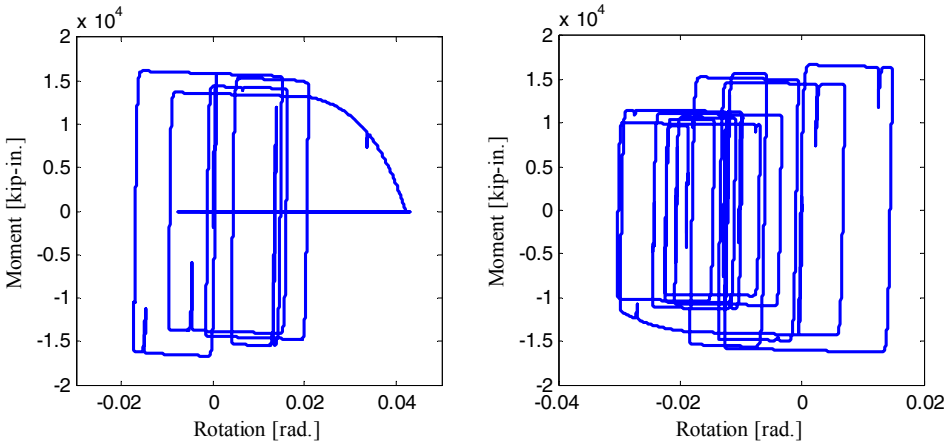


(a) Exterior Beam Plastic Hinge at First-Story Girder

(b) Interior Beam Plastic Hinge at First-Story Girder

**Figure 3-4 Moment-rotation relationships for two plastic hinges at a girder at the first story**

Figure 3-5 presents the response of the 2D frame obtained using the integration methods described in Section 3.2, namely, the implicit Newmark method (INM), the modified implicit Newmark method for hybrid simulation (INM-HS), the implicit generalized-alpha method for hybrid simulation (IGα-HS), the operator-splitting method (OS), and the generalized-alpha operator-splitting method (Gα-OS).

Each plot presented in Figure 3-5 corresponds to an integration method using various time steps. The term roof drift ratio in Figure 3-5 is defined as the lateral displacement of the building roof divided by the height of the building. The results produced by the INM method, although not an integration method used in hybrid simulation, were included in Figure 3-5 as the reference solution. Ten iterations per integration step were used for the iterative INM-HS and IGα-HS methods and a value of $\rho$ of 0.90 was used in the IGα-HS and Gα-OS methods with algorithmic damping.

It can be observed in the close-up views provided in Figure 3-5 that the five integration methods converge to the same solution as the size of the time step decreases. However, the results produced by the OS and Gα-OS methods clearly diverge from the converged solution for the two largest time steps used, namely, 0.005 and 0.010 sec. This can be also observed in Figure 3-6 where peak roof drift errors are presented for all the simulation cases presented in Figure 3-5. The results produced by the INM method with a time step of 0.001 sec. and a very stringent tolerance for the convergence test were used as the assumed exact solution for the peak roof drift error calculations. The superior accuracy of the iterative INM-HS and IGα-HS methods over the OS and Gα-OS methods is evidenced in Figure 3-6.

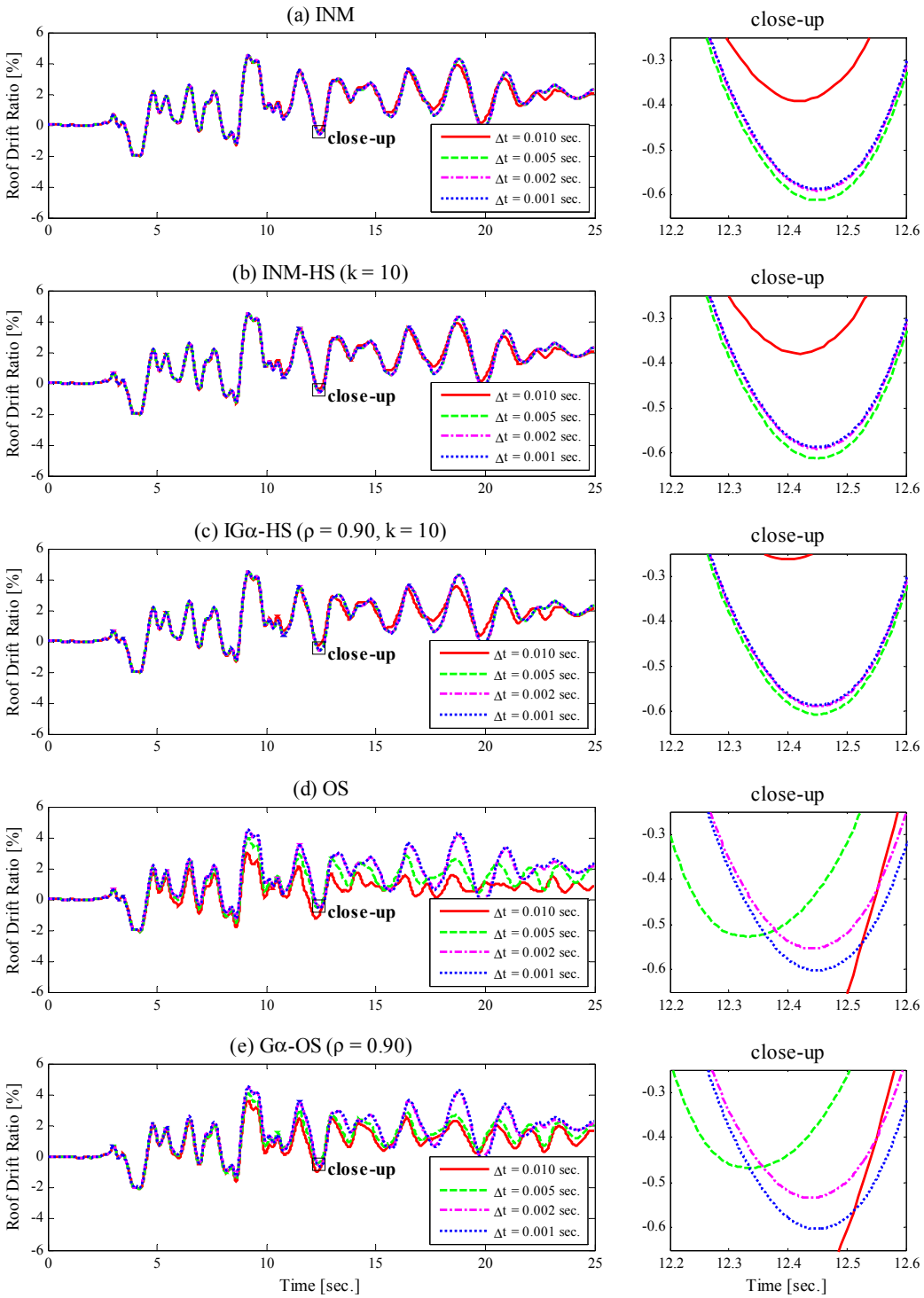


**Figure 3-5 Global results of the 2D frame using various direct integration methods**

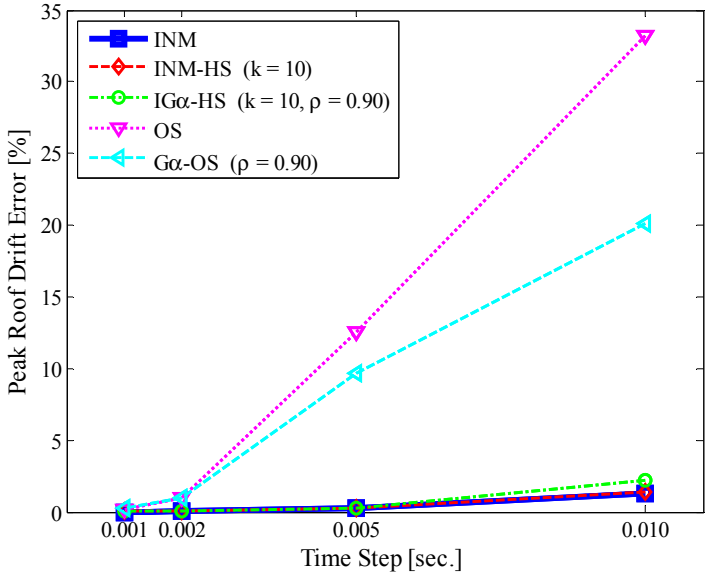


**Figure 3-6 Peak roof drift error for direct integration methods**

A more rational measure of the accuracy of the results is provided by means of energy balance calculations (Filiatrault *et al.*, 1992). The energy balance error (EBE), defined as the absolute difference between the input energy and the internal energy of the system (kinetic energy, viscous damping energy, and hysteretic energy) normalized by the input energy, was calculated for each simulation case previously presented in Figure 3-5. Maximum energy balance errors are plotted in logarithmic scale in Figure 3-7 for all integration methods except for the INM method since it presents negligible energy balance errors in the order of $1.0\times10^{-12}$ and it is not an integration method used in hybrid simulation. Some observations are made from the results presented in Figure 3-7. As expected, the accuracy of all the integration methods, as measured by the energy balance error, improves as the size of the time step decreases. However, the iterative INM-HS and IGα-HS methods (predictor-multi-corrector methods) provide significantly smaller energy balance errors than the OS and Gα-OS methods (predictor-one-corrector methods). This superior accuracy can be explained by the fact that while the internal resisting force vector is updated a constant number of times per integration step in the iterative INM-HS and IGα-HS methods, this is updated only once per integration step in the OS and Gα-OS methods. Therefore, a more fair comparison of the integration methods requires comparing, for instance, the INM-HS method with a time step of 0.010 sec. and 10 constant iterations versus the OS method with a time step of 0.001 sec., where both cases present the same number of internal resisting force vector updates. In this comparison, the INM-HS method presents lower values of energy balance error than the OS method indicating that the INM-HS method is more accurate than the OS method for the same number of model state updates.

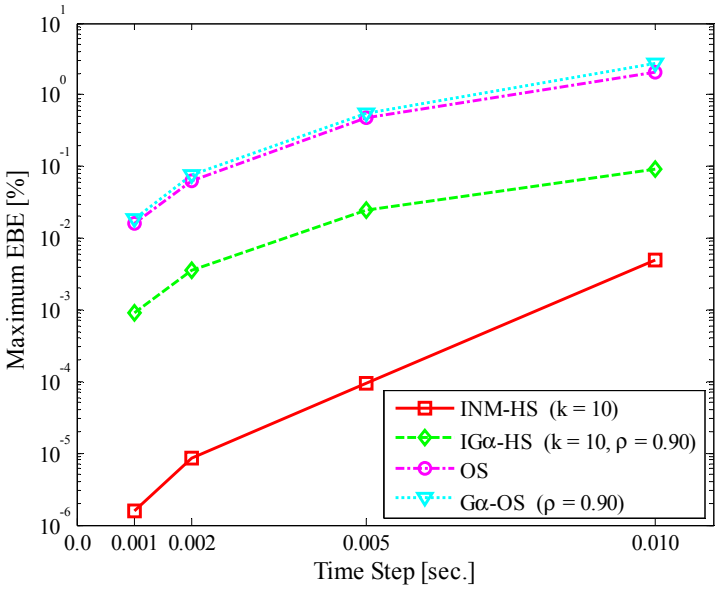


**Figure 3-7 Energy balance error for direct integration methods**

The effects of algorithmic damping on the accuracy of the integration methods can be observed by comparing the energy balance errors of the INM-HS and OS methods, methods without algorithmic damping, versus those of their corresponding integration methods with algorithmic damping, namely, the IGα-HS and Gα-OS methods, respectively. This comparison indicates that while the use of algorithmic damping in the Gα-OS method mildly increases the energy balance errors, significant increments are observed in the IGα-HS method. These observations on the accuracy of the integration methods using energy balance calculations are consistent with those obtained by visual inspection of the global response of the 2D frame presented in Figure 3-5.

To further assess the accuracy of the INM-HS method for different combinations of time steps and number of iterations, Figure 3-8 shows first the number of iterations per integration step required for convergence (using a tolerance value of $1.0\times10^{-8}$ for the "norm of unbalanced force vector" convergence test) by the original implicit Newmark method (INM) in two simulations with different time steps. It can be seen that the average number of Newton-Raphson iterations oscillate approximately around 4 or 5 per integration step and the number of iterations are well under 10 for most integration steps. This suggests that practically 10 iterations are required at most. Similar observations were made by Zhong (2005) using a similar version of the INM-HS method.

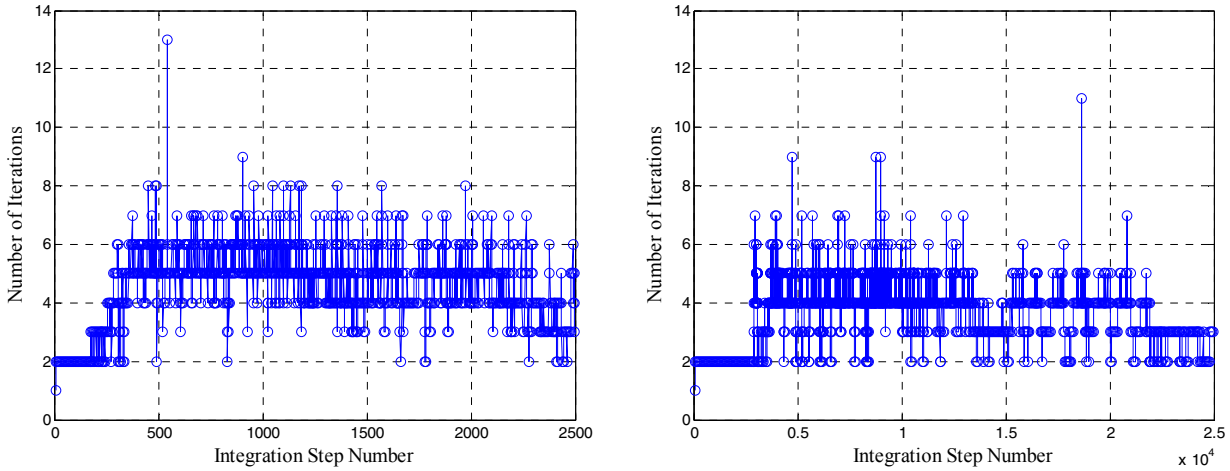


(a) INM ($\Delta t = 0.010$ sec.) (b) INM ($\Delta t = 0.001$ sec.)

**Figure 3-8 Number of iterations per integration step using the INM method**

Figure 3-9 presents peak energy balance errors for several simulation cases using the INM-HS method with different combinations of time steps (0.010, 0.005, 0.002, and 0.001 sec.) and number of iterations (10, 8, 6 and 4 iterations). Figure 3-9(a) presents the energy balance errors versus the number of iterations; however, as mentioned earlier, a more fair comparison requires presenting the energy balance error versus the ratio of time step to number of iterations shown in Figure 3-9(b). The energy balance errors are presented in logarithmic scale in both plots.

It can be seen in Figure 3-9(a) that, as expected, the accuracy of the INM-HS method, as measured by the energy balance error, increases as the size of time step decreases and the number of iterations increases. Also Figure 3-9(b) shows that when comparing simulations presenting the same time step to number of iterations ratio, the simulation with smaller time steps is more accurate in all cases. This suggests that the accuracy of the INM-HS method is more sensitive to the time step than to the number of iterations.

Another important aspect associated with integration methods for hybrid simulation is the computational time they require to execute a simulation. Figure 3-10 presents execution times of the different integration methods presented in Figure 3-5. As seen in the figure, the OS and Gα-OS methods require significantly less execution time than the iterative INM-HS and IGα-HS methods. This is due to the fact that the OS methods, unlike iterative methods, do not require the effective stiffness matrix be inverted at every integration step. Figure 3-10 shows that the execution time increases exponentially as the time step decreases.

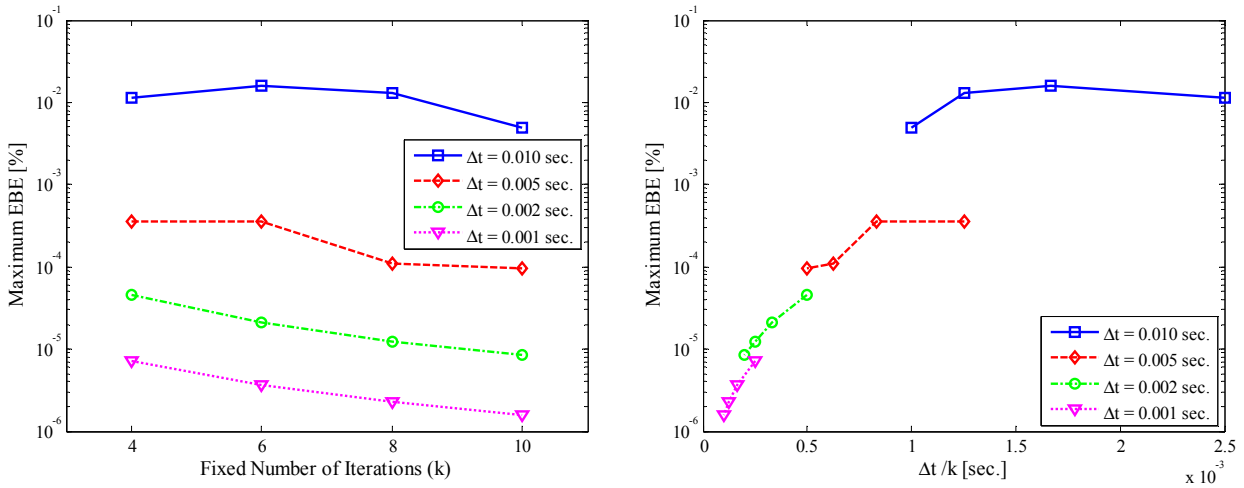


(a) Maximum EBE versus number of iteration (k)

(b) Maximum energy balance error vs $\Delta t/k$ ratio

**Figure 3-9 Maximum energy balance error for the INM-HS integration method**

While some of the integration methods evaluated in this section are more accurate than others for the 2D frame, none of them became unstable nor presented spurious high-frequency oscillations for the range of time steps used in the simulations where the smallest time step size used (0.010 sec.) was limited to the resolution of the ground motion record. However, for larger and more complex structural systems, such as the ones analyzed in subsequent sections, instability problems were frequently encountered.

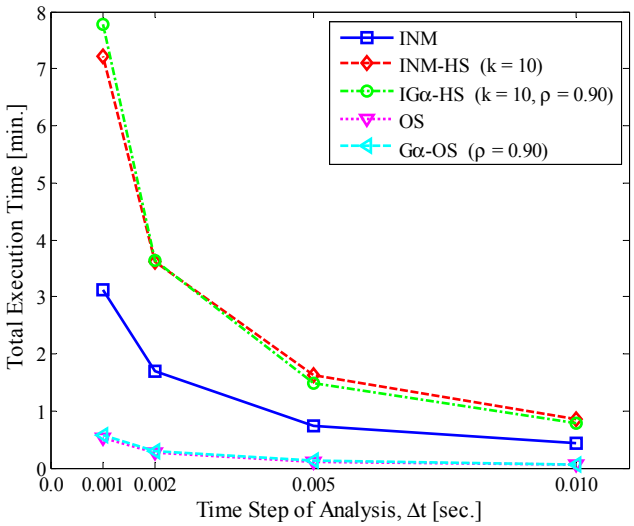


**Figure 3-10 Total execution time for direct integration methods**

The observations made in this section about the accuracy of the integration methods, where the 2D frame was subjected to the Canoga park record scaled by a factor of 3.0 resulting in a highly nonlinear response of the 2D frame, are similar to those obtained with a scale factor of 4.10 that produced sidesway collapse of the 2D frame. However, the accuracy of the integration methods improved significantly for lesser intensities of loading using ground motion scale factors less than 3.0.

### 3.3.1 Summary and Conclusions

The accuracy and stability properties of four integration methods for hybrid simulation, namely, INM-HS, IGα-HS, OS, and Gα-OS, were numerically evaluated using a 2D frame structure. Energy balance errors were computed as a measure of the accuracy of the results produced by these integration methods. The conclusions drawn and presented below are strictly valid for the model of 2D frame structure.

- The iterative INM-HS and IGα-HS methods are more accurate than the OS and Gα-OS methods as indicated by energy balance errors. However, these iterative methods are more expensive computationally than the OS and Gα-OS methods.
- The accuracy of the INM-HS method is more sensitive to the size of the time step than to the number of constant iterations. This was concluded by comparing simulations with different combinations of time step and number of constant iterations but presenting the same ratio of time step to number of iterations. In this comparison, the simulations with smaller time steps always yielded more accurate results.
- As expected, the use of algorithmic damping increased energy balance errors; however, these increments were more pronounced in the iterative IGα-HS method than in the Gα-OS method.

## 3.4 Case Study II: Experimental Evaluation of Integration Methods

In this case study, the results of twelve hybrid simulations, conducted in the single degree of freedom (SDOF) experimental test setup at the Structural and Earthquake Engineering Simulation Laboratory (SEESL) at University at Buffalo, were used to evaluate the performance of the integration methods described in Section 3.2. The hybrid simulations were conducted utilizing the Open Source Framework for Experimental Setup and Control (OpenFresco) and the Open System for Earthquake Engineering Simulation (OpenSees). Numerical simulations are presented at the end of this section to supplement the experimental evaluation.

### 3.4.1 Hybrid Model

The 2D frame structure previously presented in Section 3.3 served as the prototype structure for the hybrid simulations presented in this section. The selected numerical and physical sub-structures are indicated in Figure 3-11. A hinge was assumed at the top of the first-story column on the right to facilitate substructuring of the 2D frame.

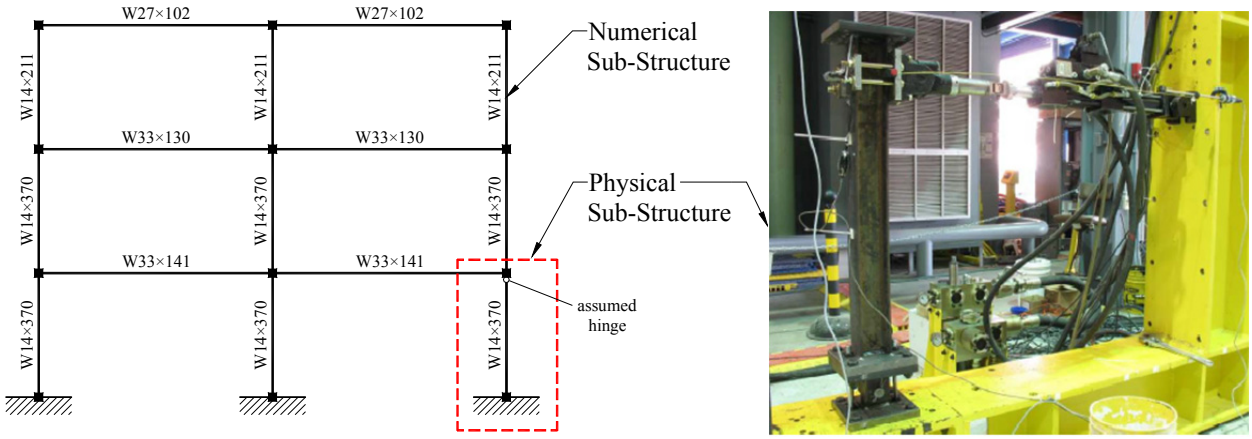


**Figure 3-11 Numerical and physical sub-structures of frame structure used in Case Study I**

The physical sub-structure consists of a steel column connected to a horizontal actuator at the top and to a clevis connection at the bottom where sacrificial steel coupons are inserted, providing repeatable low-cost nonlinear hybrid simulations. While the steel column remained elastic during the tests, the steel coupons in the clevis were designed to yield and provide different types of hysteretic response. A stable ductile hysteretic response was obtained using a pair of steel coupons with a circular cross section 1/2 in. in diameter. The steel column with this clevis connection is referred to as the ductile physical sub-structure. A second type of hysteretic response that exhibits a sudden drop of strength and stiffness was developed using the same pair of coupons, but one of them was notched 2.0 mm. all around to induce fracture of the coupon. The steel column with this clevis connection, referred to as the brittle physical sub-structure, exhibits a highly nonlinear response that could potentially challenge the ability of the numerical integration methods to produce accurate and reliable results. This hysteretic response is typically observed in fractured connections, such as the pre-Northridge beam-column connections.

The numerical sub-structure shown in Figure 3-11 was modeled in OpenSees. Similar to the Matlab model of the 2D frame described in Section 3.3, the inelastic response of the numerical sub-structure was concentrated at rotational spring elements (zero-length elements) attached at the ends of elastic beam-

column elements. The hysteretic model developed by Ibarra *et al.* (2005) and modified by Lignos and Krawinkler (2011, 2012) was assigned to the rotational spring elements. Gravity loads were applied on a leaning column to account for P-Delta effects. Panel zones were not modeled. Rayleigh damping was assigned to the model using a 2.0% damping coefficient anchored at the first two natural frequencies. Geometric nonlinearities were included using the P-Delta transformation option in OpenSees.

### 3.4.2 Coupled Simulations

Prior to conducting the hybrid simulations using the physical sub-structures assembled in the laboratory, coupled simulations were performed to verify the adequacy of data exchange between the numerical and physical sub-structures and to assist in the selection of the time steps and other relevant parameters used by the integration methods in the hybrid simulations.

In the coupled simulations presented here, the two sub-structures shown in Figure 3-11 were modeled in two separate OpenSees scripts called the master and slave scripts as illustrated in Figure 3-12. As seen in the figure, OpenFresco is the middleware that connects these two sub-structures (or more sub-structures) via interface degrees-of-freedom. The master OpenSees script models part of the structure and solves the equations of motion of the full system. At every integration step during an analysis, the master OpenSees script sends a vector of displacements to the slave OpenSees script (similar to the displacement command in a hybrid test) through OpenFresco. The slave OpenSees script imposes these displacement boundary conditions using a penalty-based algorithm and returns a vector of internal resisting forces to the master OpenSees script (similar to the force feedback in a hybrid test). This communication is given through the use of a generic super element in the master OpenSees script and an adapter element in the slave OpenSees script. More details about the theory of coupling of finite element software using OpenFresco can be found in Schellenberg *et al.* (2008).

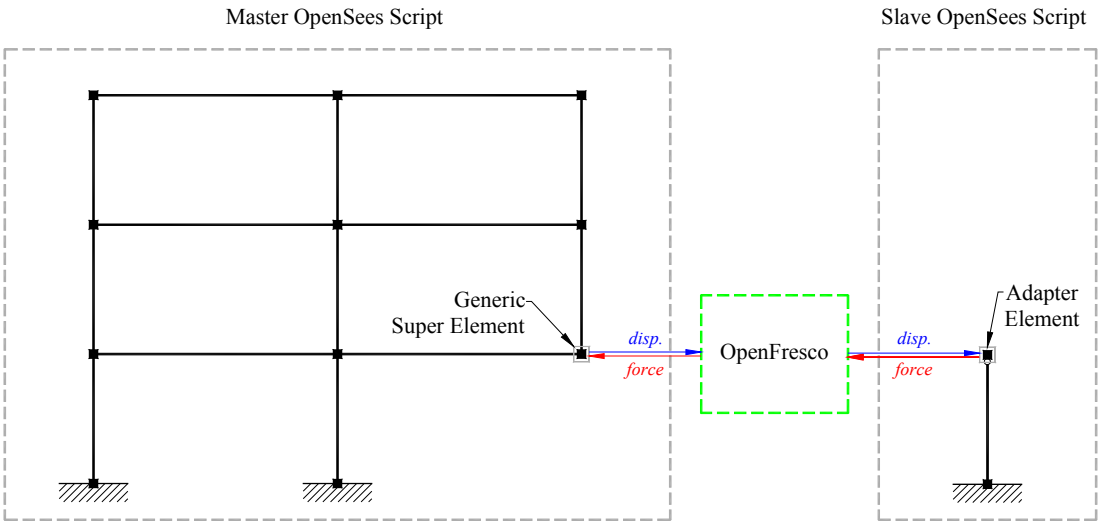


**Figure 3-12 Master and slave OpenSees scripts of the 2D frame**

The horizontal force-displacement response at the top of the column in the slave OpenSees script was modeled using the Bouc-Wen hysteretic model (Bouc 1967; Wen 1976) calibrated with data from cyclic experiments conducted on the ductile physical sub-structure prior to the hybrid simulations. The Bouc-Wen model reproduces very closely the cyclic response of the ductile physical sub-structure. The vertical DOF at the interface node in the master OpenSees script was restrained to prevent any unrealistic response as a result of the column removal for substructuring purposes.

The 2D frame model was subjected to the Canoga Park earthquake record scaled by a factor of 5.0 to induce sidesway collapse. The coupled simulations were stopped when a 15% inter-story drift was exceeded at any story. Figure 3-13 presents global response results, namely, relative roof displacement, velocity and acceleration of a conventional complete simulation (simulation using one single OpenSees script) and two coupled simulations using different integration methods used in hybrid simulation, namely, the INM-HS method presented in Section 3.2.2 with a time step of 0.002 sec. and 10 iterations per integration step and the Gα-OS method described in Section 3.2.3 with a time step of 0.001 sec. and a spectral radius ($\rho$) of 1.0, therefore, no algorithmic damping was included. The integration methods used in the coupled simulations utilized the initial stiffness matrix of the sub-structure modeled in the slave OpenSees script (similar to a hybrid test where the tangent stiffness matrix of the physical sub-structure is typically not available). The complete simulation, included for reference and assumed as the exact solution, was obtained using the INM method for purely numerical simulations with a very small time step and a stringent tolerance for the relative energy convergence test. It can be seen in Figure 3-13 that

the response of the two coupled simulations are in excellent agreement with the results of the complete simulation. This validates the correctness of the coupled simulations of the 2D frame.

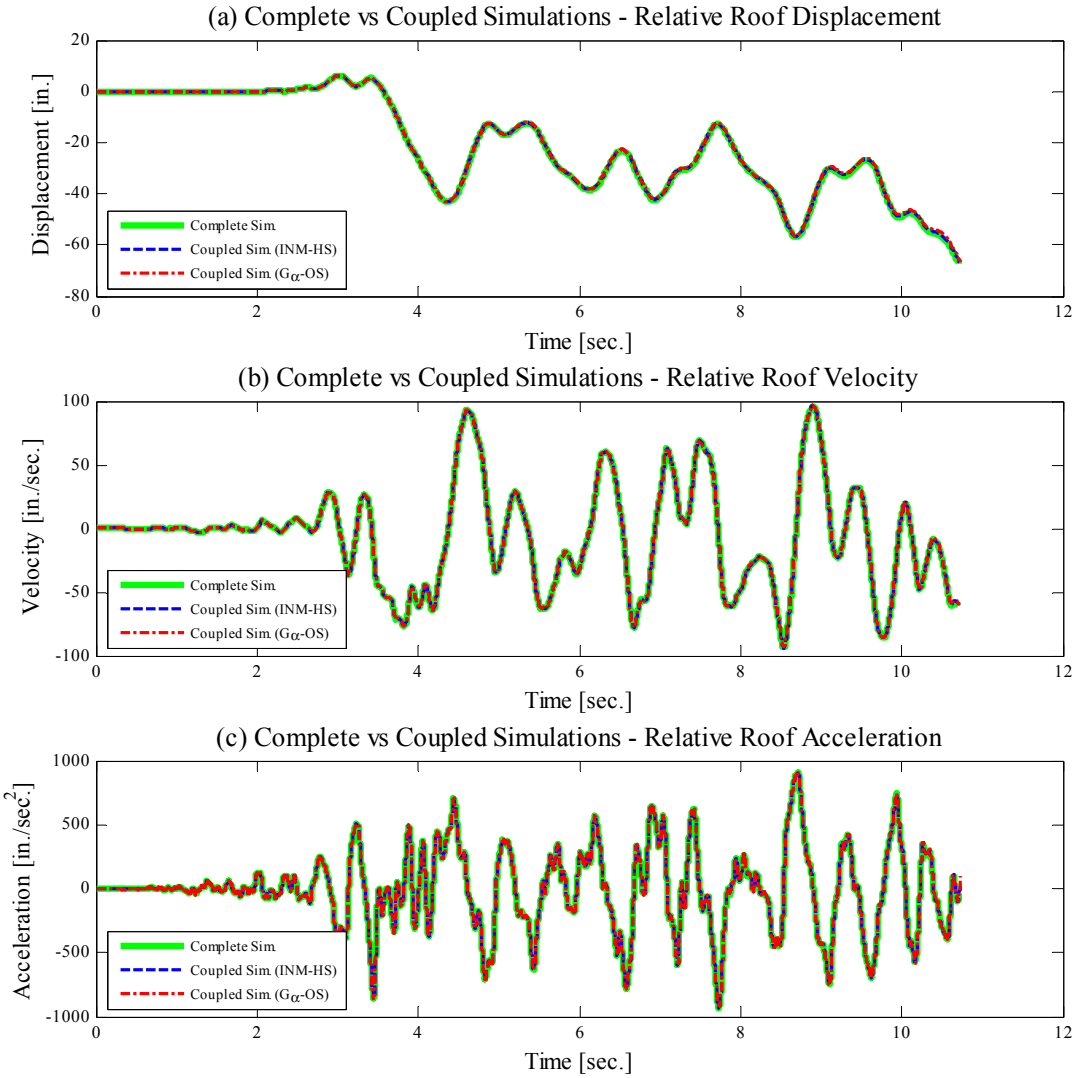


**Figure 3-13 Comparison of complete versus coupled simulations**

The accuracy and stability of the INM-HS method for increasing time step sizes and a constant number of 10 iterations is further evaluated in Figure 3-14 where global response results are presented. Figure 3-14 indicates that the INM-HS method remains accurate and stable for all time steps selected including the smallest time step of 0.010 sec. that is the resolution of the ground motion record. Additional coupled simulations (not presented here) showed that the INM-HS method remains accurate even for smaller number of iterations as low as 4.

However, the Gα-OS method produced results that visibly diverged from the converged solution for the two largest time steps used in the simulation (0.010 and 0.005 sec.) as shown in Figure 3-15 where the relative roof displacement, velocity and acceleration are presented. In the coupled simulation with a time step of 0.005 sec., the 15% inter-story drift was not exceeded and therefore the simulation continued until the end of the ground motion.

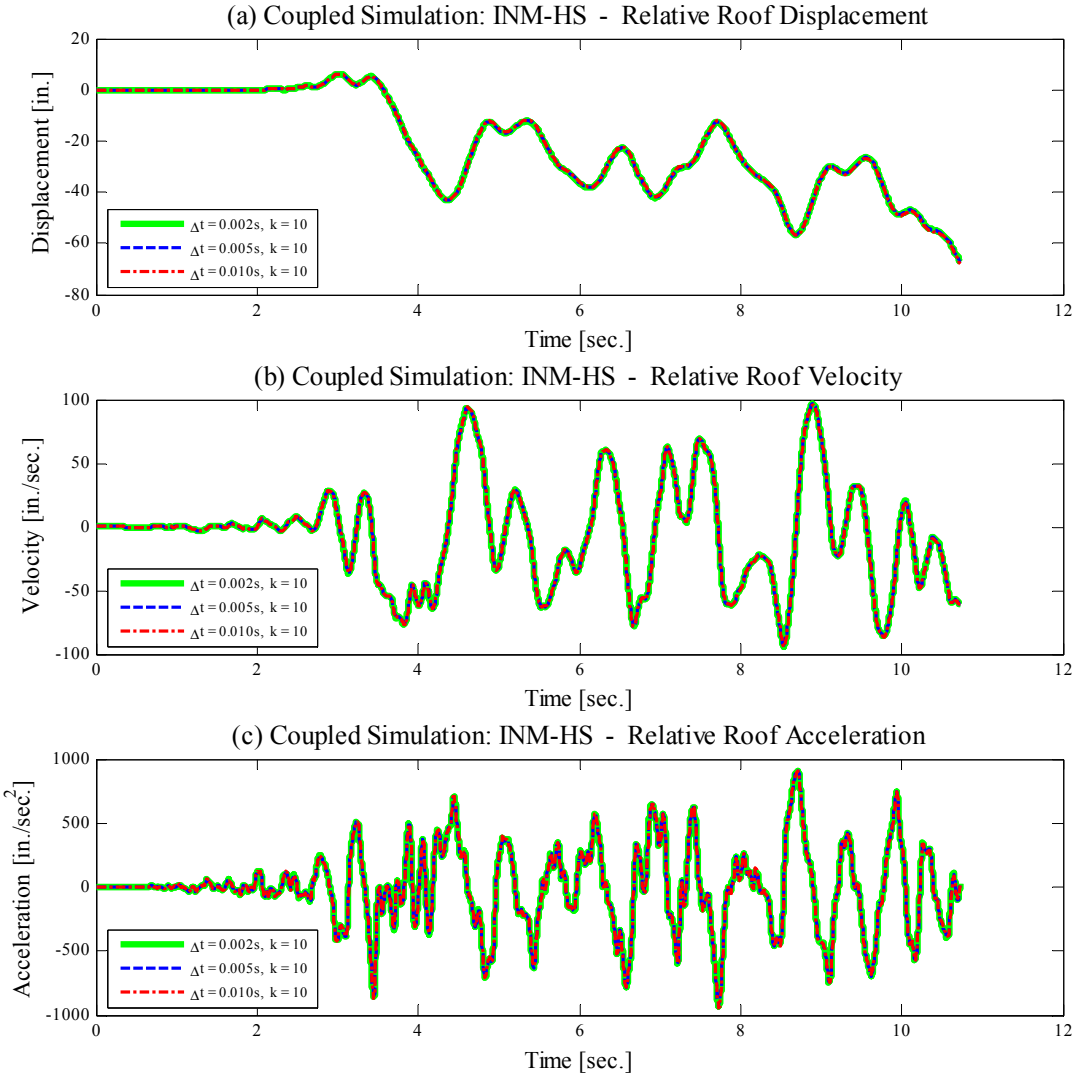


**Figure 3-14 Results of coupled simulations using the INM-HS method**

Since some effects of a hybrid test are numerically reproduced in a coupled simulation (including data communication between physical and numerical sub-structures), coupled simulations can be used to assess the accuracy and stability of the integration methods prior to conducting a hybrid test.

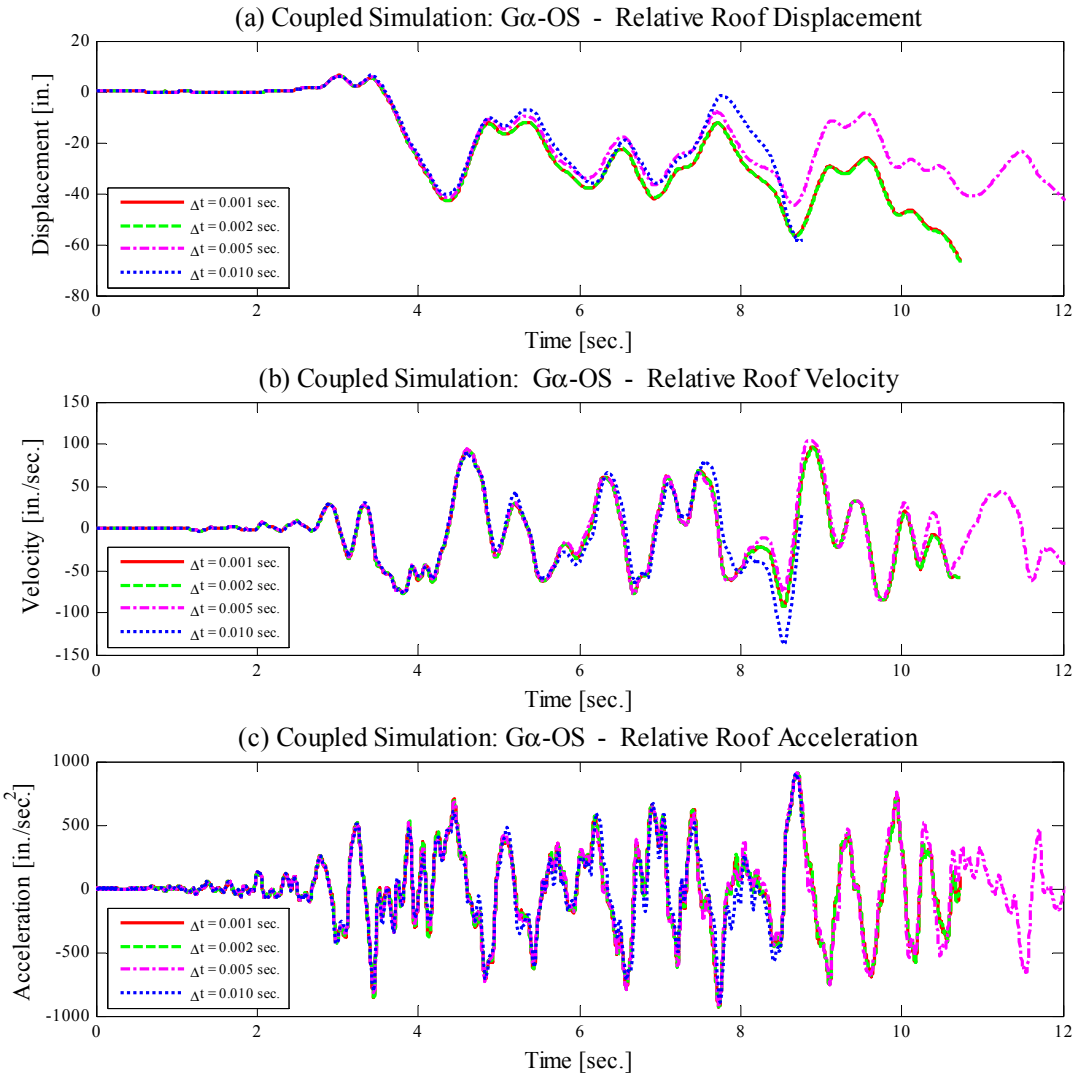


**Figure 3-15 Results of coupled simulations using the Gα-OS method**

### 3.4.3 Hybrid Simulations

.

A total of 12 hybrid simulations were conducted using different integration methods, time steps, and physical sub-structures. The coupled simulations presented in the previous section assisted in the selection of the time steps used in the hybrid tests. The tests were grouped in three series and summarized in Table 3-1 through Table 3-3.

The first test series, consisting of six tests summarized in Table 3-1, used the ductile physical sub-structure to evaluate the INM-HS method with two time step sizes (0.010 and 0.002 sec.) and two number of constant iterations (10 and 5 iterations) and the Gα-OS method with three time steps sizes (0.001,

0.002, and 0.005 sec.). The Gα-OS integration method, available in OpenSees, was used with a spectral radius ($\rho$) equal to 1.0 and therefore, this integration method is similar to the OS method where no algorithmic damping is included. The second test series, consisting of four tests summarized in Table 3-2, challenged the ability of the INM-HS and Gα-OS methods to produce accurate results using the highly nonlinear brittle physical sub-structure described in Section 3.4.1.

**Table 3-1 Test Schedule: Test Series I**

| Test ID | Integration Method | Time Step, $\Delta t$ [sec.] | Number of Iterations [$k$] | Physical Sub-Structure |
|---|---|---|---|---|
| HS01 | INM-HS | 0.002 | 10 | Ductile |
| HS02 | INM-HS | 0.010 | 10 | Ductile |
| HS03 | INM-HS | 0.010 | 5 | Ductile |
| HS04 | Gα-OS | 0.001 | NA | Ductile |
| HS05 | Gα-OS | 0.002 | NA | Ductile |
| HS06 | Gα-OS | 0.005 | NA | Ductile |

**Table 3-2 Test Schedule: Test Series II**

| Test ID | Integration Method | Time Step, $\Delta t$ [sec.] | Number of Iterations [$k$] | Physical Sub-Structure |
|---|---|---|---|---|
| HS07 | INM-HS | 0.010 | 10 | Brittle |
| HS08 | INM-HS | 0.010 | 5 | Brittle |
| HS09 | Gα-OS | 0.002 | NA | Brittle |
| HS10 | Gα-OS | 0.005 | NA | Brittle |

**Table 3-3 Test Schedule: Test Series III**

| Test ID | Integration Method | Time Step, $\Delta t$ [sec.] | Number of Iterations [$k$] | Physical Sub-Structure |
|---|---|---|---|---|
| HS11 | ENM | 0.0020 | NA | Ductile |
| HS12 | ENM | 0.0005 | NA | Ductile |

Finally, for the third test series, consisting of two tests summarized in Table 3-3, a simple approach that enables the use of explicit integration methods on structural systems having a singular mass matrix (such as the prototype model used in this section) is presented. As mentioned earlier, the explicit integration methods are typically unstable or cannot be applied at all when employed in systems with a singular mass matrix. This approach is explained in detail later in this section. Similar to the coupled simulations, all hybrid simulations were stopped when a 15% inter-story drift ratio was reached at any story or when the stroke capacity of the actuator was reached.

Figure 3-16 presents global response results of tests HS01 through HS03 using the INM-HS method. It can be seen that the global results of these three hybrid simulations are in very good agreement, indicating that the INM-HS method not only remained stable but produced accurate results for the time steps and number of iterations used. Only small differences in the results are observed at the end of the displacement response (see Figure 3-16(a)).

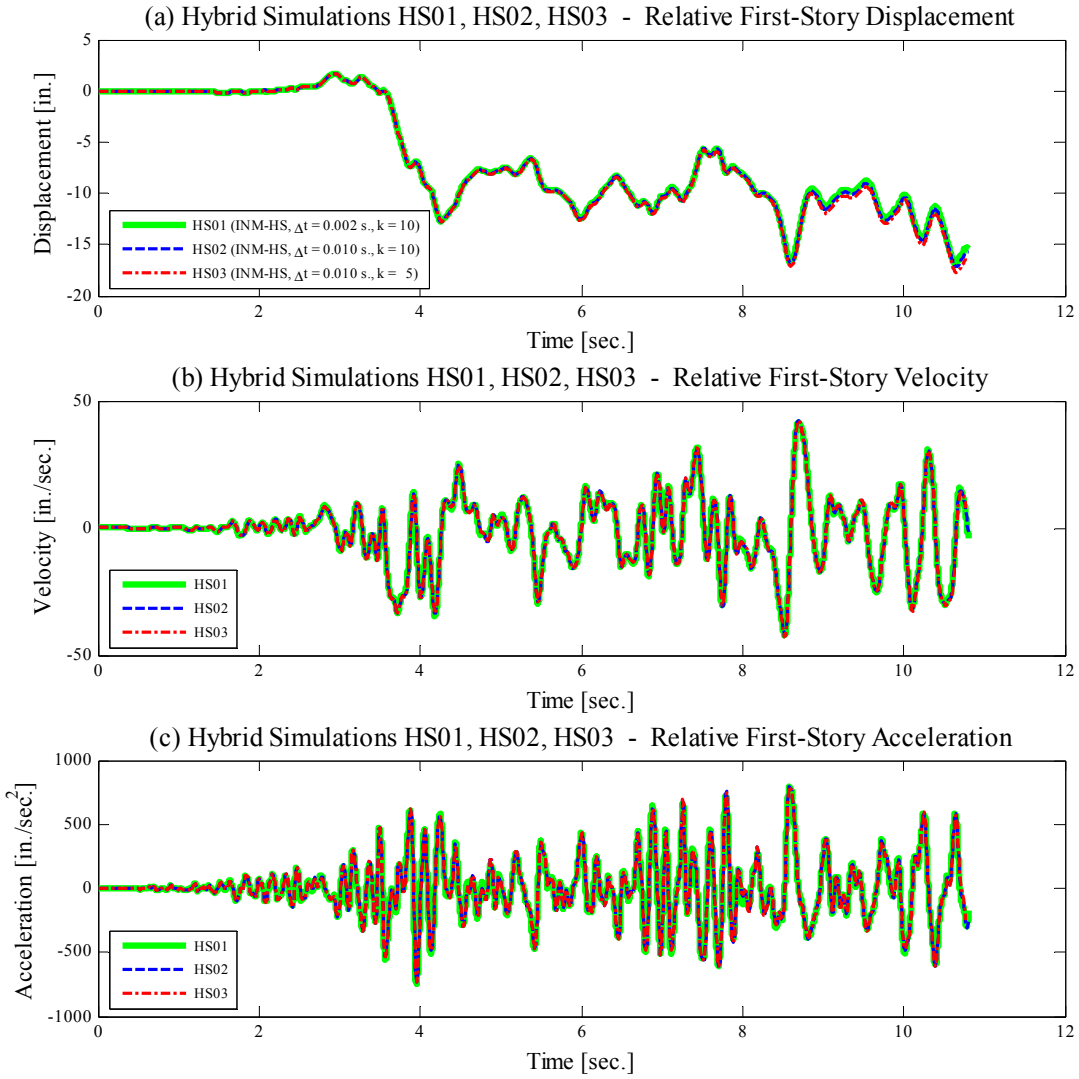


**Figure 3-16 Results of hybrid simulations HS01 through HS03**

However, as predicted by coupled simulations, the global response results of hybrid simulations HS04 through HS06 using the Gα-OS method and presented in Figure 3-17 progressively diverge as the size of the time step increases.

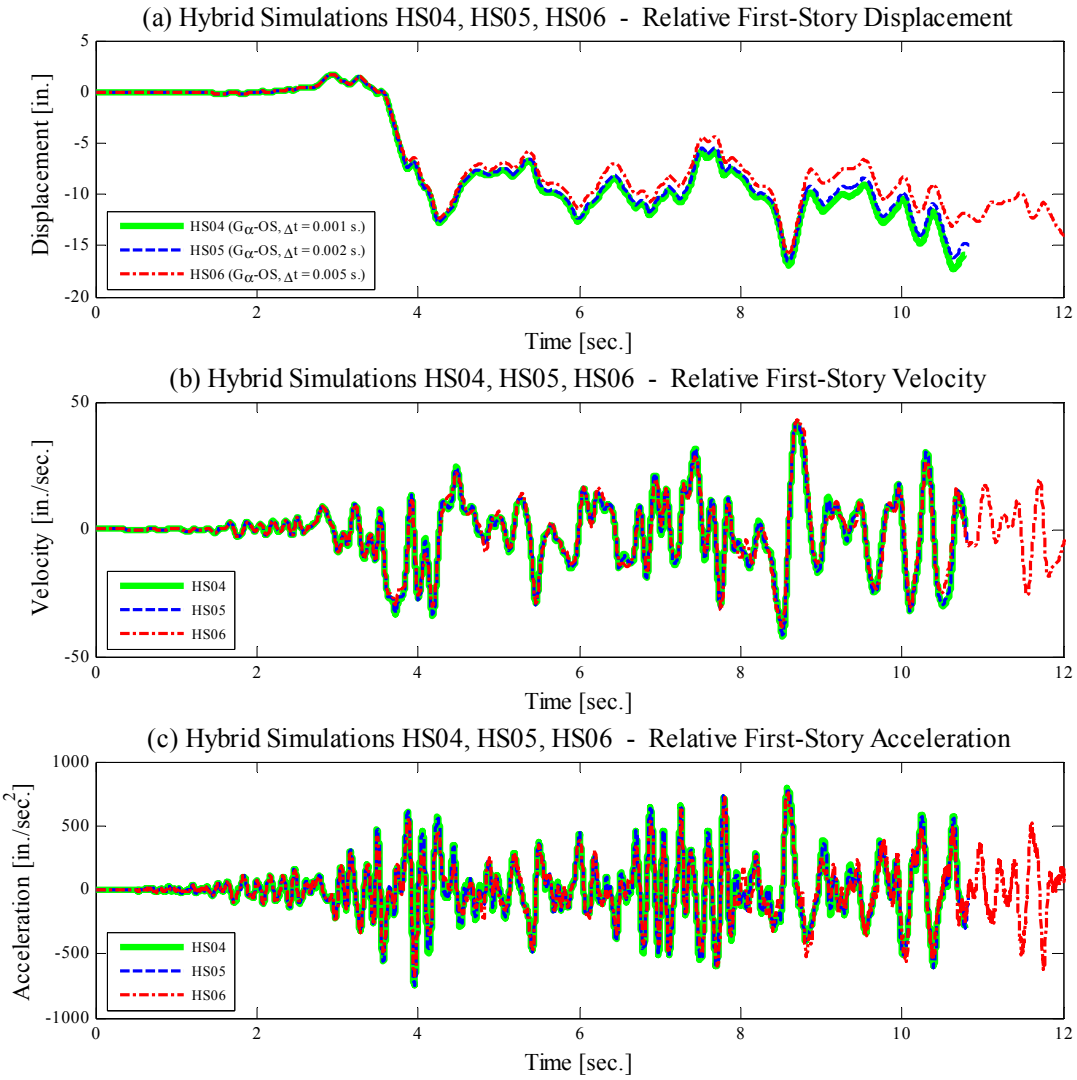


**Figure 3-17 Results of hybrid simulations HS04 through HS06**

Figure 3-18 shows the hysteretic response of the ductile physical sub-structures (tests HS01 through HS06) where the variability of the hysteretic response of the physical sub-structure can be observed. Also, it can be observed that practically no noise is observed in the force feedback.

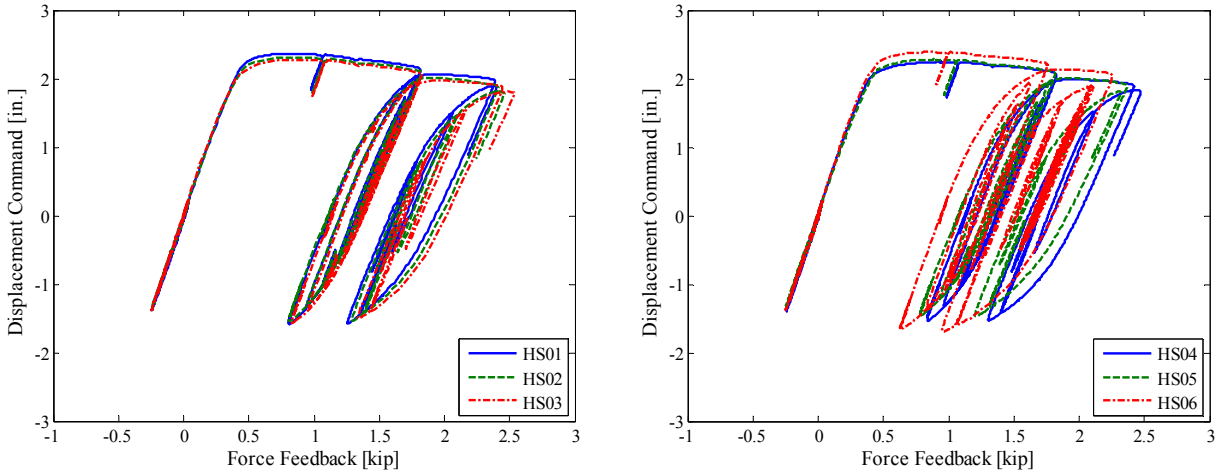


(a) Hybrid Simulations HS01 through HS03 (INM-HS) (b) Hybrid Simulations HS04 through HS06 (Gα-OS)

**Figure 3-18 Force-displacement relationships for ductile physical sub-structures**

After the execution of the first test series (tests HS01 through HS06), the parameters of the Bouc-Wen model were recalibrated using the hysteretic responses presented in Figure 3-18. Then, the results of each hybrid simulation were compared with their corresponding calibrated numerical simulations and presented in Figure 3-19. It can be seen that the numerical simulations predict very closely the global response results of the hybrid simulations except for test HS06 shown in Figure 3-19(f), where as seen before, the solution obtained in the hybrid simulation diverged due to the use of a large time step. This very good agreement was expected since the cyclic response of the physical sub-structure used in the hybrid simulation can be reproduced very well. Also, the contribution of the physical sub-structure to the global response of the prototype 2D frame is small (for instance, the lateral strength of the physical sub-structure is approximately 20% of the lateral strength of the first story of the prototype 2D frame). Finally, there is practically no noise in force feedback that could contaminate the solution.

As mentioned earlier, the highly nonlinear response of the brittle physical sub-structure used in the second test series (tests HS07 through HS10) exhibits a discontinuous non-smooth hysteretic response as a result of fracture of a steel coupon. This can challenge the accuracy and stability of the integration methods, specially of the iterative INM-HS method since the Newton-Raphson algorithm used to perform equilibrium iterations is recommended for smooth functions (in our case, smooth hysteretic models). Figure 3-20 and Figure 3-21 presents global response results for hybrid simulations HS07 and HS08 (using the INM-HS method) and HS09 and HS10 (using the Gα-OS method), respectively. It can be seen that although the physical sub-structure of both tests presents a highly nonlinear behavior (sudden drop of

strength and stiffness), the INM-HS and Gα-OS methods remained stable and converged to the same solution.

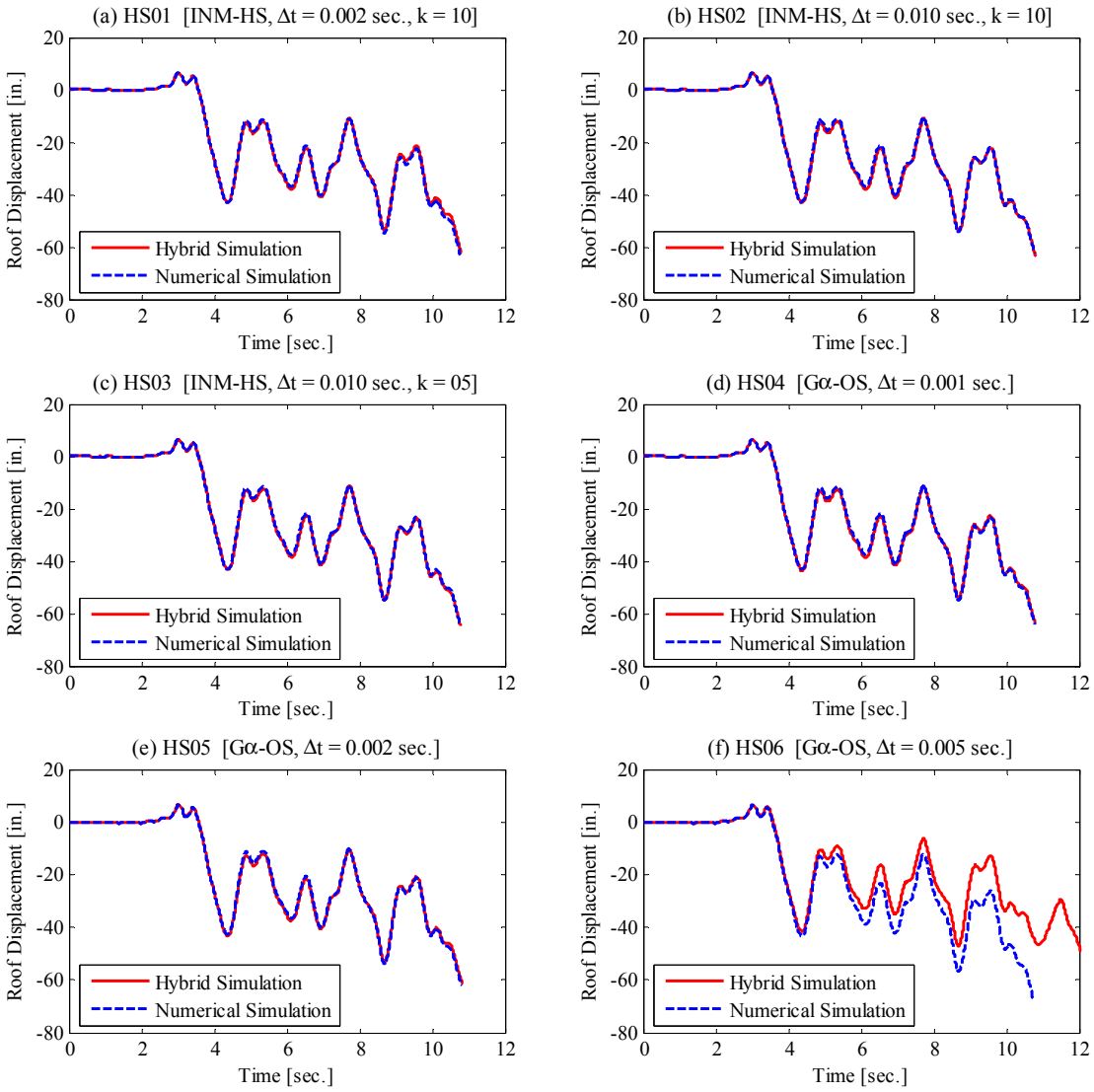


**Figure 3-19 Comparison of hybrid versus numerical simulation for HS01 through HS06**

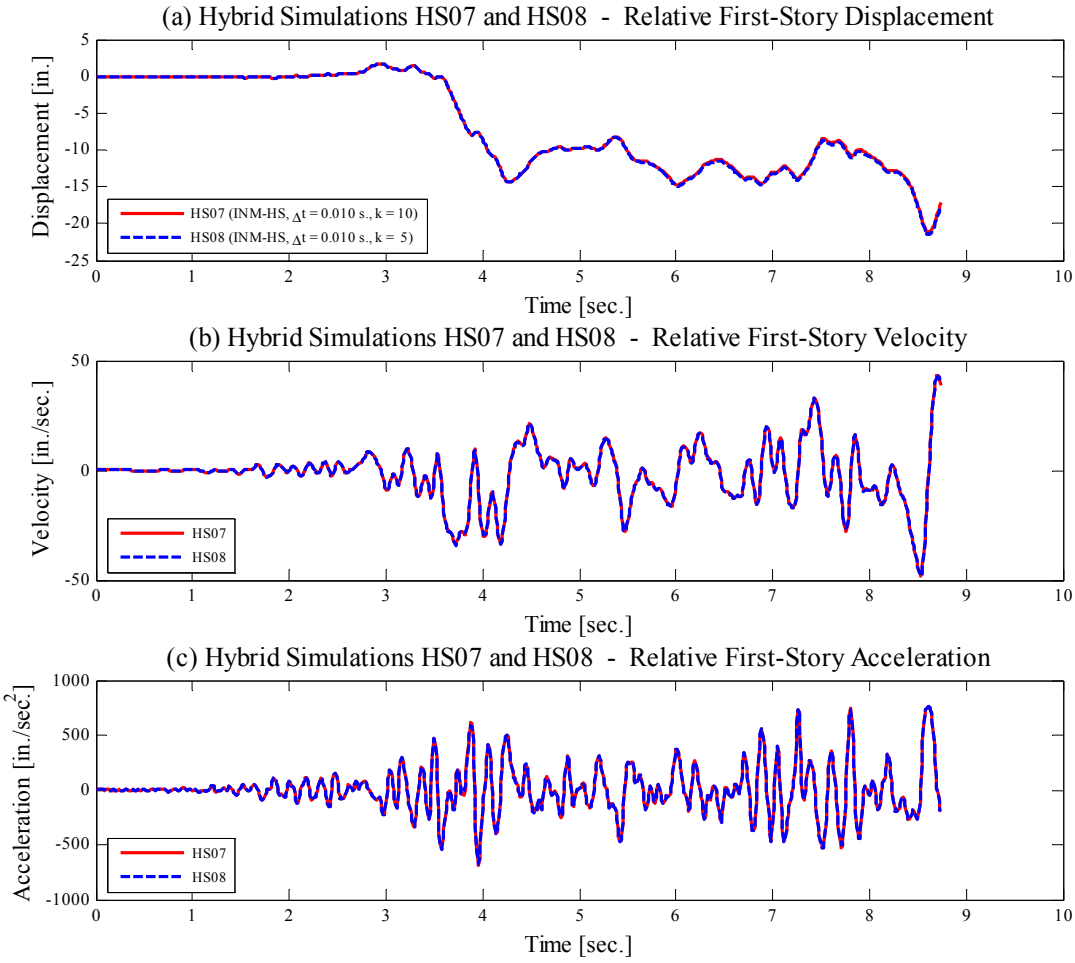


**Figure 3-20 Results of hybrid simulations HS07 and HS08**

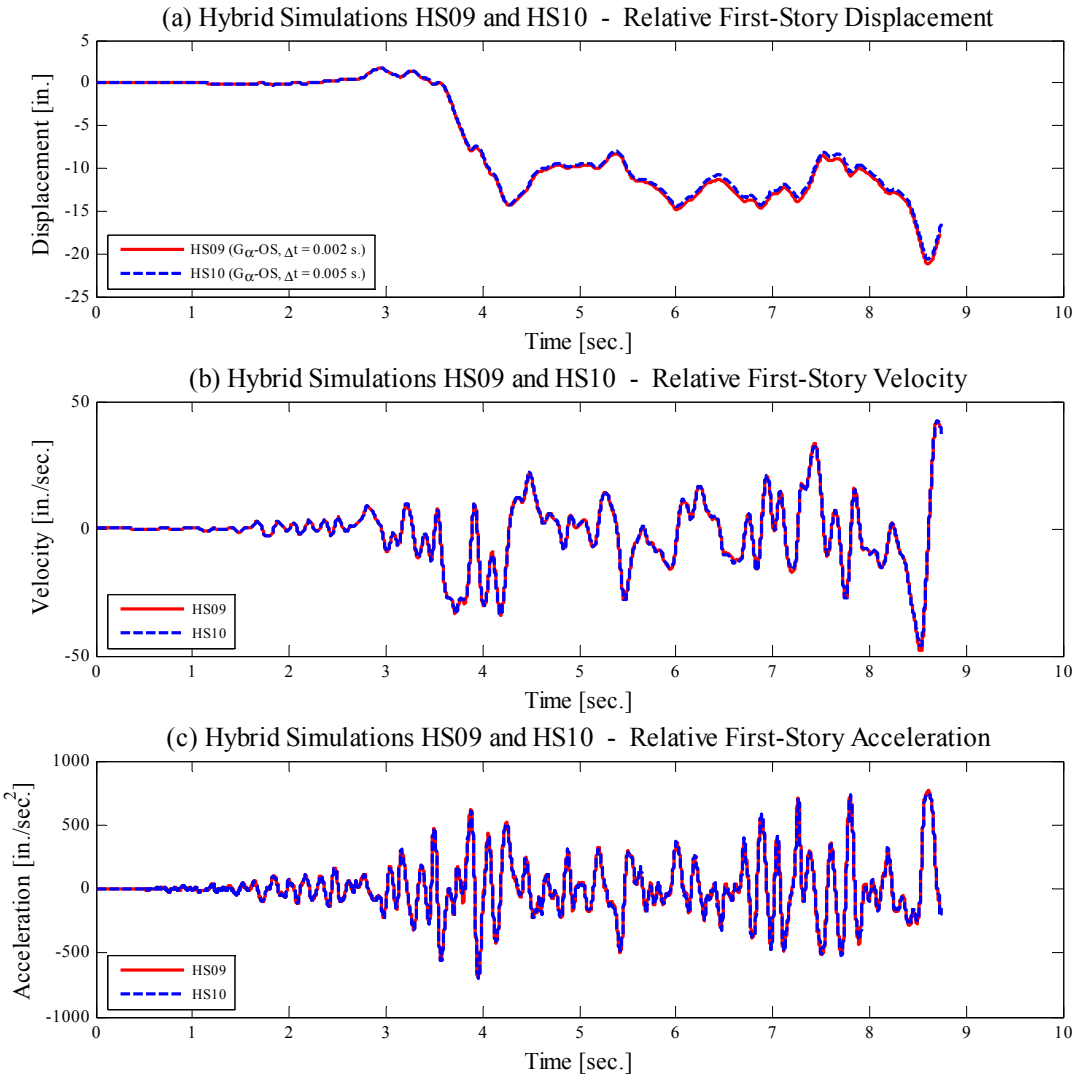


**Figure 3-21 Global response results of hybrid simulations HS09 and HS10**

To observe the effects of coupon fracture on the global response of the 2D frame, Figure 3-22 compares the global response of the first story of hybrid simulation HS02, a test without coupon fracture, against that of hybrid simulation HS07, a test with coupon fracture. In both simulations, the INM-HS method was used with a time step of 0.010 sec. and 10 fixed iterations. Fracture in the physical sub-structure occurred at the time instant of 3.79 seconds as indicated in Figure 3-22. It can be seen that up to the point of fracture, the response of 2D frame very similar in both simulations. After fracture, a divergence in the response is observed in all global responses.

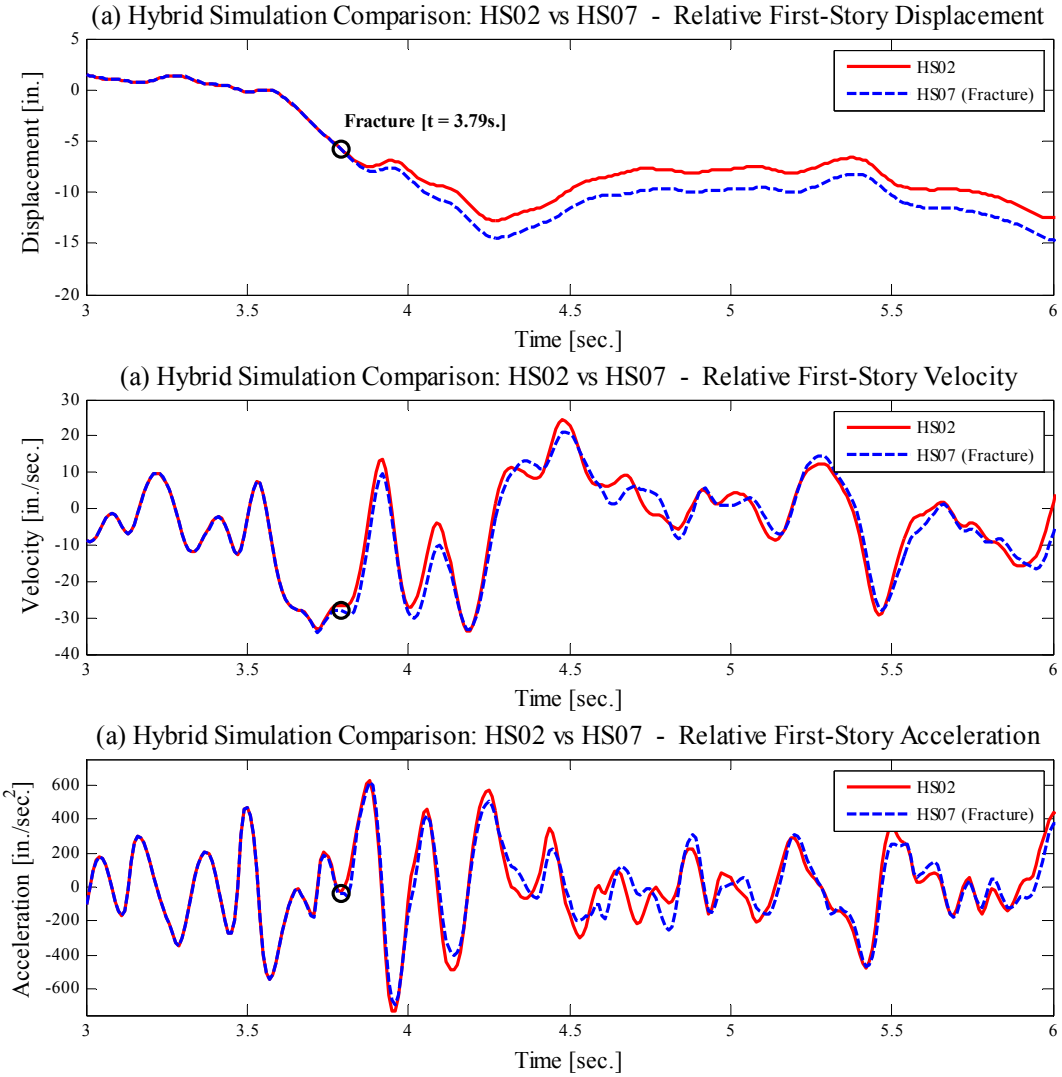


**Figure 3-22 Results of hybrid simulations HS09 and HS10**

The hysteretic response of the brittle physical sub-structure used in hybrid simulations HS07 through HS10 is presented in Figure 3-23 where the point of coupon fracture is indicated on the hysteretic response followed by a sudden drop in strength and stiffness.

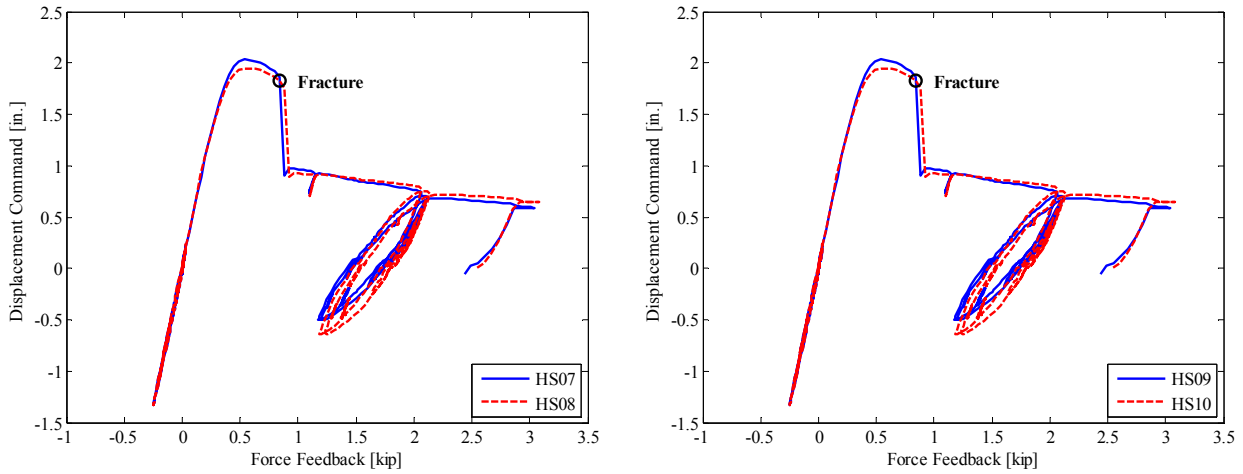


(a) Hybrid Simulations HS07 and HS08 (INM-HS) (b) Hybrid Simulations HS09 and HS10 (Gα-OS)

**Figure 3-23 Force-displacement relationships for brittle physical sub-structures**

The mass matrix of the 2D frame model shown in Figure 3-11 is singular, given that no mass was assigned to some DOFs including rotational and vertical DOFs. Therefore, explicit integration methods which require the mass matrix be inverted cannot be applied. For this reason, explicit integration methods were excluded from the evaluation presented in the previous sections. However, for the third test series, a simple approach that enables the use of explicit integration methods using coupled simulations is presented. In this approach, the numerical sub-structure (see for reference Figure 3-12) is encapsulated in a slave OpenSees script as illustrated in Figure 3-24 leaving only 3 nodes in the master OpenSees script, each one with one horizontal translational DOF (the other DOFs are restrained). Then, since the master OpenSees script solves the equations of motion, the inertial mass of each floor is assigned to the 3 nodes in the master OpenSees script. The resulting system of equations has a 3×3 non-singular mass matrix that can be solved with any explicit integration method.

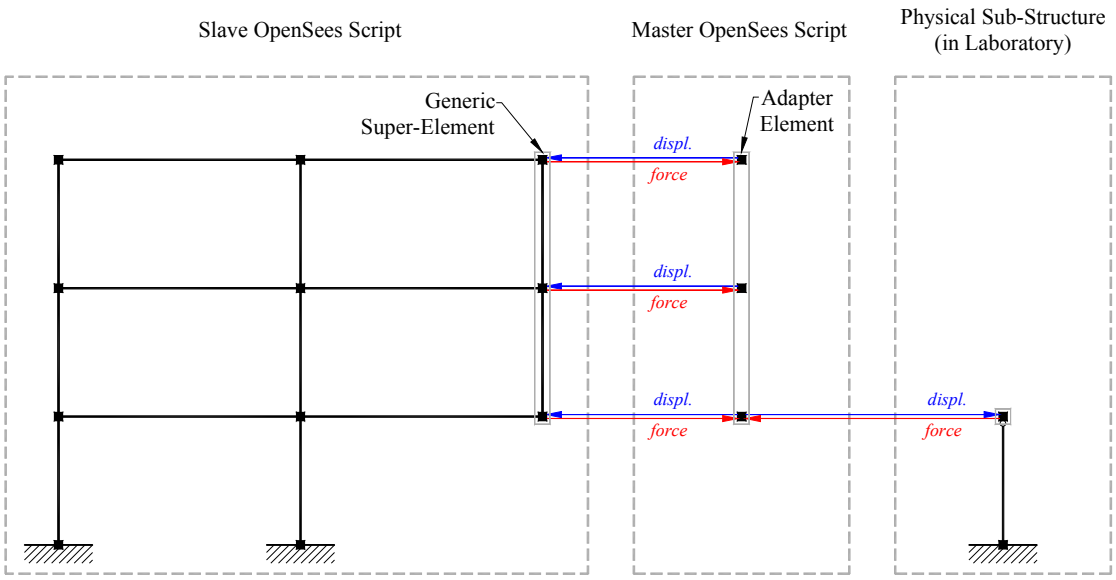


**Figure 3-24 Master and slave OpenSees Script and physical sub-structure**

This approach was first verified analytically using a coupled model where the physical sub-structure shown in Figure 3-24 was modeled in a second slave OpenSees script. It was observed that the results of these coupled simulations slightly diverged from the assumed exact solution provided by complete simulations (as mentioned earlier, a complete simulation is a conventional simulation without using coupling of FE codes) due to the different (mass and stiffness proportional) damping matrices used. While a 3×3 damping matrix is assembled in simulations following the approach illustrated in Figure 3-24, an N×N damping matrix is used in all the other simulations (N equals approximately 60 for the complete simulations).

Two hybrid simulations were conducted using the approach illustrated in Figure 3-24. The explicit Newmark Method (ENM) was used in both hybrid simulations. Figure 3-25 presents the results of tests HS11 and HS12 using two time steps. The results of HS01 (test conducted with the INM-HS method with $\Delta t = 0.002$ and $k = 10$) is included for comparison purposes.

It can be seen in Figure 3-25 that the proposed approach produces similar results as the hybrid simulation HS01. As previously mentioned, the differences observed in the results of tests HS11 and HS12 with those of test HS01 (assumed exact solution) are due to the different Rayleigh damping matrix used.

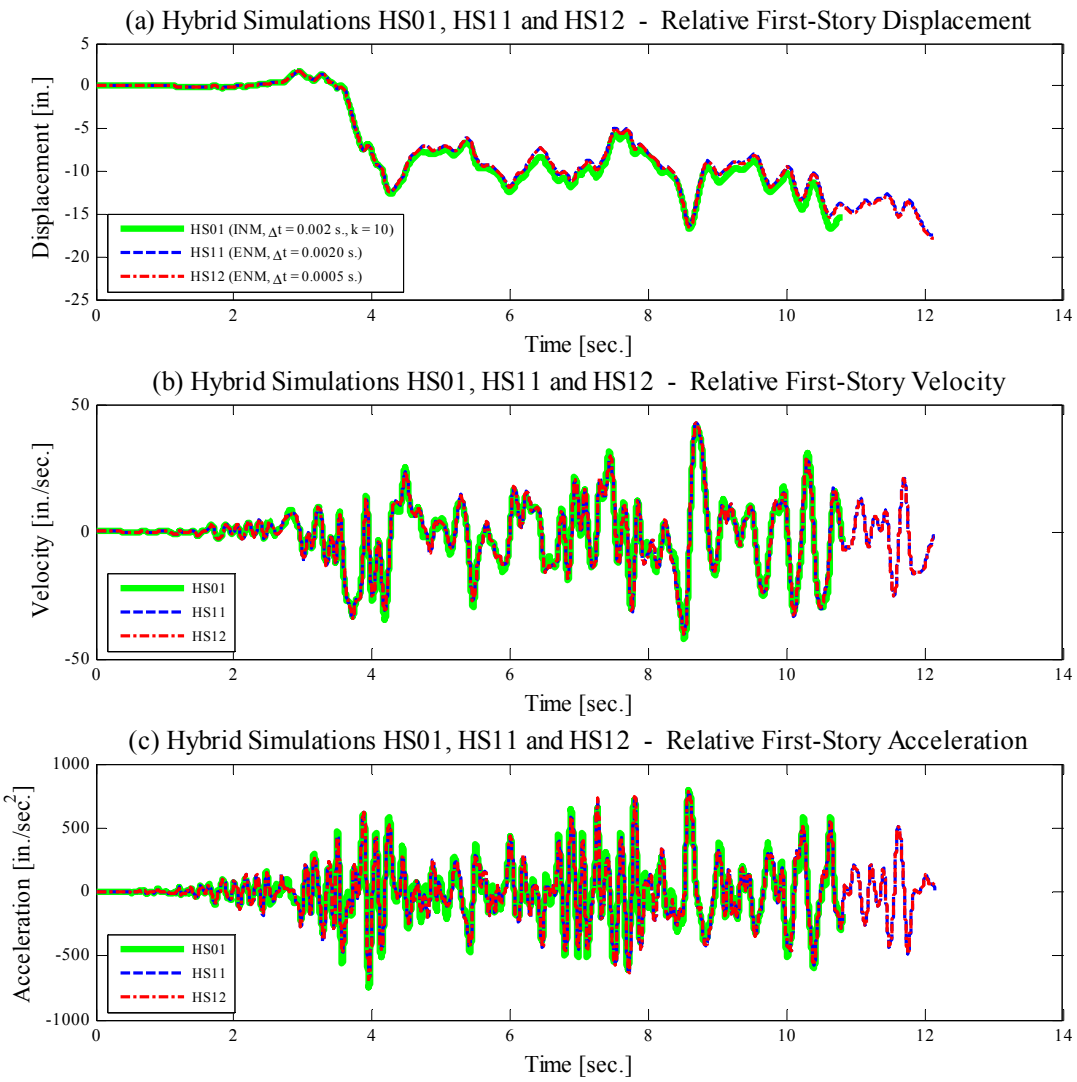


**Figure 3-25 Results of hybrid simulations HS11 and HS12 and comparison with HS01**

### 3.4.4 Summary and Conclusions

Twelve collapse hybrid simulations were conducted to evaluate the performance of the INM-HS and Gα-OS methods. Also, a simple approach that enables the use of explicit integration methods systems with a singular mass matrix was proposed. The conclusions listed below are strictly valid for the hybrid simulations of the 2D frame structure presented in this section.

- In general, the hybrid simulations conducted in this study showed that the INM-HS and Gα-OS methods produced response results with similar levels of accuracy as compared with purely numerical simulations. Both integration methods remained accurate and stable for the range of

time steps selected (the smallest time step was limited to the time step of the ground motion record equal to 0.010 sec.).

- The use of physical sub-structures with a highly nonlinear response characterized by a sudden drop in strength and stiffness did not affect the accuracy or stability of the integration methods. However, it must be recognized that: (a) the contribution of the physical sub-structure to the global response of the prototype 2D frame was small, and (b) the numerical model of the prototype 2D frame was fairly simple. Larger and more complex numerical models such as those described in Section 6 posed a challenge on the performance of these integration methods. It was observed that simulations with the INM-HS method became unstable for large levels of nonlinear response.
- The calibrated numerical simulations performed after hybrid testing reproduced very closely the results of the hybrid simulations. This is due to several reasons: (a) the cyclic response of the physical sub-structure was faithfully reproduced using the Bouc-Wen model and (b) there was practically no noise in the load cell of the actuator that could contaminate the solution.
- The INM-HS method remained accurate for large time steps (as large as 0.010 sec.) and small number of constant iterations (as low as 5 iterations). However, the Gα-OS method lost accuracy when using a time step of 0.005 seconds. Therefore, the INM-HS method is more accurate than the Gα-OS method for the same time step size or even for the same number of data communication procedures between the numerical and physical sub-structures.

# SECTION 4
# EXPERIMENTAL PROGRAM: PRELIMINARIES

## 4.1 Introduction

An experimental framework for collapse assessment was developed and implemented in this research project in response to the need for more realistic experimental information on the behavior of structures through collapse identified in the review of literature in Section 2 as well as in others (Villaverde, 2007, Lignos and Krawinkler, 2012). Hybrid simulation with substructuring was investigated as a cost-effective alternative for large-scale testing of structures to simulated dynamic earthquake loads. Through the use of substructuring techniques in hybrid simulation, only key subassemblies of a frame structure can be physically tested in a laboratory while the rest of the frame is simulated in a computer model to capture the complete system behavior. Considerable efforts were made to implement the substructuring hybrid testing approach to examine frame structures through collapse. Such efforts included evaluating the performance of integration methods and substructuring techniques for hybrid simulation which were greatly challenged when employed with large and complex numerical sub-structures exhibiting large levels of nonlinear response.

In contrast to the large number of traditional quasi-static tests conducted as part of the SAC Joint Venture (www.sacsteel.org) on cruciform or T-shaped subassemblies of beams and columns with idealized boundary conditions to prescribed cyclic loading protocols (component-level tests), larger subassemblies were subjected to more realistic loading conditions via hybrid simulation using similar laboratory equipment. Preliminary aspects of the experimental program are discussed in this section, including the objectives and scope of the experiments, descriptions of the prototype structure and reduced-scale hybrid models, and the selection of the ground motion and testing protocol.

## 4.2 Objectives and Scope of Experimental Program

The main objective of the experimental program is to obtain realistic data of the seismic response of steel moment and gravity frame subassemblies from the onset of damage through collapse. This data is valuable to assess the performance of the frame subassemblies and to investigate the capabilities of analytical models to trace the response of these frame systems through collapse. A secondary objective of

the experimental program is to evaluate a newly developed substructuring technique used for hybrid simulation of multi-story frame structures.

The experimental program comprises two series of hybrid simulations. In the first series, referred to hereafter as Hybrid Simulation #1, the focus is on the seismic behavior of a special steel moment-resisting frame. To this end, a hybrid model of a moment frame, hereafter referred to as Hybrid Model #1, was subjected to four increasing intensities of a ground motion through collapse. The physical sub-structure of this hybrid model consists of one and one-half story by one and one-half bay subassembly of a moment frame which was tested in the laboratory while the rest of the frame was simulated computationally. For the second series of hybrid simulations, referred to hereafter as Hybrid Simulation #2, the focus is shifted to the seismic behavior of the gravity framing system. In this case, a computational model of a moment frame was coupled with a hybrid model of a gravity frame. The physical sub-structure of the gravity frame is of similar overall dimensions as the previously-mentioned physical sub-structure. The hybrid model of the gravity frame coupled with the fully numerical model of the moment frame is referred to as Hybrid Model #2 in the following sections.

The experimental test setup was designed to impose lateral (seismic) as well as vertical (gravity) forces on the physical sub-structures. Lateral loading on the physical subassemblies was applied through displacement-controlled actuators commanded by the hybrid simulation algorithm. The physical sub-structures included the composite floor slab and additional dead load at the first elevated story level. The axial forces on the columns at the second story due to gravity loads of upper stories as well as seismic-induced variations from overturning forces are applied through force-controlled vertical actuators. The hybrid simulations were conducted at the Network for Earthquake Engineering Simulation (NEES) equipment site at the State University of New York at Buffalo (UB). The numerical sub-structures were developed in the Open System for Earthquake Engineering Simulation (OpenSees, 2012) platform and integrated with the physical sub-structures and laboratory hardware through the Open Source Framework for Experimental Setup and Control (OpenFresco, 2008). The physical and numerical sub-structures, briefly presented in this section, are extensively described in Section 5 and Section 6, respectively.

## 4.3 Prototype Building

The four-story office building designed and evaluated by Lignos and Krawinkler (2012) served as the prototype building for the experimental program. This building, assumed to be located in Los Angeles, CA, was designed according to U.S. codes/standards of practice, namely, IBC (2003), AISC (2005), and SEI/ASCE-02 (ASCE, 2002). Some of the column design requirements have changed in the current AISC specification (AISC, 2010b). Therefore, this building would not be exactly the same if it were designed according to current practice. The structure was classified as Category II (importance factor equal to 1.0). The building was assumed to be located on Soil Type D. The maximum considered earthquake (MCE) spectral response accelerations are $S_S$=1.5$g$, $S_1$=0.90$g$ and the design spectral response accelerations are $S_{DS}$=1.5$g$, $S_{D1}$= 0.60$g$. The seismic-force-resisting system of the prototype building consists of special steel moment-resisting frames (located around the perimeter of the building) with fully-restrained reduced beam sections (RBS) in both principal loading directions as seen in Figure 4-1. The location of the moment-resisting connections in Figure 4-1 is indicated by the "►" symbol. The inter-story heights of the four-story structure were interpreted as slab-to-slab dimensions in this study.

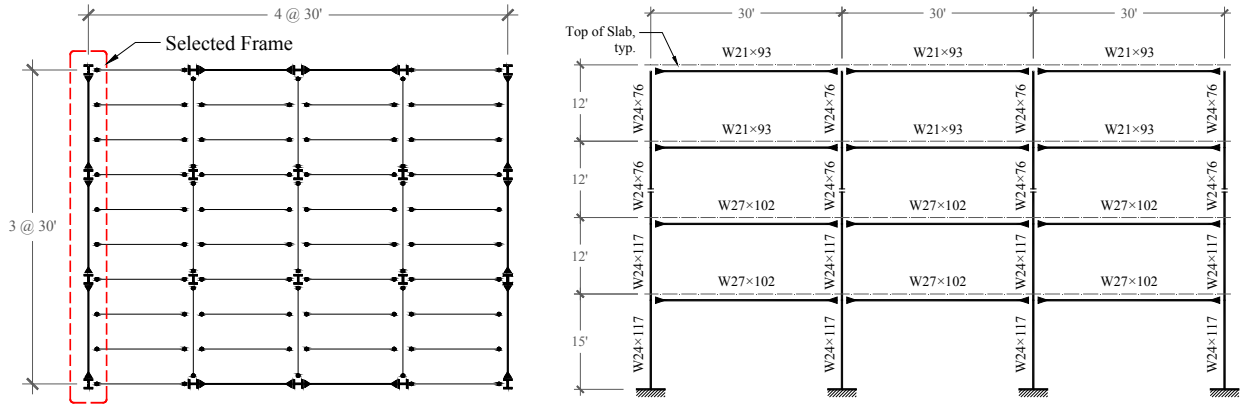


(a) Plan view of prototype building (b) Elevation of moment frame selected for testing

**Figure 4-1 Prototype building and special steel moment frame selected for hybrid testing**

Table 4-1 summarizes the dimensions and plastic modulus of the reduced beam sections and the thickness of the doubler plates provided at panel zones of the prototype moment frame selected for testing. The design of the doubler plates was performed as part of this research.

**Table 4-1 Summary of dimensions and plastic modulus of reduced beam sections and thickness of doubler plates provided at panel zones of prototype frame structure selected for testing**

| Location | Girder Section | Dimensions and Plastic Modulus of RBS | | | | Thickness of Doubler Plates | |
|---|---|---|---|---|---|---|---|
| | | *a* [in.] | *b* [in.] | *c* [in.] | $Z_{RBS}$ [in.$^3$] | Exterior Panel Zone | Interior Panel Zone |
| Roof | W21×93 | 6.28 | 18.17 | 1.88 | 144 | 1/4" | 3/4" |
| 4th Floor | W21×93 | 6.28 | 18.17 | 1.88 | 144 | 1/4" | 3/4" |
| 3rd Floor | W27×102 | 7.50 | 22.50 | 2.25 | 199 | – | 5/8" |
| 2nd Floor | W27×102 | 7.50 | 22.50 | 2.25 | 199 | – | 5/8" |

### 4.3.1 Design of Gravity-Force-Resisting System

The design of the gravity-force-resisting system of the prototype building, not addressed in Lignos and Krawinkler (2012), was performed herein in consultation with practitioner engineers from the west coast of the U.S. The gravity framing system is typically designed to carry gravity loads only. The specifications of the design of the beams and columns of the gravity framing system are summarized in Table 4-2.

**Table 4-2 Summary of structural members of gravity frames of prototype building**

| Structural Element | Section |
|---|---|
| Columns @ 1st and 2nd Story | W12×79 |
| Columns @ 3rd and 4th Story | W12×53 |
| Beams @ 2nd, 3rd, and 4th Floors | W24×68 |
| Beams @ Roof | W24×55 |
| Joists @ 2nd, 3rd, and 4th Floors | W18×35 |
| Joists @ Roof | W16×26 |

The beams and columns of the gravity frames are typically connected through simple connections. The simple shear-tab connection detail is typically used in the west coast of the U.S. The symbol "●" in Figure 4-1(a) indicates the location such type of connections. Figure 4-2 shows a typical shear-tab connection detail which was designed for the prototype building.

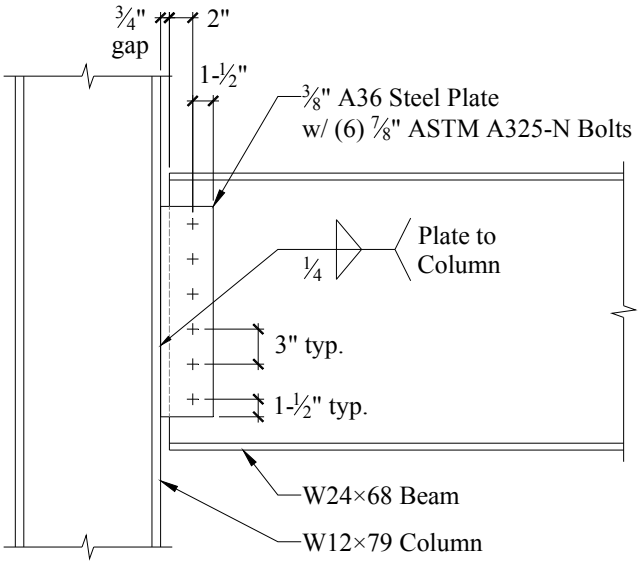


**Figure 4-2 Typical shear-tab connection detail for gravity framing system of prototype building**

The design of the shear-tab connection was performed according to AISC Steel Construction Manual (AISC, 2010b) and the recommendation of Astaneh-Asl (Steel Tips, 2005). The following limit states were checked in the shear-tab connection: (a) shear yielding of shear-tab plate, (b) bolt bearing of shear-tab plate and beam web, (c) fracture of net area of shear-tab plate, (d) bolt fracture, and (e) weld fracture. Yielding of shear-tab plate in shear was the controlling limit state.

## 4.4 Reduced-Scale Hybrid Models

### 4.4.1 Selection of Scale Factors for Hybrid Simulation

This section discusses the selection of the independent scale factors for the three fundamental dimensions, namely, mass, length and time, used in the hybrid simulations. The other scale factors can be expressed in terms of these independent scale factors following principles of dimensional analysis.

In hybrid simulation, if the physical sub-structure is scaled, the equations of motion can be solved for the prototype or the scaled model (Kumar *et al.*, 1997). If the equations of motion are solved at the prototype scale, the displacement command vector sent to the model needs to be scaled down by the corresponding length scale factor and the associated force feedback vector scaled up by the force scale factor. However, if the equations of motion are solved for the scaled model, no scaling of displacements or forces need to be applied but the time of the ground motion needs to be scaled by the time scale factor. In both cases, the

different physical and numerical sub-structures can be scaled in size using different length scale factors ($S$) as long as the displacement command and force feedback vectors are scaled accordingly. Therefore, the displacement and force scale factors are of primary importance in hybrid simulation.

For the two series of hybrid simulations conducted in this experimental program, the physical sub-structures were scaled down in size by the length scale factor of $S = 0.50$ due to cost and space limitations of the testing facility. Although a different scale factor could be used for the numerical sub-structures, the same length scale factor of 0.50 was selected for all numerical sub-structures due to the scale and size effects of the rotational capacity of the beams and columns of moment frames (as it is later explained in Section 6.2.2). Since the gravity loads on the physical sub-structures are simulated with additional weights, the arbitrary mass and time scale factors of $S^2 = 0.25$ and $S^{1/2} = 0.707$, respectively, can be chosen so as to provide a force scale factor of $S^2 = 0.25$. Therefore, the time of the ground motion was scaled down by the time scale factor of $S^{1/2} = 0.707$.

### 4.4.2 Scaling of Wide-Flange Sections

The wide-flange sections for girders and columns of the moment and gravity frames of the prototype building presented in Figure 4-1(b) and Table 4-2, respectively, were scaled down in size as follows: the wide-flange sections for the girders and columns of the half-scaled moment and gravity frames were selected to match some relevant target section properties such as moment of inertia ($I_x$), cross-sectional area ($A$), plastic modulus ($Z_x$) and compactness ratios ($b_f/2t_f$ and $h/t_w$). The compactness ratios ($b_f/2t_f$ and $h/t_w$) are very influential parameters to model cyclic deterioration in strength and stiffness of commonly-used wide-flange sections (Lignos and Krawinkler, 2011). Table 4-3 and Table 4-4 present the selected wide-flange sections of the half-scale moment and gravity frame members, respectively. The difference between the section properties of the half-scale sections and corresponding target (scaled) values are also presented where a negative value indicates that the section property of the scaled section is below its target value.

**Table 4-3 Wide-flange sections for girders and columns of half-scale moment frame**

| Structural Member | Original Section | Scaled Section | Difference in Section Property [%] | | | | |
|---|---|---|---|---|---|---|---|
| | | | $I_x$ | $A$ | $Z_x$ | $b_f/2t_f$ | $h/t_w$ |
| Girder @ 2nd & 3rd Floor | W27×102 | W14×26 | 8.3 | 2.5 | 5.4 | -0.8 | 2.1 |
| Girder @ 4th Floor & Roof | W21×93 | W12×22 | 20.6 | -5.1 | 6.1 | 4.6 | 29.4 |
| Column @ 1st & 2nd Story | W24×117 | W12×30 | 7.6 | 2.2 | 5.4 | -1.6 | 6.6 |
| Column @ 3rd & 4th Story | W24×76 | W12×19 | -1.0 | -0.5 | -1.2 | -13.5 | -5.7 |

**Table 4-4 Wide-flange sections for beams and columns of half-scale gravity frame**

| Structural Member | Original Section | Scaled Section | Difference in Section Property [%] | | | | |
|---|---|---|---|---|---|---|---|
| | | | $I_x$ | $A$ | $Z_x$ | $b_f/2t_f$ | $h/t_w$ |
| Beam @ 2nd, 3rd & 4th F. | W24×68 | W12×16 | -9.9 | -6.3 | -9.2 | -1.7 | -5.0 |
| Beam @ Roof | W24×55 | W12×14 | 5.0 | 2.7 | 3.9 | 27.1 | -0.5 |
| Column @ 1st & 2nd Story | W12×79 | W6×20 | 0.1 | 1.2 | 0.8 | 0.4 | -9.7 |
| Column @ 3rd & 4th Story | W12×53 | W6×12 | -16.8 | -9.0 | -14.8 | -17.8 | -23.1 |

### 4.4.3 Scaling of RBS Moment Connections

The RBS dimensions presented in Table 4-1 of the prototype moment frame were not simply scaled down by the length scale factor of 0.50. Instead, RBS moment connections were designed for the girders and columns shown in Table 4-3 of the half-scale moment frame as follows: while the upper limits of AISC (2010a) were selected for dimensions *a* and *b*, dimension *c* was calculated such as to match the target (scaled) value of the plastic modulus at center of the RBS ($Z_{RBS}$). Subsequently, typical design checks were performed on the resulting half-scale RBS moment connection to verify compliance with codes/standards of practice. Such design checks include: (a) check that the maximum probable moment at the face of the column does not exceed the plastic moment of the girder based on expected yield stress, (b) girder shear strength check, (c) panel zone check, and (d) column-girder moment ratio check. Table 4-5 summarizes the RBS dimensions and plastic modulus of the half-scale moment frame.

**Table 4-5 Dimensions and plastic modulus of half-scale reduced beam sections**

| | Section | *a* [in.] | *b* [in.] | *c* [in.] | $Z_{RBS}$ [in.$^3$] |
|---|---|---|---|---|---|
| Roof | W12×22 | 3.00 | 10.50 | 1.12 | 17.9 |
| 4$^{th}$ Floor | W12×22 | 3.00 | 10.50 | 1.12 | 17.9 |
| 3$^{rd}$ Floor | W14×26 | 3.75 | 11.25 | 0.32 | 25.3 |
| 2$^{nd}$ Floor | W14×26 | 3.75 | 11.25 | 0.32 | 25.3 |

### 4.4.4 Scaling of Shear-Tab Connections

Figure 4-3 presents a typical shear-tab connection detail designed for the gravity framing system of the half-scale building. This shear-tab connection was designed for the scaled gravity loading demands and checked for the actual loading demands of the test specimen. Most of the dimensions of the half-scale shear-tab connection, such as thickness of the shear-tab plate, bolt spacing, bolt edge distance, size of fillet weld, and gap between beam and column, are one-half of the full-scale connection shown in Figure 4-2. The bolts however, are not exactly half scale.

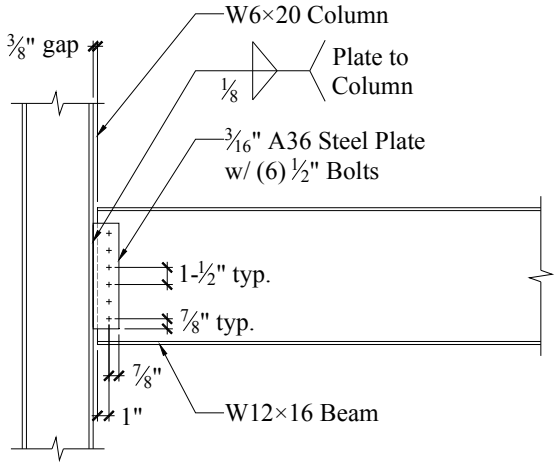


**Figure 4-3 Typical shear-tab connection detail for half-scale gravity frame**

### 4.4.5 Hybrid Model #1 (Moment Frame)

Figure 4-4 shows a schematic representation of the moment frame hybrid model used in the first series of hybrid simulations. This model is referred to hereafter as Hybrid Model #1. As seen in Figure 4-4, the physical sub-structure includes exterior and interior one-and-one-half story columns, and one-and-one-

half bay girders, and therefore, exterior and interior panel zones. The physical sub-structure was constructed so as to retain many of the features of the prototype structure including the composite floor slab. Details of the physical sub-structure are presented in Section 5.2.

The numerical sub-structure, modeled in OpenSees, was coupled with the physical sub-structure through OpenFresco using a newly developed substructuring technique (Hashemi, 2013). In the substructuring technique, there is an overlapping domain between the physical and numerical sub-structures not shown in the schematic representation of Figure 4-4. In this hybrid model, a leaning column, which is not shown in Figure 4-4, was modeled to account for P-Delta effects. A detailed description of the numerical model, as well as the substructuring technique, is presented in Section 6.2 and Section 6.4, respectively.

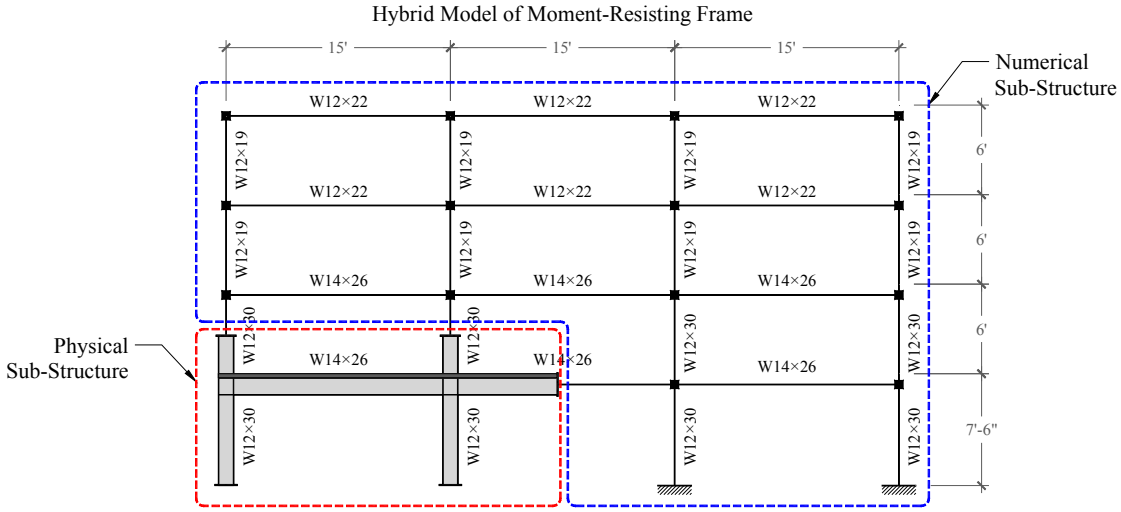


**Figure 4-4 Schematic representation of Hybrid Model #1**

### 4.4.6 Hybrid Model #2 (Moment Frame + Gravity Frame)

Figure 4-5 presents a schematic representation of the hybrid model used in the second series of hybrid simulations. This hybrid model is referred hereafter as Hybrid Model #2. It can be seen in Figure 4-5 that Hybrid Model #2 consists of a hybrid model of a gravity frame which is coupled in parallel via OpenFresco to a fully numerical model of the moment frame. To account for the actual ratio of number of moment to gravity frames in the direction of loading (2 moment frames and 3 gravity frames), the moment frame was encapsulated in a separate OpenSees script and treated as a second numerical sub-structure via OpenFresco so that the force feedback vector returned from this numerical sub-structure to

the integration algorithm (located at the OpenSees script of the numerical sub-structure of the gravity frame) is modified by a factor of 2/3.

The hybrid model of the gravity frame shown in Figure 4-5 was developed assuming that all wide-flange sections of the gravity columns are of the same size and oriented in the strong axis. Although the contribution of the gravity frames is a function of the orientation of the gravity columns, the hybrid simulations were conducted mainly to obtain experimental information on the response of the gravity frame physical subassembly rather than assessing the contribution of the gravity framing system. This experimental information is subsequently used to calibrate the numerical model of the gravity frames to assess their contribution on the collapse capacity of the building structure.

A detailed description of the physical sub-structure of the gravity frame shown in Figure 4-5 is presented in Section 5.3. This test specimen is of similar overall dimensions as the physical sub-structure of the moment frame. The development of the numerical sub-structure for the gravity frame is presented in Section 6.3. Unlike Hybrid Model #1, a leaning column was not required in Hybrid Model #2 since the gravity frame was explicitly modeled.

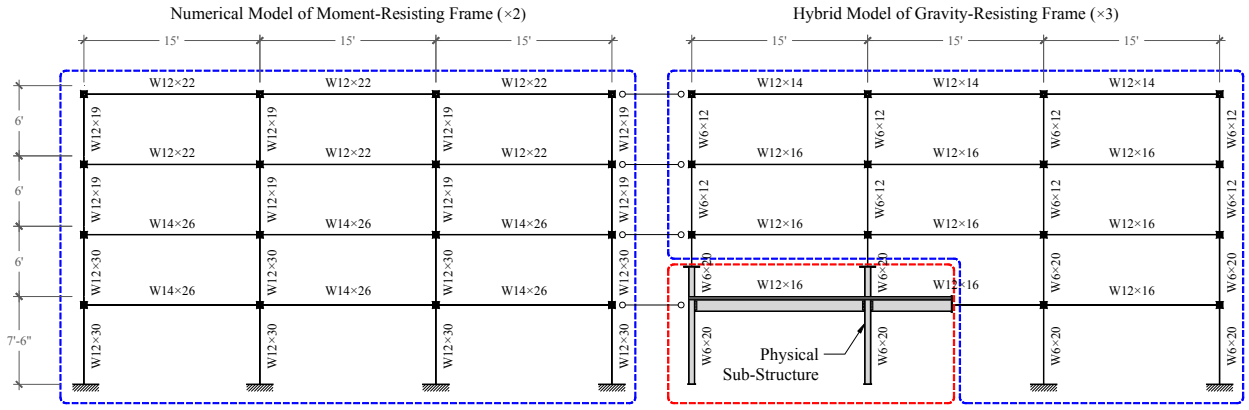


**Figure 4-5 Schematic representation of Hybrid Model #2**

## 4.5 Ground Motion Selection and Testing Program

An effort was made to find historical earthquake records whose response spectra match approximately the design response spectra of the prototype building with the potential to induce sidesway collapse of the moment frame without the use of large amplitude scale factors. In addition, only ground motions with short duration were considered for the hybrid simulations due to the following time constraint. A fixed time interval is required by each data communication procedure in hybrid simulation to calculate and send

the displacement command vector to the physical sub-structure, load the specimen and to obtain the corresponding force feedback vector. This coupled with the constraint that the hybrid simulation needs to be carried out within the eight hours of daily operation of the laboratory, yield a limit on the number of communication steps and therefore a limit on the duration of the ground motion. For this reason, the 1989 Loma Prieta earthquake recorded at Los Gatos Presentation Center (LGPC) was selected for the hybrid simulations. The duration of this ground motion is 25 seconds. However, before scaling down the ground motion by the time scale factor ($S^{1/2}$ = 0.707) for similitude, the original LGPC ground motion was shortened in length from 25.0 to 21.5 sec. due to the aforementioned time constraints by eliminating the initial 3.0 and final 0.5 sec. of the ground motion where small amplitude motion is observed. On the other hand, frequencies above 20 Hz. were filtered out from the ground motion to help convergence of the numerical integration method. Several spikes were observed in the original ground motion record, which increased the number of iterations required for convergence, since such spikes in acceleration produce large unbalanced forces. Figure 4-6 presents the acceleration response spectrum for the original ground motion and the modified ground motion (shortened and filtered) as well as the design spectrum.

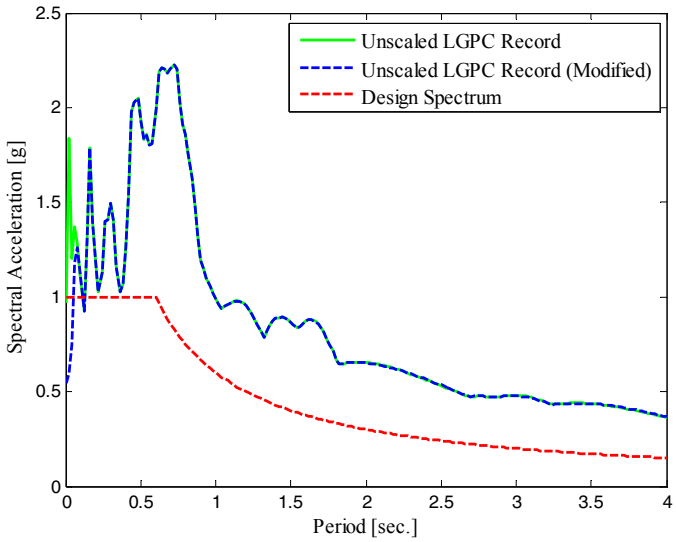


**Figure 4-6 Acceleration response spectrum of 1989 Loma Prieta ground motion recorded at Los Gatos Presentation Center station and design spectrum of prototype building**

The two hybrid models presented in Section 4.4.5 and Section 4.4.6 were subjected to increasing intensities of the LGPC ground motion shown in Table 4-6 to obtain information on the elastic response of the frame structures all the way to collapse. The last three hybrid simulations, in which the frame structures exhibited inelastic response, were conducted in a sequential fashion to carry over any residual

response to the next test in both physical and numerical sub-structures. These intensities were chosen based on pre-test numerical predictions so that the frame structures respond elastically (25% LGPC), with moderate levels of yielding (100% LGPC), severe levels of yielding (160% LGPC), and to collapse (200% LGPC). Sidesway collapse was predicted and observed in the first series of hybrid simulations at 200% of the LGPC. However, for the second series of hybrid simulation, collapse was prevented due to the addition of the gravity frames.

The 100% LGPC ground motion represents a maximum considered earthquake (MCE) ground motion. A design level earthquake (60% LGPC) ground motion intensity was not included in the testing program due to the aforementioned time constraints and because it was predicted that this ground motion intensity induced only mild levels of yielding. Various preliminary tests were conducted with the physical sub-structures prior to the two series of hybrid simulations to verify the hybrid simulation software and laboratory equipment and to identify the elastic properties of the physical test specimens. A detailed summary of all these preliminary tests is presented in Section 7.

**Table 4-6 Ground motion intensities used in testing protocol of hybrid simulations**

| Intensity | Test Description |
|---|---|
| 25% LGPC | Elastic hybrid simulation at 25% of the unscaled LGPC earthquake record (Service Level Earthquake). |
| 100% LGPC | Inelastic hybrid simulation at 100% of the unscaled LGPC earthquake record (Maxicum Considered Earthquake). |
| 160% LGPC | Inelastic hybrid simulation at 160% of the unscaled LGPC earthquake record (Near Collapse Level Earthquake). |
| 200% LGPC | Inelastic hybrid simulation at 200% of the unscaled LGPC earthquake record (Collapse Level Eartquake). |

# SECTION 5
# DESIGN AND CONSTRUCTION OF PHYSICAL SUB-STRUCTURES

## 5.1 Overview

This section presents a detailed description of the physical sub-structures selected for the two series of hybrid simulations briefly introduced in Section 4. As mentioned before, the physical sub-structures consisted of one and one-half bay by one and one-half story subassemblies of a moment and gravity frames. This section discusses the design, construction and instrumentation of the physical sub-structures as well as details of the experimental test setup used for the collapse hybrid simulations. At the end of this section, a gravity load analysis of the physical sub-structures is provided.

## 5.2 Physical Sub-Structure #1: Subassembly of Special Steel Moment Frame

### 5.2.1 Description

A physical subassembly of a special steel moment frame was tested in the first series of hybrid simulations as briefly described in Section 4. Figure 5-1 presents an elevation and a cross section of the physical sub-structure referred to hereafter as Physical Sub-Structure #1 or Test Specimen #1. Although the moment frames are located around the perimeter of the prototype building, the composite floor slab of the physical model shown in Figure 5-1 was constructed at both sides of the girder to maintain symmetry and minimize any potential out-of-plane response of the test specimen. The composite floor slab was constructed such that the ribs of the metal deck were oriented parallel to the girder.

The W8×10 floor beams or joists shown in Figure 5-1 were also included in the Physical Sub-Structure #1 to support the weight of the concrete floor slab and steel plates used to simulated gravity loads on the test specimen. The HSS6×6×½ loading beam shown in Figure 5-1 was provided as part of the experimental test setup to transfer the loads from a horizontal actuator to the test specimen. This HSS6×6×½ loading beam is further described in the subsequent sections.

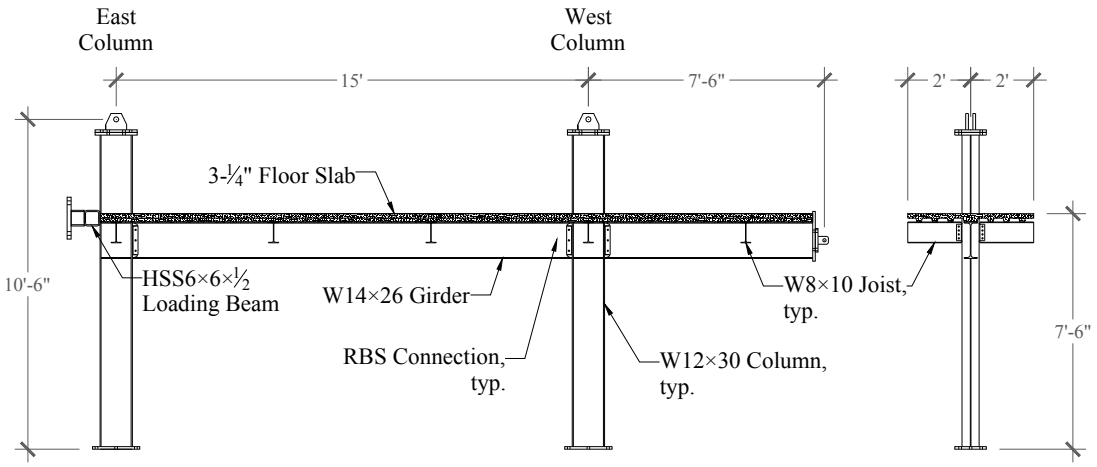


**Figure 5-1 Physical Sub-Structure #1: subassembly of special steel moment frame**

Figure 5-2 and Figure 5-3 show details of the RBS moment connections at the east and west joints of the test specimen, respectively. As mentioned before, the RBS moment connections were detailed following the recommendation of the AISC 358-10 Standard (AISC, 2010a). The doubler plate provided at the west joint was attached to the web of the column through four 3/4"-diameter plug welds and welded around the perimeter, which consisted of 3/16" fillet welds at the top and bottom sides and groove welds at the lateral sides. The material of all wide-flange sections and steel plates (continuity plates, shear-tab plates, doubler plates, etc.) was A572 Grade 50 steel.

A cross section of the composite floor slab is shown in Figure 5-4. Lightweight concrete with a specified concrete strength of 3000 psi at 28 days and a maximum aggregate size of ½" was used for the composite floor slab. A 20-gage type B steel deck manufactured by Vulcraft was selected. A standard 6×6-W1.4×W1.4 welded wire mesh was placed over the entire area of the floor slab. Also, as seen in Figure 5-1, #3 reinforcing bars spaced at 12 in. were provided across the W14×26 girder for crack control due to gravity loading. Shear studs with a diameter of 3/8" and a length of 2-½" were provided along the girder (at 6 in. on center) and floor beams (at each metal deck rib). A complete set of drawings of the test specimen is provided in Appendix A.

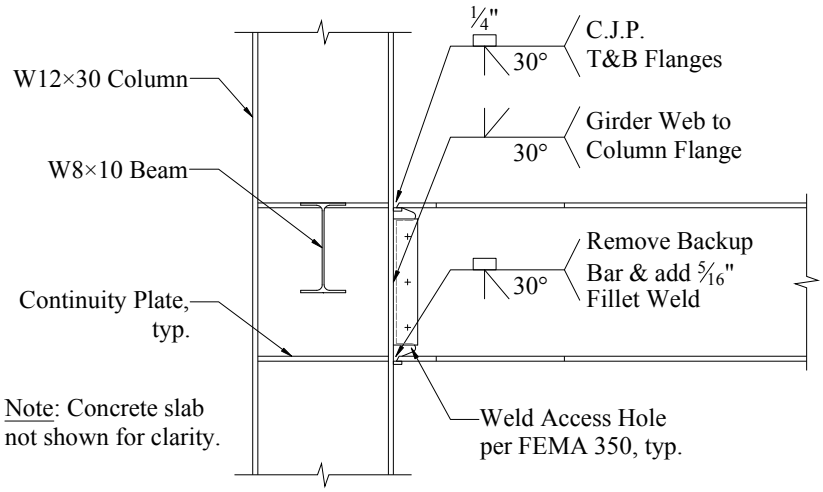


(a) Front Elevation

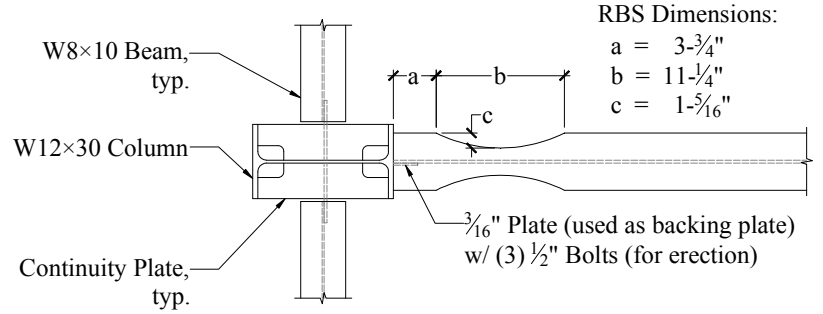


(b) Top View

**Figure 5-2 Details of RBS moment connection at east joint of Physical Sub-Structure #1**

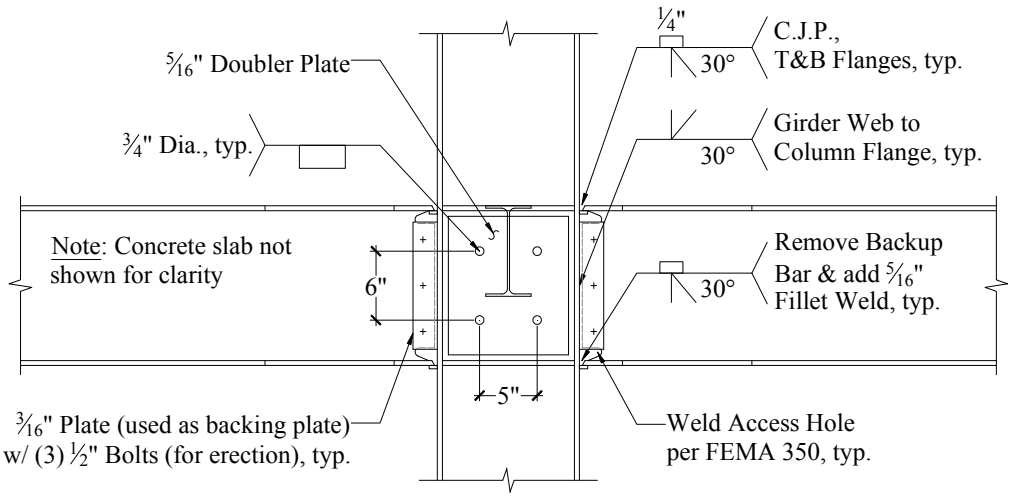


(a) Front Elevation

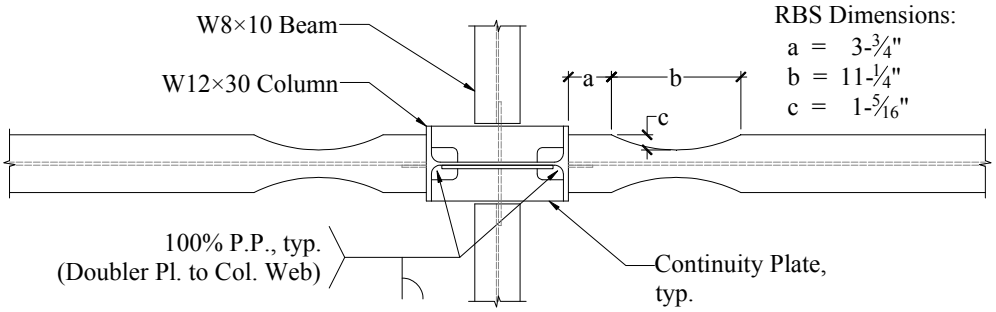


(b) Top View

**Figure 5-3 Details of RBS moment connections at the west joint of Physical Sub-Structure #1**

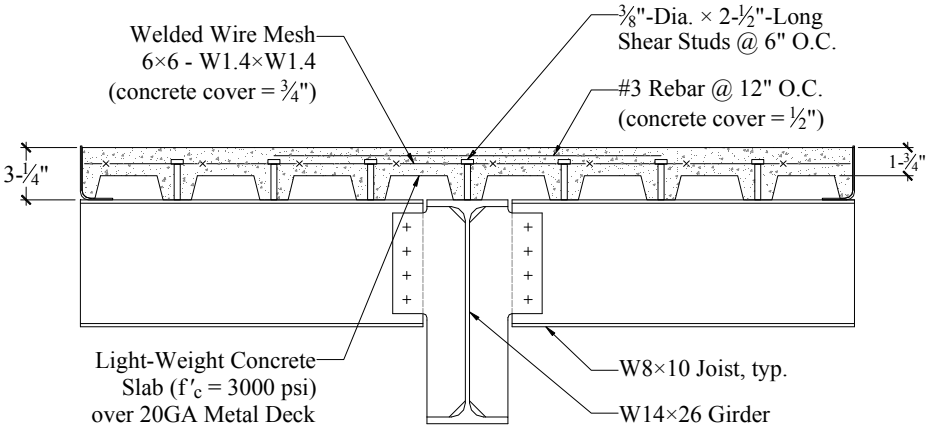


**Figure 5-4 Cross section of composite floor slab of Physical Sub-Structure #1**

### 5.2.2 Construction

The physical specimen was fully fabricated at K&E Fabricating Co. Inc. and subsequently transported to the laboratory for testing. Figure 5-5(a) and Figure 5-5(b) show respectively a photograph of the physical specimen and connection details of the east joint during construction and prior to installation of the composite floor slab. It can be seen in Figure 5-5(a) that temporary bracing was provided to avoid undesired deformations of the test specimen during construction. The closure plate provided for pouring of concrete can be seen in Figure 5-5(a) and Figure 5-5(b). Details of the composite floor slab prior to pouring of concrete are shown in Figure 5-5(c) including metal deck, shear studs, welded wire mesh and reinforcing steel bars. It can be seen in this figure that the #3 reinforcing bars were welded to the shear studs to be held in place before pouring of concrete. The physical specimen was mounted on the strong floor of the testing facility and attached through the use of two 9'×5'×1½" base plates provided at the interface of the physical specimen and the strong floor as shown in Figure 5-5(d) for the west column. The base plates of the columns of the physical specimen were attached to the interface 9'×5'×1½" base plates as seen in the structural drawings provided in Appendix A. The interface base plates were anchored to the strong floor using ten 1½" anchor bolts per plate. One of these anchor bolts is detailed in Figure 5-5(d). Base on conservative simple hand calculations, the 9'×5'×1½" base plates connected to the strong floor (selected based on available material in the laboratory) were verified to be sufficiently strong to allow for the development of the full plastic moment capacity of the columns of the special steel moment frame test specimen. However, the 9'×5'×1½" base plates connected to the strong floor provided some flexibility at the base of the columns of the physical test specimen, which was subsequently measured using the instrumentation system presented in the next section. Experimental data on the flexibility at the base of the columns of the test specimen is presented afterward in Section 7.2.1.

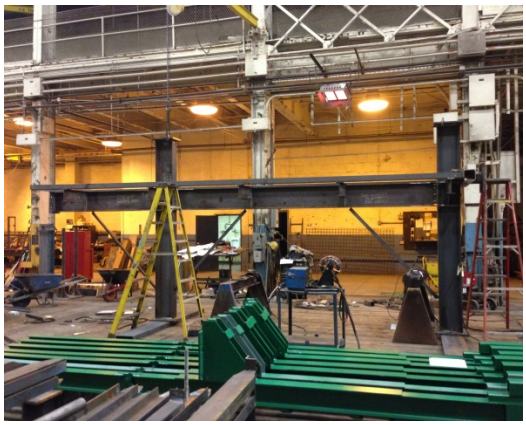

(a) Overview of specimen at construction site

(b) East joint of test specimen

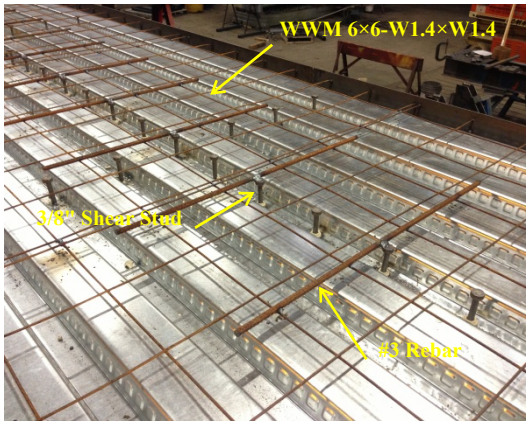


(c) Metal deck, WWM, shear studs and rebars

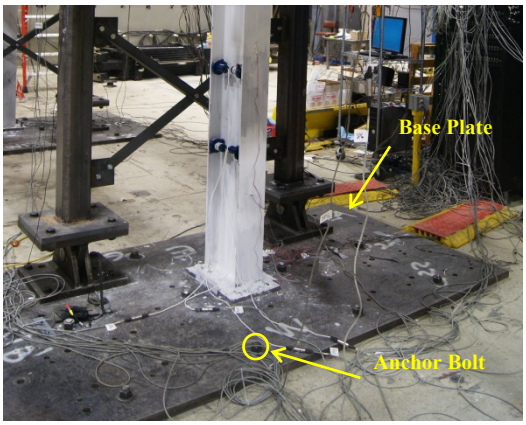


(d) Interface 9'×5'×1½" plate at west column

**Figure 5-5 Selected photographs during construction and installation of Physical Sub-Structure #1**

A total of four steel coupons were tested for each structural component, namely, W12×30 column and W14×26 girder (two coupons from web and two from flange). Figure 5-6 presents stress-strain relationships for all steel coupons of the W12×30 column and W14×26 girder sections. Table 5-1 summarizes the yield ($F_y$) and ultimate ($F_u$) stresses for each steel coupon. While the four steel coupons for the W14×26 girder exhibit approximately the same yield stress of 50 ksi, the steel coupons for the W12×30 section presents two distinct yield stress values for the web and flanges of 58 and 52 ksi, respectively.

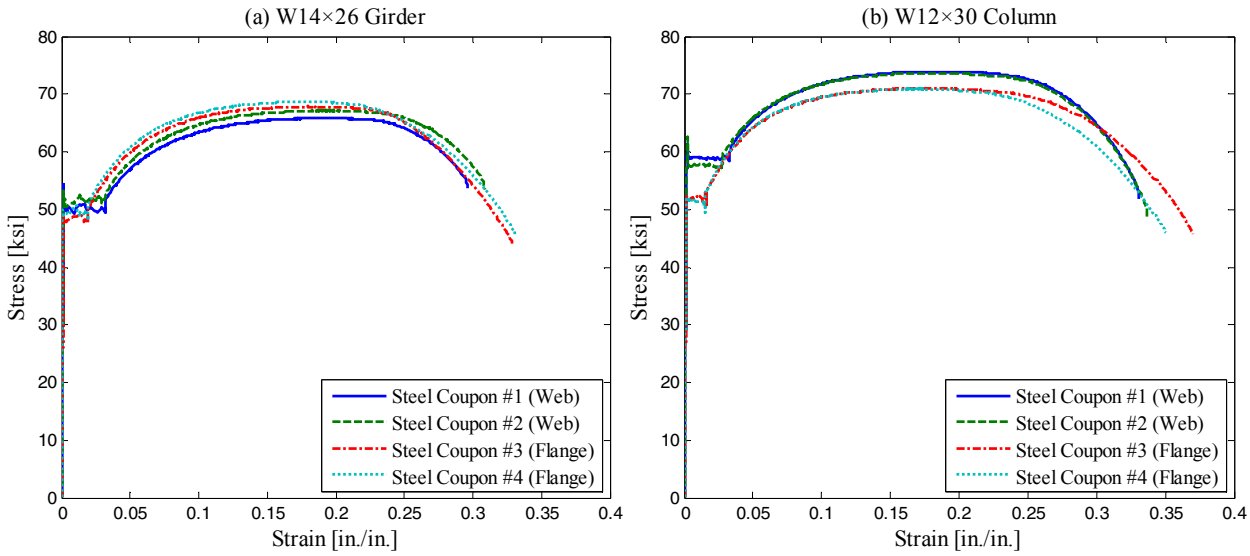


**Figure 5-6 Stress-strain relationships for the W14×26 girder and W12×30 column sections of Physical Sub-Structure #1**

**Table 5-1 Material properties for steel coupons of Physical Sub-Structure #1**

| Coupon # | Location | W14×26 Girder | | W12×60 Column | |
|---|---|---|---|---|---|
| | | $F_y$ [ksi] | $F_u$ [ksi] | $F_y$ [ksi] | $F_u$ [ksi] |
| 1 | Web | 50.1 | 65.9 | 58.8 | 73.9 |
| 2 | Web | 51.4 | 67.2 | 57.6 | 73.6 |
| 3 | Flange | 48.4 | 67.9 | 52.1 | 71.0 |
| 4 | Flange | 49.7 | 68.7 | 51.5 | 70.9 |

Similarly, Table 5-2 summarizes the results of standard concrete cylinder tests. A total of four concrete cylinders were tested for the physical test specimen. The compressive strength values shown in Table 5-2 are for individual tests. Two concrete cylinders were tested at 28 days and the remaining two on the day of the hybrid testing (at 70 days). It can be seen in Table 5-2 that the minimum specified concrete strength was not reached at 28 days. However, on the day of hybrid testing, the concrete strength reached an average value of approximately 3500 psi. All concrete cylinders were instrumented with 4 linear potentiometers as shown in Figure 5-7(a) to obtain stress-strain relationships for the material. However, reliable results were obtained only for 2 concrete cylinders. These results are presented in Figure 5-7(b) where maximum stress values are indicated. The modulus of elasticity of the concrete obtained from Figure 5-7(b) is approximately 2000 ksi. This measured value is comparatively smaller than the value predicted by ACI 318-08 (ACI, 2008) equal to 2566 ksi.

**Table 5-2 Compressive strength of standard cylinders for concrete slab of Physical Sub-Structure #1**

| Concrete Cylinder # | Age of Concrete Cylinder [days] | Compressive Strength [psi] |
|---|---|---|
| 1 | 28 | 2395 |
| 2 | 28 | 2379 |
| 3 | 70 | 3632 |
| 4 | 70 | 3510 |


(a) Standard cylinder test

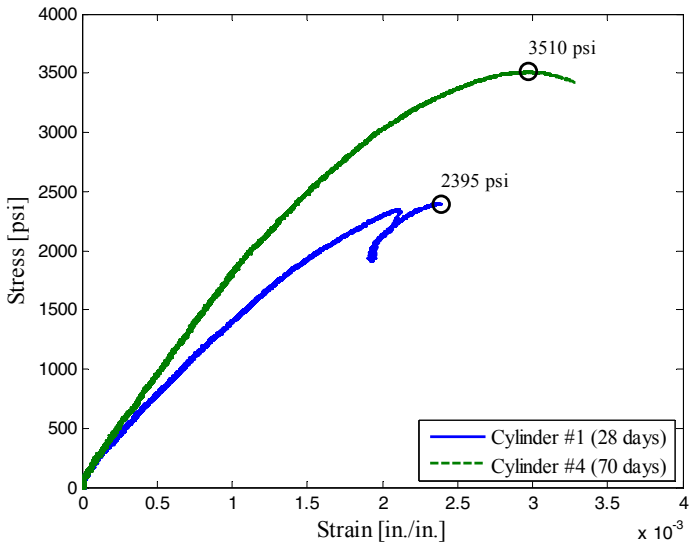


(b) Stress-strain relationship for selected concrete cylinders

**Figure 5-7 Stress-strain relationships for selected lightweight concrete cylinders of Physical Sub-Structure #1**

### 5.2.3 Instrumentation

The instrumentation system of the test specimen was designed to measure key response parameters including bending moments, chord rotation of girders and columns at plastic-hinge regions, panel zone shear distortions and deformation of the west column base plate (3D deformation). A description of the instrumentation systems is provided below.

#### 5.2.3.1 Uniaxial Strain Gages

A total of thirty nine uniaxial strain gages were strategically attached to the steel components of Physical Sub-Structure #1 as shown in Figure 5-8(a) to indirectly obtain the distribution of bending moments and

axial forces along girders and columns. The strain gages were grouped at different plane cross sections of girders and columns as shown in Figure 5-8(b). These groups were identified by one or two letters followed by a number, which denotes the steel member (EC: east column, WC: west column, or G: girder) and the location of the strain gage group along the member (cross section 1, 2 or 3), respectively. All these groups of strain gages were installed at regions of elastic response of steel components so that the stress distribution at a cross section could be derived from the engineering strain measurements using linear-elastic relationships from engineering mechanics principles. From the derived stress distribution at a cross section, bending moments and axial forces could then be obtained. However, due to the highly nonlinear response of the concrete at the composite floor slab, the derived bending moments and axial forces at girders sections were still of approximate nature.

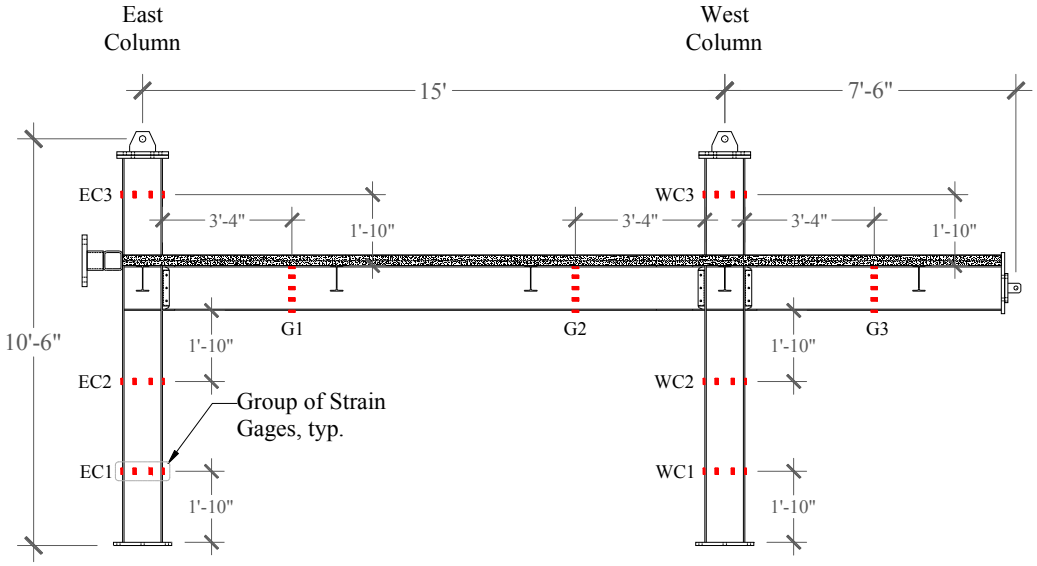


(a) Location of strain gages installed on Physical Sub-Structure #1

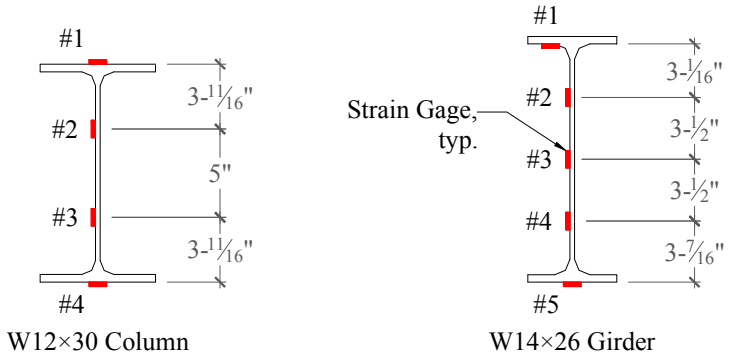


(b) Location of strain gages at a girder and column cross section of Physical Sub-Structure #1

**Figure 5-8 Location of groups of uniaxial strain gages on Physical Sub-Structure #1**

### 5.2.3.2 String and Linear Displacement Potentiometers

Eighteen string displacement potentiometers (string pots) and four linear displacement potentiometers (linear pots) were installed on Physical Sub-Structure #1 as shown in Figure 5-9 to measure chord rotations at plastic-hinge regions of columns and girders and panel zone distortions, respectively. Chord rotations were measured over a chord length of 26" for columns and 30" for girders as shown in Figure 5-9. A V-shaped arrangement of two linear pots was provided at each panel zone since the W8×10 joists, framing perpendicular to the panel zone, precluded the use of the classical X-shaped arrangement. Four additional string pots, not shown in Figure 5-9, were used to measure the out-of-plane response of the test specimen (one string pot was attached at each joint of the test specimen) and the relative displacement of the two horizontal actuators with respect to the ground floor (one string pot was placed at the head of each horizontal actuator). The string pots placed at the horizontal actuators helped synchronize the data from the different instrumentation systems.

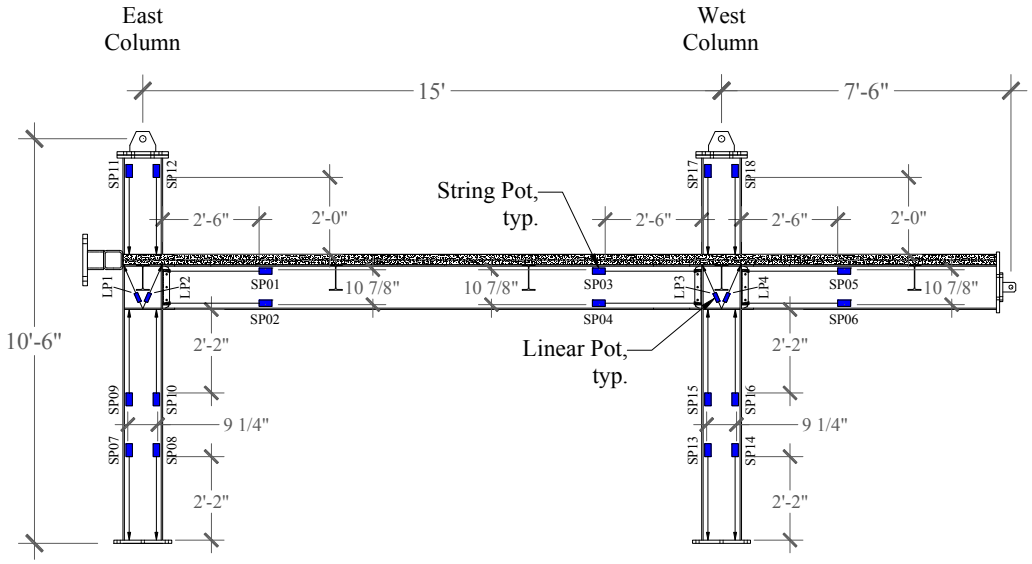


**Figure 5-9 String and linear displacement potentiometers installed on Physical Sub-Structure #1**

### 5.2.3.3 Krypton Coordinate Tracking System

A total of twenty-seven LEDs were attached at different locations around the east column of Physical Sub-Structure #1 as shown in Figure 5-10. The Krypton Coordinate Tracking System (or simply Krypton System) is a measuring device that tracks the three-dimensional position of infrared LEDs with a system of cameras. Due to limitations of the field of view of the camera system, LEDs could not be placed

around the entire physical test specimen. The arrangement of LEDs shown in Figure 5-10 permitted obtaining the following response parameters: chord rotations at the plastic-hinge regions of the west column and the girder near the west column, distortions of the east panel zone and rotation and vertical and horizontal displacement of the east column base plate. These response parameters were also obtained using the string and linear pots presented in the previous section. However, the chord rotations measured with the Krypton System were obtained over a chord length of approximately 18" for the top plastic-hinge region of the first-story column, 13" for the bottom plastic-hinge region of the first-story column, and 24" for the plastic-hinge region of the girder near the west column as shown in Figure 5-10, which were different from those of the arrangement of string pots.

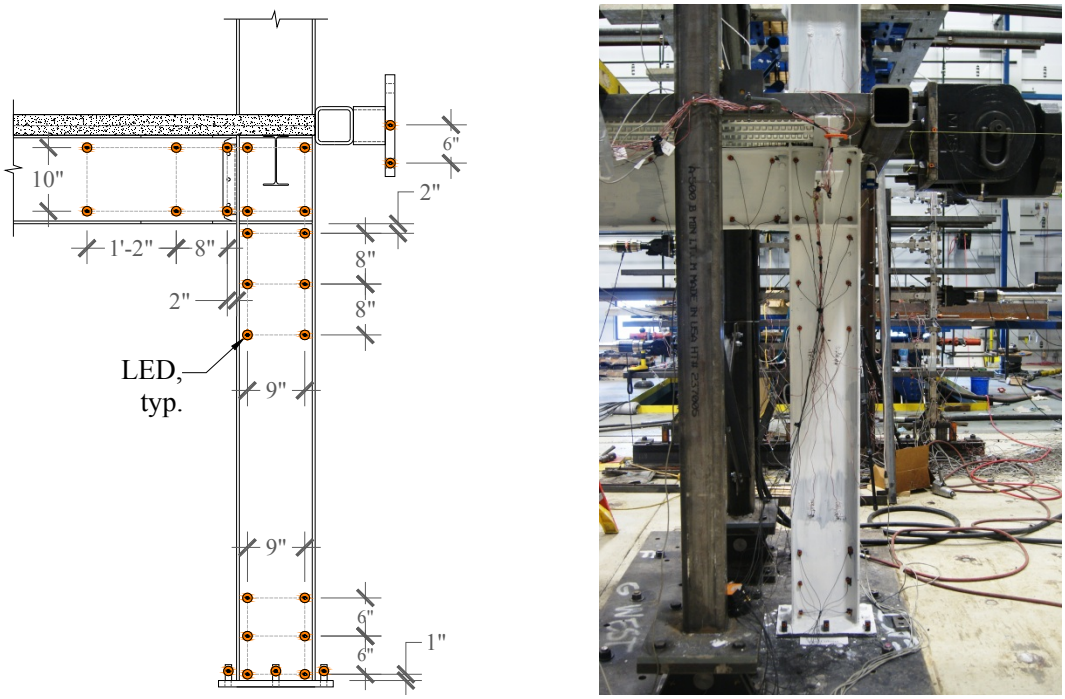


(a) Approximate location of LEDs at east col. (b) Photograph of east column with LEDs

**Figure 5-10 Physical Sub-Structure #1 instrumented with Krypton system**

A total of eight digital video cameras were used to document the progress of damage of the physical test specimen. The videos are available at the NEES central repository (nees.org/warehouse/welcome).

## 5.3 Physical Sub-Structure #2: Subassembly of Gravity Frame

### 5.3.1 Description

The physical sub-structure in the second series of hybrid simulations consisted of a gravity frame subassembly. Figure 5-11 presents an elevation and a cross section of the physical test model hereafter referred to as Physical Sub-Structure #2 or Test Specimen #2. It can be seen that the gravity frame subassembly shown in Figure 5-11 was constructed assuming that all columns of the three-bay gravity frames in the direction of loading had the same member size and were oriented in the strong axis. However, the exterior columns of these three-bay gravity frames were part of the moment frames in the orthogonal direction, as shown in the plan view of the prototype building in Figure 4-1.

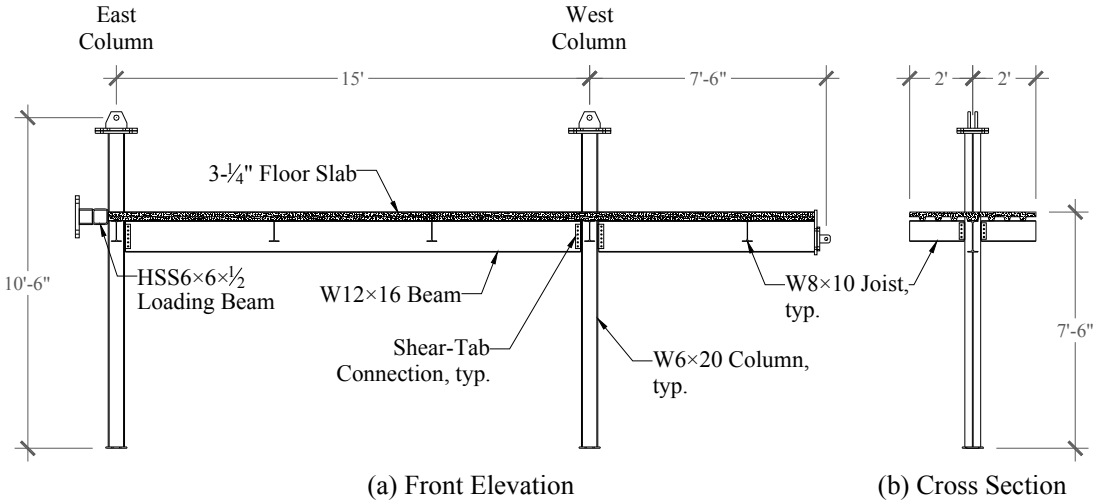


**Figure 5-11 Physical Sub-Structure #2: subassembly of gravity frame**

Similar to the previous physical test specimen, the gravity frame test specimen was constructed with a composite floor slab (see Figure 5-4 for reference). Floor joists (W8×10) were included to support the weight of the concrete floor slab as well as the steel plates used to simulate gravity loads on the elevated floor of the test specimen. As mentioned earlier, the HSS6×6×½ loading beam shown in Figure 5-11 was provided as part of the experimental test setup to transfer the loads from a horizontal actuator to the test specimen. This HSS6×6×½ loading beam is further described in subsequent sections.

Details of the shear-tab connection of the half-scale gravity frame physical subassembly are shown in Figure 5-12. As indicated before, dimensions of the connection, such as thickness of the shear-tab plate, bolt spacing, bolt edge distance, size of fillet weld, and gap distance between beam and column were

exactly half of those of the full-scale connection, except for the ½" bolts. A complete set of drawings is provided in Appendix B.

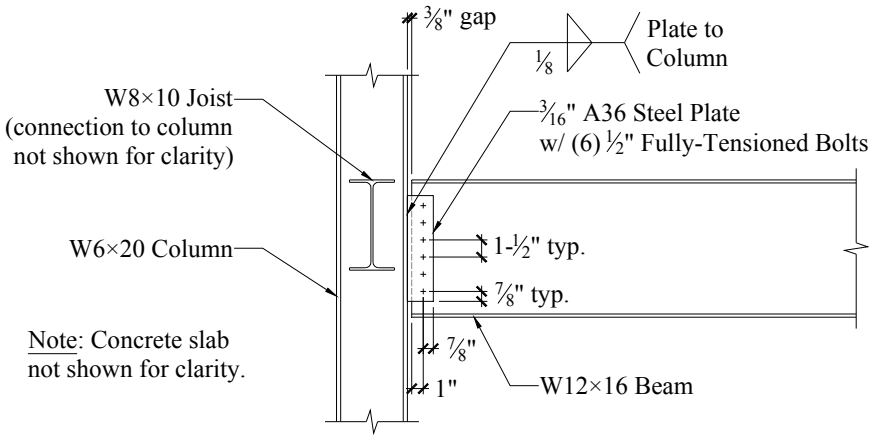


**Figure 5-12 Typical shear-tab connection detail for Physical Sub-Structure #2**

### 5.3.2 Construction

Similar to the previous physical model, the gravity frame test specimen was entirely constructed at K&E Fabricating Co. Inc. and subsequently transported to the testing facility. Figure 5-13(a) shows a photograph of the metal deck of the test specimen near the east column before the pouring of concrete. The HSS6×6×½ loading beam shown in Figure 5-13(a) was welded to the column of the test specimen and connected to the composite floor slab using four threaded rods embedded in the concrete slab, as shown in Figure 5-13(a). Details of the connection of the HSS6×6×½ loading beam to the test specimen can be found in Appendix B (structural drawings S2.06 and S2.07). The threaded rods were placed at a distance of 12" from the centerline of the beam to avoid strengthening the simple connection. Liu and Astaneh-Asl (2000b) reported that additional reinforcement placed near a simple connection did not significantly increase the resistance of the test subassembly. To avoid cracking of the concrete slab of the test specimen (which was more slender than the previous physical model) during transportation to the laboratory, a temporary bracing system was provided as shown in Figure 5-13(b). The temporary framing system consisted of braces and struts underpinning the cantilever beam and joists. The bracing system was removed before placement of the test specimen on the strong floor. Figure 5-13(d) shows a photograph of the test specimen during installation on the strong floor. The test specimen was connected to the strong floor using two 9'×5'×1½" interface plates similar to the previous test specimen. Typical simple connection details (see Appendix B, structural drawing S2.09) were provided at the base of the columns of the gravity frame physical subassembly. Although these simple connections are commonly

assumed as pinned, such connections provide some level of flexibility at the base of the columns that was measured with the Krypton System.

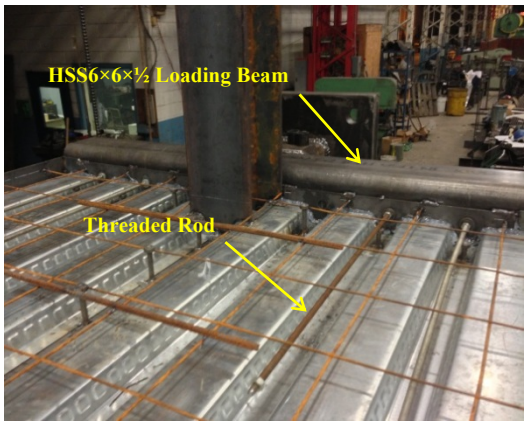


(a) HSS6×6×½ loading beam and threaded rods

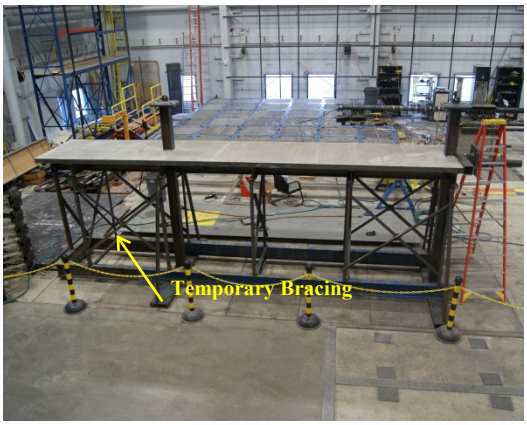


(b) Physical Sub-Structure #2 at NEES Site at UB

(c) West joint of gravity frame test specimen

(d) Placement of Physical Sub-Structure #2

**Figure 5-13 Selected photographs during construction and installation of Physical Sub-Structure #2**

Except for the A36 steel 3/16" shear-tab plate used in the simple connections (see Figure 5-12), all wide-flange sections and other plates are A572 Grade 50 steel. Similar to the previous test specimen, four steel coupons were tested for the W12×16 girder, W6×12 column and 3/16" shear-tab plate. Figure 5-14 presents stress-strain relationships for the steel coupons. Table 5-3 summarizes the yield ($F_y$) and ultimate ($F_u$) stresses of all steel coupons. The values shown in Table 5-3 are for individual tests. The average yield stress values for the W12×16 and W6×20 coupons are 49 and 53 ksi, respectively. However, the engineering stress-strain relationship for the A36 steel plate does not present a well-defined yield stress point. Therefore, Table 5-3 reports the yield stress of the A36 steel plate at an offset strain of 0.2%. Four concrete cylinders were tested. Two concrete cylinders were tested at 28 days and the remaining 2

cylinders on the day of hybrid testing (at 52 days). Table 5-4 summarizes the results of the standard concrete cylinder tests. The compressive strength of cylinder #4 was not recorded due to a malfunction of the instrumentation equipment. Although all concrete cylinders were instrumented with 4 linear pots as mentioned before, no reliable data were obtained to plot strain-stress relationships for the material.

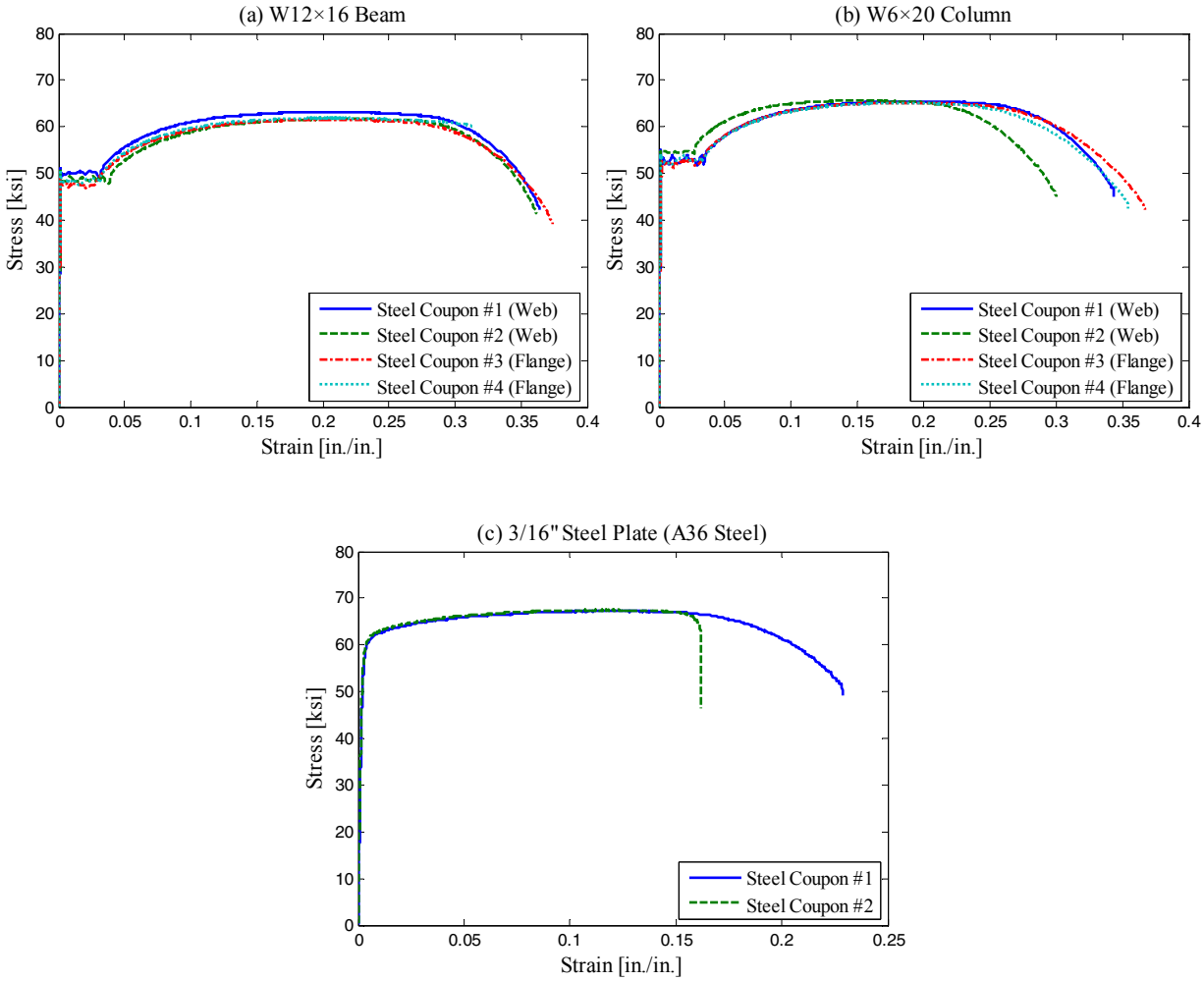


**Figure 5-14 Stress-strain relationships for W12×16 beam, W6×20 column and A36 shear-tab plate of Physical Sub-Structure #2**

**Table 5-3 Material properties for steel coupons of Physical Sub-Structure #2**

| Coupon # | Location | W12×16 Beam | | W6×20 Column | | A36 Steel Plate | |
|---|---|---|---|---|---|---|---|
| | | $F_y$ [ksi] | $F_u$ [ksi] | $F_y$ [ksi] | $F_u$ [ksi] | $F_y$ [ksi] | $F_u$ [ksi] |
| 1 | Web | 50.1 | 63.1 | 52.8 | 65.5 | 59.9 | 67.3 |
| 2 | Web | 48.8 | 61.8 | 54.6 | 65.7 | 60.3 | 67.5 |
| 3 | Flange | 47.6 | 61.6 | 52.4 | 65.2 | – | – |
| 4 | Flange | 48.4 | 61.9 | 53.0 | 65.1 | – | – |

**Table 5-4 Compressive strength of standard cylinders for concrete of Physical Sub-Structure #2**

| Concrete Cylinder # | Age of Concrete Cylinder [days] | Compressive Strength [psi] |
|---|---|---|
| 1 | 28 | NA |
| 2 | 28 | 3270 |
| 3 | 51 | 3672 |
| 4 | 51 | 3757 |

### 5.3.3 Instrumentation

The instrumentation plan for Physical Sub-Structure #2 is similar to that of the previous test specimen. A brief description of the instrumentation, highlighting the differences with the instrumentation system of Physical Sub-Structure #1, is presented in the following sections.

#### 5.3.3.1 Uniaxial Strain Gages

A total of forty-three uniaxial strain gages were employed in the second series of hybrid simulations. Thirty nine of them were attached to the test specimen similar to the previous test specimen. Figure 5-15 shows the strain gages on the Physical Sub-Structure #2. Bending moments and axial forces were obtained with the measurements of the strain gages as explained earlier in Section 5.2.3.1.

The remaining four strain gages were placed on a vertical link member which was part of the experimental test setup (described later in Section 5.4). The vertical link member was provided to underpin the girder in cantilever. Axial forces on this vertical link member were obtained using the strain gage measurements. These axial forces were subsequently used to derive bending moments along the girder in cantilever. The vertical link member was not instrumented for the first series of hybrid simulations.

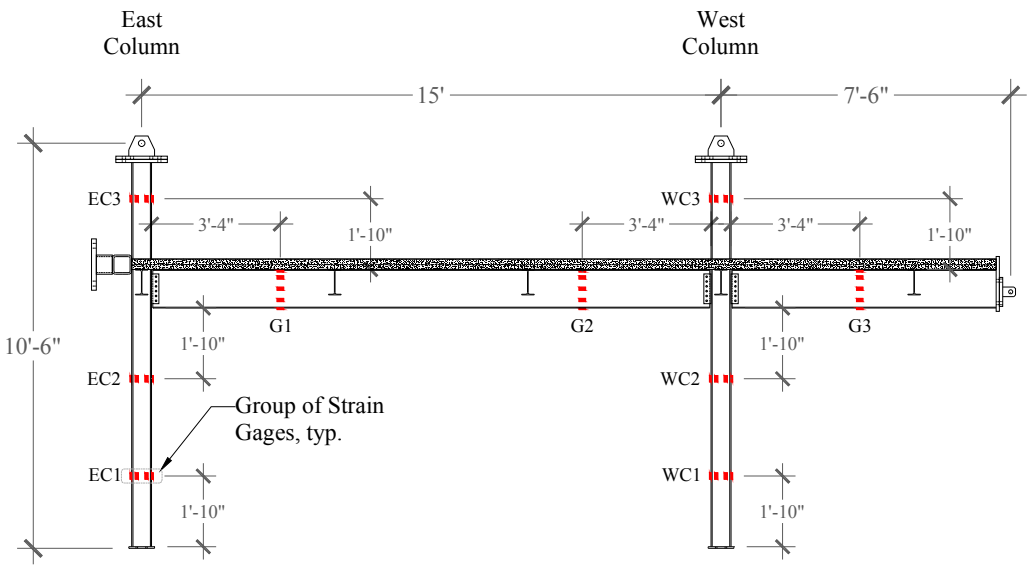


(a) Location of strain gages installed on Physical Sub-Structure #2

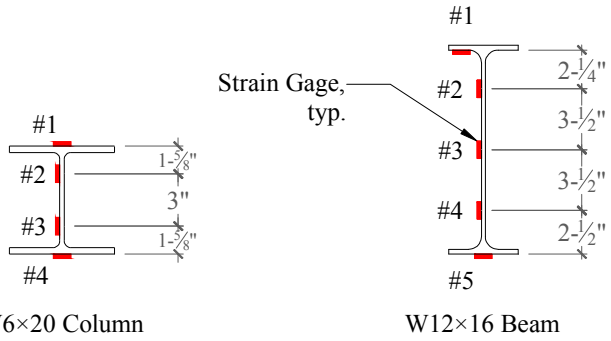


(b) Location of strain gages at a beam and column cross section of Physical Sub-Structure #2

**Figure 5-15 Location of groups of uniaxial strain gages on Physical Sub-Structure #2**

### 5.3.3.2 String and Linear Displacement Potentiometers

Eighteen string pots and six linear pots were installed on Physical Sub-Structure #2 as shown in Figure 5-9 to measure chord rotations at plastic-hinge regions within a chord length of 26" for columns and 30" for beams. Unlike the previous test specimen where the linear pots were used to obtain panel zone distortions, the aforementioned six linear pots were employed to obtain rotations of the three shear-tab connections (2 linear pots per connection).

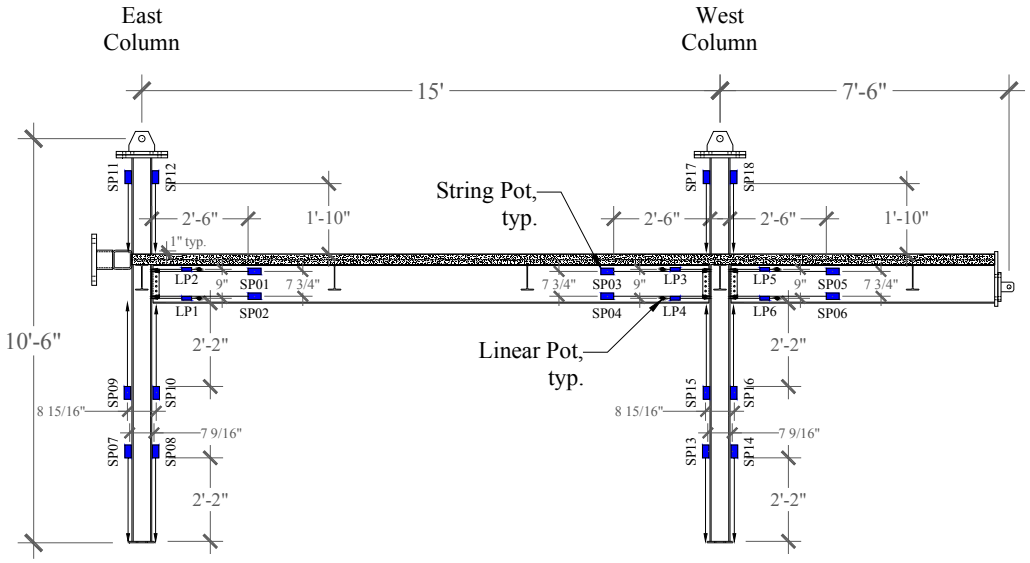


**Figure 5-16 String and linear displacement potentiometers installed on Physical Sub-Structure #2**

Four additional string pots, not shown in Figure 5-9, were used to measure the out-of-plane response of the test specimen (one string pot was attached at each joint of the test specimen) and the relative displacement of the two horizontal actuators with respect to the ground floor (one string pot was placed at the head of each horizontal actuator).

#### 5.3.3.3 Krypton Coordinate Tracking System

A total of 25 LEDs were attached around the east column of Physical Sub-Structure #2 to obtain chord rotations of columns at plastic-hinge regions, rotations of shear-tab connections, and displacement and rotation of the east column base plate. Note that the column chord rotations were measured over a length of approximately 12", which is different from the chord lengths measured by the string pots. LEDs could not be attached at the corners of a potential panel zone, given its small dimensions. However, 2 LEDs were placed at the free edge of the flanges near the corner of the panel zone.

A total of eight digital video cameras were used to document the progress of damage of the physical test specimen. The videos are available at the NEES central repository (nees.org/warehouse/welcome).

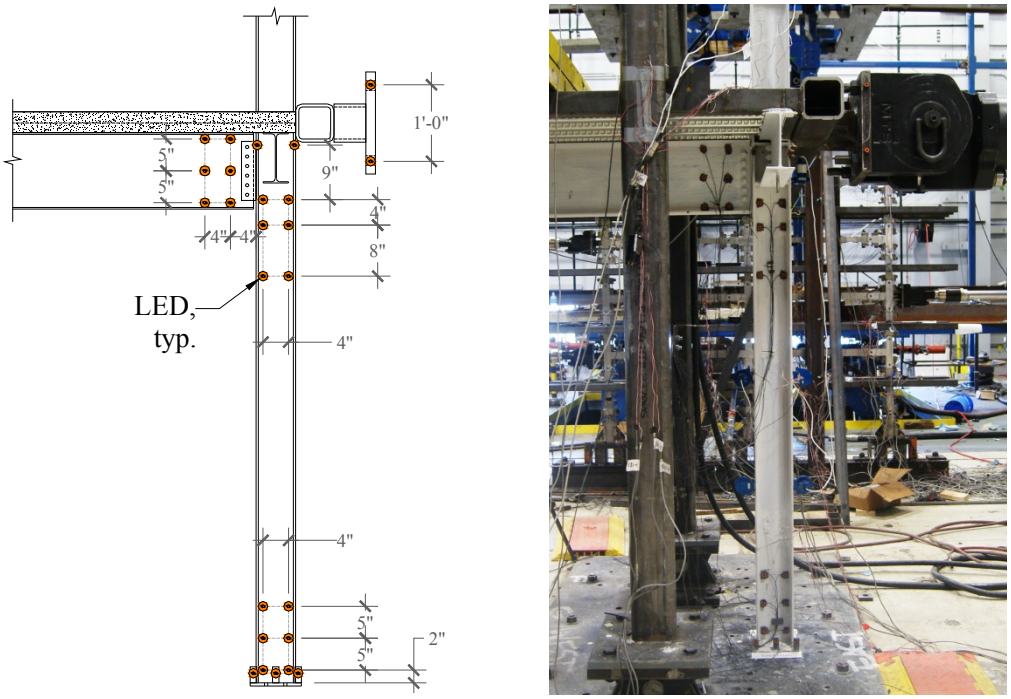


(a) Approximate location of LEDs at east col. (b) Photograph of east column with LEDs

**Figure 5-17 Physical Sub-Structure #2 instrumented with Krypton system**

## 5.4 Experimental Test Setup for Hybrid Simulation

The experimental test setup was designed to permit the application of lateral (seismic) as well as vertical (gravity) forces on the test specimens. Figure 5-18(a) and Figure 5-18(b) show an elevation and cross section, respectively, of the experimental test setup. Photographs of different views of the experimental test setup are shown in Figure 5-19. As mentioned earlier, the test specimens were anchored to the strong floor through two interface 9'×5'×1½" base plates. The end of the cantilever girder of the test specimen was supported (underpinned) with a vertical link member. A supporting frame surrounds the test specimens and provided out-of-plane support. The different elements of the supporting frame were connected through clevises so that the supporting frame sways and guides the test specimen in the direction of loading, as seen in Figure 5-18(c), providing minimal lateral resistance to the test specimen.

The two horizontal actuators shown in Figure 5-18 controlled the horizontal DOFs at the first and mid-second stories of the test specimens. The HSS6×6×½ loading beam shown in Figure 5-18 and Figure 5-19 was utilized to transfer the lateral forces from the bottom horizontal actuator to the test specimens. Details of the connection of the HSS6×6×½ loading beam to the test specimens can be found in Appendix A and Appendix B of this report. The horizontal DOFs at the top of the columns of the physical sub-structures

were coupled with a horizontal link member as seen in Figure 5-18(a). Two vertical force-controlled actuators imposed axial forces on the columns of the test specimen due to gravity loads of the stories above as well as earthquake-induced force variations from overturning forces. A reaction frame for these vertical actuators was mounted on the support frame. The gravity load at the elevated floor of the test specimens was simulated using steel plates of 8.5 kips of weight. While two steel plates were placed on the moment frame physical specimen as seen in Figure 5-19(b), four plates were used for the gravity frame physical specimen as seen in Figure 5-19(c), since the gravity load tributary area for a gravity frame is twice that of a moment frame, as can be seen in the plan view of the building structure in Figure 4-1(a). The reaction frame for the vertical actuators and the horizontal link member were connected through a vertical guide connection consisting of a steel pipe sliding inside another to uncouple the vertical connection and thus provide only horizontal connection.

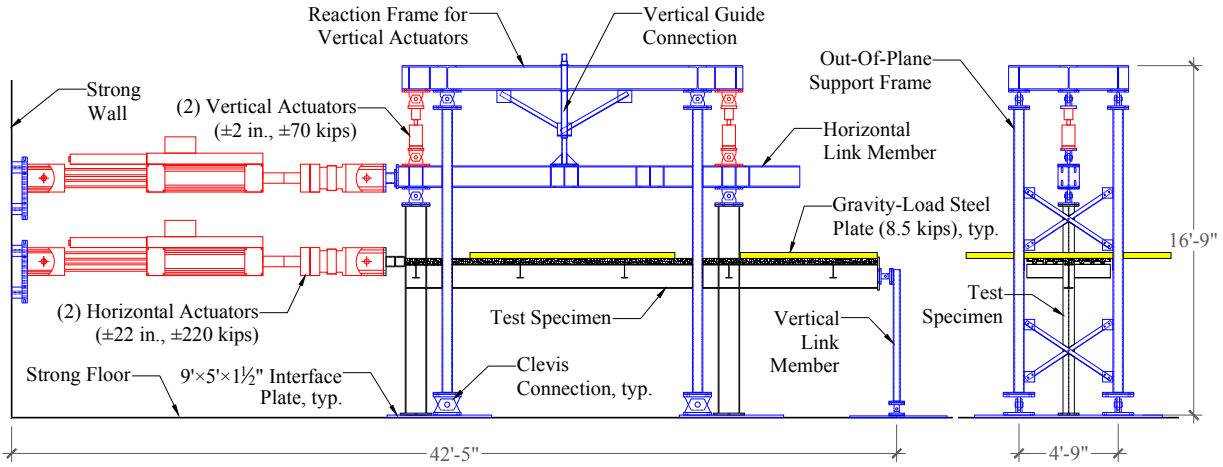


(a) Front Elevation (b) Cross Section

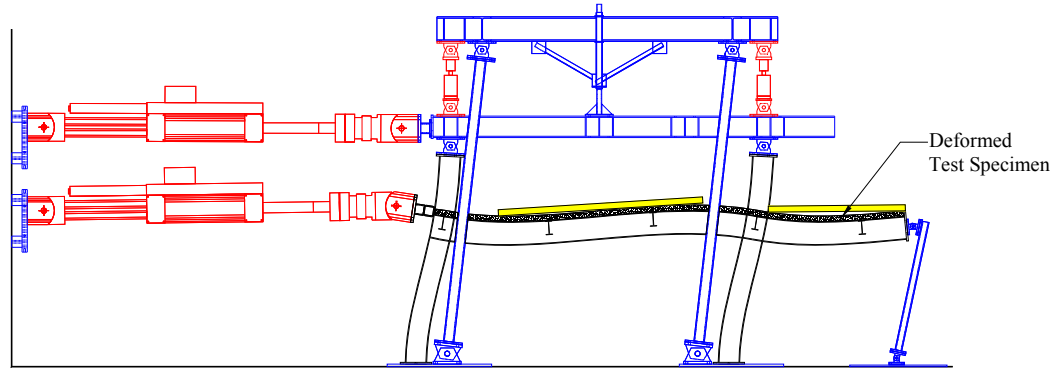


(c) Front Elevation (Deformed Configuration)

**Figure 5-18 Experimental test setup for collapse hybrid simulation**

(a) Panoramic south view of experimental test setup and Physical Sub-Structure #2

(b) North-east view of test setup and Physical Sub-Structure #1

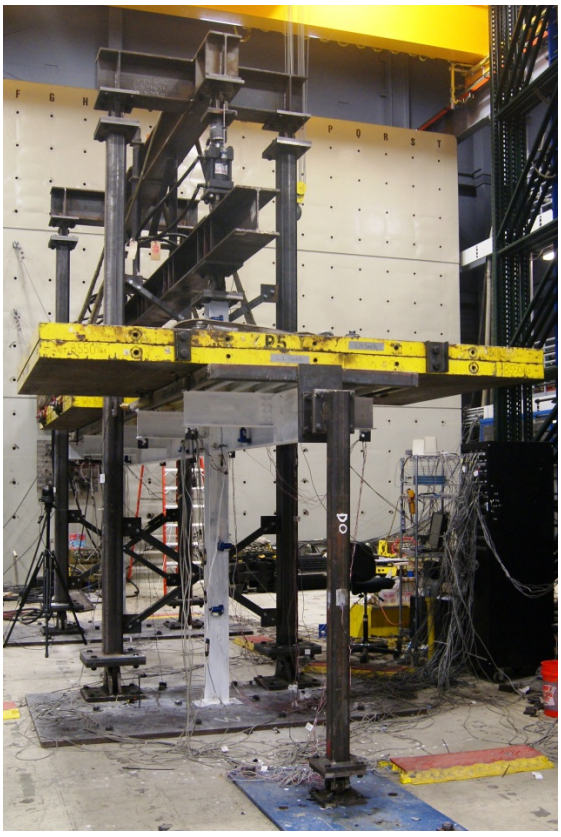

(c) West-north view of test setup and Physical Sub-Structure #2

**Figure 5-19 Photographs of experimental test setup for collapse hybrid simulation**

Figure 5-20 shows additional details of the experimental test setup. Figure 5-20(a) shows a roller that was provided at the interface of the physical specimens with each one of the four long columns of the supporting frame to minimize friction during lateral loading. The supporting frame with the four rollers provided out-of-plane support to the physical specimens. However, it did not restrain the girder of the Physical Sub-Structure #1 for lateral-torsion bucking, as is discussed later in Section 7. Figure 5-20(b) shows the clevis provided between the girder in cantilever of the test specimens and the vertical link member.

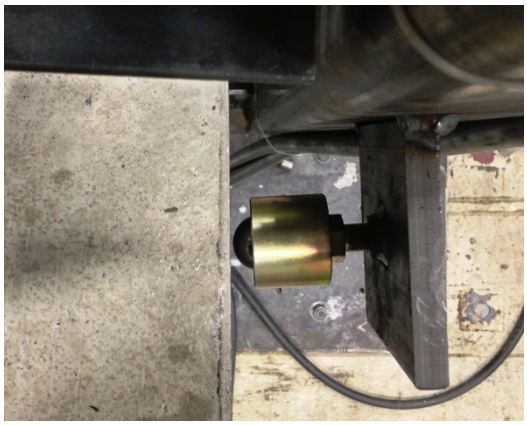

(a) Roller between supporting frame and test specimens

(b) Clevis between test specimens and vertical link member

**Figure 5-20 Selected photographs of experimental test setup for collapse hybrid simulation**

In the experimental test setup shown in Figure 5-18 and Figure 5-19, the degrees of freedom (DOFs) of the physical sub-structures at the interface with the numerical sub-structures (boundary DOFs) were simplified. For instance, the rotational DOFs at the top of the columns and at the end of the cantilever girder of the physical sub-structures were not controlled. Also, the vertical DOF at the end of the cantilever girder was constrained with the vertical link member. Hybrid simulation with these simplified boundary conditions were addressed in the substructuring technique developed for multi-story frame structures. This substructuring technique is described in detail in Section 6.4.

## 5.5 Gravity Load Analysis of Physical Sub-Structures

Prior to conducting the series of hybrid simulations with the physical model of the gravity frame (Physical Sub-Structure #2), it was necessary to verify that the shear-tab connections of the test specimen were subjected to realistic values of shear forces and rotation demands induced by gravity loading since

the seismic behavior of these simple connections are significantly influenced by these two response parameters (see Astaneh-Asl *et al.*, 1989, and Liu and Astaneh-Asl, 2000b). To this end, two simple elastic models were prepared in SAP2000 (CSI, 2012) including: (a) a reference model of the entire gravity frame subjected to the assumed gravity loads (DL = 90 psf and 25% LL = 25×50 psf), which served as the assumed realistic condition, and (b) a model of Physical Sub-Structure #2 including the horizontal and vertical link members which were subjected to the actual gravity loading conditions of the test specimen in the laboratory (four steel plates of 8.5 kips). The flexibility of the simple connections was modeled using linear elastic rotational spring elements with an elastic stiffness of 35000 kip-in/rad. This value was obtained following the recommendations of Liu and Astaneh-Asl (2000b, 2004). Table 5-5 compares the shear force and bending moment diagrams of these two simple models. Bending moment diagrams were included to calculate the rotation demands of the shear-tab connections. It can be seen that the shear-tab connections of the model of Physical Sub-Structure #2 are subjected to shear forces that are, at most, 25% larger than those of the complete gravity frame, which was assumed to be the realistic case. The rotation demands (calculated by dividing the bending moments by the spring elastic stiffness of 35,000 kip-in/rad.) of the left and right shear-tab connections of the full span of the Physical Sub-Structure #2 are 15% and 5% larger than those of the realistic case, respectively. However, the shear-tab connection of the half span is approximately 55% smaller than the assumed realistic value. The lack of rotation demand on this shear-tab connection was compensated similar to Liu and Astaneh-Asl (2000b) by providing a vertical link member 0.25" shorter so as to lower the tip of the cantilever girder enough to compensate for the absent rotation.

Although the influence of these two response parameters (shear force and rotation demand) on the seismic response of moment-resisting connections is less critical, the same comparison is provided in Table 5-6 for the physical model of the moment frame (Physical Sub-Structure #1) for the sake of completeness. The shear forces and rotation demands on the moment connections of Physical Sub-Structure #1 are on average 40% and 25% larger, respectively, than those of the referential model.

**Table 5-5 Comparison of bending-moment and shear-force diagrams for complete gravity frame model and Physical Sub-Structure #2 model subjected to gravity loads**

| a) Complete Gravity Frame | b) Physical Sub-Structure #2 |
|---|---|
| a.1) SAP2000 Model and Gravity Loading | b.1) SAP2000 Model and Gravity Loading |
| 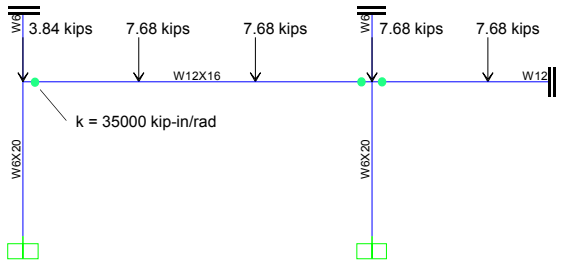 | 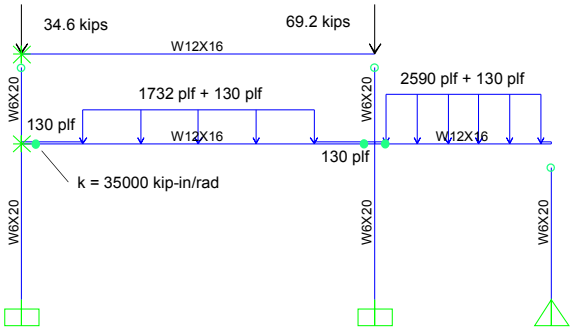 |
| a.2) Shear Force Diagram | b.2) Shear Force Diagram |
| 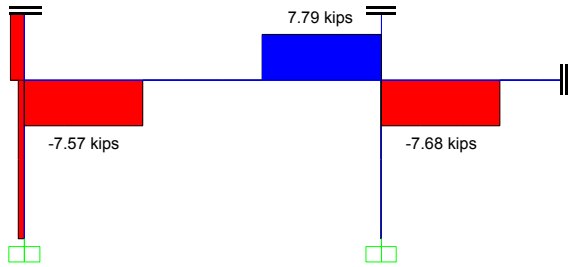 | 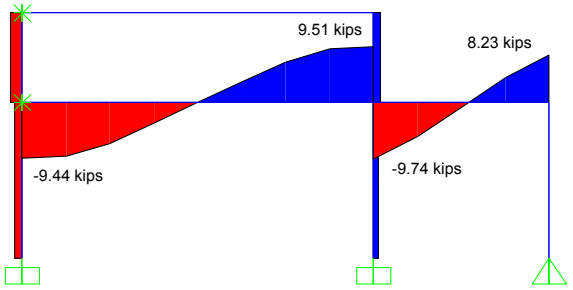 |
| a.3) Bending Moment Diagram | b.3) Bending Moment Diagram |
| 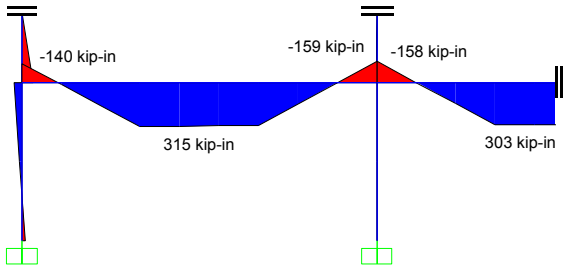 | 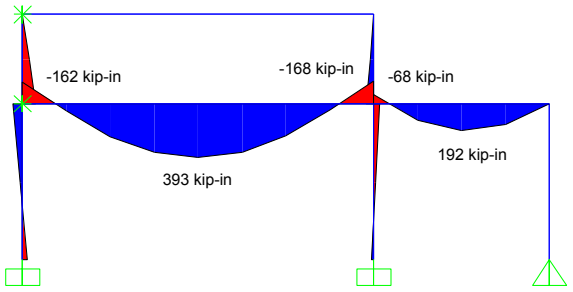 |

**Table 5-6 Comparison of bending-moment and shear-force diagrams for complete moment frame model and Physical Sub-Structure #1 subjected to gravity loads**

| a) Complete Moment Frame | b) Physical Sub-Structure #1 |
|---|---|
| a.1) SAP2000 Model and Gravity Loading | b.1) SAP2000 Model and Gravity Loading |
| 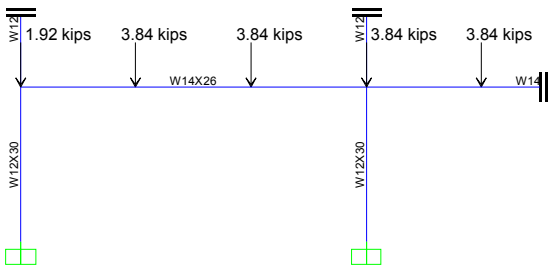 | 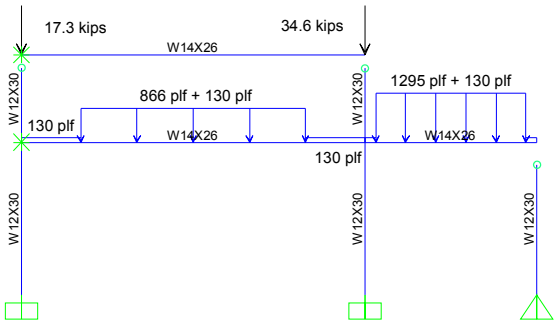 |
| a.2) Shear Force Diagram | b.2) Shear Force Diagram |
| 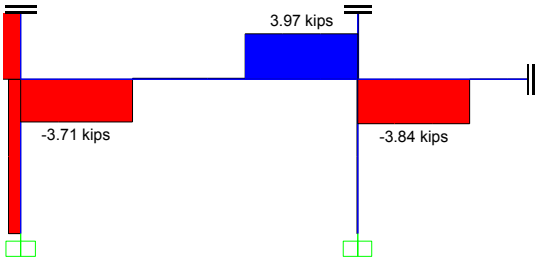 | 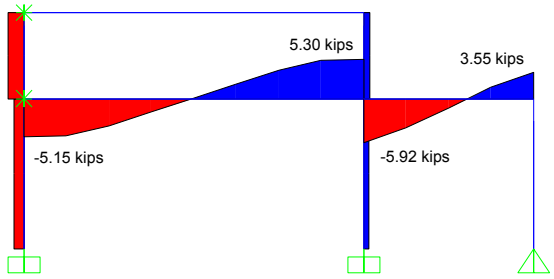 |
| a.3) Bending Moment Diagram | b.3) Bending Moment Diagram |
| 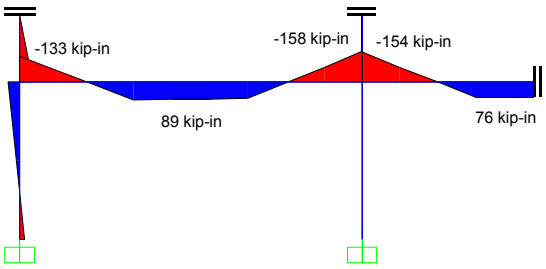 | 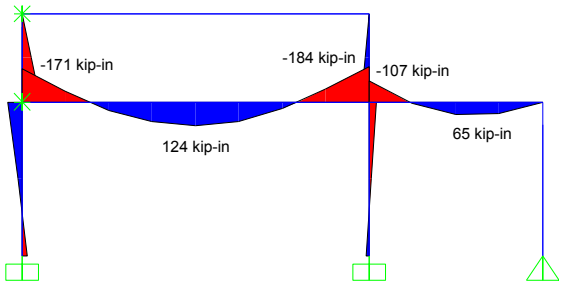 |

# SECTION 6
# NUMERICAL SUB-STRUCTURES AND SUBSTRUCTURING TECHNIQUE

## 6.1 Overview

This section presents a detailed description of the numerical models and substructuring technique used in the series of hybrid simulations. Section 6.2 and Section 6.3 describe the numerical models of the moment and gravity frames, respectively. A study conducted to improve the stability of the hybrid simulations is included in Section 6.2. Finite element studies of shear-tab connections are presented in Section 6.3. Section 6.4 presents the substructuring technique used to partition the frame structures into physical and numerical sub-structures as described in Section 4. An extensive evaluation of the substructuring technique is provided in Section 6.4. The selection of the integration method, time steps and number of iterations for the two series of hybrid simulations is discussed in Section 6.6. Finally, a description of the procedure followed to apply gravity loads on the hybrid models is presented in Section 6.7.

## 6.2 Numerical Model of Special Steel Moment Frame

### 6.2.1 General Description of Numerical Model

Figure 6-1 illustrates the two-dimensional OpenSees model of the moment-resisting frame. A concentrated plasticity approach was adopted herein to reproduce the inelastic behavior of the frame structure. The flexural response of girders and columns of the moment frame was modeled using two rotational springs (zero-length elements in OpenSees) attached at both ends of an elastic beam-column element as seen in Figure 6-1. A phenomenological hysteretic model was assigned to the rotational springs to reproduce the inelastic flexural response of girders and columns. Such an ensemble of elements in series is known as the one-component model (Giberson, 1967).

The rotational springs (zero-length elements) of the one-component model have a finite initial elastic stiffness in OpenSees, unlike the rigid-plastic rotational springs used in other structural analysis software (e.g., SAP2000). Similar to Ibarra and Krawinkler (2005), the elastic stiffness of these rotational springs is selected to be $n$ times the rotational stiffness of the beam-column element located in between the

rotational springs. Therefore, the elastic stiffness of such elastic beam-column element needs to be increased by $n + 1$ so that the rotational stiffness at the ends of the one-component model produces the same stiffness of the original elastic element. The value of $n = 10$ used in previous studies (e.g., Ibarra and Krawinkler, 2005, Medina, 2002) was preliminarily selected for the OpenSees model. Afterward, this value was refined based on studies presented in Section 6.2.5.

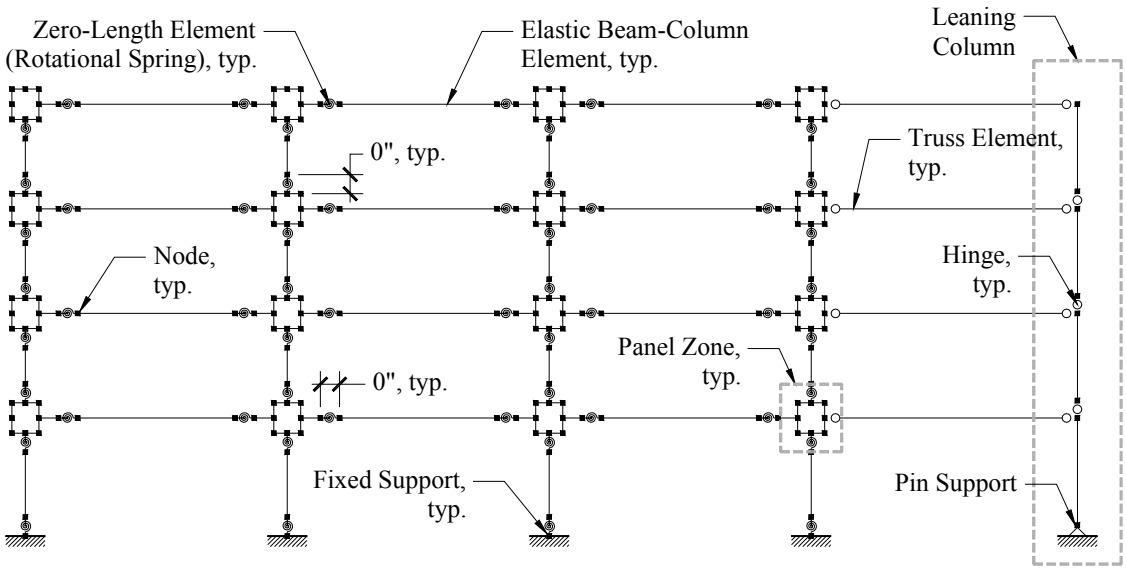


**Figure 6-1 Schematic representation of OpenSees model of moment-resisting frame**

Inherent damping in the frame structure was modeled using the Rayleigh damping model with modifications proposed by Zareian and Medina (2010). A damping ratio of 2.0% was anchored at the first two natural frequencies. In this modified version, the stiffness-proportional component of the damping matrix was assembled only from elastic elements (such as elastic beam-column elements, truss elements, etc.). Consequently, zero stiffness-proportional damping was assigned to all inelastic elements (such as zero-length elements at girders, columns, panel zones, etc.). Therefore, the stiffness-proportional damping multiplier was increased to compensate for the contribution of the nonlinear elements to the damping matrix. This approach was suggested to overcome some of the limitations of the classical Rayleigh damping model associated with unrealistic damping forces when used with the one-component model described above. Zareian and Medina found that such unrealistic damping forces have a significant influence on the collapse capacity of a system. A discussion about modeling of damping in nonlinear structures can be found in Ray *et al.* (2013).

The panel zones were explicitly modeled following the recommendations of the FEMA 355F report (FEMA, 2000) as shown in Figure 6-2. The inelastic behavior of the panel zone was captured using a tri-linear hysteretic model assigned to the rotational spring (zero-length element) located at the upper-left corner of the panel zone. The rigid links shown in Figure 6-2 consisted of elastic beam-column elements with a moment of inertia ($I_x$) and cross-sectional area ($A$) of the second-floor girder section, both amplified by a factor of 1000 (stiffness multiplier).

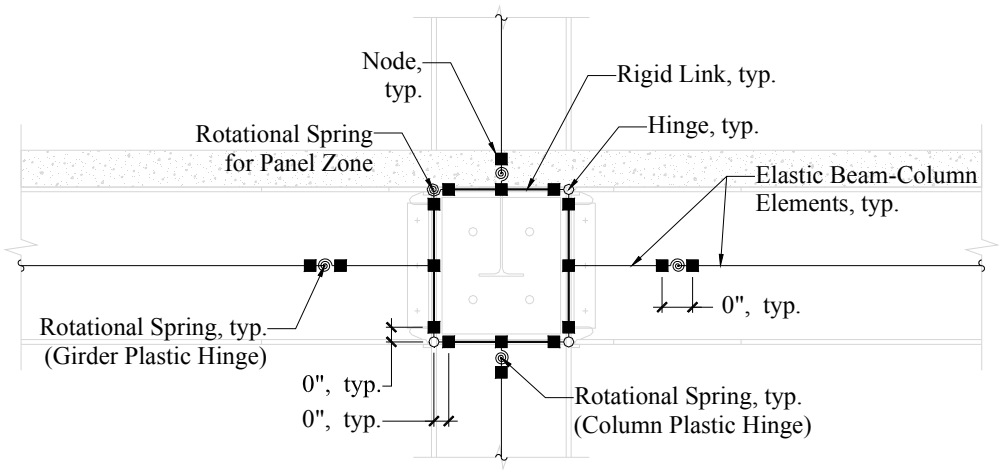


**Figure 6-2 Schematic representation of panel zone model in OpenSees**

Geometric nonlinearities were captured using the corotational transformation in OpenSees. Afterwards, the P-Delta transformation was selected given that its simple formulation provides improvements in the stability of the simulation (see Section 6.2.5). A leaning column was included in the absence of the gravity framing system to account for P-Delta effects of the gravity loads acting on such frames. As shown in Figure 6-1, the leaning column was connected to the moment frame through truss elements, which have a cross-sectional area equal to that of the first-story column section amplified by 1000 (stiffness multiplier). The aforementioned modeling assumptions have been widely adopted in the past and implemented in other structural analysis software such as DRAIN-2D (Prakash *et al.*, 1994, Kanaan and Powell, 1973) and IDARC (Reinhorn *et al.*, 2009).

The seismic weight of the prototype as well as the half-scale frame structure is summarized in Table 6-1. Since only one out of the two moment frames is modeled, only half of the seismic weight of the building structure is listed in Table 6-1. The seismic weights were scaled down by the weight scale factor of $0.50^2 = 0.25$. The gravity loading of the prototype building consisted of a dead load of 90 psf and 25% of the code-specified live load of 50 psf, both uniformly distributed on the full floor area.

**Table 6-1 Seismic weight of prototype and half-scale moment frame structures**

| Level | Seismic Weight of Prototype [kip] | Seismic Weight of Half-Scale Model [kip] |
|---|---|---|
| Roof | 1181 | 295 |
| 4th Floor | 1054 | 264 |
| 3rd Floor | 1054 | 264 |
| 2nd Floor | 1064 | 264 |
| Total | 4349 | 1086 |

### 6.2.2 Modified Ibarra-Medina-Krawinkler (IMK) Model

The one-dimensional hysteretic model developed by Ibarra *et al.* (2005) and subsequently modified by Lignos and Krawinkler (2011, 2012) was used to simulate the inelastic flexural response of girders and columns of the moment frame. This model, hereafter referred as the modified-IMK model, is capable of simulating the basic modes of strength and stiffness deterioration observed in steel members. Figure 6-3(a) shows the parameters which characterize the backbone curve of the modified-IMK model including i) three strength parameters: effective yield moment ($M_y$), capping moment strength ($M_c$) and the residual moment ($M_r$) (defined by the $\kappa$ factor), and ii) four deformation parameters: yield rotation ($\theta_y$) (defined by the elastic stiffness, $K_e$), pre-capping plastic rotation ($\theta_p$), post-capping plastic rotation ($\theta_{pc}$) and ultimate rotation capacity ($\theta_u$). A reference cumulative rotational capacity ($\Lambda$) defines the rate of cyclic deterioration illustrated in Figure 6-3(b).

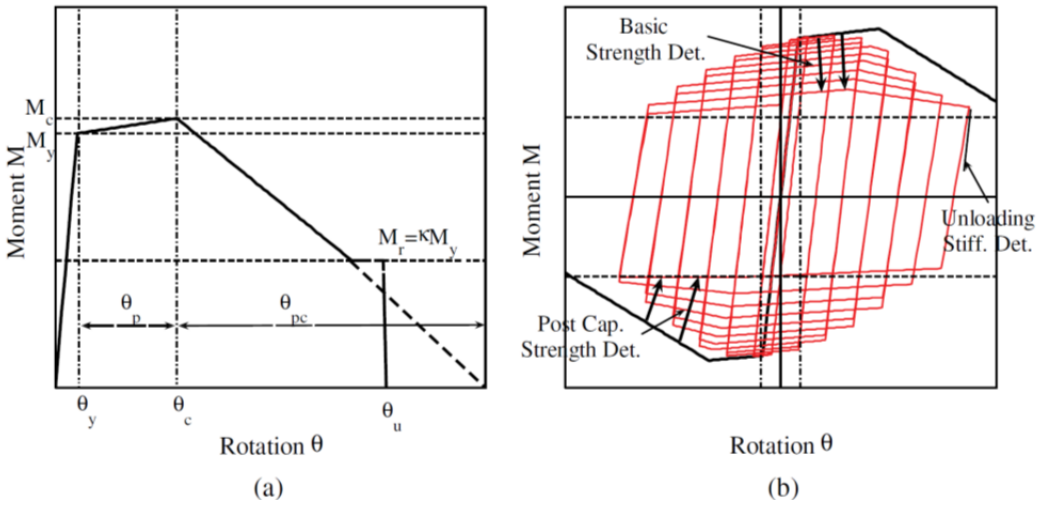


**Figure 6-3 Modified-IMK model: (a) monotonic curve, (b) basic modes of cyclic deterioration and associated definitions (Lignos and Krawinkler, 2011)**

The parameters of the modified-IMK model were calibrated by Lignos and Krawinkler (2011, 2012) using an extensive database of structural steel components (available from the following link: dimitrios-lignos.research.mcgill.ca/databases/). As a result of such calibration studies, regression equations were provided to estimate the pre- and post-capping plastic rotations and the reference cumulative rotation capacity ($\Lambda$) of beams with RBS and beams-other-than-RBS. Table 6-2 and Table 6-3 summarize these parameters for the girder and column sections of the prototype and half-scale moment frame, respectively. Although the regression equations were calibrated for beams, these equations provide the best estimates for columns until more experimental data become available (Lignos and Krawinkler, 2012). The yield moment strength was increased to an effective value to account for, on average, the effect of isotropic hardening. This was done because the modified IMK model is not able to simulate the effect of cyclic hardening on the hysteretic response of a steel component. Therefore, the predicted yield strength (defined as the plastic section modulus times the measured yield strength obtained from coupon testing) of girders and columns was increased by the 1.06 and 1.17 factors, respectively, as recommended in Lignos and Krawinkler (2011). The modified-IMK model, as currently implemented in OpenSees, does not account for axial force-bending moment (P-M) interaction. The use of this one-dimensional hysteretic model to simulate the response of the columns represents a reasonable assumption for low-rise structures where the level of column axial forces is low. This has been validated through collapse simulations of recent small and full-scale collapse tests (see Lignos *et al.*, 2011a, Suita *et al.*, 2008, and Lignos *et al.*, 2013).

**Table 6-2 Modeling parameters for sections of prototype moment-resisting frame**

| Structural Member | Original Section | $\theta_p$ [rad.] | $\theta_{pc}$ [rad.] | $\Lambda$ |
|---|---|---|---|---|
| Girder @ 2nd & 3rd Floor | W27×102 | 0.023 | 0.183 | 1.043 |
| Girder @ 4th Floor & Roof | W21×93 | 0.032 | 0.280 | 1.860 |
| Column @ 1st Story | W24×117 | 0.021 | 0.135 | 1.091 |
| Column @ 2nd Story | W24×117 | 0.019 | 0.135 | 1.091 |
| Column @ 3rd & 4th Story | W24×76 | 0.019 | 0.133 | 0.874 |

A comparison of the plastic rotation capacities presented in Table 6-2 and Table 6-3 indicates that, although non-dimensional magnitudes, the rotational capacity of girders and columns of the half-scale moment frame are larger than those of the prototype for most cases. This is attributed to the smaller $h/t_w$ slenderness ratios of the W14×26 and W12×30 sections compared to the W24 sections that are used as part of the design of the prototype building.

**Table 6-3 Modeling parameters for sections of half-scale moment-resisting frame**

| Structural Member | Scaled Section | $\theta_p$ [rad.] | $\theta_{pc}$ [rad.] | $\Lambda$ |
|---|---|---|---|---|
| Girder @ 2nd & 3rd Floor | W14×26 | 0.038 | 0.183 | 1.025 |
| Girder @ 4th Floor & Roof | W12×22 | 0.043 | 0.234 | 1.325 |
| Column @ 1st Story | W12×30 | 0.033 | 0.153 | 0.977 |
| Column @ 2nd Story | W12×30 | 0.030 | 0.153 | 0.977 |
| Column @ 3rd & 4th Story | W12×19 | 0.030 | 0.179 | 0.996 |

### 6.2.3 Effects of Composite Floor Slab

Previous studies have shown that the composite action of the floor slab has a significant influence on the seismic behavior of moment frame structures (Lee and Lu, 1989, Leon *et al.*, 1998). Some of the effects of the composite floor slab were accounted for in the OpenSees model as described below.

#### 6.2.3.1 Girder Stiffness

Experimental studies have confirmed that the composite action of the floor slab increases the elastic stiffness of composite girders. Lee (1987) reported that the experimental elastic stiffness under negative moment of two composite beams was 13.6% and 10.3% higher than the theoretical values calculated for the composite section. However, under positive moment, the experimental stiffness reached values of 74% and 85% of the theoretical stiffness for the composite section (or 106% and 135% of the theoretical stiffness calculated for the bare steel section). Also, Nam and Kasai (2012) found experimentally that the ratio of moment of inertia of composite beam to that of bare steel beam varied from 2.0 to 3.0 for the collapse test at E-Defense (Suita *et al.*, 2008).

In view of this, the flexural elastic stiffness of the girder of the half-scale moment frame OpenSees is increased to account for composite action. The theoretical moment of inertia under positive and negative bending for the composite W14×26 girder is 235% and 147% higher than the moment of inertia of the bare steel girder. However, since experimental data (Lee, 1987) suggests smaller increments of 135% under positive bending and, given that such elastic stiffness deteriorates near the joint upon cyclic loading, the flexural elastic stiffness of the one-component model for the girders in OpenSees was modified by increasing the moment of inertial ($I_x$) by a factor of 1.20 to account for composite action.

### 6.2.3.2 Girder Plastic Hinges

Some of the modeling parameters of the modified-IMK model were modified following the recommendation of Lignos *et al.* (2011b) to account for the effects of composite action of the floor slab as shown in Table 6-4.

**Table 6-4 Modeling parameters for composite girders of half-scale moment-resisting frame**

| Scaled Section | $M_y^+ = 1.25M_y^{bare}$ [kip-in.] | $M_y^- = 1.15M_y^{bare}$ [kip-in.] | $\theta_p^+ = 2.0\,\theta_p^{bare}$ [rad.] | $\theta_p^- = 0.9\,\theta_p^{bare}$ [rad.] | $\theta_{pc}^+ = 1.5\,\theta_p^{bare}$ [rad.] | $\theta_{pc}^- = 1.0\,\theta_p^{bare}$ [rad.] | $D^+$ | $D^-$ |
|---|---|---|---|---|---|---|---|---|
| W14×26 | 1678.7 | 1544.4 | 0.0756 | 0.0340 | 0.2742 | 0.1828 | 0.85 | 1.00 |
| W12×22 | 1192.2 | 1096.8 | 0.0862 | 0.0388 | 0.3509 | 0.2339 | 0.85 | 1.00 |

Such recommendations were based on a series of observations made on experimental data of steel composite beam-to-column subassemblies. The "bare" superscript used in Table 6-4 denotes the modeling parameters of the bare steel section previously presented in Table 6-3. It can be seen that the yield moment is increased for positive and negative bending. Also, the rotational capacity parameters ($\theta_p$, $\theta_{pc}$) are also modified. The asymmetric hysteretic response of the composite girder is simulated with the parameter $D$ that defines the decrease in rate of cyclic deterioration under positive or negative moment. For a bare steel section, the value of $D$ is 1.0. Figure 6-4 illustrates the moment-rotation relationships of the modified-IMK model for the bare and composite W27×102 and W21×93 girder sections.

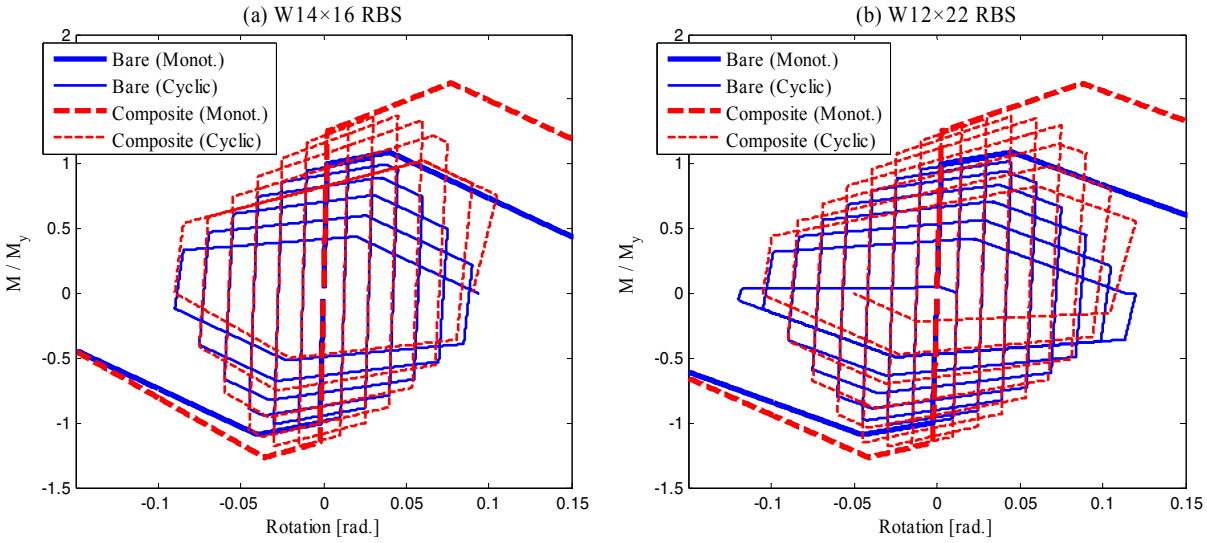


**Figure 6-4 Moment-rotation relationships for bare and composite half-scale reduced beam sections obtained with modified-IMK model**

#### 6.2.3.3 Response of Panel Zones

Experimental studies have shown that the composite floor slab increases the stiffness and strength of panel zones due to the enlargement of the panel zone dimensions (Lee and Lu, 1989). However, only limited experimental data of panel zones is available to refine the analytical models used to capture the cyclic behavior (Kim and Engelhardt, 2002). For this reason and for simplicity, the panel zones were not modified to account for slab effects.

Finally, a rigid diaphragm effect produced by the floor slab was also accounted for by assigning a rigid diaphragm to each floor level.

### 6.2.4 Comparison of Numerical Models of Prototype and Half-Scale Moment Frame

Since the plastic rotation of girders and columns of the half-scale moment frame are larger than that of the prototype (see Section 6.2.2), this section presents a comparison of the global response of the OpenSees model of the prototype and half-scale moment frame. To provide unbiased comparisons, the yield stress for all steel members was set to 50 ksi in both OpenSees models instead of using the available measured values presented in Section 4.

Table 6-5 presents the first four natural periods of the prototype and half-scale model of the moment frame. The natural periods of the half-scale model are compared with corresponding target scaled values which are defined and shown in Table 6-5. The natural periods of the half-scale OpenSees model are smaller than the target scaled values. This observation is consistent with the differences observed in the moment of inertia of the half-scale and original wide-flanged sections presented in Table 4-3 where the positive values indicate that the moment of inertia of the half-scale sections is greater than the target scaled values. In all cases, the differences in period are below 6%.

**Table 6-5 Comparison of natural periods of OpenSees model of prototype and half-scale structures**

| Mode | Natural Period of Prototype Frame | Natural Period of Scaled Frame | Target Scaled Period | Period Difference |
|---|---|---|---|---|
| | $T_n^p$ [sec.] | $T_n^m$ [sec.] | $T_n^t=\sqrt{0.5}\ T_n^p$ [sec.] | $100\times\frac{\lvert T_n^s - T_n^t\rvert}{T_n^t}\%$ |
| 1 | 0.996 | 0.673 | 0.704 | 4.4 |
| 2 | 0.318 | 0.212 | 0.225 | 5.7 |
| 3 | 0.155 | 0.105 | 0.110 | 4.2 |
| 4 | 0.092 | 0.062 | 0.065 | 4.7 |

Figure 6-5 presents pushover curves for the prototype and half-scale OpenSees model of the moment frame. A code-based inverse-triangular lateral force distribution was used for the pushover analysis. The term roof drift ratio in Figure 6-5 (and Figure 6-6) is defined as the lateral displacement at the roof level divided by the roof height. The lateral forces were normalized by the corresponding seismic weight of the steel moment frame. Normalization of lateral displacements and forces in Figure 6-5 permits a direct comparison of the two pushover plots. Although the peak normalized lateral strength of both OpenSees models are similar as expected, plastic deformation capacity of the half-scale model is higher than that of the prototype as predicted by the nonlinear static analysis. Since the dimensions of the RBS of the half-scale moment frame were scaled down to match exactly the target scaled plastic modulus of the prototype RBS connection (and therefore the target yield strength of the RBS moment connection), a reasonably good comparison of the peak lateral strength is observed. The larger deformation capacity of the half-scale model is a result of the aforementioned differences in rotation capacity of girders and columns of the prototype and half-scale model.

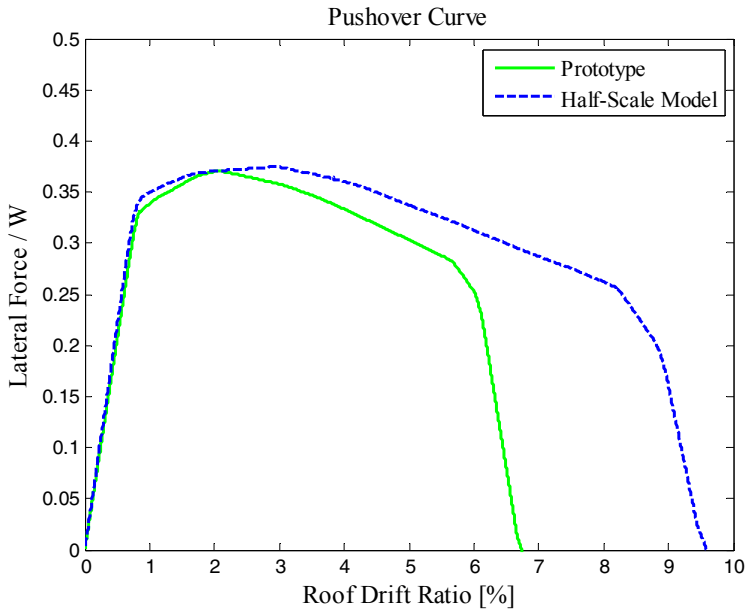


**Figure 6-5 Comparison of pushover curves of OpenSees model of prototype and half-scale moment-resisting frames**

Figure 6-6 compares the dynamic response of the prototype and half-scale OpenSees models subjected sequentially to increasing intensities of the LGPC ground motion, namely, 25%, 100%, 160%, and 200%, which are the same intensity levels used for the two series of hybrid simulations conducted in the experimental program. In order to compare the response history of the two OpenSees models in the same

plot, two different axes are provided for the time of the prototype and half-scale model. These two axes are related by the time scale factor of 0.707 selected in Section 4.4.1. Some observations can be made with respect to the results presented in Figure 6-6.

- The comparison of the elastic response of the two OpenSees models shown in Figure 6-6(a) shows a significant difference in the amplitude of the motion after the first oscillations. The different periods of vibration, previously shown by the eigenvalue analysis, are also observed in Figure 6-6(a).
- The response of the two OpenSees models under moderate and severe levels of yielding shown in Figure 6-6(b) and Figure 6-6(c), respectively, shows a better comparison. This could be attributed to the fact the yielding capacity of the half-scale OpenSees model matches very closely its target scaled value. However, a noticeable difference in residual drifts is observed at the end of the 160% ground motion, as shown in Figure 6-6(c).
- Although the last analysis cases started with different residual drifts, both OpenSees models presented similar roof drift response at collapse, as shown in Figure 6-6(d).

In summary, the global response of the OpenSees model of the half-scale frame structure compares very well with that of the prototype. The pushover analysis demonstrated a slightly larger deformation capacity than the half-scale model. However, the dynamic response of both OpenSees models was very similar when subjected to the same ground motion intensities used for the two series of hybrid simulations, as shown in Table 4-6. The largest differences were observed for the elastic response.

(a) Comparison of Roof Drift Ratio Response for 25% LGPC

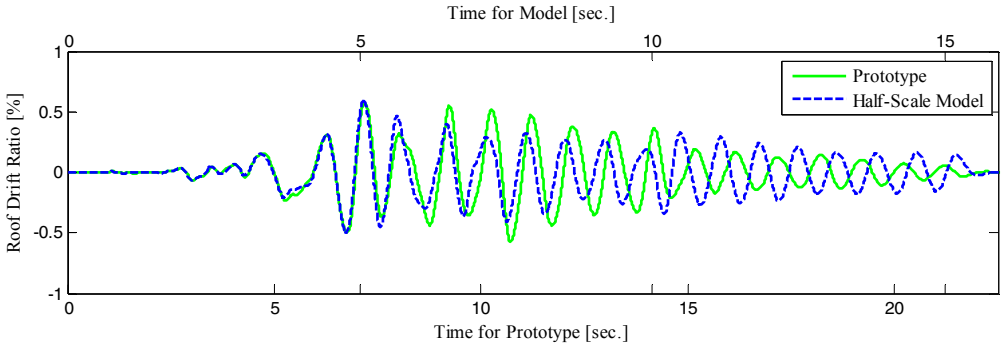


(b) Comparison of Roof Drift Ratio Response for 100% LGPC

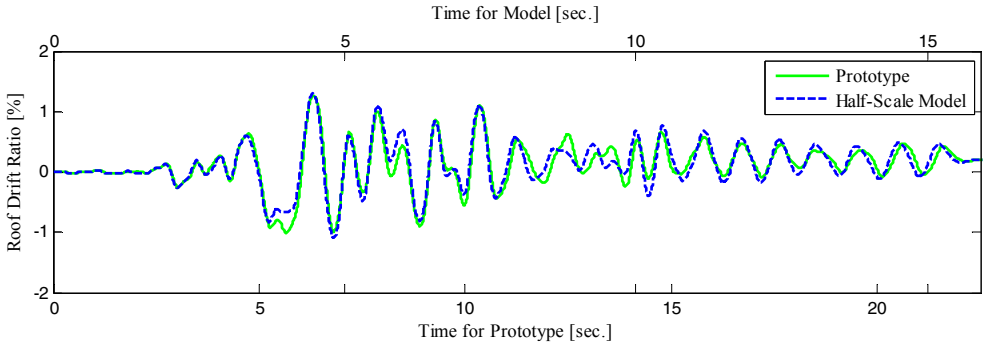


(c) Comparison of Roof Drift Ratio Response for 160% LGPC

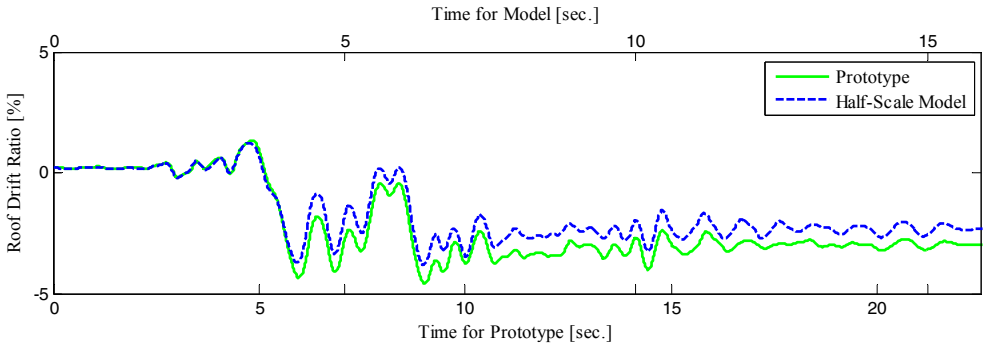


(d) Comparison of Roof Drift Ratio Response for 200% LGPC

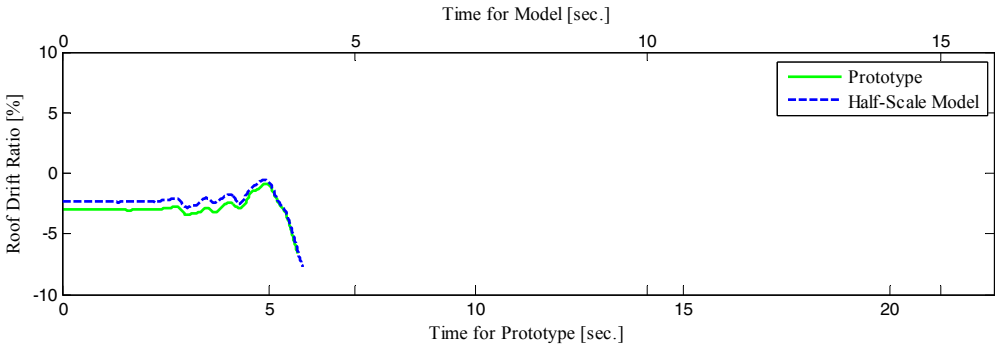


**Figure 6-6 Comparison of dynamic response of OpenSees model of prototype and half-scale moment-resisting frame subjected to increasing intensities of the LGPC ground motion**

### 6.2.5 Evaluation of Robustness of the Numerical Model

Through a series of response history analyses carried out using the INM-HS algorithm (described in Section 3.2.2) to integrate the equations of motion of the OpenSees model, stability problems were frequently encountered due to the complexity of the analytical model, the high levels of nonlinear response, and the use of large time steps which are typically preferred in hybrid simulation. Upon further investigation, it was noticed that an analysis became unstable whenever spikes in the values of unbalanced forces were observed. Similar observations were reported by Hashemi (2013). Therefore, this section investigates some modifications made to the OpenSees model which could potentially lead to reductions in the magnitude of such unbalanced forces and consequently improve the stability of the analysis and robustness of the OpenSees model.

The modifications included softening the elastic stiffness of rigid links in the panel zones and leaning column. The stiffness multiplier used for the elastic beam-column and truss elements was reduced from 1000 to 100. Also, the elastic stiffness of the rotational springs (zero-length elements) at columns and girders, which is defined by the parameter $n$, was softened using a value of $n = 1$ instead of $n = 10$. Another modification to the model is the use of the HHT integration method with algorithmic damping modified for hybrid simulation available in OpenFresco as the HHT-HS integration method. The HHT integration method is known to improve the stability of the simulation and eliminate spurious high-frequency vibrations. Also, the use of the P-Delta instead of the corotational formulation was investigated. All these changes were implemented in six OpenSees models which are summarized in Table 6-6. All OpenSees models in Table 6-6 were subjected to 200% of the LGPC ground motion, which resulted in a highly nonlinear response of the frame structure.

Figure 6-7 presents the maximum norm of the unbalanced force vector recorded for the different OpenSees models using several time steps and number of iterations for the integration methods. The vertical axis used for the unbalanced forces is in logarithmic scale. Each data point in Figure 6-7 corresponds to an analysis case. The data points circled in back indicate that the analysis became unstable. The time step and number of iterations used in each analysis is indicated next to the data point where $\Delta t$ is the scaled time step of the ground motion equal to 0.0035 sec. ($0.5^{1/2} \times 0.005$ sec.).

**Table 6-6 Summary of different OpenSees models used in robustness studies**

| Model # | Model Description |
|---|---|
| 1 | Original model as described in Section 6.2.1 through Section 6.2.3. |
| 2 | The following changes were made to the original model (Model #1):<br>(a) The ***stiffness muliplier*** for rigid links in panel zones was changed from 1000 to **100**.<br>(b) The ***stiffness multiplier*** for rigid links connecting the momenr frame to the leaning column was changed from 1000 to **100**. |
| 3 | In addition to the changes made in Model #2, the ***HHT-HS integration method*** with alg orithmic damping modified for hybrid simulation was selected instead of the INM-HS i ntegration method used in all previous models. |
| 4 | In addition to the changes made in Model #3, the elastic stiffness of the zero-length elements (rotational springs) was softened using a value of $\boldsymbol{n = 1}$ instead of $n = 10$. |
| 5 | In addition to the changes made in Model #4, the ***P-Delta transformation*** was used instead of the corotational transformation used in all the previous models. |
| 6 | The following changes were made to the original model (Model #1):<br>(a) The ***stiffness muliplier*** for rigid links in panel zones and leaning column was changed from 1000 to **100**.<br>(b) The ***INM-HS Integration method*** was selected.<br>(c) The elastic stiffness of the rotational springs at girders and columns was softened using $\boldsymbol{n = 1}$ instead of $n = 10$.<br>(d) The ***P-Delta transformation*** was selected instead of the corotational transformation. |

Some observations are made from Figure 6-7.

- All of the analysis cases presented for Model #1 (original model as described in Section 6.2.1 through Section 6.2.3) became unstable for the time steps and number of iterations shown in Figure 6-7.
- Softening the elastic stiffness of highly-stiff elements (rigid links) in Model #2 did not prevent instability of any of the analysis cases.
- In Model #3, although it was observed that the use of the HHT-HS integration method with algorithmic damping eliminated some of the spurious high-frequency oscillations, it did not improve the stability of the simulations.
- The use of $n = 1$ instead of $n = 10$ in Model #4, which softened the elastic stiffness of the rotational springs at beams and columns, decreased significantly the maximum norm of the unbalanced force vector for the smallest time steps used ($1/4\,\Delta t$).
- The use of the P-Delta formulation in Model #5 significantly reduced the magnitude of the unbalanced forces and consistently improved the instability of the analysis cases, even for the

largest time step ($\Delta t$) used. The complexity of the corotational formulation, although it produces slightly different results than the P-Delta formulation near collapse, requires smaller time steps and a larger number of iterations for convergence.

- The norms of the unbalanced force vector shown for Model #6, which is similar to Model #5 except for the selection of the integration method, indicates that the INM-HS integration method presents lower values of unbalanced forces as compared to the HHT-HS algorithm.

In summary, the selection of the P-Delta formulation and the use of $n = 1$ instead of $n = 10$ to define the elastic stiffness of the rotational springs at girders and columns resulted in the largest reductions in the norm of the unbalanced force vector and therefore the best improvements to the stability of the numerical simulation and robustness of the OpenSees model. The use of the HHT-HS integration method did not provide better results than the INM-HS method as measured by the unbalanced forces. Note that these observations are valid only for the OpenSees model presented in this section. Extrapolation of such observations to other cases requires further studies. In view of this, the followings modifications were permanently implemented in all the subsequent OpenSees models of the moment frame: (a) the use of the P-Delta formulation instead of the corotational, (b) the use of $n = 1$ to define the elastic stiffness of the rotational springs at girders and columns, (c) the use of the INM-HS integration method to solve the equations of motion and (d) the use of a stiffness multiplier of 100 to soften the elastic stiffness of rigid links.

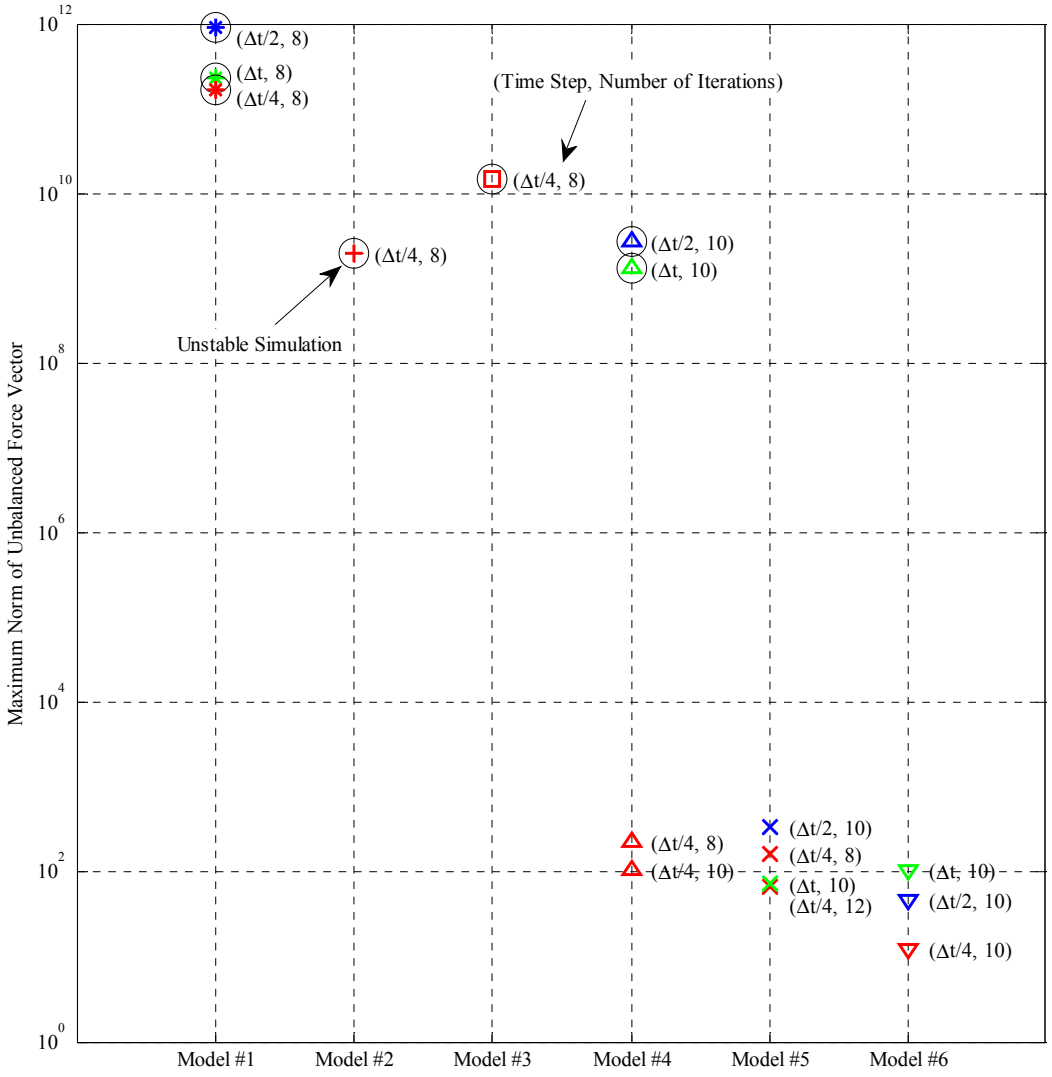


**Figure 6-7 Maximum norm of unbalanced force vector for different OpenSees models**

## 6.3 Numerical Model of Gravity-Resisting Frame

### 6.3.1 General Description of Numerical Model

Figure 6-8 illustrates the two-dimensional OpenSees model of a gravity-resisting frame of the building structure. Note that the building structure presents a total of three gravity frames in the direction of loading (see Figure 4-1). In this model, the columns were oriented in the strong axis for consistency with the gravity frame physical sub-structure previously presented in Section 5.3. A concentrated plasticity model of the gravity frame was developed similar to the OpenSees model of the moment frame presented in Section 6.2. It can be seen in Figure 6-8 that the gravity columns were assumed pinned at the base. However, flexible support boundary conditions were subsequently considered based on experimental data on the physical sub-structure. This is discussed in detail in Section 7.3. The joints of the gravity frame were modeled using a panel zone model (FEMA, 2000) to account for joint deformation since some panel zone yielding of gravity frame subassemblies was reported by Liu and Astaneh-Asl (2000b) due to binding of beam flanges on the column flange at large rotations.

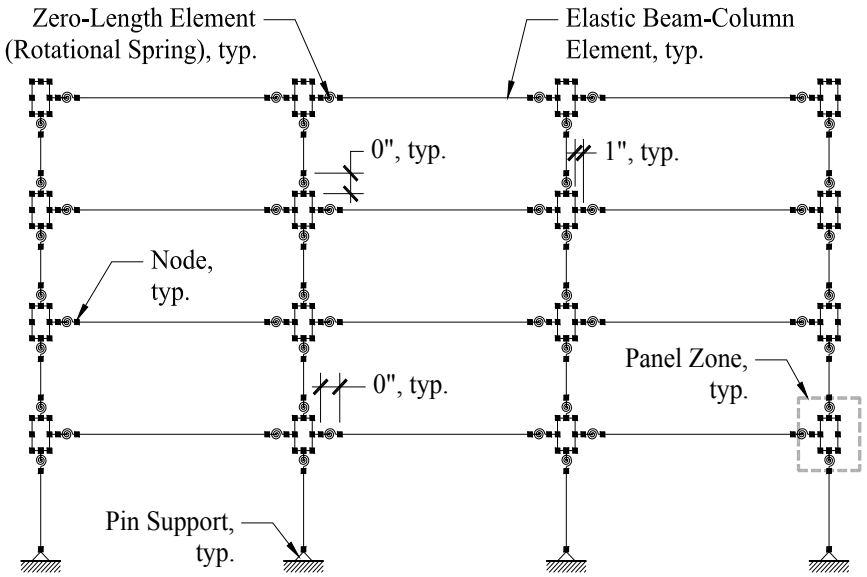


**Figure 6-8 Schematic representation of OpenSees model of gravity frame**

The one-dimensional hysteretic model developed by Lowes and Altoontash (2003) and subsequently modified by Mitra (2007) was used to reproduce the inelastic moment-rotation response of the shear-tab connections. This hysteretic model, available in OpenSees as the Pinching4 material model, is capable of reproducing the main characteristics of the cyclic response of a shear-tab connection including pinching,

deterioration of both strength and stiffness and stiffening at large deformations. However, limited experimental data on shear-tab connections is available to calibrate such phenomenological model. By far, the most extensive experimental program was conducted by Liu and Astaneh-Asl (2000b) where sixteen full-scale simple connections were tested under cyclic loading. Finite element studies were conducted and presented in the next section in an attempt to supplement the limited experimental data and assist in the calibration of the Pinching4 model. Similar to the moment frame OpenSees model, the modified-IMK model was utilized to capture any inelastic action in the columns of the gravity frame.

The OpenSees model of the gravity frame described above was coupled with the OpenSees model of the moment frame via OpenFresco as shown in Figure 6-9. The concept of coupling finite element codes with OpenFresco was previously introduced in Section 3.4.2 (for reference, see Schellenberg *et al.*, 2008). In the coupled model of Figure 6-9, the gravity and moment frames are modeled in two separate OpenSees scripts referred as the master and slave OpenSees scripts. Only 2/3 of the internal resisting force vector of the moment frame is returned to the master OpenSees script to account for the actual ratio of number of moment to gravity frames. Since only one gravity frame is modeled, the mass of the coupled model in Figure 6-9 is one third of the total mass of the half-scale building structure. The response of the moment frame together with the gravity frames was simulated using the coupled modeled shown in Figure 6-9 since a conventional numerical simulation (without coupling of finite element codes) would require modeling two moment frames together with three gravity frames in a single OpenSees script, resulting in a very computationally expensive numerical model.

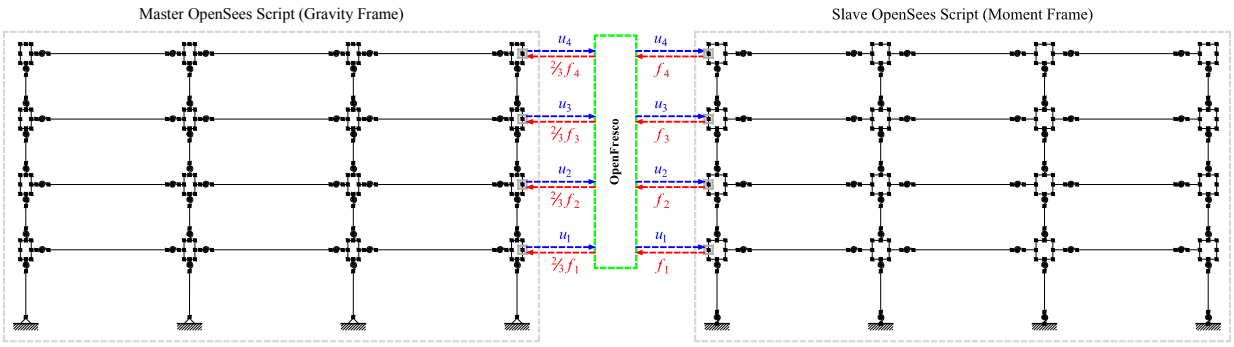


**Figure 6-9 Coupled model used to simulate the response of moment and gravity frames**

### 6.3.2 Finite Element Modeling of Shear-Tab Connections

Finite element studies were conducted to assess the ability of simple finite element models to predict some of the main characteristics of the moment-rotation response of shear-tab connections and to subsequently predict the response of the shear-tab connections of the half-scale gravity frame previously

presented in Figure 5-12. Due to the complex behavior of this type of connection, preliminary results showed deficiencies of the finite element models' ability to trace the cyclic response of these connections, especially when including the composite floor slab. Based on these results, further studies such as refinement of finite element models and mesh sensitivity studies were not pursued in this report. However, these studies are documented and presented in this section. In these studies, the experimental response of two specimens with shear-tab connections tested by Liu and Astaneh-Asl (2000b) were simulated using a general-purpose finite element code. While both specimens consisted of a steel subassembly of beams and columns with shear-tab connection details, the second specimen included a concrete floor slab.

#### 6.3.2.1 Description of Specimens 2A and 6A of Liu and Astaneh-Asl

Liu and Astaneh-Asl tested a total of sixteen cruciform gravity frame subassemblies with several simple connection details as shown in Figure 6-10. Two of these test specimens, namely, Specimen 2A and Specimen 6A, were constructed with shear-tab connection details typical of the west coast of the U.S. as shown in Figure 6-11. Specimen 6A is identical to Specimen 2A but included a floor slab.

As seen in Figure 6-11, both test specimens consisted of W24×55 beams connected to a W14×90 column face through shear-tab connections. The shear-tab connection detail consisted of a 3/8 in. steel plate (A36 steel) attached to the column flange with a 1/4 in. fillet weld provided at both sides of the plate. This plate, referred to as the shear-tab plate, was connected to the beam web through six equally spaced A325N tension-control bolts of 7/8 in. of diameter. The material of all wide-flanged sections was A572 grade 50 steel. The floor slab of Specimen 6A consisted of lightweight concrete poured over a 20-gage W3-36 metal deck manufactured by Verco Decking, Inc. The overall depth of the floor slab was 6-1/4 in., the depth of the metal deck ribs was 3 in. and the width of the concrete slab was 8.0 ft. The nominal strength of the lightweight concrete was 3000 psi. The concrete slab was reinforced with a 6×6-W1.4×W1.4 welded wire mesh for temperature and shrinkage control and #3 reinforcing bars spaced at 12 in. across the W24×55 beams for crack control.

The two gravity load actuators shown in Figure 6-10(b) were located at 5.0 ft. and 6.0 in. away from the centerline of the column and imposed a vertical downward force of 50.0 and 40.0 kips to Specimen 2A and Specimen 6A, respectively. Before the application of the gravity load, an initial downward deflection of 0.375 in. was applied at the free end of the beams supported by struts in both specimens. The application of the gravity forces at the specified distance and the girder-end downward deflections provided realistic combinations of shear forces and rotations on the shear-tab connections.

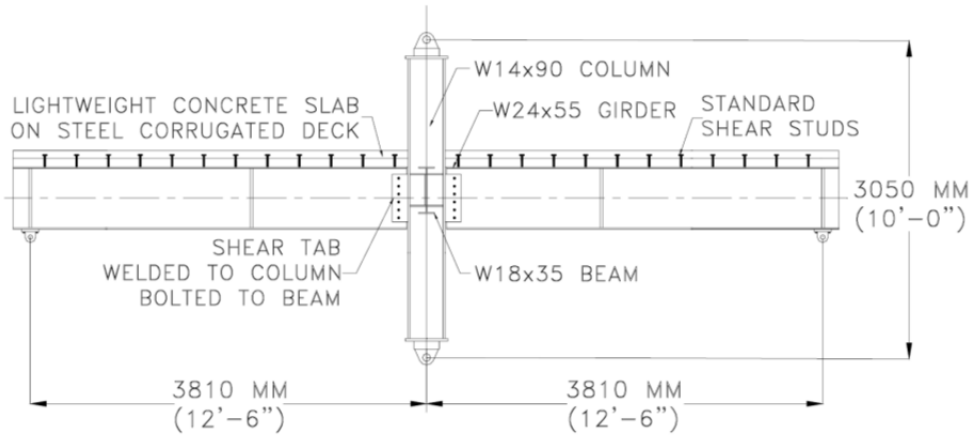


(a) Test specimen with floor slab

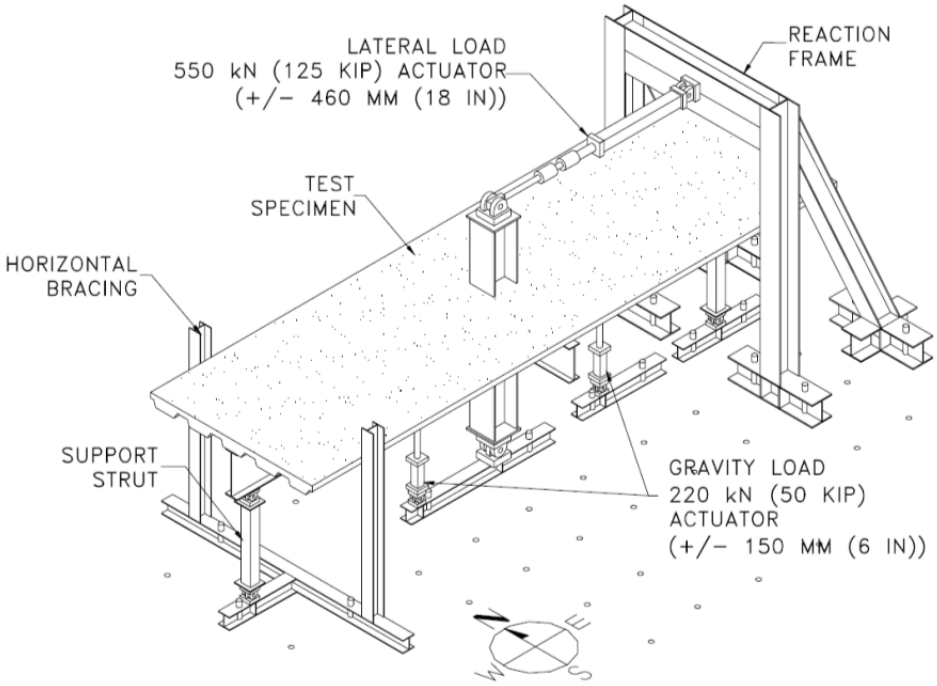


(b) Experimental test setup

**Figure 6-10 Experimental program of Liu and Astaneh-Asl (2000a)**

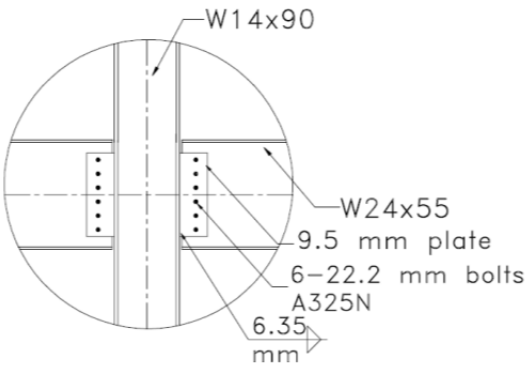


(a) Specimen 2A

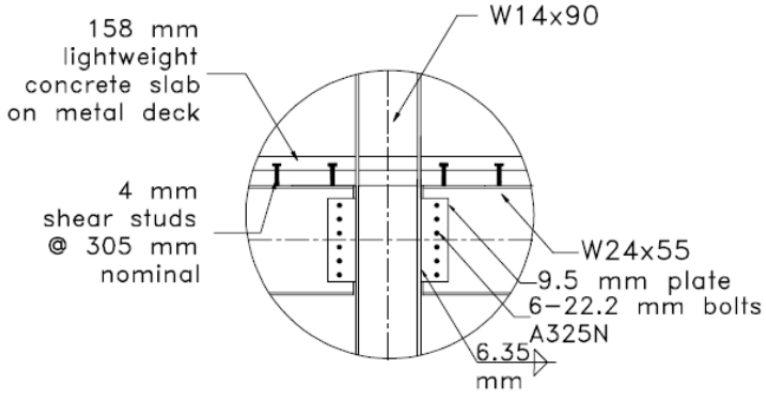


(b) Specimen 6A

**Figure 6-11 Connection details of Specimen 2A and Specimen 6A of Liu and Astaneh-Asl (2000a)**

#### 6.3.2.2 Finite Element Model of Specimen 2A

Figure 6-12(a) shows a three-dimensional ABAQUS (DS Simulia, 2010) model used to simulate the response of Specimen 2A. Due to limitation in computational time, only the beam at one side of the column (and therefore one shear-tab connection) was modeled instead of the full cruciform subassembly. The simple shear-tab connections of Specimen 2A (and Specimen 6A) lacked symmetry since although the centerlines of beams and column were aligned, the shear-tab plate was provided only at one side of the beam web. Because of this lack of symmetry, the finite element model shown in Figure 6-12(c) included the entire geometry of one shear-tab connection. The cyclic response of Specimen 2A was primarily governed by (a) slippage between shear-tab plate and girder web and (b) yielding of the shear-tab plate, especially around the bolt holes (elongation of bolt holes) as reported by Liu and Astaneh-Asl. Due to these observations, the finite element model of Specimen 2A focused on modeling these two phenomena as closely as possible. All other mechanisms, such as fracture of shear-tab plate, were simplified or not included at all.

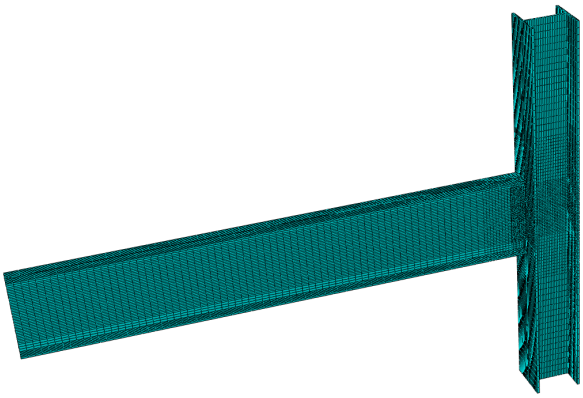

(a) Three-dimensional ABAQUS model

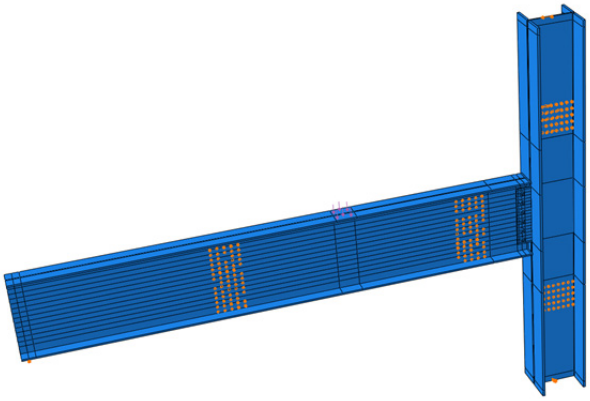

(b) Loads and boundary conditions

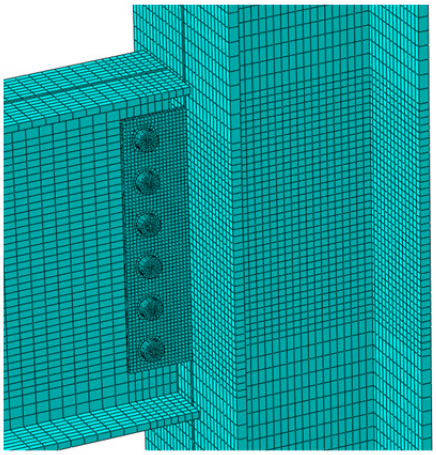

(c) Close-up of shear-tab connection

(d) Mesh of 3/8" shear-tab plate

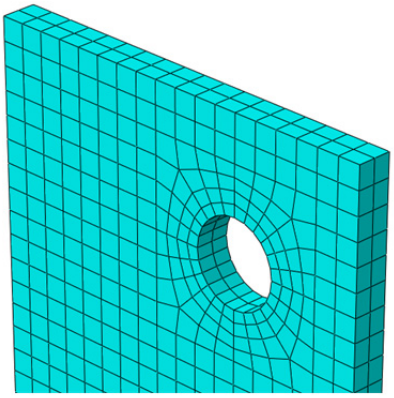

(e) Close-up of 3/8" shear-tab plate

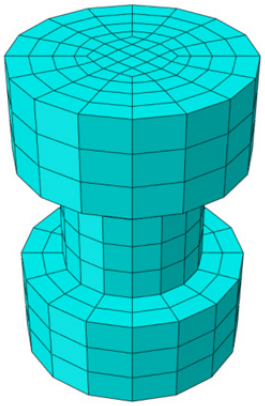

(f) Mesh of 7/8" bolt and nut

**Figure 6-12 ABAQUS model used to simulate the response of Specimen 2A of Liu and Astaneh-Asl (2000a)**

Figure 6-12(b) shows the loads and boundary conditions of the ABAQUS model. The vertical loads applied by the gravity load actuators and the girder-end deflections described in the previous section were also simulated in the ABAQUS model. A roller support condition was modeled at the bottom of the column and at the free end of the beam. The lateral displacement protocol was applied at the top of the column as in the actual test. An elastic material model with a high modulus of elasticity was assigned to the elements in the vicinity of the boundary conditions and point of application of the lateral load to avoid stress concentration. Some nodes on the web of the beam and column were restrained in the out-of-plane direction as shown in Figure 6-12(b) to prevent excessive out-of-plane response of the ABAQUS model.

The classical metal plasticity model with kinematic hardening available in ABAQUS was selected for the steel components. This simple model considers a linear hardening and is used for cyclic loading. Measured material properties reported by Liu and Astaneh-Asl were used for the plasticity model. The modulus of elasticity of all steel material models was set to 29000 ksi. Three-dimensional solid elements with reduced integration (C3D8R) were utilized.

The ABAQUS model shown in Figure 6-12(a) was composed of several parts, namely, W24×55 beam, W14×90 column, shear-tab plate and bolt-and-nut parts. The interaction between these parts was captured using the general contact formulation in ABAQUS. The general contact formulation permits tangential and normal contact between all surfaces. A coefficient of friction of 0.60 was used between steel elements. The explicit formulation in ABAQUS was used in all simulations due to the lack of convergence of the implicit formulation in ABAQUS Standard, especially when the general contact formulation option is used. Below is a summary of the different parts of the ABAQUS model.

**W24×55 Beam and W14×90 Column**

The W24×55 beam and W14×90 column were discretized into 10244 and 8300 cubic elements, respectively. Since very little inelastic response was reported for these two members, an elastic material model was assigned to all cubic elements in the column while the metal plasticity model described before was assigned to a few elements for the beam near the connection (elements within a beam length of 6.0" close to the connection). A yield stress of 61.0 ksi (that is approximately the average of the measured yield (52.2 ksi) and ultimate (68.6 ksi) stress reported for the beam) and no strain hardening were set for the model. A linear-elastic material model was used for rest of elements of the girder.

**Shear-Tab Plate**

Figure 6-12(d) shows the shear-tab plate. Since the behavior of Specimen 2A was governed mainly by slippage and yielding of the shear-tab plate, a fine mesh was provided as seen in the close-up view in Figure 6-12(e). The shear-tab plate comprises a total of 3024 solid elements. The diameter of the bolt holes was 1/16" larger than that of the bolts due to structural tolerances. A yield stress of 56.0 ksi (average of the measured yield (45.7 ksi) and ultimate (66.1 ksi) stress reported for the shear-tab plate) and no strain hardening was set for the metal plasticity model. This simple plasticity model of the shear-tab plate does not include damage models that capture cyclic deterioration or fracture.

**Bolts, Nuts and Pretension Forces**

Figure 6-12(f) shows the ABAQUS model for the bolt and nut. It can be seen that the geometry of the bolt and nut in the model was simplified as follows: (a) the bolt was modeled together with its nut as one piece, (b) washers were not modeled, and (c) a rounded bolt head and a nut were modeled instead of the hexagonal shape. A total of 672 elements were used for one bolt and nut model shown in Figure 6-12(f) (4032 elements in total for the six bolts). Since low levels of bolt yielding were reported for the experiments, these high-strength bolts (with a yield stress of 90 ksi) were modeled elastically to reduce computational time. It was noticed that the results did not change when an inelastic material model was used for the bolt and nut model. Given that slippage between the shear-tab plate and web of the girder, both clamped by bolts, governed the cyclic behavior of the simple connection, pretension forces on the bolts were modeled as follows. The pretension forces in the bolts can be directly modeled in ABAQUS/Standard using bolt forces. However, this option is not available in ABAQUS/Explicit. For this reason, a few steps were taken to model bolt pretension forces similar to Citipitioglu *et al.* (2002). The pretension force in the bolts was achieved in several steps using shorter bolts. Initially, the head and nut of a bolt is overlapping with the shear-tab plate and beam web. Displacements were imposed at both ends of the bolt elements (head and nut), stretching the bolt until the surface of the bolt ends were in contact with the respective surfaces, but not overlapping. Then, the general contact option was activated and the bolts were released. To obtain the correct shortening of the bolts that provides the required clamping force, a few small models were created with different length bolts. Bolts undersized by 0.002 in. were found to produce an average pretension stress of 40 ksi that produces a force of 40.0 kips as required per code.

**Fillet Weld**

A “tie” constraint in ABAQUS/Explicit was used to simulate the welded connection (1/4" fillet weld) between the shear-tab plate and the column flange. In a tie constraint, the DOFs of a master surface are

imposed on those of a slave surface. In this case, the surface of the column that is in contact with the shear-tab plate was selected as the master surface. Consequently, the surface of the shear-tab plate that is in contact with the column was selected as the slave surface. This simplification was adopted to minimize computational time since the behavior of the weld contributed very little to the response of the connections.

**Finite Element Results for Specimen 2A**

The finite element model shown in Figure 6-12(a) was subjected to monotonic and cyclic lateral displacements at the tip of the column with increasing amplitude. Note that due to the size of the ABAQUS model, the full loading history of the actual test could not be used in the finite element simulations. Figure 6-13 presents the monotonic and cyclic moment-rotation relationships for the shear-tab connection of Specimen 2A predicted by ABAQUS. The experimental test results of Liu and Astaneh-Asl are also provided for comparison. The rotation of the shear-tab connection is defined as the relative rotation of the beam with respect to the column near the connection. Due to the use of the explicit formulation in ABAQUS, some level of noise is observed in the response as seen in Figure 6-13. This noise could be minimized at the expense of longer real time duration of the simulation.

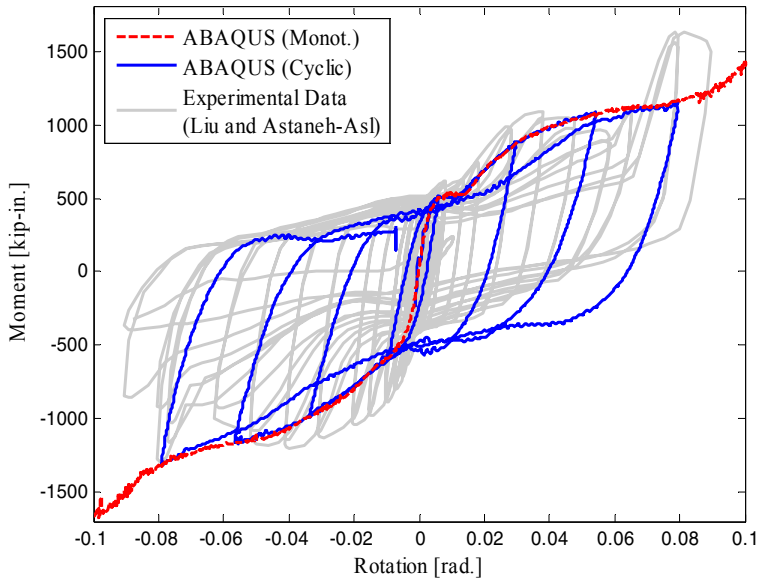


**Figure 6-13 Predicted moment-rotation relationships for shear-tab connection of Specimen 2A using ABAQUS Explicit**

Some observations can be made based on the results presented in Figure 6-13. In general, the envelope of the moment-rotation relationship for the shear-tab connection without concrete slab is slightly under-predicted in the ABAQUS model. However, the envelope of the predicted cyclic response presents minimal cyclic strength deterioration. Consequently, the predicted envelopes of both monotonic and cyclic response are similar. The stiffening of the connection under positive bending due to binding of beam flanges on column flanges at large rotations is not captured. Also, the observed strength deterioration under negative bending at around 0.08 rad. due to fracture of the shear-tab plate is not captured by the ABAQUS model since fracture models were not included.

#### 6.3.2.3 Finite Element Model of Specimen 6A

Figure 6-14(a) shows the ABAQUS model used to simulate the response of the shear-tab connection of Specimen 6A, which included a floor slab. The model of the bare steel subassembly is similar to that of Specimen 2A presented in Section 6.3.2.2. Only the region of the floor slab near the joint was modeled to reduce computational time. A description of the floor slab model is provided below.

Only the lightweight concrete, shear studs and welded wire mesh were included in the ABAQUS model. The metal deck and #3 reinforcing bars were neglected. The concrete damage plasticity model available in ABAQUS was utilized to model the lightweight concrete of the floor slab of Specimen 6A. The stress-strain relationship for the concrete was developed using the Mander model (Mander *et al.*, 1988) with the measured concrete compressive strength of 6230 and the modulus of elasticity of the concrete estimated using the ACI-318 formula for lightweight concrete. The concrete slab shown in Figure 6-14(a) consists of 41460 cubic elements. A finer mesh was provided near the joint. The shear studs, provided to attach the concrete slab to the W24×55 beam, were modeled as follows. An elastic material model with the modulus of elasticity of steel was assigned to the cubic elements of the concrete slab where the shear studs are located to simulate the response of the shear studs. These elements, highlighted in Figure 6-14(b), were attached to the upper face of the top flange of the W24×55 beam using a tie constraint in ABAQUS. To ensure the composite action of the W24×55 beam with the concrete slab, the face of beam in contact with concrete slab was connected using a tie constraint. The welded wire mesh placed over the entire area of the floor slab was modeled using the cubic elements of the concrete slab mesh for simplicity. The classic metal plasticity model was assigned to these elements which are highlighted in Figure 6-14(c). The cross-sectional area of the cubic elements simulating the response of the welded wire mesh in ABAQUS was larger than the actual area to avoid a very fine mesh which increases the size of the model and the computational time. Consequently, the modulus of elasticity and yield strength of the material model for the welded wire mesh were modified accordingly.

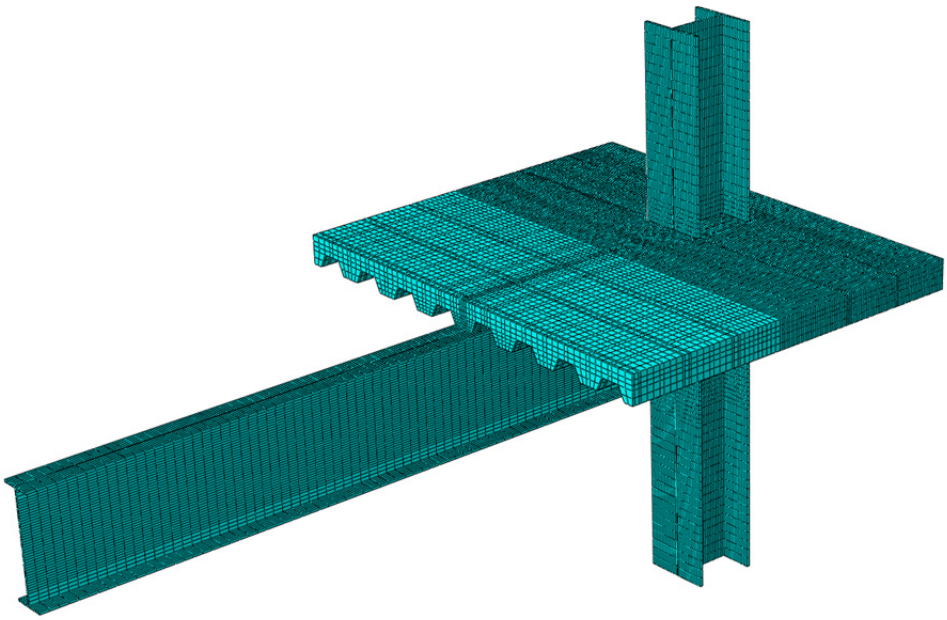

(a) Three-dimensional ABAQUS model

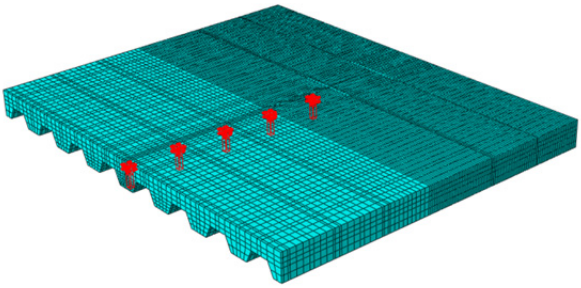

(b) Elements for modeling shear studs

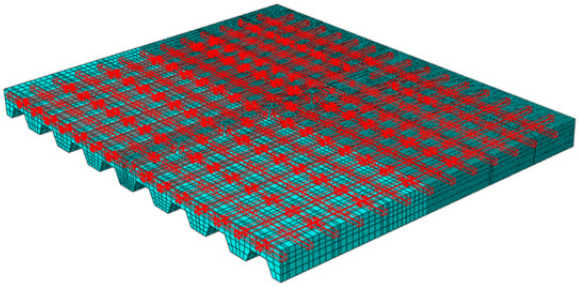

(c) Elements for modeling welded wire mesh

**Figure 6-14 ABAQUS model used to simulate the response of Specimen 6A in Liu and Astaneh-Asl (2000a)**

**Finite Element Results for Specimen 6A**

Figure 6-15 presents the monotonic and cyclic moment-rotation relationships for the shear-tab connection of Specimen 6A predicted using ABAQUS as well as the theoretical envelope constructed following the guidelines of Liu and Astaneh-Asl (2004). The experimental test results of Liu and Astaneh-Asl are also provided for comparison. It can be seen in Figure 6-15 that the ABAQUS model significantly underestimates the moment strength of the shear-tab connection. When the concrete slab is in tension, the lack of reinforcement in the model is possibly the cause of the lower prediction in strength. The strength deterioration, especially under positive bending is not captured, nor is the stiffening of the connection under negative bending due to binding of the beam flange on the column flange. The cyclic response

predicted by the ABAQUS model presents a pinched hysteretic behavior typical of shear-tab connections. In summary, the ABAQUS model presented herein does not reproduce the response of the shear-tab connection with the composite floor slab. The complex behavior of the concrete floor slab and its interaction with the steel subassembly is not captured with this simple ABAQUS model.

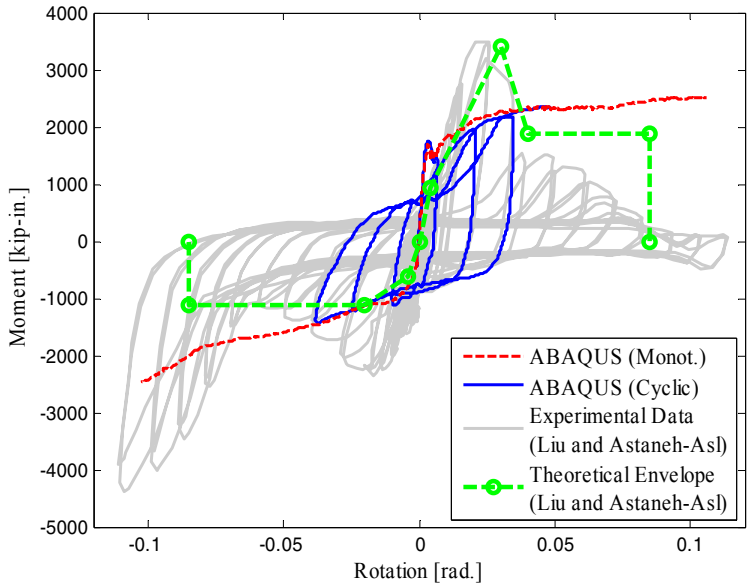


**Figure 6-15 Predicted moment-rotation relationships for shear-tab connection of Specimen 6A using ABAQUS and theoretical relationships proposed by Liu and Astaneh-Asl (2000a)**

However, some parameters characterizing the moment-rotation response of the shear-tab connection can be obtained using the theoretical envelope proposed by Liu and Astaneh-Asl shown in Figure 6-15. The guidelines of Liu and Astaneh-Asl were developed based on experimental data which includes the experimental results of Specimen 6A. Therefore, the theoretical moment-rotation relationship proposed by Liu and Astaneh-Asl predicts closely the peak moment strength of Specimen 6A under positive bending. However, in the guidelines, the calculation of the moment capacity under negative bending neglects both the contribution of the floor slab and binding of the beam on the column flange. Also, the maximum rotation capacity is based on the limit state of binding of the beam flange on the column flange since this was followed by shearing of bolts or fracture of shear-tab plate (Liu and Astaneh-Asl, 2004).

#### 6.3.2.4 Finite Element Model of Shear-Tab Connection of Half-Scale Gravity Frame

Figure 6-16 presents the ABAQUS model used to simulate the response of the shear-tab connection of the half-scale gravity frame presented in Section 5.3. All modeling assumptions and simplifications adopted

for the previous ABAQUS models described in Section 6.3.2.2 and Section 6.3.2.3 were also adopted in this model. The measured modulus of elasticity of 2000 psi and the measured concrete compressive strength of 3510 psi (see Figure 5-7(b)) were used for the concrete plasticity damage model. Figure 6-16 shows the number of cubic elements in which the different elements were discretized.

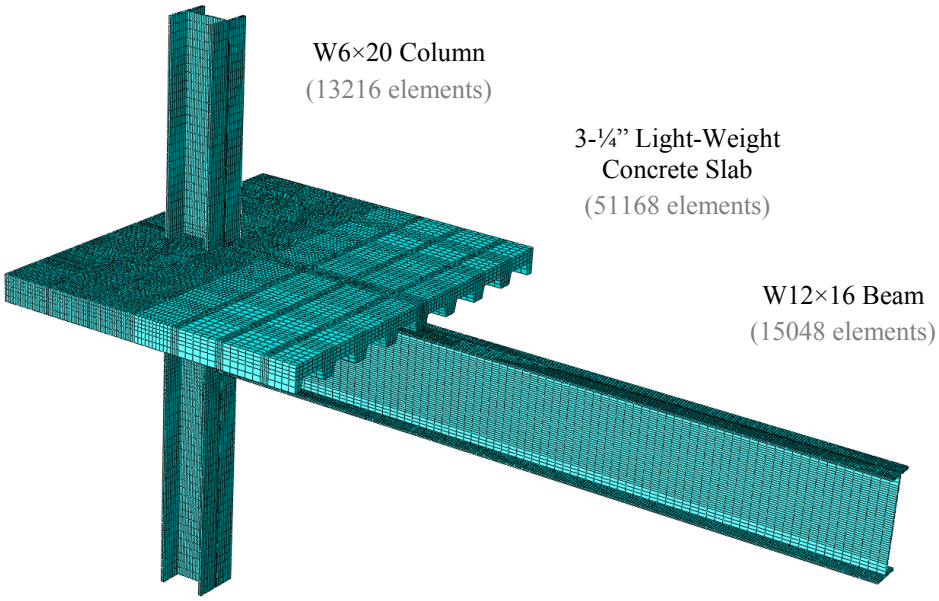


(a) Three-dimensional ABAQUS model

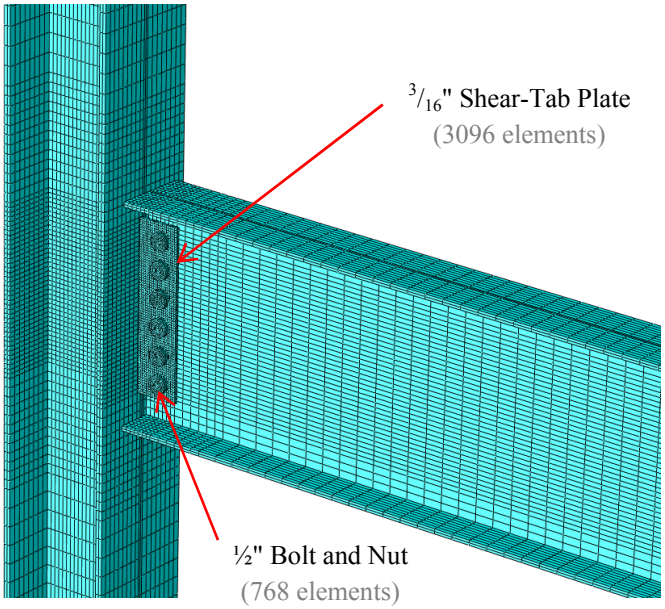


(b) Close-up of shear-tab connection (floor slab not shown)

**Figure 6-16 ABAQUS model used to simulate the response of shear-tab connection of the half-scale gravity frame**

Figure 6-17 presents predicted monotonic and cyclic moment-rotation relationships for the shear-tab connection of the half-scale gravity frame using ABAQUS as well as the theoretical moment-rotation envelope of Liu and Astaneh-Asl. Since the dimensions of the shear-tab connection of the half-scale gravity frame are approximately half of those of Specimen 6A, the scaled moment-rotation response of Specimen 6A (the bending moments were scaled down by the bending moment scale factor of $0.5^3$) is plotted in Figure 6-15 for reference.

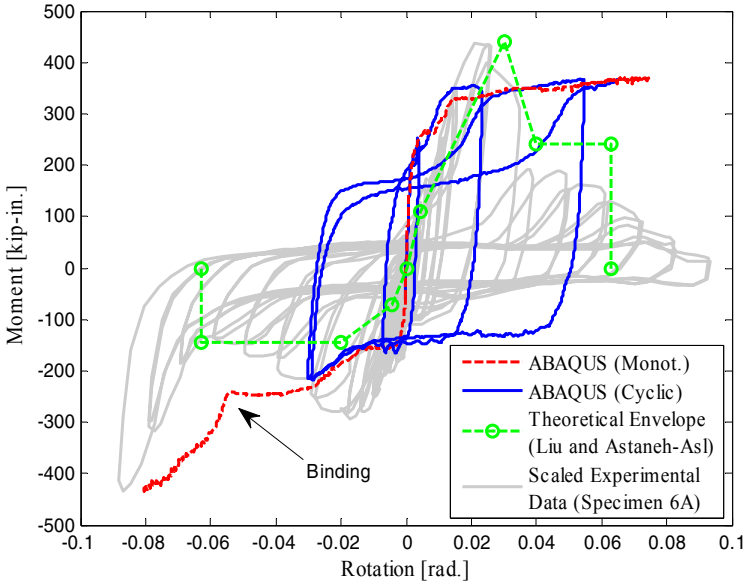


**Figure 6-17 Predicted moment-rotation relationships for shear-tab connection of half-scale gravity frame using ABAQUS and guidelines of Liu and Astaneh-Asl (2000a)**

It can be observed that the theoretical envelope of Liu and Astaneh-Asl predicts a similar bending strength as that of the scaled experimental response under positive bending. Also, the monotonic response predicted by ABAQUS simulates the response of the shear-tab connection after binding as shown in Figure 6-17 at a rotation value of approximately 0.055 rad. However, since it was previously shown that the simple models described above do not reproduce faithfully the response of the shear-tab connections of Specimen 6A, the results presented in Figure 6-17 were not used to assist in the calibration of the numerical model of the gravity frame for the hybrid simulations.

### 6.3.3 Calibration of Pinching4 Hysteretic Model

Based on the observations presented in Section 6.3.2, the Pinching4 hysteretic model was calibrated to reproduce the moment-rotation response of the shear-tab connections of the half-scale gravity frame used in the second series of hybrid simulations. The guidelines of Liu and Astaneh-Asl were employed to estimate the moment capacity under positive bending and the initial stiffness of the shear-tab connection. However, since the guidelines were based on cyclic test results, such positive moment capacity was increased by a factor of 1.10 for monotonic loading. Since, as explained before, the dimensions of the shear-tab connections of the half-scale gravity frame are approximately half of those of Specimen 6A, the scaled moment-rotation response of Specimen 6A (moments were scaled down by $0.5^3$) was utilized to estimate the parameters of the Pinching4 model defining pinching. Also, the negative moment capacity of the connections was selected to match the scaled moment capacity of Specimen 6A. The stiffening of the connection under negative bending at large rotations due to binding of the beam flange on column flange was ignored since this stiffening effect is not always exhibited by a shear-tab connection. Figure 6-18 presents several windows of the calibration of the Pinching4 hysteretic model. Figure 6-18(a) and Figure 6-18(b) show that the calibrated Pinching4 model reproduces reasonably well the initial stiffness and pinching response of the connection at small rotations. Figure 6-18(c) shows that the calibrated model captures very well the pinched hysteretic response of the referential data. As mentioned earlier, the response of the connection after binding of beam flange on the column flange was purposely not capture by the Pinching4 model as shown in Figure 6-18(e) and Figure 6-18(f).

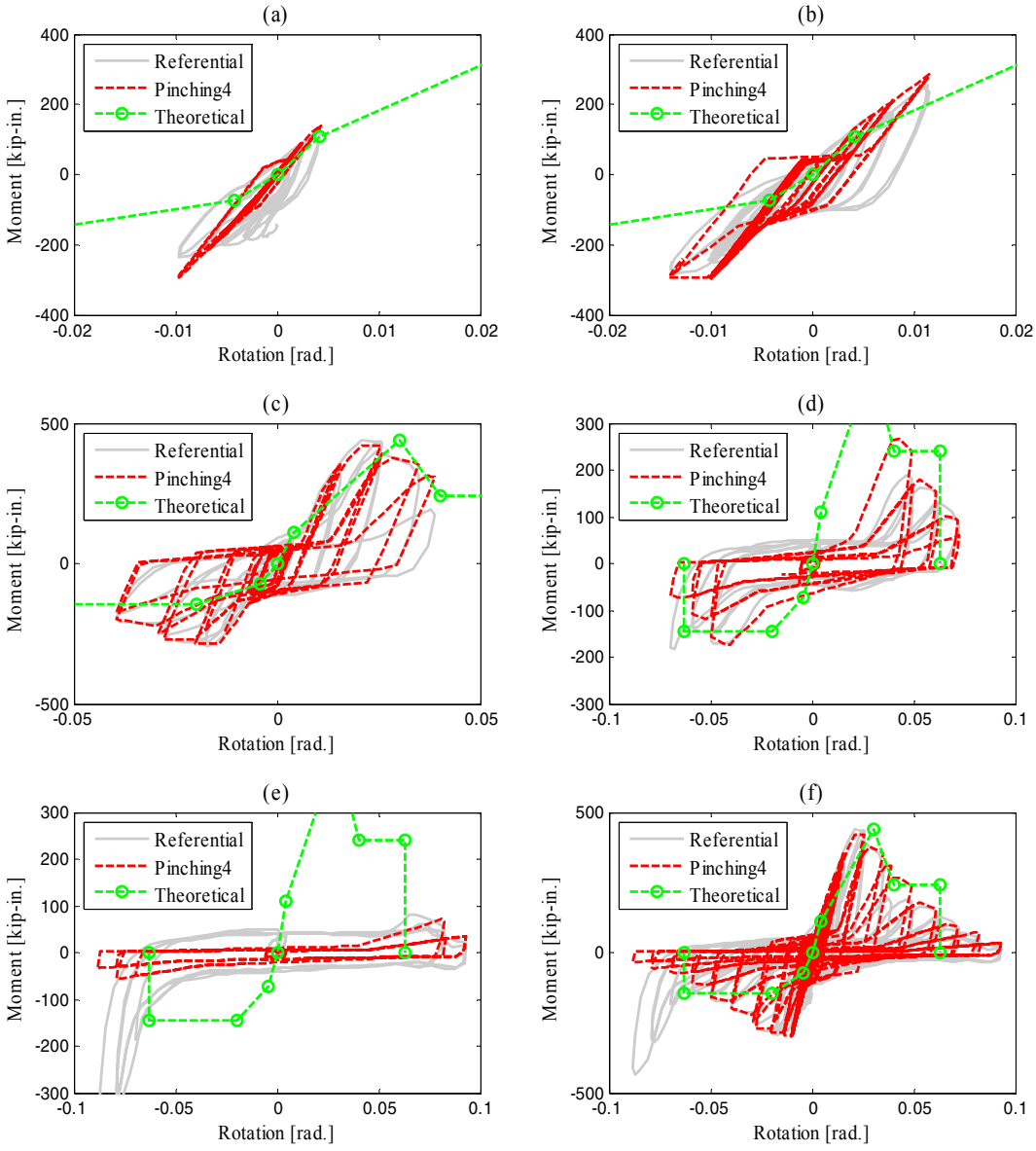


**Figure 6-18 Calibration of Pinching4 hysteretic model to reproduce the cyclic moment-rotation response of shear-tab connections of half-scale gravity frame**

## 6.4 Substructuring Technique for Hybrid Simulation

### 6.4.1 Introduction

As mentioned earlier in Section 4, the use of substructuring in hybrid simulation permits physical testing of only key subassemblies of a frame structure in a laboratory while the response of the rest of the structure is simulated in a computer model. In substructuring, equilibrium and compatibility should be satisfied at the interface nodes between the physical and numerical sub-structures. However, limitations on the number of actuators available in a testing facility make difficult to control physical sub-structures presenting a large number of boundary DOFs such as those sub-structures selected for this experimental program which present 9 boundary DOFs as shown in Figure 6-19.

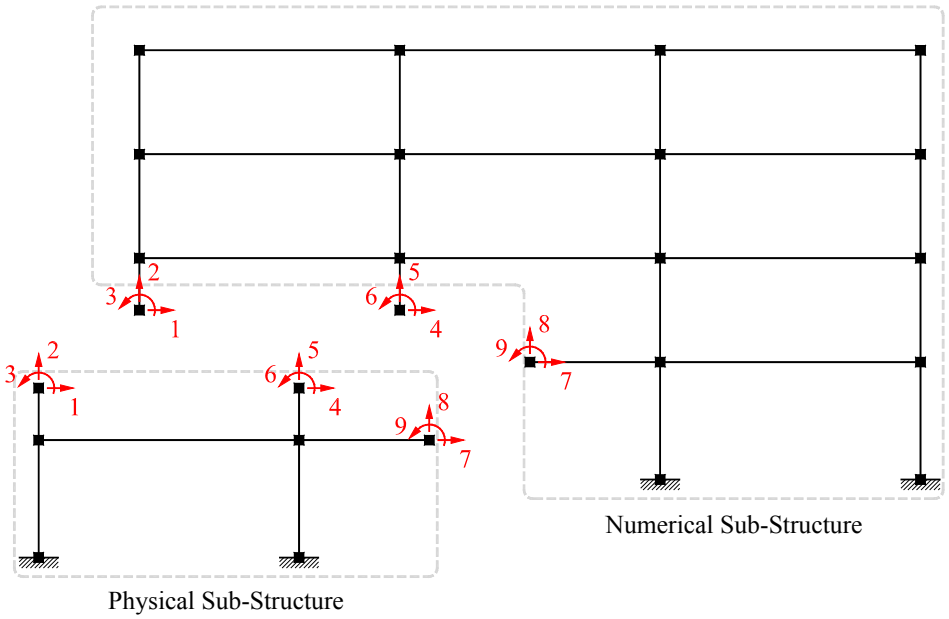


**Figure 6-19 Degrees of freedom at the interface between the physical and numerical sub-structures**

Simplifications of the boundary conditions between the physical and numerical sub-structures have been proposed to reduce the number of actuators. Schneider and Roeder (1994) suggested substructuring frame structures at points of inflection where hinges can be assumed to eliminate the rotational DOFs at the interface nodes. This substructuring technique provides reasonable results when the frame structure experiences moderate levels of yielding. However, for collapse assessment, significantly different results were observed which changed the collapse mechanism of a frame structure. On the other hand, Cortes-Delgado (2013) tested a physical subassembly similar to those selected for this experimental program

using a substructuring technique developed by Wang *et al.* (2011) with simplified boundary conditions and an overlapping domain between the physical and numerical sub-structures. This technique was subsequently refined by Hashemi *et al.* (2013). Hashemi *et al.* validated this technique through a series of hybrid simulations conducted on a 1/8-scale aluminum frame structure which was previously tested in a shake table. The substructuring algorithm used in the series of hybrid simulations in this research project was based on the work of Hashemi *et al.* and was extended to account for varying axial loads on the columns. This section presents a description and a numerical evaluation of the performance of the substructuring technique.

### 6.4.2 Substructuring Technique with Simplified Boundary Conditions

To illustrate the substructuring technique adopted herein to conduct the two series of hybrid simulations, Figure 6-20 shows a detailed diagram of the physical and numerical sub-structures of the Hybrid Model #1 (moment frame). Unlike the schematic representation of the Hybrid Model #1 previously shown in Figure 4-4, it can be seen in Figure 6-20 that the domain of the numerical sub-structure was extended and consequently, there is an overlapping domain (indicated in the figure) between the physical and numerical sub-structures. Also, Figure 6-20 shows that the boundary conditions of the physical sub-structure at the interface with the numerical sub-structure were simplified. Note that the exact boundary DOFs (DOF 1 through 9) are shown in Figure 6-20. Such simplifications were necessary to control the physical sub-structures using the experimental test setup shown in Figure 6-19 with four actuators. The overlapping domain helps to minimize the loss of accuracy of the simulation as a consequence of the simplified boundary conditions. The leaning column, part of the numerical sub-structure, is not shown in Figure 6-20 for clarity.

The boundary DOFs of the physical sub-structure were simplified as follows. Hinges were provided at the boundaries of the physical sub-structure to eliminate the rotational DOFs (i.e., DOF 3, 6 and 9). Due to the difficulties associated with controlling the stiff axial DOFs in columns, the vertical DOFs at the top of the columns (i.e., DOF 2 and 5) were not controlled in displacement. Instead, axial forces at these DOFs were imposed using force-controlled actuators to satisfied equilibrium. Therefore, only equilibrium and not compatibility was satisfied at these vertical DOFs. Also, the vertical DOF at the end of the girder (DOF 8) was restrained by the vertical link member. The horizontal DOFs at the top of the columns (i.e., DOF 1 and 4) were coupled using the horizontal link member. Therefore, the boundary conditions of the physical sub-structure at the interface with the numerical sub-structure were simplified to two horizontal DOFs which are controlled by two displacement-controlled horizontal actuators.

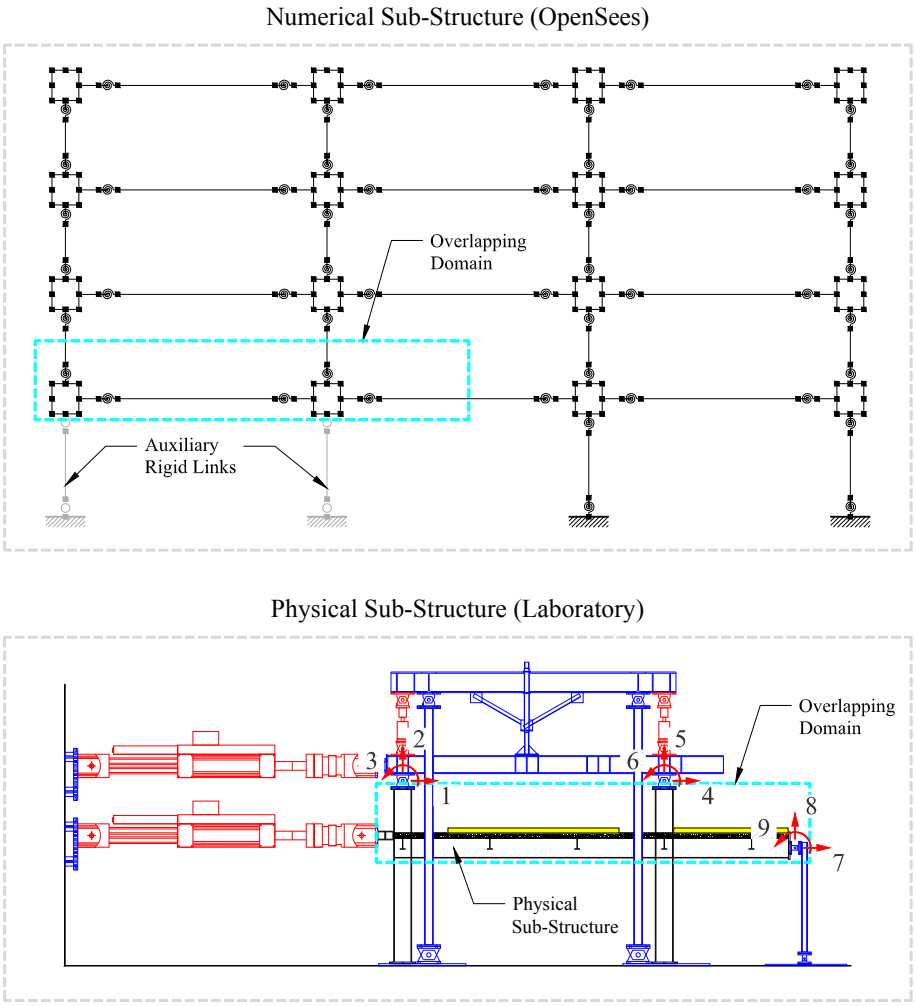


**Figure 6-20 Physical and numerical sub-structures of Hybrid Model #1, overlapping domain and exact boundary DOFs of physical sub-structure**

Figure 6-21 is used to explain and illustrate the data exchange between the physical and numerical sub-structures using the substructuring algorithm with overlapping domains. As mentioned before, the physical and numerical sub-structures are coupled through OpenFresco. At each data communication step, the top and bottom horizontal actuators are commanded by $1/2\,(u_1+u_2)$ and $u_1$, respectively, where $u_1$ and $u_2$ are the first- and second-story lateral displacements, respectively, calculated by the integration algorithm. Instead of returning the actuator forces to the integration algorithm or the reactions at the boundary of the physical sub-structure which are not accurate due to the simplifications, reactions within the physical sub-structure at the boundary of the numerical sub-structure (i.e., $M_1$, $V_1$, $M_2$, $V_2$) are returned as shown in Figure 6-21 (force feedback vector). These reactions are indirectly obtained from measurements of the strain gages previously shown in Figure 5-8 (and Figure 5-15 for Hybrid Model #2).

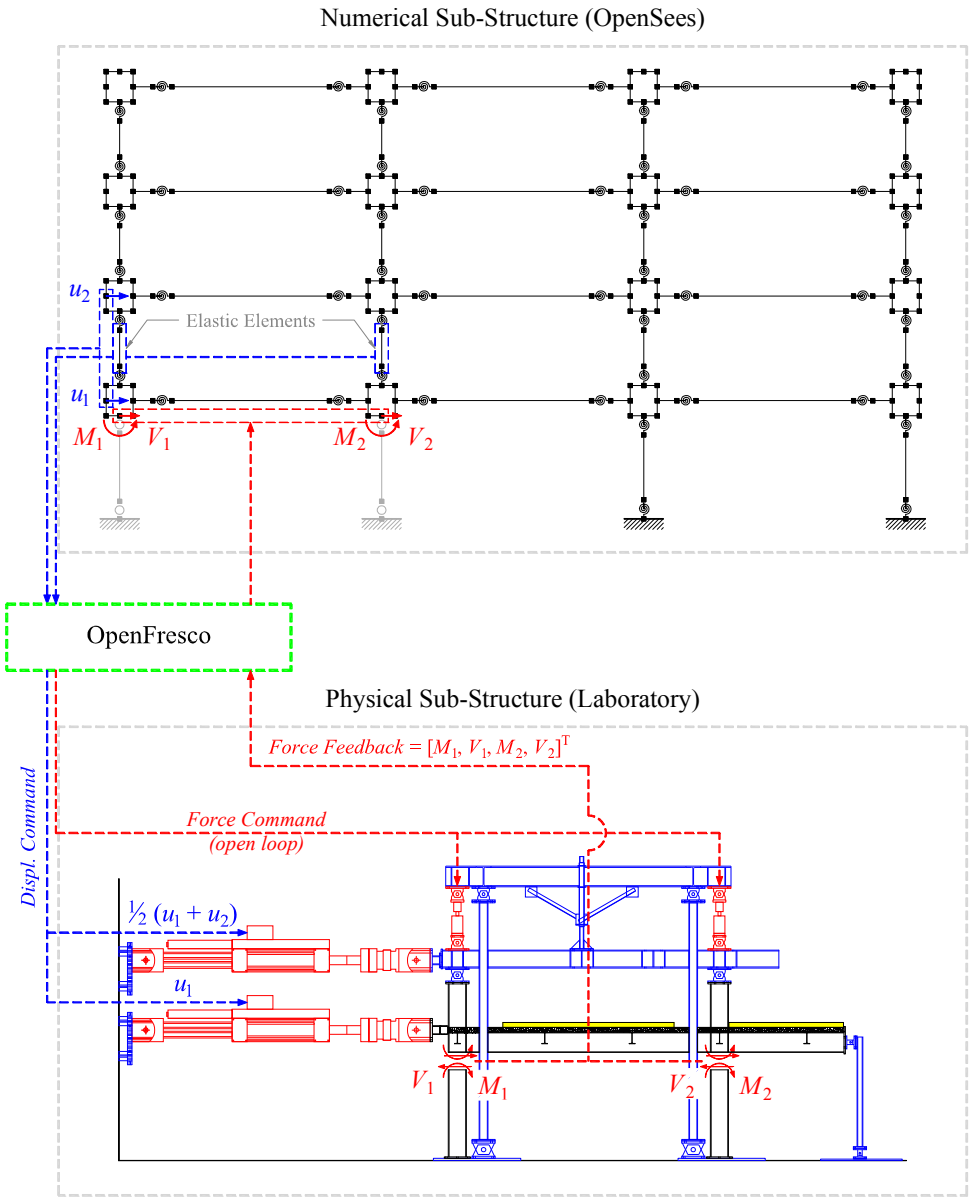


**Figure 6-21 Schematic representation of data exchange between physical and numerical sub-structures using substructuring algorithm with overlapping domains**

Given that a hybrid simulation is carried out in displacement control with OpenFresco, the force command for the vertical actuators cannot be sent directly from the numerical to the physical sub-structure. Instead, the displacement vectors of the elastic beam-column elements indicated in Figure 6-21 are sent to OpenFresco to be transformed into a force vector (using the elastic stiffness matrix of such elastic elements) which is then used to obtain the command signal for the force-controlled vertical actuators. Since this is done using an open-loop control which means that no axial forces are returned to

the integration algorithm, the vertical DOFs at the boundary of the numerical sub-structure are constrained with auxiliary link elements as shown in Figure 6-20.

### 6.4.3 Evaluation of Substructuring Technique with Simplified Boundary Conditions

The substructuring technique described above in Section 6.4.2 was numerically evaluated through a series of coupled simulations. The coupled simulations are used to reproduce numerically the data communication algorithm between the physical and numerical sub-structures during a hybrid simulation. The concept of coupled simulations was previously introduced in Section 3.4.2. This section presents an evaluation of the substructuring algorithm implemented particularly for the two hybrid models presented previously in Section 4.4.5 and Section 4.4.6.

#### 6.4.3.1 Evaluation of Substructuring Technique for Hybrid Model #1 (Moment Frame)

In the coupled simulations presented in this section, the numerical and physical sub-structures of the Hybrid Model #1 shown in Figure 6-20 are modeled in two separate OpenSees scripts referred to as the master and slave OpenSees scripts, respectively, as shown in Figure 6-22. These two OpenSees scripts are coupled through OpenFresco as explained in Section 3.4.2 (for reference, see Schellenberg *et al.*, 2008). However, modifications were made to the generic Experimental Element (*expElement generic*) object in OpenFresco to implement the data communication algorithm of the substructuring technique described in Section 6.4.2. Figure 6-22 illustrates the data communication algorithm between the master and slave OpenSees scripts during a coupled simulation. At each integration step in a coupled simulation, a vector of displacements is sent from the master to the slave OpenSees script. Such displacements are imposed to the sub-structure contained in the slave OpenSees script and the vector of internal resisting forces is returned to the integration algorithm in the master OpenSees script. Since only displacement boundary conditions can be imposed to the sub-structure inside the slave OpenSees script, the axial forces at the top of the columns in the slave OpenSees script cannot be applied similar to the open-loop force command shown in Figure 6-21. Therefore, only axial forces from gravity loads were applied on the columns of the slave OpenSees script. The coupled model shown in Figure 6-22 was subjected to four increasing intensities of the LGPC ground motion (similar to the testing program of the two series of hybrid simulations presented in Section 7). The results of these coupled simulations are compared with those of conventional numerical simulations where the complete model of the moment frame structure was encapsulated in one single OpenSees script. The results of such conventional simulations are assumed as the exact solution. Dynamic analysis of the coupled model requires the specialized implicit Newmark

method with fixed number of iterations (INM-HS) (see Section 3.2.2) to integrate the equations of motion. On the other hand, the conventional implicit Newmark method (see Section 3.2.1) was used for the conventional simulations.

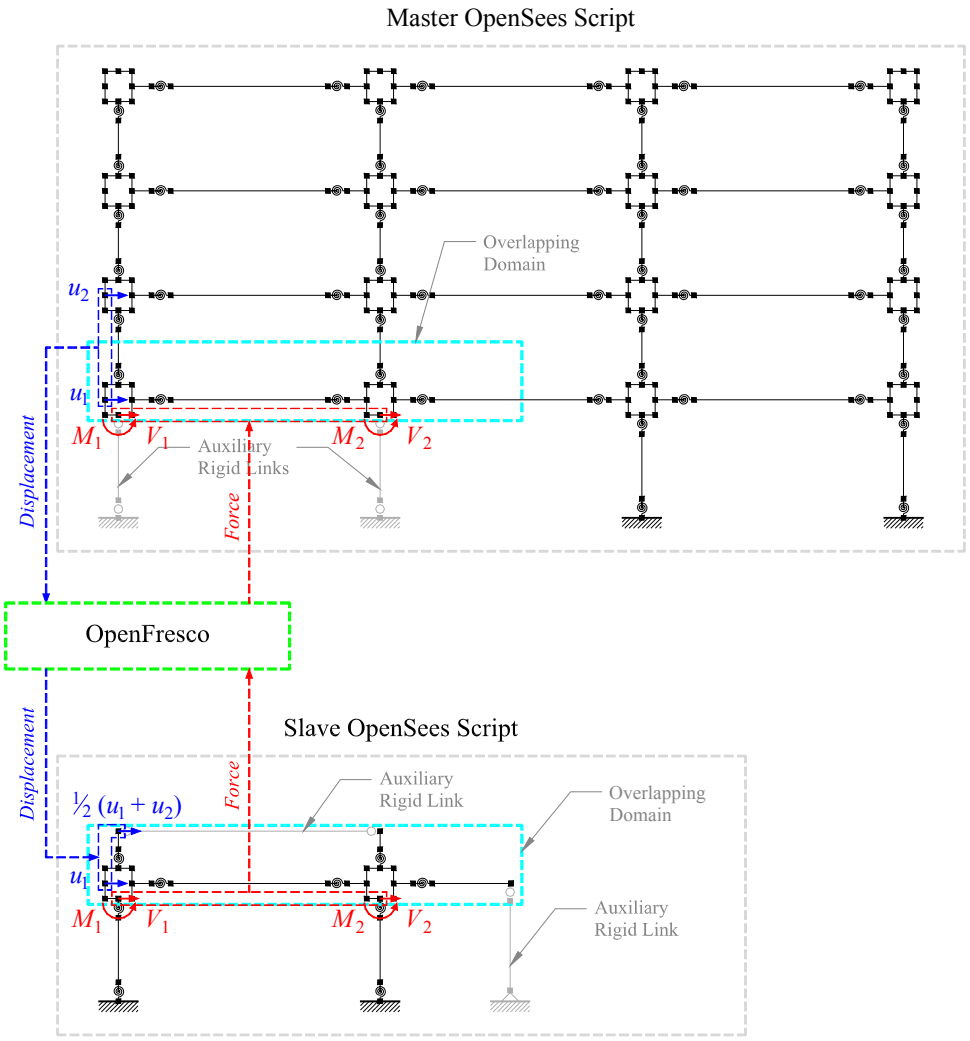


**Figure 6-22 Master and slave OpenSees scripts of coupled simulations with substructuring technique used to simulate the response of Hybrid Model #1**

Figure 6-23 and Figure 6-24 present global response results, namely, roof drift ratio and base shear, respectively, predicted for the Hybrid Model #1. It can be seen that the results of the coupled simulations with the substructuring algorithm are in close agreement with the assumed exact solution all the way through collapse. Similar analysis carried out with other substructuring techniques without the overlapping domain (e.g., Schneider and Roeder, 1994) were not only not able to trace the global response to collapse with similar levels of accuracy but also resulted in a completely different collapse

mechanism. The good agreement in the global response shown in Figure 6-23 and Figure 6-24 made the substructuring technique with simplified boundary conditions and overlapping domain a viable alternative for hybrid testing of large frame subassemblies (with a large number of DOFs) using a reduced number of actuators available in a testing facility to load the physical specimen in the laboratory.

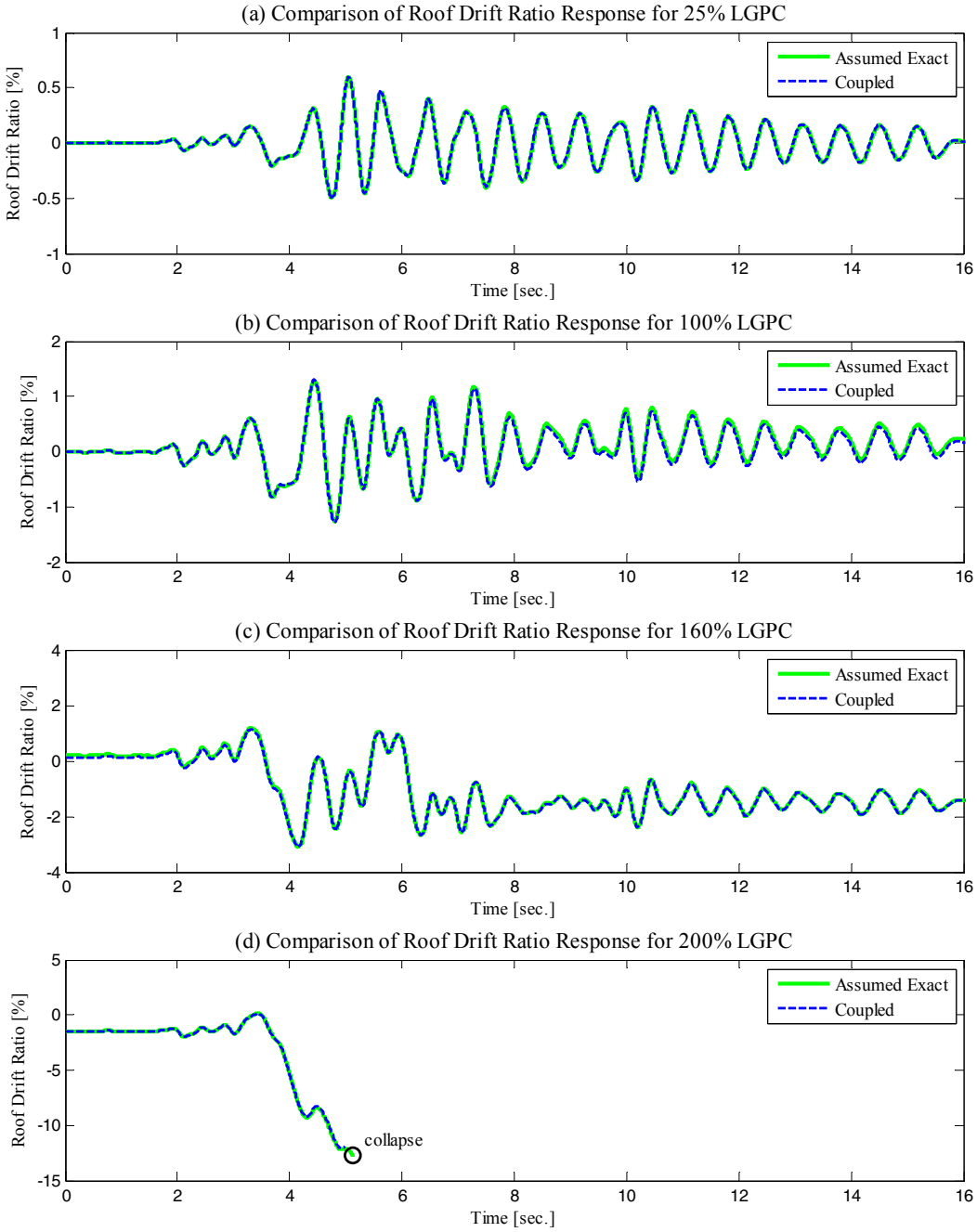


**Figure 6-23 Comparison of roof drift ratio of complete (assumed exact) and coupled models used to simulate the response of Hybrid Model #1**

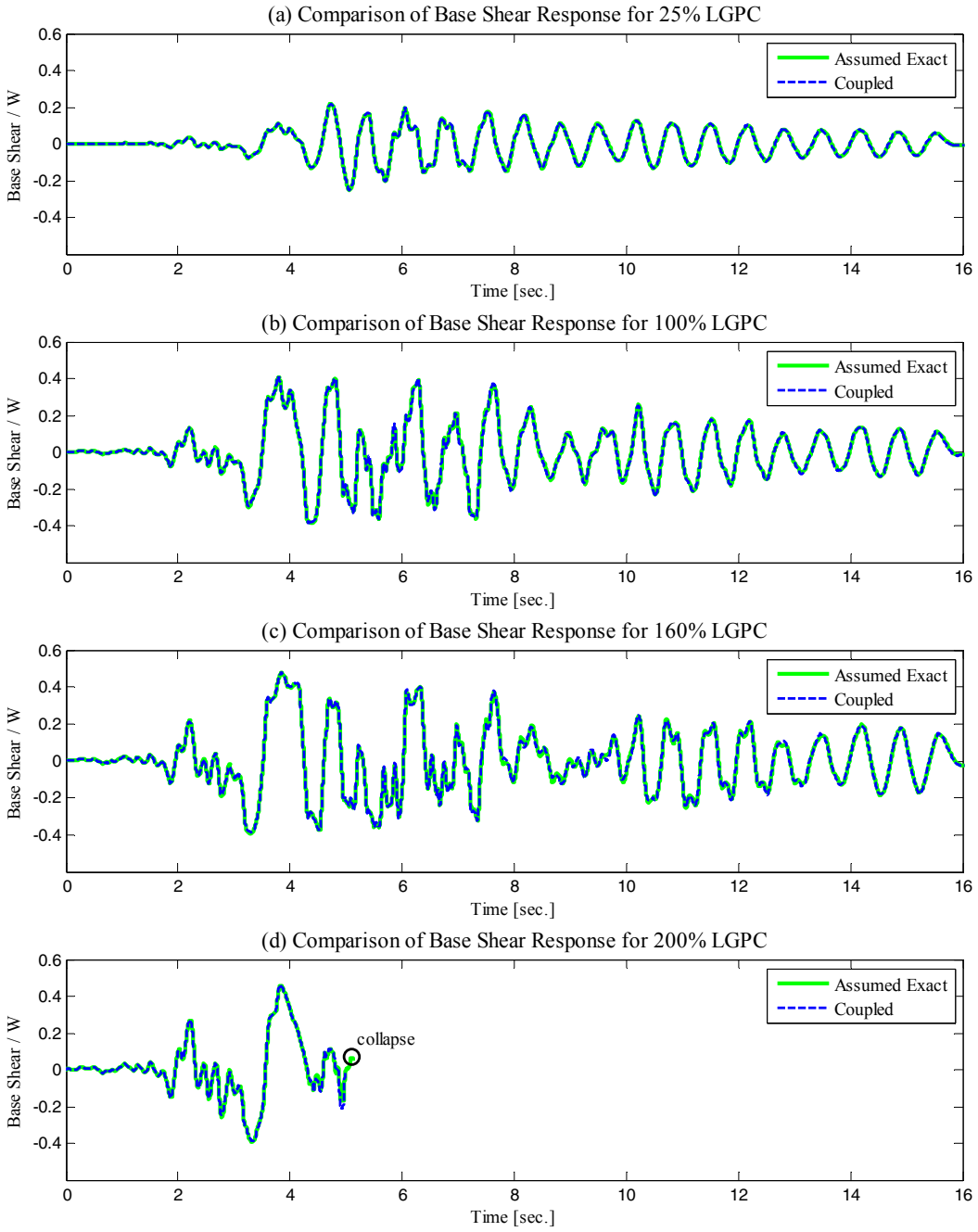


**Figure 6-24 Comparison of base shear of complete (assumed exact) and coupled model used to simulate the response of Hybrid Model #1**

However, compared to the assumed exact response of the frame structure, some differences were observed in the local response of the master and slave OpenSees scripts as a consequence of the simplified boundary conditions. Because of this, the ability of the substructuring technique to subject the physical sub-structures to realistic loading conditions through collapse is evaluated below.

Figure 6-25 through Figure 6-27 compare moment-rotation relationships for selected column plastic-hinge regions of the coupled model with those of the assumed exact response. The location of the plastic-hinge regions is indicated with sketches provided at the top of each plot set. As indicated before, the slave OpenSees script of the coupled model (shown as Coupled(S) in the legends of Figure 6-25 through Figure 6-27) simulates the response of the moment frame physical sub-structure in the first series of hybrid simulations.

Figure 6-25 shows that the response of the plastic hinges at the base of the columns of the slave OpenSees script compares very well with those of the assumed exact response. However, the slave OpenSees script presents slightly smaller rotations. Also, while the response at the top of the first-story columns shown in Figure 6-26 compares reasonably well when the response is elastic (25% through 160% LGPC), significant differences are observed towards collapse (200% LGPC) as seen in Figure 6-26(g) and Figure 6-26(h). Figure 6-27 shows the response of column plastic-hinge regions at the bottom of the second story. In these plots, the response of the coupled model is shown for the master and slave OpenSees scripts since the column plastic-hinge regions at these locations are within the overlapping domain. The response of the columns at the bottom of the second story is elastic for all ground motion intensities except for the exterior column at 200% LGPC (see Figure 6-27(g)). Typically, the moment demand at the bottom of the second-story columns of the slave OpenSees script is somewhat smaller than the assumed exact response.

The aforementioned observations indicate that, as expected, the column plastic hinges of the frame subassembly in the slave OpenSees script (which simulates the response of the physical sub-structure) away from the simplified boundary conditions exhibit a more similar response to the assumed exact solution than those located near. For this particular model, only minor differences in the response of the column plastic hinges of the frame subassembly in the slave OpenSees script were observed. The largest differences were found for the top plastic hinges of the first-story columns near collapse.

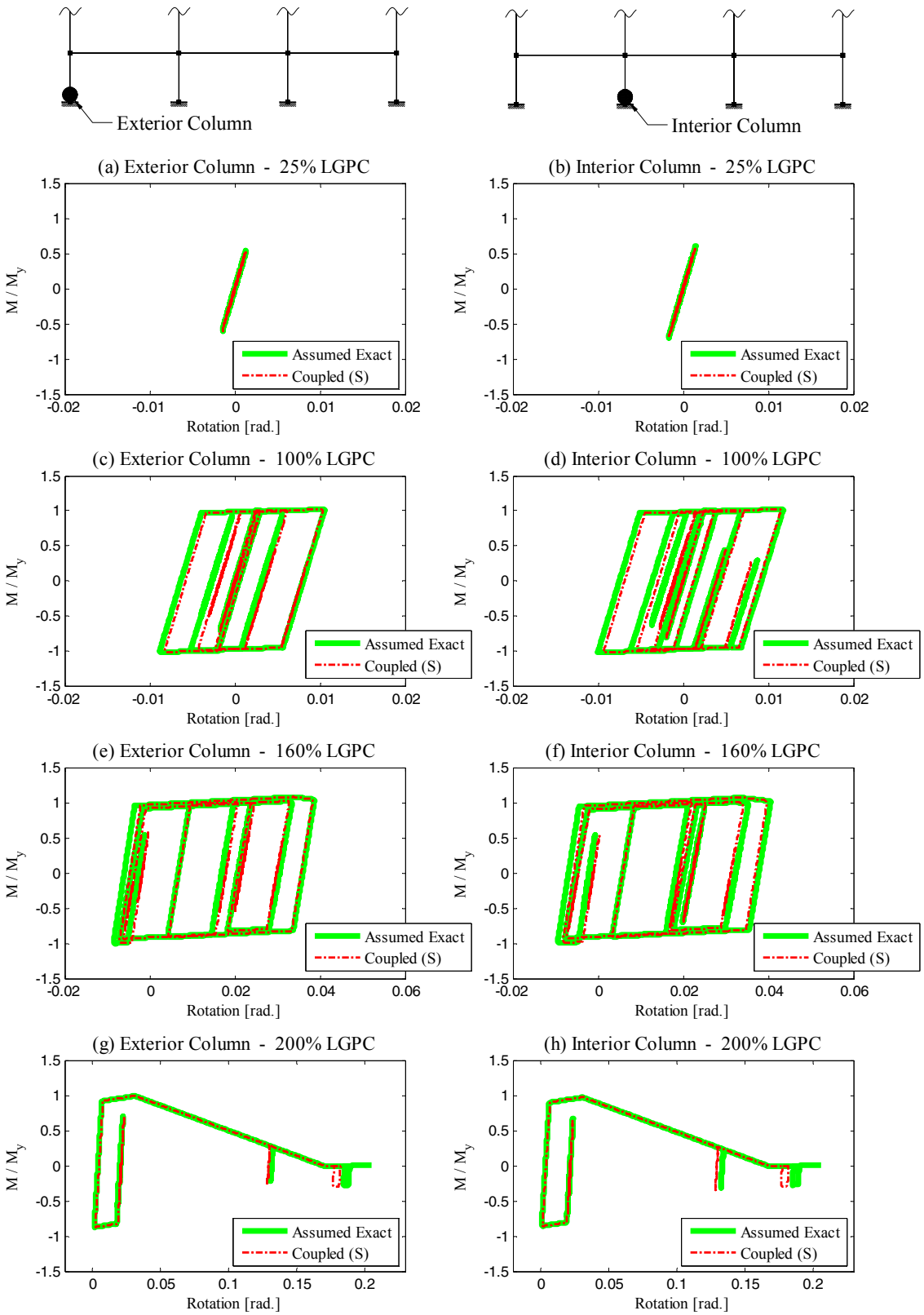


**Figure 6-25 Comparison of moment-rotation relationships for selected columns of complete (assumed exact) and coupled models used to stimulate the response of Hybrid Model #1 (Part I)**

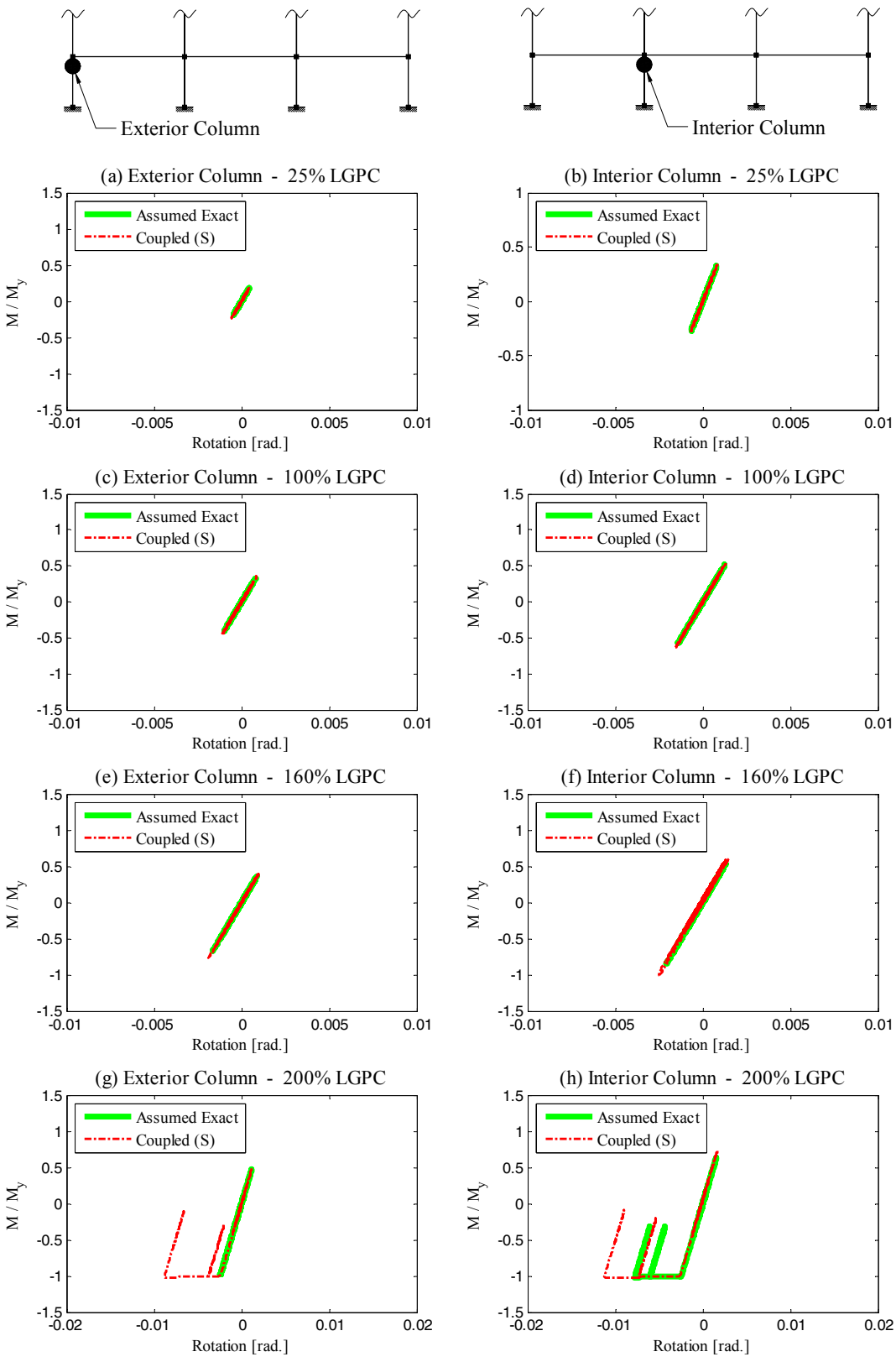


**Figure 6-26 Comparison of moment-rotation relationships for selected columns of complete (assumed exact) and coupled models used to stimulate the response of Hybrid Model #1 (Part II)**

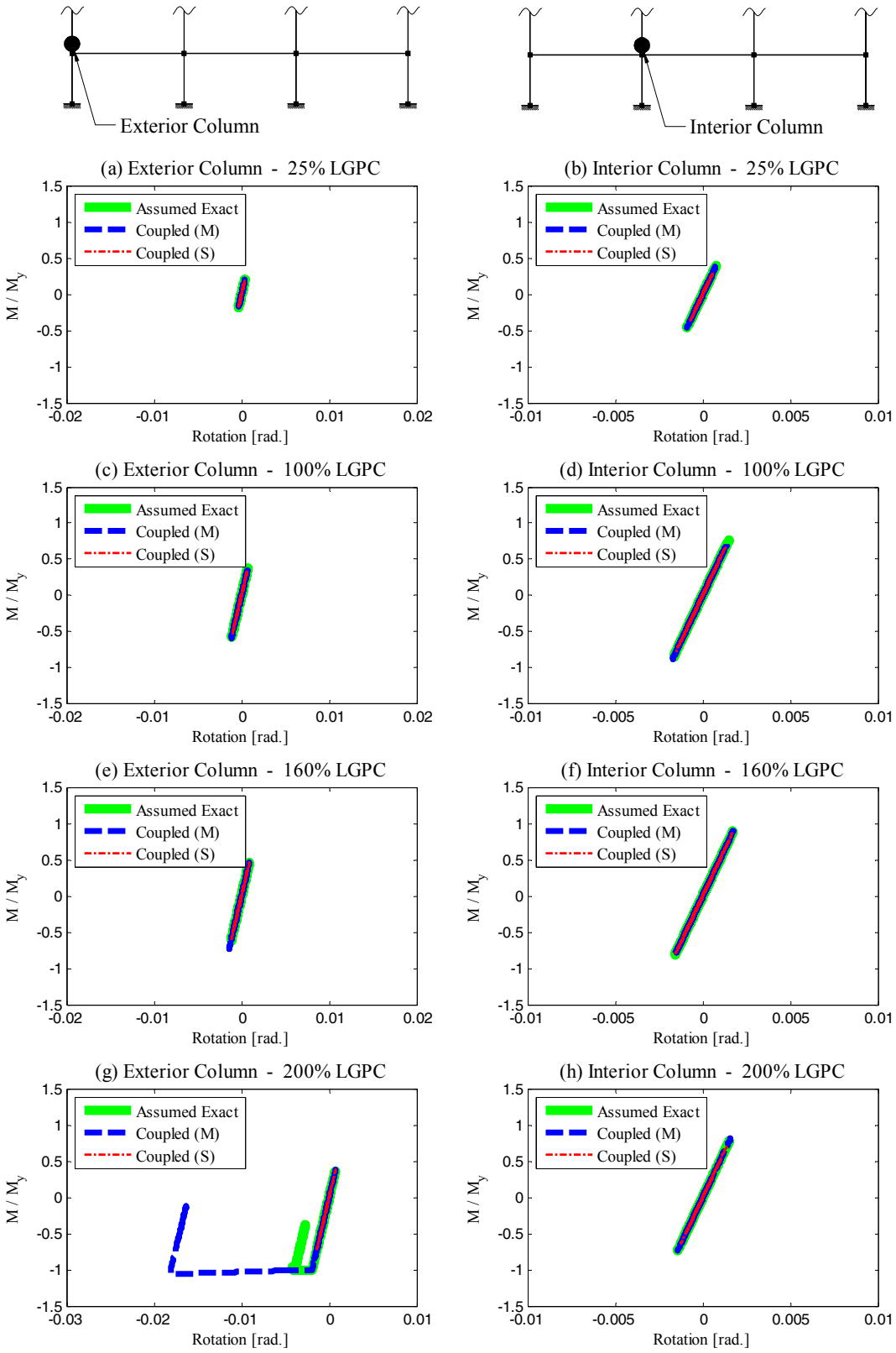


**Figure 6-27 Comparison of moment-rotation relationships for selected columns of complete (assumed exact) and coupled models used to stimulate the response of Hybrid Model #1 (Part III)**

Figure 6-28 compares moment-rotation relationships for girders with RBS (plastic-hinge regions) within the overlapping domain between the master and slave OpenSees scripts (see Figure 6-22 for reference). Sketches provided at the top of Figure 6-28 are used to indicate the location of the girder plastic-hinge regions. Figure 6-28 presents the response of the girder of both the master and slave OpenSees scripts.

Figure 6-28 shows that the girders of the slave OpenSees script (simulating the response of the physical sub-structure) exhibit significantly smaller rotations than the assumed exact response. On the contrary, larger rotations are experienced by the girders of the frame subassembly in the master OpenSees script as compared to the assumed exact response.

To better observe the distribution of the plastic deformation in the frame structure, Figure 6-29 compares moment-distortion relationships for panel zones within the overlapping domain. Similar to Figure 6-28, sketches provided at the top of Figure 6-29 show the location of the panel zones. Contrary to the observations provided for Figure 6-28, Figure 6-29 shows that the panel zones in the slave OpenSees script exhibits significant larger deformation demands than the assumed exact response and the deformation demands on the panel zones in the master OpenSees script are comparatively smaller.

Both, Figure 6-28 and Figure 6-29, indicate that the distribution of the plastic deformation at the joints of the frame structure within the overlapping domain is somewhat different from that of the assumed exact response. The distribution of the plastic deformation at the exterior and interior joints within the overlapping domain is presented in Figure 6-30 and Figure 6-31, respectively. The response of the panel zones as well as girders and columns framing into the joint in Figure 6-30 and Figure 6-31 are associated with the 160% LGPC ground motion intensity. As observed previously, the response of the columns, which remained elastic, is reasonably similar in both the coupled model and the assumed exact model. However, it appears that the plastic deformation shifts from the girders to the panel zones for both joints of the frame subassembly in the slave OpenSees script as seen in Figure 6-30(a) and Figure 6-30(c). These observations are made particularly for the coupled model analyzed here and are potentially very sensitive to the relative strength of the girder, column and panel zone.

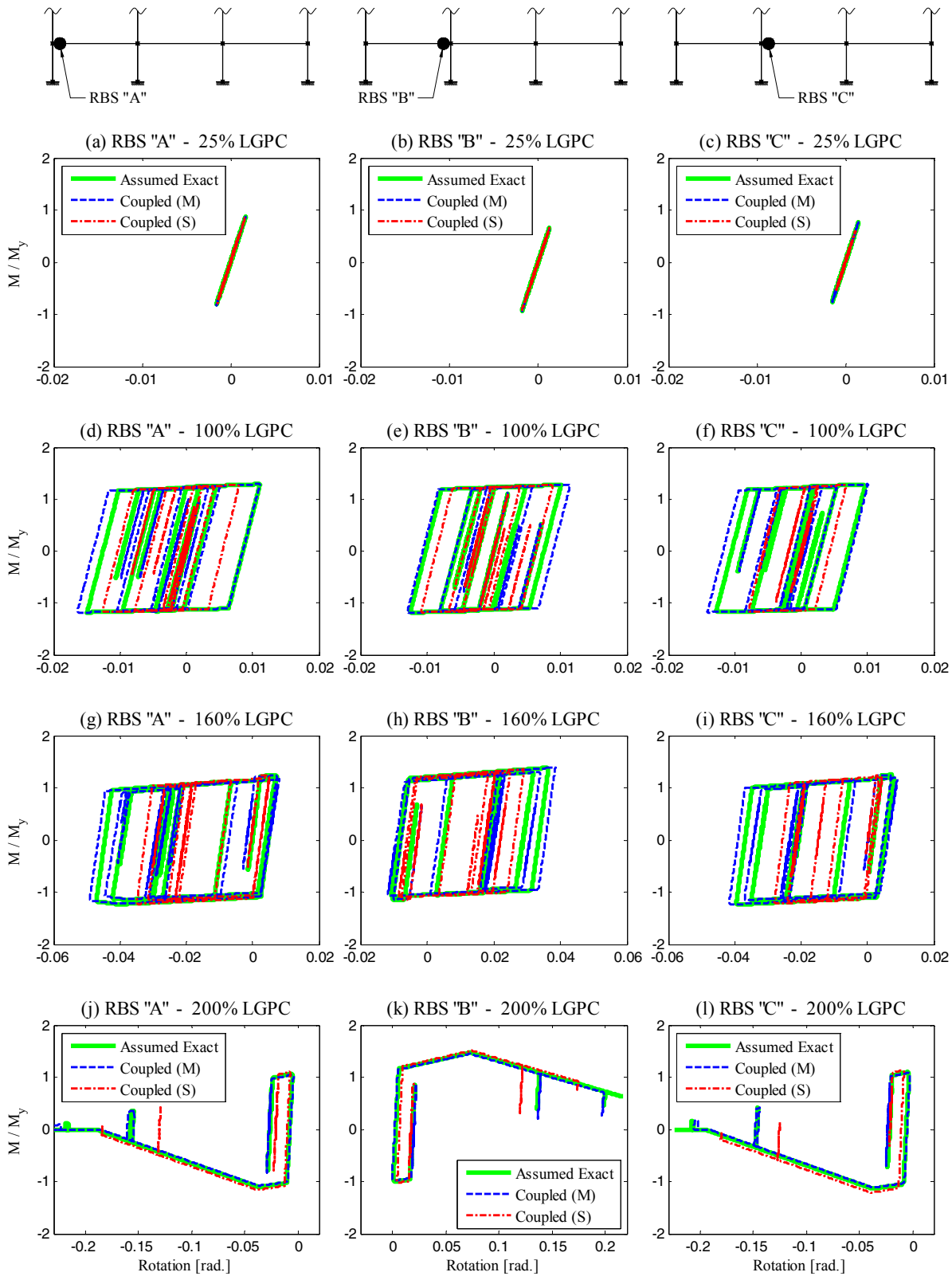


**Figure 6-28 Comparison of moment-rotation relationships for selected girders of complete (assumed exact) and coupled models used to simulate the response of Hybrid Model #1**

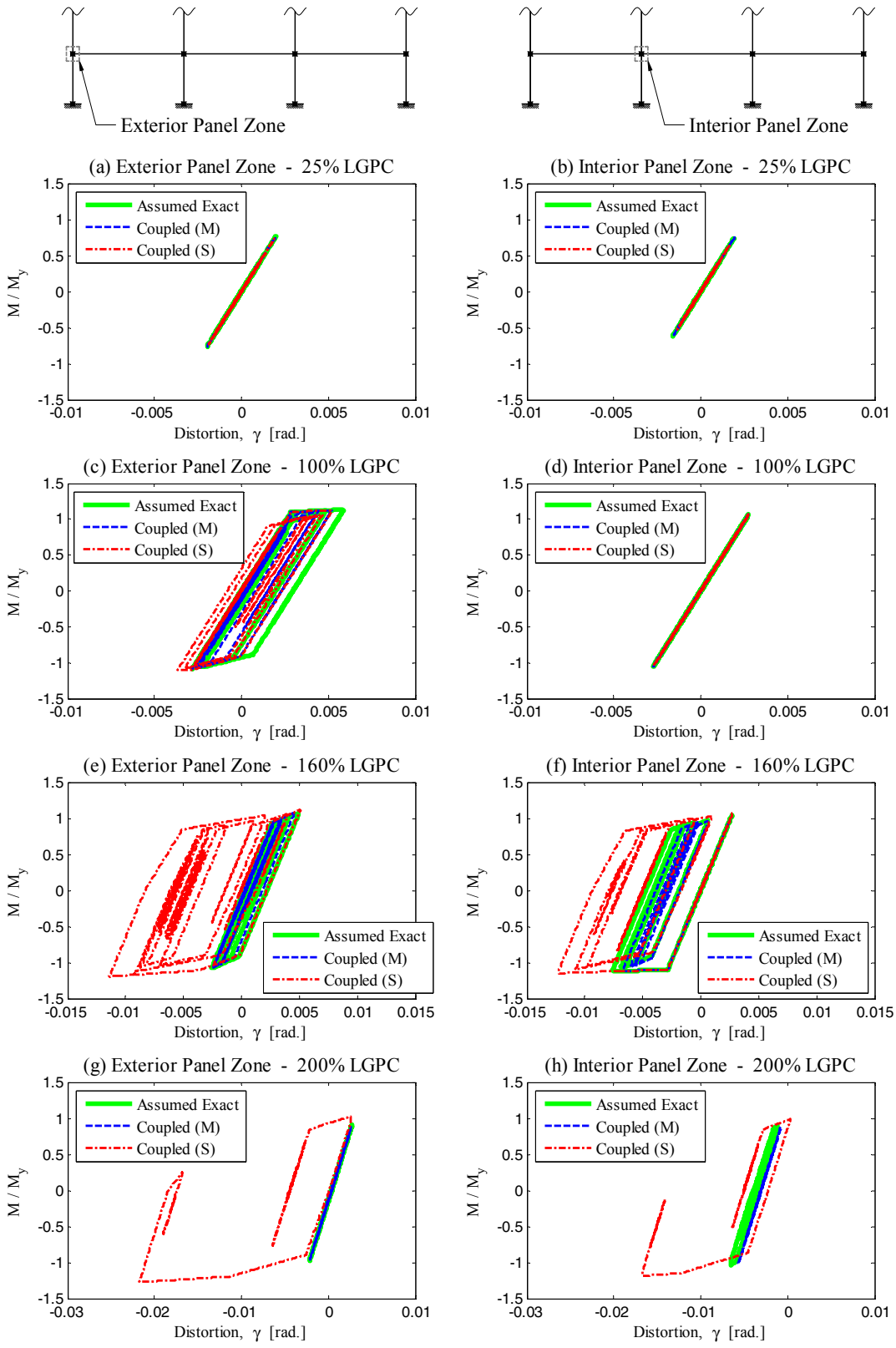


**Figure 6-29 Comparison of moment-distortion relationships for selected panel zones of complete (assumed exact) and coupled models used to simulate the response of Hybrid Model #1**

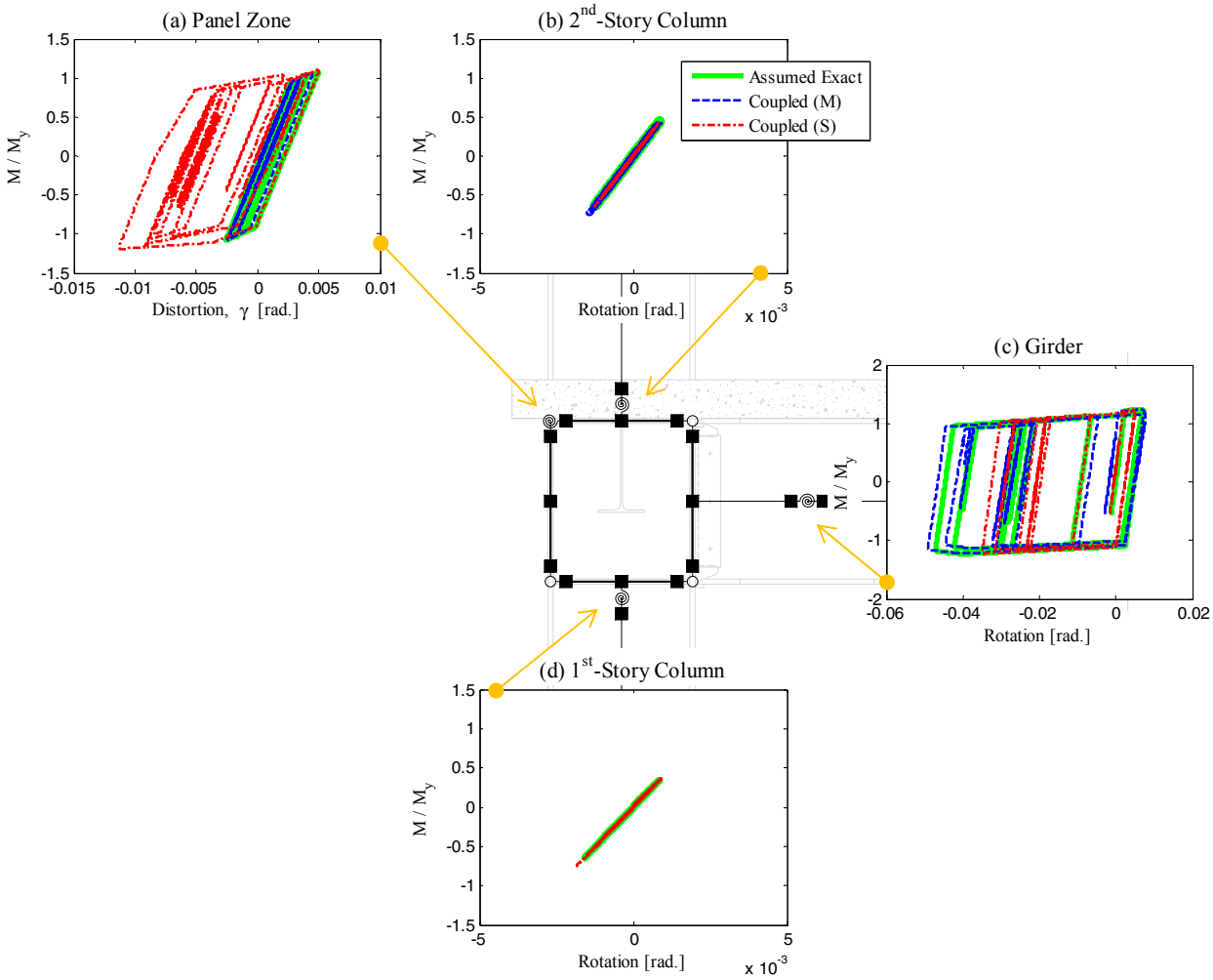


**Figure 6-30 Comparison of moment-deformation relationships for columns, girder and panel zone at exterior joint within the overlapping domain for the 160% LGPC**

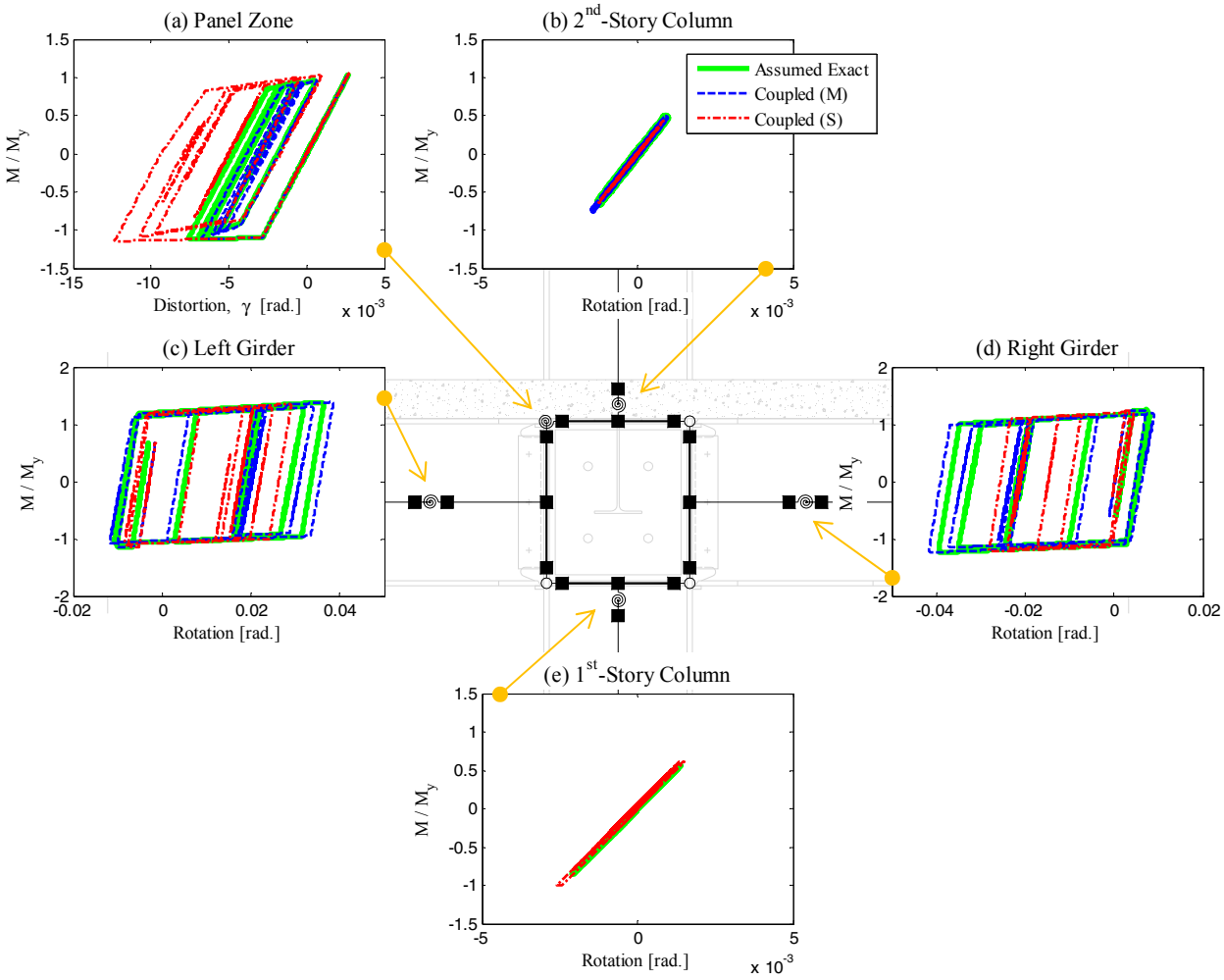


**Figure 6-31 Comparison of moment-deformation relationships for columns, girders and panel zone at interior joint within the overlapping domain for the 160% LGPC**

#### 6.4.3.2 Evaluation of Substructuring Technique for Hybrid Model #2 (Gravity Frame)

This section presents an evaluation of the substructuring technique implemented for Hybrid Model #2. The coupled model shown in Figure 6-32 was used to simulate the response of Hybrid Model #2. In this model, the numerical and physical sub-structures of the gravity frame are modeled in master and slave OpenSees scripts and the moment frame is encapsulated in a second slave OpenSees script. The substructuring algorithm described in Section 6.4.2 is used to couple the master and slave OpenSees scripts of the gravity frame. This coupled model (of the gravity frame) is in turn coupled with the numerical model of the moment frame at each floor level. However, only 2/3 of the internal resisting force vector from the moment frame OpenSees script is returned to the master OpenSees script to account for the actual ratio of number of gravity to moment frames since only one gravity frame is modeled. Consequently, the mass of the coupled model in Figure 6-32 is one third of the total mass of the building structure.

Similar to the previous section, the coupled model shown in  shown in Figure 6-32 was subjected to the same four increasing intensities of the LGPC ground motion (similar to the testing program of the series of hybrid simulations). The results of these coupled simulations are compared with those of coupled simulations using the model previously shown in Figure 6-9 where the complete model of the gravity frame structure was encapsulated in one single OpenSees script and therefore the substructuring algorithm was not utilized. The results of such coupled simulations are assumed as the exact response. Dynamic analysis of both coupled models requires the specialized implicit Newmark method with fixed number of iterations presented in Section 3.2.2.

Figure 6-33 and Figure 6-34 present global response results, namely, roof drift ratio and base shear, respectively, predicted for the Hybrid Model #2. Figure 6-34 presents the base shear of the gravity frames only. As it was observed before, it can be seen that the results of the coupled simulations with the substructuring algorithm are in close agreement with the assumed exact response. However, the local response of the slave OpenSees script, which simulates the response of the physical sub-structure, exhibits some differences as explained below.

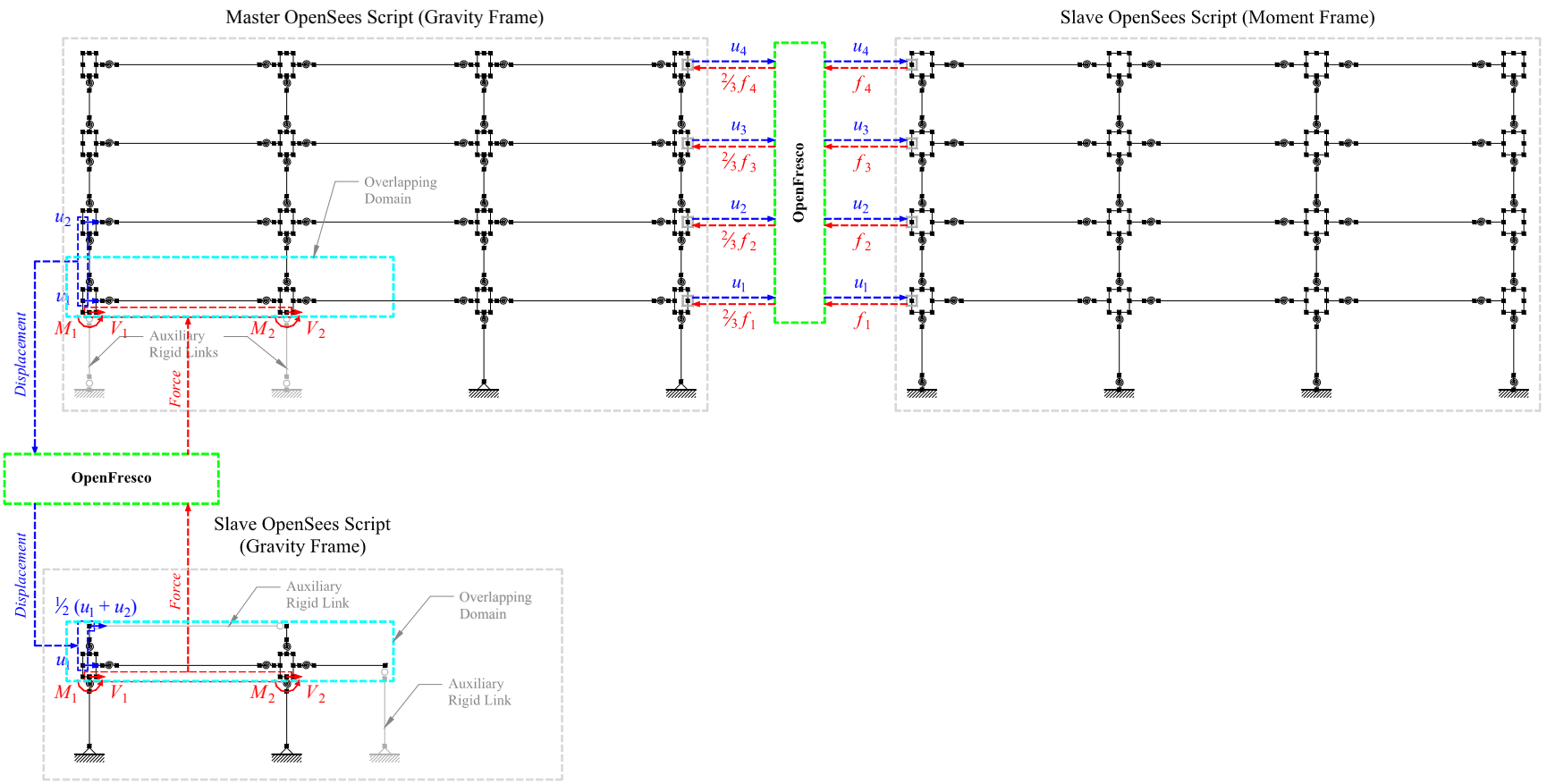


**Figure 6-32 Coupled model used to simulate the response of Hybrid Model #2**

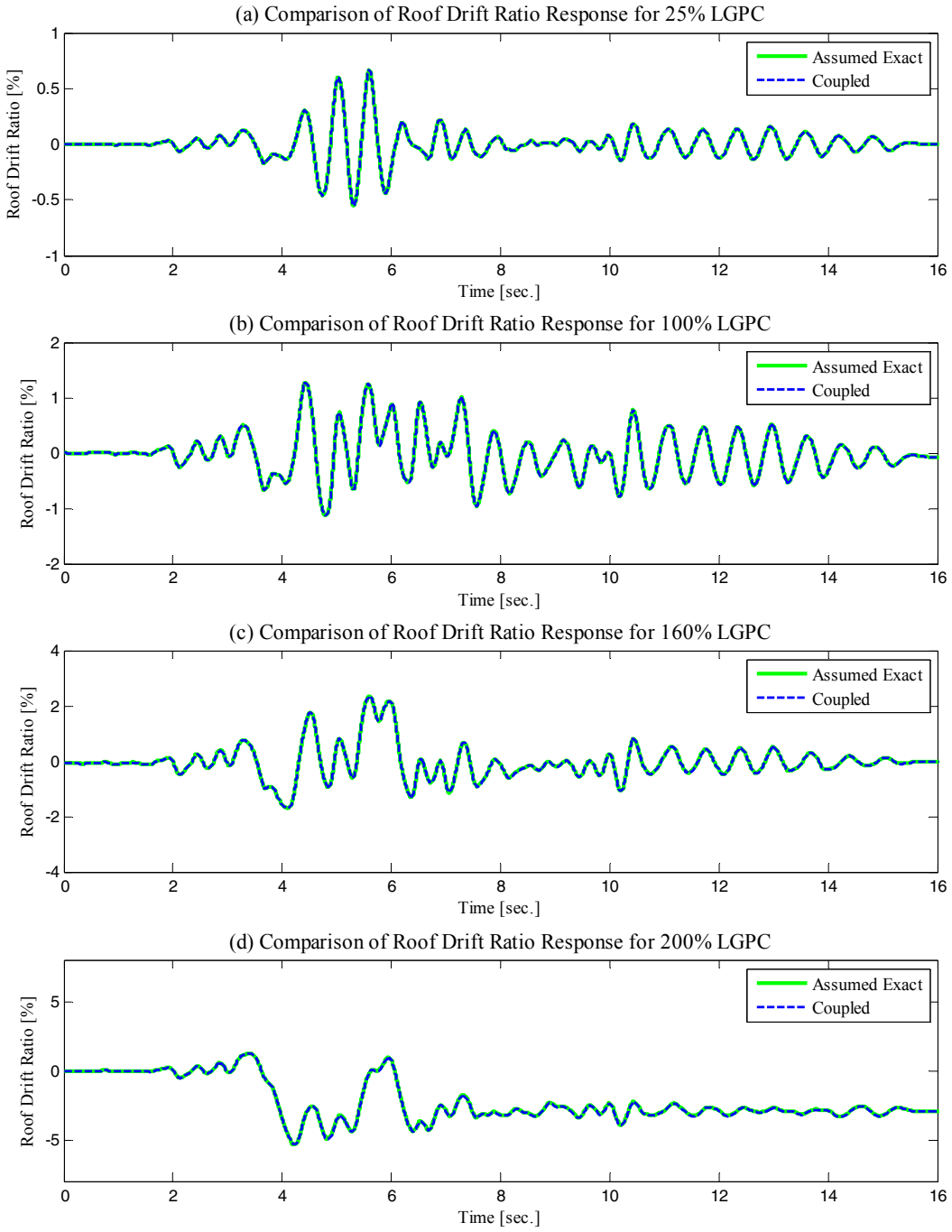


**Figure 6-33 Comparison of roof drift ratio of complete (assumed exact) and coupled models used to stimulate the response of Hybrid Model #2**

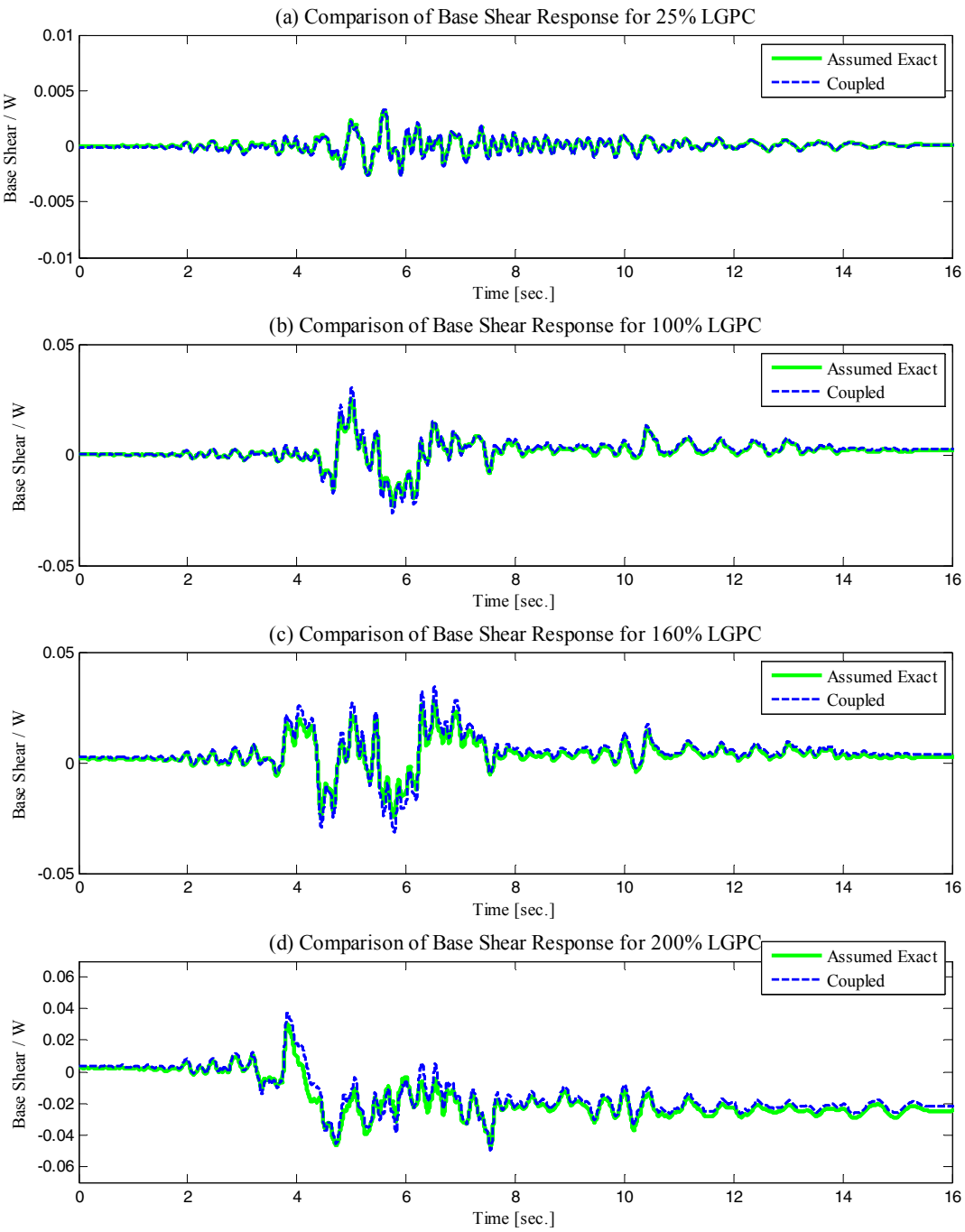


**Figure 6-34 Comparison of base shear of complete (assumed exact) and coupled models used to stimulate the response of Hybrid Model #2**

Figure 6-35 and Figure 6-36 compare moment-rotation relationships for an exterior and interior column at selected plastic-hinge regions. Note that the columns of the gravity frames are pinned at the base. The location of the plastic-hinge regions is indicated with sketches provided at the top of each plot set. Although the response of the columns is elastic, it can be clearly seen in Figure 6-35 that the bending moments at the top of the first-story columns of the slave OpenSees script (simulating the physical sub-structure) are consistently larger compared to the assumed exact solution.

Figure 6-37 compares moment-rotation relationships for shear-tab connections within the overlapping domain between the master and slave OpenSees scripts (see Figure 6-32 for reference). Sketches provided at the top of Figure 6-37 are used to indicate the location of the shear-tab connection (denoted as STC "A", "B", and "C" in the figures). The response of the shear-tab connections in both the master and slave OpenSees scripts is presented in Figure 6-37. In general, Figure 6-37 shows that the shear-tab connections of the slave OpenSees script (which simulates the response of the gravity frame physical sub-structure) exhibit smaller rotations as compared to the assumed exact response. Such differences increase with increasing levels of shaking. This observation was slightly more pronounced for Hybrid Model #1. On the contrary, the master OpenSees script (simulating the response of the gravity frame numerical sub-structure) typically experiences larger levels of rotations.

Figure 6-38 compares moment-distortion relationships for panel zones within the overlapping domain. Sketches provided at the top of Figure 6-38 show the location of the panel zones. Similar to the panel zones of the moment frame in Section 6.4.3.1, Figure 6-38 shows that the panel zones in the slave OpenSees script exhibit significantly larger deformation demands than the assumed exact response for the largest shaking intensity of 200% LGPC as observed in Figure 6-38 (h). This supports previous observations in which it appears that the distribution of inelastic deformation in the joints of the frame's physical sub-structures changes due to the simplified boundary conditions of the substructuring algorithm.

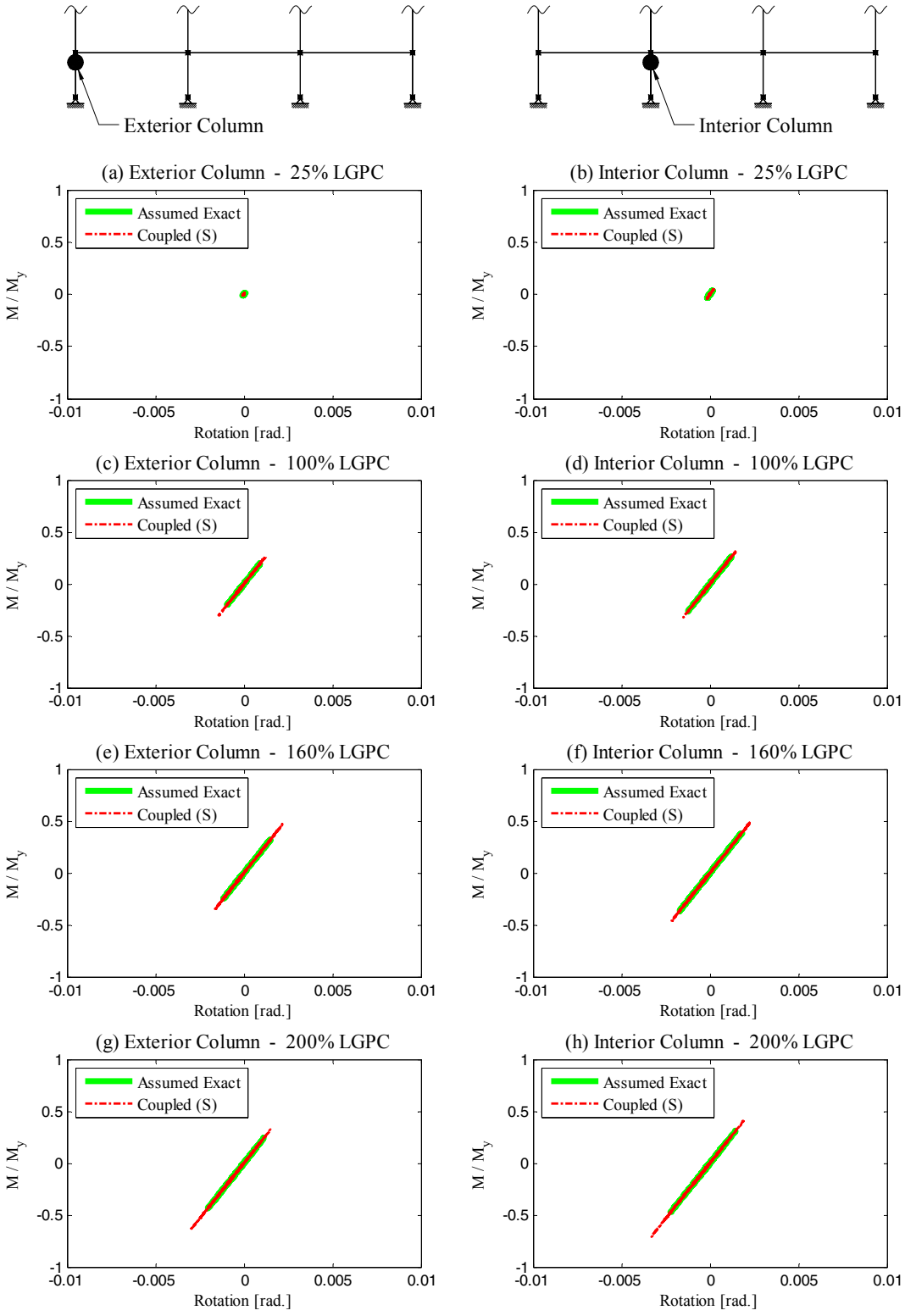


**Figure 6-35 Comparison of moment-rotation relationships for selected columns of complete (assumed exact) and coupled models used to stimulate the response of Hybrid Model #2 (Part I)**

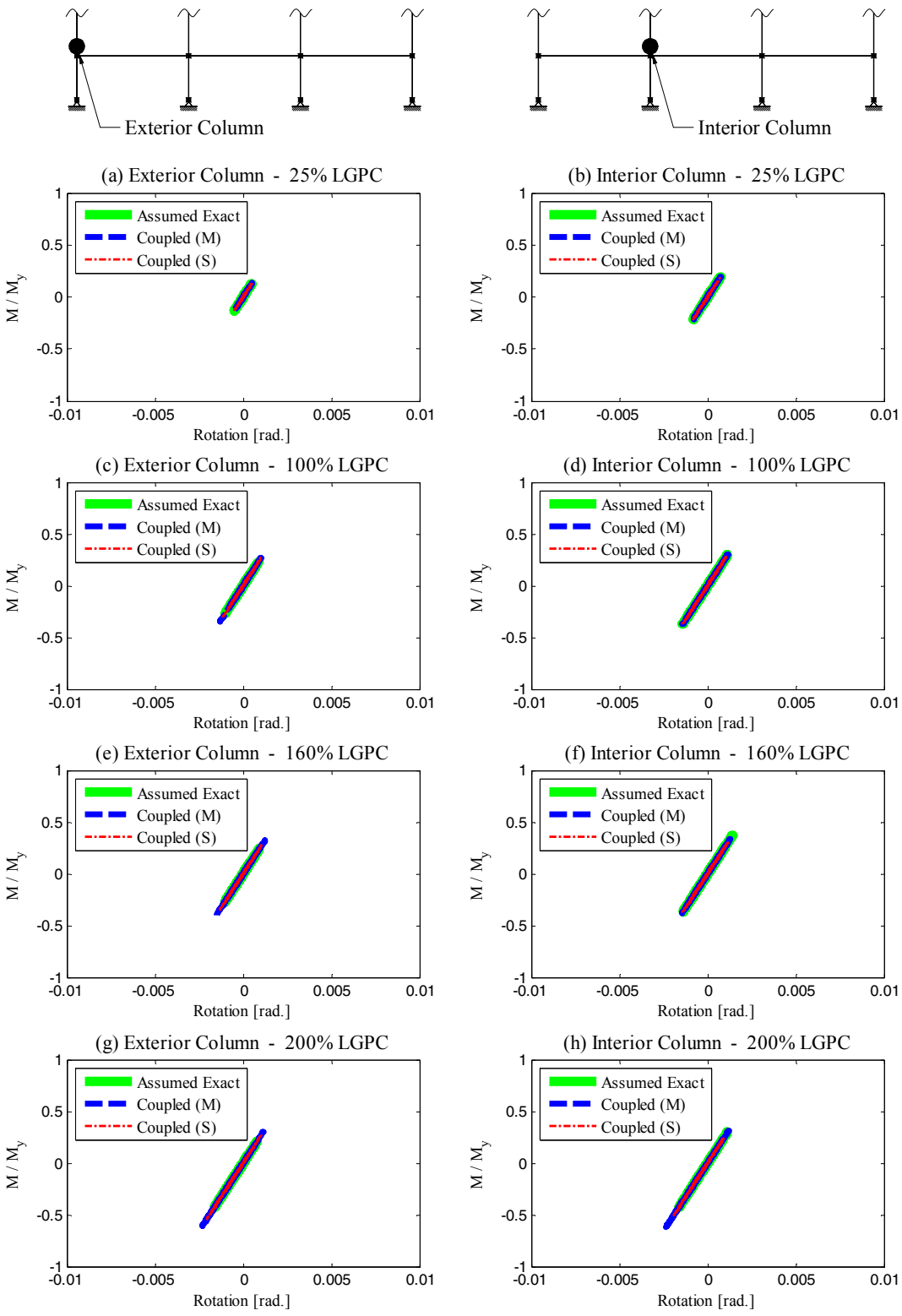


**Figure 6-36 Comparison of moment-rotation relationships for selected columns of complete (assumed exact) and coupled models used to stimulate the response of Hybrid Model #2 (Part II)**

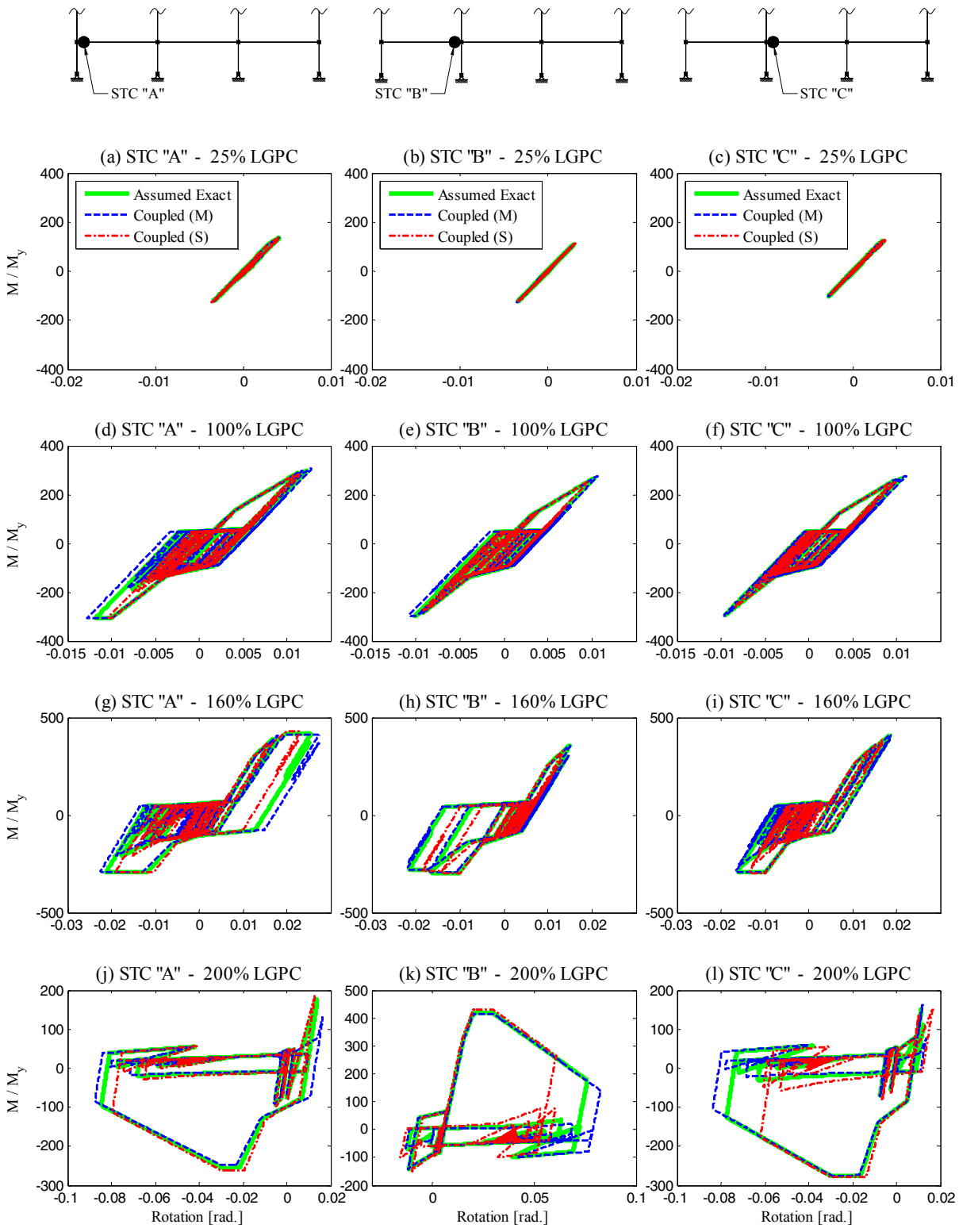


**Figure 6-37 Comparison of moment-rotation relationships for selected girders of complete (assumed exact) and coupled models used to stimulate the response of Hybrid Model #2**

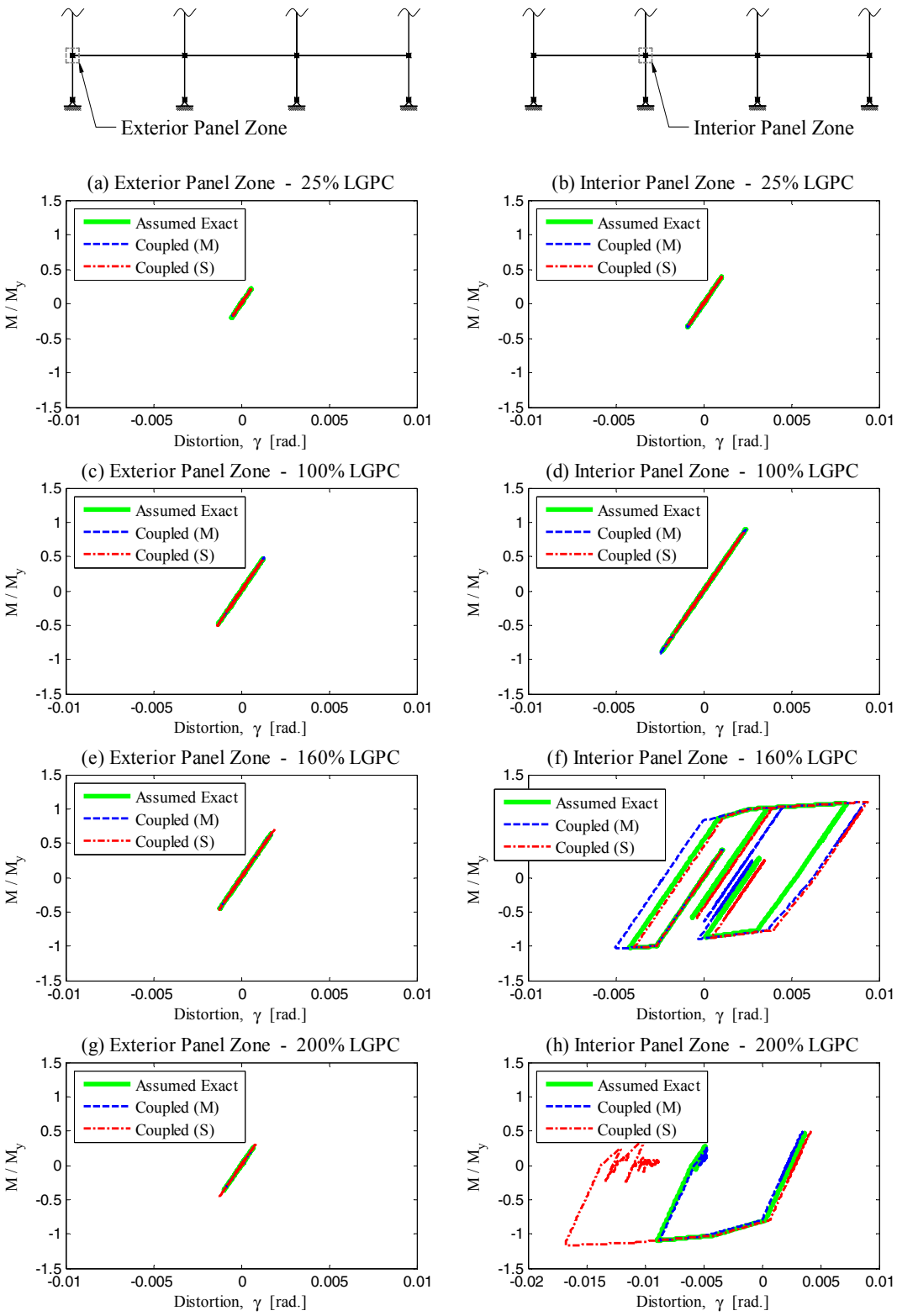


**Figure 6-38 Comparison of moment-distortion relationships for selected panel zones of complete (assumed exact) and coupled models used to stimulate the response of Hybrid Model #2**

#### 6.4.3.3 Summary

The analytical studies conducted here show that the substructuring technique with simplified boundary conditions and an overlapping domain produces global response results that are in close agreement with a conventional numerical simulation (assumed as the exact response) all the way through collapse. Other substructuring techniques without overlapping domain (e.g., Schneider and Roeder, 1994) did not trace the global response to collapse and resulted in a completely different collapse mechanism. Hashemi (2013) reported similar observations. However, these analytical studies also showed that there are some differences in the local response of the physical sub-structure in a hybrid simulation as compared to a conventional numerical simulation. As mentioned earlier, the response of the physical sub-structure in a hybrid simulation was simulated using the slave OpenSees scripts in coupled simulations. It was found that the regions of the physical sub-structure near the simplified boundary conditions will exhibit the largest differences. The response of the columns of the physical sub-structure was faithfully reproduced. However, it appears that the inelastic response in the physical sub-structure with the simplified boundary conditions shifts from the beams to the panel zones. This observation is more pronounced for the moment frame structure.

## 6.5 Hybrid Simulation Architecture

The substructuring technique described above requires additional sensing to measure the shear forces and bending moments at the top of the first-story columns (see Figure 6-21). This requires integration of the data acquisition system into the feedback loop of the hybrid control system. At the NEES equipment site at University at Buffalo, the data acquisition system (DAQ) is integrated in the SCRAMNet+ (Systran, 2004) loop along with the xPC used for the hybrid control system as shown in Figure 6-. The hybrid simulation control systems using xPC Target is three-loop architecture (Stojadinovic *et al.*, 2006). The innermost Servo-Control Loop contains the actuator controller that sends command displacements and forces to the actuator-specimen and reads back measured displacements and forces. The middle loop runs the Predictor-Corrector actuator command generator on the xPC-Target real-time digital signal processor (DSP) and delivers the command displacements to the actuator controller in real-time through the shared memory SCRAMNet+. Finally, the outer Integrator loop runs on the xPC-Host PC and includes OpenSees, Matlab (MathWorks , 2011), and OpenFresco communicating with the xPC-Target through TCP/IP. For this particular setup, the xPC was programmed to read the DAQ system data directly from SCRAMNet+. The programmable xPC obtained the strain gauge data and converted it to the required columns forces as feedback for the hybrid simulation. While this control system is designed for real-time

testing, the use of the DAQ feedback data with filtering added significant delays to each iteration step and limited the rate of testing to 0.22 sec. per step.

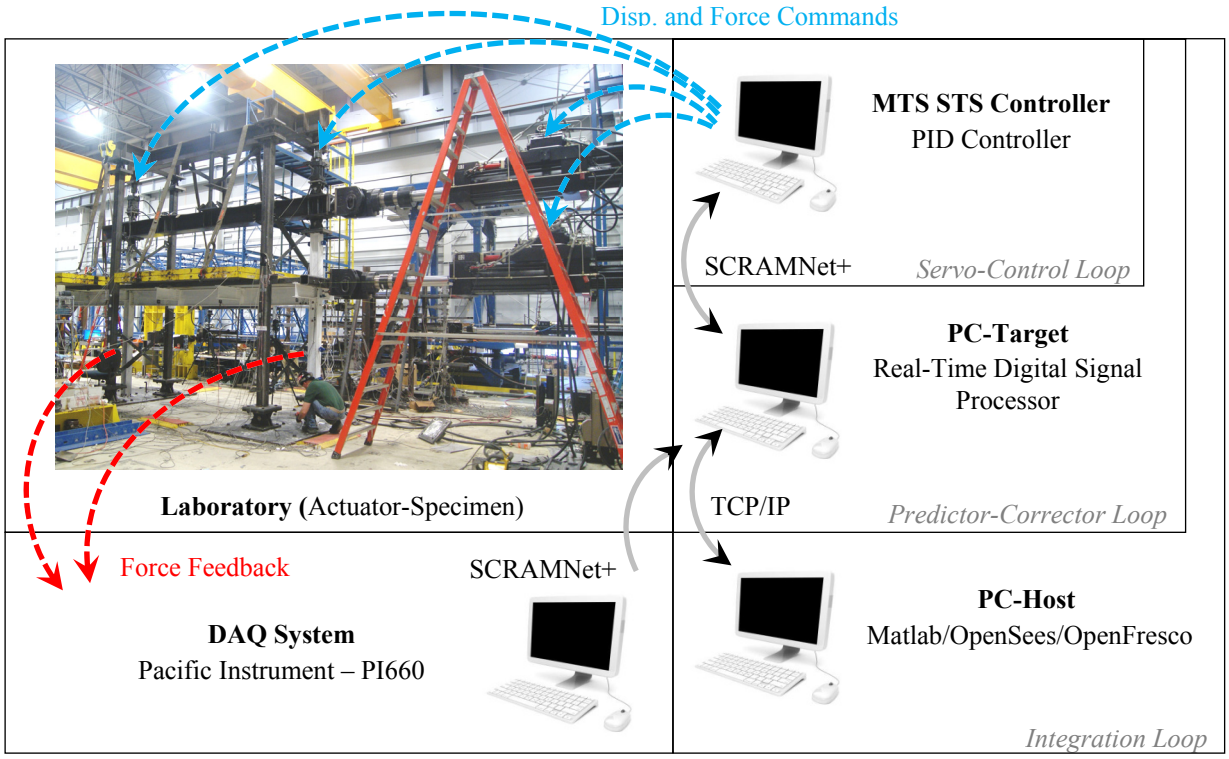


**Figure 6-39 Hybrid simulation hardware architecture at NEES equipment Site at University at Buffalo (adapted from Hashemi, 2013)**

## 6.6 Selection of Integration Method, Time Steps and Number of Iterations for Hybrid Simulations

The implicit Newmark method modified for hybrid simulation (INM-HS) (Schellenberg *et al.*, 2009), as implemented in OpenSees, was selected to integrate the equations of motion during the two hybrid simulations in this report. In this modified version, the number of iterations per integration step is fixed to a constant value and the displacement increments modified to make them more uniform. A detailed description of the integration method was provided in Section 3.2.2. The selection of this integration method was based on the studies presented in Section 3. The selection of the time steps and number of iterations for each hybrid simulation of the two series of hybrid simulations (Hybrid Simulation #1 and #2) is discussed here.

As mentioned before, small time steps and a large number of iterations provide improved stability and accuracy of the simulation. However, the eight hours of daily operation of the laboratory coupled with the fact that a data communication procedure between the physical and numerical sub-structures carried out at every iteration requires a fixed time interval of 0.22 sec. yield a limit on the minimum size of the time step and maximum number of iterations. The time interval of 0.22 sec. was allocated to calculate and send a displacement command vector to the physical sub-structure, obtain the corresponding force feedback vector and return it to the numerical integration algorithm to calculate the displacement command vector for the next iteration. Since the last three hybrid simulations of the two series of hybrid simulations according to the testing program presented in Table 4-6, namely, 100%, 160% and 200% LGPC, are inelastic hybrid simulations, they need to be conducted in sequence to carry over any residual response of the numerical sub-structure to the next simulation. Therefore, the time steps and number of iterations for these three sequential hybrid simulations need to be selected so that the total real time duration of the simulation remains approximately within the eight hours of daily operation of the laboratory. Analytical studies were conducted to assist in the selection of the time steps and number of iteration of the INM-HS integration method for the two series of hybrid simulations. These studies are presented below.

### 6.6.1 Studies for Hybrid Simulation #1

Figure 6- shows ten alternative cases with different combinations of time steps and number of iterations for the three sequential hybrid simulations of Hybrid Simulation #1. Maximum norms of the unbalanced force vector are presented in Figure 6- as a measure of the stability of the simulation as described in Section 6.2.5. The coupled model previously shown in Figure 6-22 is used simulate the response of the sequential hybrid simulations. The time steps and number of iterations for each alternative case are shown in the legend of Figure 6- where $1/2\Delta t$@6 denotes the time step ($1/2\Delta t$) and the number of iterations (6 iterations) selected for each of the three sequential hybrid simulations. The time step $\Delta t$ is the scaled time step (resolution) of the original ground motion record. The estimated total real time duration of the sequential hybrid simulations (calculated with the 0.22 sec. time interval for a data communication step) is shown in parenthesis in the figure legend next to each alternative case.

As expected, the case with the largest time step sizes and consequently the shortest real-time duration (Case 04) presents, on average, the largest unbalanced forces. In contrast, the case with the smallest time step sizes and largest number of iterations and consequently the longest real-time duration (Case 07) presents, on average, the smallest unbalanced forces. The time steps and number of iterations of Case 08,

which presents the lowest values of unbalanced forces and approximately remains within 8 hours, was selected for Hybrid Simulation #1.

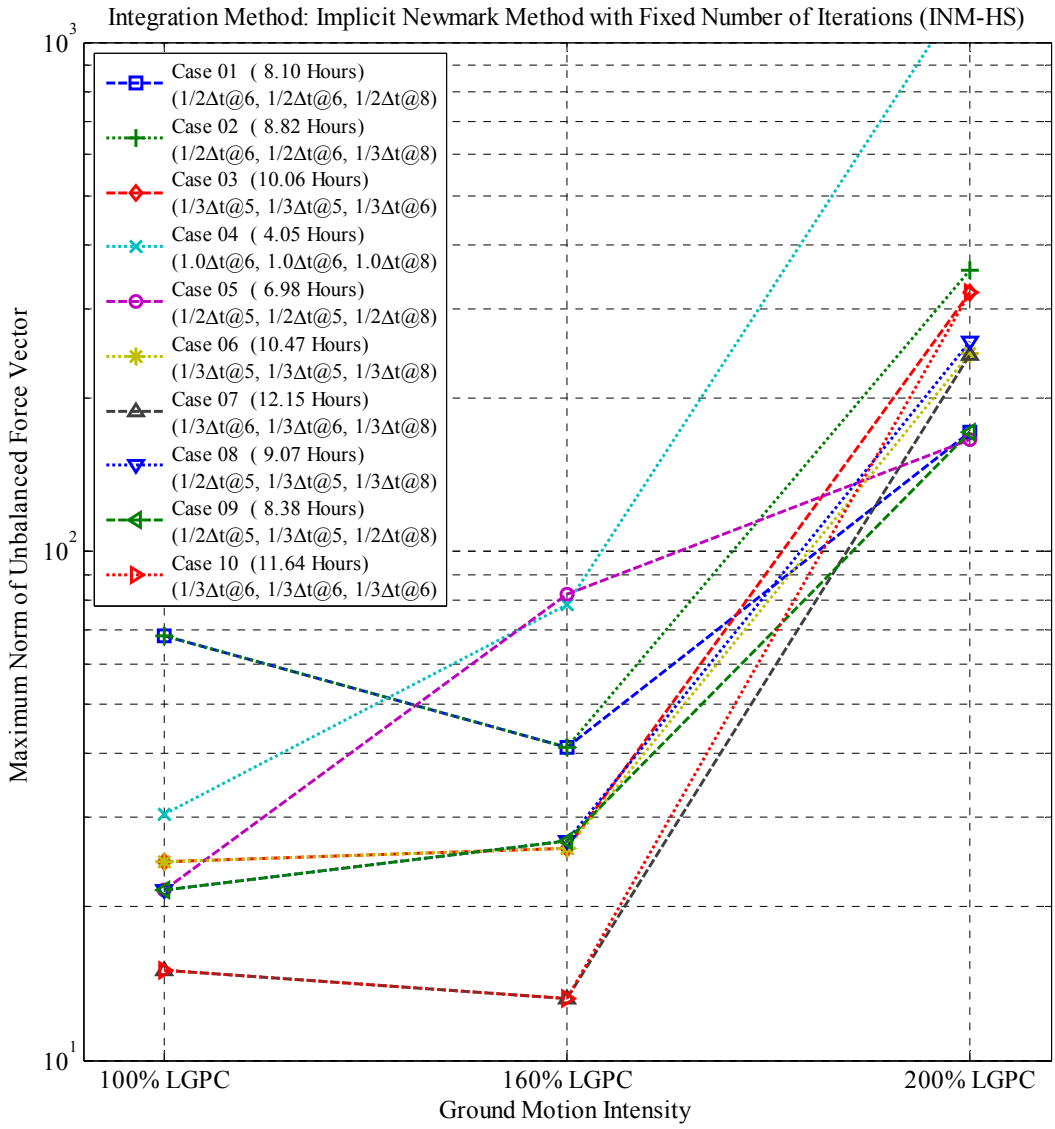


**Figure 6-40 Study to assist in the selection of time steps and number of iterations for the INM-HS integration method used in Hybrid Simulation #1**

Table 6-7 summarizes the time steps, number of iterations, total number of integration steps and estimated real time duration for each hybrid simulation of the testing program for Hybrid Simulation #1. The first hybrid simulation shown in Table 6-7 (25% LGPC) is an elastic test and produces the lowest values of

unbalanced forces. Also, sidesway collapse was predicted during the first 4.1 sec. of the last simulation (200% LGPC) and therefore this simulation is shorter than the previous one.

**Table 6-7 Selected time steps and number of iterations for INM-HS integration method used for Hybrid Simulation #1**

| Ground Motion Intensity | Time Step [$\Delta t_{gm}$ [1]] | Number of Iterations per Integration Step | Total Number of Integration Steps | Real Time Duration of Simulation |
|---|---|---|---|---|
| 25% LGPC | 1/2 | 4 | 9166 | 2h:14m |
| 100% LGPC | 1/2 | 5 | 9166 | 2h:48m |
| 160% LGPC | 1/3 | 5 | 13749 | 4h:12m |
| 200% LGPC | 1/3 | 8 | 3571 | 1h:45m |

[1] $\Delta t_{gm}$: scaled size of the time step of the ground motion equal to $0.5^{0.5} \times 0.005$ sec. = 0.003536 sec.

### 6.6.2 Studies for Hybrid Simulation #2

A similar study was conducted to assist in the selection of the time steps and number of iterations for Hybrid Simulation #2. As mentioned before, the gravity framing system of the building structure is included in Hybrid Model #2 where the physical sub-structure is a subassembly of a gravity frame. The coupled model shown previously in Figure 6-32 was used to simulate the response of Hybrid Model #2.

It was predicted using this coupled model with substructuring that inclusion of the gravity frames in the second series of hybrid simulations prevented sidesway collapse under the same increasing intensity ground motions of the previous section. Therefore, the duration of the second series of hybrid simulations (Hybrid Simulation #2) is longer than that of the first series (Hybrid Simulation #1) and consequently larger time steps and smaller number of iterations need to be selected in Hybrid Simulation #2 to accommodate the sequential hybrid simulations within the hours of operation of the laboratory.

Figure 6-41 presents five alternative cases with different combinations of time steps and number of iterations for the last three sequential hybrid simulations of Hybrid Simulation #2. The time steps and number of iterations of Case 04 produces, on average, the lowest unbalanced forces and therefore was selected for Hybrid Simulation #2.

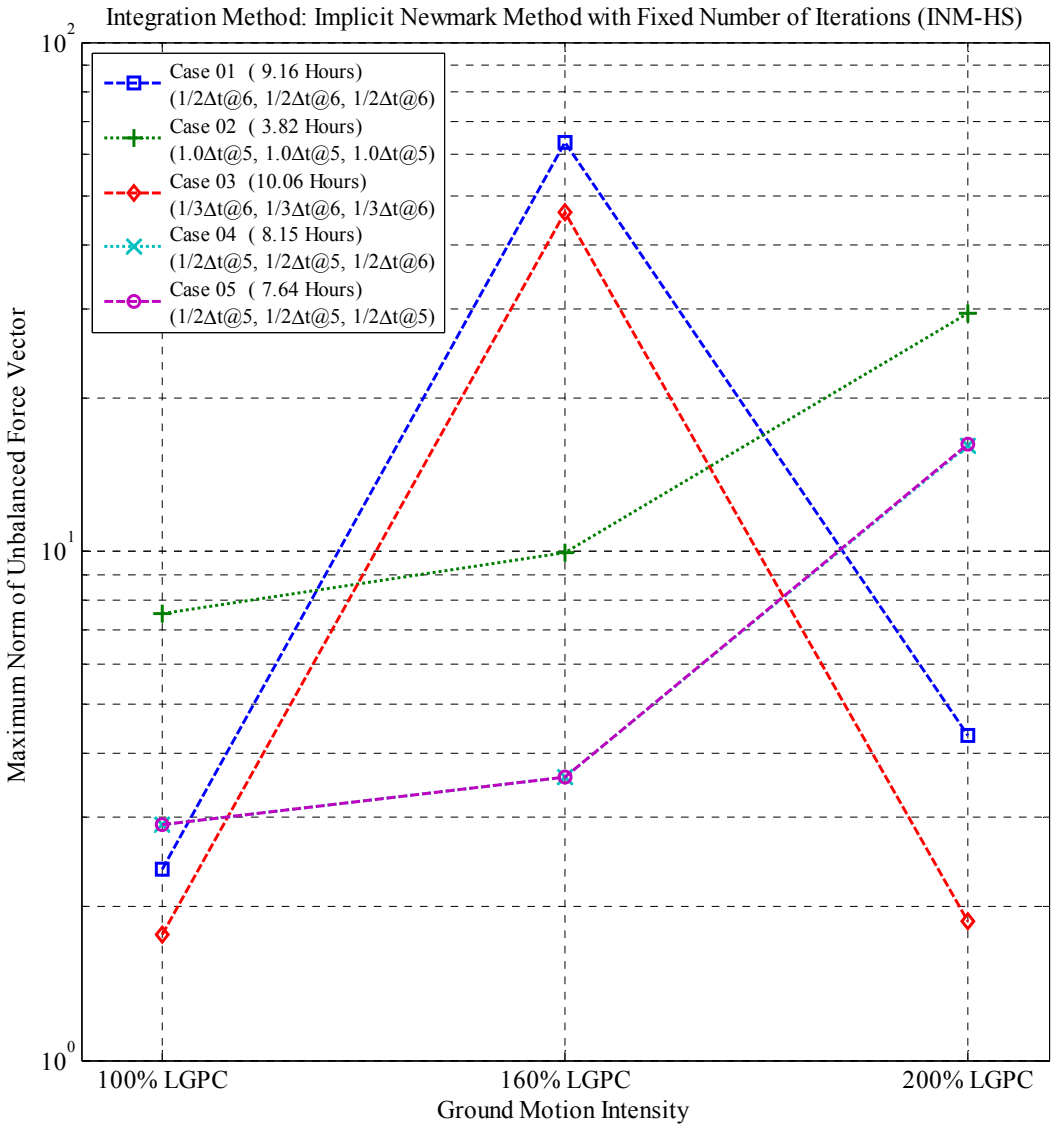


**Figure 6-41 Study to assist in the selection of time steps and number of iterations for the INM-HS integration method used in Hybrid Simulation #2**

Table 6-8 summarizes the time steps, number of iterations, total number of integration steps and real time duration for all hybrid simulations of the testing program for Hybrid Simulation #2.

**Table 6-8 Selected time steps and number of iterations for INM-HS integration method used for Hybrid Simulation #2**

| Ground Motion Intensity | Time Step [$\Delta t_{gm}$ [1]] | Number of Iterations per Integration Step | Total Number of Integration Steps | Real Time Duration of Simulation |
|---|---|---|---|---|
| 25% LGPC | 1/2 | 6 | 9166 | 3h:22m |
| 100% LGPC | 1/2 | 5 | 9166 | 2h:48m |
| 160% LGPC | 1/2 | 5 | 9166 | 2h:48m |
| 200% LGPC | 1/2 | 6 | 9166 | 3h:22m |

[1] $\Delta t_{gm}$: scaled size of the time step of the ground motion equal to $0.5^{0.5} \times 0.005$ sec. = 0.003536 sec.

## 6.7 Gravity Loading of Hybrid Models

This section presents the procedure followed to apply the gravity loads on the hybrid (physical and numerical) models prior to the hybrid simulations. The experimental test setup shown previously in Figure 5-19 was designed to apply gravity forces on the physical sub-structures. The first elevated story level of the test specimens was loaded with steel plates. The weight of each steel plate is 8.5 kips. While two steel plates were placed on the moment frame physical sub-structure, four plates were used to load the gravity frame physical sub-structure since the gravity load tributary area for a gravity frame is twice of that for a moment frame (see Figure 4-1(a) for reference). The gravity forces on the columns of the physical sub-structures from upper stories as well as seismic-induced variations from overturning forces were applied through force-controlled actuators as shown in Figure 5-18. The force-controlled actuators were commanded by the hybrid simulation algorithm presented in Section 6.4.2.

On the other hand, gravity loading of the numerical sub-structures was carried out before the initiation of the hybrid simulation using a load-control algorithm with Newton-Raphson iterations. This was done to avoid iterations with the physical sub-structure during gravity loading (and because the load-control algorithm with Newton-Raphson iterations is not compatible with hybrid simulation). After applying the gravity loads on the numerical sub-structure, the physical sub-structure was integrated via OpenFresco to start the hybrid simulations. At the beginning of the hybrid simulation, the force-controlled actuators imposed gravity forces from upper stories using a ramp function. This ramp function was created using the "rate limiter" option in Simulink (MathWorks, 2011) to avoid jerky loading of the physical columns.

Gravity loading of the physical sub-structures with a ramp function took place within the first milliseconds of the ground motion where very little motion was observed. Gravity loading of the physical and numerical sub-structures was completed after this and the hybrid model was ready for seismic loading.

Also, it is important to mention that gravity loads on the numerical sub-structures were not applied along the girders/beams of the frame structure in order to avoid inducing initial moments and rotations on the moment and simple connections. Rather, the gravity loads were concentrated at point loads and applied on the columns only. This was done since such initial bending moments resulted in large unbalanced forces at the first integration steps during the hybrid simulations. It was verified numerically that such gravity loading did not change the results of the simulation if the gravity loads are applied along girders or beams (more realistic case).

# SECTION 7
# EXPERIMENTAL PROGRAM: TEST RESULTS

## 7.1 Overview

This section presents results of the two series of hybrid simulations successfully conducted at the University at Buffalo NEES equipment site. A total of two half-scale physical subassemblies of a special steel moment-resisting frame as well as a gravity-resisting frame were tested via hybrid simulation with substructuring techniques. Preliminary tests conducted prior to the hybrid simulations to verify the software and laboratory equipment are presented as well.

In the first series of hybrid simulations (Hybrid Simulation #1), a hybrid model of a special steel moment resisting frame was subjected to increasing intensities of the Loma Prieta ground motion all the way to collapse. The physical sub-structure of this hybrid model spanned one and one half bays by one and one half stories of the moment frame structure. In the second series of hybrid simulations (Hybrid Simulation #2), a similar-sized physical subassembly of a gravity frame was tested to the same increasing ground motion intensities. More specifically, the second series of hybrid simulations were conducted on a hybrid model of a gravity frame coupled with a fully numerical model of the moment frame to capture the complete system response. Both physical sub-structures were constructed with a composite floor slab and included the dead load on the slab at the first elevated story and vertical loads from upper stories accounting for overturning forces. Sidesway collapse was observed in the first series of hybrid simulations while the addition of the gravity frames in the second series prevented collapse under the same intensity of shaking.

## 7.2 Results of Hybrid Simulation #1

Table 7-1 summarizes the first series of hybrid simulations (HS01 test series) conducted on a moment frame subassembly and includes a set of four preliminary tests (PT01 test series) conducted to verify the adequacy of the hybrid simulation software and laboratory equipment and to identify the elastic properties of the physical sub-structure. The tests listed in Table 7-1 are identified by a test ID. The test ID for the preliminary tests (PT01) is followed by a sequence number. For the hybrid simulations, the test ID denotes the hybrid simulation series (HS01: first series of hybrid simulations) followed by the ground motion intensity (25% through 200%). For the specific case of the preliminary hybrid simulation HS01-

Sine, “Pulse” denotes a sine-pulse ground motion. All tests summarized in Table 7-1 are listed in chronological order. A detailed description of each test is provided below.

**Table 7-1 Summary of tests conducted on Physical Sub-Structure #1 (moment frame subassembly)**

| Test # | Test ID | Test Type | Test Description |
|---|---|---|---|
| 01 | PT01-01 | Quasi-Static | Preliminary elastic test. The physical sub-structure was subjected to a displacement protocol generated by a coupled simulation using a low-frequency sine-pulse ground motion (sine function: period = 0.67 sec. and amplitude = 0.10g). |
| 02 | PT01-02 | Quasi-Static | Preliminary elastic test. The physical sub-structure was subjected to a displacement protocol generated by a coupled simulation using a high-frequency sine-pulse ground motion (sine function: period = 0.05 sec. and amplitude = 2.00g). |
| 03 | PT01-03 | Quasi-Static | Preliminary elastic test. The physical sub-structure was subjected to a prescribed cyclic displacement protocol to measure the elastic properties of the first story. Both horizontal actuators were commanded with a triangular one-cycle displacement protocol (peak displacement amplitude = 1/4", duration = 2.0 min.). |
| 04 | PT01-04 | Quasi-Static | Preliminary test where the physical sub-structure was subjected to a prescribed cyclic displacement protocol to measure the elastic properties of the mid-second story. While the bottom horizontal actuator remained in position, only the top horizontal actuator was commanded with a triangular one-cycle displacement protocol (peak displacement amplitude = 1/8", duration = 2.0 min.). |
| 05 | HS01-Sine | Hybrid | Preliminary elastic hybrid simulation conducted using a high-frequency sine-pulse ground motion (sine function: period = 0.05 sec. and amplitude = 2.00g). |
| 06 | HS01-25% | Hybrid | Elastic hybrid simulation conducted with 25% of the unscaled LGPC earthquake record (Service Level Earthquake). |
| 07 | HS01-100% | Hybrid | Inelastic hybrid simulation conducted with 100% of the unscaled LGPC earthquake record (Maximum Considered Earthquake). |
| 08 | HS01-160% | Hybrid | Inelastic hybrid simulation conducted with 160% of the unscaled LGPC earthquake record (Near Collapse Level Earthquake). |
| 09 | HS01-200% | Hybrid | Inelastic hybrid simulation conducted with 200% of the unscaled LGPC earthquake record (Collapse Level Earthquake). |

In the preliminary tests PT01-01 and PT01-02, the physical sub-structure was subjected to a lateral displacement protocol generated by coupled simulations which were executed in parallel with loading of the physical specimen. The coupled model previously shown in Figure 6-22, in which the physical and numerical sub-structures of Hybrid Model #1 were numerically simulated in two separate OpenSees scripts, was subjected to sine-pulse ground motions. At each integration step during the coupled simulations, the displacement vector sent from the master to the slave OpenSees script was also sent to the laboratory as a displacement command to load the physical sub-structure. However, the force

feedback vector obtained from the physical sub-structure as shown in Figure 6-21 was recorded but not returned to OpenSees. Therefore, the numerical sub-structure contained in the slave OpenSees script (which simulates the response of the physical sub-structure) and the physical sub-structure in the laboratory were subjected to the same lateral displacements. Also, the force command vector, previously described in Section 6.4.2, was sent to the physical sub-structure to impose axial forces on the physical columns. These two tests were performed mainly to verify that (a) the displacement and force command vectors sent through OpenFresco were correctly applied by the actuators and (b) the feedback from strain gauges were properly transformed to obtain the force feedback vector. Sine functions with different periods and amplitudes were used for the sine-pulse ground motions (listed in Table 7-1) in tests PT01-01 and PT01-02 to excite the first and fourth vibration modes of the moment frame model, respectively. All sine-pulse ground motions included one complete sine wave.

These tests were followed by two quasi-static tests, namely, PT01-03 and PT01-04, conducted mainly to obtain the flexibility of the moment frame physical sub-structure and to measure the flexibility of the support boundary conditions. The flexibility (rotational and horizontal) at the base of the east column of the physical sub-structure was obtained using the Krypton instrumentation system. This information was utilized to update the support boundary conditions of the numerical sub-structure.

Once the displacement and force command vectors as well as the force feedback vector from the physical sub-structure were verified, the first preliminary elastic hybrid simulation, HS01-Sine, was conducted to verify the data exchange between the physical and numerical sub-structures. Interlocks on the actuator displacements were set to prevent undesired damage of the physical sub-structure in case of equipment malfunctioning or software instability. This hybrid simulation which was subjected to a sine-pulse ground motion was successfully conducted and provided the final check to proceed with the execution of the first series of hybrid simulations. As indicated earlier in Section 6.6, the inelastic hybrid simulations HS01-100% through HS01-200% were conducted in sequence to carry over any residual response of the numerical sub-structure to the next simulation. Table 7-2 summarizes the time steps and number of iterations for the INM-HS integration method, the total number of integration steps and the real time duration of each test of the first series of hybrid simulation.

**Table 7-2 Summary of time steps and number of iterations for the INM-HS integration method, total number of integration steps and real time duration of Hybrid Simulation #1**

| Test ID | Time Step [$\Delta t_{gm}$ [1]] | Number of Iterations per Integration Step | Total Number of Integration Steps | Real Time Duration of Simulation |
|---|---|---|---|---|
| HS01-25% | 1/2 | 4 | 9166 | 2h:14m |
| HS01-100% | 1/2 | 5 | 9166 | 2h:48m |
| HS01-160% | 1/3 | 5 | 13749 | 4h:20m |
| HS01-200% | 1/3 | 8 | 3457 | 1h:41m |

[1] $\Delta t_{gm}$: scaled size of the time step of the ground motion equal to $0.5^{0.5} \times 0.005$ sec. = 0.003536 sec.

An additional 1.0 sec. of highly-damped free vibration (50% damping ratio) was added at the end of each sequential hybrid simulation to fully damp the vibration of the hybrid model before the initiation of the next hybrid simulation. The high damping ratio was used to shorten the duration of the free vibration. The last hybrid simulation at the collapse level earthquake, HS01-200%, was stopped when the stroke capacity of the actuators of 20 in. was reached at the top horizontal actuator. A lateral displacement of 20 in. at the top of the physical sub-structure represents approximately a 15% inter-story drift ratio. The information provided in Table 7-2 is similar to the pre-test predictions presented previously in Table 6-7 except for the last hybrid simulation (HS01-200%) where the collapse criteria (20 in.) was reached slightly earlier than the pre-test prediction.

### 7.2.1 Results of Preliminary Tests (PT01 Test Series)

A key objective of preliminary tests PT01-01 and PT01-02 was to verify the data communication between the numerical and physical models, specifically, the transfer of displacement and force command vectors to the actuators and the force feedback vector obtained from the physical sub-structure. Figure 7-1 and Figure 7-2 compare the response of the four components of the force feedback vector obtained from the physical sub-structure with numerical predictions from the slave OpenSees script of the coupled simulations for the PT01-01 and PT01-02 tests, respectively. As indicated before, the slave OpenSees script was developed to simulate numerically the response of the physical sub-structure. The location of the four response quantities of the force feedback vector is indicated with a sketch above each figure. It can be seen in Figure 7-1 and Figure 7-2 that the numerical predictions largely overestimate the values of the measured force feedback vector. It was found afterwards that such differences were mainly due to the fact that while fixed supports were modeled in the slave OpenSees script (numerical predictions), the physical sub-structure exhibited flexible support boundary conditions at the base of the columns due to

the interface 9'×5'×1½" base plates used to attach the columns of the physical sub-structure to the strong floor in the laboratory. Such degree of flexibility at the base of the columns cannot be ignored in the numerical predictions.

In view of this, the second set of preliminary tests, namely, PT01-03 and PT01-04, were used to quantify the support flexibility of the physical sub-structure. The rotational and horizontal stiffness at the base of the east column of the physical sub-structure was obtained using measurements from the Krypton system. However, no experimental information was obtained for the west column. Afterwards, the numerical model of the physical sub-structure (slave OpenSees script in the coupled simulations) was updated using this experimental information. More specifically, rotational and horizontal elastic spring elements were added at the base of the columns of the numerical model to simulate the flexible supports. Table 7-3 shows the elastic stiffness for the rotation and horizontal springs at the base of the columns. Since no experimental measurements were available for the west column, similar elastic values were assumed for the west column with some modifications to better match the measured force feedback vector.

**Table 7-3 Elastic stiffness of flexible supports of the Physical Sub-Structure #1**

| Column | Rotational Stiffness at Support [kip-in./rad.] | Horizontal Stiffness at Support [kip/in.] |
|---|---|---|
| East Column [1] | 229775.8 | 3916.6 |
| West Column [2] | 183820.7 | 3916.6 |

[1] Values obtained from experimental information.

[2] Assumed values.

Figure 7-3 and Figure 7-4 compare the response of the four components of the force feedback vector measured from the physical sub-structure with the updated numerical predictions based on the numerical model with flexible supports for the PT01-01 and PT01-02 tests, respectively. Although for both tests the updated numerical predictions are closer to the experimental data, better improvements are observed for the PT01-01 test where the numerical model of the moment frame responded in its fundamental mode of vibration. This is because the calibration of the flexible supports was mainly based on the experimental data from the PT01-01 test where only the fundamental mode of the moment frame was excited. It is evident from Figure 7-1 through Figure 7-4 that flexible supports need to be accounted for in the numerical models for better predictions of the response of the physical sub-structure.

Therefore, the support boundary conditions of the numerical sub-structure of Hybrid Model #1 were updated using the information presented in Table 7-3. Calibration of this numerical model was important in order to improve numerical predictions of the expected results from the hybrid tests.

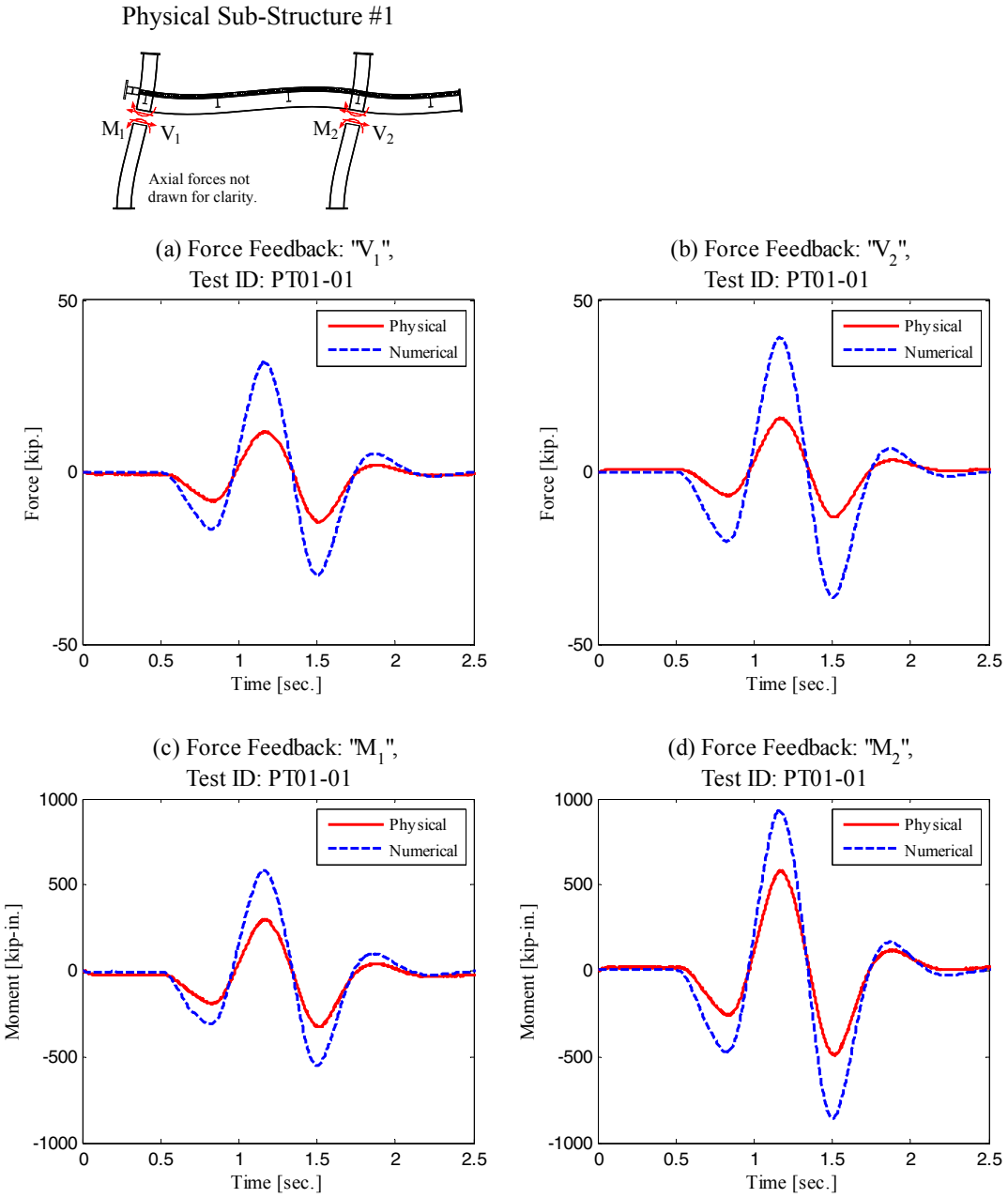


**Figure 7-1 Comparison of force feedback vector obtained from Physical Sub-Structure #1 and corresponding numerical prediction for PT01-01 test**

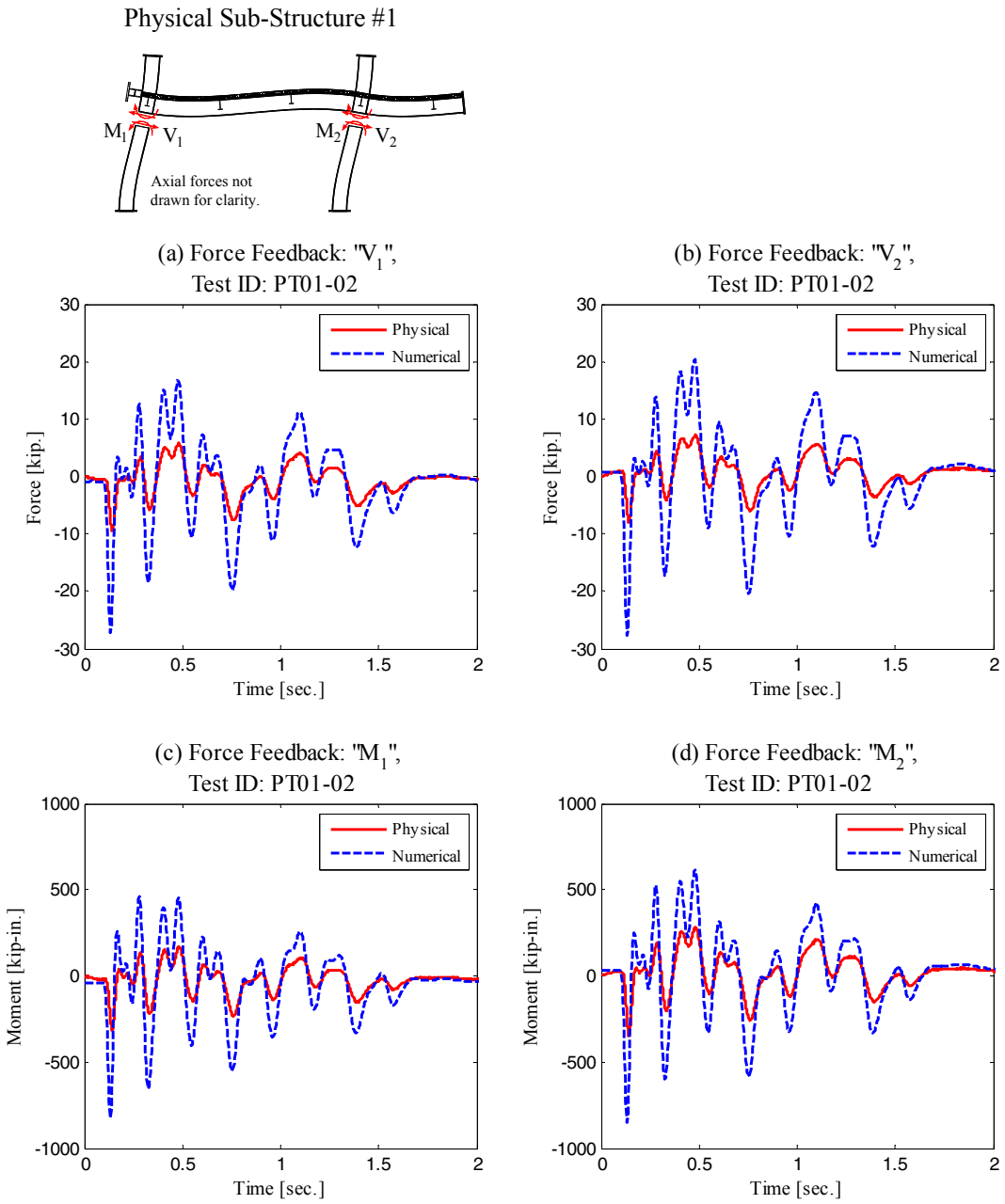


**Figure 7-2 Comparison of force feedback vector obtained from Physical Sub-Structure #1 and corresponding numerical prediction for PT01-02 test**

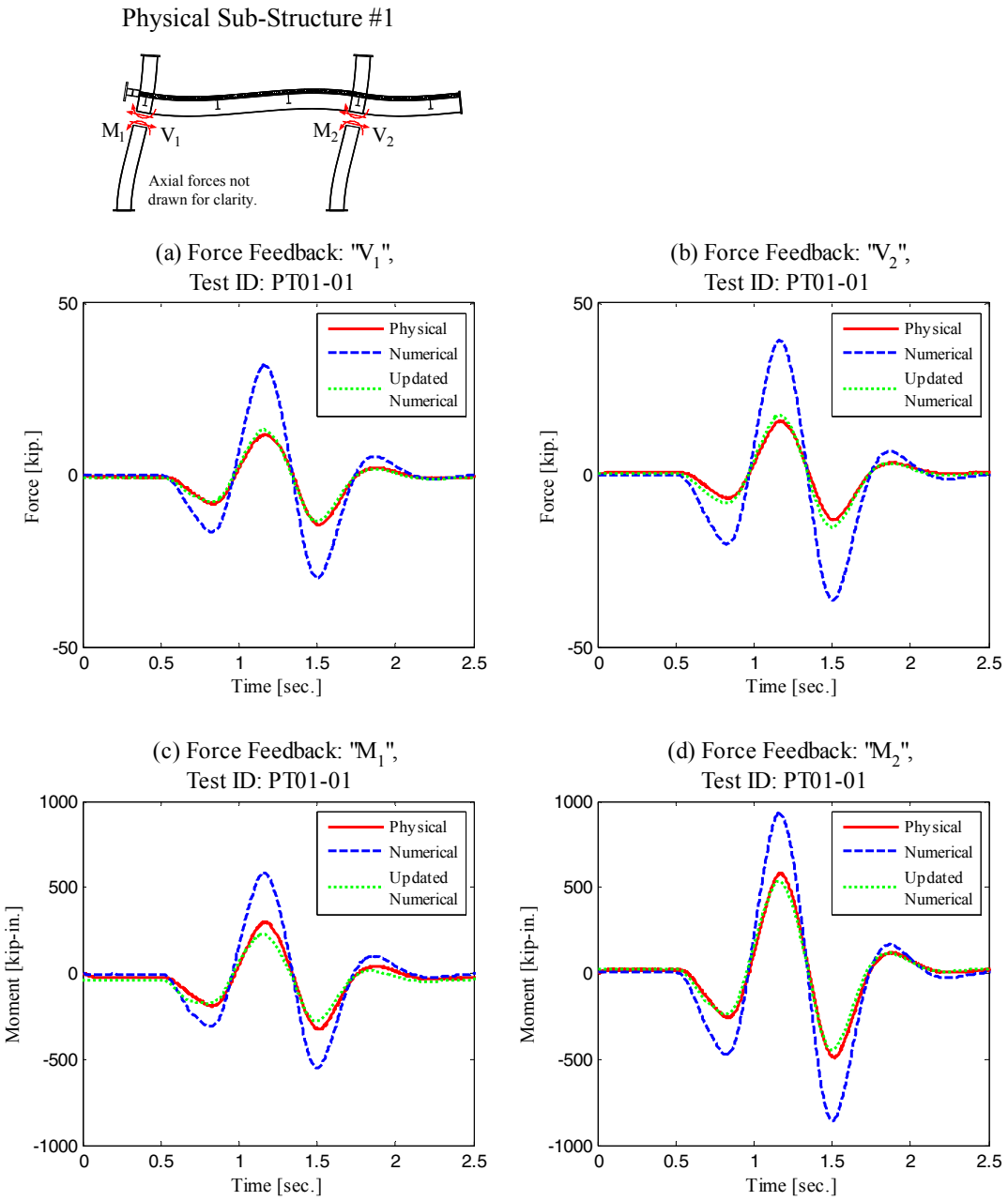


**Figure 7-3 Comparison of force feedback vector obtained from Physical Sub-Structure #1 and corresponding updated numerical prediction for PT01-01**

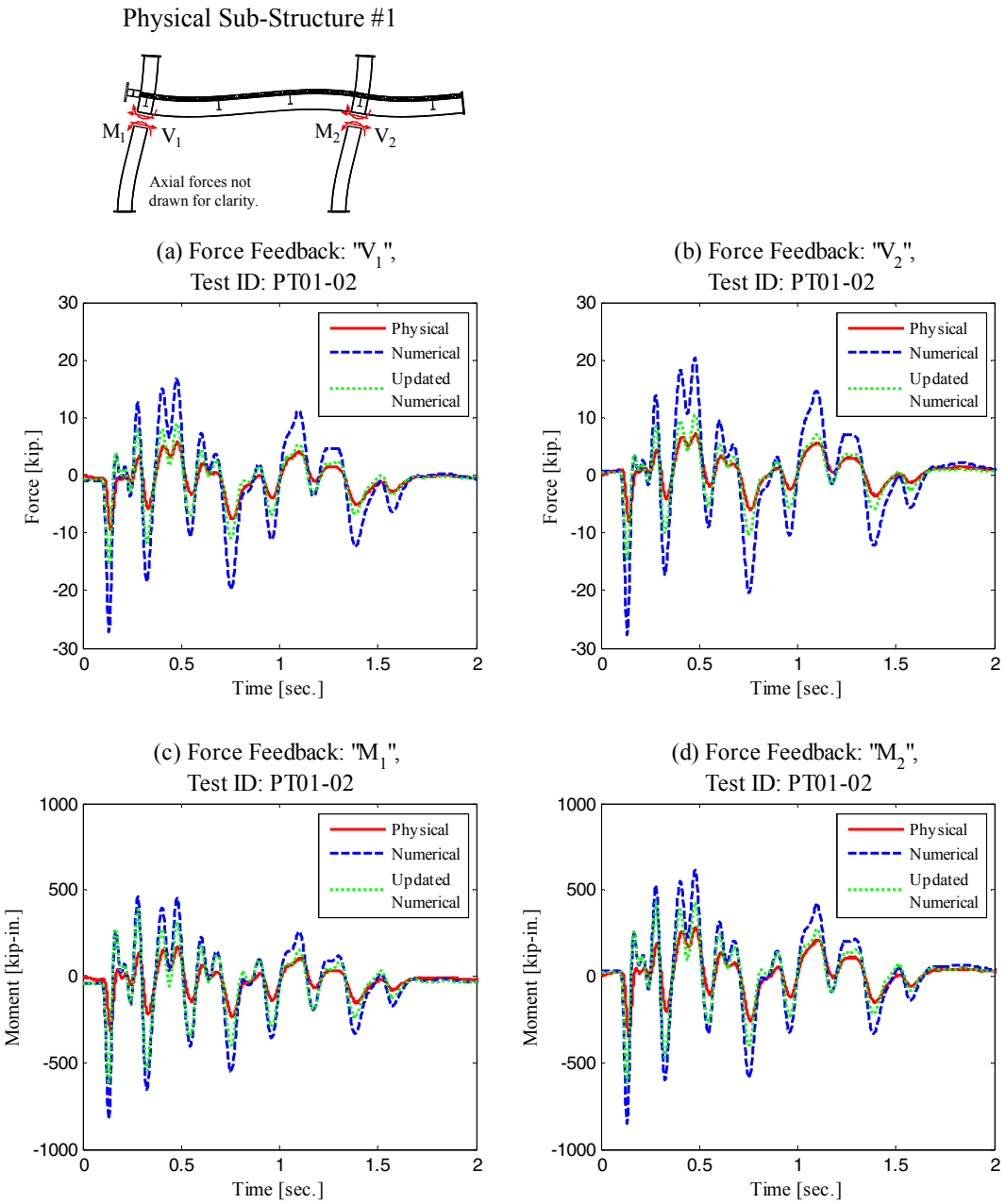


**Figure 7-4 Comparison of force feedback vector obtained from Physical Sub-Structure #1 and corresponding updated numerical prediction for PT01-02**

### 7.2.2 Results of Hybrid Simulations (HS01 Test Series)

The first series of hybrid simulations (Hybrid Simulation #1) were successfully conducted using the substructuring technique described in Section 6.4 and the INM-HS integration method with the time steps and number of iterations presented in Section 6.6.1. This section presents the results of this first series of hybrid simulations. The results of the preliminary elastic hybrid simulation HS01-Sine are not presented since the physical and numerical sub-structures in this hybrid simulation remained elastic and information on the elastic response of the hybrid model can be obtained from the hybrid simulation at 25% of the ground motion (HS01-25%).

In order to first examine the stability and accuracy of Hybrid Simulation #1, Figure 7-5 presents the norm of the unbalanced force vector, $norm(P_{eff})$, for the first series of hybrid simulations compared to pre-test numerical predictions. The unbalanced force vector was previously defined in Section 3.2.1 and it was shown in Section 6.2.5 that unbalanced forces provide an indirect measure of the stability of a simulation since simulations with large unbalanced forces tend to become unstable. For comparison purposes, the pre-test predictions were obtained using coupled numerical simulations conducted with the same integration method (INM-HS), time steps, and number of iterations used in the hybrid simulations. The flexible support boundary conditions were also included in the coupled simulations. The maximum norm of the unbalanced force vector is identified in Figure 7-5 for each simulation. As expected, the unbalanced forces for the hybrid simulations are, on average, larger than the numerical predictions but of the same order of magnitude. The differences can be mainly attributed to the noise in the force feedback from the physical sub-structure. Only the maximum norm of the unbalanced force vector of the HS01-160% hybrid simulation is significantly larger than its predicted value. Also, only the maximum norm of the unbalanced force vector for the HS01-100% hybrid simulation is smaller than its predicted value. The hybrid simulations did not present any instability problems. Since unbalanced forces are mostly similar, it can be concluded that the accuracy of the hybrid simulations is similar to that of the numerical predictions.

In the first part of this section, global response results of the hybrid simulation models are presented in Section 7.2.2.1 and compared with pre-test numerical predictions to assess the accuracy of the hybrid simulations. Subsequently in Section 7.2.2.2, local response results are presented to assess the behavior of the physical sub-structure.

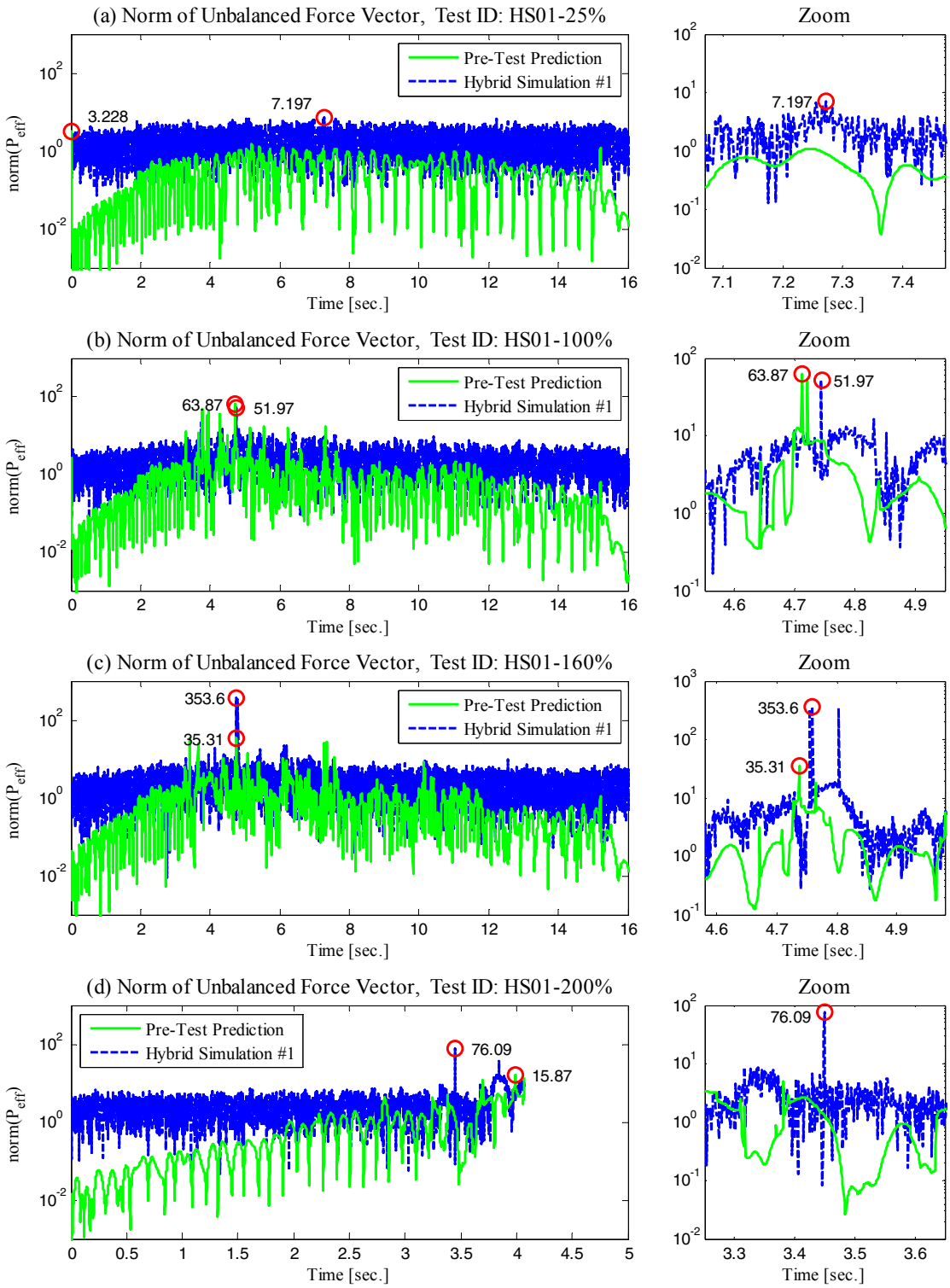


**Figure 7-5 Norm of unbalanced force vector for Hybrid Simulation #1 and pre-test numerical predictions**

#### 7.2.2.1 Global Response Results and Comparison with Pre-Test Predictions

This section presents selected global response results of the first series of hybrid simulations including roof drift ratios, inter-story drift ratios, base shears, force-displacement relationships for the first story, column axial forces and out-of-plane displacement of the physical sub-structure. Pre-test numerical predictions are also presented for comparison purposes. The pre-test predictions were based on a conventional purely numerical simulation using the implicit Newmark method (INM) with comparatively smaller time steps and a stringent tolerance for the converge test. The numerical models used for the pre-test numerical predictions were updated using the flexible support information obtained from the preliminary tests for consistency with the flexible supports of the hybrid model.

Figure 7-6 presents the roof drift ratio response for the first series of hybrid simulations (Hybrid Simulation #1) as well as pre-test numerical predictions. The term roof drift ratio in Figure 7-6 (and in all subsequent figures) is defined as the lateral displacement at the roof level divided by the roof height (306 in.). Maximum roof drift ratio values are indicated in Figure 7-6 for each hybrid simulation. In general, the results of the hybrid simulations are in good agreement with the pre-test predictions. However, Figure 7-6(a) and Figure 7-6(b) show that the fundamental period of the frame structure is slightly larger in the hybrid simulations. Therefore, the physical sub-structure is more flexible than its corresponding numerical model. Since the elastic properties of bare steel components can be closely predicted, such differences can be mostly due to some of the modeling assumptions (see Section 6.2.3) adopted to account for the effects of the composite floor slab. One of these assumptions included a 20% increase in the flexural stiffness of the girders. Also, the residual drift at the end of the HS01-160% test is significantly larger than its predicted value as seen in Figure 7-6(c). This could be attributed to the fact that residual drifts are significantly influenced by the type of hysteresis (Ruiz-Garcia and Miranda, 2006). In this case, inelastic response in the numerical portion of the hybrid simulation model was simulated with multi-linear springs (i.e., not smooth hysteresis models). Despite the before-mentioned differences, the time instant of collapse of the hybrid model was closely predicted as shown in Figure 7-6(d).

To better observe differences in the displacement response, Figure 7-7 presents inter-story drift ratios for all story levels of the hybrid model as well as numerical pre-test predictions. Similar to Figure 7-6, maximum inter-story drift ratio values are indicated in Figure 7-7 for each hybrid simulation. It can be seen that the smallest differences with the pre-test numerical predictions occur at the fourth story. Figure 7-9 also shows a sidesway collapse mechanism that is based on the lower three stories of the four-story hybrid model.

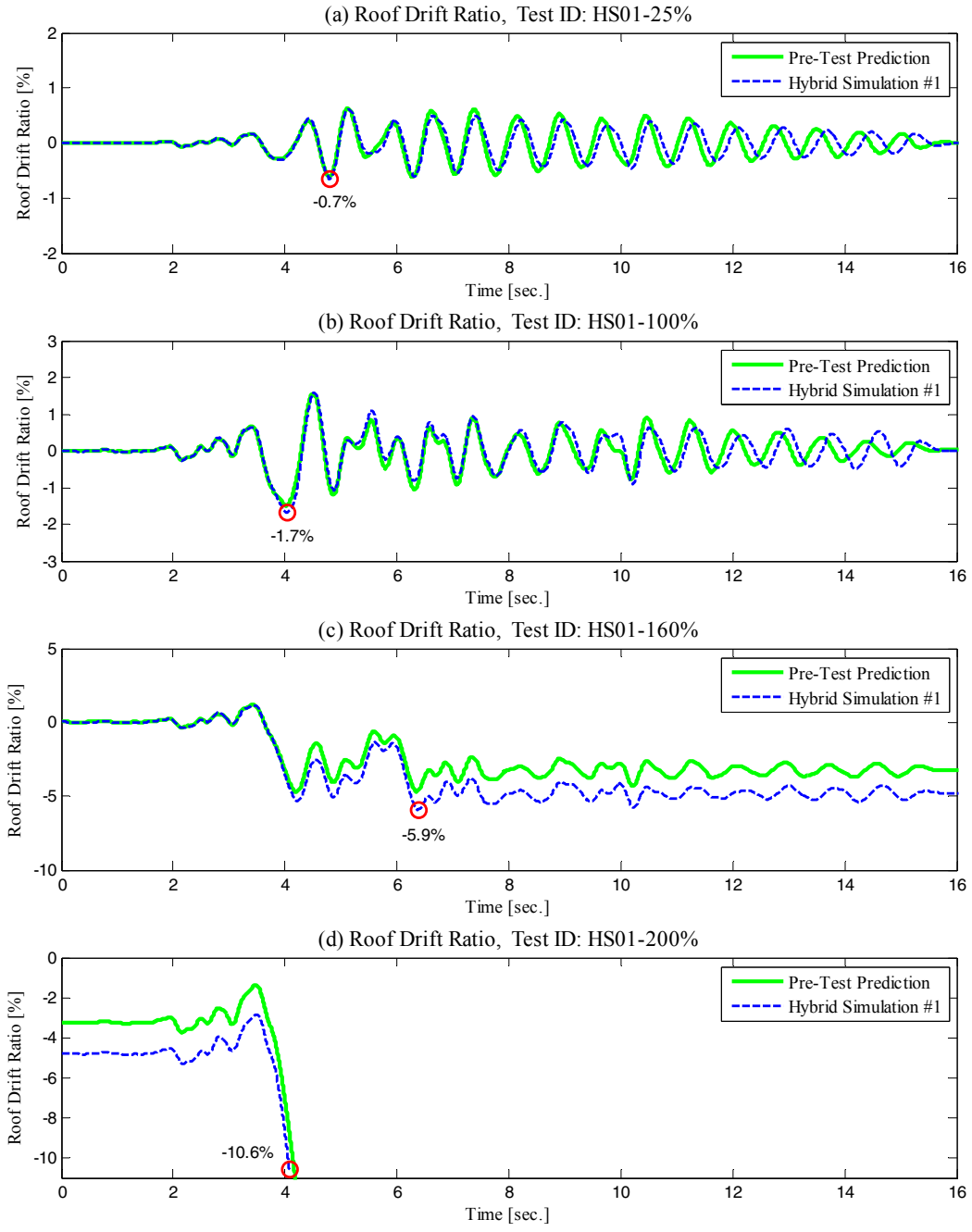


**Figure 7-6 Roof drift ratio response for Hybrid Simulation #2 and pre-test numerical predictions**

Figure 7-8 presents the base shear response of the hybrid model as well as pre-test numerical predictions. The base shear values presented in Figure 7-8 (and Figure 7-9) were normalized by the scaled seismic weight of the model of 544 kips (which is half of the total seismic weight presented in Table 6-1 for one moment frame). Maximum normalized base shear values are indicated in Figure 7-8 for each hybrid simulation. On average, the base shear values of the Hybrid Model #1 are smaller than the predicted values. This can be attributed to the fact that the physical subassembly of the hybrid model is slightly more flexible that the pure analytical model that was used for the pre-test predictions. Also, the maximum normalized base shear of the hybrid model, which occurs at 160% of the ground motion intensity, is 0.46 as seen in Figure 7-8(c).

Figure 7-9 presents the inter-story drift ratio of the first story versus the total base shear for the Hybrid Model #1 as well as pre-test predictions. Figure 7-9(a) and Figure 7-9(b) show the slightly larger flexibility of the Hybrid Model #1 as compared to the pre-test numerical model. From Figure 7-9(d), it is observed that structural collapse due to sidesway instability took place because the base shear of the hybrid model approaches zero after the first story exceeds an inter-story drift ratio of 15%.

Figure 7-10 presents axial forces at the base of the east and west columns of the physical sub-structure for the first series of hybrid simulations. Numerical pre-test predictions are also presented in Figure 7-10 for comparison purposes. The axial forces were normalized by $P_{y,p}$, which is defined as the column cross-sectional area times the measured material yield strength obtained from coupon testing. Maximum normalized axial force values are indicated in Figure 7-10 for each hybrid simulation. The axial forces in the physical columns were obtained using the groups of strain gages "EC1" and "WC1" previously presented in Figure 5-8. Since the measurements of the strain gages were set to zero at the beginning of the hybrid simulations, initial axial forces on the columns of the physical sub-structure due to gravity loads were added to the values shown in Figure 7-10. Such initial axial forces were estimated based on the results presented earlier in Table 5-6. In most cases, the axial forces measured in the physical columns were smaller than the predicted values. Also, Figure 7-10 shows, as expected, a larger axial force variation in the exterior column (east column) as compared to the interior column (west column) due to overturning effects of the seismic forces. While the exterior column experienced a maximum compressive axial force of $0.18P_{y,p}$, a value of $0.10P_{y,p}$ was observed for the interior column.

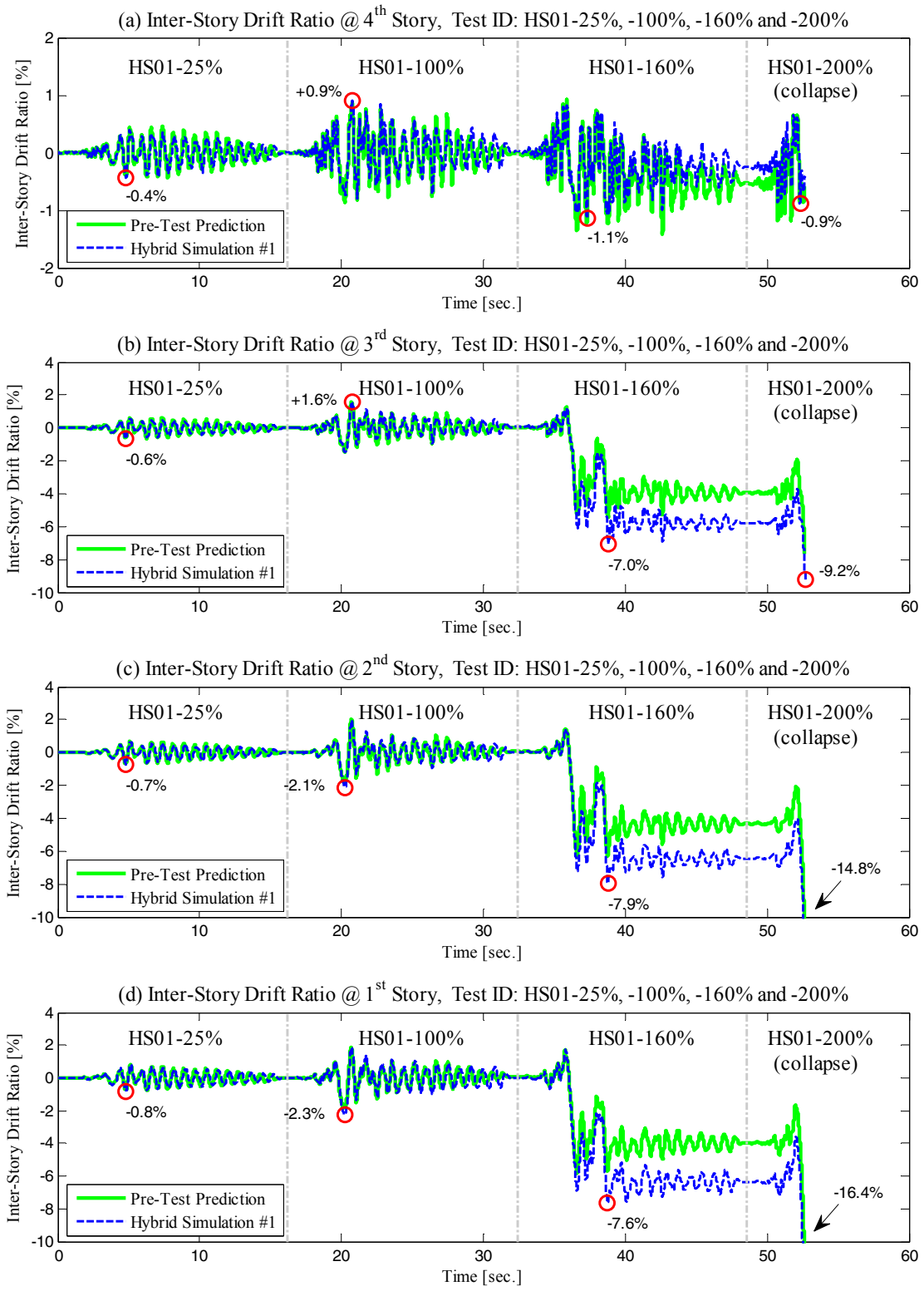


**Figure 7-7 Inter-story drift ratios for Hybrid Simulation #1 and pre-test numerical predictions**

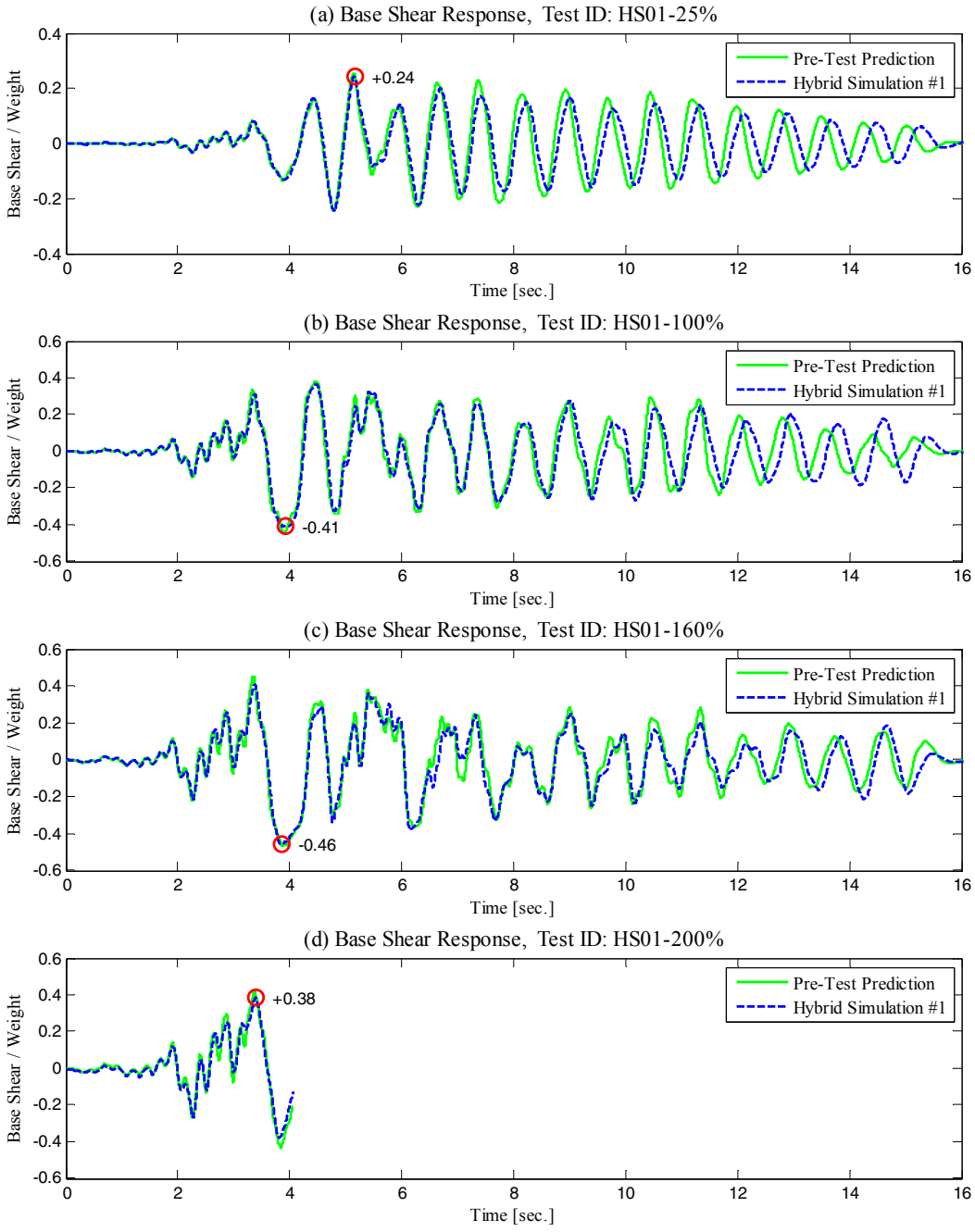


**Figure 7-8 Base shear response for Hybrid Simulation #1 and pre-test numerical predictions**

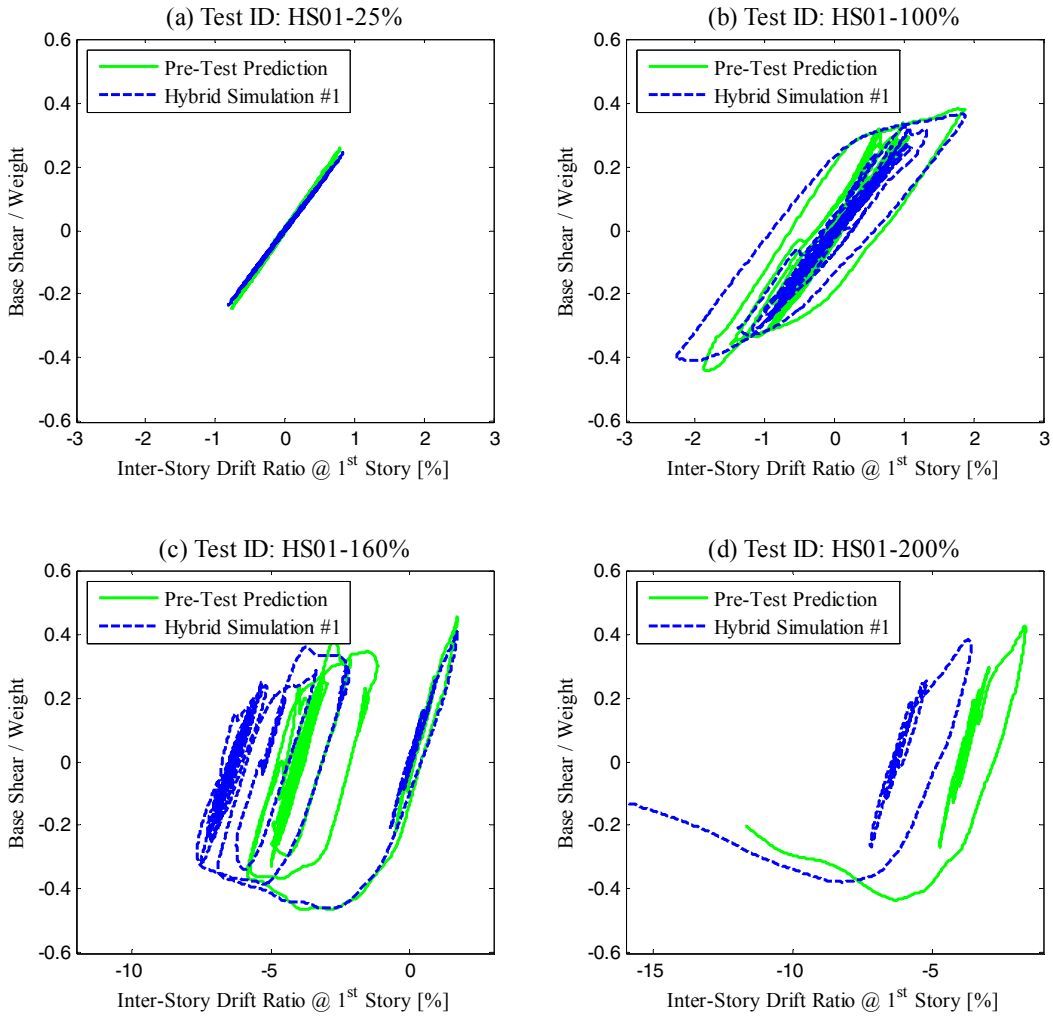


**Figure 7-9 Total base shear versus inter-story drift ratio at first story for Hybrid Simulation #1 and pre-test numerical prediction**

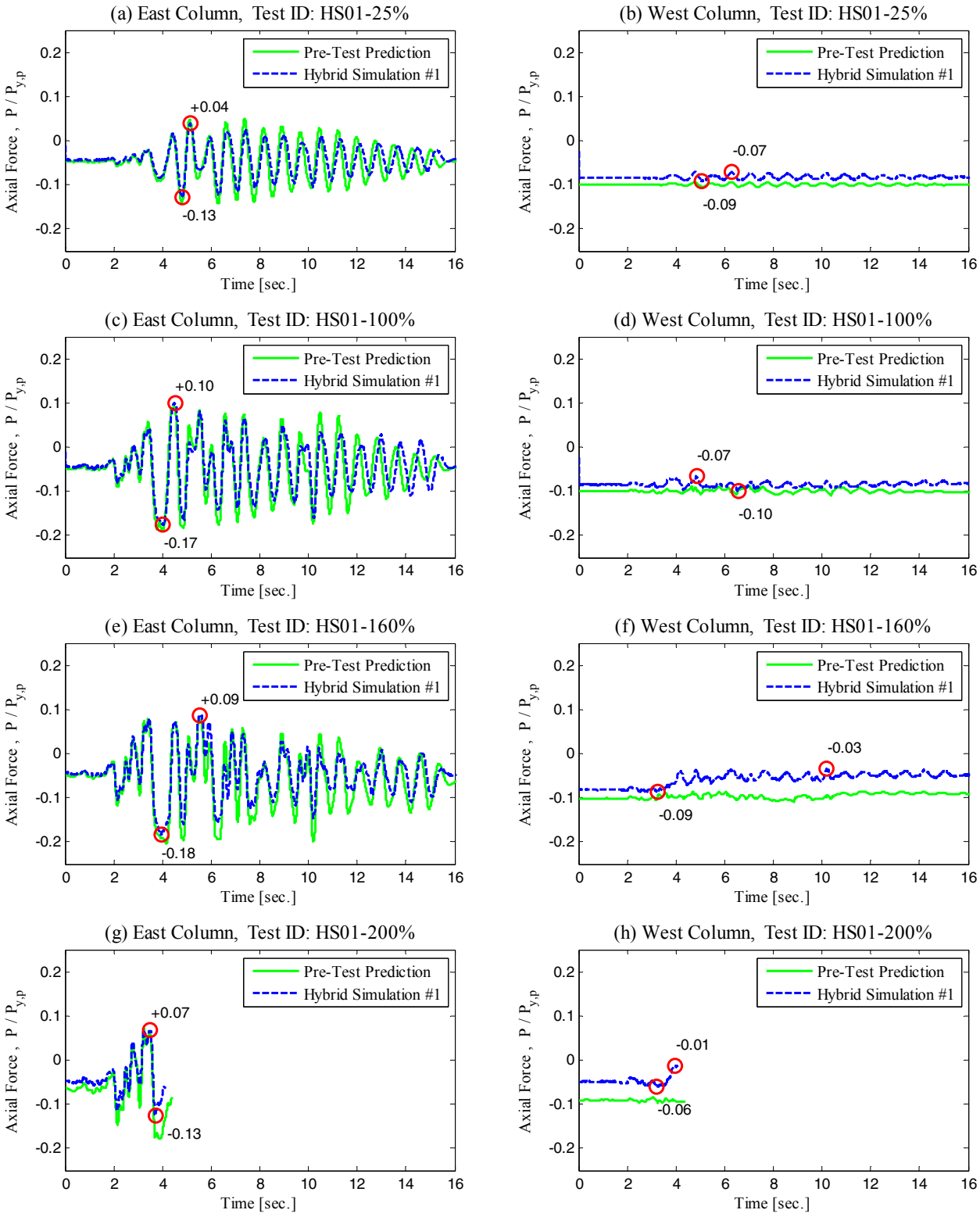


**Figure 7-10 Axial force at base of first-story columns of physical sub-structure for Hybrid Simulation #1 and pre-test numerical prediction**

Figure 7-11 presents the out-of-plane response of the joints of the physical sub-structure during the first series of hybrid simulations. As it was described in Section 5.2.3.2, two string pots monitored the out-of-plane displacement at the east and west joints of the physical sub-structure. Before approaching collapse, the maximum out-of-plane displacement of the physical sub-structure was approximately 2% of the peak lateral displacement. Also, Figure 7-11 shows that the physical specimen twisted as the structure collapsed.

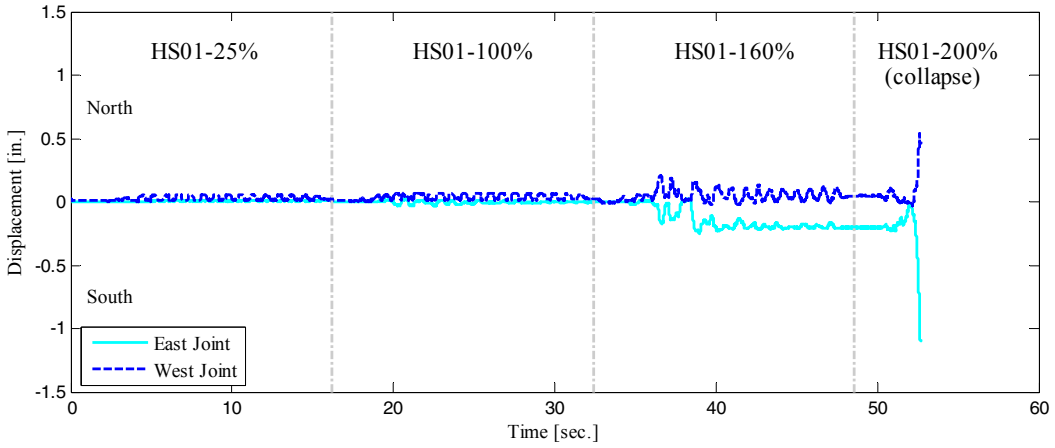


**Figure 7-11 Out-of-plane response of the physical sub-structure during Hybrid Simulation #1**

Figure 7-12 shows the deformed configuration of the Physical Sub-Structure #1 at the end the collapse hybrid simulation (HS01-200%). From the rotated position of the steel plate (yellow plate) used to simulate gravity forces on the slab, it can be seen that the girder twisted toward the end of the simulation. This is not expected to happen in frame structures with parallel bays. The lateral support of the experimental test setup did not restrain lateral torsional buckling of the girder. As it will be shown later in this section, twisting of the girder induced some yielding on the columns via out-of-plane bending. This could affect the outcome of the results, such as the post-capping rotation capacity of girders and columns. However, twisting of the girder occurred only at the very end of the simulation. Also, in realistic three-dimensional building structures, some level of out-of-plane bending is expected in the columns due to bi-directional loading.

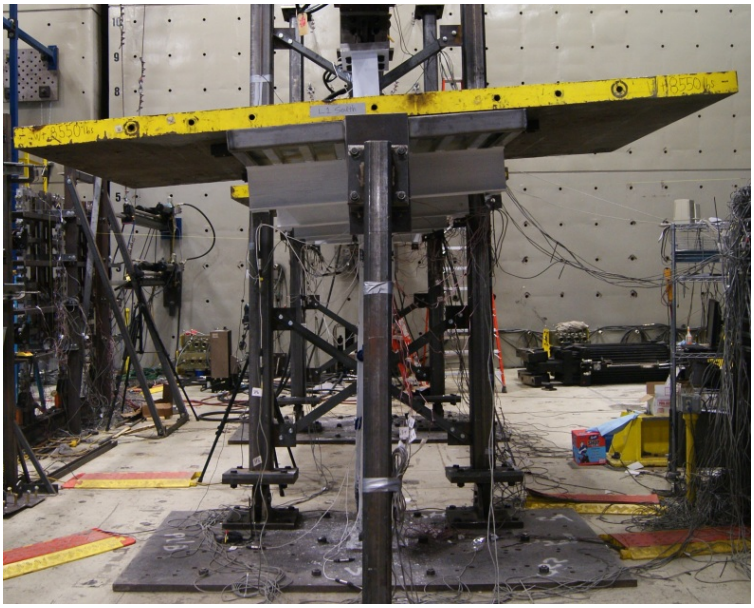

**Figure 7-12 Twisting of girder of the Physical Sub-Structure #1 at the end of first series of hybrid simulations**

#### 7.2.2.2 Local Response Results

This section more closely examines the local response of the special steel moment frame hybrid model tested in the first series of hybrid simulations. The inelastic response of physical components is compared with the computed inelastic response from similar numerical components to provide complete information on the hybrid model. As mentioned before, all hybrid simulations from the first series are presented except for the preliminary elastic hybrid simulation HS01-Sine.

Figure 7-13 presents the inter-story drift ratio of the first story versus the physical and numerical components of the base shear in Hybrid Model #1. Unlike similar plots presented previously in Figure 7-9, Figure 7-13 presents separately the numerical and physical components of the base shear. A sketch is provided above Figure 7-13 to better illustrate the base shear components. As seen in the sketch, the numerical component does not include the base shear from the leaning column. Although the numerical sub-structure was calibrated with experimental information on the flexible support condition of the physical sub-structure, Figure 7-13(a) indicates a higher flexibility of the physical sub-structure as compared to the numerical sub-structure. Also, the peak base shear of the physical portion of the frame structure is smaller than that of the numerical sub-structure as observed in Figure 7-13(c). This could be partly attributed to the assumptions adopted to simulate the response of the slab in the numerical model (see Section 6.2.3 for reference). Also, as is shown later in this section, the bending strength of the

columns was overestimated in the numerical model and, consequently, the lateral strength of the numerical model observed in Figure 7-13 is higher than the physical portion. Although the shear forces at the base of the two exterior (or interior) columns are not necessarily similar, analytical simulations indicated that for this particular model such shear forces are very similar (the largest difference was 9% of the smallest shear force).

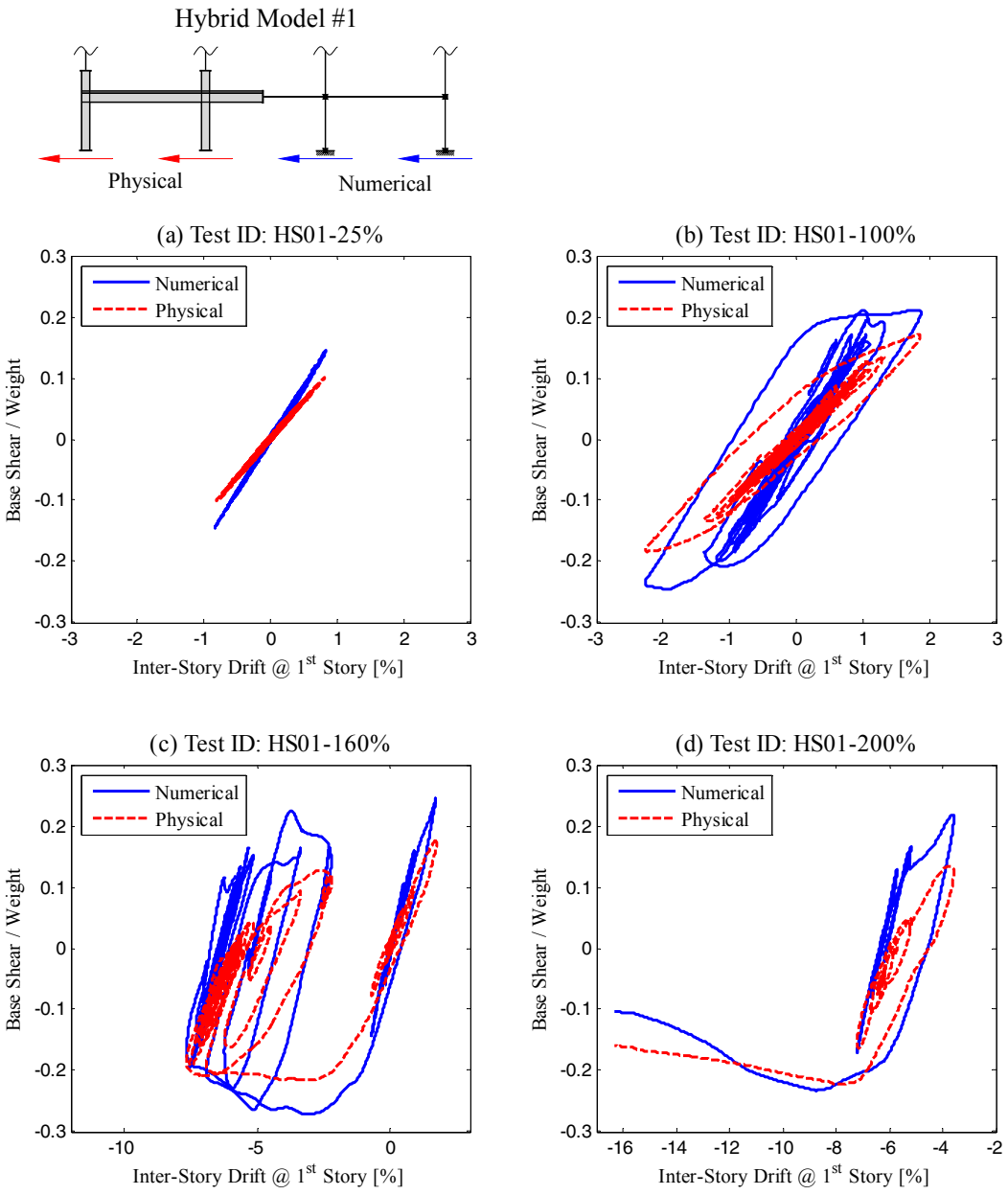


**Figure 7-13 Physical and numerical components of the base shear versus inter-story drift ratio of first story for Hybrid Simulation #1**

The physical component of the base shear (base shear from physical portion of hybrid model) was obtained indirectly using measurements from the strain gages. To assess the accuracy of the base shear forces, Figure 7-14 compares the sum of the shear forces at the base of the east and west columns of the physical sub-structure ($V_{EC}+V_{WC}$) with the sum of the horizontal actuator forces ($F_{act1}+F_{act2}$) obtained from certified actuator load cells. It can be seen that the shear forces at the base of the east and west columns compare very well with the actuator lateral forces all the way to collapse. Note that the shear force at the base of the vertical link member due to P-Delta effects (as well as the base shear of the long columns of the supporting frame shown in Figure 5-18) were not included in the equilibrium check of Figure 7-14 since these values are negligible compared to the shear forces in the moment frame.

Photographs of the damage state of the east and west columns of the physical sub-structure at the end of the hybrid simulations are shown in Figure 7-15. The damage corresponds to a maximum inter-story drift ratio of 16.4% at the first story. It can be seen that damage on the physical sub-structure was mainly concentrated at the base of the columns, panel zones and reduced beam sections. Also, significant yielding at the top of the first-story west column is observed. Yielding at this location was mostly due to twisting of the girder as seen in earlier in Figure 7-12. This is further discussed in the next sections.

The observed behavior of the frame with damage distributed throughout the various components highlights the benefits to this hybrid test approach with large subassemblies. This is in contrast to the single connection tests that have been conducted in the past.

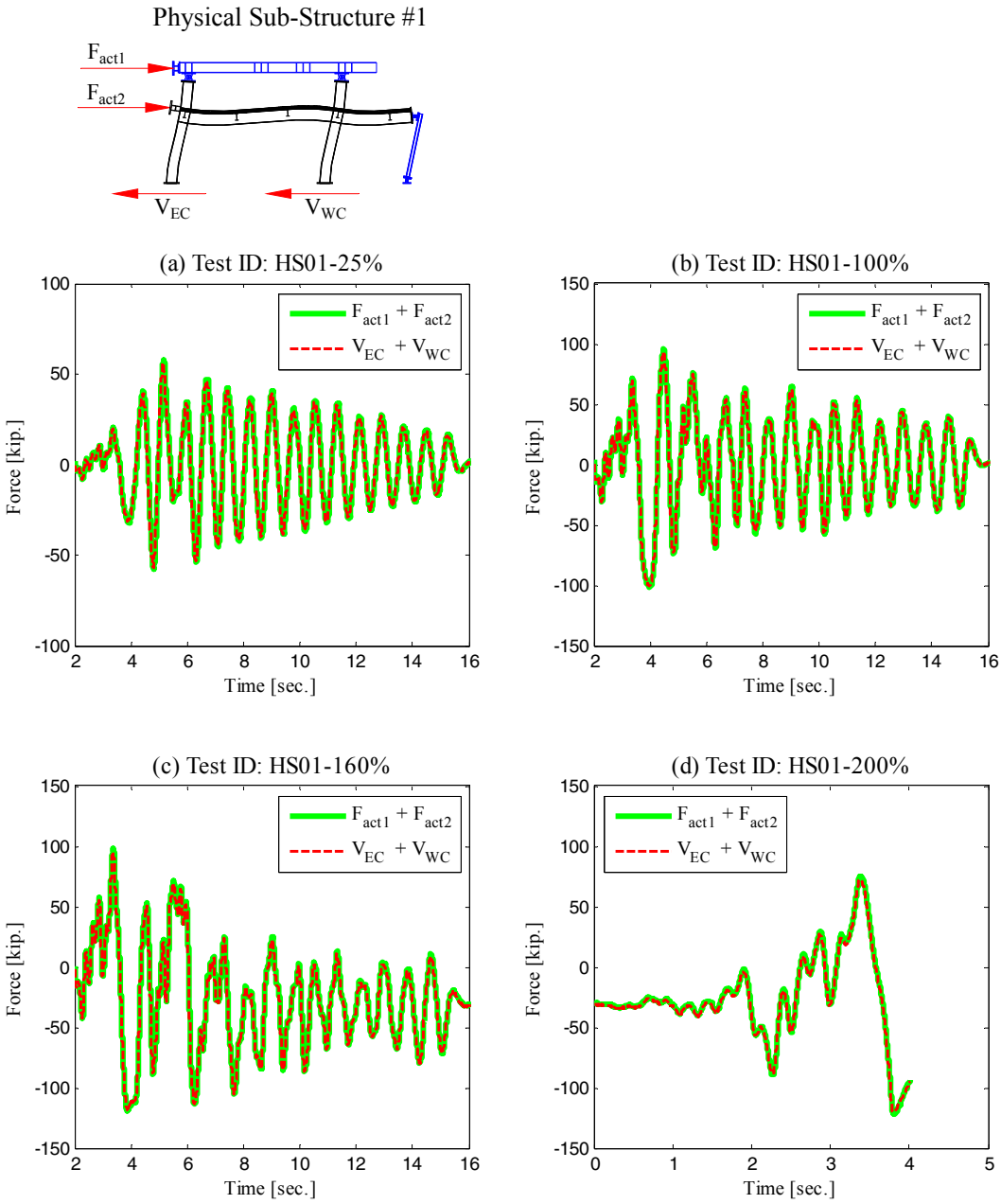


**Figure 7-14 Verification of column shear forces derived from strain gage measurements ($V_{EC}$+$V_{WC}$) using certified actuator load cells for Hybrid Simulation #1**

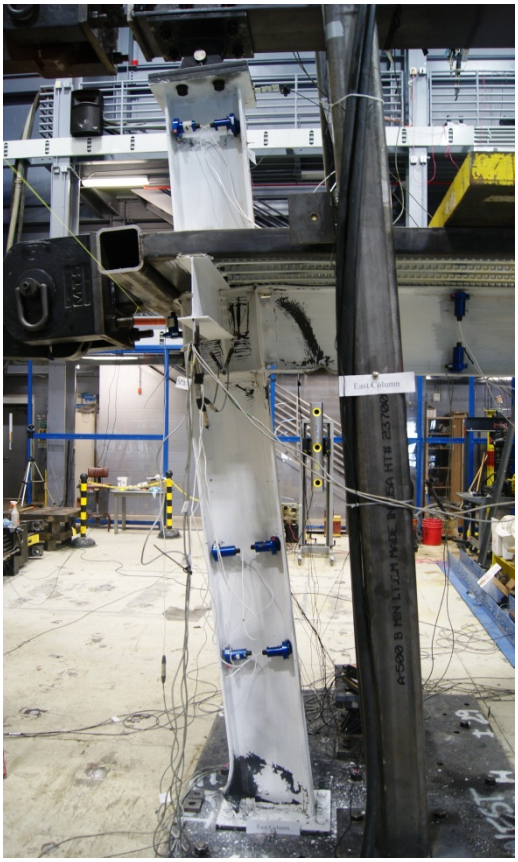

(a) North view of deformed east column

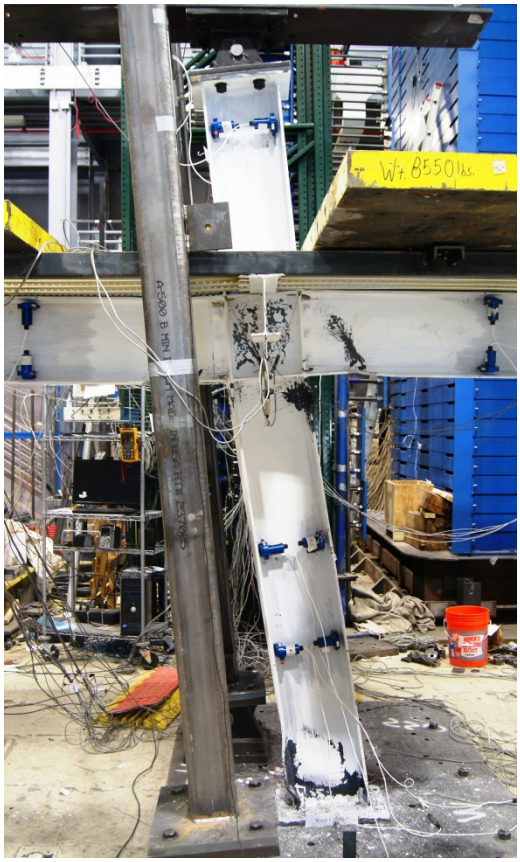


(b) North view of deformed west column

**Figure 7-15 Deformed configuration of east and west columns of physical sub-structure after Hybrid Simulation #1**

**Response of Moment Frame Columns**

Figure 7-16 through Figure 7-18 present moment-rotation relationships for the columns of the physical sub-structure at plastic-hinge regions. The location of the plastic-hinge regions is indicated with a sketch provided above each plot. The sketches do not show the overlapping domain between the physical and numerical sub-structures (for reference, see Figure 6-20). In each plot, the response of physical columns is presented together with the response of similar columns from the numerical sub-structure of the moment frame for comparison purposes. Although the response of such physical and numerical components is different, some observations can be carefully made. All bending moments were normalized by the predicted moment strength ($M_{y,p}$) of the W12×30 column, which was defined as the plastic section modulus ($Z$) times the measured material yield strength obtained from coupon testing. The elastic component of the rotations was removed so that only plastic rotations are presented in all figures. To this end, the elastic stiffness was first obtained using linear regression of the data from the elastic hybrid simulation HS01-25%. Such elastic stiffness was then utilized to estimate the elastic component of the rotations presented in the inelastic hybrid simulations HS01-100% through HS01-200%. Maximum plastic rotation values are indicated in some moment-rotation plots.

Some observations can be made with respect to the results presented in Figure 7-16 through Figure 7-18. In general, the inelastic response of the columns of the moment frame was mainly concentrated at the base of the columns, as seen in Figure 7-16. Significant yielding was also observed at the top of the first-story west column, as seen in Figure 7-17(f) and Figure 7-17(h). However, visual inspection of the damage indicated that yielding at this location was partly due to lateral-torsional buckling of the girder (as seen earlier in Figure 7-12) which induced out-of-plane bending of the column. String pot measurements indicated that while a maximum plastic rotation of 0.10 rad. was experienced at this location by the west column (see Figure 7-17(h)), the east column only presented a plastic rotation of 0.03 rad. (see Figure 7-17(g)). Also, Figure 7-18 shows that there was practically no yielding of columns at the bottom of the second story. With regards to the numerical model, Figure 7-16 shows that the bending moment at yielding was over-predicted in the numerical sub-structure. This was mainly due to the fact that the yield moment of the numerical sub-structure was increased by a factor of 1.17 to account for the effect of isotropic hardening. To a lesser extent, such yield moment over-predictions could be attributed to the fact that the hysteretic model for columns did not account for axial force-bending moment (P-M) interaction. The east and west columns of the physical model experienced compressive axial forces equal to 18% and 10% of the axial strength at yielding ($P_{y,p}$), respectively (see Figure 7-10 for reference). The reduced bending capacity of the columns for such levels of axial loads is less than 5%.

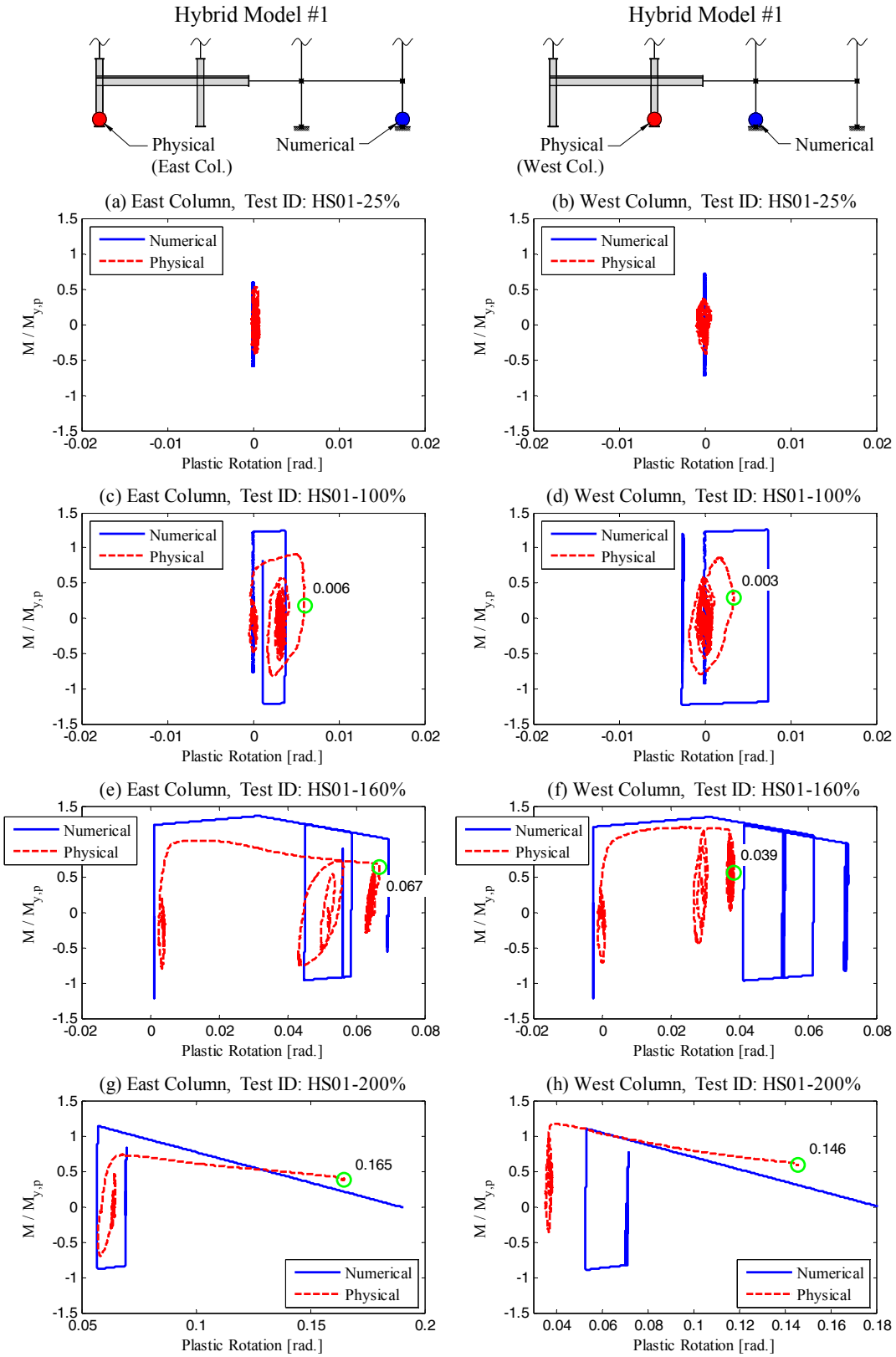


**Figure 7-16 Moment-rotation relationships for column plastic-hinge regions of moment frame during Hybrid Simulation #1 (Part I)**

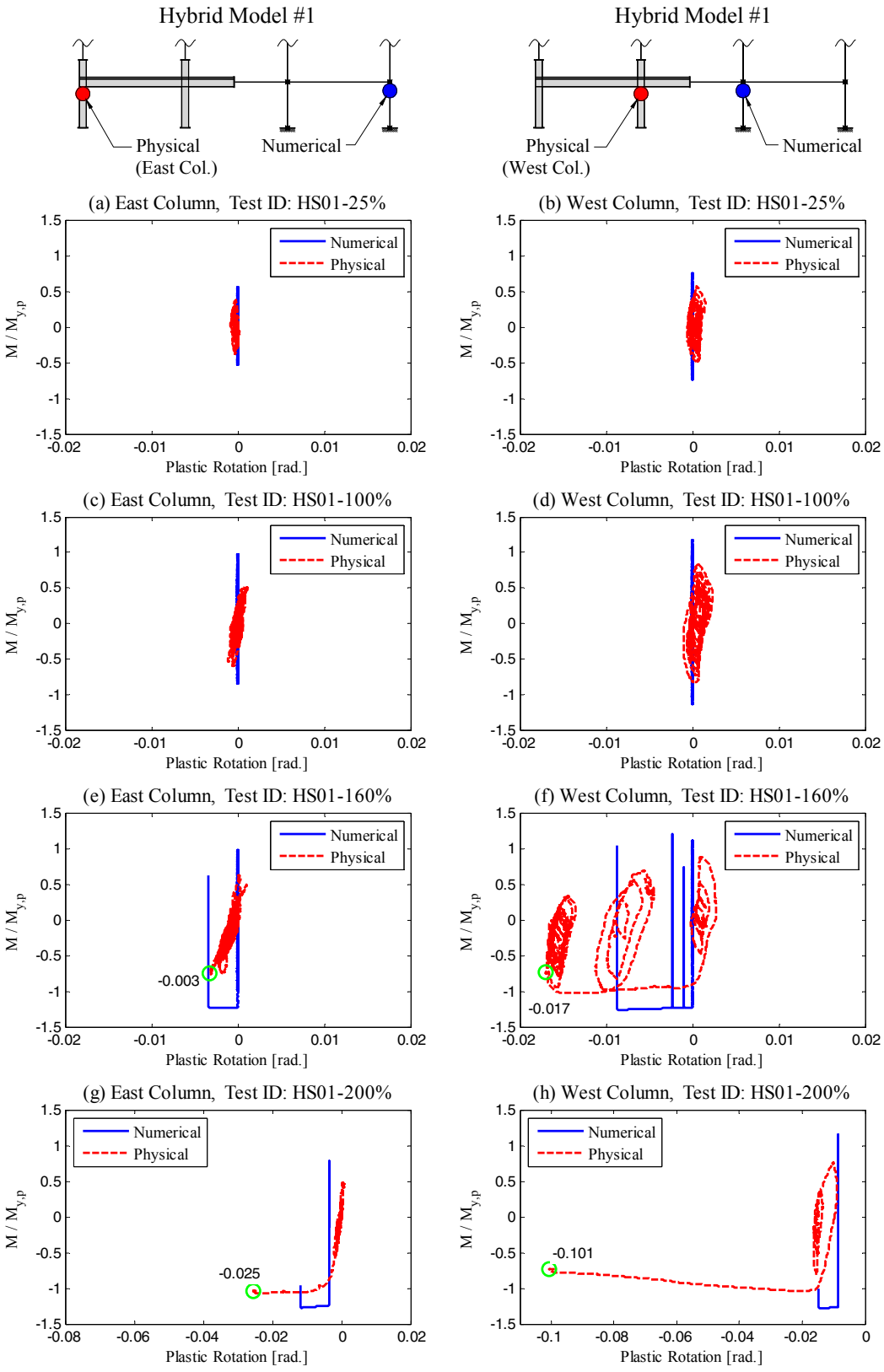


**Figure 7-17 Moment-rotation relationships for column plastic-hinge regions of moment frame during Hybrid Simulation #1 (Part II)**

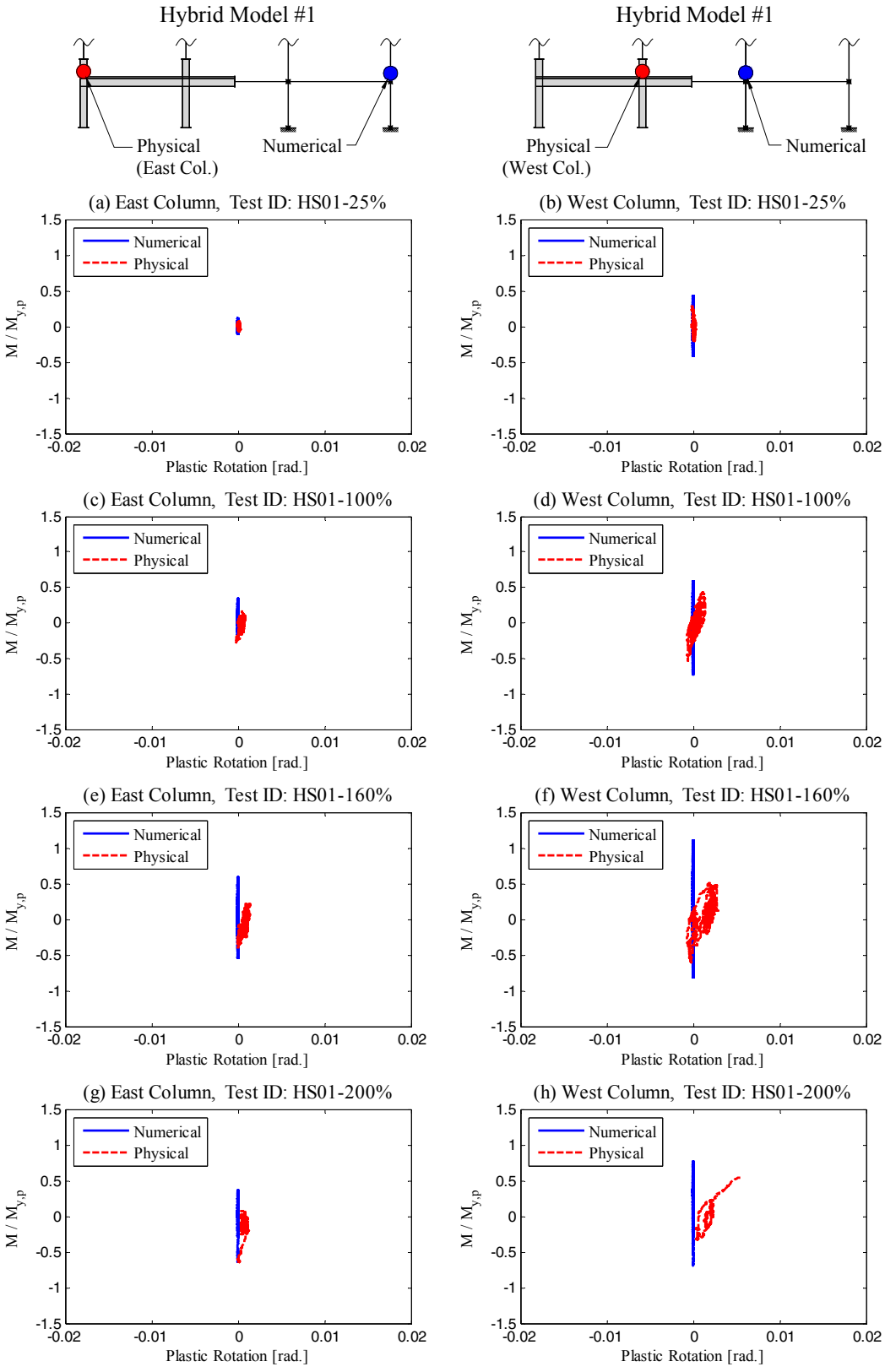


**Figure 7-18 Moment-rotation relationships for column plastic-hinge regions of moment frame during Hybrid Simulation #1 (Part III)**

The post-capping strength deterioration clearly observed in Figure 7-16(g) and Figure 7-16(h) indicates that the post-capping rotation of the W12×30 column was under-predicted in the numerical sub-structure. This was expected since, as mentioned before, the post-capping plastic rotation for girders and columns of the numerical sub-structure were obtained using the regression equations of Lignos and Krawinkler which were derived with an experimental database of sections larger than or equal to W21. Smaller sections such as the W12×30 tested here exhibit larger plastic rotation capacities as compared to predictions by the regression equations. In collapse assessment of structural systems, the post-capping plastic rotation is one of the most influential parameters (Ibarra and Krawinkler, 2005).

The information presented in Figure 7-16 through Figure 7-18 is useful to assess the performance of the substructuring technique. Figure 7-16 shows that the columns of the physical sub-structure at the base exhibit typically smaller rotations than those of the numerical sub-structure. This was previously predicted in the numerical evaluation of the substructuring technique. However, in the hybrid simulations, the interior physical column (west column) was subjected to significantly smaller rotations than the similar interior numerical column. Also, Figure 7-17(h) shows that the interior first-story column presents larger rotations at the top than the numerical sub-structure as the frame structure collapsed. This is also in good agreement with the numerical evaluation of the substructuring technique (see Figure 6-26(h) for reference).

As indicated before, the bending moments presented in Figure 7-16 through Figure 7-18 were indirectly obtained from strain gage measurements. Such measurements were verified to be reliable in Figure 7-14. Similarly, the plastic rotations presented in Figure 7-16 through Figure 7-18 obtained from measurements from string pot data were also verified in Figure 7-19. Figure 7-19 presents the plastic rotation at the base of the east column obtained from the Krypton system and string pot data. The elastic component of the rotations was removed for comparison purposes. It can be seen in Figure 7-19 that the rotations obtained at the plastic hinge region at the base of the columns compares well with the rotations obtained by the Krypton system.

Figure 7-20 shows photographs of the damage state at the base of the east and west columns of the physical sub-structure for hybrid simulation HS01-100% through HS-200%. The photographs were taken either at the end of the simulation indicated in the photograph or during the simulation but after the maximum deformation. Values of maximum plastic rotation are indicated for each photograph. It can be seen that significant web and local buckling are observed for the last hybrid simulation at collapse (see Figure 7-20(e) and Figure 7-20(f).

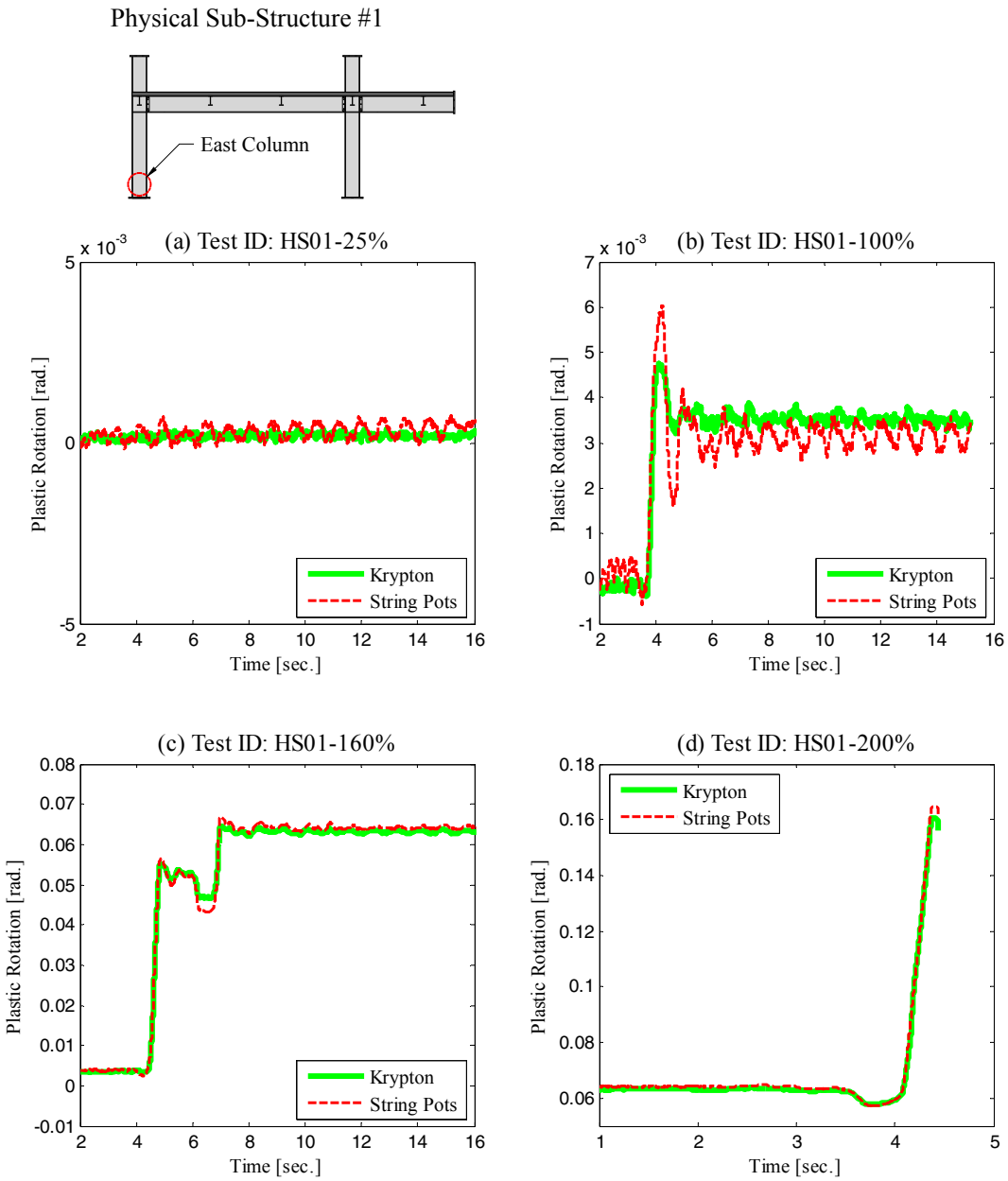


**Figure 7-19 Comparison of plastic rotations at base of east column obtained with data from Krypton system and string pots**

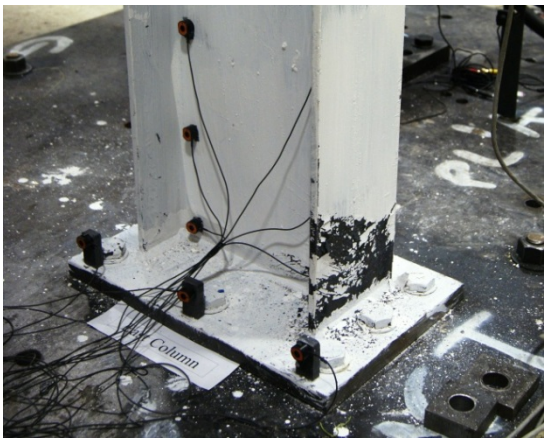

(a) East Column [0.006 rad.]; Test ID: HS01-100%

(b) West Column [0.003 rad.]; Test ID: HS01-100%

(c) East Column [0.067 rad.]; Test ID: HS01-160%

(d) West Column [0.039 rad.]; Test ID: HS01-160%

(e) East Column [0.165 rad.]; Test ID: HS01-200%


(f) West Column [0.146 rad.]; Test ID: HS01-200%

**Figure 7-20 Photographs of the damage state at the base of columns of moment frame physical subassembly during Hybrid Simulation #1**

**Response of Panel Zones**

The shear distortions of the panel zones in the physical sub-structure were obtained using measurements from the linear pots arranged in a V-shaped configuration as previously shown in Figure 5-9 as well as measurements from the Krypton system (see Figure 5-10). The derived distortions using the Krypton system are very reliable due to the high precision of the measuring device. Also, it was found that the linear pots detached from the panel zone during loading of the physical sub-structure. Figure 7-21 compares the distortion of the east panel zone obtained with data from the Krypton system and from linear pots. The location of the east panel zone within the physical sub-structure is indicated with a sketch provided at the top of the Figure 7-21. It can be seen that the derived panel zone distortions from both instrumentation devices compare very well until the beginning of the HS01-160% test. After that, the linear pots detached from the physical sub-structure and produced erratic measurements as seen in Figure 7-21(c) and Figure 7-21(d). The erratic measurements of the linear pots are more evident in Figure 7-22 where moment-distortion relationships for the east panel zone are presented. The term $\sum M_{column}/M_{y,p}$ in Figure 7-22 is defined as the sum of column bending moments above and below the panel zone normalized by the predicted panel zone yield moment strength of $M_{y,p} = 0.55F_y\, d_c\, t\, d_b$, where $F_y$ is measured material yield strength obtained from coupon testing, $d_c$ is the column depth, $t$ is the panel zone thickness and $d_b$ is the girder depth. The strings pots installed at the west column presented the same problems. Therefore, accurate distortions for the west panel zone could not be obtained.

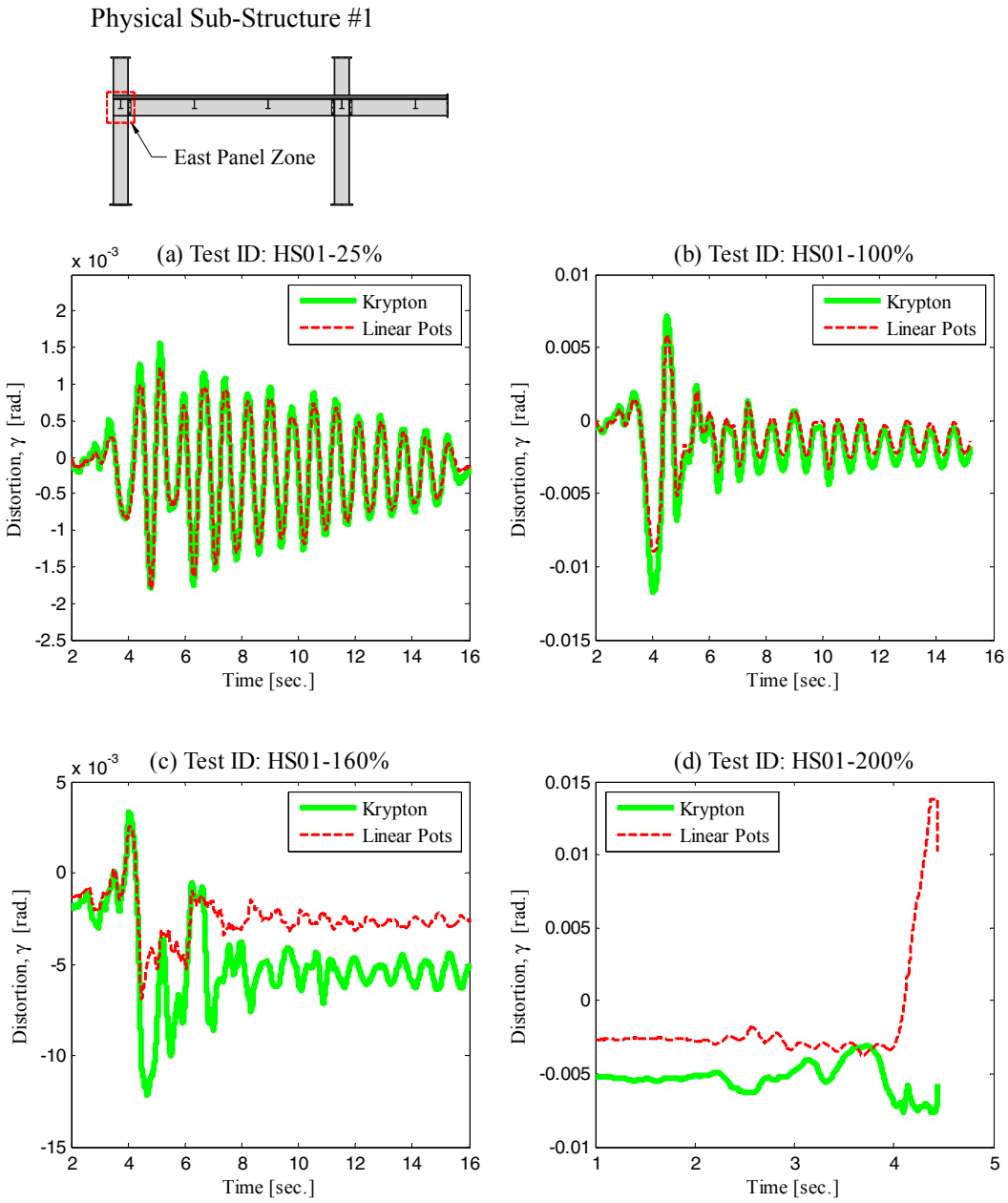


**Figure 7-21 Comparison of panel zone distortion obtained with data from Krypton system and string pots**

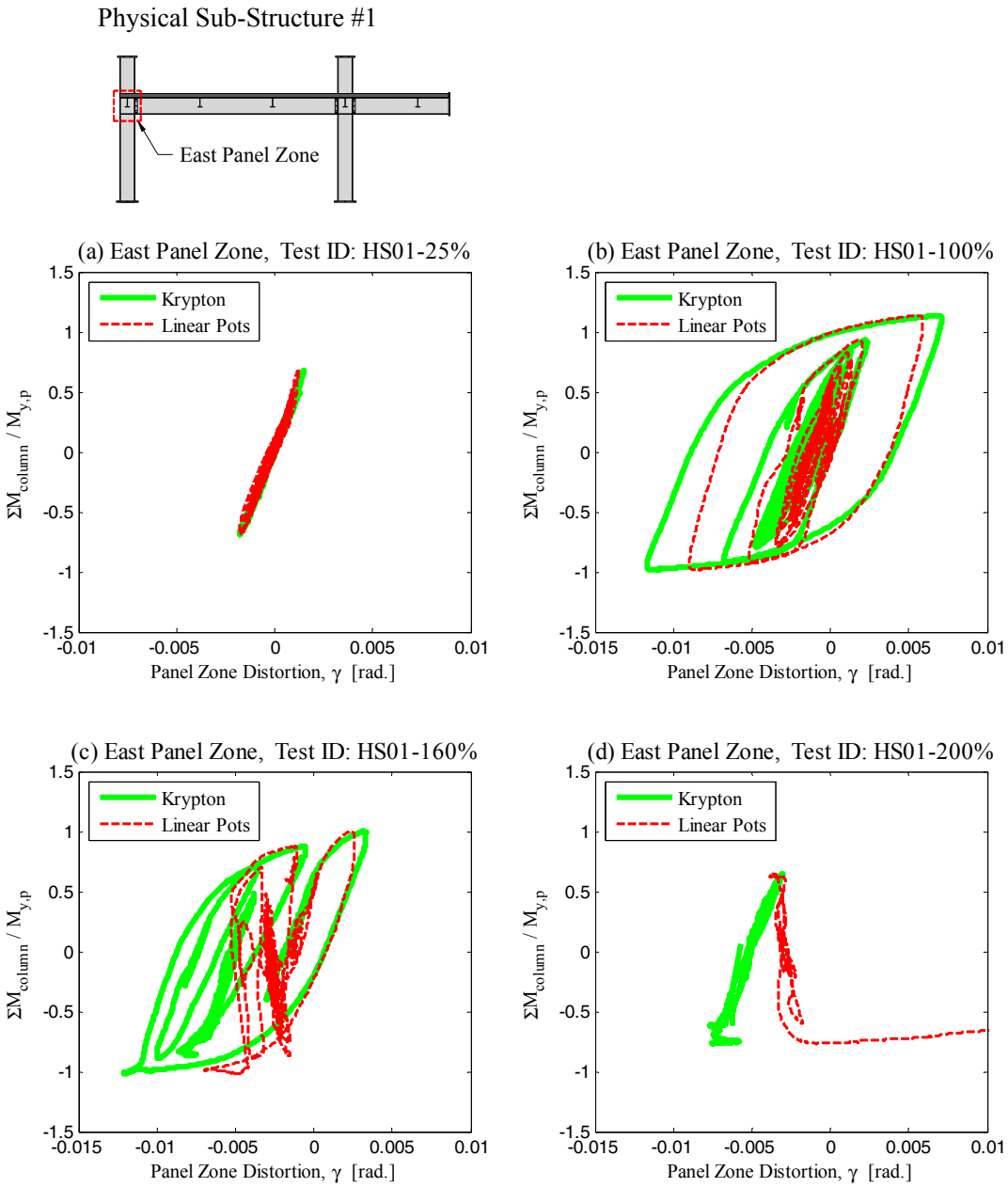


**Figure 7-22 Comparison of moment-distortion relationships for east panel zone where distortions were obtained with Krypton system and string pots**

Figure 7-23 presents moment-distortion relationships for panel zones of the physical sub-structure. The location of the panel zones was indicated with sketches provided at the top of Figure 7-23. Since the panel zones indicated in these sketches are located within the overlapping domain between the physical and numerical sub-structures (see Section 6.4 for reference), the response of the panel zones from the numerical sub-structure is also presented. While the distortions shown for the east panel zone were reliably obtained with the krypton system, the distortions obtained for the west panel zone are evidently erratic as discussed earlier. Some observations can be made from Figure 7-23, which focuses on the east panel zone.

From Figure 7-23(a), it was found that the elastic stiffness of the physical panel zone is 30% stiffer than that of the numerical sub-structure. This can be attributed to the presence of the floor slab which was not considered in the numerical model. The largest deformation demands on the east panel zone are observed for the HS01-100% test. The response of the east panel zone during the collapse level test (HS01-200%) was practically elastic since the strength of girders and columns at plastic-hinge regions significantly deteriorated at this point, which transferred minimum bending moments to the panel zone. Note that the predicted shear capacity according to the Krawinkler (1978) equations was fairly close to the observed yield shear resistance of both panel zones as seen in Figure 7-23. This is to be expected for this size of cross sections with thin webs as discussed in Krawinkler and Mohasseb (1987). Also, the physical and numerical responses shown in Figure 7-23(c) for the hybrid simulation HS01-160% appeared to have an offset. Verification of the data showed that both responses started from values of force and displacement close to zero but the physical sub-structure shifted upon loading of the specimen.

With regards to the performance of the substructuring technique, the deformation demand on the east panel zone was larger than its corresponding numerical model for the HS01-100% test. This was numerically predicted in the evaluation of the substructuring technique presented in Section 6.4.3.

Figure 7-24 shows photographs of the damage state of the east and west joints of the moment frame physical sub-structure for hybrid simulations HS01-100% through HS01-200%. The photographs shown in Figure 7-24 were taken either at the end of the simulation or during the simulation but after the maximum deformation of the test specimen.

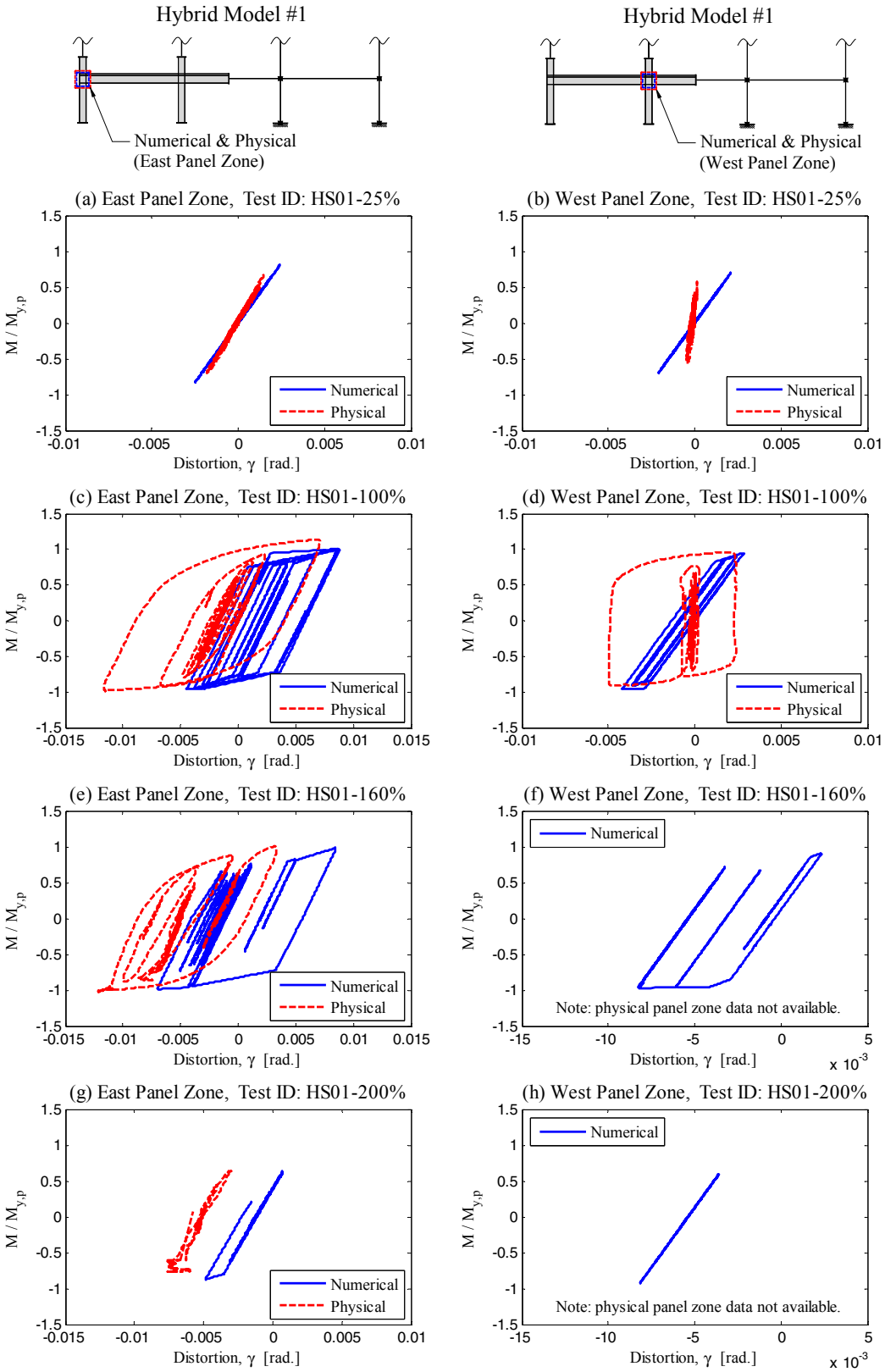


**Figure 7-23 Moment-distortion relationships for panel zones of moment frame during Hybrid Simulation #1**

(a) North-west view of east joint; HS01-100%

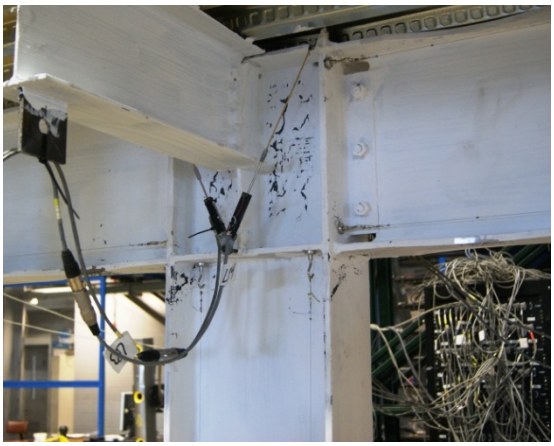

(b) North-west view of west joint; HS01-100%

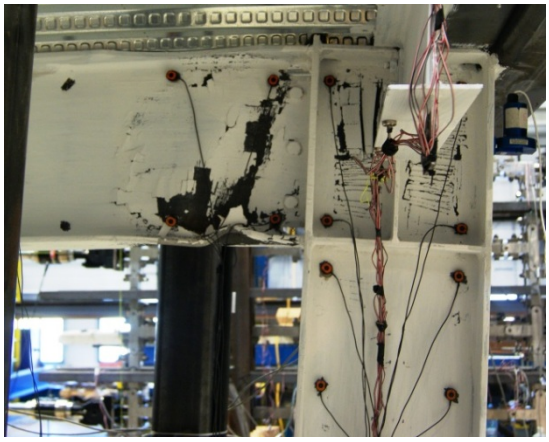

(c) South view of east joint; HS01-160%

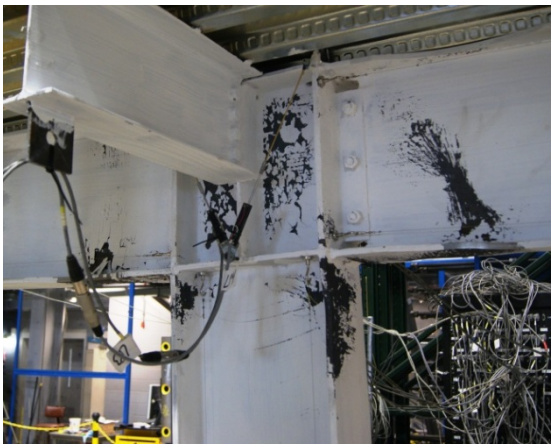

(d) North-west view of west joint; HS01-160%


(e) North-west view of east joint; HS01-200%

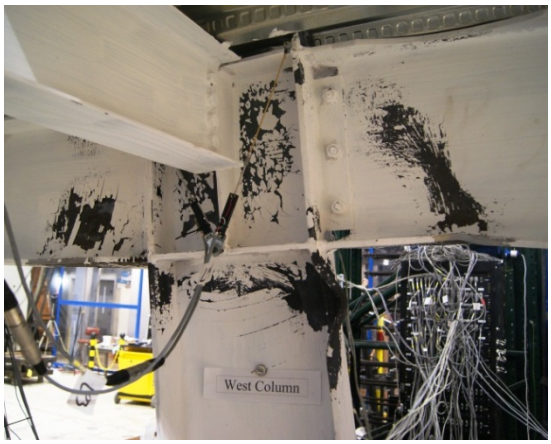


(f) North-west view of west joint; HS01-200%

**Figure 7-24 Photographs of the damage state of east and west joints of moment frame physical subassembly during Hybrid Simulation #1**

**Response of Girders with RBS**

The distribution of bending moments along girders of the physical sub-structure was obtained using a procedure similar to the one followed for columns. However, only approximate estimates of the bending moments were obtained because of the presence of the concrete slab. The procedure followed is described below.

Initially, curvatures at the instrumented girder cross sections shown previously in Figure 5-8 were obtained by interpolating strain gage data. Then, an elastic fiber model of the cross section of the composite girder was scripted in Matlab using the measured elastic properties of the concrete and steel materials. The elastic fiber model included the W14×26 girder, concrete slab (with the measured modulus of elasticity of 2000 psi), metal deck and welded wire mesh. Therefore, the previously-calculated curvatures were used as input for the elastic fiber model to obtain theoretical bending moments. These theoretical bending moments at the instrumented cross sections were extrapolated to obtain the distribution of the bending moments along the girders. To assess the accuracy of the derived girder bending moments, an equilibrium check was performed in Figure 7-25 where the sum of column bending moments is compared with the sum of girder bending moments at the east and west joints of the physical sub-structure. Although this equilibrium check ignores the contribution of shear forces, it serves as an approximate measure of the accuracy of the derived bending moment along the girders.

Some observations can be made with respect to the accuracy of the derived girder bending moments by virtue of Figure 7-25. In general, larger differences are observed for the moment equilibrium at the east joint. This is due to the swivel of the actuators connected to the side of the east joint. Because of friction, the swivel has a moment resistance that is not considered in the joint moment equilibrium. Since the theoretical girder bending moments are derived using linear-elastic relationships, these are, as expected, over-estimated in all cases. It cannot be determined from Figure 7-25 if the largest over-predictions occur when the girder is under negative or positive moment. In summary, the approximate bending moments derived for the girders are reasonable. However, these values should be used with caution.

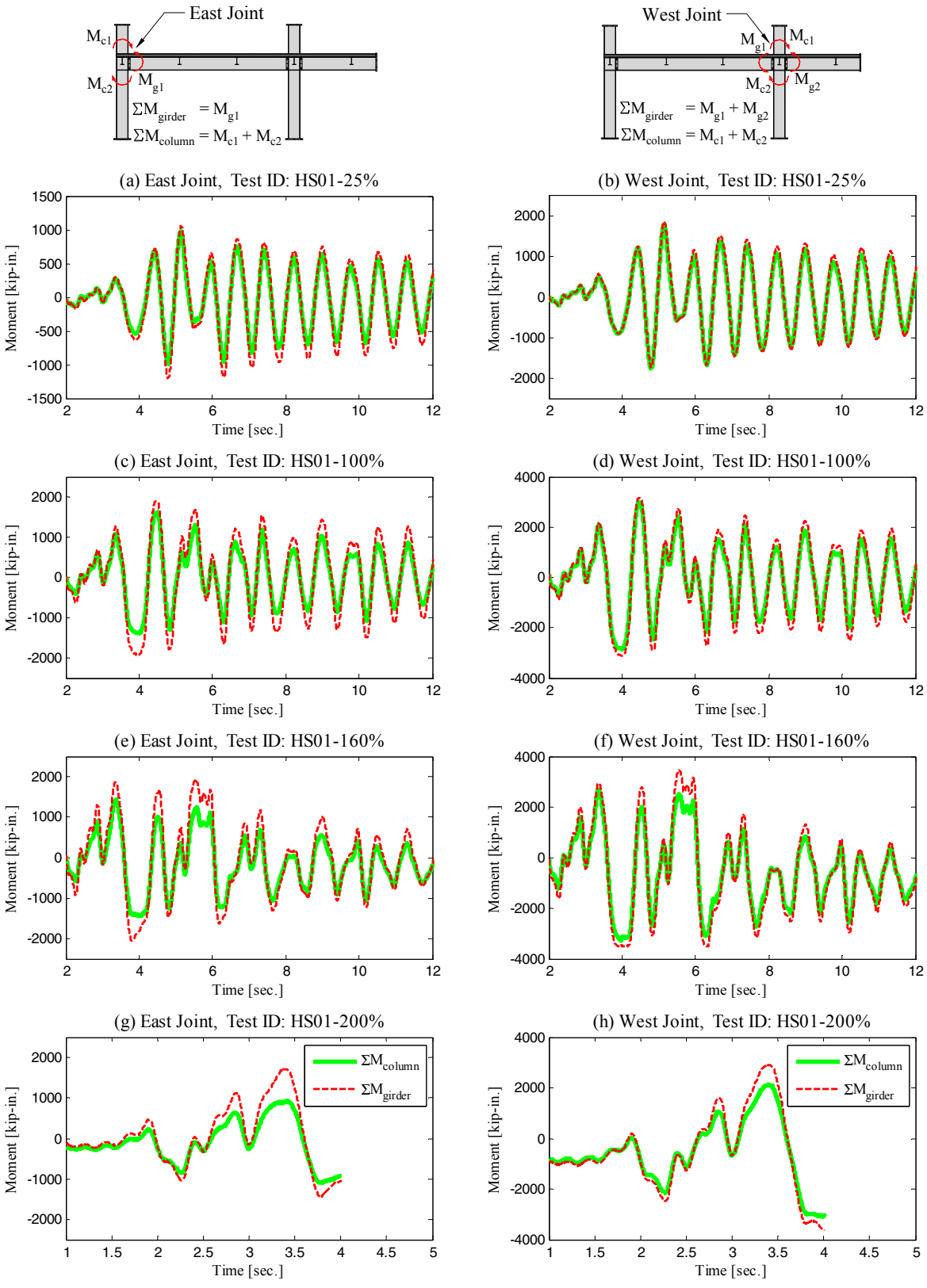


**Figure 7-25 Verification of derived bending moments at composite girders of moment frame physical subassembly using moment equilibrium at joints for Hybrid Simulation #1**

Figure 7-26 presents moment-rotation relationships for the three reduced beam sections (RBS) of the physical sub-structure of the moment frame. Sketches provided at the top of Figure 7-26 indicate the location of the RBS. Since the reduced beam sections of the physical sub-structure are located within the overlapping domain with the numerical sub-structure, moment-rotation relationships for the numerical reduced beam sections are also presented. Bending moments were normalized by the predicted moment strength ($M_{y,p}$) of the W14×26 girder, which is defined as the plastic section modulus ($Z$) times the measured material yield strength obtained from coupon testing. In Figure 7-26, only plastic rotations similar to the moment-rotation relationships for columns are presented. Also, maximum plastic rotations are indicated for the physical model.

Some observations can be made from Figure 7-26. The yield moment strength of the reduced beam sections was reasonably predicted in the numerical sub-structure. Also, the pre- and post-capping plastic rotations of the beams with RBS were predicted fairly well in the numerical portion of the hybrid model for the W14×26 girder. These values were obtained based on multivariate regression equations by Lignos and Krawinkler (2011). The physical sub-structure of the moment frame was subjected to smaller rotation demands than the numerical sub-structure as predicted in the evaluation of the substructuring technique in Section 6.4.3.

Figure 7-27 shows photographs of two beams with RBS at the end of the first series of hybrid simulations. Lateral torsional buckling of the girders is evident from this figure. The maximum levels of plastic rotation were 0.16 and 0.08 rad. for the east and west girders with RBS, respectively. Figure 7-27 shows that towards the end of the simulation (at collapse), the RBS section twisted. This is consistent with prior sub-assemblage tests conducted by Chi and Uang (2002). The eccentric beam flange force due to lateral-torsional buckling of the steel beam caused twisting to the steel columns of the first story of the physical subassembly of the hybrid model. This could have been avoided by using additional lateral braces near the RBS location.

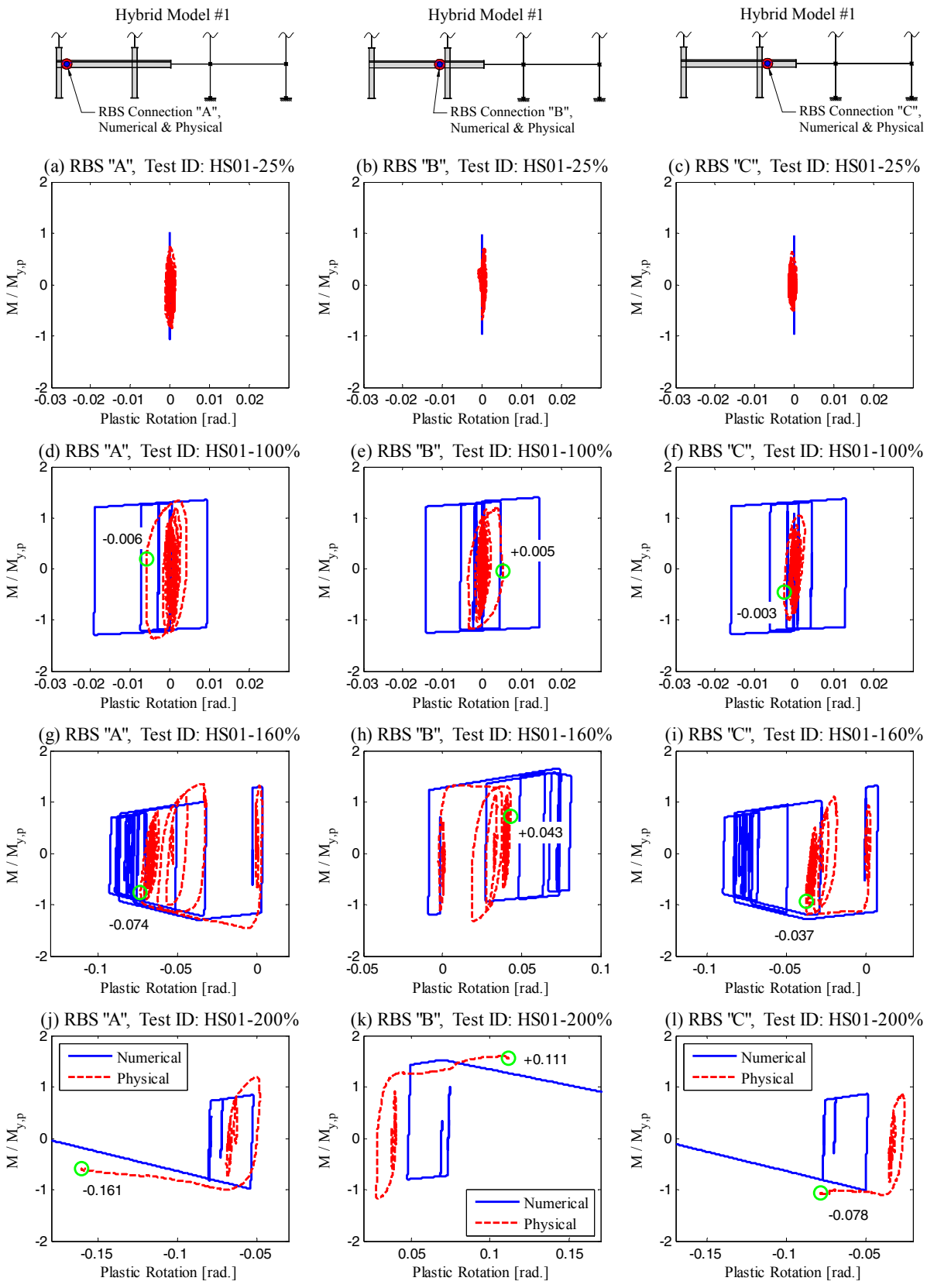


**Figure 7-26 Moment-rotation relationships for girders with RBS during Hybrid Simulation #1**

(a) Girder with RBS at east joint [–0.161 rad.] (b) Girder with RBS at west joint [–0.078 rad.]

**Figure 7-27 Photographs of lateral-torsional buckling of girders with RBS after Hybrid Simulation #1**

**Response of Column Base Plate**

The response of the east column base plate was monitored with the Krypton instrumentation system. Figure 7-28 shows the numbering convention of selected LEDs of the Krypton system attached near the base plate of the east column. Three LEDs (23, 24 and 25) were attached to the base plate near the bolts using magnet supports as seen in Figure 7-28 and two LEDs (21 and 22) directly to the web of the column.

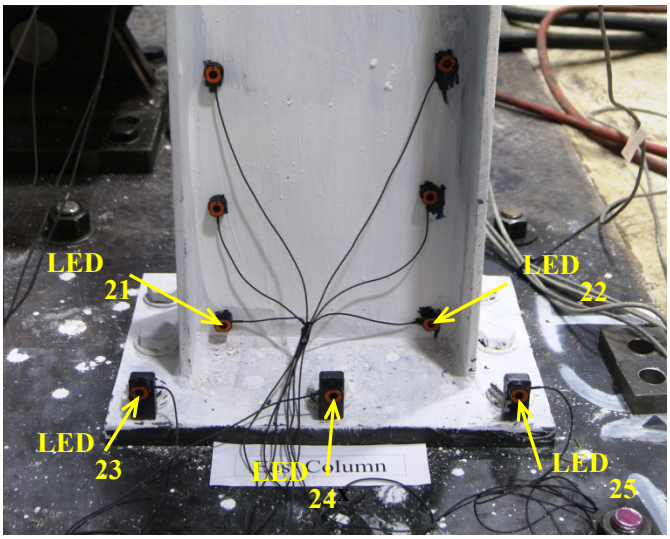


**Figure 7-28 Selected LEDs at bottom of east column of moment frame physical sub-structure**

Figure 7-29 shows the vertical deformation of the LEDs at maximum (positive and negative) column bending moments at the base. A dashed line was drawn joining the data points of the three LEDs attached to the base plate and the two upper LEDs attached to the web of the column to approximate the rotations at the base. It can be seen that the column base plate rotated, and its response is mostly rigid since the three data points of the LED attached to the base plate remained in a straight line. However, some bending of the column base plate is observed at the collapse hybrid simulation (HS01-200%) as seen in Figure 7-29(d). Also, one LED on the web of the column (LED 21) detached from the test specimen during the last hybrid simulation (HS01-200%). Because of the rigid behavior of the column base plate, the rotation of the column at the support level can be reliably obtained interpolating the data from the LEDs attached to the base plate (LED 23, 24 and 25).

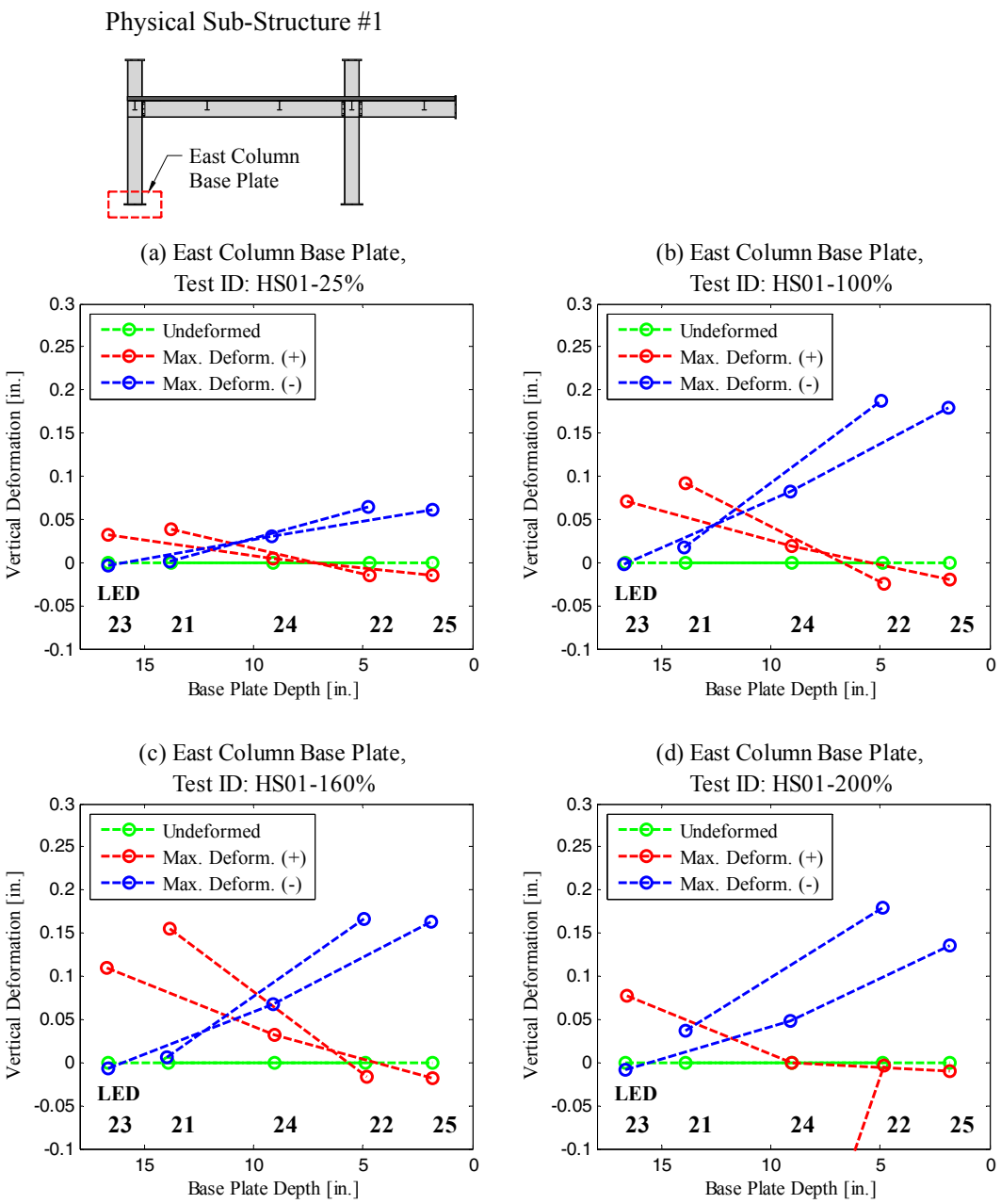


**Figure 7-29 Vertical deformation of LEDs located near the base of east column of moment frame physical subassembly during Hybrid Simulation #1**

Figure 7-30 shows the rotation of the base plate (obtained through data interpolation from LED 23, 24 and 25) versus the bending moment at the base of the east column of the physical sub-structure. Moment-rotation relationships for the flexible support of the exterior column of the numerical sub-structure of the moment frame are also presented for comparison purposes. Bending moments were normalized by the

predicted moment strength of the column. It can be seen that the response of the physical and numerical support boundary conditions at the support compares very well. An elastic behavior is mostly observed.

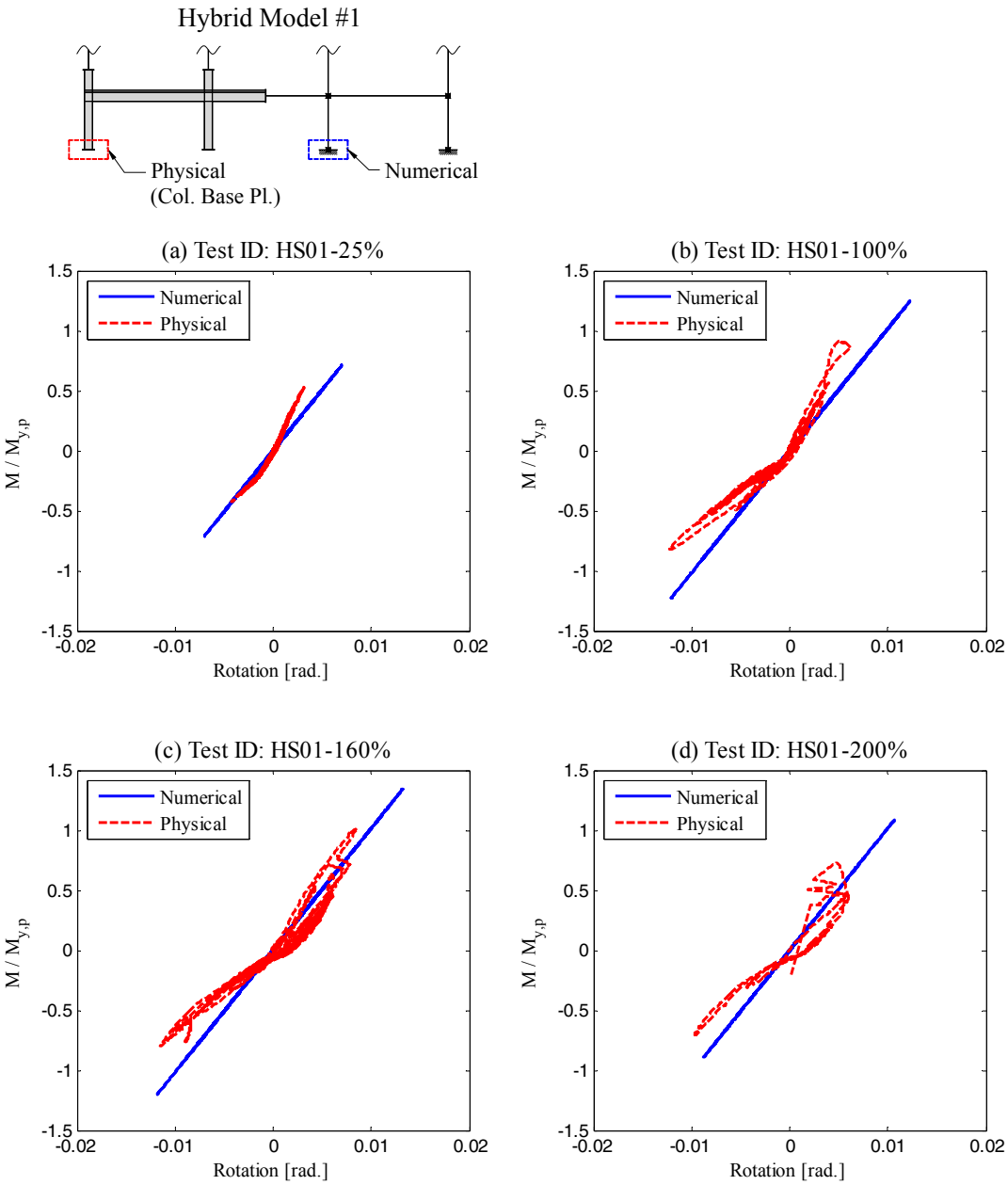


**Figure 7-30 Moment-rotation relationships for supports during Hybrid simulation #1**

**Response of Concrete Slab**

Photographs of the damage state of the concrete floor slab could only be obtained at the end of the hybrid simulations. The configuration of the experimental test setup, such as the steel plates providing supplementary dead load and safety measures of the testing facility, did not allow for photographs in between tests. Figure 7-31 shows the damage state of the concrete floor slab of the physical sub-structure near the columns at the end of the hybrid simulations. Damage was limited to the region around the column (plastic hinge region). Some concrete spalling was observed around the west column. Despite the damage observed on the concrete slab, the concrete floor slab did not lose its vertical load carrying capacity.

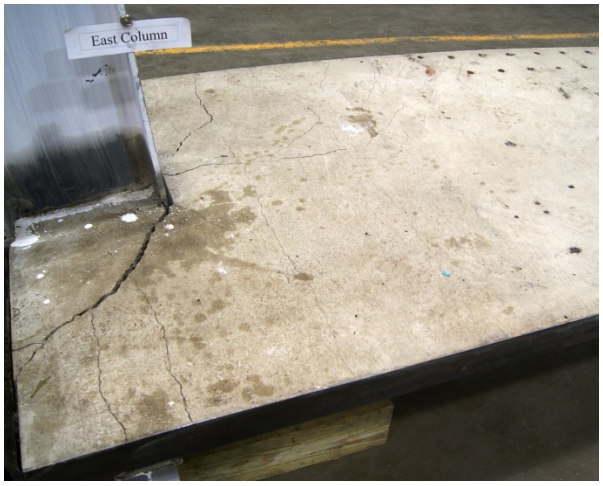


(a) North view of concrete slab at east column

(b) South view of concrete slab at east column


(c) North-west view of concrete slab at west column


(d) South-east view of concrete slab at west column

**Figure 7-31 Photographs of the damage state of the concrete slab of the moment frame physical subassembly after Hybrid Simulation #1**

## 7.3 Results of Hybrid Simulation #2

Table 7-4 summarizes the second series of hybrid simulations (HS02 test series) conducted on the gravity frame physical subassembly, a set of four preliminary tests (PT02 test series) conducted prior to the hybrid simulations and a cyclic test (Cyclic02 test) conducted at the end of the test series. The tests listed in Table 7-4 are identified by a test ID. The test ID for the preliminary tests (i.e., PT02) is followed by a sequence number. For the hybrid simulations, the test ID denotes the hybrid simulation series (HS02: second series of hybrid simulations) followed by the ground motion intensity (25% through 200%). The hybrid simulation HS02-25%F denotes a failed hybrid simulation as it is discussed later. In the preliminary hybrid simulation HS02-Sine, "Pulse" denotes a sine-pulse ground motion. All tests summarized in Table 7-4 are listed in chronological order. A description of the sequence of testing is provided below.

The first two preliminary tests, namely, PT02-01 and PT02-02, were conducted first to quantify the flexibility of the support boundary conditions of the Physical Sub-Structure #2. In these tests, the physical sub-structure remained elastic with a maximum inter-story drift ratio at the first story limited to 0.3%. For the hybrid simulations, the numerical sub-structure of the gravity frame was updated with the experimentally-measured flexible support conditions. The Physical Sub-Structure #2 in the preliminary tests HS02-03 and HS02-04 was subjected to a displacement protocol produced by coupled simulations (similar to Section 7.2). However, the preliminary test PT02-03, conducted to verify the transfer of displacement and force command vectors as well as the force feedback vector, was stopped due to instability of the controller of the vertical actuators. This test was successfully repeated and listed as PT02-04 in Table 7-4.

The first preliminary elastic hybrid simulation, HS02-Sine, was conducted to verify the data communication between the physical and numerical sub-structures. Similar to the previous hybrid simulations, interlocks on the actuator displacements were set to prevent undesired damage of the physical sub-structure in case of equipment or software malfunctioning. This hybrid simulation was successfully conducted and provided the final check to proceed with the execution of the second series of hybrid simulations.

**Table 7-4 Summary of tests conducted on Physical Sub-Structure #2 (gravity frame subassembly)**

| Test # | Test ID | Test Type | Test Description |
|---|---|---|---|
| 01 | PT02-01 | Quasi-Static | Preliminary elastic test. The physical sub-struture was subjected to a prescribed cyclic displacement protocol to measure the elastic properties of the first story. Both horizontal actuators were commanded with a triangular one-cycle displacement protocol (peak displacement amplitude = 1/4", duration = 2.0 min.). |
| 02 | PT02-02 | Quasi-Static | Preliminary elastic test. The physical sub-structure was subjected to a prescribed cyclic displacement protocol to measure the elastic properties of the second story. While the bottom horizontal actuator remained in position, only the top horizontal actuator was commanded with a triangular one-cycle displacement protocol (peak displacement amplitude = 1/8", duration = 2.0 min.). |
| 03 | PT02-03 | Quasi-Static | Preliminary elastic test. The physical sub-structure was subjected to a displacement protocol generated by a coupled simulation using a high-frequency sine-pulse ground motion (sine function: period = 0.05 sec., amplitude = 1.00g). Tests were stopped due to malfunctioning of one of the actuators. |
| 04 | PT02-04 | Quasi-Static | Preliminary elastic test. Previous preliminary test was succesfully repeated. The physical sub-structure was subjected to a displacement protocol generated by a coupled simulation using a high-frequency sine-pulse ground motion (sine function: period = 0.05 sec., amplitude = 1.00g). |
| 05 | HS02-Pulse | Hybrid | Preliminary elastic hybrid simulation conducted using a high-frequency sine-pulse ground motion (sine function: period = 0.05 sec. and amplitude = 1.00g). |
| 06 | HS02-25%F | Hybrid | Failed hybrid simulation conducted with 25% of the unscaled LGPC earthquake record. The hybrid simulation stopped unexpectedly due to malfunctioning of one of the computers. An 1.5% inter-story drift was unexpectedly imposed at the first story of the physical sub-structure. |
| 07 | HS02-25% | Hybrid | Elastic hybrid simulation conducted with 25% of the unscaled LGPC earthquake record (Service Level Earthquake). |
| 08 | HS02-100% | Hybrid | Inelastic hybrid simulation conducted with 100% of the unscaled LGPC earthquake record (Maximum Considered Earthquake). |
| 09 | HS02-160% | Hybrid | Inelastic hybrid simulation conducted with 160% of the unscaled LGPC earthquake record (Near Collapse Level Earthquake). |
| 10 | HS02–200% | Hybrid | Inelastic hybrid simulation conducted with 200% of the unscaled LGPC earthquake record (Collapse Level Earthquake). |
| 11 | Cyclic02 | Quasi-Static | The physical sub-structure was subjected to a cyclic displacement protocol to obtain information on the residual strenght of the speciment and the behavior of shear-tab connections at large rotations. |

At the beginning of the first hybrid simulation conducted with 25% of the LGPC ground motion (listed as HS02-25%F in Table 7-4), one of the computers crashed (due to a conflicting computer program running in parallel but not part of the hybrid simulation software) and consequently the test was stopped. The

hydraulic system for the actuators was immediately shut down, both horizontal actuators retracted to their mid-stroke positions and, as a consequence, undesired lateral displacements of 1.80" and 1.33" were imposed on the physical sub-structure at the first and mid-second story levels, respectively. Such lateral displacements represented a 1.5% inter-story drift ratio at the first story of the physical sub-structure. The actuator interlocks did not work when the hydraulic system was turned off.

In view of this failed hybrid simulation, the response of the physical sub-structure during this unexpected loading is presented in the following sections to assess the damage to the physical sub-structure. This test at 25% of the LGPC ground motion was repeated and successfully completed.

As mentioned earlier in Section 6.6, the inelastic hybrid simulations HS02-100% through HS02-200% were conducted in sequence to carry over any residual response of the numerical sub-structure to the next simulation. Although the time steps and number of iterations for the INM-HS integration method were previously presented in Table 6-8 together with the total number of integration steps and real time duration of the series of simulation simulations, this information is presented again in Table 7-5 for the sake of completeness.

**Table 7-5 Summary of time steps and number of iterations for the INM-HS integration method, total number of integration steps and real time duration of Hybrid Simulation #2**

| Test ID | Time Step [$\Delta t_{gm}$ [1]] | Number of Iterations per Integration Step | Total Number of Integration Steps | Real Time Duration of Simulation |
|---|---|---|---|---|
| HS02-25% | 1/2 | 6 | 9166 | 3h:22m |
| HS02-100% | 1/2 | 5 | 9166 | 2h:48m |
| HS02-160% | 1/2 | 5 | 9166 | 2h:48m |
| HS02-200% | 1/2 | 6 | 9166 | 3h:22m |

[1] $\Delta t_{gm}$: scaled size of the time step of the ground motion equal to $0.5^{0.5} \times 0.005$ sec. = 0.003536 sec.

As predicted before the test, the building structure did not collapse in the second series of hybrid simulation due to the contribution of the gravity frames. Therefore, the gravity frame physical subassembly was subjected to a quasi-static cyclic loading protocol (Cyclic02 test) after Hybrid Simulation #2 to obtain information on the residual capacity of the shear-tab connections after the hybrid test series.

### 7.3.1 Results of Preliminary Tests (PT02 Test Series)

Table 7-6 presents the flexibility at the base of the east and west columns of the physical sub-structure (gravity frame) obtained from the preliminary tests PT02-01 and PT02-02. The rotational and horizontal stiffness at the base of the east column of the physical sub-structure was obtained using the Krypton system. However, due to the limitations of the Krypton camera, no experimental information could be obtained for the west column. Because of this, the same information was assumed for the west column.

**Table 7-6 Elastic stiffness of flexible supports of the Physical Sub-Structure #2**

| | Rotational Stiffness at Support [kip-in./rad.] | Horizontal Stiffness at Support [kip/in.] |
|---|---|---|
| East Column [1] | 58097.0 | 498.4 |
| West Column [2] | 58097.0 | 498.4 |

[1] Values obtained from experimental information.

[2] Assumed values based on experimental information obtained for east column.

The numerical models used to execute the coupled simulations for the preliminary tests PT02-03 and PT02-04 as well as for the second series of hybrid simulations were updated with the flexible support information provided in Table 7-6. Figure 7-32 compares the response of the four components of the force feedback vector of the physical sub-structure with those of the slave OpenSees script used in the coupled simulation for the preliminary test PT02-04.

It can be seen that the components of the force feedback vector of the physical sub-structure start with an initial value due to the application of the gravity loads at the beginning of the simulation using a ramp function. This offsets the response of the force feedback vector from physical sub-structure as compared to the numerical values. Despite this, the force feedback obtained from the physical sub-structure compares reasonably with the corresponding numerical model (slave OpenSees Script).

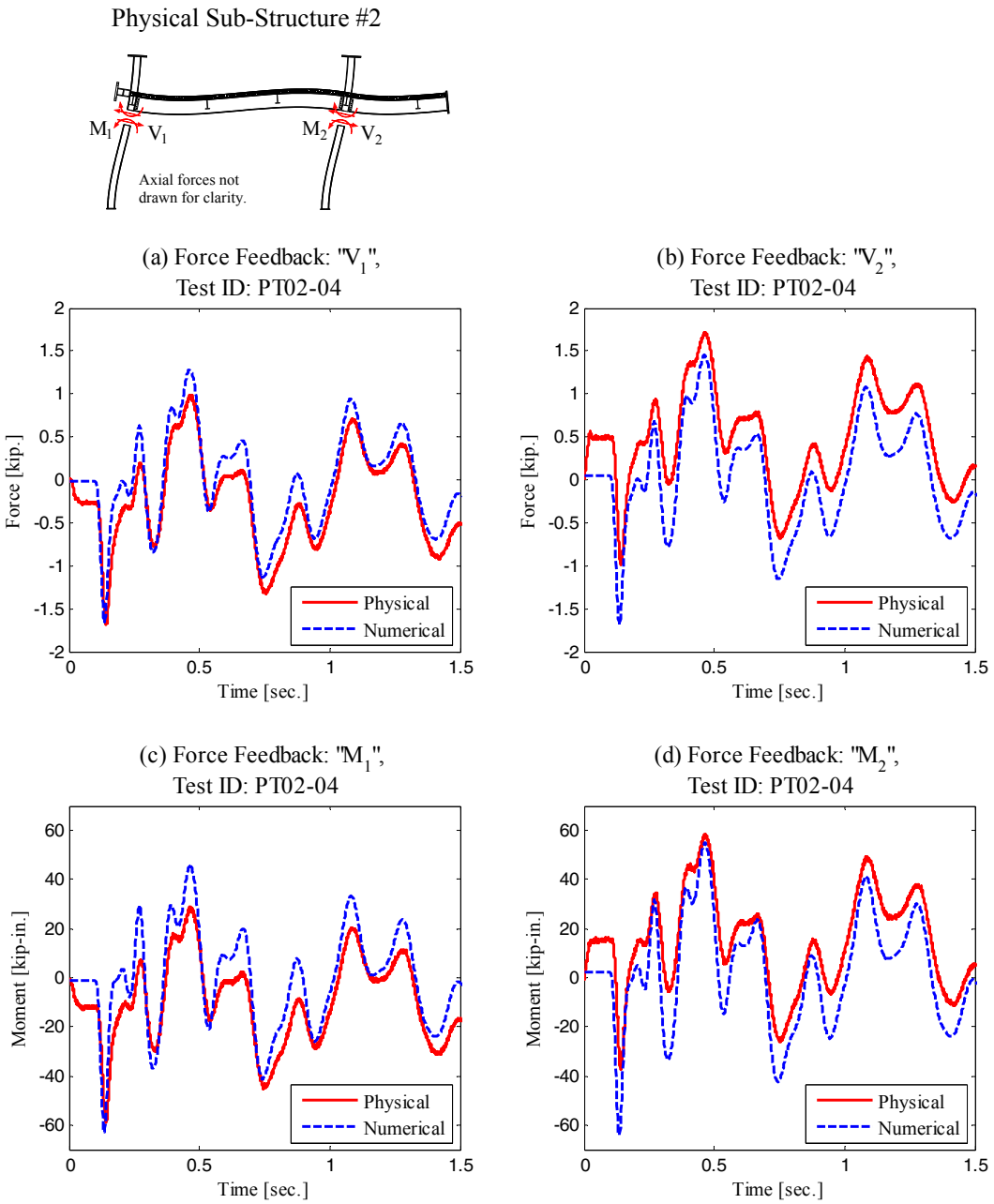


**Figure 7-32 Comparison of force feedback vector obtained from Physical Sub-Structure #2 and corresponding numerical prediction for PT02-04 test**

### 7.3.2 Results of Hybrid Simulations (HS02 Test Series)

The second series of hybrid simulations conducted on a gravity frame subassembly were successfully carried out with the substructuring technique and integration method described in previous sections. The results of all hybrid simulations summarized in Table 7-4, including the preliminary elastic hybrid simulation (HS02-Sine) and the failed hybrid simulation (HS02-25%F) are presented in this section since the shear-tab connections exhibited a hysteretic response even at the small rotations of the HS02-Sine test. In order to first examine the stability and accuracy of Hybrid Simulation #2, Figure 7-33 presents the norm of the unbalanced force vector, norm($P_{eff}$), for the second series of hybrid simulations. It was shown previously in Section 6.2.5 that unbalanced forces (defined in Section 3.2.1) provide an indirect measure of the stability of a simulation since simulations with large unbalanced forces tend to become unstable. The pre-test numerical predictions, also presented in Figure 7-33, were based on coupled simulations with the same integration method (INM-HS), time steps, and number of iterations used in the hybrid simulations for comparison purposes. Maximum values of the norm of the unbalanced force vector are indicated in Figure 7-33. In all cases, the hybrid simulations present larger values of unbalanced forces. This can be attributed to the noise in the force feedback signal. However, since the unbalanced forces of the hybrid simulations and the coupled simulations are mostly in the same order of magnitude, it can be concluded that the accuracy of the hybrid simulations is similar to that of the numerical predictions.

The first part of this section compares the global response results for the second series of hybrid simulations with pre-test numerical predictions. Subsequently, local response results are presented to examine more closely the behavior of the physical sub-structure and to assess the ability of the numerical model to trace the response of the gravity frame.

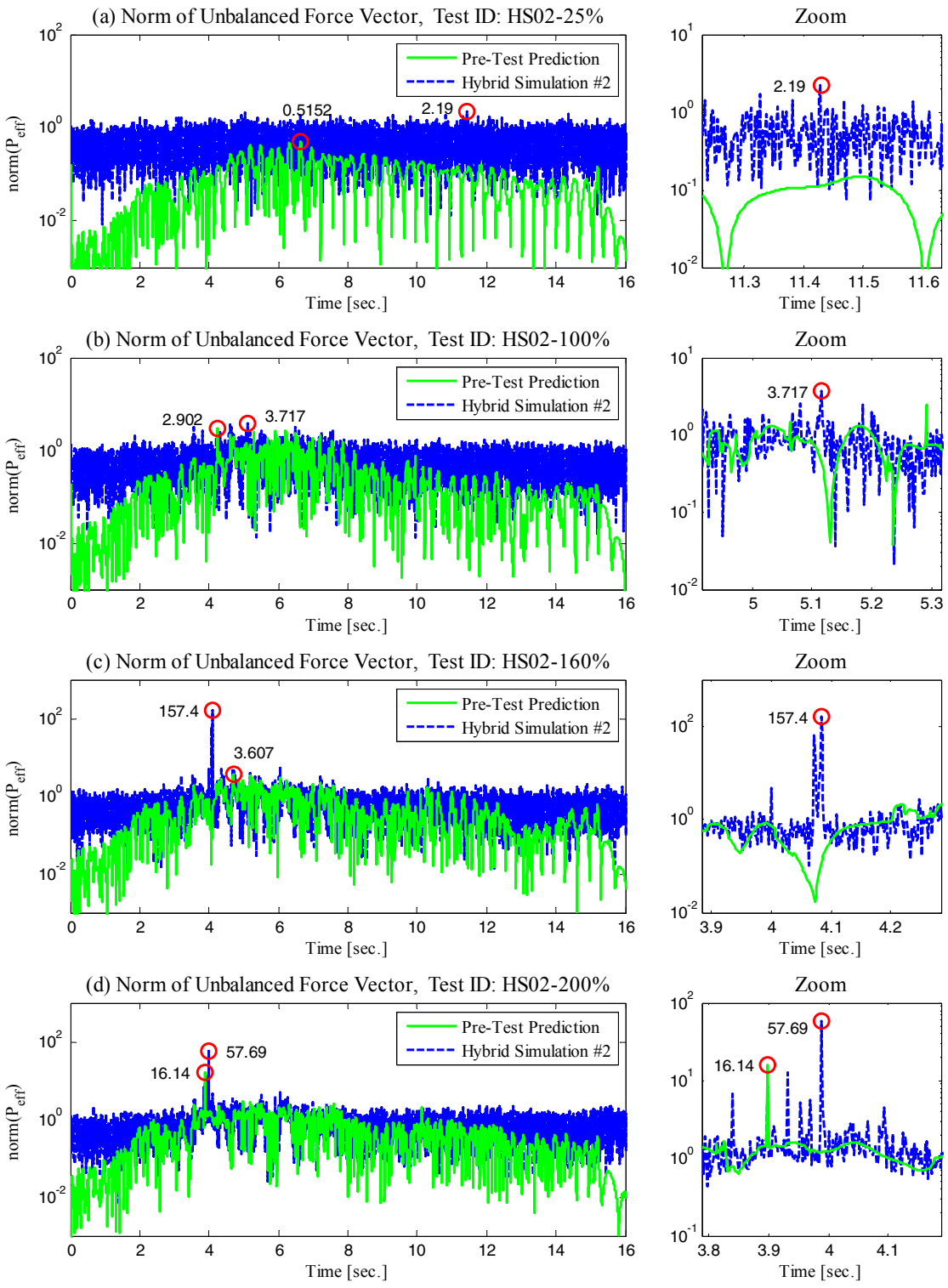


**Figure 7-33 Norm of unbalanced force vector for Hybrid Simulation #2 and pre-test numerical predictions**

#### 7.3.2.1 Global Response Results and Comparison with Pre-Test Predictions

In this section, global response results of the second series of hybrid simulations are presented together with pre-test numerical predictions for comparison purposes. The pre-test predictions were based on a purely numerical simulation using the coupled model shown earlier in Figure 6-9. The INM-HS integration method was used with small time steps and large number of iterations for accuracy of the solution. The flexible support boundary conditions, as measured in the preliminary tests (PT02-01 and PT02-02), were included in the numerical model for the pre-test predictions for consistency with the hybrid model with flexible supports.

Figure 7-34 compares the roof drift ratio response for the second series of hybrid simulations (Hybrid Simulation #2) with pre-test numerical predictions. The term roof drift ratio was previously defined in Figure 7-6. Maximum drift ratios are shown for each hybrid simulation in Figure 7-34. As previously mentioned, the building structure did not collapse in the second series of hybrid simulation. The maximum roof drift ratio for the HS02-200% test was 6.5%. Since there is only a small contribution of the physical sub-structure to the response of the frame structure, the pre-test numerical simulations predict very closely the response of the hybrid model as observed in Figure 7-34. However, despite this small contribution of the physical sub-structure, there is a difference in the residual deformation at the end of the hybrid simulations. This is due to the fact that residual drifts are very sensitive to many modeling parameters including the type of hysteresis.

Figure 7-35 presents inter-story drift ratios for all story levels of the hybrid model as well as pre-test predictions. Similar to the previous series of hybrid simulations, the smallest differences with the pre-test predictions are observed for the fourth story. In the lower three stories, the main difference appears to be a residual offset after a large inelastic excursion in each story. From Figure 7-35, it can be seen that the potential collapse mechanism of the frame structure with the gravity frame is based on a sidesway mode of the lower three stories which is similar to the Hybrid Model #1.

Figure 7-36 presents the response of the total base shear (moment and gravity frame components) for the second series of hybrid simulations. Pre-test predictions are also presented. The base shear values were normalized by the corresponding seismic weight of the hybrid model, which is one third of the total seismic weight of the half-scale building structure presented in Table 6-1. The total base shear compares very well with pre-test predictions. A comparison of the maximum normalized base shear for the Hybrid Model #1 in Figure 7-8 (moment frame only) with that for Hybrid Model #2 in Figure 7-36 (moment and

gravity frames) indicates a significant increment of 35% which prevented the Hybrid Model #2 from collapsing under the same intensity of shaking of the Hybrid Model #1. This significant contribution of the gravity frame to the base shear response is partly attributed to the orientation of the gravity columns (oriented in the strong axis) as indicated previously in Section 4.4.6 and Section 6.3.1.

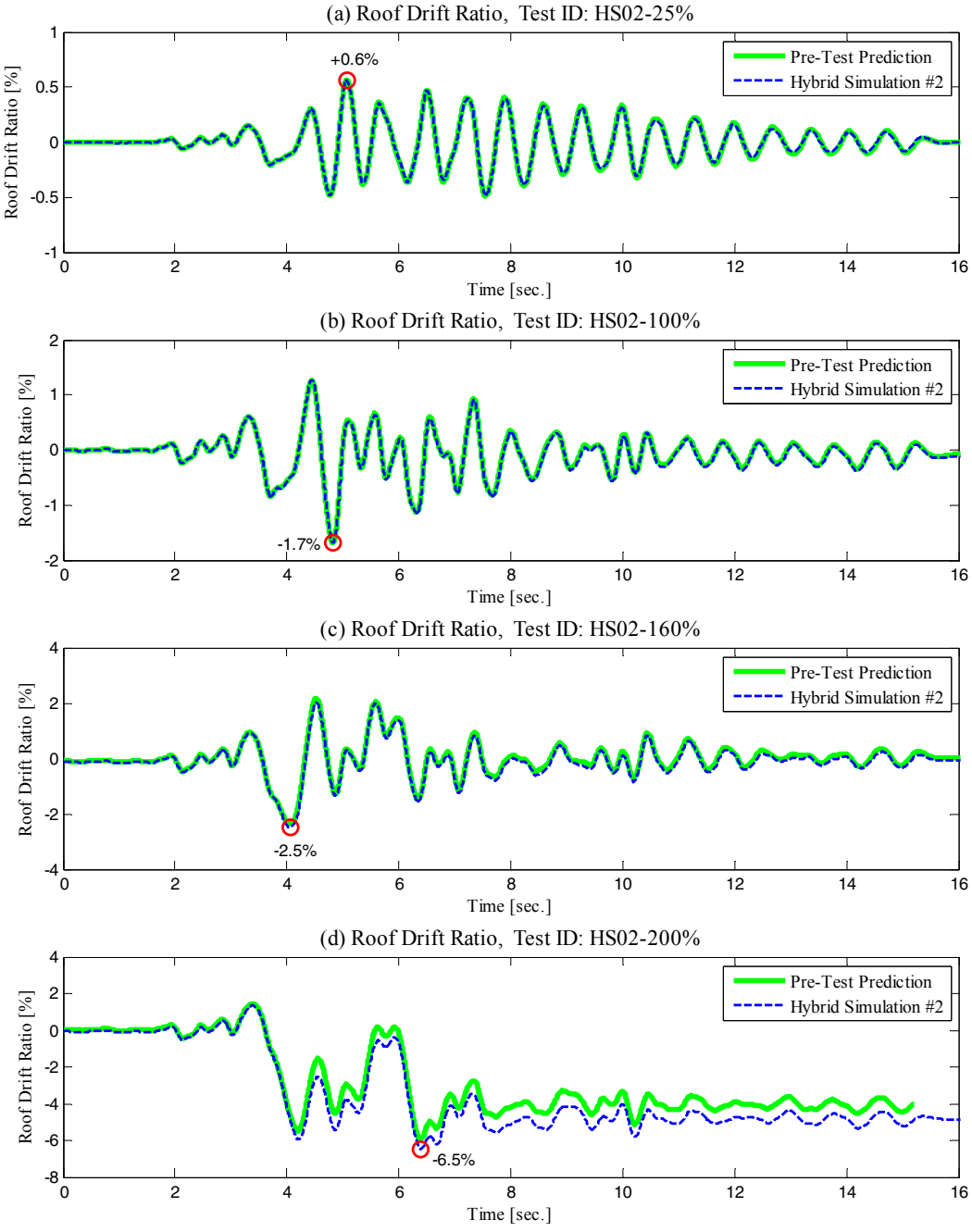


**Figure 7-34 Roof drift ratio response for Hybrid Simulation #2 and pre-test numerical predictions**

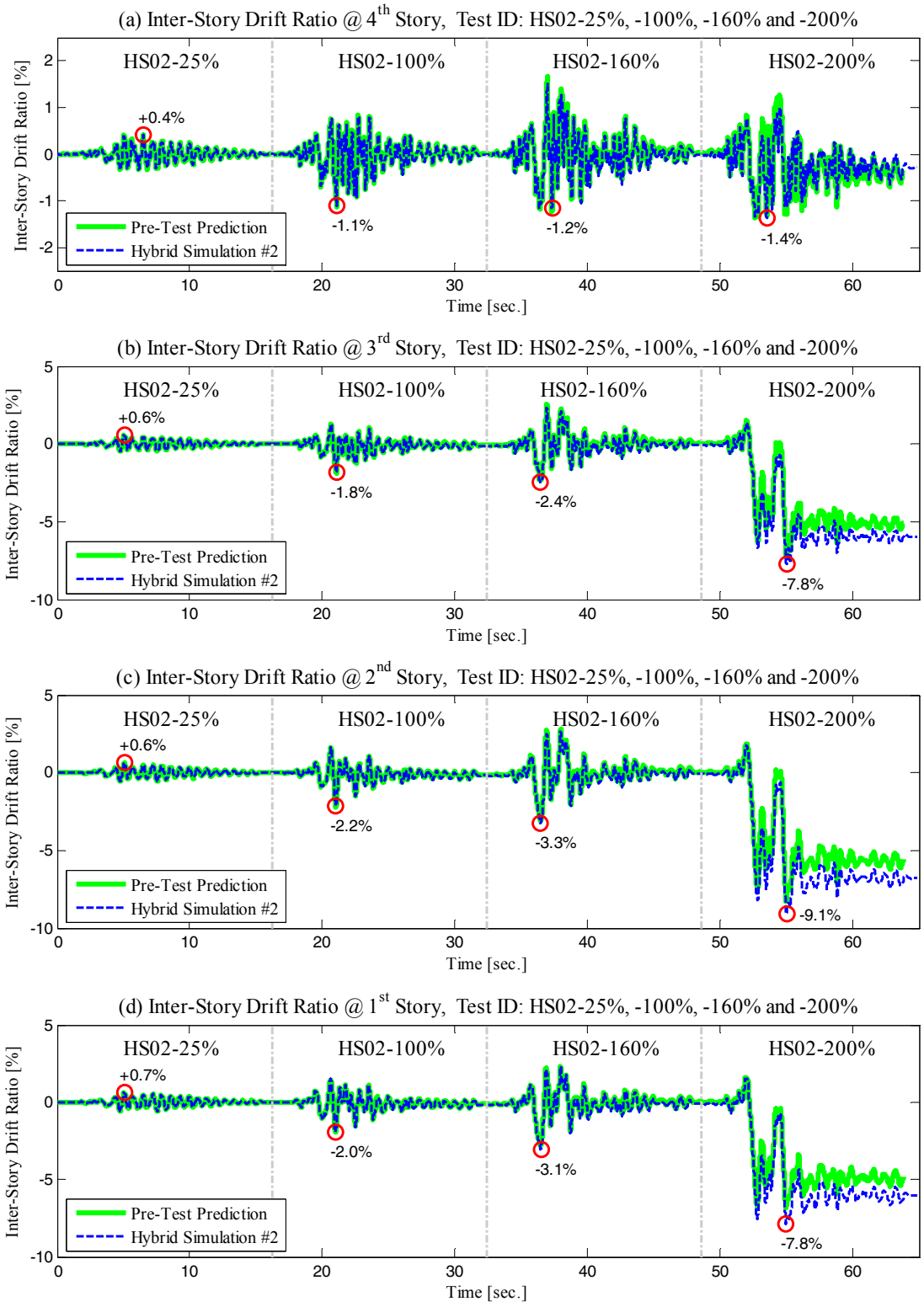


**Figure 7-35 Inter-story drift ratios for Hybrid Simulation #2 and pre-test numerical predictions**

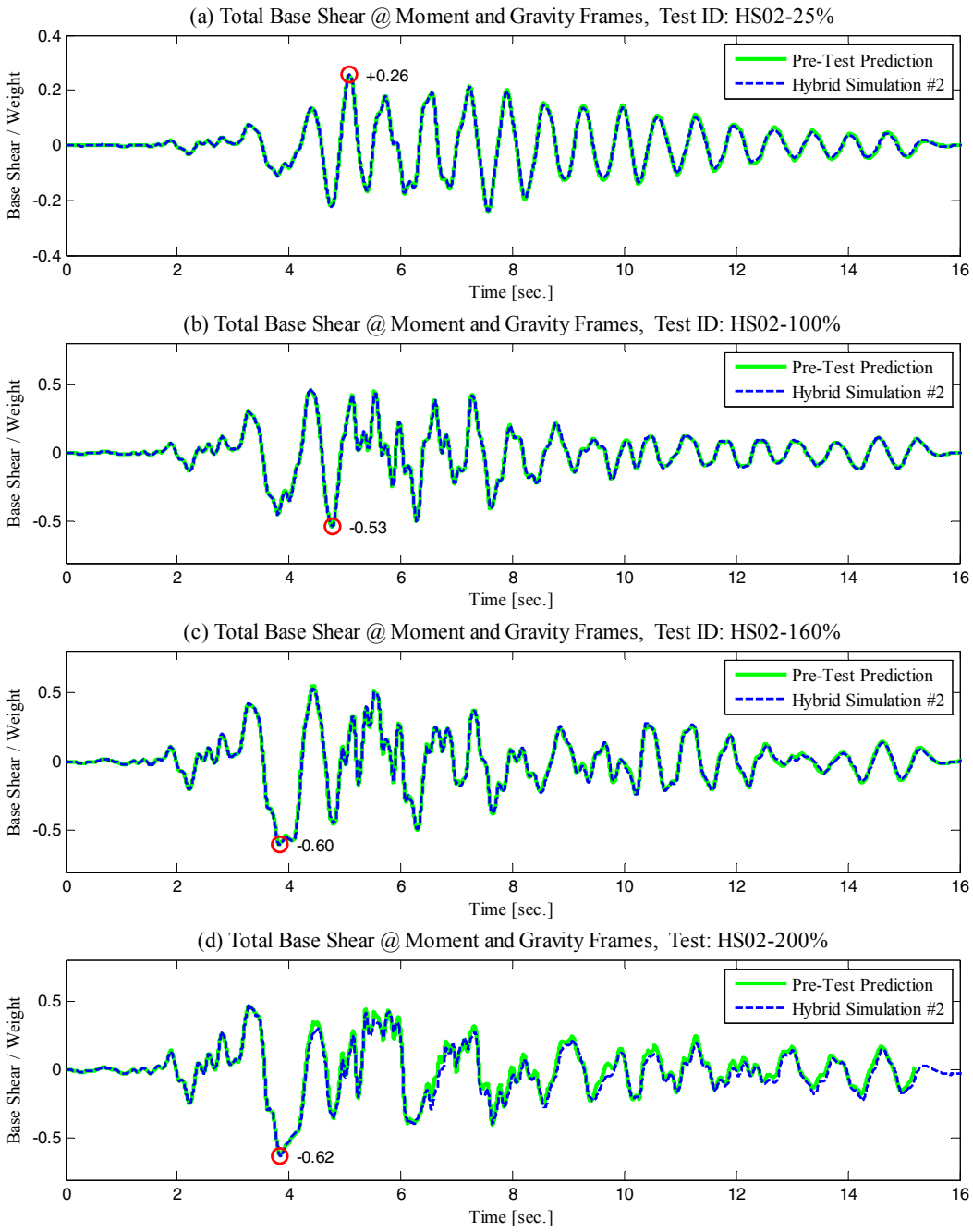


**Figure 7-36 Total base shear response for Hybrid Simulation #2 and pre-test numerical predictions**

Figure 7-37 presents the base shear response of the gravity frame component for the second series of hybrid simulations. It can be seen that the gravity frames attracted a maximum base shear of approximately 0.16W (where W is the corresponding seismic weight of the hybrid model) which represents 25% of the total base shear. Also, the pre-test predictions over-estimate the base shear at the

gravity frame since as it is examined later, the gravity frame physical sub-structure is more flexible and weaker than the corresponding numerical model.

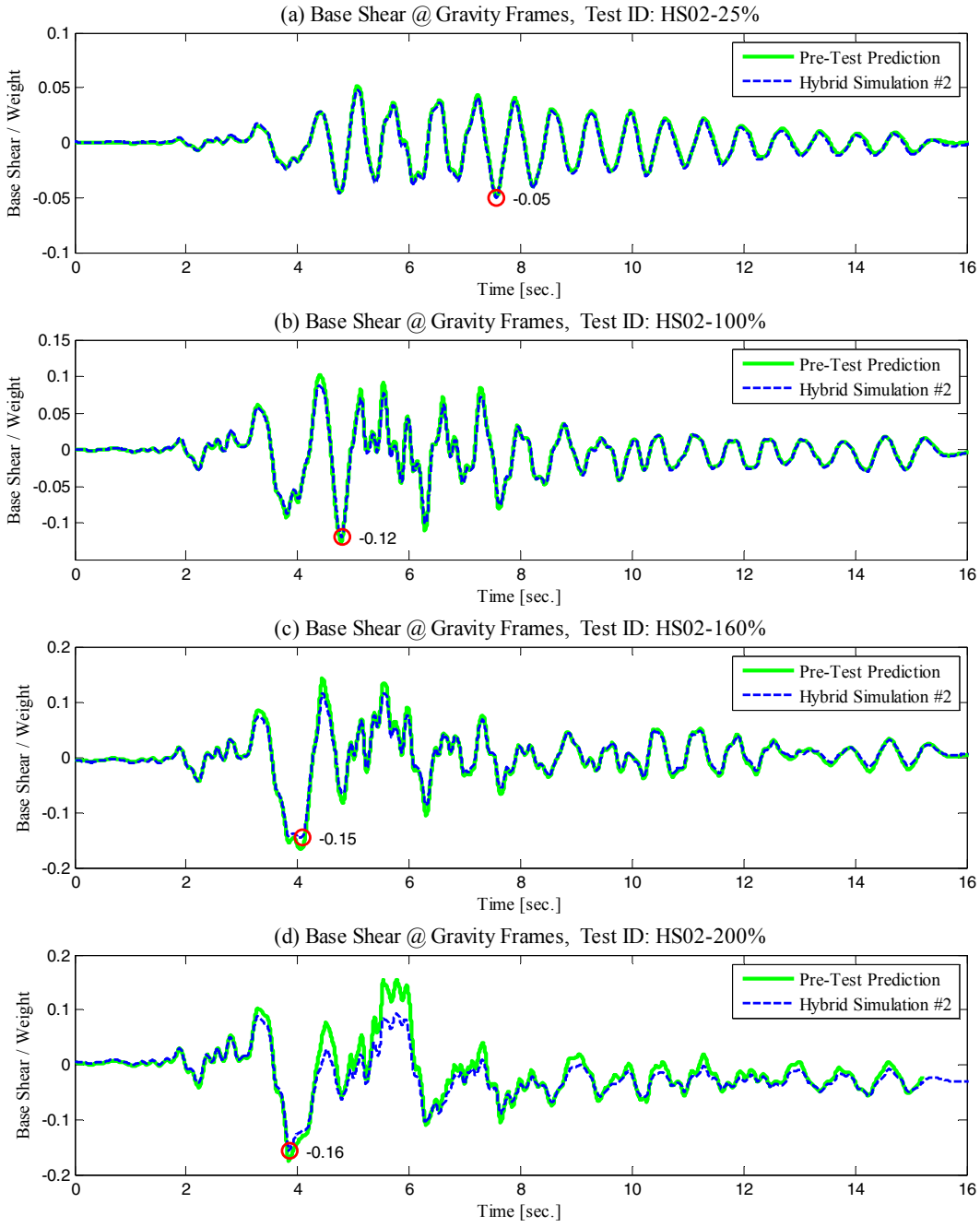


**Figure 7-37 Response of the gravity frame component of the base shear for Hybrid Simulation #2 and pre-test numerical predictions**

Figure 7-38 presents the inter-story drift ratio at the first story versus the total base shear (moment and gravity frame components) for Hybrid Simulation #2 as well as for pre-test numerical predictions. Comparing the strength deterioration of Hybrid Model #2 (moment and gravity frames) observed in Figure 7-38(d) versus the strength deterioration of the collapsing Hybrid Model #1 (moment frame only) observed in Figure 7-9(d), it can be seen that the post-capping slope (negative slope) of the force-displacement relationships of the frame structure is reduced due to the contribution of the gravity frames. This post-capping slope is a very influential parameter in collapse assessment (Ibarra and Krawinkler, 2005)

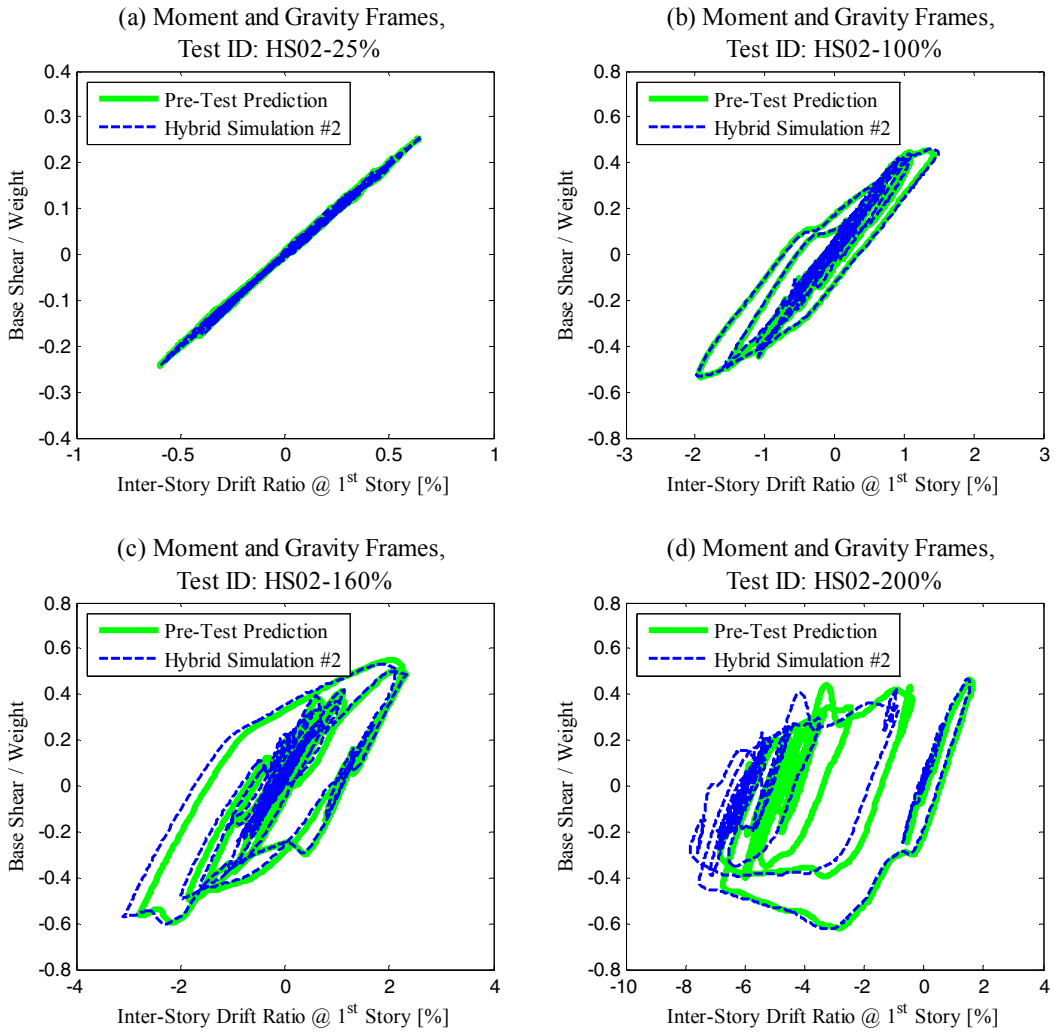


**Figure 7-38 Total base shear versus inter-story drift ratio at first story for Hybrid Simulation #2 and pre-test numerical prediction**

Figure 7-39 presents the inter-story drift ratio at the first story versus the gravity frame component of the base shear for Hybrid Simulation #2. Pre-test numerical predictions are also presented for comparison. It can be seen that the force-displacement plots exhibit a pinched hysteretic response typical of gravity frames. Also, the pre-test numerical simulations over-predict the strength of the hybrid model. As it is seen later, this is mostly attributable to differences in the support boundary conditions.

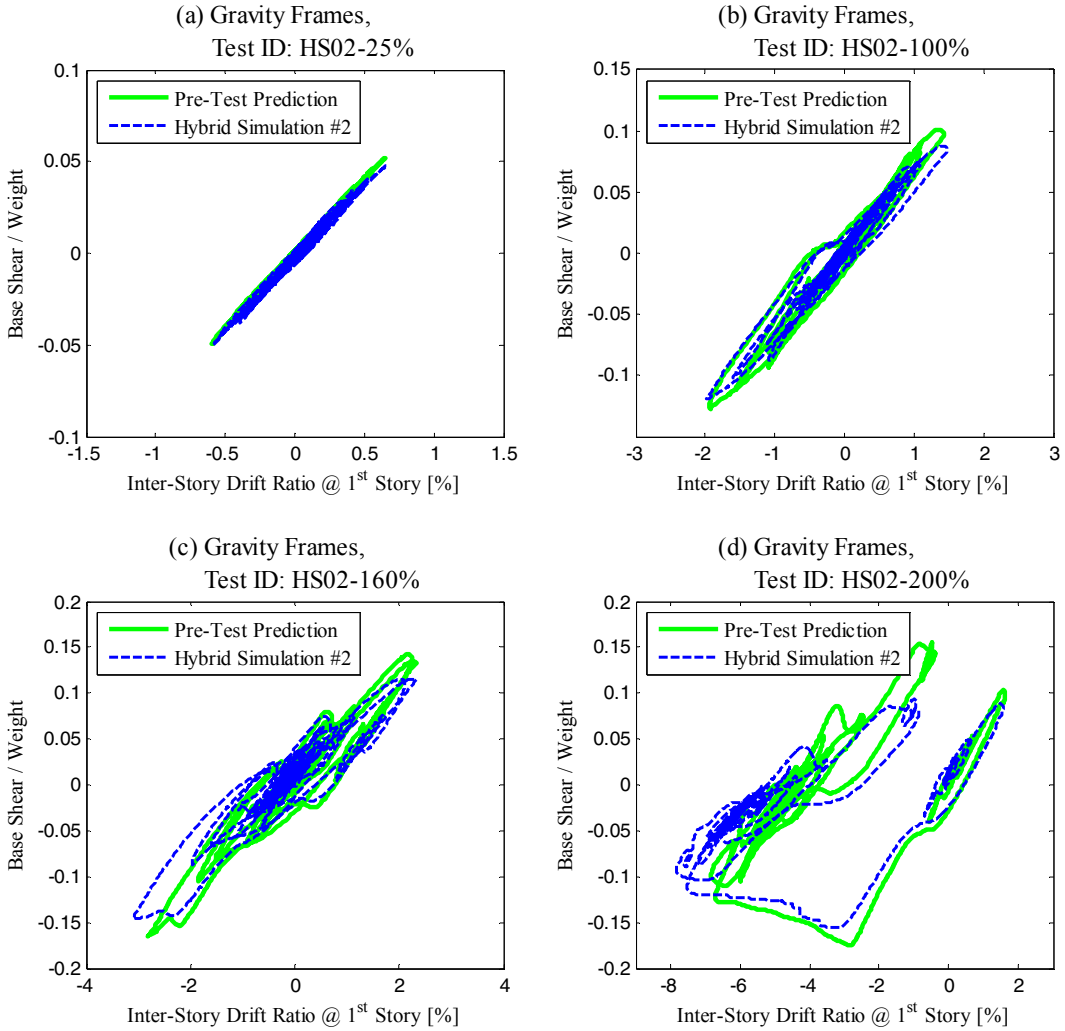


**Figure 7-39 Gravity frame component of the base shear versus inter-story drift ratio at first story for Hybrid Simulation #2 and pre-test numerical prediction**

Figure 7-40 presents the axial force response at the base of the east and west columns of the gravity frame physical sub-structure for Hybrid Simulation #2. Numerical pre-test predictions are also presented. All axial forces were normalized by the predicted column axial strength ($P_{y,p}$) defined in Section 7.2.2.1. Maximum axial force values are presented in Figure 7-40 for the hybrid simulations. As mentioned

before, axial forces were obtained using the groups of strain gage “EC1” and “WC1” (see Figure 5-15 for reference). Since the readings of the strain gages were set to zero at the beginning of the test, initial axial forces due to gravity loading of the physical sub-structure (theoretically obtained from Table 5-5) were added to the values shown in Figure 7-40 for comparison purposes. Despite the fact that the force-controlled vertical actuators were commanded by the correct gravity forces from upper stories at the beginning of the hybrid simulation, Figure 7-40 shows that the axial forces measured at the bottom of the physical model are significantly smaller than the predicted values. Although the sources for such differences were not fully clarified after a verification of the data, this can be attributed to several reasons including (a) gravity loads not accounted for in the theoretical values obtained from Table 5-5 and (b) mistuning of force-controlled actuators. On the other hand, Figure 7-10 shows that the exterior physical column (east column) exhibits larger axial force variations than the interior column (west column) due to overturning forces.

Figure 7-41 presents the out-of-plane displacement response of the east and west joints of the physical sub-structure. As indicated before in Section 5.3.3.2, two string pots (attached at the two joints of the physical sub-structure) monitor the out-of-plane response of the test specimen. It can be seen in Figure 7-41 that the west joint of the physical sub-structure moved north 0.18" upon application of the gravity forces on the physical sub-structure (which is approximately 2% of the peak lateral displacement). It can be seen that the support frame part of the test setup provided adequate out-of-plane support where the maximum out-of-place displacement (observed at the end of the hybrid tests) is less than 5% of the peak lateral displacement. Minor twisting of the physical sub-structure is observed toward the end of the hybrid simulations.

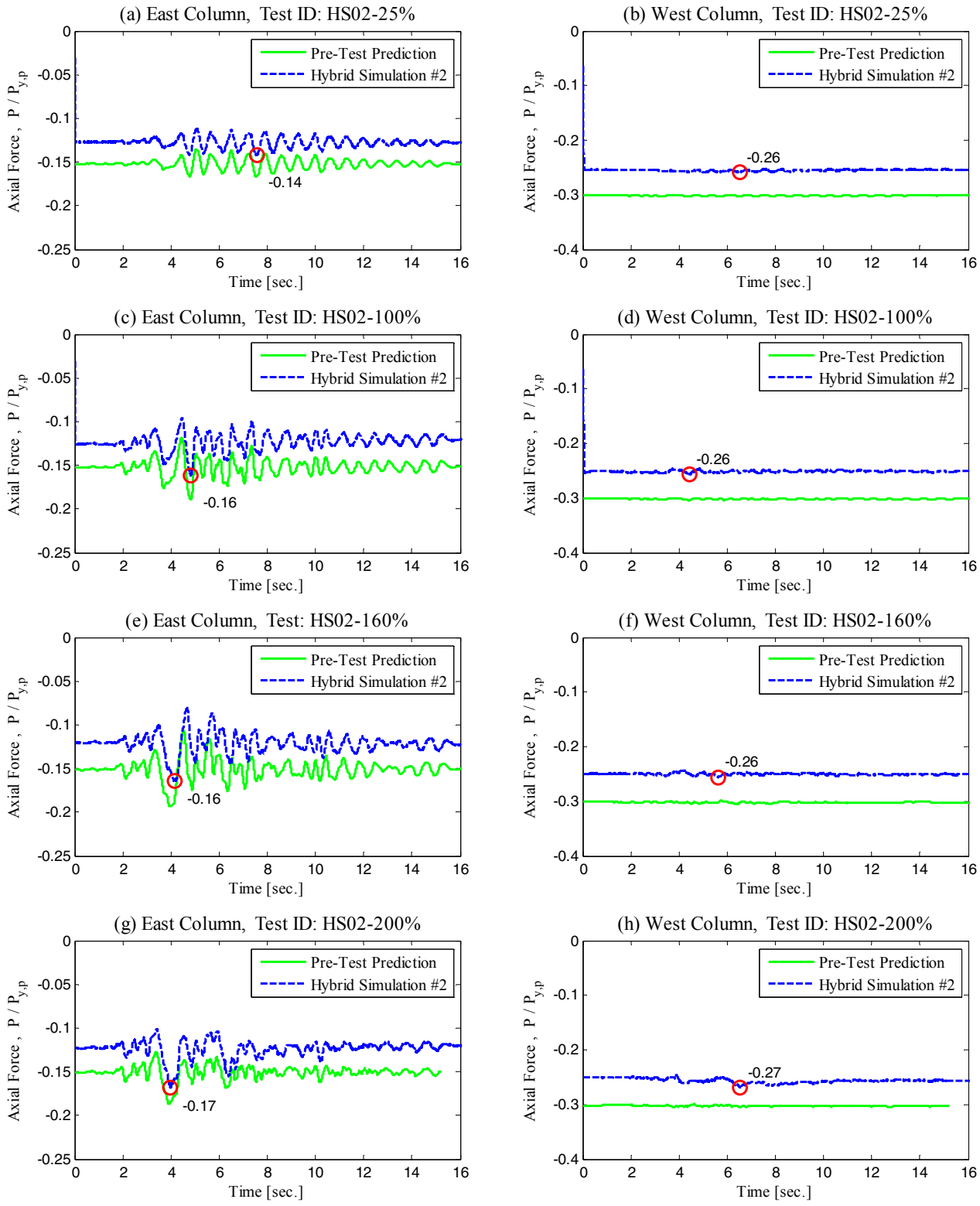


**Figure 7-40 Axial force at base of first-story columns of physical sub-structure for Hybrid Simulation #2 and pre-test numerical prediction**

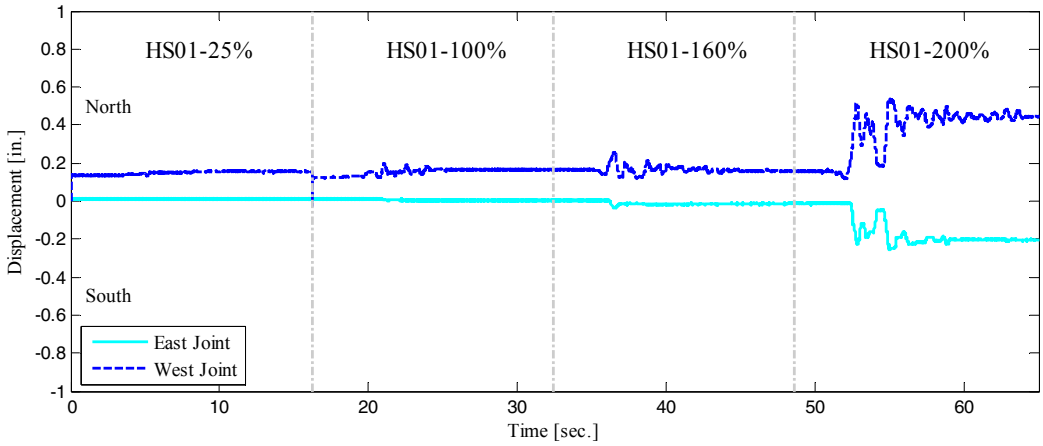


**Figure 7-41 Out-of-plane response of the physical sub-structure during Hybrid Simulation #2**

#### 7.3.2.2 Local Response Results

This section presents local response results to examine more closely the behavior of the gravity frame physical sub-structure. The response of different components of the physical sub-structure is presented together with similar components of the numerical sub-structure for the adjacent gravity frame. As mentioned before, the response of the physical sub-structure for all hybrid simulations of the second series are presented.

Figure 7-42 presents the inter-story drift ratio at the first story versus the physical and numerical components of the base shear at a gravity frame for the second series of hybrid simulations. The base shear values were normalized by one third of the total seismic weight of the half-scale building structure. Therefore, the normalized shear values presented in Figure 7-42 represent the base shear at all gravity frames. It can be seen in Figure 7-42(a) that the flexibility of both portions (physical and numerical) of the hybrid model are similar. However, Figure 7-42(b) through Figure 7-42(d) show that the numerical sub-structure over-predicted the lateral yield strength of the physical model. As it is discussed later, this was partly attributed to the fact that the elastic springs at the base of the columns used to simulate the flexibility of the supports permitted yielding of the numerical columns at the base. This was unrealistic since the physical model did not present yielding at the base of the columns. The bolts of the column base plates fractured in tension as indicated in Figure 7-42(d) and accommodated larger rotations at the base of the columns without column yielding.

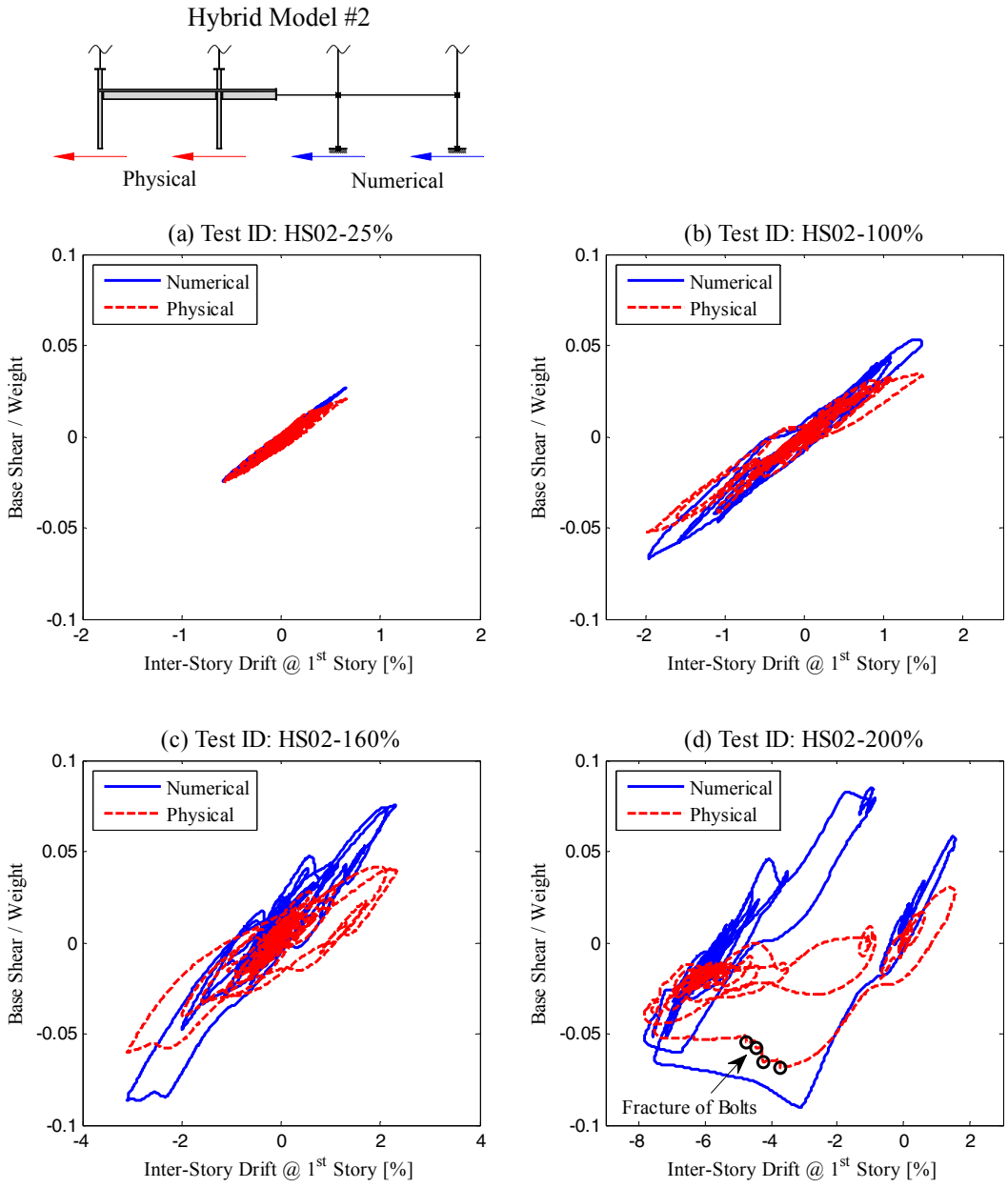


**Figure 7-42 Physical and numerical components of the base shear versus inter-story drift ratio of first story for Hybrid Simulation #2**

The shear values at the base of the columns presented in Figure 7-42 were obtained indirectly from the distribution of moments along columns which were obtained using strain gages. To verify the accuracy of these values, Figure 7-43 compares the sum of the shear forces at the base of the east and west columns of the physical sub-structure ($V_{EC}+V_{WC}$) with the sum of the horizontal actuator forces ($F_{act1}+F_{act2}$) obtained from certified actuator load cells. It can be seen that the sum of shear forces at the base of the

east and west columns compare very well with the sum of actuator lateral forces except for the last hybrid test HS02-200%. However, when the shear due to the P-Delta effects ($V_{P\text{-}\Delta}$) from the vertical link member as well as from the four long columns of the supporting frame of the test setup is added to the shear at the base of the columns, they matched the total force of the actuators. These shear forces ($V_{P\text{-}\Delta}$) were negligible in the moment frame but not in the gravity frame examined here.

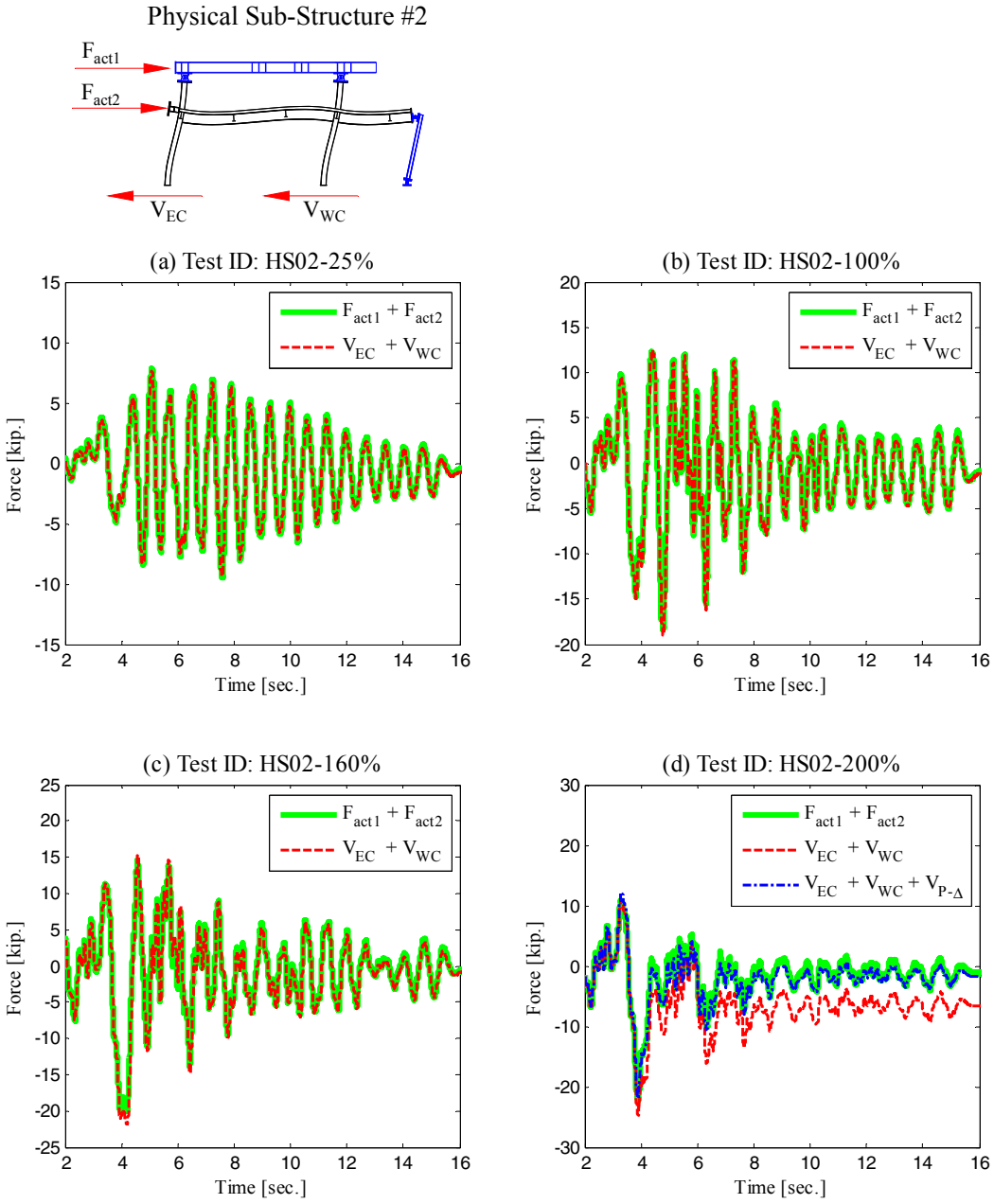


**Figure 7-43 Verification of column shear forces derived from strain gage measurements ($V_{EC}$+$V_{WC}$) using certified actuator load cells for Hybrid Simulation #2**

**Response of Shear-Tab Connections**

Figure 7-44 through Figure 7-49 show moment-rotation relationships as well as photographs of the damage state of the three shear-tab connections of the gravity frame physical sub-structure. The location of the shear-tab connections (designated as shear-tab connection "A", B" and "C") is indicated with sketches above each figure. Since the three shear-tab connections are located within the overlapping domain between the physical and numerical sub-structures, moment-rotation relationships for the numerical shear-tab connections are also presented. Maximum rotations are indicated in each plot. The damage state photographs were either taken at the end of the simulation or after the maximum deformation demands, so that the damage observed can be associated with the maximum rotations indicated in the figures. The response of the shear-tab connections for all hybrid simulations is presented, including the preliminary elastic hybrid simulation HS02-Sine and the failed hybrid simulation HS02-25%F since the shear-tab connections exhibited a hysteretic response in all these tests. Photographs of the damage state are only presented for the last four hybrid simulation where visible damage is observed. For the first two hybrid simulations, namely, HS02-Sine and HS02-25%F, minimal or no visible damage could be observed. It is important to mention that, due to the application of the gravity load on the physical specimen at the beginning of the hybrid simulation, the moment-rotation curves of the physical shear-tab connections shifted vertically, as seen in Figure 7-48. Rather than attempting to remove this vertical offset between the physical and numerical components for a better match, the unmodified physical data is presented.

Several comments can be made from the information provided in Figure 7-44 through Figure 7-49. The response of the three shear-tab connections (physical and numerical) remained elastic for the first hybrid simulation conducted with the sine-pulse ground motion, HS02-Sine, as observed in Figure 7-44(a), Figure 7-46(a) and Figure 7-48(a). In all these cases, the rotational elastic stiffness of the shear-tab connections was significantly underestimated in the numerical sub-structure of the gravity frame. The elastic rotational stiffness of the shear-tab connections "A", "B", and "C" are $2.0\times10^5$, $3.0\times10^5$, and $1.3\times10^5$ kip-in./rad., respectively, as estimated from Figure 7-44(a), Figure 7-46(a) and Figure 7-48(a). All these values are comparatively larger than the predicted value in the numerical model of $0.4\times10^5$ kip-in./rad. Also, note that the shear-tab connections experienced a maximum rotation demand of +0.001 rad. (under positive bending) in the HS02-Sine test as seen Figure 7-46(a) and Figure 7-48(a).

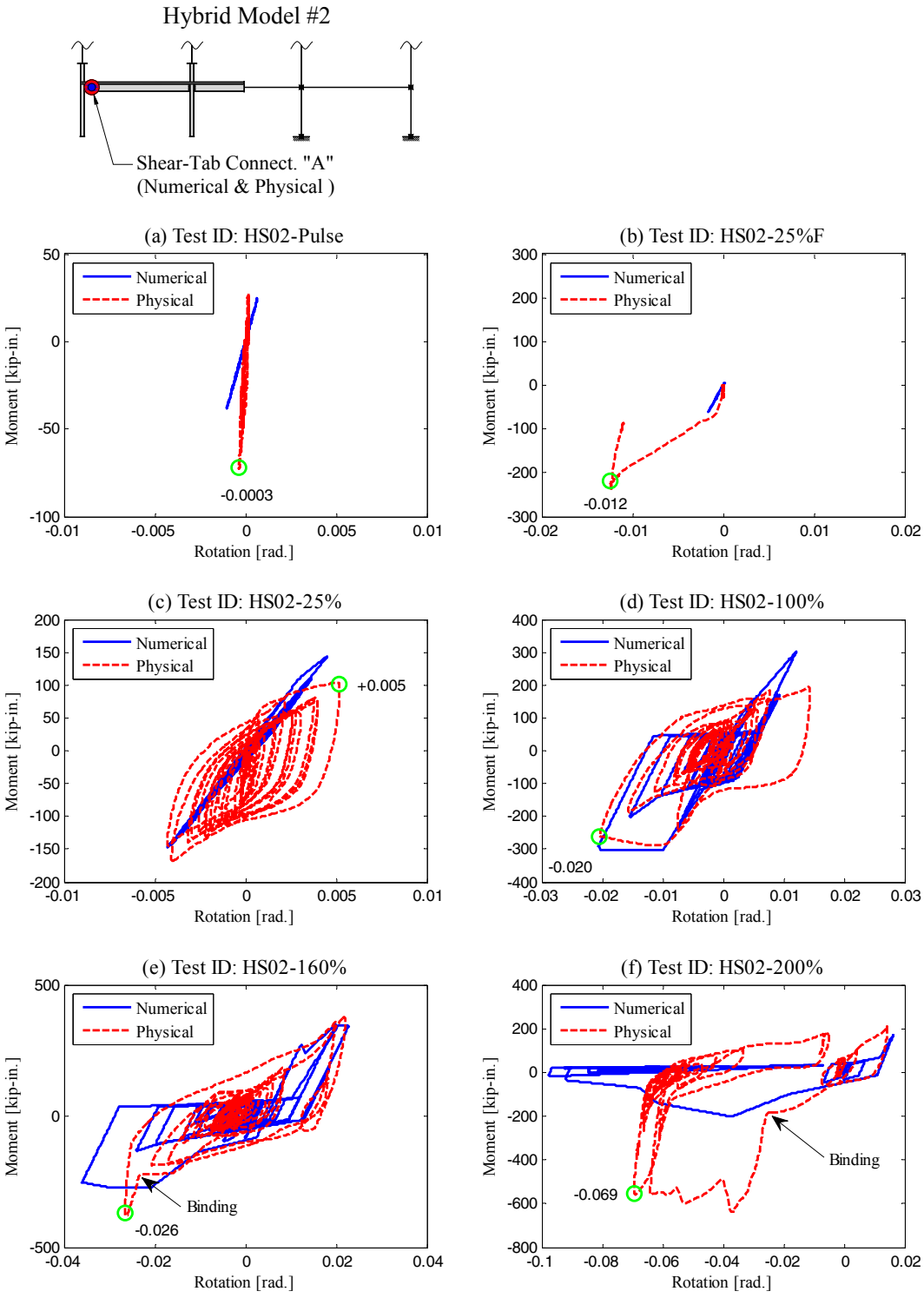


**Figure 7-44 Moment-rotation relationships for shear-tab connection "A" of gravity frame during Hybrid Simulation #2**

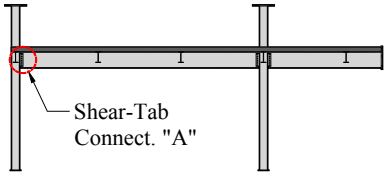


(a) Location of Shear-Tab Connection “A”

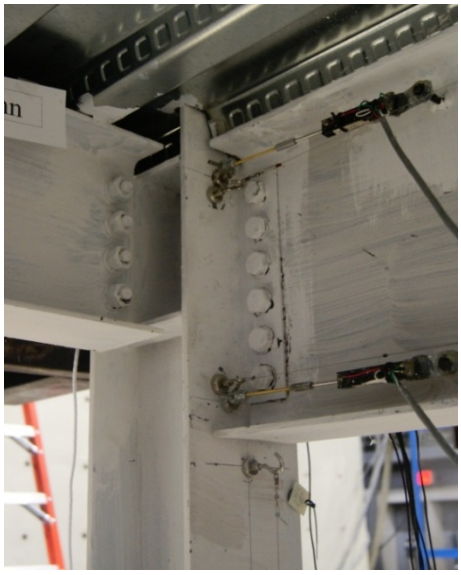

(b) Shear-Tab Conn. “A” [+0.005 rad.], HS02-25%

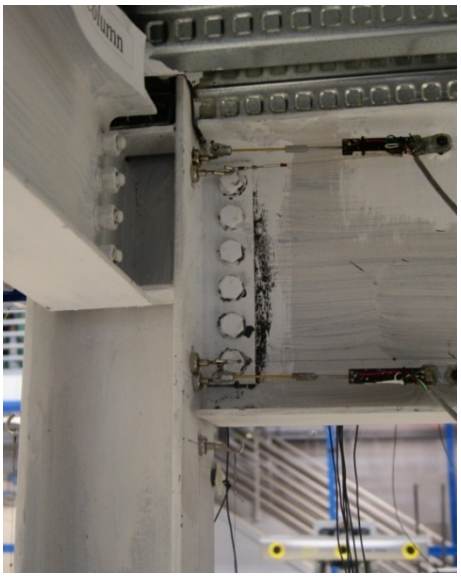

(c) Shear-Tab Conn. “A” [–0.020 rad.], HS02-100%

(d) Shear-Tab Conn. “A” [–0.026 rad.], HS02-160%

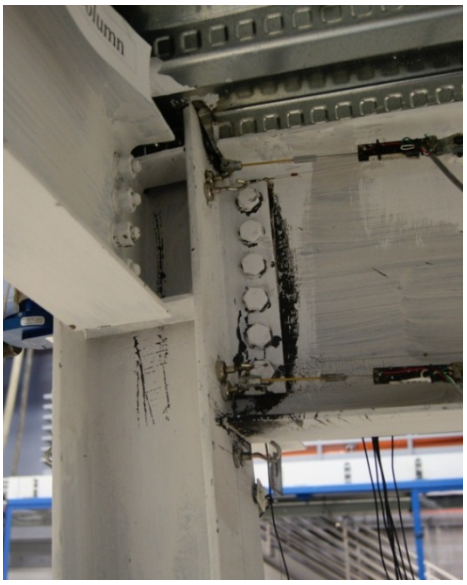

(e) Shear-Tab Conn. “A” [–0.069 rad.], HS02-200%

**Figure 7-45 Photographs of the damage state of shear-tab connection “A” of gravity frame physical subassembly during Hybrid Simulation #2**

During the failed hybrid simulation (HS02-25%F), the first story of the physical sub-structure was unexpectedly subjected to a maximum inter-story drift ratio of 1.5%. Figure 7-44(b), Figure 7-46(b), and Figure 7-48(b) show the moment-rotation response of the shear-tab connections for this failed test. The shear-tab connections exhibited a mild inelastic response (with rotations in the order of 0.01 rad.) mainly due to friction between shear-tab plate and beam web. Also, minor stiffening is observed in the response of the shear-tab connections "A" and "B". This can be due to bearing of the bolts on the bolt holes of the shear-tab plate and beam web. Visual inspection of shear-tab connections with flaking of whitewash near the connections indicated that the hysteretic response observed at this failed hybrid simulation was mostly due to friction between the shear-tab plate and beam web.

During the hybrid simulation at the service level earthquake (HS02-25%), a stable hysteretic response is observed for all the shear-tab connections of the physical sub-structure as shown in Figure 7-44(c), Figure 7-46(c), and Figure 7-48(c). This hysteretic response is mostly due to friction between the shear-tab plate and the beam web. However, the numerical sub-structure of the gravity frame did not capture this hysteretic response at small rotations. Minor flaking of the whitewash, indicating minor or no yielding of the connection, is observed at the end of this test in Figure 7-45(b), Figure 7-47(b), and Figure 7-49(b).

A pinched hysteretic response of the shear-tab connections is observed during the hybrid simulation at the MCE ground motion (HS02-100%). The pinched response at this point was due to bearing of the bolts on the bolt holes of the shear-tab plate and beam web. In this case, the numerical model reasonably captured the pinching response of the physical shear-tab connection, especially of the exterior shear-tab connection (identified as connection "A") as seen in Figure 7-44(d). As expected, this exterior shear-tab connection "A" exhibits the largest rotation demands. For this level of loading (MCE ground motion), some yielding of the beam web near the connection is observed for the shear-tab connection "A" as shown in Figure 7-45(c).

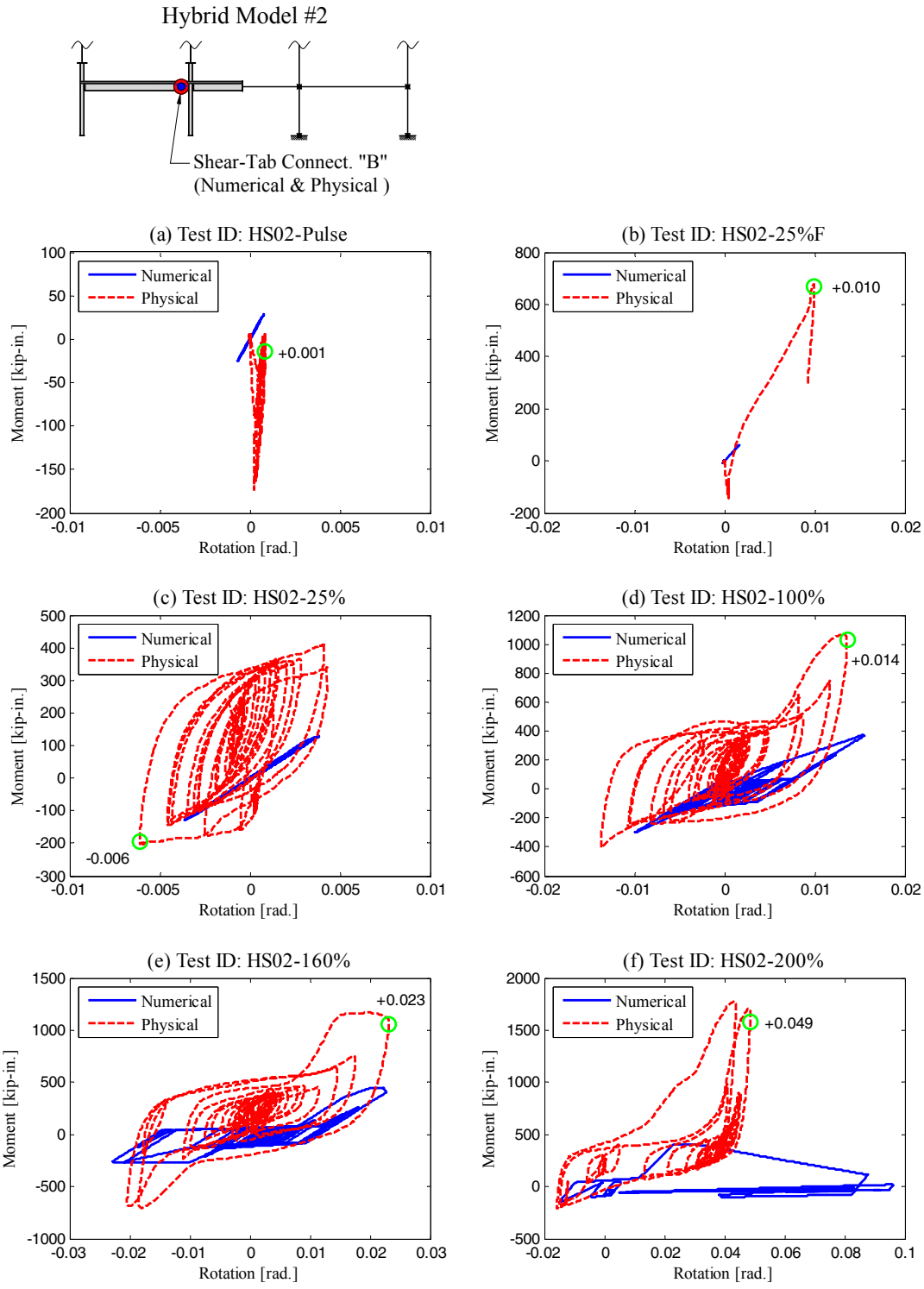


**Figure 7-46 Moment-rotation relationships for shear-tab connection "B" of gravity frame during Hybrid Simulation #2**

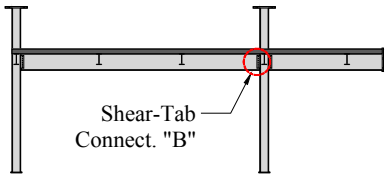


(a) Location of Shear-Tab Connection “B”

(b) Shear-Tab Conn. “B” [–0.006 rad.], HS02-25%

(c) Shear-Tab Conn. “B” [+0.014 rad.], HS02-100%

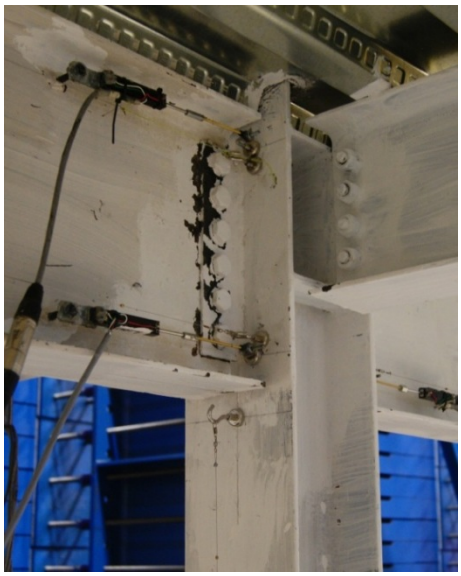

(d) Shear-Tab Conn. “B” [+0.023 rad.], HS02-160%

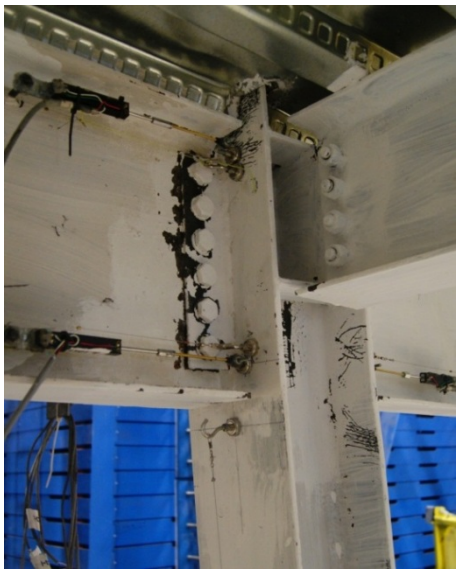

(e) Shear-Tab Conn. “B” [+0.049 rad.], HS02-200%

**Figure 7-47 Photographs of the damage state of shear-tab connection “B” of gravity frame physical subassembly during Hybrid Simulation #2**

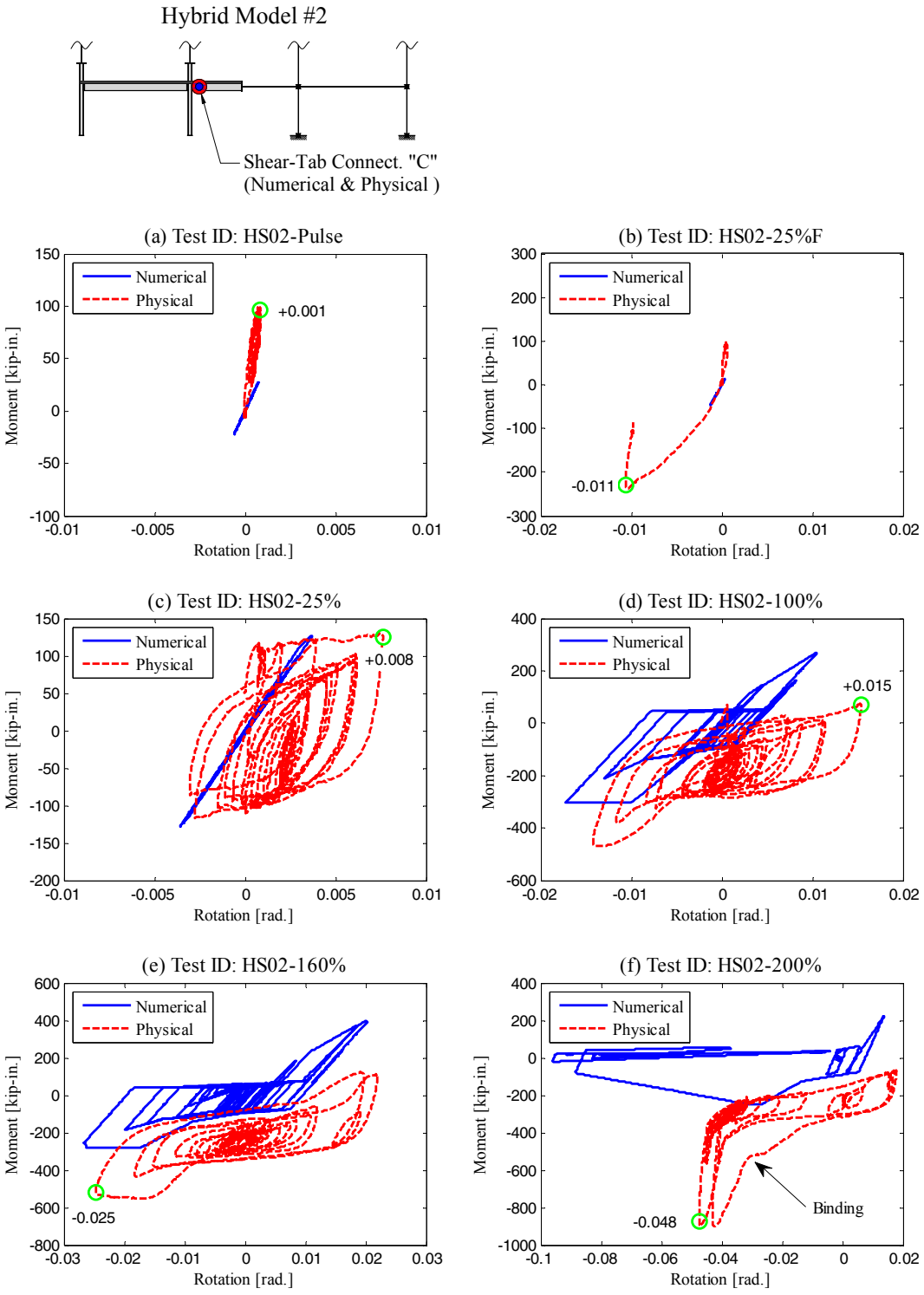


**Figure 7-48 Moment-rotation relationships for shear-tab connection "C" of gravity frame during Hybrid Simulation #2**

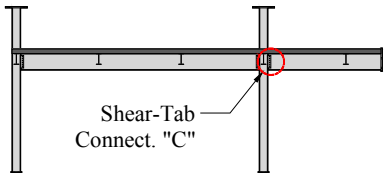


(a) Location of Shear-Tab Connection “C”

(b) Shear-Tab Conn. “C” [+0.008 rad.], HS02-25%

(c) Shear-Tab Conn. “C” [+0.015 rad.], HS02-100%

(d) Shear-Tab Conn. “C” [–0.025 rad.], HS02-160%

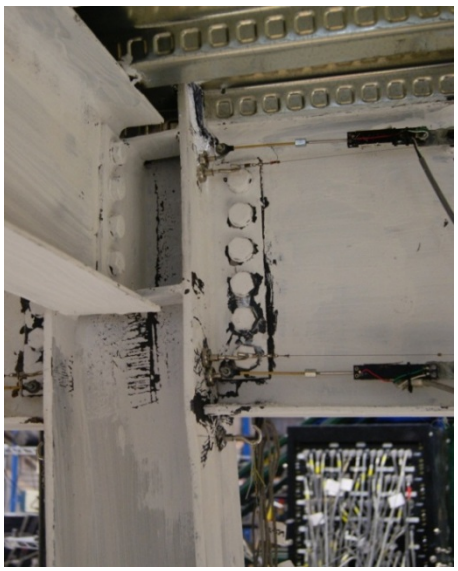

(e) Shear-Tab Conn. “C” [–0.048 rad.], HS02-200%

**Figure 7-49 Photographs of the damage state of shear-tab connection “C” of gravity frame physical subassembly during Hybrid Simulation #2**

For the hybrid simulation at 160% of the LGPC ground motion (HS02-160%), the shear-tab connections of the physical sub-structure were subjected to rotation demands of 0.025 rad., on average. At this level of loading, binding of one corner of the lower beam flange on the column flange was observed for the exterior shear-tab connection "A" as indicated in Figure 7-44(e) (also see photograph in Figure 7-45(d) for reference). Binding occurred approximately at a rotation of 0.022 rad. in negative bending. The moment-rotation response suddenly stiffened as a result of binding. Binding did not occur in the other shear-tab connections ("B" and "C") since these interior connections typically present smaller rotation demands.

For the last hybrid simulation at 200% of the LGPC ground motion (HS02-200%), significant binding of the lower beam flange on the column flange is observed for the shear-tab connections "A" and "C" as indicated clearly in Figure 7-44(f) and Figure 7-48(f), respectively. Photographs of binding at these connections are shown in Figure 7-45(e) and Figure 7-49(e). As observed before, binding at these two connections occurred at an approximate rotation of -0.022 rad. (under negative bending). Since the shear-tab connection "B" was loaded mostly under positive bending, binding of the beam lower flange on the column flange did not occur for this connection. Yielding of the shear-tab plate of the exterior connection is observed in Figure 7-45(e).

In summary, a ductile behavior of the shear-tab connections was observed. The behavior up to the MCE ground motion was governed mainly by (a) friction between the shear-tab plate and beam web and (b) yielding of the shear-tab plate near the bolt holes. Some yielding of the beam web was observed for the exterior shear-tab plate (see Figure 7-45(e)). At the ground motion intensities beyond MCE, significant binding of the lower beam flange on the column flange governed the response of the shear-tab connections. However, no bolt fracture or shear-tab plate fracture was observed. This is in contrast to the experimental program of Liu and Astaneh-Asl (2000b) where fracture of bolts and shear-tab plates were reported typically after binding. This is primarily attributed to the fact that the shear connections as part of the hybrid model experienced much less cumulative damage prior to structural collapse compared to the component tests that were conducted as part of the testing program of Liu and Astaneh-Asl (2000b). In this testing program, the SAC symmetric loading protocol was employed. This agrees with earlier findings regarding the loading protocol prior to collapse as discussed in Lignos *et al.* (2011a) and Lignos and Krawinkler (2012). Also, it is important to mention that the yield strength of the shear-tab plates in the gravity frame subassembly was 30% larger than that of Specimen 6A of Liu and Astaneh-Asl. This could be another reason for the different behavior of the shear-tab connections tested here and those of Liu and Astaneh-Asl.

The data presented above provides valuable experimental information to assess the performance of the substructuring algorithm. In general, the shear-tab connections of the physical and numerical sub-structure were subjected to similar rotation demands for all hybrid simulations (see Figure 7-48(e) for reference) except for the last hybrid simulation HS02-200% where the shear-tab connections of the physical sub-structure stiffened after binding of beam flange on column flange and did not exhibit large rotations as compared to the numerical shear-tab connections where the stiffening effect was not included as seen in Figure 7-44(f), Figure 7-46(f) and Figure 7-48(f). Also, the numerical evaluation of the substructuring technique showed that such differences in rotations became more pronounced with increasing levels of shaking.

In contrast to the procedure followed to derive bending moments along girders of the moment frame physical subassembly (see Section 7.2.2.2), bending moments on the shear-tab connections of the gravity frame physical subassembly were obtained as follows. The vertical link member part of the test setup and shown in Figure 5-18(a) was instrumented with four strain gages for Hybrid Simulation #2 to obtain axial forces on this member as indicated previously in Section 5.3.3.1. Since the vertical member underpinned the beam of the physical sub-structure in cantilever, bending moments at this cantilever beam were obtained using the derived axial forces of the vertical link member. Therefore, bending moments at the shear-tab connection "C" were obtained. Then, the moment at shear-tab connection "B" was obtained using moment equilibrium at the west joint. This was possible since bending moments along columns can be accurately obtained as discussed before. Similarly, bending moments at shear-tab connection "A" were obtained using moment equilibrium at the east joint of the physical sub-structure. These derived moments are approximate in nature since shear forces are not included in the joint equilibrium. Also, the resisting bending moment of the actuators attached near the east joint was not accounted for. Therefore, conclusions based on these approximate bending moments are carefully drawn.

Also, it is important to mention that since the measurements of the instrumentation system were set to zero at the beginning of the hybrid simulation, the moments and rotations of the physical sub-structure presented in Figure 7-44, Figure 7-46, and Figure 7-48 do not include initial values from gravity loading of the physical subassembly using the four 8.5-kip steel plates shown previously in Figure 5-19. The physical sub-structure was loaded with these four 8.5-kip steel plates prior to the hybrid simulations. Also, as it was explained before in Section 6.7, the gravity frame numerical sub-structure do not present initial values of moments and rotations from gravity loading. More details of gravity loading of the hybrid model can be found in Section 6.7 of this report.

**Response of Concrete Slab**

Figure 7-50 shows photographs of the damage state of the concrete slab after the completion of the second series of hybrid simulations. Due to safety measures, photographs of the concrete slab were only obtained at the end of the hybrid simulations. In general, damage of the concrete slab was limited to the regions around the columns. While minimal concrete spalling was observed around the west column, a diagonal crack was observed around the east column due to the lateral forces transferred by the horizontal actuator. Despite the damage observed on the concrete slab, the concrete floor slab did not lose its vertical load carrying capacity.

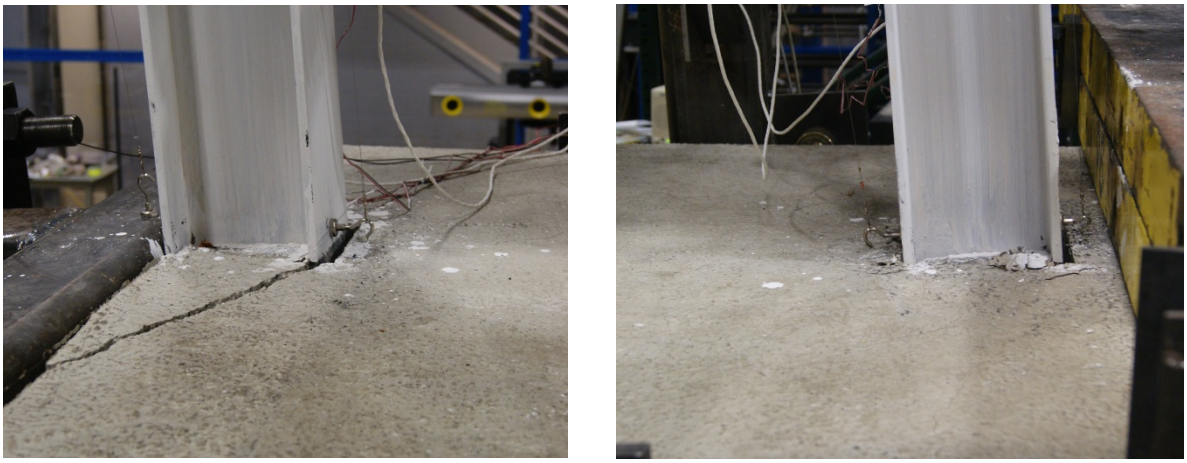

(a) North view of concrete slab around east column (b) North view of concrete slab around west column

**Figure 7-50 Photographs of the damage state of the concrete slab of the gravity frame physical subassembly after Hybrid Simulation #2**

**Response of Gravity Frame Columns**

Figure 7-51 through Figure 7-56 present moment-rotation relationships for columns of the gravity frame physical sub-structure at plastic-hinge regions. In each plot, the response of the physical column is presented together with the response of a similar column from the numerical sub-structure. Although the response of such physical and numerical components is different, some observations can be carefully made. The location of the plastic-hinge regions is indicated with a sketch above each figure. All bending moments were normalized by the predicted moment strength ($M_{y,p}$) of the W6×20 column. The predicted moment strength is defined as the plastic section modulus ($Z$) times the measured material yield strength obtained from coupon testing. The elastic component of the rotations was removed so that only plastic rotations are presented in all figures for comparison purposes. Photographs of the damage state at the base of the physical columns are presented in Figure 7-57 for hybrid simulations HS02-100% through HS02-

200% where damage is visible. These photographs were taken at the end of each hybrid simulation or after maximum loading of the specimen (maximum displacement).

In general, the moment-rotation relationships presented in Figure 7-51 through Figure 7-56 indicate that the gravity columns of the physical specimen exhibit low levels of yielding which concentrated at the base only. This is confirmed by photographs of the damage state at the base of columns provided in Figure 7-57. Also, photographs presented previously in Figure 7-45, Figure 7-47, Figure 7-49 and Figure 7-50 confirm that the columns remained elastic at the top of the first story and at the bottom of the second story of the physical test specimen (potential plastic-hinge regions). It is important to point out that the string pots shown in Figure 7-50(b) installed to monitor chord rotations on the west gravity column above the concrete slab were pushed by the concrete slab upon loading of the physical specimen during Hybrid Simulation #2 and consequently provided erratic rotation measurements as seen in Figure 7-56(f). Therefore, the yielding-like response observed in Figure 7-56(f) does not indicate column yielding but rather malfunctioning of the instrumentation system for rotations (string pots). On the contrary, the bending moments presented in Figure 7-51 through Figure 7-56 are reasonably accurate.

During the last hybrid simulation at 200% of the LGPC ground motion (HS02-200%), two bolts at each column base plate (4 bolts total) fractured in tension as seen in Figure 7-57(e) and Figure 7-57(f). Fracture of bolts is indicated in the moment-rotation plots in Figure 7-51(f) and Figure 7-54(f) for the east and west columns, respectively. The previously presented Figure 7-42 shows that bolt fracture occurred at first story inter-story drift ratios between 3.7% and 4.7%. A sudden drop in strength is observed in the moment-rotation response at the instant of bolt fracture. Fracture of bolts at the column base plates helped to accommodate large rotations at the base without yielding of the columns. However, the flexible supports of the numerical sub-structure (modeled with elastic springs) allowed for yielding at the base of the numerical columns as seen in Figure 7-51(e), Figure 7-51(f), Figure 7-54(e) and Figure 7-54(f) for the last two hybrid simulations (HS01-160% and HS01-200%). Therefore, although the flexible supports helped to improve the predictions for low levels of loading, they turned out to be unrealistic for large levels of loading such as in hybrid simulation HS02-160% and HS02-200%.

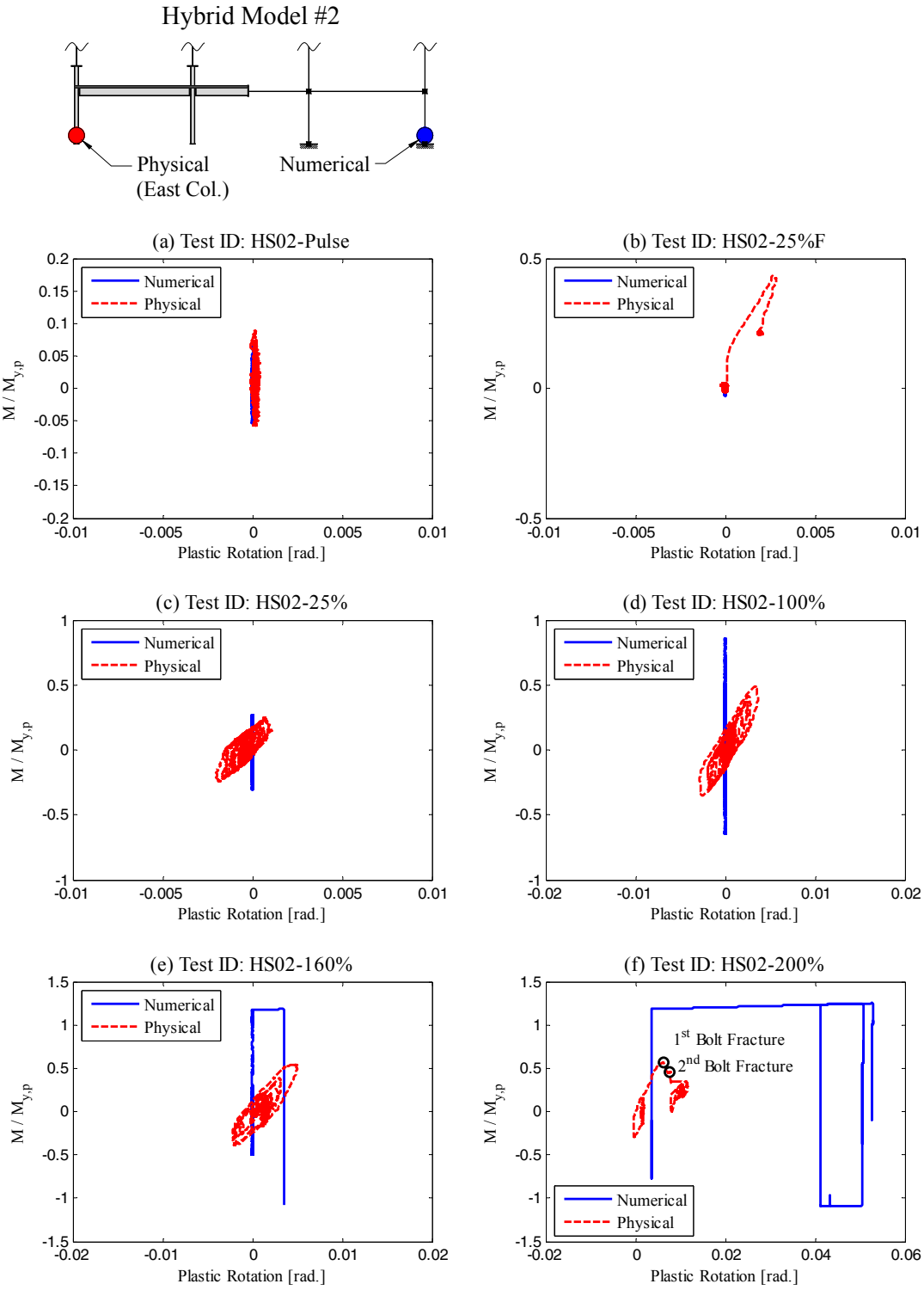


**Figure 7-51 Moment-rotation relationships for east column plastic-hinge regions of gravity frame during Hybrid Simulation #2 (Part I)**

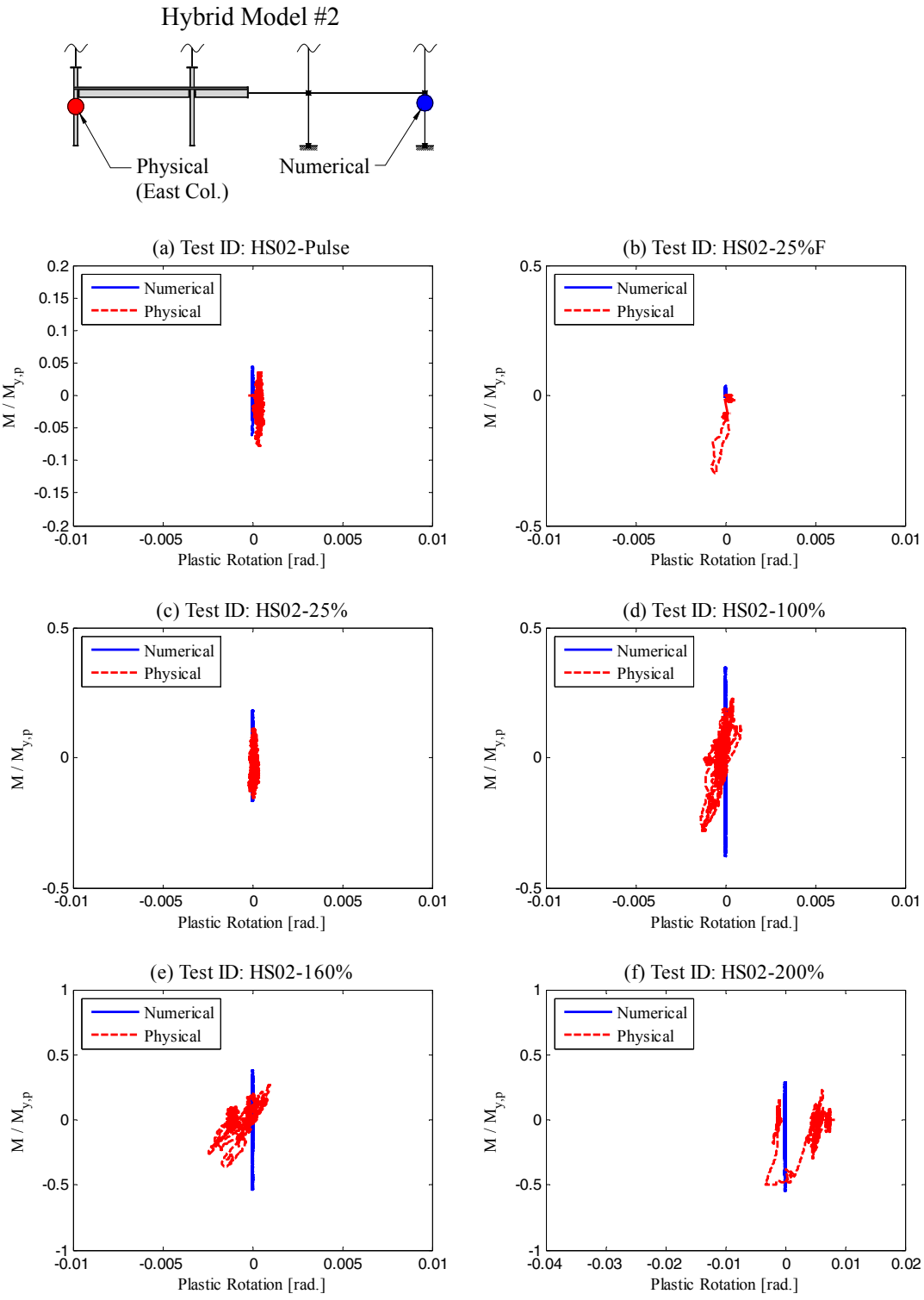


**Figure 7-52 Moment-rotation relationships for east column plastic-hinge regions of gravity frame during Hybrid Simulation #2 (Part II)**

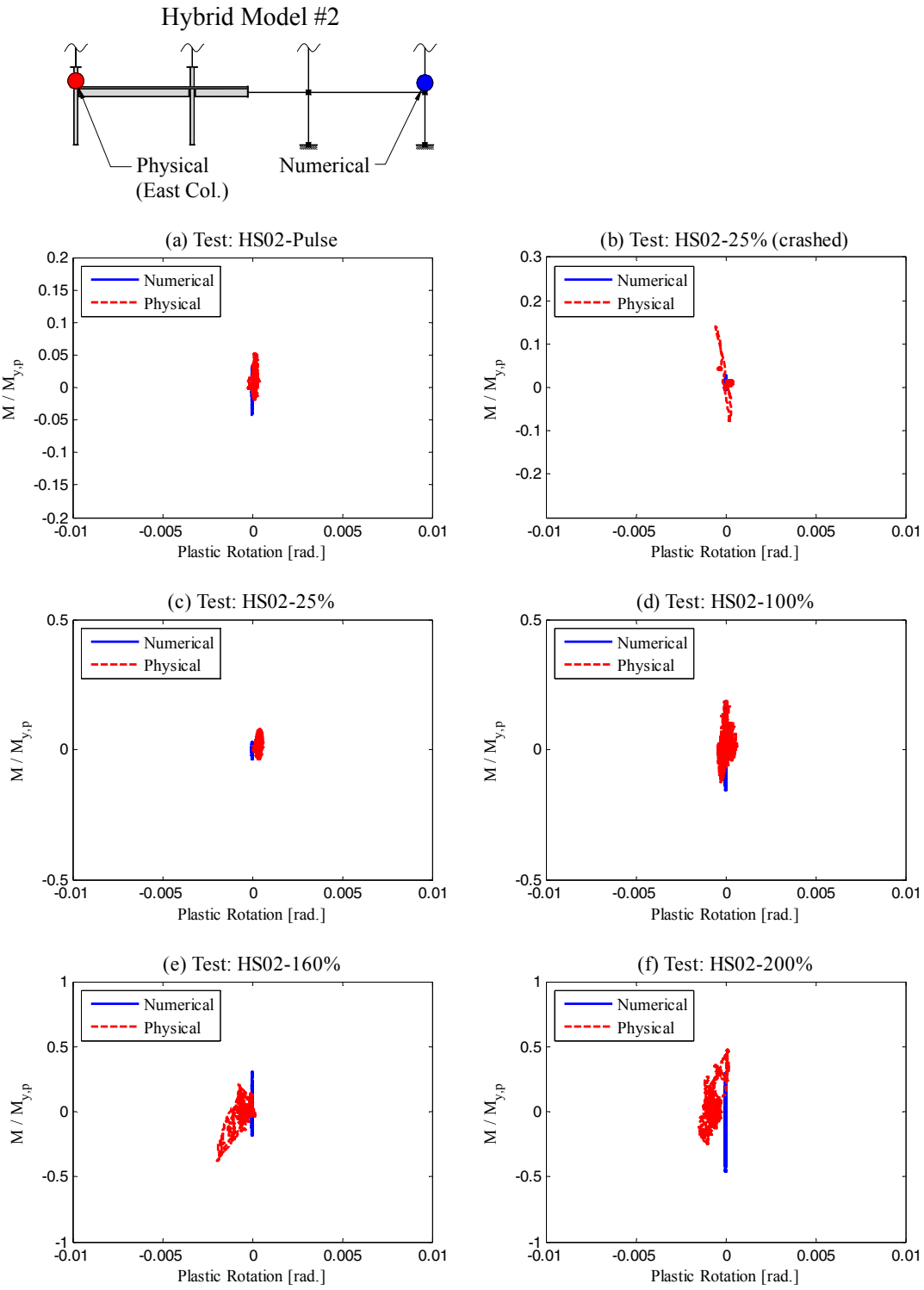


**Figure 7-53 Moment-rotation relationships for east column plastic-hinge regions of gravity frame during Hybrid Simulation #2 (Part III)**

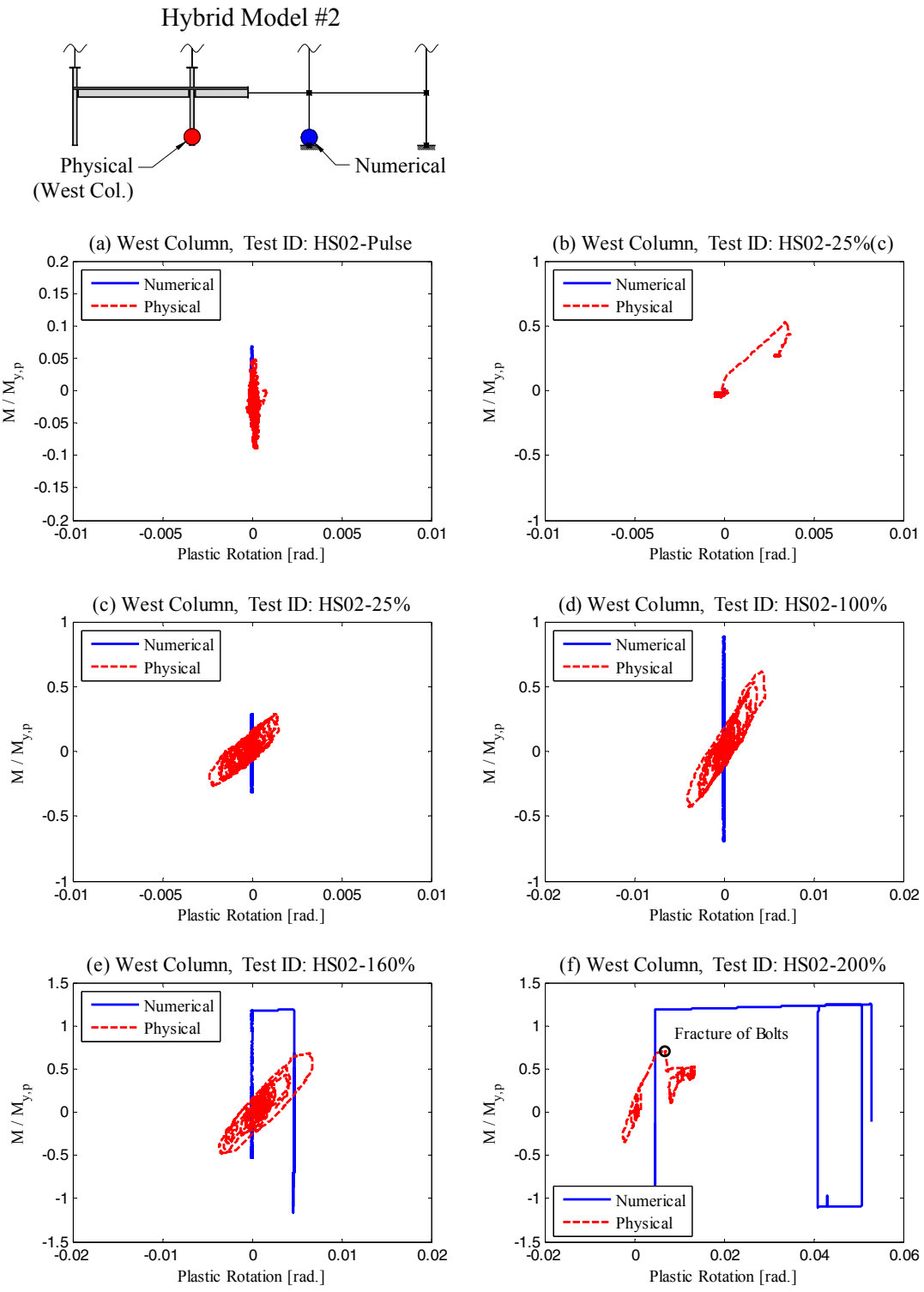


**Figure 7-54 Moment-rotation relationships for west column plastic-hinge regions of gravity frame during Hybrid Simulation #2 (Part I)**

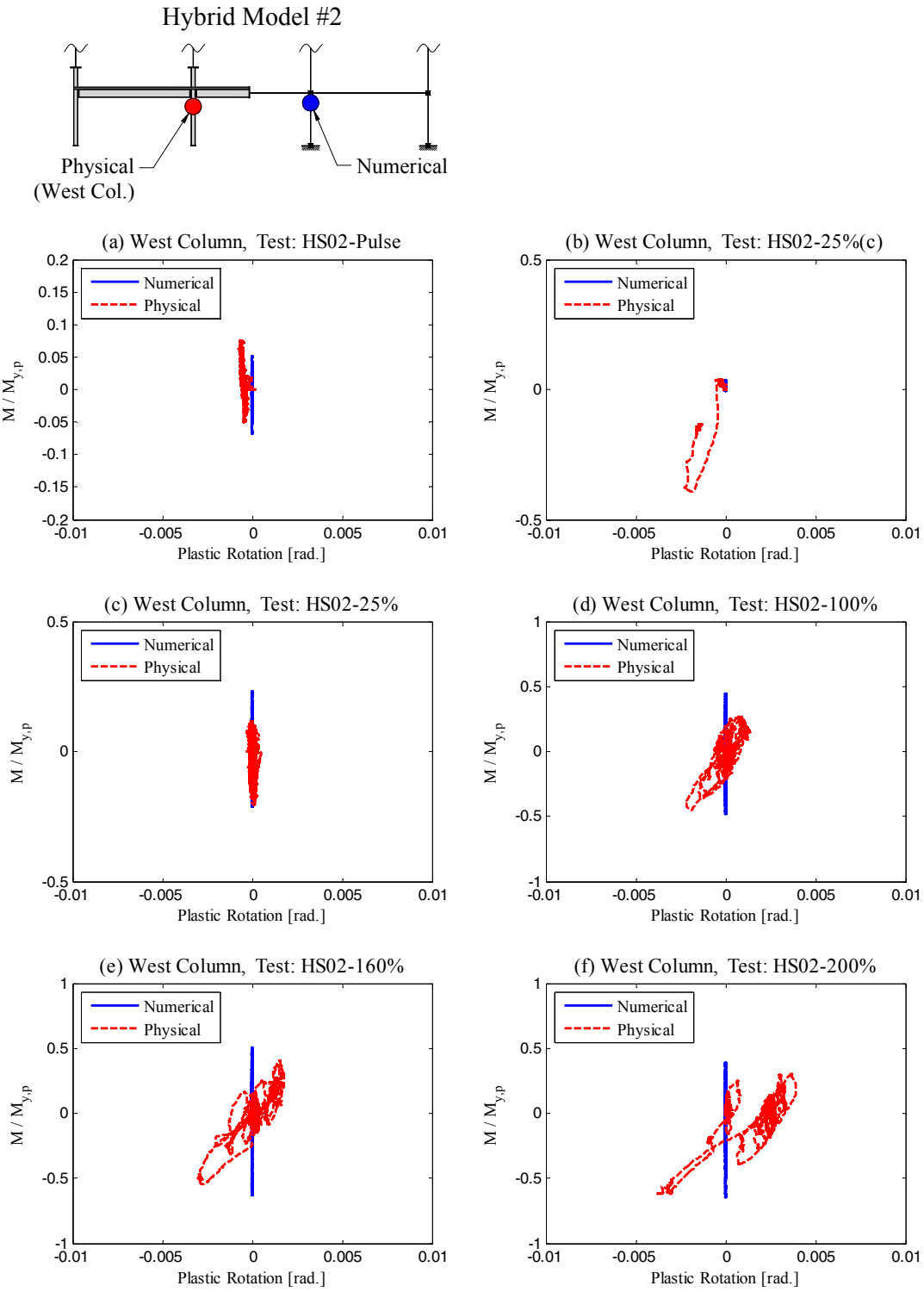


**Figure 7-55 Moment-rotation relationships for west column plastic-hinge regions of gravity frame during Hybrid Simulation #2 (Part II)**

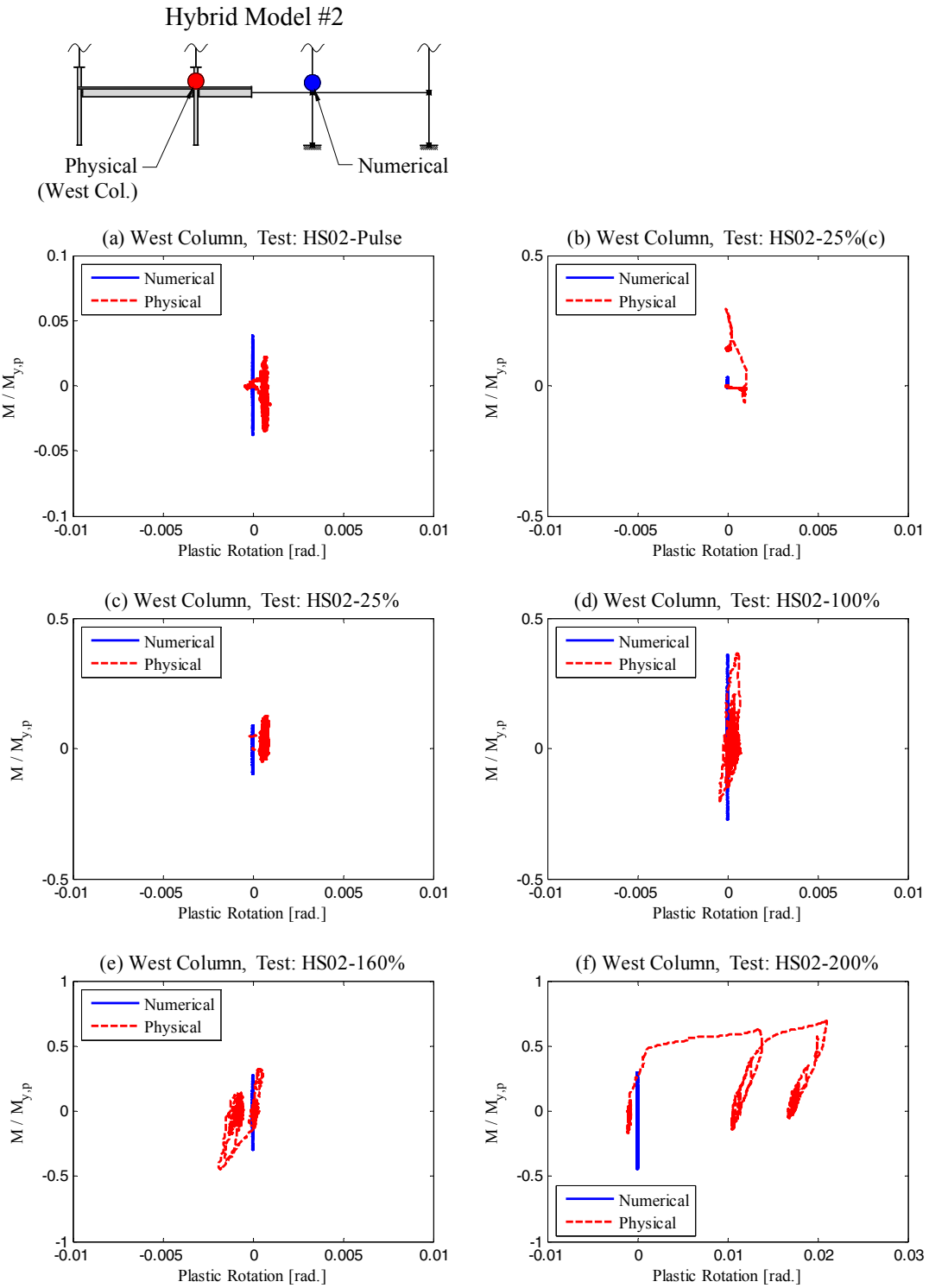


**Figure 7-56 Moment-rotation relationships for west column plastic-hinge regions of gravity frame during Hybrid Simulation #2 (Part III)**

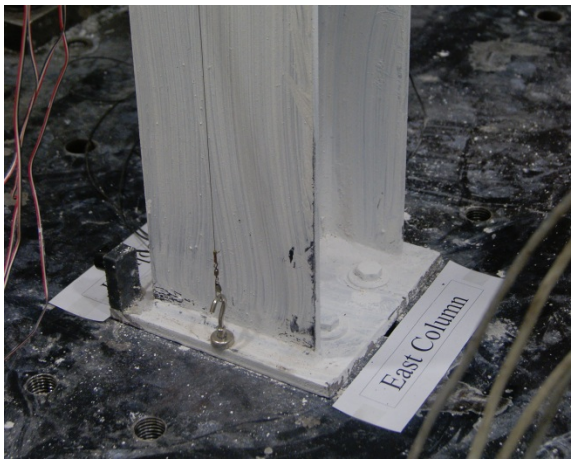


(a) East-north view of east column; HS02-100%

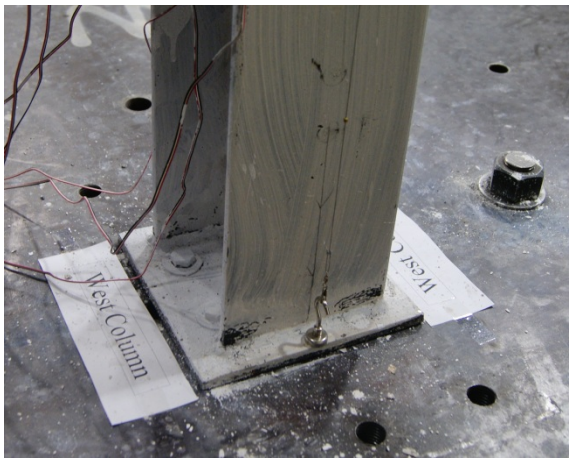


(b) East-south view of west column; HS02-100%

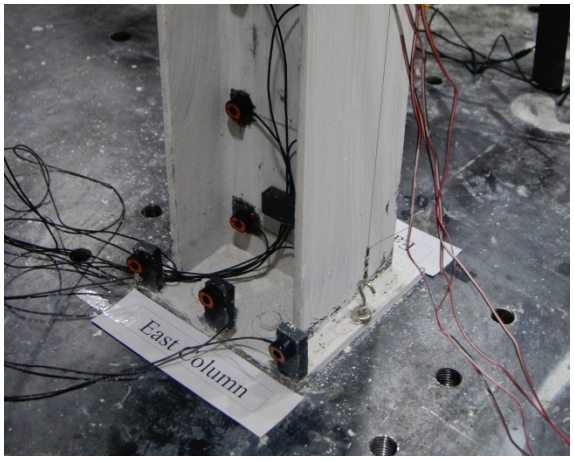


(c) South-east view of east column; HS02-160%


(d) East-north view of west column; HS02-160%

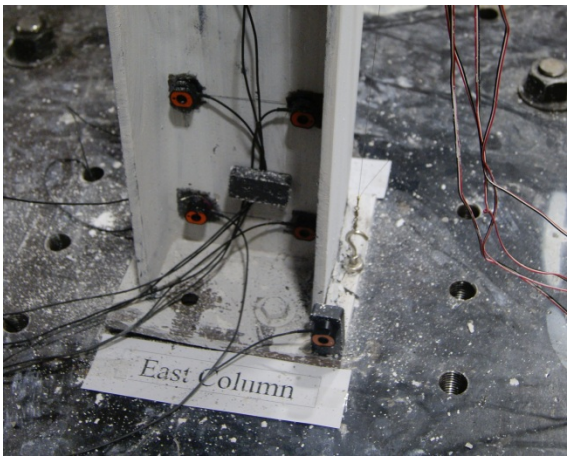


(e) South-east view of east column; HS02-200%


(f) North-west view of west column; HS02-200%

**Figure 7-57 Photographs of the damage state at base of columns of gravity frame physical subassembly during Hybrid Simulation #2**

**Response of Panel Zones**

Previously presented photographs of the damage state of the gravity frame physical sub-structure in Figure 7-45(e), Figure 7-47(e), and Figure 7-49(e) showed some yielding at the panel zones for the last hybrid simulation at 200% of the LGPC ground motion (HS02-200%). It appears from flaking of the whitewash that the panel zones were subjected to a combination of shear, bending, and high axial forces rather than pure shear. Measurements of the panel zone distortion could not be obtained due to the floor beams attached transversely to the panel zone which blocked the vision of the Krypton camera and precluded installation of linear pots.

**Response of Column Base Plate**

As indicated before, the response of the east column was monitored with the Krypton instrumentation system. Figure 7-58 shows the numbering convention of selected LEDs near the base plate of the east column of the physical sub-structure. Three LEDs (21, 22 and 23) were attached to the column base plate using magnet supports and two LEDs (19 and 20) directly to the web of the gravity column.

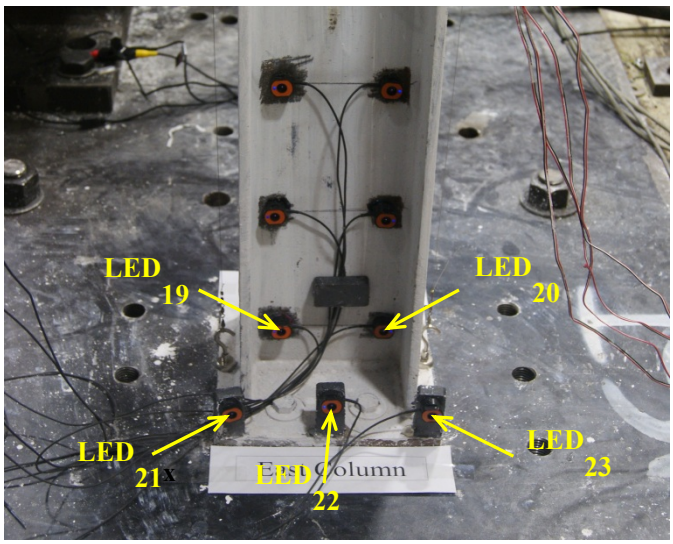


**Figure 7-58 Selected LEDs at bottom of east column of gravity frame physical sub-structure**

Figure 7-59 shows the vertical deformation of the LEDs at maximum (positive and negative) column bending moments at the base. The data points for the three LEDs attached to the column base plate and the two LEDs attached to the column web are connected with a dashed line to approximate rotations at these two planes. Bending of the column base plate is evident after the first hybrid simulation (HS02-25%). Bending of the column base plate significantly increased upon further loading.

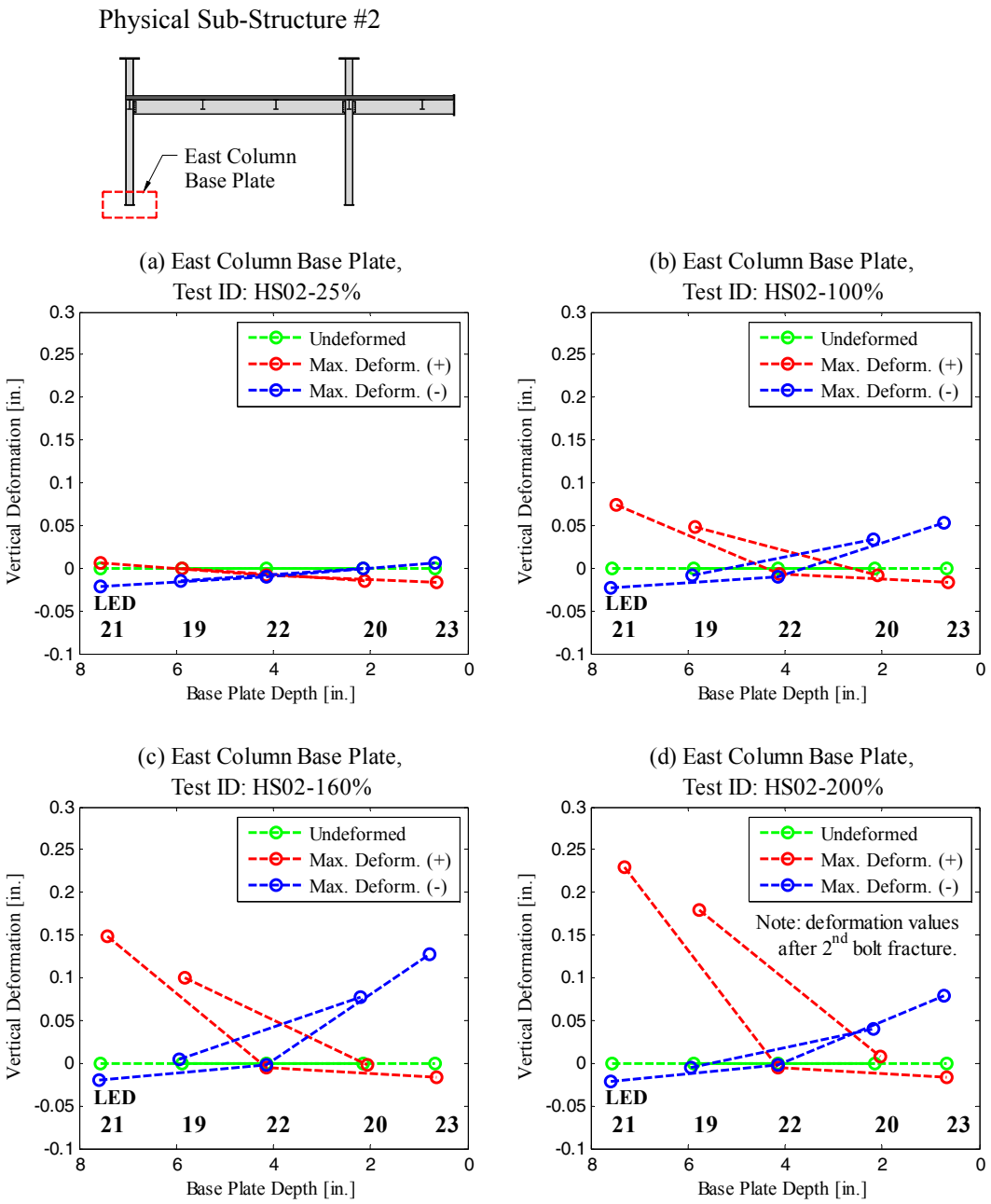


**Figure 7-59 Vertical deformation of LEDs located near the base of east column of gravity frame physical subassembly during Hybrid Simulation #2**

The rotation at the base plate of the east physical column (obtained approximately through data interpolation of LED 21, 22 and 23) versus the bending moment at the base of the same column is presented in Figure 7-60 for the second series of hybrid simulations. For comparison purposes, the rotation of the flexible support of the exterior column of the numerical sub-structure versus the column bending moment at the base is also presented in Figure 7-60. The physical and numerical moment-rotation relationships presented in Figure 7-60 provide information of the flexible support of the gravity frame hybrid model. A comparison of Figure 7-60(a) and Figure 7-60(c) indicates a degradation of the elastic rotational stiffness of the base plate support connection mostly due to the unexpected loading of the test specimen during the HS02-25%F test. The response of the base plate support during hybrid simulation HS02-100% in Figure 7-60(d) resembles a self-centering hysteretic response as a result of rocking of gravity columns. The column base plate, initially straight, bended and adopted a rounded convex shape upon cyclic loading and, consequently, flattened the flag-type hysteretic response as observed in Figure 7-60(e). Fracture of the first bolt at the east column base plate occurred at approximately 0.03 rad. as indicated in Figure 7-60(f). Fracture of the second bolt moved the LEDs of the Krypton instrumentation system and did not allow capturing the subsequent response.

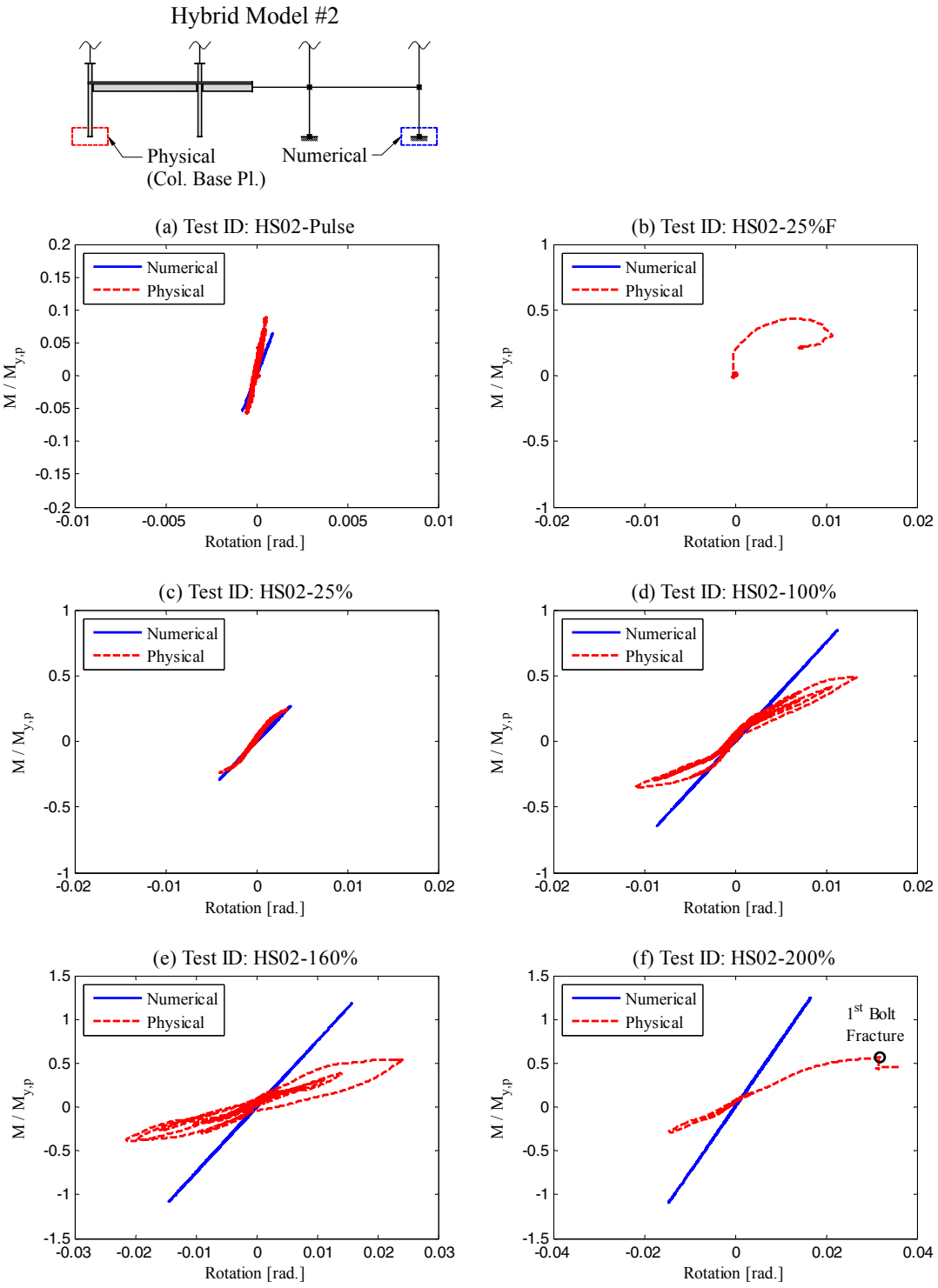


**Figure 7-60 Moment-rotation relationships for supports during Hybrid simulation #2**

### 7.3.3 Results of Cyclic02 Test

As mentioned before, the main objective of the Cyclic02 test was to obtain information on the shear-tab connections at large rotations. Figure 7-61 presents the displacement protocol selected for the top and bottom horizontal actuators. The vertical actuators were set to impose a constant vertical force on the columns corresponding to the gravity load of the stories above.

Since some of the bolts of the column base plates fractured in tension during the second series of hybrid simulations, the column base plates of the physical sub-structure were welded to the interface 9'×5'×1½" base plates as shown in Figure 7-62 before conducting the Cyclic02 test.

Figure 7-63 and Figure 7-64 show, respectively, moment-rotation relationships and photographs of the damage state for the three shear-tab connections of the physical subassembly for the Cyclic02 test. During the execution of the cyclic test, one of the actuators exhibited a high frequency response likely due to instability of the controller. Therefore, the bending moments presented in Figure 7-63 were smoothed. During the last loading cycle of the test specimen, one of the linear pots at the exterior shear-tab connection (shear-tab connection "A") detached from the specimen as seen in Figure 7-64(b).

Some observations can be made based on the information provided in Figure 7-63 and Figure 7-64. In general, the shear-tab connections exhibited a significant reserved capacity after the hybrid simulations. The low stiffness and strength of the shear-tab connections at small rotations typifies the pinched hysteretic behavior that shear-tab connections exhibit. The shear-tab connections stiffened upon further loading due to binding of the beam flanges on the column flanges. Also, significant damage is observed in the interior physical column (west column) as seen in Figure 7-64(c) and Figure 7-64(d). This can be attributed to a combination of significant binding of beam flanges on the column flanged and high axial forces on such internal gravity column.

The shear-tab plates did not show signs of fracture. However, significant yielding is observed near the bolt holes, especially in the exterior shear-tab connection (shear-tab connection "A") as seen in Figure 7-64(b).

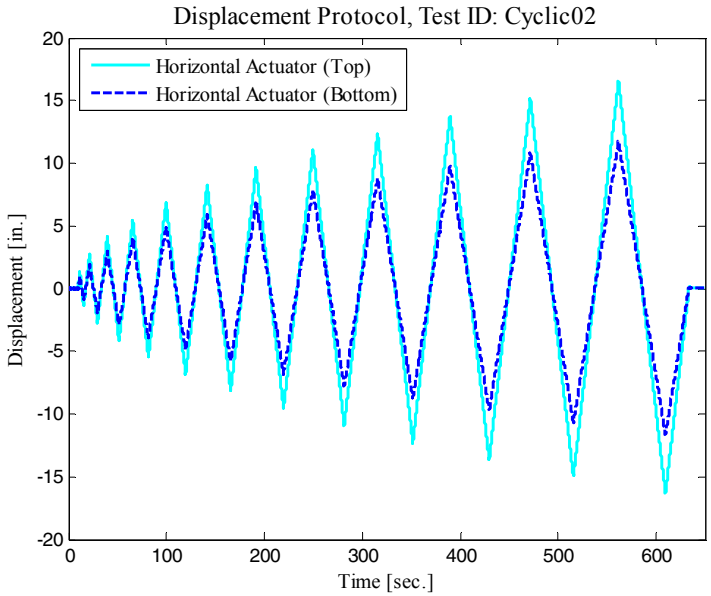


**Figure 7-61 Displacement protocol for Cyclic02 test**

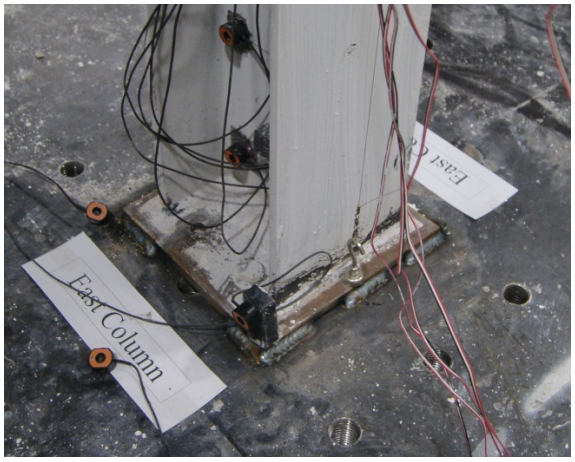


(a) South-east view of east column base plate

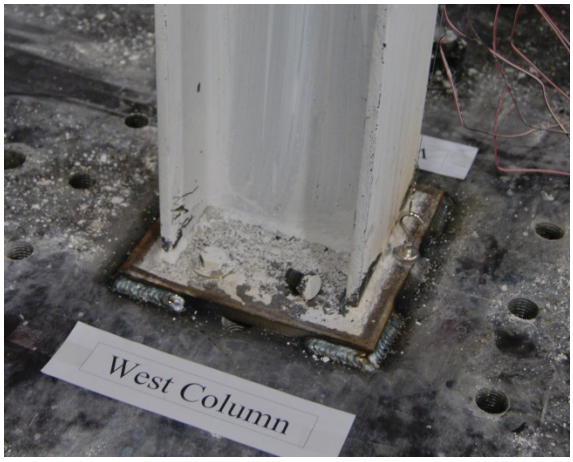


(b) South-west view of west column base plate

**Figure 7-62 Welding of column base plates of gravity frame subassembly prior to Cyclic02 test**

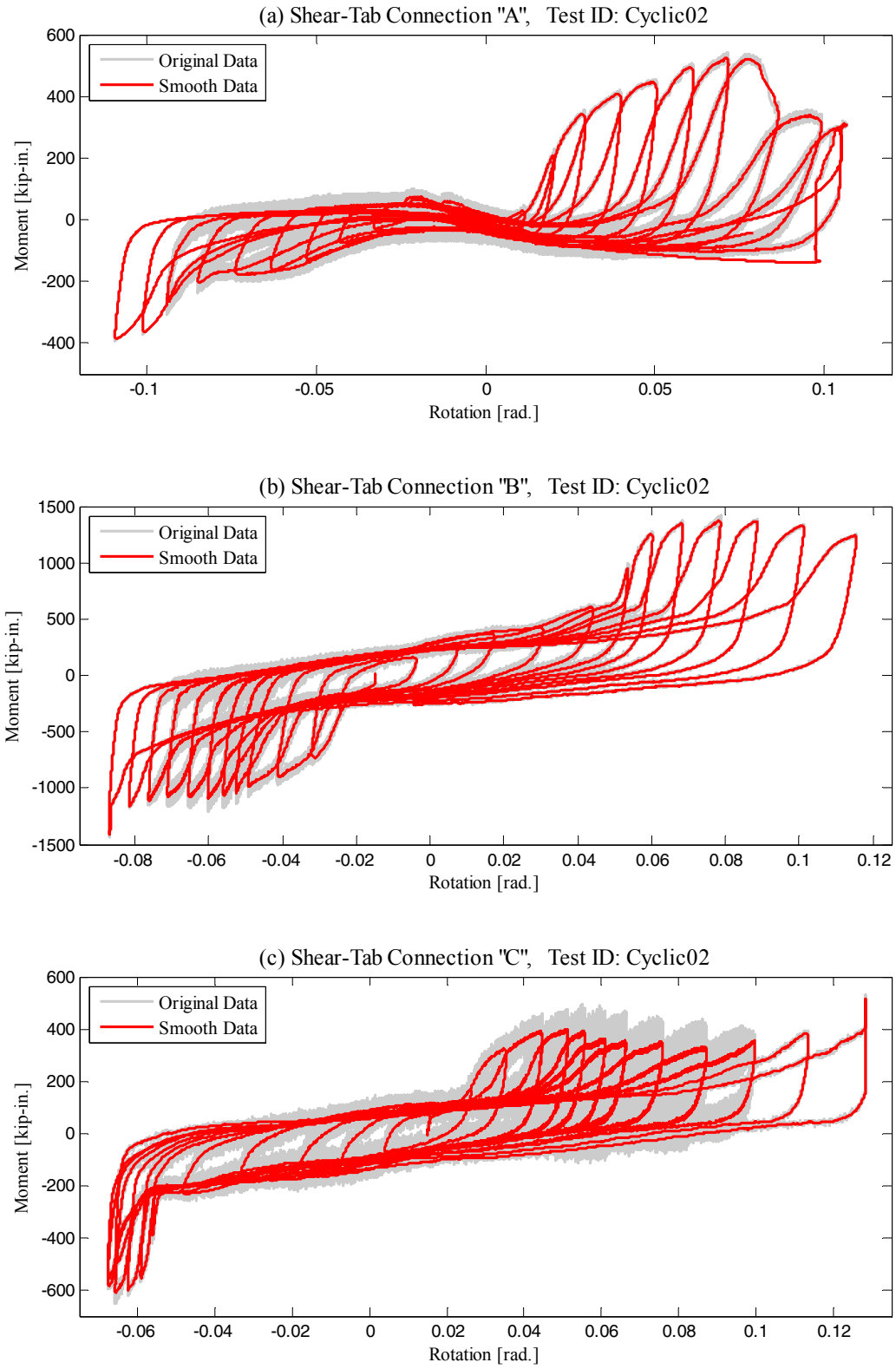


**Figure 7-63 Moment-rotation relationships for shear-tab connections of gravity frame physical subassembly during Cyclic02 test**


(a) Location of shear-tab connections

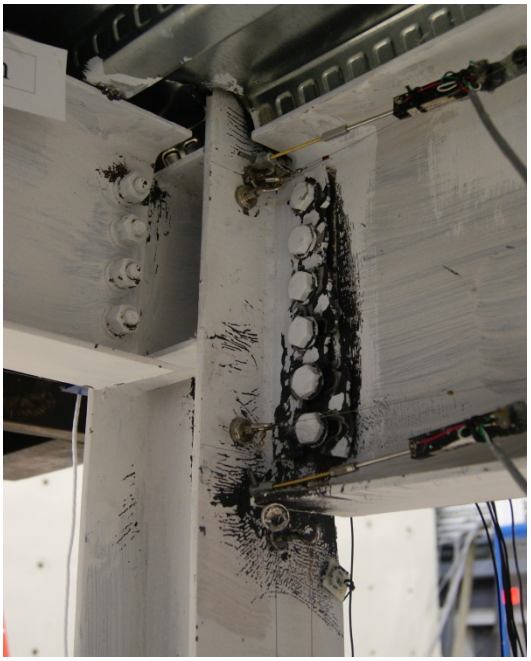

(b) Shear-tab connection "A" after Cyclic02 test

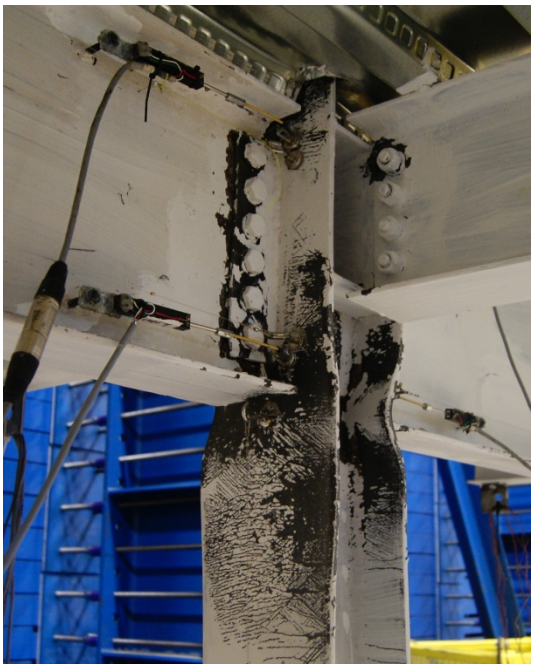

(c) Shear-tab connection "B" after Cyclic02 test

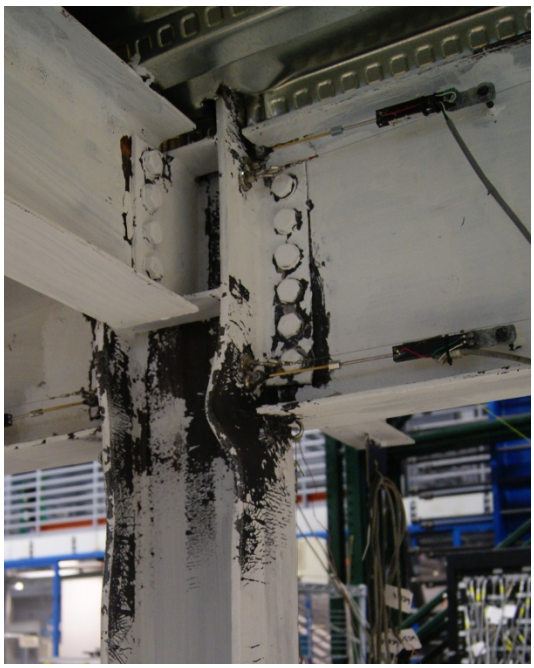

(d) Shear-tab connection "C" after Cyclic02 test

**Figure 7-64 Photographs of the damage state of shear-tab connections of gravity frame physical subassembly after Cyclic02 test**

Figure 7-65 shows photographs of the damage state of the concrete slab after the Cyclic02 test. Significant concrete spalling around both columns is observed. Despite such level of damage in the shear-tab connections and concrete slab, the floor slab did not lose its vertical load carrying capacity.

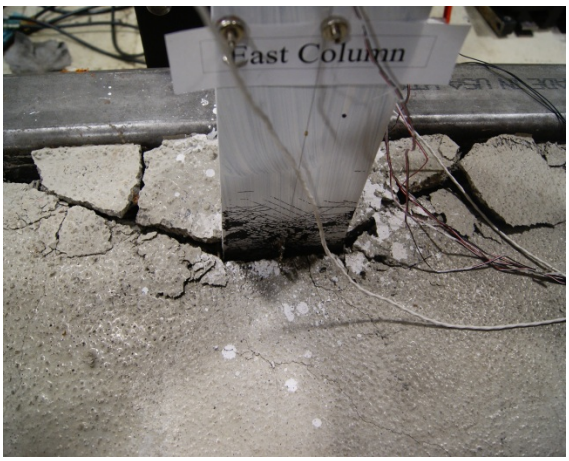


(a) West view of slab around east column

(b) East view of slab around west column

**Figure 7-65 Photographs of the damage state of the concrete slab of the gravity frame physical subassembly after Cyclic02 test**

In summary, a great deal of experimental information was obtained for the seismic response of a special steel moment frame subassembly as well as for a gravity frame. The two series of hybrid simulations were successfully conducted using the integration method and substructuring technique previously evaluated. Experimental information was presented mainly in the general form of force-displacement relationships for different components of the frame structures, including girder and column plastic-hinge regions, panel zones and column base plates. This data was used for seismic assessment and model validation. In general, the global response results of the hybrid simulations compare favorably with pre-test numerical predictions and with previous results of the substructuring technique evaluation. The experimental data also supplemented studies for the evaluation of the substructuring technique for collapse assessment. The differences observed in the global response results of the hybrid models with pre-test predictions were mainly due to over-predictions of the elastic stiffness of the physical sub-structure, as well as to the moment strength at yielding of columns.

# SECTION 8
# COLLAPSE EVALUATION OF A STEEL MOMENT FRAME BUILDING STRUCTURE

## 8.1 Introduction

The collapse performance of the steel moment frame building structure presented in Section 4 is further evaluated in this section using a seismic fragility framework. The evaluation presented in this section was based on the methodology proposed in FEMA P695 (FEMA, 2009). Although the FEMA P695 methodology provides a rational basis for quantifying the performance of new seismic-force-resisting systems for inclusion in building codes, it also addresses collapse evaluation of existing seismic-force-resisting systems specified in current building codes. The response of the prototype building structure is evaluated for three cases to assess the influence of the composite floor slab and the gravity-force-resisting system. In the first case, the response of a special steel moment frame structure without slab effects was assessed. This case served as the baseline for the other two cases. For the second case, the effect of the composite floor slab on seismic response of the steel moment frame structure was included. In the third case, the gravity-force-resisting system was explicitly modeled to examine its contribution to the response of the building structure.

## 8.2 Scope of Collapse Evaluation

The methodology proposed in FEMA P695 (FEMA, 2009) was simplified and implemented herein to evaluate the collapse performance of the building structure presented in Section 4. While the FEMA P695 requires the development of a set of building configurations or "index archetype configurations" to describe a range of permissible configuration of a structural system, the methodology, as implemented in this study, was used for three single models. Although the FEMA P695 methodology requires modeling only components specifically designed as part of the seismic-force-resisting system, the evaluation presented in this section was extended to include frames of the gravity-force-resisting system to assess their influence on the collapse capacity.

The FEMA P695 methodology uses the collapse margin ratio (*CMR*), defined as the ratio between the median collapse intensity ($\hat{S}_{CT}$) and the Maximum Considered Earthquake (MCE) ground motion intensity ($S_{MT}$), as the primary parameter to characterize the collapse safety of a structural system.

Nonlinear dynamic analyses are used to assess median collapse capacities ($\hat{S}_{CT}$) and collapse margin ratios (*CMR*). For collapse evaluation, a set of ground motions are scaled systematically to increasing intensities until median collapse is established. The methodology defines median collapse as the ground motion intensity in which half of the records in a ground motion set cause collapse of an index archetype model. This process is similar to the concept of Incremental Dynamic Analysis (IDA) as proposed by Vamvatsikos and Cornell (2002). Acceptable values of the collapse margin ratios (*CMR*) are defined in terms of an acceptably low probability of collapse for MCE ground motions, considering uncertainty in collapse fragility. The probability of collapse due to MCE ground motions applied to a population of archetypes is limited to 10%, on average. The probability of collapse for individual archetypes is limited to 20% or twice the average value to evaluate acceptability of potential outliers. The FEMA P695 methodology, as simplified and implemented in this study for collapse evaluation, is summarized in the following steps:

### 8.2.1 Development of Models

The FEMA P695 methodology requires only nonlinear models of the seismic-force-resisting system for collapse evaluation. However, nonlinear models of the gravity-force-resisting system were also included in the collapse evaluation presented in this study to explicitly assess its influence on the collapse capacity of the structural system. The FEMA P695 methodology writes that the analytical models should, to the extent possible, include explicit simulation of all significant deterioration mechanisms that could lead to structural collapse. Models need to be calibrated using test data at the material, component or assembly level or other substantial evidence to verify their ability to simulate expected nonlinear behavior. In this study, the nonlinear models were initially calibrated using existing experimental data of steel components. Subsequently, these nonlinear models were refined based on the experimental results obtained from the two series of hybrid simulations presented in Section 7.

### 8.2.2 Analysis of Models

Collapse assessment is conducted using results from both nonlinear static (pushover) and nonlinear dynamics (response history) analysis procedures. Nonlinear dynamic analyses are employed to estimate median collapse capacities ($\hat{S}_{CT}$) and collapse margin ratios (*CMR*). A set of 22 ground motion pairs from sites located greater than or equal to 10 km from fault rupture, referred in the methodology as the Far-Field record set, were used for collapse assessment using nonlinear dynamic analysis. Table 8-1 summarizes the Far-Field ground motion set.

**Table 8-1 Summary of Far-Field ground motion record set for collapse assessment (FEMA, 2009)**

| Pair No. | EQ ID | Mag. | Year | Event | Fault Type | Station Name | Campbell Dist. (km) |
|---|---|---|---|---|---|---|---|
| 1 | 12011 | 6.7 | 1994 | Northridge | Thrust | Beverly Hills – Mulhol | 17.2 |
| 2 | 12012 | 6.7 | 1994 | Northridge | Thrust | Canyon Country – WLC | 12.4 |
| 3 | 12041 | 7.1 | 1999 | Duzce, Turkey | Strike-slip | Bolu | 12.4 |
| 4 | 12052 | 7.1 | 1999 | Hector Mine | Strike-slip | Hector | 12.0 |
| 5 | 12061 | 6.5 | 1979 | Imperial Valley | Strike-slip | Delta | 22.5 |
| 6 | 12062 | 6.5 | 1979 | Imperial Valley | Strike-slip | El Centro Array #11 | 13.5 |
| 7 | 12071 | 6.9 | 1995 | Kobe, Japan | Strike-slip | Nichi-Akashi | 25.2 |
| 8 | 12072 | 6.9 | 1995 | Kobe, Japan | Strike-slip | Shin-Osaka | 28.5 |
| 9 | 12081 | 7.5 | 1999 | Kocaeli, Turkey | Strike-slip | Duzce | 15.4 |
| 10 | 12082 | 7.5 | 1999 | Kocaeli, Turkey | Strike-slip | Arcelik | 13.5 |
| 11 | 12091 | 7.3 | 1992 | Landers | Strike-slip | Yermo Fire Station | 23.8 |
| 12 | 12092 | 7.3 | 1992 | Landers | Strike-slip | Coolwater | 20.0 |
| 13 | 12101 | 6.9 | 1989 | Loma Prieta | Strike-slip | Capitola | 35.5 |
| 14 | 12102 | 6.9 | 1989 | Loma Prieta | Strike-slip | Gilroy Array #3 | 12.8 |
| 15 | 12111 | 7.4 | 1990 | Manjil, Iran | Strike-slip | Abbar | 13.0 |
| 16 | 12121 | 6.5 | 1987 | Superstition Hills | Strike-slip | El Centro Imp. Co. Cent | 18.5 |
| 17 | 12122 | 6.5 | 1987 | Superstition Hills | Strike-slip | Poe Road (temp) | 11.7 |
| 18 | 12132 | 7.0 | 1992 | Cape Mendocino | Thrust | Rio Dell Overpass | 14.3 |
| 19 | 12141 | 7.6 | 1999 | Chi-Chi, Taiwan | Thrust | CHY101 | 15.5 |
| 20 | 12142 | 7.6 | 1999 | Chi-Chi, Taiwan | Thrust | TCU045 | 26.8 |
| 21 | 12151 | 6.6 | 1971 | San Fernando | Thrust | LA – Hollywood Stor | 25.9 |
| 22 | 12171 | 6.5 | 1976 | Friuli, Italy | Thrust | Tolmezzo | 15.8 |

Scaling of ground motion records in the methodology involves two steps. First, individual records in the set are normalized by their respective peak ground velocity. This step is intended to remove unwarranted variability between records due to inherent differences in event magnitude. Second, the normalized ground motions are collectively scaled (or "anchored") to a specific ground motion intensity such that the median spectral acceleration of the record matches the spectral acceleration at the fundamental period ($T$) of the index archetype being analyzed which is calculated using the period formula of Section 12.8.2.1 of ASCE/SEI 7-05 provided below:

$$T = C_u T_a = C_u \, C_t \, h_n^x \geq 0.25 \text{ sec.} \tag{8-1}$$

where $h_n$ is the building height, the values of the coefficient, $C_u$, are given in Table 12.8-1 of ASCE/SEI 7-05, and values of period parameters $C_t$ and $x$ are given in Table 12.8-2 of ASCE/SEI 7-05. In the

collapse evaluation, the ground motions are systematically scaled to increasing intensities until median collapse is established. Median collapse is the ground motion intensity in which half of the ground motions records cause collapse of the structural system. Unlike the procedure proposed by Vamvatsikos and Cornell (2002) in which a full increment dynamic analysis (IDA) is required, the FEMA P695 methodology only requires calculating the response of the structure at the median collapse point. Also, these two methods are different in terms of scaling the ground motions. In the FEMA P695 methodology, the set of ground motion intensities are defined in terms of the median spectral intensity of the far-field record set rather than the spectral intensity of each individual record as in the IDA.

### 8.2.3 Evaluate the Performance

The results from the nonlinear static and dynamic analyses are used to evaluate the acceptability of the calculated collapse margin ratio (*CMR*). Acceptability is measured by comparing the collapse margin ratio, after some adjustments, to acceptable values that depend on the quality of information used to define the system, total system uncertainty and established limits on acceptable probabilities of collapse. The FEMA P695 methodology limits the probability of collapse due to Maximum Considered Earthquake (MCE) ground motions to 10%. Each performance group is required to meet this collapse probability limit, on average. A limit of twice this value or 20% is suggested as a criterion for evaluating the acceptability of potential "outliers" within a performance group. The collapse margin ratio (*CMR*) can be significantly influenced by the frequency content (spectral shape) of the ground motion set. To account for the effects of spectral shape, a simplified procedure is provided in the FEMA P695 methodology to adjust the median collapse capacities ($\hat{S}_{CT}$) using a spectral shape factor (*SSF*). Consequently, the collapse margin ratio (*CMR*) is also modified to an adjusted collapse margin ratio (*ACMR*) as follows:

$$ACMR = SSF \times CMR \tag{8-2}$$

The spectral shape factor (*SSF*) is a function of the fundamental period (*T*), the period-based ductility ($\mu_T$) and the applicable Seismic Design Category. The spectral shape factor can be obtained from Table 7-1a and Table 7-1b from the FEMA P695 report (2009). A nonlinear static pushover analysis is used to quantify the period-based ductility ($\mu_T$) as shown in Figure 8-1.

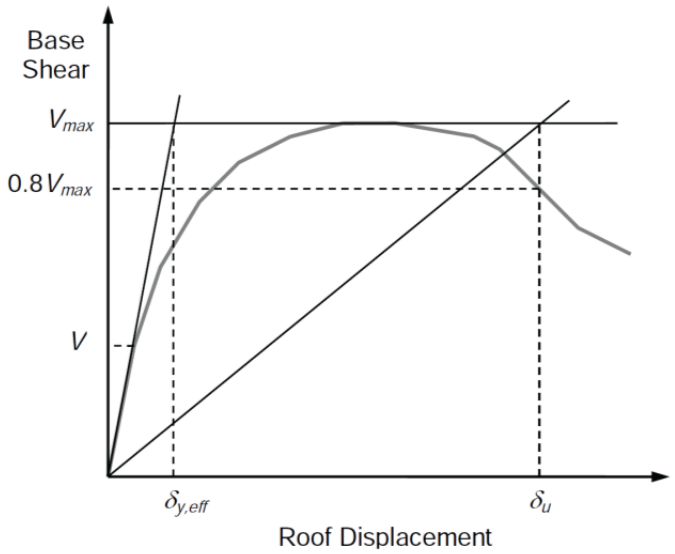


**Figure 8-1 Idealized nonlinear static pushover curve (FEMA, 2009)**

For a given archetype model, the period-based ductility ($\mu_T$) is defined as the ratio of ultimate roof drift displacement ($\delta_u$) to the effective yield roof drift displacement ($\delta_{y,eff}$):

$$\mu_T = \frac{\delta_u}{\delta_{y,eff}} \tag{8-3}$$

The acceptable values of adjusted collapse margin ratio are based on total system uncertainty ($\beta_{TOT}$) and established values of acceptable probabilities of collapse. Many sources of uncertainty contribute to variability in collapse capacity. The following sources of uncertainty are considered in the collapse assessment process:

- Record-to-Record Uncertainty (RTR): uncertainty due to variability in the response of index archetypes to different ground motion records. Based on previous studies using the far-field ground motion record set, a fixed value of record-to-record variability ($\beta_{RTR}$) of 0.40 is assumed in the performance evaluation of systems with significant period elongation (i.e., period-based ductility, $\mu_T \geq 3$). For systems with little or no period elongation, values of record-to-record variability can be reduced as follows (where $\beta_{RTR}$ must be greater than or equal to 0.20):

$$\beta_{RTR} = 0.1 + 0.1\mu_T \leq 0.40 \tag{8-4}$$

- Design Requirements Uncertainty (DR): uncertainty related to the completeness and robustness of the design requirements and the extent to which they provide safeguards against anticipated failure modes. Qualitative values of design requirements-related collapse uncertainty ($\beta_{DR}$) can be obtained from Table 3-1 from the FEMA P695 report and range from $\beta_{DR}$ = 0.10 (superior) to $\beta_{DR}$ = 0.50 (poor).

- Test Data Uncertainty (TD): uncertainty related to the completeness and robustness of the test data used to define the system. This type of uncertainty is closely associated with, but distinct from, modeling-related uncertainty. Qualitative values of test data-related collapse uncertainty ($\beta_{TD}$) can be obtained from Table 3-2 from the FEMA P695 report and range from $\beta_{TD}$ = 0.10 (superior) to $\beta_{TD}$ = 0.50 (poor).

- Modeling Uncertainty (MDL): type of uncertainty related to how well index archetype models represent the full range of structural response characteristics and associated design parameters for the archetype design space and how well the analysis model captures structural collapse behavior through direct simulation or non-simulated component checks. Modeling-related uncertainties ($\beta_{MDL}$), quantified in terms of the quality of index archetype models, can be obtained from Table 5-3 from FEMA (2009) and range from $\beta_{MDL}$ = 0.10 (superior) to $\beta_{MDL}$ = 0.50 (poor).

The total system collapse uncertainty is given by:

$$\beta_{RTR} = \sqrt{\beta_{RTR}^2 + \beta_{DR}^2 + \beta_{TD}^2 + \beta_{MDL}^2} \tag{8-5}$$

Acceptable performance is defined in the FEMA P695 methodology by two basic collapse prevention objectives:

- The probability of collapse for MCE ground motions is approximately 10%, or less, on average across a performance group.
- The probability of collapse for MCE ground motions is approximately 20%, or less, for each index archetype within a performance group.

This is achieved when the adjusted collapse margin ratios (*ACMR*) for each index archetype meet the following two criteria:

$$\overline{ACMR_i} \geq ACMR_{10\%} \quad (8\text{-}6)$$

$$ACMR_i \geq ACMR_{20\%} \quad (8\text{-}7)$$

While $ACMR_i$ is the adjusted collapse margin ratio for each index archetype within a performance group, $\overline{ACMR_i}$ is the average value of the adjusted collapse margin ratio for the performance group. Table 7-3 of the FEMA P695 report provides acceptable values of adjusted margin ratio $ACMR_{10\%}$ and $ACMR_{20\%}$, based on the total system collapse uncertainty and values of acceptable collapse probability, taken as 10% and 20%, respectively.

## 8.3 Collapse Evaluation of a Special Steel Moment Frame Building Structure

The steel moment frame building structure presented in Section 4 was evaluated using the FEMA P695 methodology as simplified and summarized earlier in this section. The seismic-force-resisting system of the prototype building structure consists of special steel moment frames with reduced beam sections (RBS). As mentioned previously in Section 4, the building structure was designed according to the SEI/ASCE-02 (2002), AISC (2005), and IBC (2003) design provisions. The building was assumed to be located on Soil type D in Los Angeles. The Maximum Considered Earthquake (MCE) spectral response acceleration at short ($S_S$) and 1.0-second ($S_1$) periods were assumed to be 1.5g and 0.9g, respectively. The design spectral response acceleration parameters $S_{DS}$ and $S_{D1}$ are 1.0g and 0.6g, respectively.

The analytical models developed for the collapse evaluation also included explicit models of the gravity-force-resisting system to assess its influence on the collapse capacity of the building structure. The analytical models were initially calibrated using an existing experimental database of steel components (Lignos and Krawinkler, 2012, Liu and Astaneh-Asl, 2000b) and subsequently refined using the experimental results of the two half-scale moment and gravity frame subassemblies tested via hybrid simulation. The inelastic response of the building structure was simulated using a concentrated plasticity model as described in Section 6.2.1. Three numerical models, progressively more sophisticated, were developed for the collapse evaluation and summarized in Table 8-2.

The first analytical model (MF model), used as the baseline case for the subsequent two cases, consists of a half-scale model of a steel moment frame system as described previously in Section 6.2.1 and Section 6.2.2. The effects of the composite floor slab were not included in this model. The second model (CMF model) is similar to the previous MF model but included the effects of the composite floor slab as described in Section 6.2.3. In this model, the elastic stiffness of the girder was increased by a factor of

1.20 (to account for stiffening of the concrete slab) and the modeling parameters of the modified-IMK model for girder elements were modified according to the recommendation of Lignos *et al.* (2011b). Finally, the third model (CMF+GF model) includes the frames of the gravity-force-resisting system (as described previously in Section 6.3) in addition to the steel moment frame structure as modified to include the effect of the composite floor slab. These three numerical models were developed to assess the influence of the composite floor slab and gravity framing system, two modeling aspects typically ignored in collapse seismic assessment of structures.

**Table 8-2 Summary of analytical models used in collapse evaluation of prototype building structure**

| Model ID | Model Description |
|---|---|
| MF | Analytical model of a half-scale bare steel moment frame as described in Section 6.2 except for the modifications presented in Section 6.2.3 to include slab effects. A leanin g column was modeled to include the P-Delta effects. |
| CMF | Analytical model of a half-scale steel moment frame as described in Section 6.2 includi ng the effect of the composite floor slab as described in Section 6.2.3. |
| CMF+GF | Analytical model of the half-scale steel moment frame as described in Section 6.2 inclu ding the effect of the composite floor slab as described in Section 6.2.3 and the gravity -force-resisting system. |

### 8.3.1 Calibration of Analytical Models

The numerical models of the moment and gravity frame structures, previously calibrated prior to the hybrid simulations, were refined based on observations of the experimental results of the two series of hybrid simulations presented previously in Section 7. A brief description of the refinement process of the numerical models is provided below.

#### 8.3.1.1 Calibration of Numerical Model of Moment Frame

The results of the first series of hybrid simulations clearly showed that the numerical model of the moment frame underestimated the post-capping plastic rotation capacity ($\theta_{pc}$) of the W12×30 columns as shown in Figure 7-16(g) and Figure 7-16(h). As mentioned before, the post-capping plastic rotation capacity is one of the most influential parameters in collapse assessment of structural systems (Ibarra and Krawinkler, 2005) and, therefore, accurate estimates of this modeling parameter are important. Also, the yield moment capacity ($M_y$) of the W12×30 columns was previously overestimated, mainly due to the 1.17 factor used to increase the yield moment capacity to an effective value to account for isotropic hardening. These two modeling parameters ($\theta_{pc}$, $M_y$) were calibrated as shown in Figure 8-2.

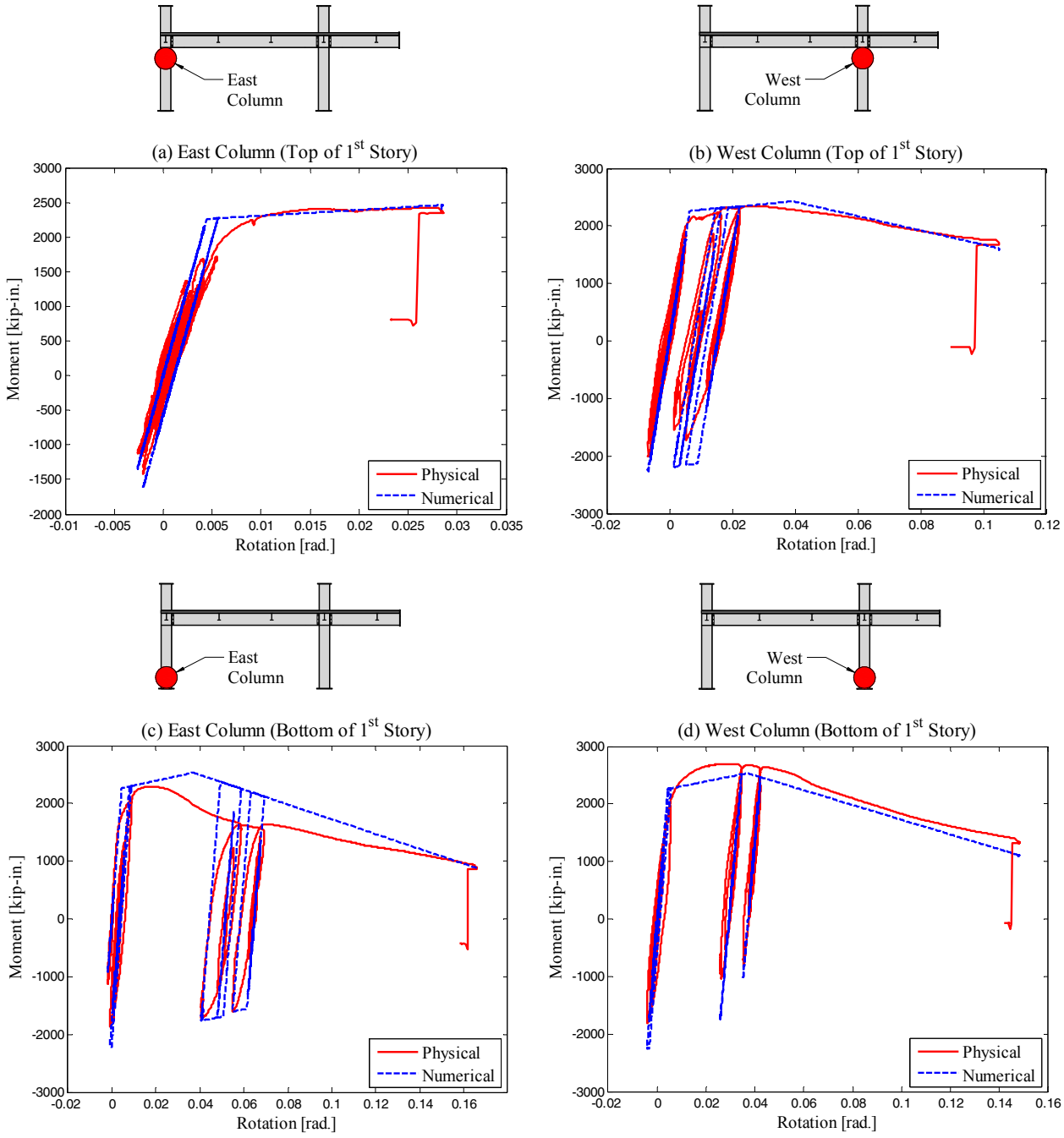


**Figure 8-2 Calibration of modified-IMK hysteretic model using data from Hybrid Simulation #1**

It can be seen in Figure 8-2 that calibration was based on the experimental moment-rotation relationships obtained from four plastic-hinge regions at the W12×30 columns of the moment frame subassembly used in the first series of hybrid simulations. The location of the plastic-hinge regions from which the experimental data was obtained is indicated with a sketch above each plot in Figure 8-2.

Table 8-3 summarizes modeling parameters of the modified-IMK model for the W12×30 columns. It can be seen in Figure 8-2 that that moment-rotation relationships of the numerical model with the calibrated parameters matches, on average, the four experimental moment-rotation relationships. The pre-capping plastic rotation ($\theta_p$) and reference cumulative rotation capacity ($\Lambda$), also included in Table 8-3 for completeness, were not modified since the experimental data does not clearly and consistently suggests a better estimate. A larger number of loading cycles as compared to those in the hybrid simulations are needed to obtain better estimates of the reference cumulative rotation capacity ($\Lambda$).

**Table 8-3 Calibration of modified-IMK model parameters using data from Hybrid Simulation #1**

| | Parameters per Lignos and Krawinkler (2011) | Calibrated Parameters using Hybrid Simulation #1 |
|---|---|---|
| Effective Yield Moment, $M_y$ [kip-in.] | $1.17M_{y,p}$ | $1.00M_{y,p}$ |
| Pre-Capping Plastic Rotation, $\theta_p$ [rad.] | 0.033 | 0.033 |
| Post-Capping Plastic Rotation, $\theta_{pc}$ [rad.] | 0.153 | 0.200 |
| Reference Cumulative Rotation Capacity, $\Lambda$ | 0.977 | 0.977 |

[1] $M_{y,p}$: predicted yield moment defined as plastic modulus ($Z$) times measured material yield stress.

As mentioned earlier in Section 7, the experimental moment-rotation relationships for girders of the moment frame subassembly should be carefully used to assess the numerical model of the moment frame structure since very approximate estimates of bending moments were obtained along the girders as explained in Section 7.2.2.2. Recognizing this, the experimental data previously presented in Figure 7-26 suggested that the numerical model of the moment frame reasonably predicted the yield moment capacity ($M_y$) under positive and negative bending, pre-capping ($\theta_p$) and post-capping ($\theta_{pc}$) plastic rotation capacity of the composite W14×26 girder. Because of this, the modeling parameters of girders are not further refined in this section. Similar observations were made for the numerical model of the panel zone. In summary, the numerical model of the moment frame structure was calibrated as follows:

- The yield moment capacity ($M_y$) and post-capping plastic rotation capacity ($\theta_{pc}$) of the W12×30 column (located at the first and second stories) were modified according to Table 8-3.
- Since no experimental data was obtained for the W12×19 column (located at the third and fourth stories), only the 1.17 factor used to increase the yield moment capacity to an effective value was removed.

- No other modeling parameters including those for girders or panel zones were calibrated or modified.
- A fixed support boundary condition was assumed at the base of the moment frame structure.

The aforementioned refinements of the modeling parameters were implemented in the numerical model of the special steel moment frame used to conduct the FEMA P-695 analysis in Section 8.3. In an attempt to further assess the accuracy of the hybrid simulations presented in Section 7, the response of the first series of hybrid simulations is numerically reproduced herein through coupled simulations which were updated with the calibrated modeling parameters described above. Since the only difference between the hybrid simulations and corresponding coupled simulations is the physical sub-structure, only the slave OpenSees script of the couple model, which simulates the response of the physical sub-structure, was updated with the calibrated modeling parameters to better match the hybrid simulations results.

To this end, the slave OpenSees script for the coupled simulations was updated as follows. The modeling parameters of the W12×30 column were modified according to Table 8-3. Since it was observed that Hybrid Model #1 is more flexible than the corresponding numerical model, some modifications were made to the flexibility of the support boundary conditions. While the support flexibility at the east column of the physical sub-structure of the moment frame was closely estimated in the numerical model as shown previously in Figure 7-30, it was noticed that the flexibility of the west column, which could not be obtained experimentally, was possibly larger than for the east column due to the arrangement of anchor bolts near the column used to attach the interface 9'×5'×1½" base plates to the strong floor. While the east column is located near four closely-spaced anchor bolts, larger spaced anchor bolts were provided around the west column. Because of this, it was assumed that the stiffness of the support boundary condition at the west column was 75% of that of the east column. Finally, the corotational transformation formulation was selected in the slave OpenSees script to better capture the response of the physical sub-structure at large deformations.

Figure 8-3 compares the roof drift ratio response of the coupled simulations (post-test predictions with updated slave OpenSees script only) and Hybrid Simulation #1. It can be noted that the post-test predictions are closer than the pre-test predictions presented previously in Figure 7-6. The fundamental period of vibration of the coupled model is closer to that of Hybrid Model #1 as observed in Figure 8-3(a). However, a difference in residual roof drift ratio at the end of hybrid simulation HS01-160% can

still be observed. In summary, it can be noticed that the hybrid simulations and numerical simulations predict the response of the frame structure with similar levels of accuracy.

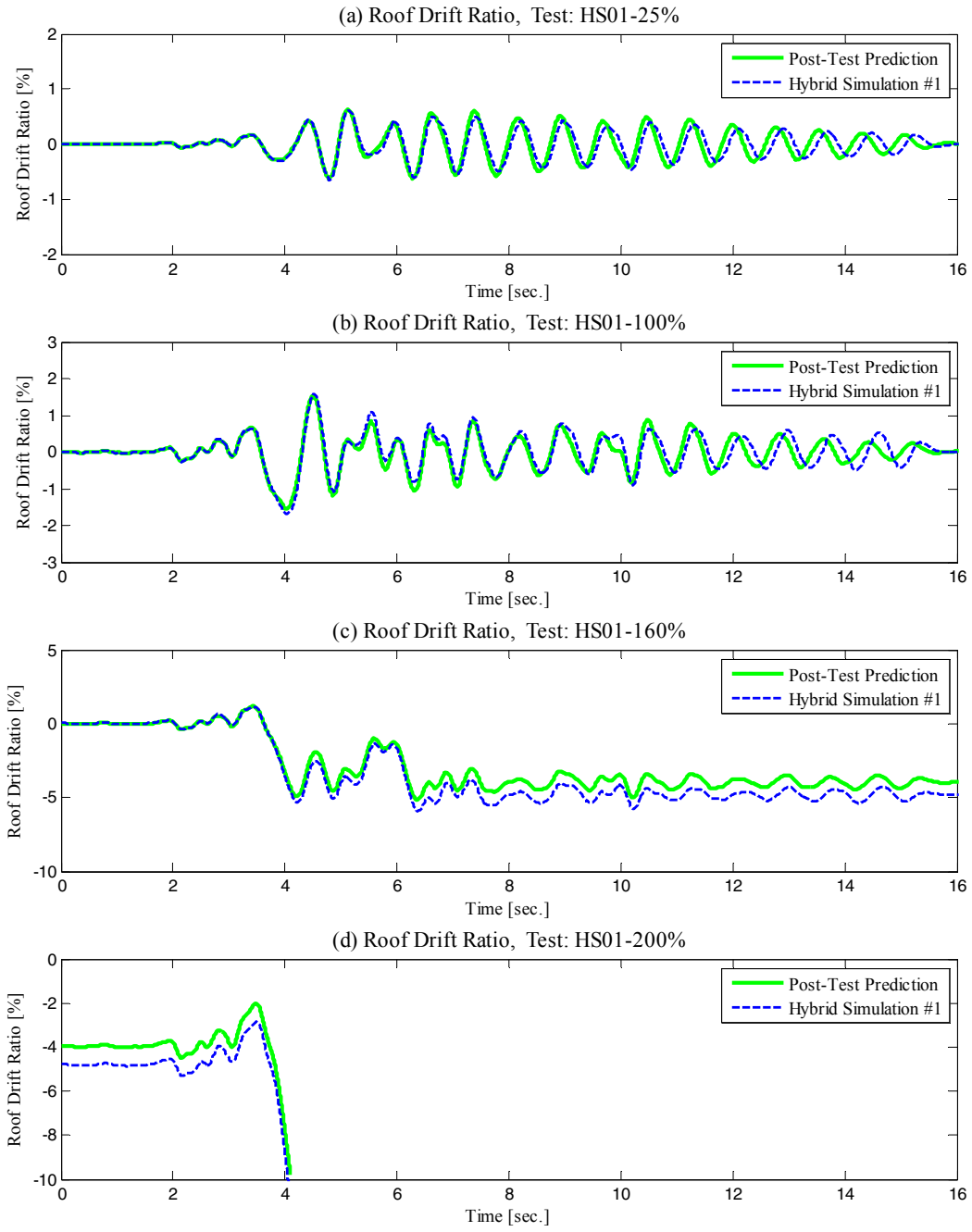


**Figure 8-3 Roof drift ratio response for calibrated numerical simulation after test and Hybrid Simulation #1**

#### 8.3.1.2 Calibration of Numerical Model of Gravity Frame

The numerical model of the gravity frame, which was initially calibrated using the guidelines and experimental data of Liu and Astaneh-Asl (2000b, 2004), was subsequently refined using the experimental results of the half-scale gravity frame subassembly tested via hybrid simulation. A description of the post-test calibration of the numerical model of the gravity frame is provided below.

Figure 8-4 compares experimental moment-rotation relationships for the shear-tab connection "C" of the gravity frame subassembly with numerical predictions using the Pinching4 hysteretic model calibrated prior to the hybrid simulations (see Section 6.3.3). The location of the shear-tab connection "C" within the gravity frame subassembly is indicated in the sketch above Figure 8-4. The data from the second series of hybrid simulations is presented in Figure 8-4(a) through Figure 8-4(d). Figure 8-4(e) shows the data of the Cyclic02 test and Figure 8-4(f) presents the response of the shear-tab connection for the combined hybrid simulation (HS02) and cyclic test (Cyclic02) to capture the cumulative damage in the numerical model. For comparison purposes, the rotations of the physical response in Figure 8-4 were used as input for the Pinching 4 hysteretic model. Since the pre-test calibration of the Pinching4 hysteretic model was based on the guidelines of Liu and Astaneh-Asl (2004), the moment-rotation envelope constructed using such guidelines is also provided in Figure 8-4 to establish comparisons.

Some observations can be made based on the results presented in Figure 8-4. The pre-test calibration of the Pinching4 hysteretic model does not reproduce the hysteretic response of the shear-tab connections under low-amplitude loading as shown in Figure 8-4(a). Although the pinched hysteretic response of the shear-tab connection is reasonably captured as shown in Figure 8-4(b) and Figure 8-4(c), the hysteretic model does trace the response of the shear-tab connections after binding of the beam flange on the column flange. In general, it can be seen that the Pinching4 hysteretic model (as calibrated prior to the hybrid simulations) as well as the guidelines of Liu and Astaneh-Asl under-predicts the moment-rotation envelope of the shear-tab connection "C". Although the numerical models seem to predict very reasonably the moment strength of the shear-tab connections as shown in Figure 8-4(f), the rate at which such moment strength deteriorates upon cyclic loading was over-estimated in the pre-test calibration of the Pinching4 model. As discussed earlier in Section 7.3.2.2, this was attributed to two reasons. First, the strength deterioration parameters of the Pinching4 hysteretic model were calibrated based on cyclic test results of Specimen 6A of Liu and Astaneh-Asl. Specimen 6A was subjected to a larger number of cycles (SAC symmetric loading protocol) as compared to the hybrid simulations and the response of Specimen 6A under large deformation was governed by fracture of shear-tab plate. Second, the material yield

strength of the shear-tab plates for the gravity frame subassembly including connection "C" was 30% larger than for Specimen 6A. The strength deterioration at large deformation is an important parameter in collapse predictions and good estimates should be obtained for the gravity frame.

Based on the above observations, the modeling parameters of the Pinching4 hysteretic model were refined using experimental information of the shear-tab connection "C". Figure 8-5 presents the experimental response of the shear-tab connection "C" as well as numerical predictions using the Pinching4 hysteretic model as calibrated after the test. To trace the moment-rotation response of the shear-tab connections after binding of the beam flange on the column flange, which is characterized by an increasing stiffness and strength at large rotations, a rotational gap spring element (elastic-perfectly plastic gap material in OpenSees) was modeled in parallel with the rotation spring element with the Pinching4 hysteretic model. It can be seen that the post-test calibration of the Pinching4 hysteretic model together with the rotational gap spring element reproduce very closely the response of the shear-tab connection.

Figure 8-6 compares the model for the shear-tab connection calibrated after the test with experimental data obtained for the shear-tab connection "A". It can be seen that the calibrated parameters for the Pinching4 hysteretic model also predicts reasonably well the response of the shear-tab connection "A". Therefore, the numerical model for the shear-tab connections consisting of two rotational springs with the Pinching4 hysteretic model and the gap material, as calibrated after the test, were used for the collapse evaluation in this section. The experimental information of shear-tab connection "C" was used to calibrate the modeling parameters of the Pinching4 hysteretic model since this data is more reliable than the other two shear-tab connections ("B" or "C") as explained in Section 5.3.3.1.

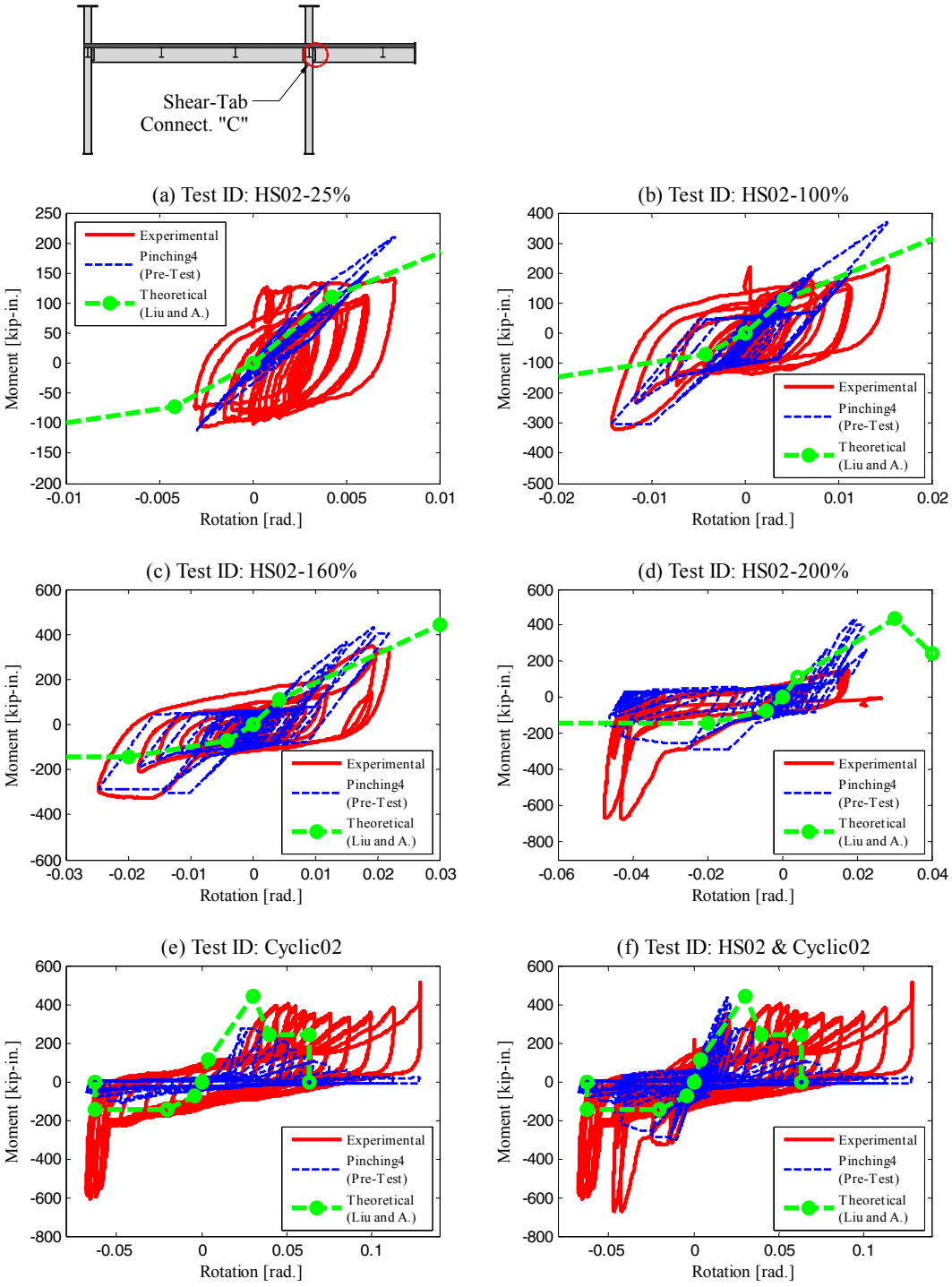


**Figure 8-4 Comparison of experimental moment-rotation relationships for shear-tab connection "C" versus numerical predictions using Pinching4 model (calibrated before the test) and theoretical envelope of Liu and Astaneh-Asl (2000b)**

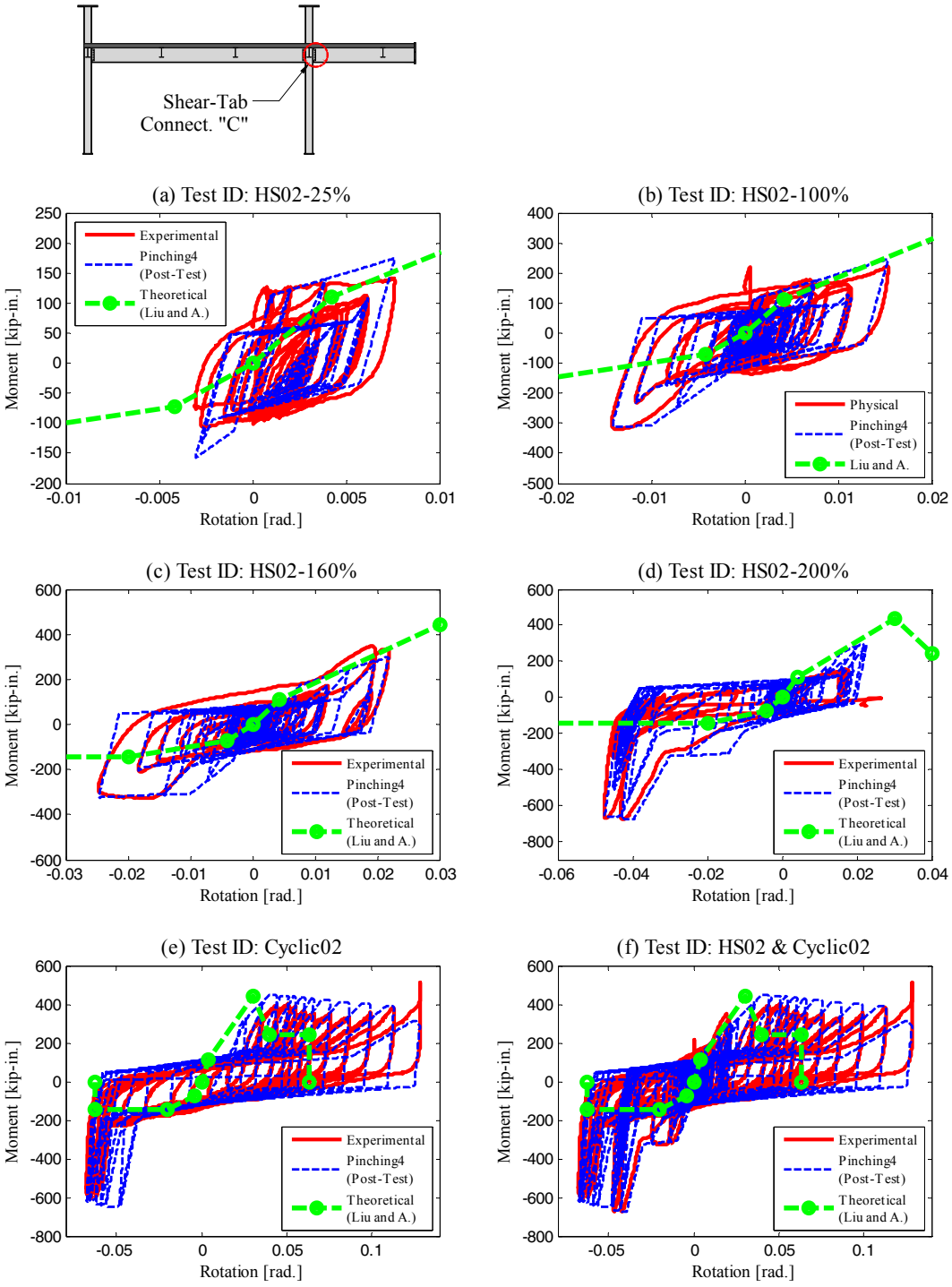


**Figure 8-5 Comparison of experimental moment-rotation relationships for shear-tab connection "C" versus numerical predictions using Pinching4 model (calibrated after the test) and theoretical envelope of Liu and Astaneh-Asl (2000b)**

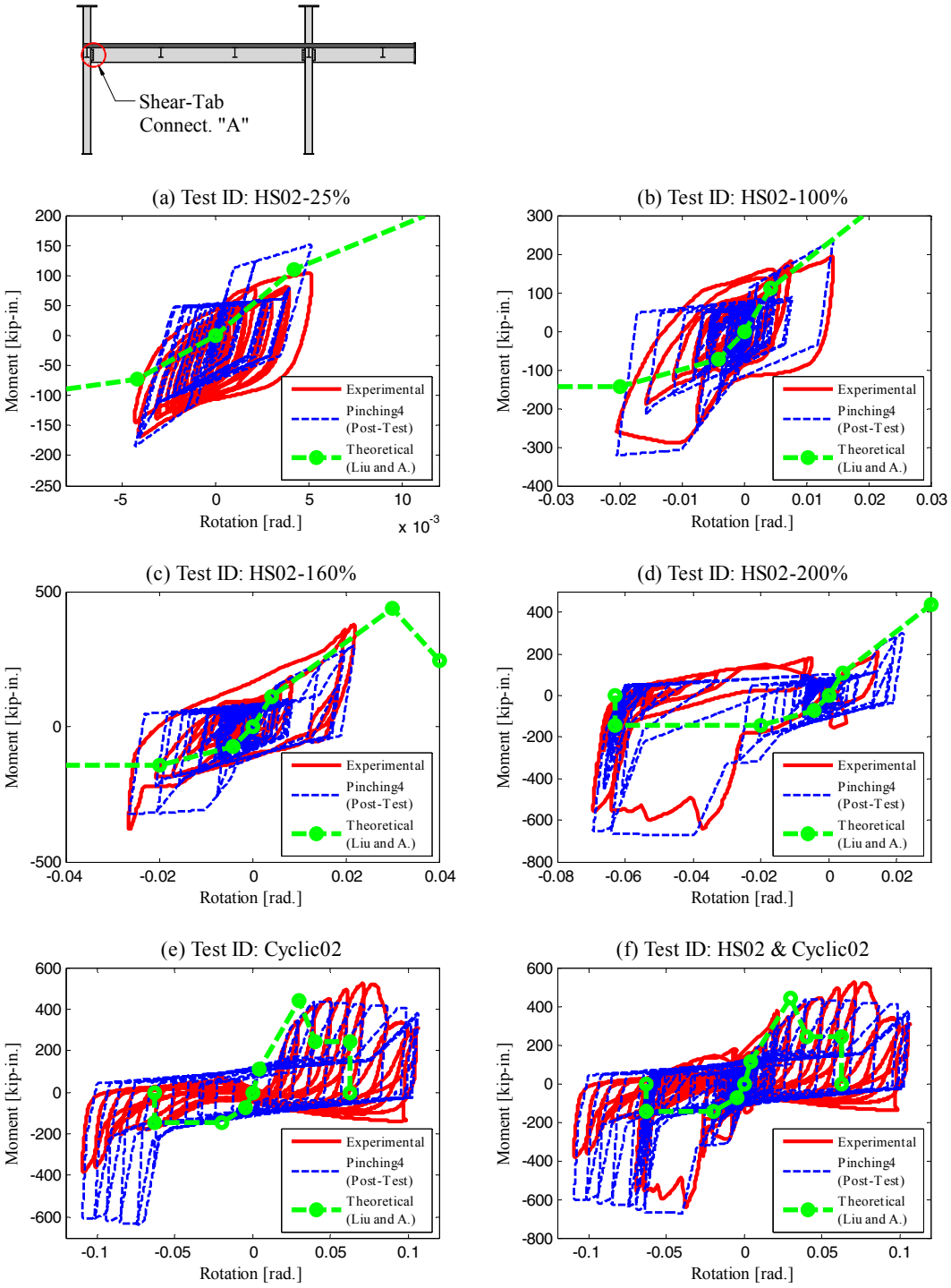


**Figure 8-6 Comparison of experimental moment-rotation relationships for shear-tab connection "A" versus numerical predictions using Pinching4 model (calibrated before the test) and theoretical envelope of Liu and Astaneh-Asl (2000b)**

### 8.3.2 Results from Nonlinear Static Analysis

In the methodology as summarized in the previous section, the results from nonlinear static analysis are used to calculate the period-based ductility ($\mu_T$) defined by Equation 8-3. The vertical distribution of the lateral force used in the nonlinear static analysis was proportional to the fundamental mode shape of the numerical models. Figure 8-7 presents the lateral force versus the roof drift ratio (pushover curve) for the steel moment frame structures with ("CMF" model) and without the composite floor slab ("MF" model). The lateral forces in Figure 8-7 were normalized by the corresponding seismic weight. The ultimate roof drift displacement ($\delta_u$) and the effective yield roof drift displacement ($\delta_{y,eff}$), both normalized by the building roof height, are indicated in Figure 8-7. The period-based ductility ($\mu_T$) was calculated with these two parameters using Equation 8-3 for the "MF" and "CMF" analytical models and are equal to $\mu_T = 6.4$ and $\mu_T = 8.0$, respectively. The period-based ductility of the third model ("CMF+GF" model) can be safely assumed to be larger than 8.0 since the addition of the gravity frames reduces the post-capping strength deterioration (negative slope) of the moment frame structure shown in Figure 8-7(b) and consequently results in larger values of period-based ductility. This was previously shown in Figure 7-38. Also, the moment and gravity frames in the "CMF+GF" model were simulated through coupled simulations. A coupled simulation in OpenSees and OpenFresco is not compatible with the nonlinear static (pushover) solvers.

### 8.3.3 Results from Nonlinear Dynamic Analysis

Nonlinear dynamic analyses were conducted to calculate the median value of the collapse ground motion intensity ($\widehat{S}_{CT}$) and the collapse margin ratio ($CMR$). Although not required, a full incremental dynamic analysis was carried out. The far-field ground motion set previously presented in Table 8-1 was used to conduct the incremental dynamic analysis on the three analytical models described in Table 8-2. Scaling of the normalized ground motion records was based on the median spectral acceleration of the ensemble of ground motion records at the scaled fundamental period of the building structure of 0.64 sec. defined by Equation 8-1 (fundamental period of steel moment frame calculated with the following parameters: $h_n = 612$ in., $C_u = 1.4$, $C_t = 0.028$, $x = 0.80$) and scaled down by the time scale factor of $S^{1/2} = 0.707$ defined in Section 4.4.1.

Figure 8-8 presents results of the incremental dynamic analysis conducted for the three analytical models presented in Table 8-2, namely, bare steel moment frame (MF model), steel moment frame with

composite floor slab (CMF model) and steel moment frame and gravity frame with composite floor slab (CMF+GF model). Empirical collapse fragility curves, constructed from the IDA results, are provided in Figure 8-8 where lines of bet-fit lognormal cumulative distribution functions are provided. Median values ($\mu$) and dispersion factor ($\beta$) are also provided. The horizontal dashed line in Figure 8-8(a), Figure 8-8(c) and Figure 8-8(e) indicate the Maximum Considered Earthquake ground motion intensity ($S_{MT}$). The median values of the collapse ground motion intensity ($\hat{S}_{CT}$) are indicated in Figure 8-8(b), Figure 8-8(d) and Figure 8-8(f). The collapse criterion was the ground motion intensity at which the IDA curve becomes flat. Also, convergence of the coupled simulations for the "CMF+GF" model was not achieved for all the ground motions. Therefore, a total of ten ground motions were removed for the IDA analysis as seen in Figure 8-8 due to lack of convergence of the simulations.

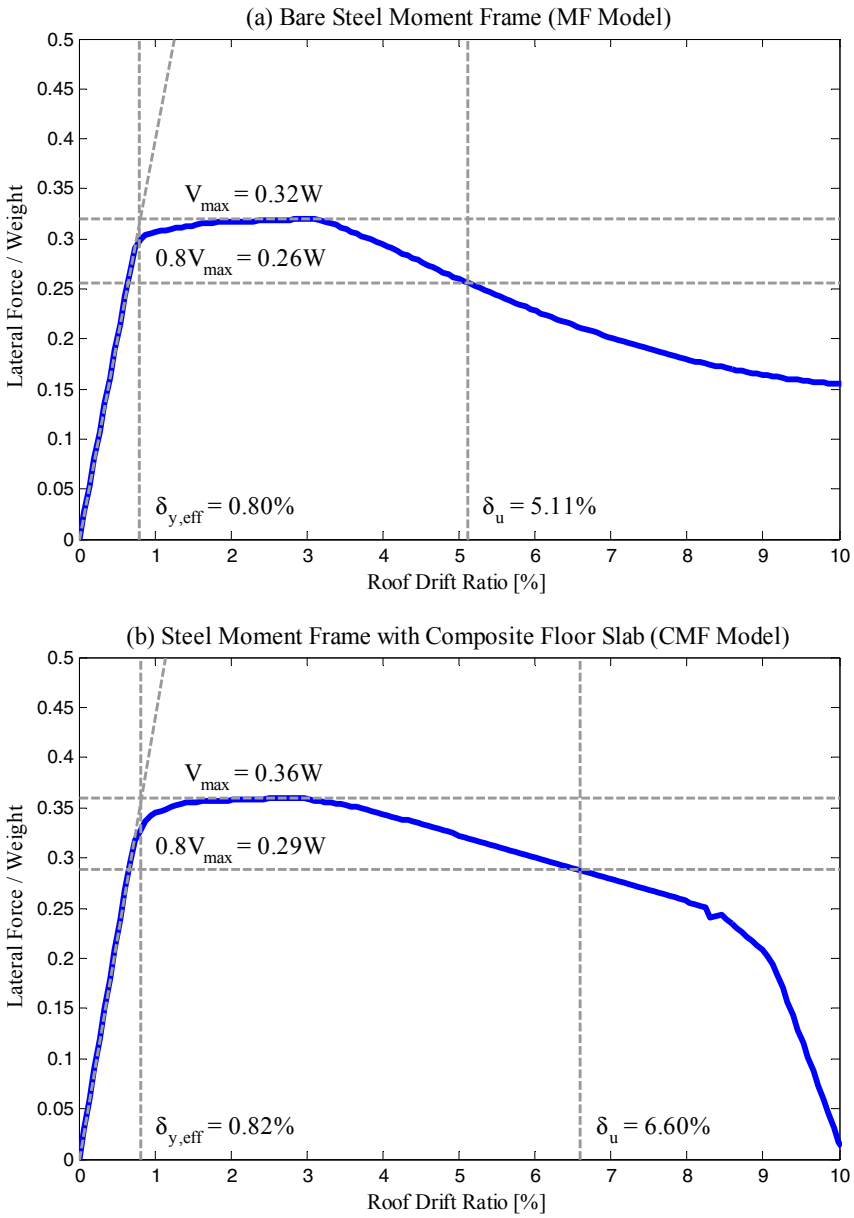


**Figure 8-7 Results of nonlinear static (pushover) analysis for steel moment frame building structure**

(a) IDA curves for "MF" Model

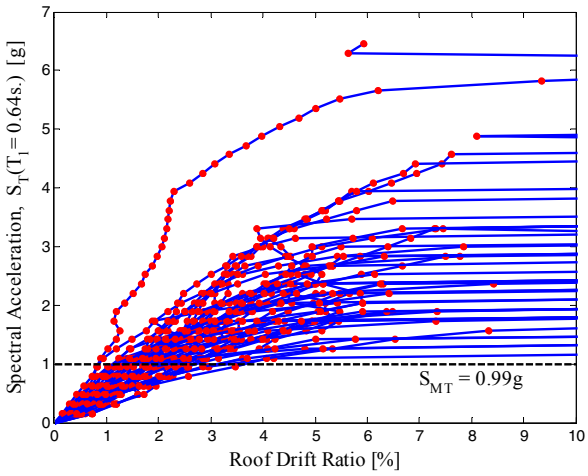


(b) Collapse fragility curve for "MF" Model

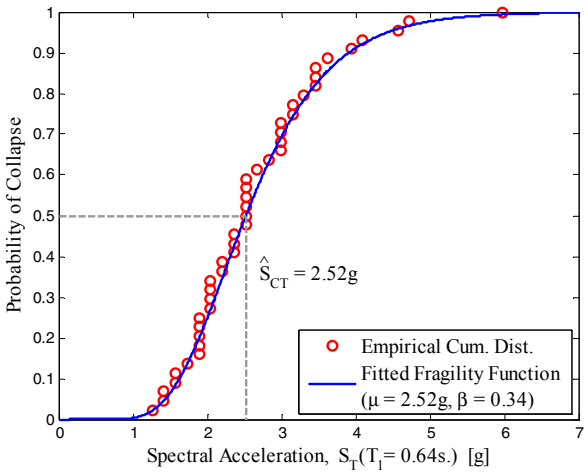


(c) IDA curves "CMF" Model

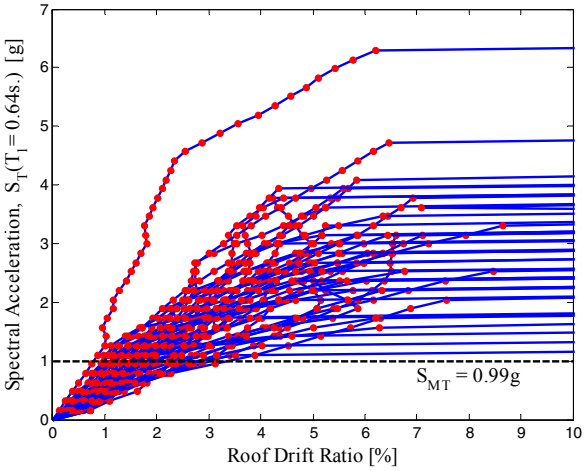


(d) Collapse fragility curve for "CMF" Model

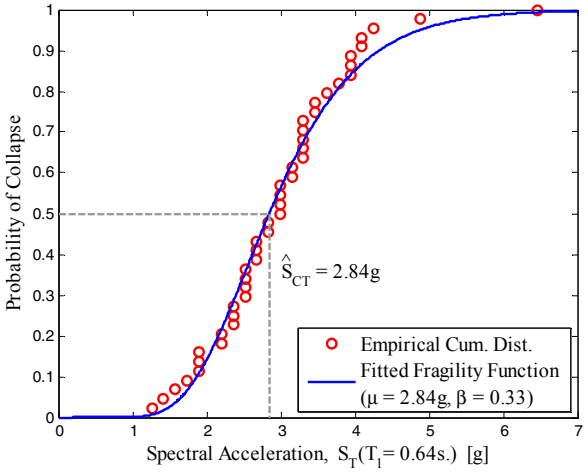


(e) IDA curves for "CMF+GF" Model

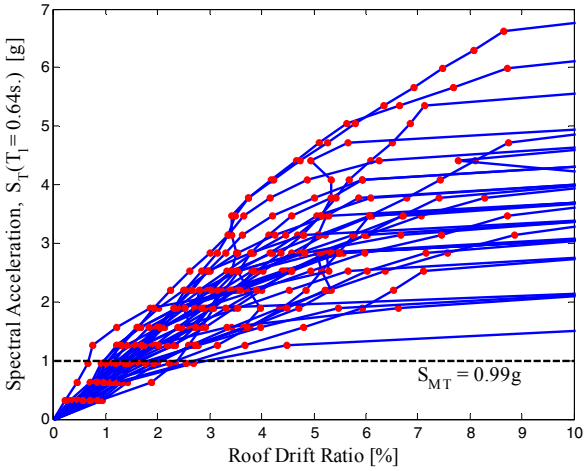


(f) Collapse fragility curve "CMF+GF" Model

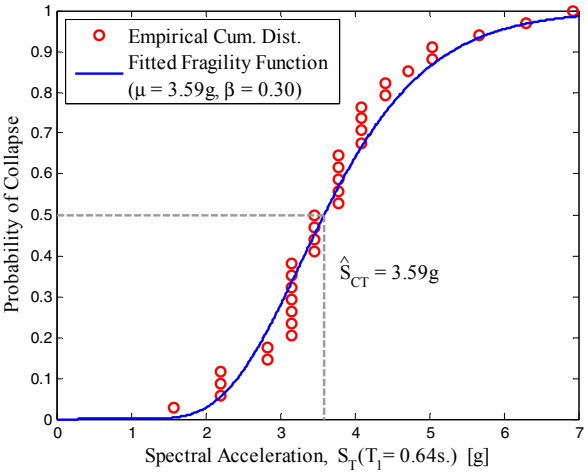


**Figure 8-8 Results of incremental dynamic analytic for steel moment frame building structure**

Based on the results obtained from the incremental dynamic analysis, collapse margin ratios (*CMR*) were calculated for the three analytical models of the building structure which are summarized in Table 8-4 together with selected results of the incremental dynamics analysis including the median collapse capacity ($\hat{S}_{CT}$), the uncertainty factor ($\beta$) associated with the ground motion uncertainty, and the collapse probability at 150% of the MCE ground motion (since the collapse probabilities at the MCE ground motion intensity are very small for the moment frame building structure in the direction of loading).

**Table 8-4 Summary of incremental dynamic analysis results for collapse evaluation**

| Model | Median Collapse Capacity ($\hat{S}_{CT}$) | Uncertainty ($\beta$) | Collapse Margin Ratio (*CMR*) | Collapse Probability at 150% MCE (%) |
|---|---|---|---|---|
| Moment Frame (MF) | 2.52 | 0.34 | 2.55 | 6.2 |
| Moment Frame with Floor Slab (CMF) | 2.84 | 0.33 | 2.87 | 2.4 |
| Moment and Gravity Frames with Floor slab (CMF+GF) | 3.59 | 0.30 | 3.63 | 0.2 |

As expected, it can be seen in Table 8-4 that the median collapse capacity increases as slab effects and gravity frames are included in the analytical models. However, while the inclusion of slab effects results in a 13% increment of the median collapse capacity with respect the moment frame (MF) model, a 42% increment is observed when the gravity frames were also included. Note that the composite floor slab and the gravity frames have a very positive influence on the collapse probability of the frame structure.

### 8.3.4 Calculation of Acceptable Collapse Margin Ratios ($ACMR_{10\%}$, $ACMR_{20\%}$)

Acceptable values of the adjusted collapse margin ratios for 10% and 20% probability of collapse for MCE ground motions ($ACMR_{10\%}$ and $ACMR_{20\%}$, respectively) are based on the total system uncertainty ($\beta_{TOT}$) which is calculated combining four previously-described sources of uncertainties ($\beta_{RTR}$, $\beta_{TD}$, $\beta_{TD}$, and $\beta_{MDL}$) using Equation 5-1. A brief description of the selection of these uncertainty parameters is provided below using similar criteria to that provided in the examples of the FEMA P695 report.

A value of $\beta_{RTR} = 0.40$ is selected for the record-to-record uncertainty since values of the period-based ductility obtained in Section 8.3.2 are $\mu_T \geq 3$. Since the prototype office building was designed according to the AISC (2005), SEI/ASCE-02 (2002) and IBC (2003) design provisions, the design requirement uncertainty was categorized as superior (A). Such design provisions represent many years of development

and include lessons learned from a number of major earthquakes (FEMA, 2009). Therefore, a value of $\beta_{DR} = 0.10$ is selected for the design requirement uncertainty.

To quantify the uncertainty related to the quality of data ($\beta_{TD}$), it is recognized that the numerical models of the steel moment frame were calibrated using a large test database of beam components (Lignos and Krawinkler, 2012). The test database included limited beam components with the composite floor slab but did not include column elements. Further, the hysteretic model used for the column does not account for axial force-bending moment (P-M) interaction. The numerical model of the gravity frame was calibrated based on a very limited test data of shear-tab connections (Liu and Astaneh-Asl, 2000b). The two aforementioned numerical models were subsequently refined using the experimental results of the two series of hybrid simulations conducted herein. In view of this and following recommendations in the FEMA P695 report, the test data uncertainty is selected as good (B) and consequently a value of $\beta_{TD} = 0.20$ is selected. According to the guidelines of Section 5.7 of the FEMA P695 report, the model-related uncertainty is characterized as good (B) and a value of $\beta_{MDL} = 0.20$ is selected since the primary expected failure mode is flexural hinging leading to sidesway collapse. This collapse mechanism is reasonably well predicted as shown in the two series of hybrid simulations. Therefore, the total system uncertainty calculated with Equation 5-1 is $\beta_{TOT} = 0.50$. Per Table 7-3 of the FEMA P695 report, the acceptable values of adjusted collapse margin ratio for a system uncertainty $\beta_{TOT} = 0.50$ are $ACMR_{10\%} = 1.90$ and $ACMR_{20\%} = 1.52$.

### 8.3.5 Evaluation of Adjusted Collapse Margin Ratios

The collapse margin ratios (*CMR*) obtained in Section 8.3.3 and summarized in Table 8-4 need to be adjusted by a spectral shape factor (*SSF*) to account for the spectral shape of the ground motion set using Equation 8-2. The spectral shape factor (*SSF*) is a function of the code-specified fundamental period (*T*), the period-based ductility ($\mu_T$) calculated in Section 8.3.2 and the applicable Seismic Design Category (SDC).

In the FEMA P695 methodology, maximum and minimum ground motions are defined for the SDC B, C and D based on respective upper- and lower-bound values of Maximum Considered Earthquake (MCE) and Design Earthquake (DE) spectral accelerations as given in Table 11.6-1 of ASCE/SEI 7-05 for short-period response and in Table 11.6-2 of ASCE/SEI 7-05 for 1-second response. In the FEMA P695 report, Table 7-1a provides values of spectral shape factors (*SSF*) for archetypes designed for Seismic Design

Category (SDC) B, C, and $D_{min}$ and Table 7-1b of the FEMA P695 report provides *SSF* values for SDC $D_{max}$.

Based on the occupancy category of the building structure and the fact that the MCE spectral response acceleration values ($S_S$, $S_1$) assumed for the steel moment frame building structure corresponds to the maximum values of spectral acceleration for SDC D ($D_{max}$) ($S_S$=1.5*g*, $S_1$=0.60*g*), the Seismic Design Category (SDC) of D was assigned to the steel moment frame structure under evaluation. Therefore, Table 8-5 summarizes the collapse margin ratio (*CMR*), the spectral shape factor (*SSF*), the adjusted collapse margin ratio (*ACMR*), and the acceptable adjusted margin ratio ($ACMR_{10\%}$) for the three analytical models.

**Table 8-5 Summary of adjusted collapse margin ratios and acceptable values**

| Model | Collapse Margin Ration (*CMR*) | Spectral Shape Factors (*SSF*) | Adjusted Collapse Margin Ratio (*ACMR*) | Acceptable Adjusted Margin Ratio ($ACMR_{10\%}$) |
|---|---|---|---|---|
| Moment Frame (MF) | 2.52 | 1.32 | 3.33 | 1.90 |
| Moment Frame with Floor Slab (CMF) | 2.84 | 1.37 | 3.90 | 1.90 |
| Moment and Gravity Frames with Floor Slab (CMF + GF) | 3.59 | 1.37 | 4.92 | 1.90 |

It can be seen in Table 8-5 that the adjusted collapse margin ratios of the three analytical models largely pass the acceptable value ($ACMR_{10\%}$) of the FEMA P695 methodology. As expected, the gravity frames and the composite action of the floor slab on the moment frames increase the collapse margin ratio. Increments in the adjusted collapse margin ratio (*ACMR*) of 17% and 47% are obtained for inclusion of (i) slab effects, and (ii) gravity frames in addition to slab effects, respectively. This indicates an important contribution of the gravity-force-resisting system on the collapse capacity of the steel moment frame building structure. However, as it was mentioned early, this could be considered as an upper limit since all the columns of the gravity frame were oriented in the strong axis (the contribution of the gravity frames is a function of the orientation of the gravity columns).

Figure 8-9 presents the adjusted fragility curves for the three analytical models described in Table 8-2. The fragility curves previously presented in Figure 8-8 were adjusted as follows. The median collapse ground motion intensity ($\hat{S}_{CT}$) was adjusted by the spectral shape factor (*SSF*) and the uncertainty factor modified by the total system uncertainty ($\beta_{TOT}$ = 0.50) to account for other sources of uncertainties. It can be seen in Figure 8-9 that the collapse probabilities of the building structure at the MCE ground motion

spectral acceleration ($S_{MT} = 0.99g$) are significantly lower than the acceptable probability of 10% suggested in the FEMA P695 methodology.

Since the collapse probabilities of this steel moment frame building structure are very low, Figure 8-9 reports collapse probabilities at 150% of the MCE ground motion spectral acceleration. It can be seen that inclusion of slab effects and gravity frames results in a decrease of the collapse probability from 5.4% to 1.0%.

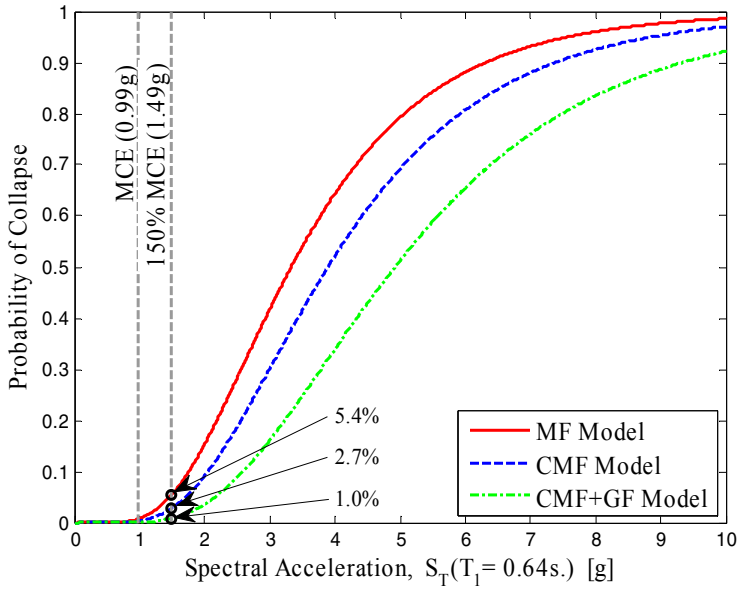


**Figure 8-9 Adjusted collapse fragility curves for steel moment frame building structure**

In summary, the FEMA P695 methodology was utilized to assess the collapse capacity of the steel moment frame building structure presented in Section 4 using three analytical models which simulate the response of (i) a special steel moment frame, (ii) a special steel moment frame including slab effects, and (iii) a special steel moment frame including slab effects and the gravity frames. The analytical models were calibrated with experimental data. In this evaluation, it was found that the collapse probability at the MCE ground motion intensity was significantly below the acceptable 10% suggested in the FEMA P695 methodology for the three analytical models. Also, while the composite action of the floor slab resulted in a 17% increment in the adjusted collapse margin ratio, an increment of 47% was obtained when the moment frames were also included. This indicated an important contribution of the gravity-force resisting system on the collapse capacity for this particular building structure.

# SECTION 9
# SUMMARY AND CONCLUSIONS

## 9.1 Summary

The overarching objective of this research project is to advance knowledge on collapse assessment of structural systems through experimental testing. Hybrid simulation with substructuring was evaluated and implemented as a cost-effective experimental framework for large-scale system-level testing of frame structures under simulated dynamic earthquake loading. Several challenges were encountered during the implementation of the hybrid testing method to evaluate frame structures through collapse. After addressing these concerns, the experimental framework was implemented to examine the seismic response of two half-scale subassemblies of a moment and a gravity frame from the onset of damage through collapse.

A brief description of the analytical and experimental studies conducted in this research project followed by a list of the most important conclusions of each study is presented in the following two sections. Section 9.2 presents the studies associated with the development of the experimental framework, including an evaluation of integration methods and substructuring techniques for hybrid simulation. Section 9.3 presents the implementation of the experimental framework to test two half-scale frame subassemblies through collapse. At the end of this section, suggestions for future research are provided in Section 9.4.

## 9.2 Development of Experimental Framework for Collapse Assessment

The review of past studies in support of collapse assessment in Section 2 indicated that there is a need for large-scale experimental tests examining the system-level response of structures through collapse. These experiments are key for a better understanding of collapse and essential to assist in the development and improvement of analytical tools for collapse prediction. In response to this lack of experimental data, an experimental framework was evaluated and developed to subject large subassemblies of frame structures to more realistic loading conditions via hybrid simulation. The test method was found to be reliable and provided insight into experimental behavior of structural subassemblies under realistic seismic loads. However, the implementation of the hybrid testing method presented various challenges to simulate the seismic response of frame structures through collapse. Two major challenges were addressed in this

report and included the performance of the integration methods and substructuring techniques used in hybrid simulation. A summary and a list of conclusions of these studies are presented below.

### 9.2.1 Evaluation of Integration Methods for Hybrid Simulation

The performance of numerical integration methods for hybrid simulation are greatly challenged when employed with large and complex numerical sub-structures exhibiting large levels of inelastic response. Numerical simulation of structural collapse is a highly nonlinear problem that requires the use of sophisticated integration methods together with small time steps for convergence, accuracy and stability of the results. Analytical studies conducted prior to the two series of hybrid simulations (Section 6.2.5) showed that the integration methods often became unstable for the selected hybrid models. In response to these studies, Section 3 presents an analytical and experimental evaluation of the performance of two integration methods used in hybrid simulation; namely, a modified version of the implicit Newmark method (Schellenberg *et al.*, 2009) (referred as the INM-HS method) and the operator-splitting method developed by Nakashima *et al.* (1989) (referred as the OS method). The conclusions of these studies are summarized below:

- The iterative INM-HS method is more accurate than the OS method as indicated by energy balance calculations. However, this method is comparatively more expensive computationally.
- The accuracy of the INM-HS method is more sensitive to the size of the time step than to the number of selected constant iterations. This was concluded by comparing numerical simulations with different combinations of time steps and numbers of constant iterations but presenting the same ratio of time step to number of iterations. In this comparison, the simulations with smaller time steps always yielded more accurate results.
- As expected, the use of algorithmic damping increased energy balance errors. However, these increments were more pronounced in the iterative INM-HS method than in the OS method.
- A series of hybrid simulations showed that the INM-HS and OS methods produced response results with similar levels of accuracy of purely numerical simulations.
- The use of physical sub-structures exhibiting a highly nonlinear response characterized by a sudden drop in strength and stiffness did not affect the accuracy or stability of the integration methods for the hybrid models presented in Section 3.4.

### 9.2.2 Evaluation of Substructuring Technique with Simplified Boundary Conditions

The use of substructuring techniques with simplified boundary conditions in hybrid simulation permits testing larger frame subassemblies (presenting a large number of boundary DOFs) using a reduced number of actuators to load the physical test specimen in the laboratory. An overlapping domain provided between the numerical and physical sub-structures minimizes the loss of accuracy of the simulation as a consequence of the simplified boundary conditions. The substructuring technique used in the hybrid simulations in this research project was based on the work of Hashemi (2013) and it was extended to include column axial forces. Section 6 presented an analytical evaluation of the accuracy of the substructuring technique and the ability to subject the physical frame subassemblies to realistic loading conditions despite the simplified boundary conditions. This substructuring technique was further evaluated using the test results of the hybrid simulations presented in Section 7. The major conclusions of these studies are summarized below:

- Hybrid simulations conducted with the substructuring technique with simplified boundary conditions and overlapping domain faithfully reproduced the global response of a frame structure. Other substructuring techniques with simplified boundary conditions but without an overlapping domain (e.g., Schneider and Roeder, 1994) did not trace the global response to collapse and resulted in a different collapse mechanism.
- However, compared to fully numerical simulations, the loading conditions of the physical sub-structure in a hybrid simulation present some differences as a consequence of the simplified boundary conditions. The portions (structural components) of the physical sub-structure further away from the simplified boundary conditions exhibited the smallest differences.

## 9.3 Implementation of Experimental Framework for Two Collapse Tests

The experimental framework developed in this research project was implemented to examine the seismic response of two half-scale subassemblies from the onset of damage through collapse. The test specimens consisted of a one and one half bay by one and one half story subassemblies of a special steel moment and gravity frames. These large frame subassemblies which included the concrete floor slab were subjected to realistic loading conditions via hybrid simulation to obtain response data at the system level. The following objectives were accomplished with the results of this experimental program:

- Data of the seismic response of two half-scale subassemblies of a steel moment and gravity frames through collapse was obtained. Testing these large subassemblies allowed for the observation of component behavior (girder, column, panel zones, etc.), their connections, and interactions with neighboring members which resulted in improved system-level simulations. This data is archived at the NEES central repository (nees.org/warehouse/welcome).
- The seismic performance of the steel moment and gravity frame subassemblies was assessed using the data obtained from the experimental program. Analysis of the test data allowed for documentation of the progress of damage and correlation with engineering demand parameters such as drifts and rotations.
- The capabilities of analytical models to trace the response of frame structures through collapse were assessed using the data obtained from the experimental program. Recommendations were included to improve collapse simulations.
- Using a seismic fragility framework (based on the FEMA P695 methodology), the contribution of the gravity-force-resisting system on the collapse capacity of a steel moment frame building structure was evaluated. The analytical models of the building structure were calibrated using the experimental data. For this particular building structure, the seismic fragility studies suggested that the gravity frames have a very positive impact on the collapse probability.
- The experimental program conducted as part of this research project provided data to evaluate the performance of the substructuring technique for hybrid simulation of multi-story frame structures through collapse. The ability of the substructuring technique to subject the test specimens to realistic loading conditions was assessed. The findings were summarized previously in Section 9.2.1.

## 9.4 Suggestions for Future Work

The following areas of research were identified as future work which could complement the research in this report:

- Large-scale frame structures can be evaluated using the experimental framework developed in this research project to examine other steel or reinforced concrete frame structures. Also, similar testing strategies can be used for taller building structures.
- The substructuring technique with simplified boundary conditions and overlapping domain between the physical and numerical sub-structures was evaluated here particularly for the hybrid

models employed in this research project. The evaluation can be extended to hybrid models with sub-structures of different sizes, configurations and behavior.

- More studies are needed to assess the contribution of the gravity-force-resisting system on the seismic response of steel moment frame building structures. The study presented in this report can be extended by examining building configurations with various ratios of number of moment to gravity frames.
- Earlier in the definition of the scope of this research project, the development of smooth hysteretic models for collapse prediction (e.g., Sivaselvan and Reinhorn, 2000) was identified as one potential area of research. Internal discussions suggested that smooth hysteretic models could possibly better capture acceleration and residual drifts as compared to multi-linear (non-smooth) models.
- While the effects of the axial force and bending moment (P-M) interaction in columns have minimal effect in low-rise buildings such as the one examined herein, the development of analytical models that includes the effects of P-M interaction are required for collapse assessment of taller building structures.

# SECTION 10

# REFERENCES


Abolmaali, A., Kukreti, A. R., and Razavi, H. (2003). "Hysteresis Behavior of Semi-Rigid Double Web Angle Steel Connections." Journal of Constructional Steel Research, Vol. 59, Iss. 8, pp. 1057-1082.

ACI (2008). "Building Code Requirements for Structural Concrete (ACI 318-08) and Commentary (ACI 318R-08)." American Concrete Institute, Farmington Hills, MI.

Ahmadizadeh, M. and Mosqueda, G. (2008). "Hybrid Simulation with Improved Operator-Splitting Integration Using Experimental Tangent Stiffness Matrix Estimation." Journal of Structural Engineering, Vol. 134, Iss. 12, pp. 1829-1838.

AISC (2005). "Manual of Steel Construction, Load and Resistance Factor Design (Thrid Ed.)." American Institute of Steel Construction, Chicago, IL.

AISC (2010a). "Prequalified Connections for Special and Intermediate Steel Moment Frames for Seismic Applications (AISC 358-10)." American Institute of Steel Construction, Chicago.

AISC (2010b). "Seismic Provisions for Structural Steel Buildings (AISC 341S1-10)." American Institute of Steel Construction, Chicago.

ASCE (2002). "Minimum Design Loads for Buildings and Other Structures." American Society of Civil Engineers (SEI/ASCE-02).

Astaneh-Asl, A. (2005). "Design of Shear Tab Connections for Gravity and Seismic Loads." Steel Tips, Structural Steel Educational Council.

Astaneh-Asl, A., Call, S. M., and McMullin, K. M. (1989). "Design of Single Plate Connections." AISC Engineering Journal, First Quarter, pp. 21-31.

Aycardi, L. E., J. M., Mander, J. B., and Reinhorn, A. M. (1992). "Seismic Resistance of Reinforced Concrete Frame Structures Designed Only for Gravity Loads: Part II – Experimental Performance of Subassemblages." Technical Report NCEER-92-0028, National Center for Earthquake Engineering Research, State University of New York at Buffalo, NY.

Bouc, R. (1967). "Forced Vibration of Mechanical Systems with Hysteresis." Proccedings of 4th Conference on Non-linear Oscillations, Prague.

Bracci, J. M., Reinhorn, A. M., and Mander, J. B. (1992a). "Seismic Resistance of Reinforced Concrete Frame Structures Designed Only for Gravity Loads: Part I – Design and Properties of a One-Third Scale Model Structure." Technical Report NCEER-92-0027, National Center for Earthquake Engineering Research, State University of New York at Buffalo, NY.

Bracci, J. M., Reinhorn, A. M., and Mander, J. B. (1992b). "Seismic Resistance of Reinforced Concrete Frame Structures Designed Only for Gravity Loads: Part III – Experimental Performance and Analytical Study of a Structural Model." Technical Report NCEER-92-0029, National Center for Earthquake Engineering Research, State University of New York at Buffalo, NY.

Calvi, G.M., Magenes, G., and Pampanin, S. (2002). "Experimental Test on a Three Storey R.C. Frame Designed for Gravity Only." 12th European Conference on Earthquake Engineering, London, paper no. 727.

Chen, C. and Ricles, J. (2008). "Development of Direct Integration Algorithms for Structural Dynamics Using Discrete Control Theory." Journal of Engineering Mechanics, Vol. 134, Iss. 8, pp. 676-683.

Chi, B. and Uang, C. M. (2002). "Cyclic Response and Design Recommendations of Reduced Beam Section Moment Connections with Deep Columns." Journal of Structural Engineering (ASCE), Vol. 128, Iss. 4, pp. 464-473.

Chung, J. and Hulbert, G. M. (1993). "A Time Integration Algorithm for Structural Dynamics with Improved Numerical Dissipation: The Generalized-Alpha Method." Journal of Applied Mechanics, ASME, Vol. 60, Iss. 2, pp. 371-375.

Citipitioglu, A. M., Haj-Ali, R. M., and White, D. W. (2002). "Refined 3D Finite Element Modeling of Partially-Restrained Connections including Slip." Journal of Constructional Steel Research, Vol. 58, Iss. 5-8, pp. 995-1013.

Cortes-Delgado, M. (2013). "Hybrid Simulation with Distributed Substructures including Overlapping Domains." PhD Dissertation, Department of Civil, Structural and Environmental Engineering, State University of New York at Buffalo, NY.

Crocker, J. and Chambers, J. (2004). "Single Plate Shear Connection Response to Rotation Demands imposed by Frames undergoing Cyclic Lateral Displacements." Journal of Structural Engineering, Vol. 130, Iss. 6, pp. 934-941.

CSI (2012). "SAP2000: Integrated Finite Element Analysis and Design of Structures, Version 14." Computers and Structures Inc., Berkeley, CA.

Dermitzakis, S. N. and Mahin, S. A. (1985). "Development of Substructuring Techniques for On-Line Computer Controlled Seismic Performance Testing." Earthquake Engineering Research Center, Berkeley, CA, 153 pp.

Dorka, U. E. and Heiland, D. (1991). "Fast Online Earthquake utilizing a Novel PC Supported Measurement and Control Concept." 4th Conference on Structural Dynamics, Southampton, UK.

DS Simulia (2010). "ABAQUS Software, Version 6.10-EF2". Dassault Systèmes Simulia Corp., Providence, RI, USA.

El-Attar, A. G., White R. N., and Gergely, P. (1991). "Shake Table Test of a 1/6 Scale Two-Story Lightly Reinforced Concrete Building." Technical Report NCEER-90-0017, National Center for Earthquake Engineering Research, State University of New York at Buffalo, NY.

Elwood, K. J. and Moehle, J. P. (2003). "Shake Table Tests and Analytical Studies on the Gravity Load Collapse of Reinforced Concrete Frames." PEER Report 2013/01.

Elwood, K. J. and Moehle, J. P. (2005). "Drift Capacity of Reinforced Concrete Columns with Light Transverse Reinforcement." Earthquake Spectra, Vol. 21, No. 1, pp. 71-89.

FEMA (2000). "State of the Art Report on Performance Prediction and Evaluation of Steel Moment-Frame Buildings (FEMA 355F)." Federal Emergency Management Agency, Washintong, DC.

FEMA (2009). "Quantification of Building Seismic Performance Factors (FEMA P695)." Federal Emergency Management Agency, Washington, DC.

Filiatrault, A., Tinawi, R., and Leger, P. (1992). "The Use of Energy Balance in Nonlinear Seismic Analysis." 10th World Conference in Earthquake Engineering, Madrid, Spain, pp. 4111-4116.

Foutch, D. A. and Yun, S. Y. (2002). "Modeling of Steel Moment Frames for Seismic Loads." Journal of Constructional Steel Research, Vol. 58, Iss. 5-8, pp. 529-564.

Giberson, M. F. (1967). "The Response of Nonlinear Multi-Story Structures subjected to Earthquake Excitation." PhD Dissertation, California Institute of Technology, Pasadena, CA.

Gong, Y. (2010). "Plastic Behavior of Shear Tabs Welded to Flexible Wall Support." Journal of Structural Engineering, Vol. 136, Iss. 10, pp. 1197-1204.

Gupta, A. and Krawinkler, H. (1999). "Seismic Demands for Performance Evaluation of Steel Moment Resisting Frame Structures." Report No. 132, John A. Blume Earthquake Engineering Center, Stanford University, CA.

Gupta, A. and Krawinkler, H. (2000). "Behavior of Ductile SMRFs at various Seismic Hazard Levels." Journal of Structural Engineering (ASCE), Vol. 126, Iss. 1, pp. 98-107.

Haselton, C. B. and Deierlein, G. G. (2006). "Assessing Seismic Collapse Safety of Modern Reinforced Concrete Moment Frame Buildings." Report No. TR 156, John A. Blume Earthquake Engineering Center. Department of Civil Engineering, Stanford University.

Hashemi, M. J. (2013), "Collapse Simulation of Multi-Story Buildings through Hybrid Testing with Substructuring Techniques." PhD Dissertation, Department of Civil, Structural and Environmental Engineering, State University of New York at Buffalo, NY, 293 pp.

Hashemi, M. J., Del Carpio, R. M., and Mosqueda, G. (2013). "Substructuring Techniques for Hybrid Simulation of Complex Structural Systems through Collapse." 5th International Conference on Advances in Experimental Structural Engineering. Taipei, Taiwan.

Huang, Z. and Foutch, D. A. (2009). "Effect of Hysteresis Type on Drift Limit for Global Collapse of Moment Frame Structures under Seismic Loads." Journal of Earthquake Engineering, Vol. 13, Iss. 7, pp. 939-964.

Hughes, T. J. R. and Liu, W. K. (1978). "Implicit-Explicit Finite Elements in Transient Analysis: Implementation and Numerical Examples." Journal of Applied Mechanics, ASME, Vol. 45, Iss. 2, pp. 375-378.

Hughes, T. J. R., Pister, K. S., and Taylor, R. L. (1979). "Implicit-Explicit Finite Elements in Nonlinear Transient Analysis." Computer Methods in Applied Mechanics and Engineering, Vols. 17-18, Part 1, pp. 159-182.

Ibarra, L. F. and Krawinkler, H. (2005). "Global Collapse of Frame Structures under Seismic Excitations." Report No. PEER 2005/06, Pacific Earthquake Engineering Research Center, University of California at Berkeley, Berkeley, California.

Ibarra, L. F., Medina, R. A., and Krawinkler, H. (2005). "Hysteretic Models that Incorporate Strength and Stiffness Deterioration." Earthquake Engineering and Structural Dynamics. Vol. 34, Iss. 12, pp. 1489-1511.

IBC (2003). "International Building Code (IBC) 2003." International Code Council, Birmingham, AL.

Ji, X., Kato, M., Wang, T., Hitaka, T., and Nakashima, M. (2009). "Effect of Gravity Columns on Mitigation of Drift Concentration for Braced Frames." Journal of Constructional Steel Research, Vol. 65, Iss. 12, pp. 2148-2156.

Kanaan, A. E. and Powell, G.H. (1973). "DRAIN-2D-A General Purpose Computer Program for Dynamic Analysis of Inelastic Plane Structures." Reports No. UCB/EERC/73/06 and 73/22. University of California, Berkeley, CA.

Kanvinde, A. M. (2003). "Methods to Evaluate the Dynamic Stability of Structures – Shake Table Tests and Nonlinear Dynamic Analyses." EERI Paper Competition Winner, Proceedings of EERI Meeting, Portland.

Kato, B., Akiyama, H., Suzuki, H., and Fukuzawa, Y. (1973). "Dynamic Collapse Tests of Steel Structural Models." Preprints, 5th World Conference on Earthquake Engineering, Rome.

Kim, K. D. and Engelhardt, M. D. (2002). "Monotonic and Cyclic Loading Models for Panel Zones in Steel Moment Frames." Journal of Constructional Steel Research, Vol. 58, Iss. 5-8, pp. 605-635.

Kim, Y., Kabeyasawa, T., Matsumori, T. and Kabeyasawa, T. (2012). "Numerical Study of a Full-Scale Six-Story Reinforced Concrete Wall-Frame Structure Tested at E-Defense." Earthquake Engineering and Structural Dynamics, Vol. 41, Iss. 8, pp. 1217-1239.

Krawinkler, H. (1978). "Shear in Beam-Column Joints in Seismic Design of Steel Frames." Engineering Journal, American Institute of Steel Construction, Vol. 5, No. 3, pp. 82-91.

Krawinkler, H. and Mohasseb, S. (1987). "Effects of Panel Zone Deformations on Seismic Response." Journal of Constructional Steel Research, Vol. 8, pp. 233-250.

Kumar, S., Itoh, Y., Saizuka, K., and Usami, T. (1997). "Pseudodynamic Testing of Scaled Models. Journal of Structural Engineering." Vol. 123, Iss. 4, pp. 524-526.

Lee, S. J. (1987). "Seismic Behavior of Steel Building Structures with Composite Slabs." PhD Dissertation, Lehigh University at Bethlehem, PA.

Lee, S. and Lu, L. (1989). "Cyclic Tests of Full-Scale Composite Joint Subassemblages." Journal of Structural Engineering, Vol. 115, Iss. 8, pp. 1977-1998.

Leon, R., Hajjar, J., and Gustafson, M. (1998). "Seismic Response of Composite Moment-Resisting Connections. I: Performance." Journal of Structural Engineering, Vol. 124, Iss. 8, pp. 868-876.

Lignos, D., Chung, Y-L., Nagae, T., Nakashima, M. (2011a). "Numerical and Experimental Evaluation of Seismic Capacity of High-Rise Steel Buildings subjected to Long Duration Earthquakes." Journal of Computers and Structures, Vol. 89, Iss. 11-12, pp. 959-967.

Lignos, D., Eads, L., and Krawinkler, H. (2011b). "Effect of Composite Action on Collapse Capacity of Steel Moment Frames under Earthquake Loading." EUROSTEEL, Budapest, Hungary.

Lignos, D. and Krawinkler, H. (2011). "Deterioration Modeling of Steel Components in Support of Collapse Prediction of Steel Moment Frames under Earthquake Loading." Journal of Structural Engineering (ASCE), Vol. 137, Iss. 11, pp. 1291-1302.

Lignos, D. and Krawinkler, H. (2012). "Sidesway Collapse of Deteriorating Structural Systems under Seismic Excitations." Report No. TB 172, John A. Blume Earthquake Engineering Center, Stanford University, CA.

Lignos, D., Hikino, T., Matsuoka, Y., and Nakashima, M. (2013). "Collapse Assessment of Steel Moment Frames Based on E-Defense Full-Scale Shake Table Collapse Tests." Journal of Structural Engineering (ASCE), Vol. 139, Iss. 1, pp. 120-132.

Liu, J. and A. Astaneh-Asl (2000a). "Cyclic Testing of Simple Connections including Effects of Slab." Journal of Structural Engineering (ASCE), Vol. 126, Iss. 1, pp. 32-39.

Liu, J. and A. Astaneh-Asl (2000b). "Experimental and Analytical Studies of the Cyclic Behavior of Simple Connections in Steel Frame Buildings." UCB/CEE-STEEL-2000/01. Berkeley, California, Deptarment of Civil and Environmental Engineering, University of California, Berkeley.

Liu, J. and Astaneh-Asl, A. (2004). "Moment-Rotation Parameters for Composite Shear Tab Connections." Journal of Structural Engineering, Vol. 130, Iss. 9, pp. 1371-1380.

Lowes, L. and Altoontash, A. (2003). "Modeling Reinforced-Concrete Beam-Column Joints subjected to Cyclic Loading." Journal of Structural Engineering, Vol. 129, Iss. 12, pp. 1686-1697.

Mahin, S. A., Shing, P. B., Thewalt, C. R., and Hanson, R. D. (1989). "Pseudodynamic Test Method - Current Status and Future Direction." Journal of Structural Engineering, ASCE, Vol. 115, Iss. 8, pp. 2113-2128.

Mahmoud, H. (2011). "Seismic Behavior of Semi-Rigid Steel Frames." PhD Dissertation, University of Illinois, Urbana, IL.

Mahmoud, H., Elnashai, A., Spencer, B., Jr., Kwon, O., and Bennier, D. (2013). "Hybrid Simulation for Earthquake Response of Semirigid Partial-Strength Steel Frames. Journal of Structural Engineering." 139, SPECIAL ISSUE: NEES 1: Advances in Earthquake Engineering, pp. 1134-1148.

Mander, J. B., Priestley, M. J. N., and Park, R. (1988). "Theoretical Stress-Strain Model for Confined Concrete." Journal of Structural Engineering, Vol. 114, No. 8, pp. 1804-1826.

Marosi, M., D'Aronco, M., Tremblay, R., and Rogers, C. A. (2011). "Multi-Row Bolted Beam to Column Shear Tab Connections." EUROSTEEL, Budapest, Hungary.

MathWorks (2011). "MATLAB and Simulink R2011b." MathWorks, Natick, MA.

Matsumori T., Shirai K., and Kabeyasawa, T. (2006). "Simulated Earthquake Test on a Full-Scale Six-Story Reinforced Concrete Building at E-Defense, Part 1: Outline of Test Program." Proceedings of The 2nd NEES/E-Defense Workshop on Collapse Simulation of Reinforced Concrete building Structures, Miki Japan.

Medina, R. (2002). "Seismic Demands for Nondeteriorating Frame Structures and their Dependence on Ground Motions." PhD Dissertation, Department of Civil Engineering, Stanford University, CA.

Mitra, N. (2007). "An Analytical Study of Reinforced Concrete Beam-Column Joint Behavior under Seismic Loading." PhD Dissertation, University of Washintong, WA.

Mosqueda, G. and Ahmadizadeh, M. (2011). "Iterative Implicit Integration Procedure for Hybrid Simulation of Large Nonlinear Structures." Earthquake Engineering and Structural Dynamics, Vol. 40, Iss. 9, pp. 945-960.

Nakashima, M., Kaminoso, T., Ishida, M., and Kazuhiro, A. (1990). "Integration Techniques for Substructure Online Test." 4th U.S. National Conference of Earthquake Engineering, Palm Springs, CA, Earthquake Engineering Research Institute.

Nakashima, M., Matsumiya, T., Suita, K., and Liu, D. (2006). "Test on Full-Scale Three-Storey Steel Moment Frame and Assessment of Ability of Numerical Simulation to Trace Cyclic Inelastic Behaviour." Earthquake Engineering and Structural Dynamics, Vol. 35, Iss. 1, pp. 3-19.

Nam, T. T. and Kasai, K. (2012). "Study on Shake Table Experimental Results regarding Composite Action of a Full-Scale Steel Building tested to Collapse." 9th International Conference on Urban Earthquake Engineering/4th Asia Conference on Earthquake Engineering, Tokyo Institute of Technology, Tokyo, Japan.

Newmark, N. M. (1959). "A Method of Computation for Structural Dynamics." Journal of Engineering Mechanics (ASCE) 67.

OpenFresco (2008). "Open Framework for Experimental Setup and Control. Pacific Earthquake Engineering Research Center (PEER)". Available from: http:// http://openfresco.berkeley.edu.

OpenSees (2012). "Open System for Earthquake Engineering Simulation. Pacific Earthquake Engineering Research Center (PEER)." Available from: http:// http://opensees.berkeley.edu.

Prakash, V., Powell, G. H., and Campbell, S. D. (1994). "DRAIN-3DX: Base Program Description and User Guide: Version 1.10." UCB/SEMM-1994/07, Department of Civil Engineering, University of California, Berkeley, CA.

Ray, T., Reinhorn, A. M., and Nagarajaiah, S. (2013). "Nonlinear Elastic and Inelastic Spectra with Inherent and Supplemental Damping." Earthquake Engineering and Structural Dynamics, Vol. 42, Iss. 14, pp. 2151-2165.

Reinhorn, A. M., Roh, H. S., Sivaselvan, M. V., Kunnath, S. K., Valles, R. E., Madan, A., Li, C., Lobo, R., and Park, Y. J. (2009). "IDARC2D Version 7.0: A Program for the Inelastic Damage Analysis of Structures." Technical Report MCEER-09-0006, State University of New York at Buffalo, NY.

Rodgers, J. and Mahin, S. (2006). "Effects of Connection Fractures on Global Behavior of Steel Moment Frames Subjected to Earthquakes." Journal of Structural Engineering (ASCE), Vol. 132, No. 1, pp. 78-88.

Ruiz-García, J. and Miranda, E. (2006). "Evaluation of Residual Drift Demands in Regular Multi-Storey Frames for Performance-Based Seismic Assessment." Earthquake Engineering Structuctural Dynamics, Vol. 35, Iss. 13, pp. 1609-1629.

Schellenberg, A. H., Huang, Y., and Mahin, S. A. (2008). "Structural FE-Software Coupling through the Experimental Software Framework, OpenFresco." Proceeding of the 14th World Conference on Earthquake Engineering, Beijing, China.

Schellenberg, A. H. and Mahin, S. A. (2006). "Integration of Hybrid Simulation within the General-Purpose Computational Framework OpenSees." Proceedings, 8th National Conference on Earthquake Engineering, EERI, San Francisco, CA.

Schellenberg, A. H., Mahin, S. A., and Fenves, G. L. (2009). "Advanced Implementation of Hybrid Simulation." Report PEER 2009/104. Pacific Earthquake Engineering Research Center, University of California, Berkeley, CA.

Schneider, S. P. and Roeder, C. W. (1994). "An Inelastic Substructure Technique for the Pseudodynamic Test Method." Earthquake Engineering and Structural Dynamics, Vol. 23, Iss. 7, pp. 761-775.

Sherman, D. R. and Ghorbanpoor, A. (2002). "Design of Extended Shear Tabs." Report submitted to American Institute of Steel Construction, University of Wisconsin, Milwaukee.

Shing, P. S. B., Vannan, M. T., and Cater, E. (1991). "Implicit Time Integration for Pseudodynamic Tests." Earthquake Engineering and Structural Dynamics, Vol. 20, Iss. 6, pp. 551-576.

Shing, P. B., Nakashima, M. and Bursi, O.S. (1996). "Application of Pseudodynamic Test Method to Structural Research." Earthquake Spectra, EERI, Vol. 12, Iss. 1, pp. 29-54.

Shirai, K., Matsumori, T., and Kabeyasawa, T. (2006). "Simulated Earthquake Test on a Full-Scale Six-Story Reinforced Concrete Building at E-Defense, Part 2: Study on Distribution of Seismic Forces." Proceedings of the 2nd NEES/E-Defense Workshop on Collapse Simulation of Reinforced Concrete building Structures, Miki Japan.

Sivaselvan, M. V. and Reinhorn, A. M. (2000). "Hysteretic Models for Deteriorating Inelastic Structures." Journal of Engineering Mechanics (ASCE), Vol. 126, Iss. 6, pp. 633-640.

Sivaselvan, M. V. and Reinhorn, A. M. (2006). "Lagrangian Approach to Structural Collapse Simulation." Journal of Engineering Mechanics (ASCE), Vol. 132, Iss. 8, pp. 795-805.

Stojadinovic, B., Mosqueda, G., and Mahin, S. A. (2006). "Event-driven control system for geographically distributed hybrid simulation." Journal of Structural Engineering (ASCE), Vol. 132, Iss. 1, pp. 68-77.

Suita, K., Yamada, S., Tada, M., Kasai, K., Matsuoka, Y., and Shimada, Y. (2008). "Collapse Experiment on Four-Story Steel Moment Frame: Part 2." Proceeding of the 14th World Conference on Earthquake Engineering, Beijing, China.

Systran, C. (2004). The SCRAMNet+ Network (Shared Common RAM Network).

Tagawa, H., Macrae, G., and Lowes, L. (2010). “Continuous Column Effects of Gravity Columns in U.S. Steel Moment-Resisting Frame Structures.” Journal of Struc. Constr. Eng., AIJ, Vol. 75, No. 650, pp. 761-770. (in Japanese)

Takanashi, K. (1975). “Non-Linear Earthquake Response Analysis of Structures by a Computer-Actuator On-Line System.” Bulletin of Earthquake Resistant Structure Research Center, The Institute of Industrial Science, University of Tokyo, No. 8, pp.1-17.

Takanashi, K. and Nakashima, M. (1987). “Japanese Activities on On-Line Testing.” Journal of Engineering Mechanics, ASCE, Vol. 113, Iss. 7, pp. 1014-1032.

Vamvatsikos, D. and Cornell, C.A. (2002) . “Incremental dynamic analysis.” Earthquake Engineering Structuctural Dynamics, Vol. 31, Iss. 3, pp. 491-514.

Vian, D. and Bruneau, M. (2001). “Experimental Investigation of P-Delta Effects to Collapse during Earthquakes.” Technical Report MCEER-01-0001. Multidisiplinary Center for Earthquake Engineering Research, State University of New York at Buffalo, NY.

Vian, D. and Bruneau, M. (2003). “Tests to Structural Collapse of Single Degree of Freedom Frames subjected to Earthquake Excitations.” Journal of Structural Engineering (ASCE), Vol. 129, Iss. 12, pp. 1676-1685.

Villaverde, R. (2007). “Methods to Assess the Seismic Collapse Capacity of Building Structures: State of the Art.” Journal of Structural Engineering, Vol. 133, Iss. 1, pp. 57-66.

Wang, T., McCormick, J., Yoshitake, N., Pan, P., Murata, Y. and Nakashima, M. (2008). “Collapse Simulation of a Four-Story Steel Moment Frame by a Distributed Online Hybrid Test.” Earthquake Engineering and Structural Dynamics, Vol. 37, Iss. 6, pp. 955-974.

Wang, T., Mosqueda, G., Jacobsen, A., and Cortes-Delgado, M. (2011). “Performance Evaluation of a Distributed Hybrid Test Framework to Reproduce the Collapse Behaviour of a Structure.” Earthquake Engineering Structuctural Dynamics, Vol. 41, Iss. 2, pp. 295-313.

Wen, Y. K. (1976). “Method for Random Vibration of Hysteretic Systems.” Journal of Engineering Mechanics Division (ASCE), Vol. 102, No. 2, pp. 249-263.

Zareian, F. and Medina, R. A. (2010). “A Practical Method for Proper Modeling of Structural Damping in Inelastic Plane Structural Systems.” Computers and Structures, Vol. 88, Iss. 1-2, pp. 45-53.

Zhong, W. (2005). “Fast Hybrid Test System for Substructure Evaluation.” PhD Dissertation, University of Colorado at Boulder, CO, 123 pp.

# APPENDIX A: DRAWINGS OF TEST SPECIMEN #1



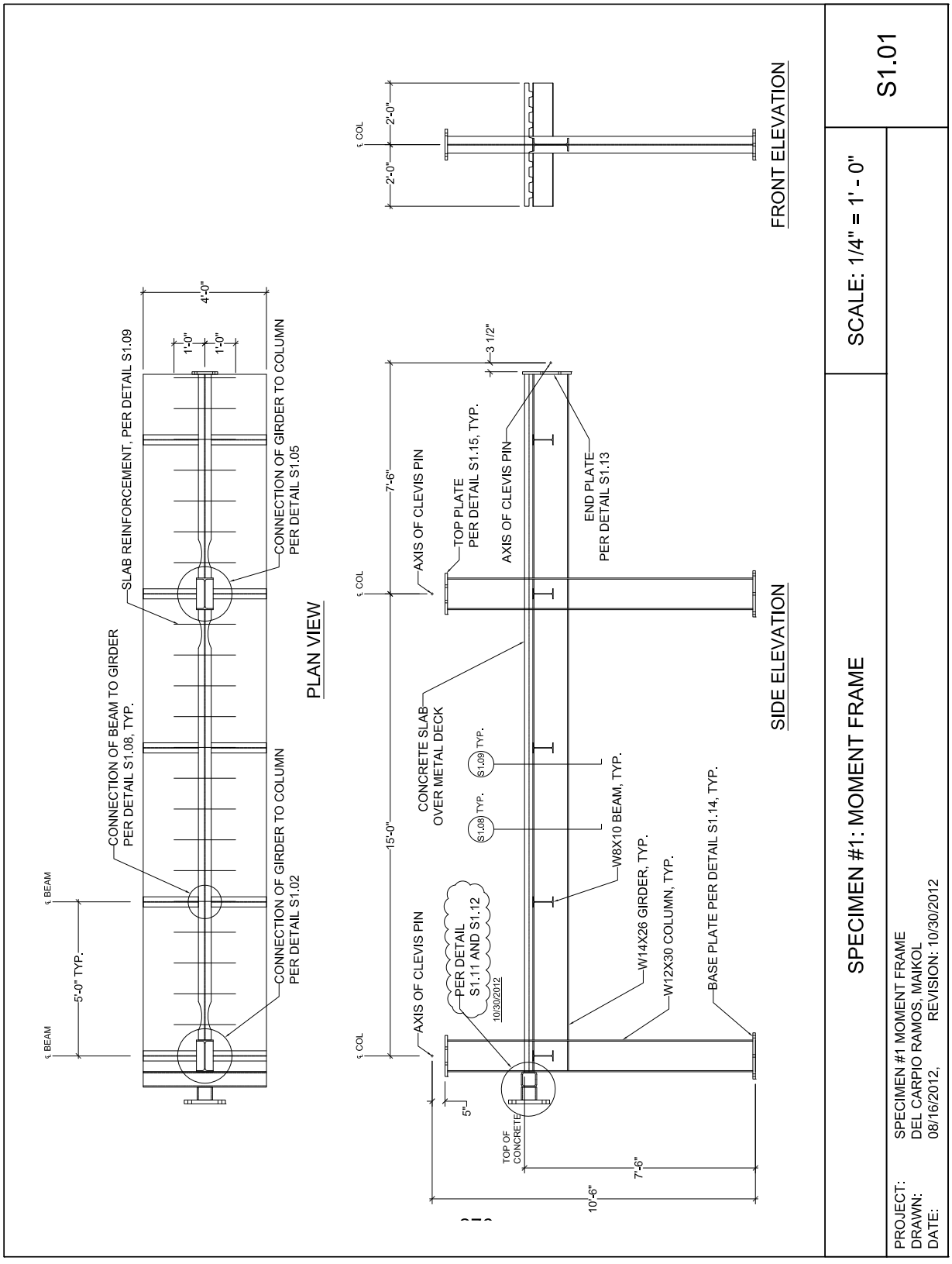




PRODUCED BY AN AUTODESK EDUCATIONAL PRODUCT

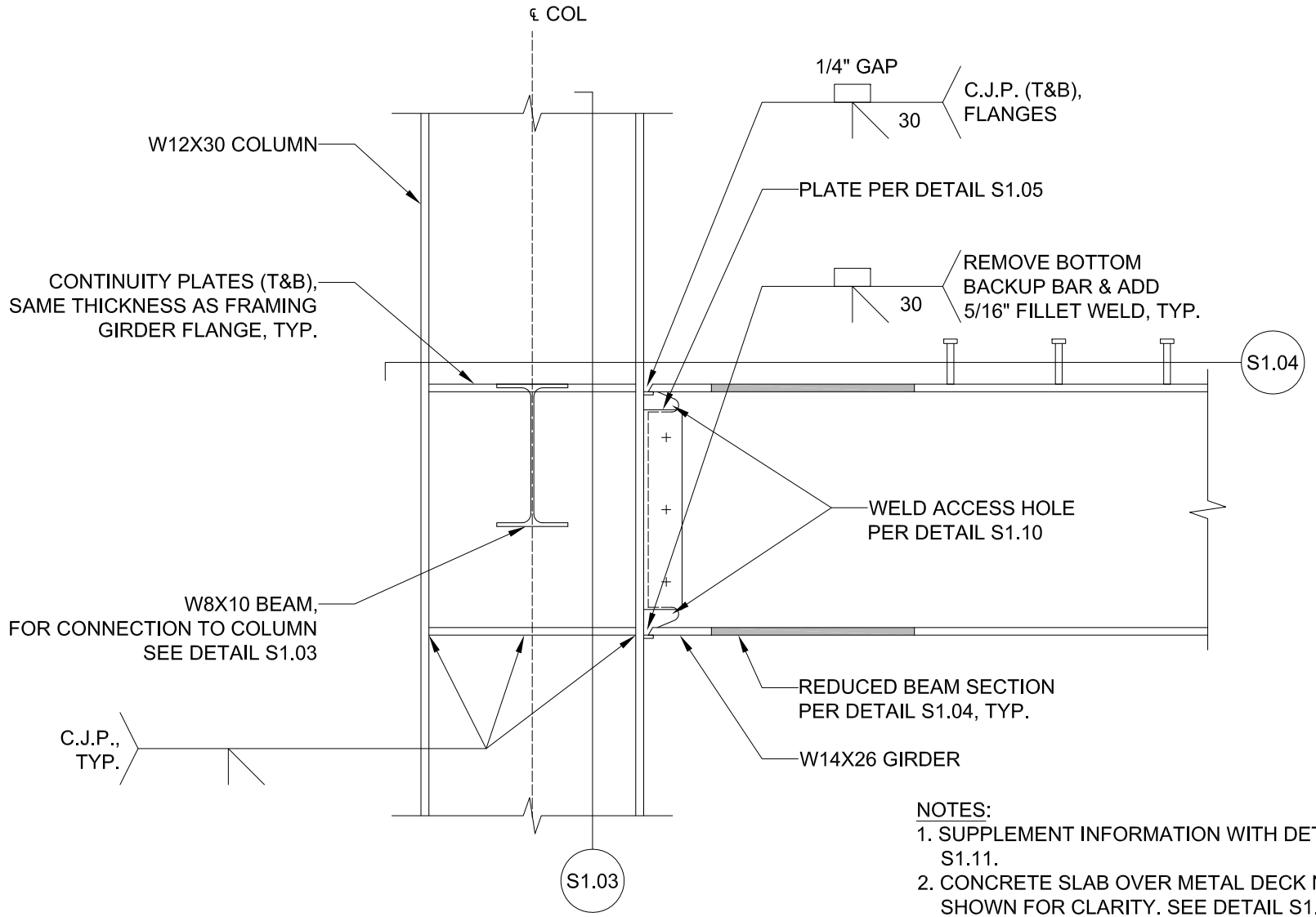


NOTES:
1. SUPPLEMENT INFORMATION WITH DETAIL S1.11.
2. CONCRETE SLAB OVER METAL DECK NOT SHOWN FOR CLARITY. SEE DETAIL S1.09.

| CONNECTION OF GIRDER TO EXTERIOR COLUMN (EXTERIOR MOMENT CONNECTION) | SCALE: 1-1/2" = 1' - 0" | S1.02 |
|---|---|---|

PROJECT: SPECIMEN #1 MOMENT FRAME
DRAWN: DEL CARPIO RAMOS, MAIKOL
DATE: 08/16/2012

PRODUCED BY AN AUTODESK EDUCATIONAL PRODUCT



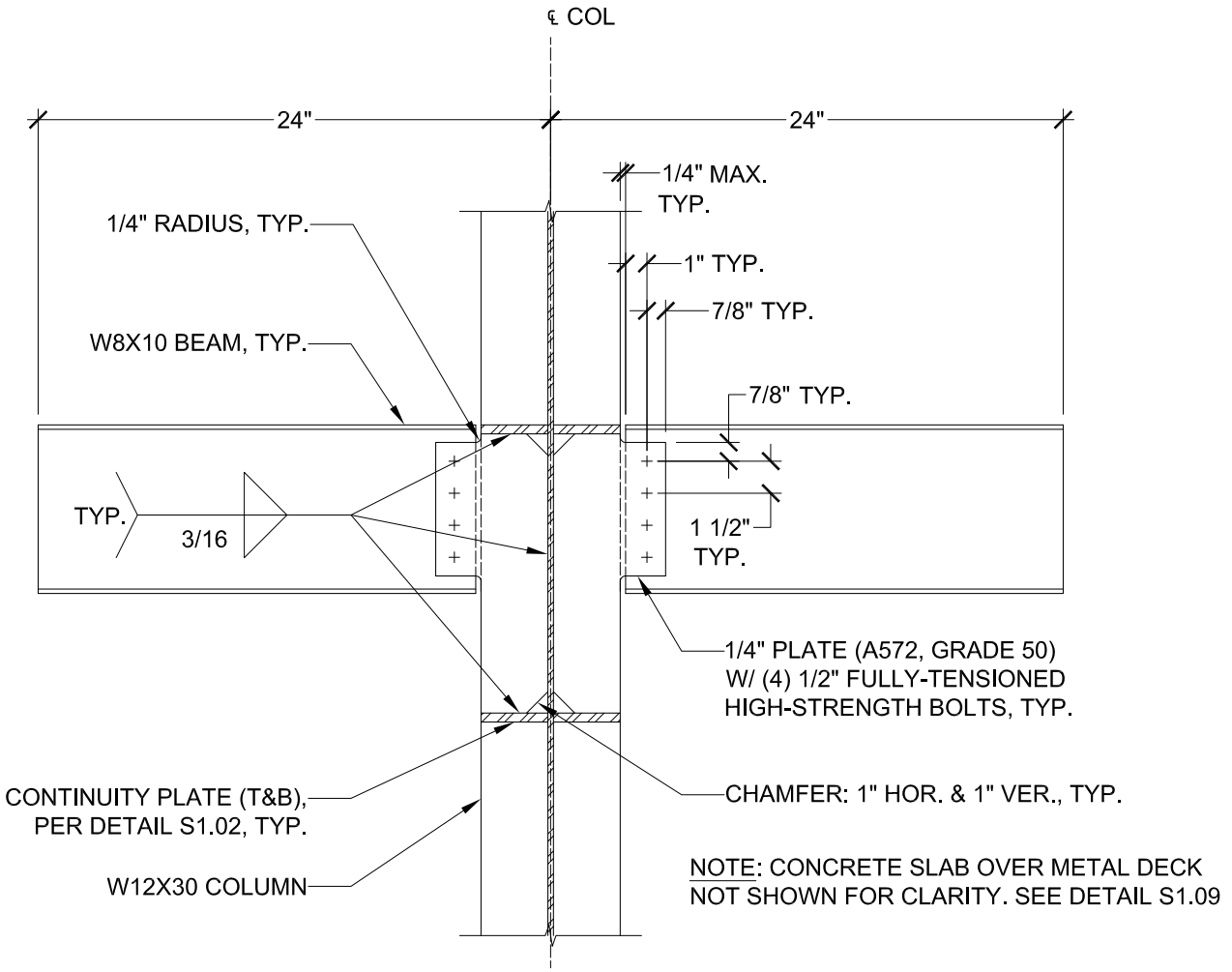


| CONNECTION OF BEAM TO COLUMN | SCALE: 1-1/2" = 1' - 0" | S1.03 |
|---|---|---|

PROJECT: SPECIMEN #1 MOMENT FRAME
DRAWN: DEL CARPIO RAMOS, MAIKOL
DATE: 08/16/2012

PRODUCED BY AN AUTODESK EDUCATIONAL PRODUCT

PRODUCED BY AN AUTODESK EDUCATIONAL PRODUCT



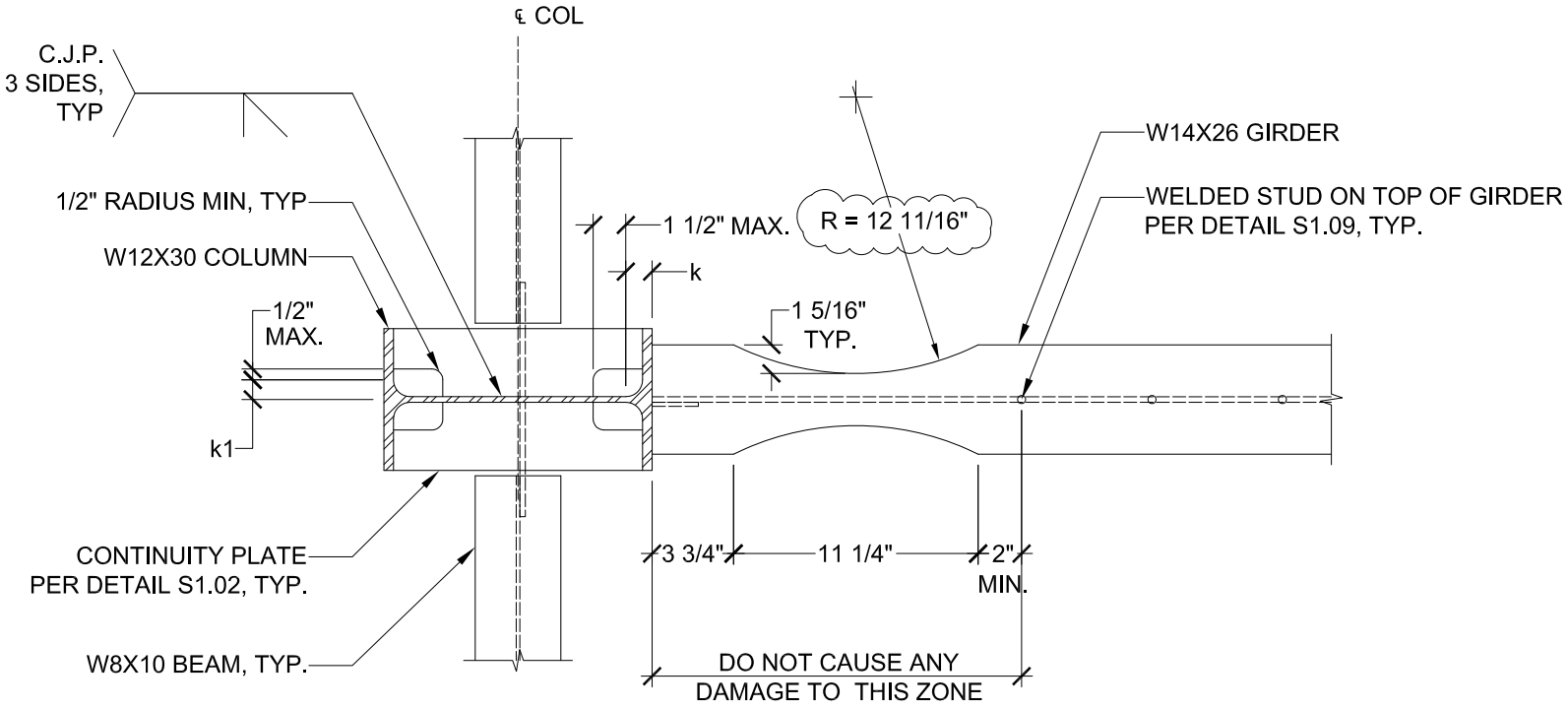


| EXTERIOR MOMENT CONNECTION - PLAN VIEW | SCALE: 1-1/2" = 1' - 0" | S1.04 |
|---|---|---|

PROJECT: SPECIMEN #1 MOMENT FRAME
DRAWN: DEL CARPIO RAMOS, MAIKOL
DATE: 08/16/2012

PRODUCED BY AN AUTODESK EDUCATIONAL PRODUCT

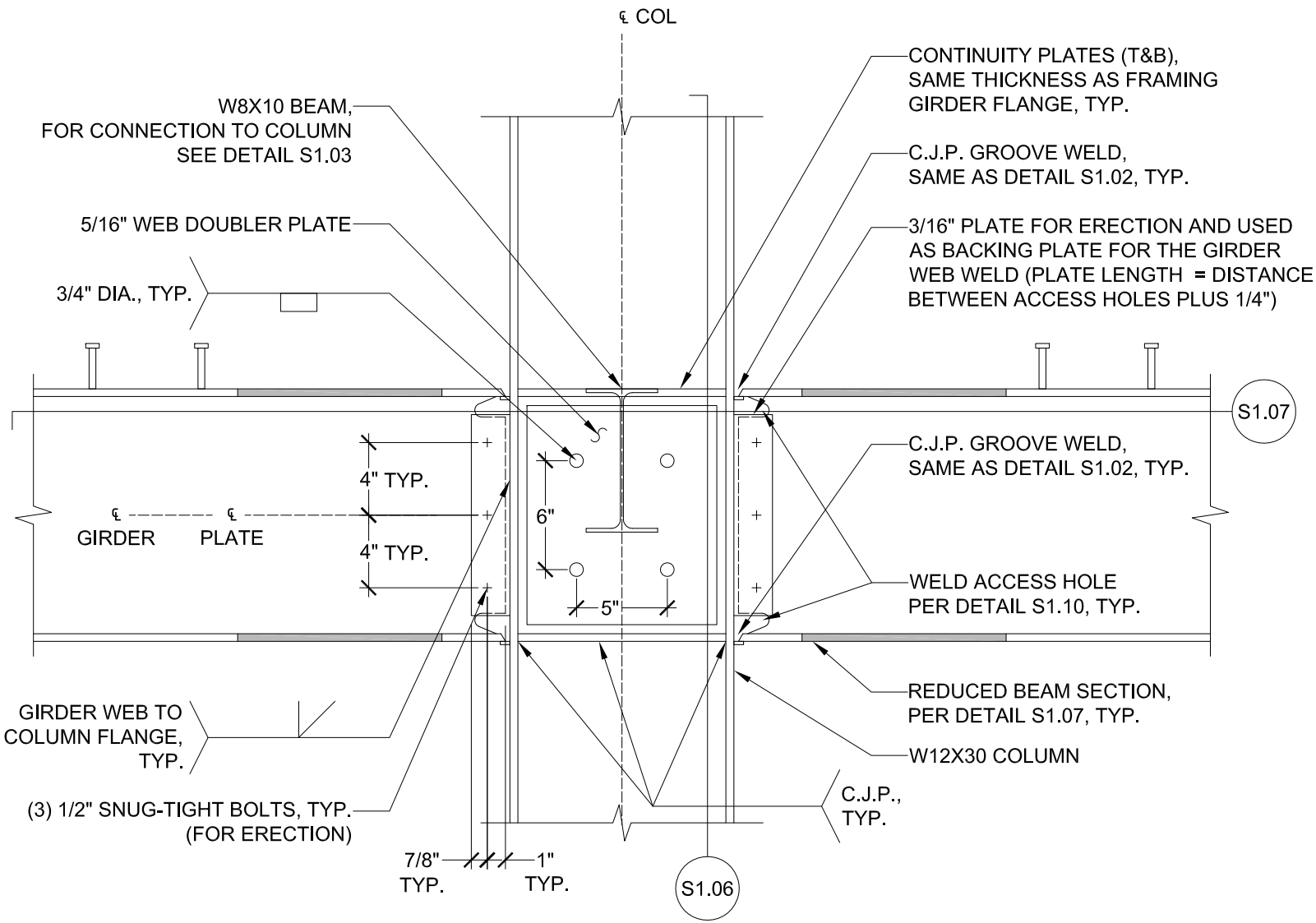


| | | |
|---|---|---|
| CONNECTION OF GIRDER TO INTERIOR COLUMN (INTERIOR MOMENT CONNECTION) | SCALE: 1-1/2" = 1' - 0" | S1.05 |

PROJECT: SPECIMEN #1 MOMENT FRAME
DRAWN: DEL CARPIO RAMOS, MAIKOL
DATE: 08/16/2012

PRODUCED BY AN AUTODESK EDUCATIONAL PRODUCT



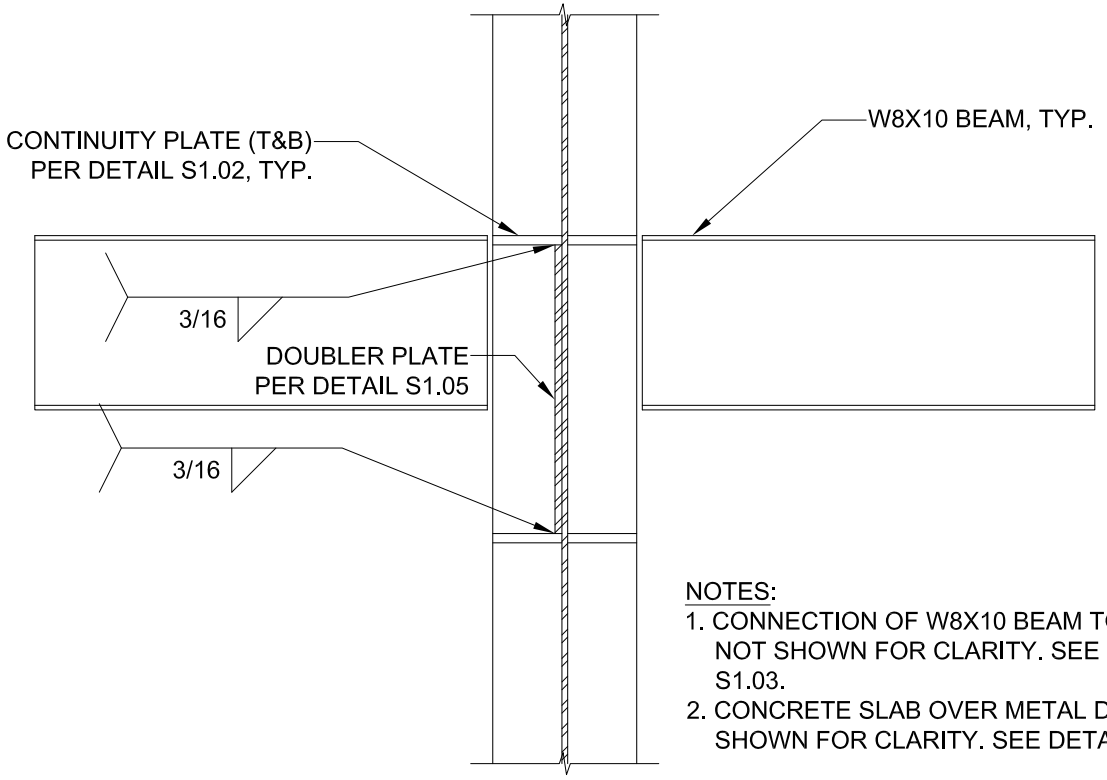


NOTES:
1. CONNECTION OF W8X10 BEAM TO COLUMN NOT SHOWN FOR CLARITY. SEE DETAIL S1.03.
2. CONCRETE SLAB OVER METAL DECK NOT SHOWN FOR CLARITY. SEE DETAIL S1.09.

| INTERIOR MOMENT CONNECTION - SECTION | SCALE: 1-1/2" = 1' - 0" | S1.06 |
|---|---|---|

PROJECT: SPECIMEN #1 MOMENT FRAME
DRAWN: DEL CARPIO RAMOS, MAIKOL
DATE: 08/16/2012

PRODUCED BY AN AUTODESK EDUCATIONAL PRODUCT

PRODUCED BY AN AUTODESK EDUCATIONAL PRODUCT



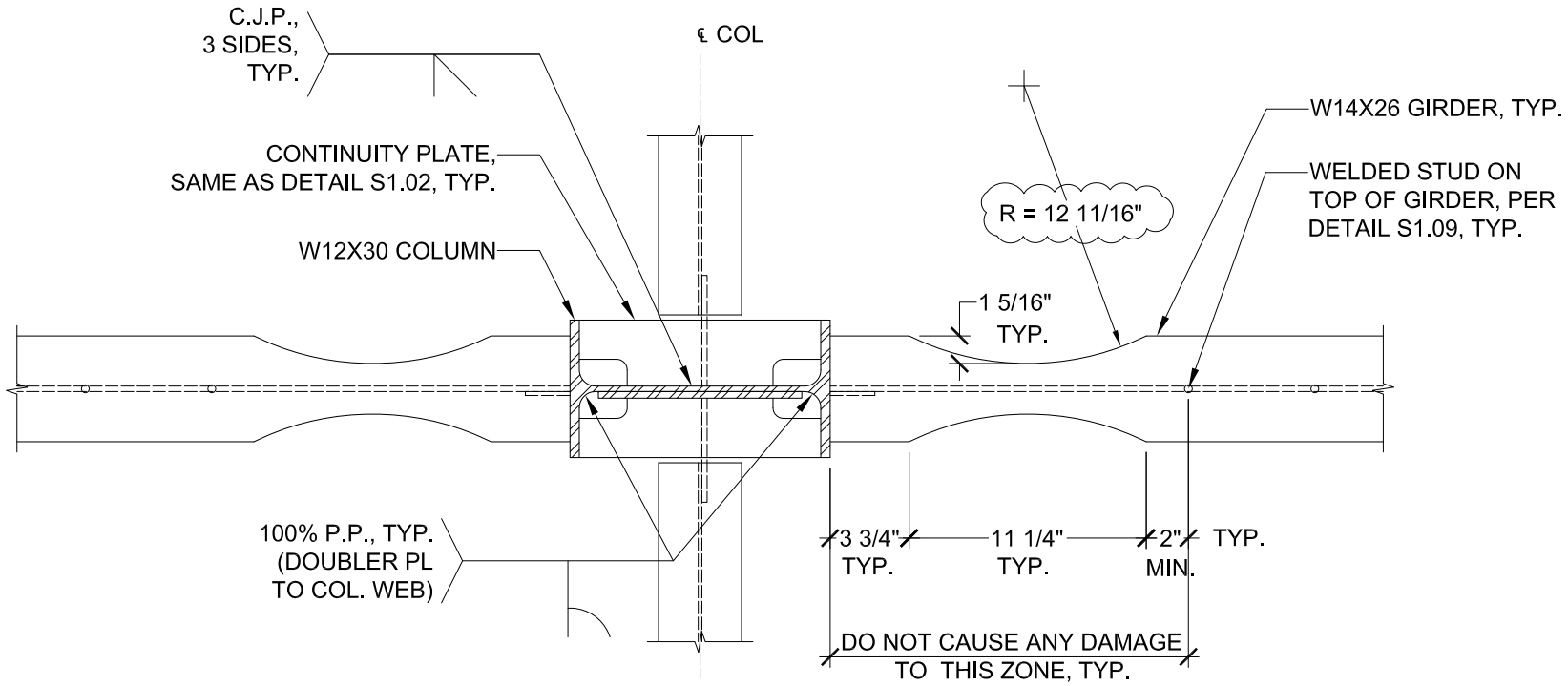


| | | |
|---|---|---|
| INTERIOR MOMENT CONNECTION - PLAN VIEW | SCALE: 1-1/2" = 1' - 0" | S1.07 |
| PROJECT: SPECIMEN #1 MOMENT FRAME<br>DRAWN: DEL CARPIO RAMOS, MAIKOL<br>DATE: 08/16/2012 | | |

PRODUCED BY AN AUTODESK EDUCATIONAL PRODUCT

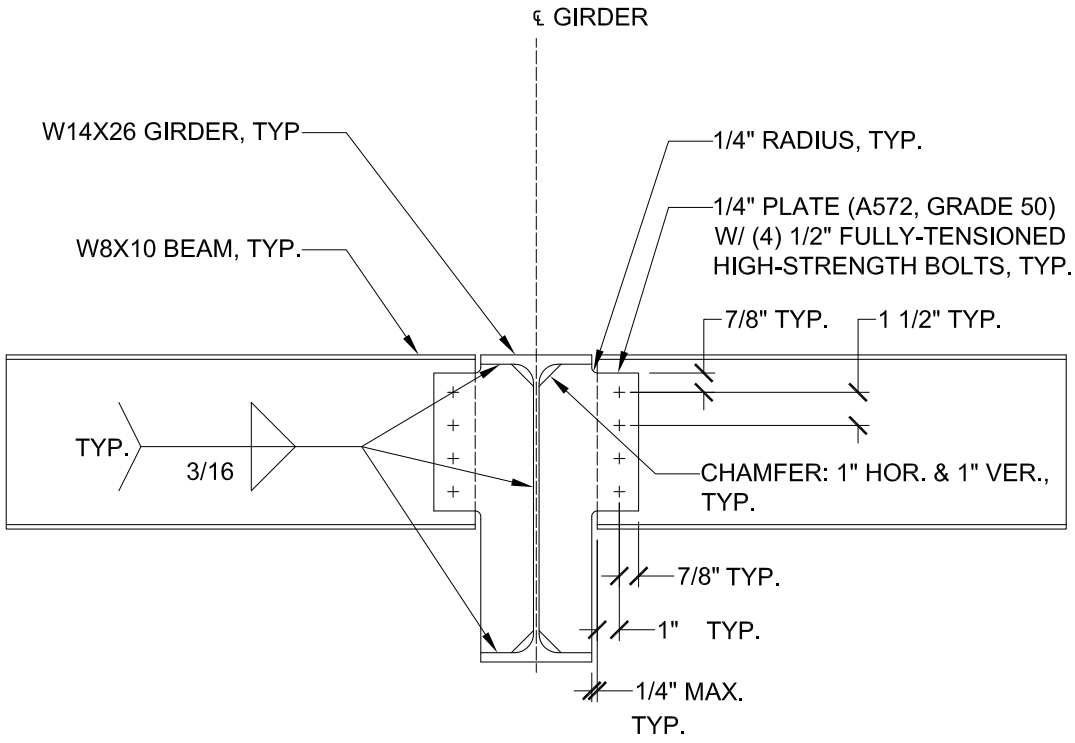


NOTE: CONCRETE SLAB OVER METAL DECK IS NOT SHOWN FOR CLARITY. SEE DETAIL S1.09

| CONNECTION OF BEAM TO GIRDER | SCALE: 1-1/2" = 1' - 0" | S1.08 |
|---|---|---|

PROJECT: SPECIMEN #1 MOMENT FRAME
DRAWN: DEL CARPIO RAMOS, MAIKOL
DATE: 08/16/2012

PRODUCED BY AN AUTODESK EDUCATIONAL PRODUCT

PRODUCED BY AN AUTODESK EDUCATIONAL PRODUCT

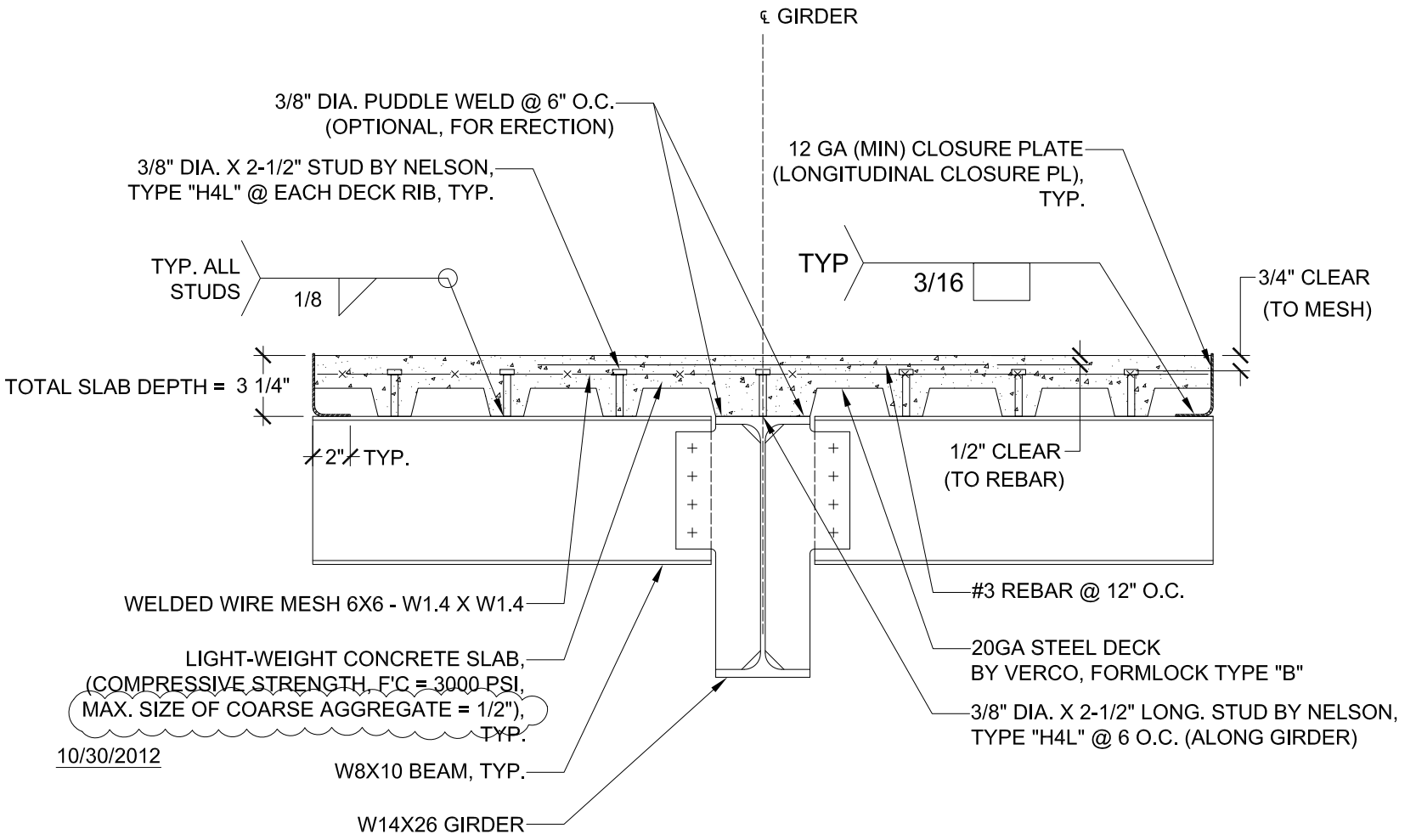


NOTE: SUPPLEMENT INFORMATION WITH DETAIL S1.08

| CONCRETE SLAB OVER METAL DECK DETAIL | SCALE: 1-1/2" = 1' - 0" | S1.09 |
|---|---|---|

PROJECT: SPECIMEN #1 MOMENT FRAME
DRAWN: DEL CARPIO RAMOS, MAIKOL
DATE: 08/16/2012

PRODUCED BY AN AUTODESK EDUCATIONAL PRODUCT

PRODUCED BY AN AUTODESK EDUCATIONAL PRODUCT

**NOTES:**

1. BEVEL AS INDICATED
2. LARGER OF "tf" OR 1/2" (PLUS 1/2 tf OR MINUS 1/4 tf)
3. 3/4" tf TO tf, 3/4" MIN (±1/4")
4. 3/8" MIN RADIUS (PLUS NOT LIMITED, OR MINUS 0)
5. 3 tf (±1/2")
6. FOR CUTTING METHODS AND SMOOTHNESS, SEE REQUIREMENTS OF SECTION 4.4 OF FEMA 353.

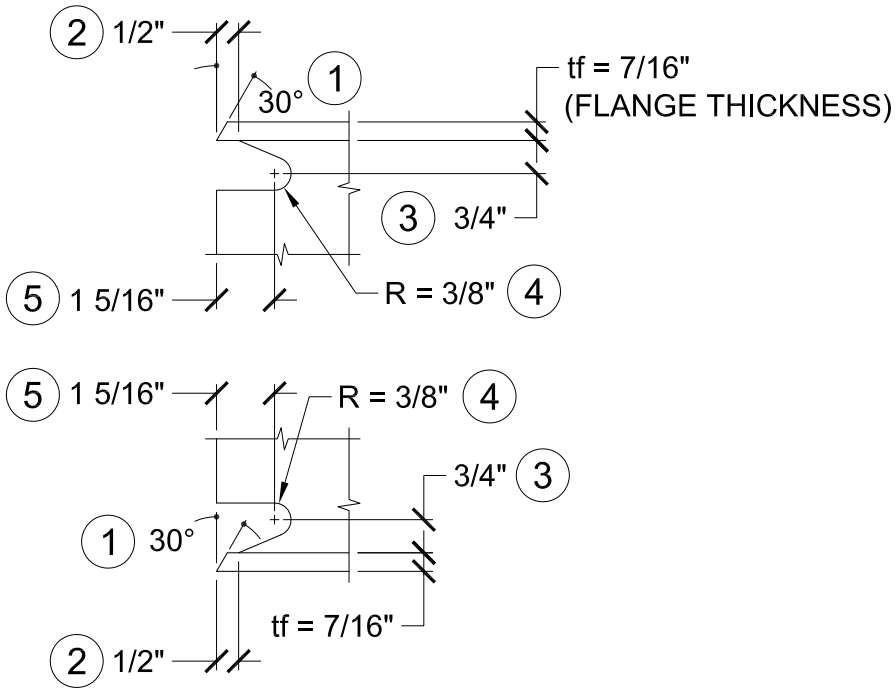


| WELD ACCESS HOLE DETAIL | SCALE: 3" = 1' - 0" | S1.10 |
|---|---|---|

PROJECT: SPECIMEN #1 MOMENT FRAME
DRAWN: DEL CARPIO RAMOS, MAIKOL
DATE: 08/16/2012

PRODUCED BY AN AUTODESK EDUCATIONAL PRODUCT

PRODUCED BY AN AUTODESK EDUCATIONAL PRODUCT

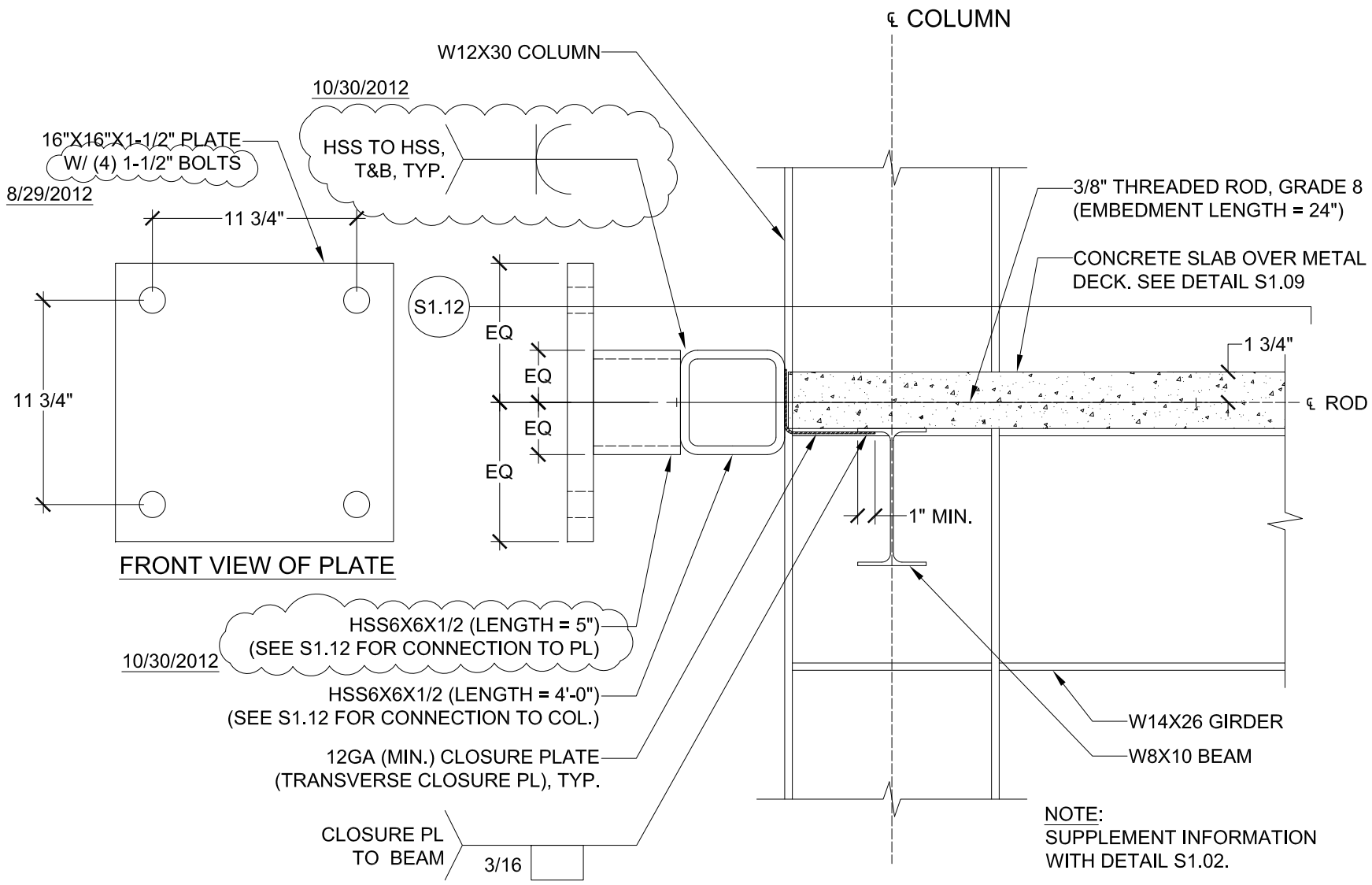


| CONNECTION OF HSS6X6X1/2 AND PLATE TO FRAME - ELEVATION | SCALE: 1-1/2" = 1' - 0" | S1.11 |
|---|---|---|

PROJECT: SPECIMEN #1 MOMENT FRAME
DRAWN: DEL CARPIO RAMOS, MAIKOL
DATE: 08/16/2012, REVISION 1: 08/29/2012 REVISION 2: 10/30/2012

PRODUCED BY AN AUTODESK EDUCATIONAL PRODUCT

PRODUCED BY AN AUTODESK EDUCATIONAL PRODUCT

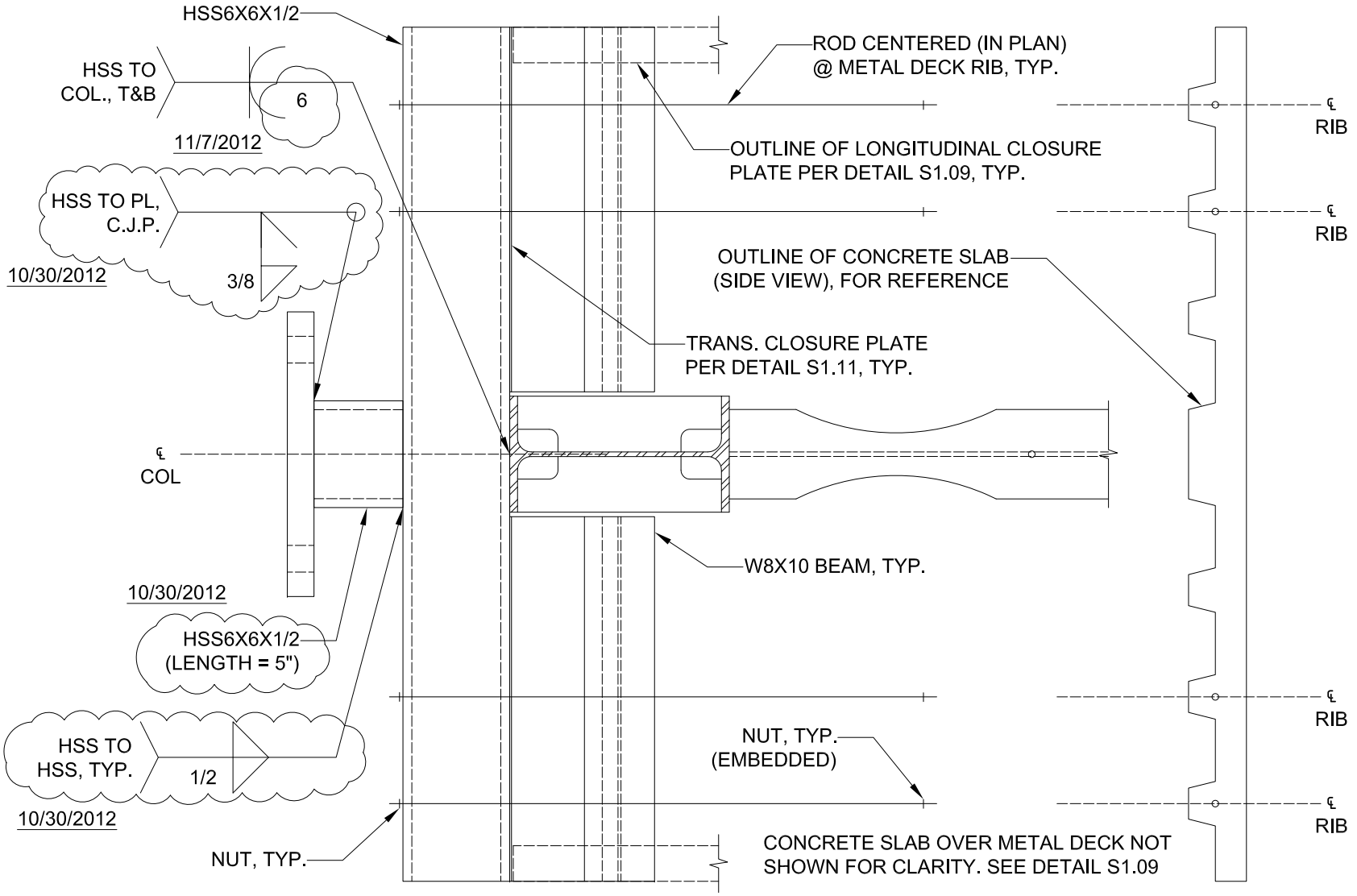


| CONNECTION OF HSS6X6X1/2 TO FRAME - PLAN VIEW | SCALE: 1-1/2" = 1' - 0" | S1.12 |
|---|---|---|

PROJECT: SPECIMEN #1 MOMENT FRAME
DRAWN: DEL CARPIO RAMOS, MAIKOL
DATE: 08/16/2012, REVISION 1: 10/30/2012 REVISION 2: 11/07/2012

PRODUCED BY AN AUTODESK EDUCATIONAL PRODUCT



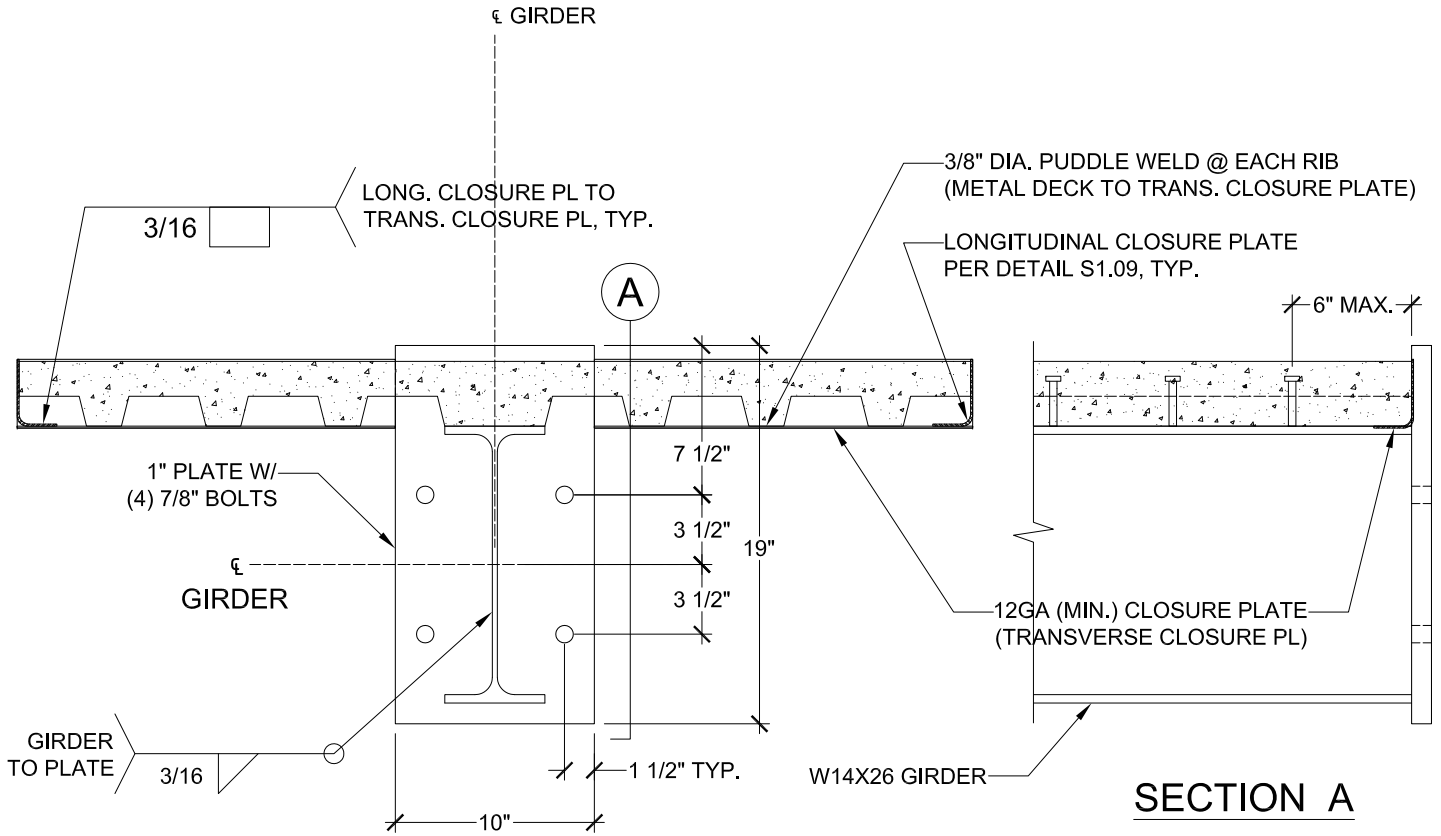


| | | |
|---|---|---|
| END PLATE DETAIL | SCALE: 1-1/2" = 1' - 0" | S1.13 |
| PROJECT: SPECIMEN #1 MOMENT FRAME<br>DRAWN: DEL CARPIO RAMOS, MAIKOL<br>DATE: 08/16/2012 | | |

PRODUCED BY AN AUTODESK EDUCATIONAL PRODUCT

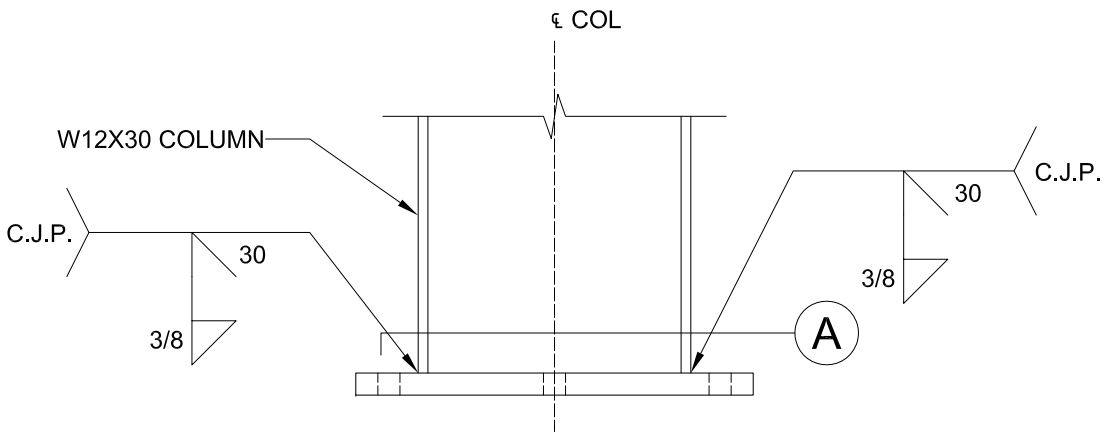


ELEVATION

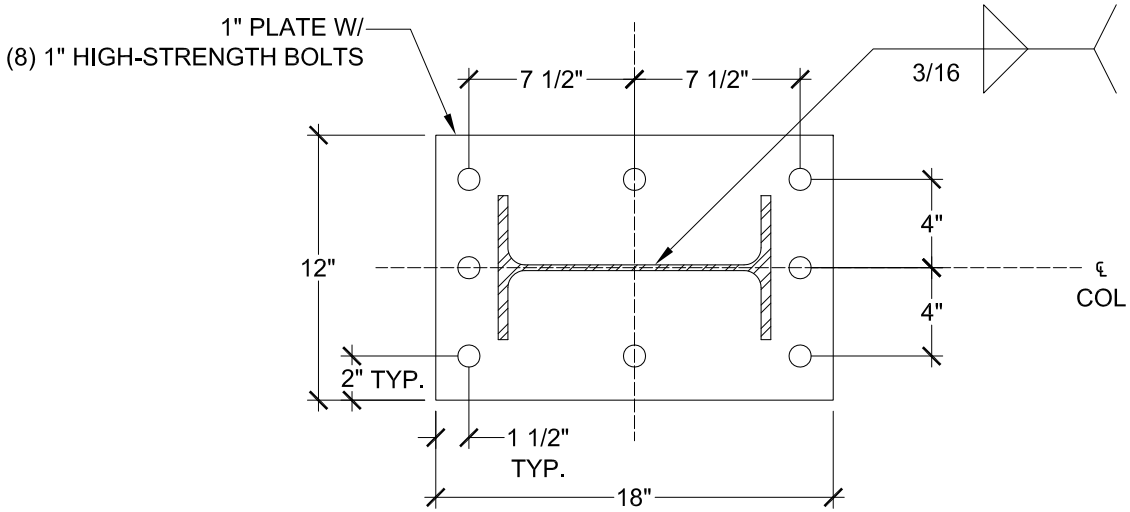


SECTION A

| | | |
|---|---|---|
| BASE PLATE DETAIL | SCALE: 1-1/2" = 1' - 0" | S1.14 |
| PROJECT: SPECIMEN #1 MOMENT FRAME<br>DRAWN: DEL CARPIO RAMOS, MAIKOL<br>DATE: 08/16/2012 | | |

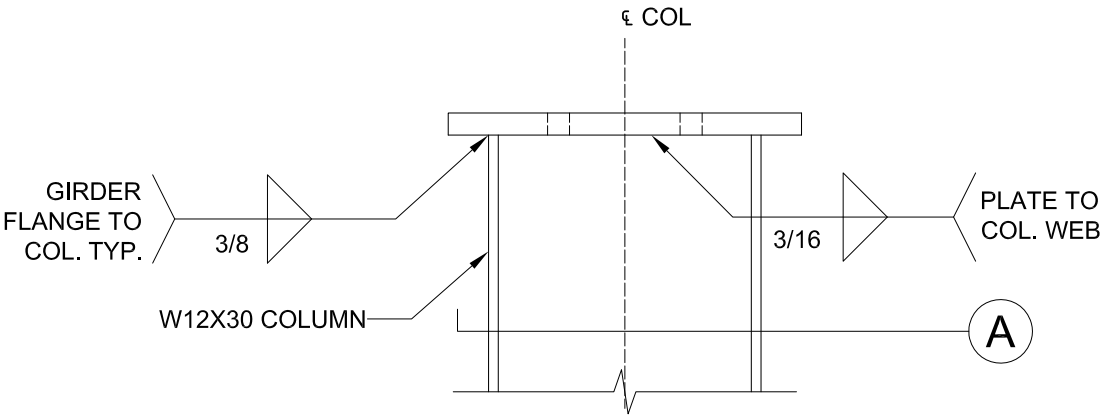


ELEVATION

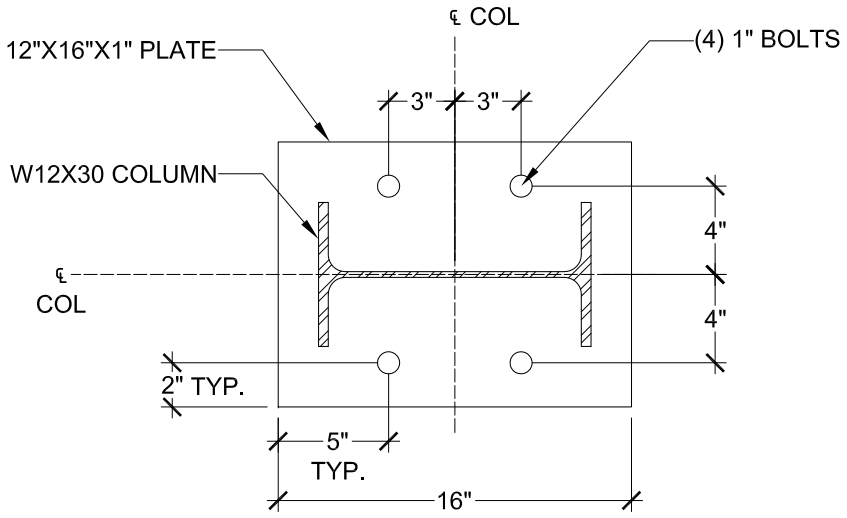


SECTION A

| | | |
|---|---|---|
| TOP PLATE DETAIL | SCALE: 1-1/2" = 1' - 0" | S1.15 |
| PROJECT: SPECIMEN #1 MOMENT FRAME<br>DRAWN: DEL CARPIO RAMOS, MAIKOL<br>DATE: 08/16/2012 | | |

PRODUCED BY AN AUTODESK EDUCATIONAL PRODUCT

PRODUCED BY AN AUTODESK EDUCATIONAL PRODUCT

# APPENDIX B: DRAWINGS OF TEST SPECIMEN #2



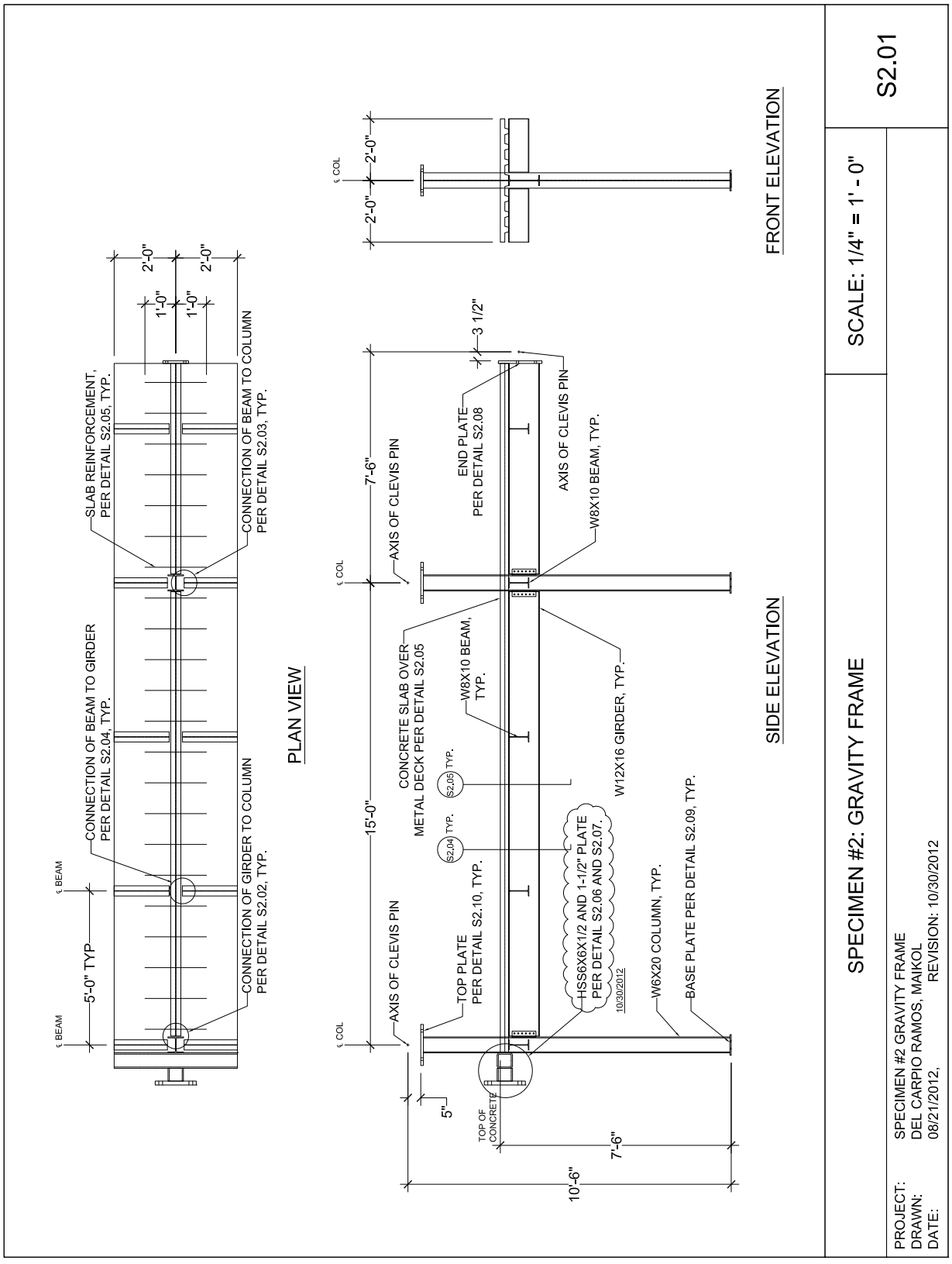

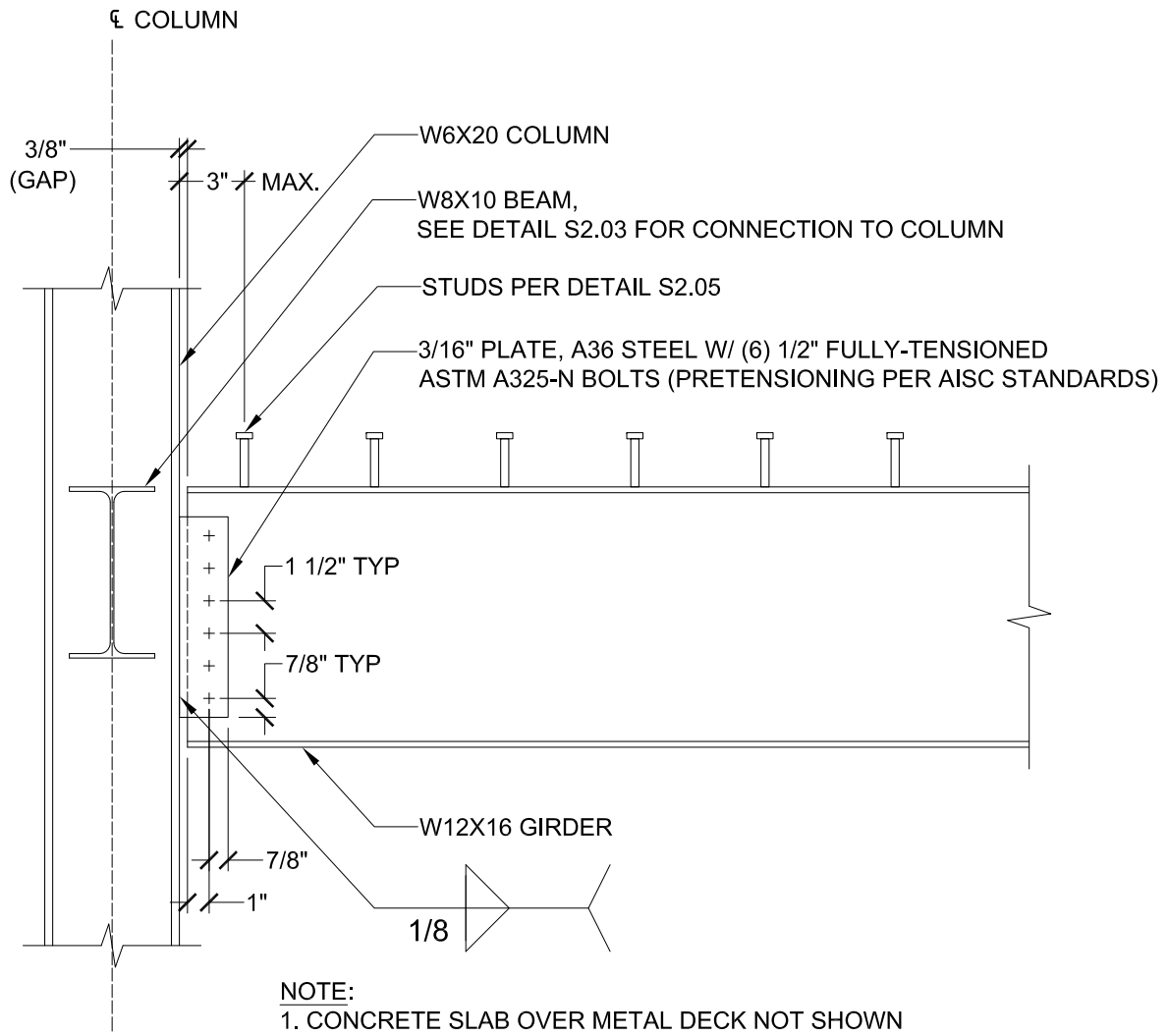


NOTE:
1. CONCRETE SLAB OVER METAL DECK NOT SHOWN FOR CLARITY. SEE DETAIL S2.05.
2. SUPPLEMENT INFORMATION WITH DETAIL S2.06

| CONNECTION OF GIRDER TO COLUMN (SHEAR-TAB CONNECTION) | SCALE: 1-1/2" = 1' - 0" | S2.02 |
|---|---|---|

PROJECT: SPECIMEN #2 GRAVITY FRAME
DRAWN: DEL CARPIO RAMOS, MAIKOL
DATE: 08/21/2012

PRODUCED BY AN AUTODESK EDUCATIONAL PRODUCT

PRODUCED BY AN AUTODESK EDUCATIONAL PRODUCT

PRODUCED BY AN AUTODESK EDUCATIONAL PRODUCT



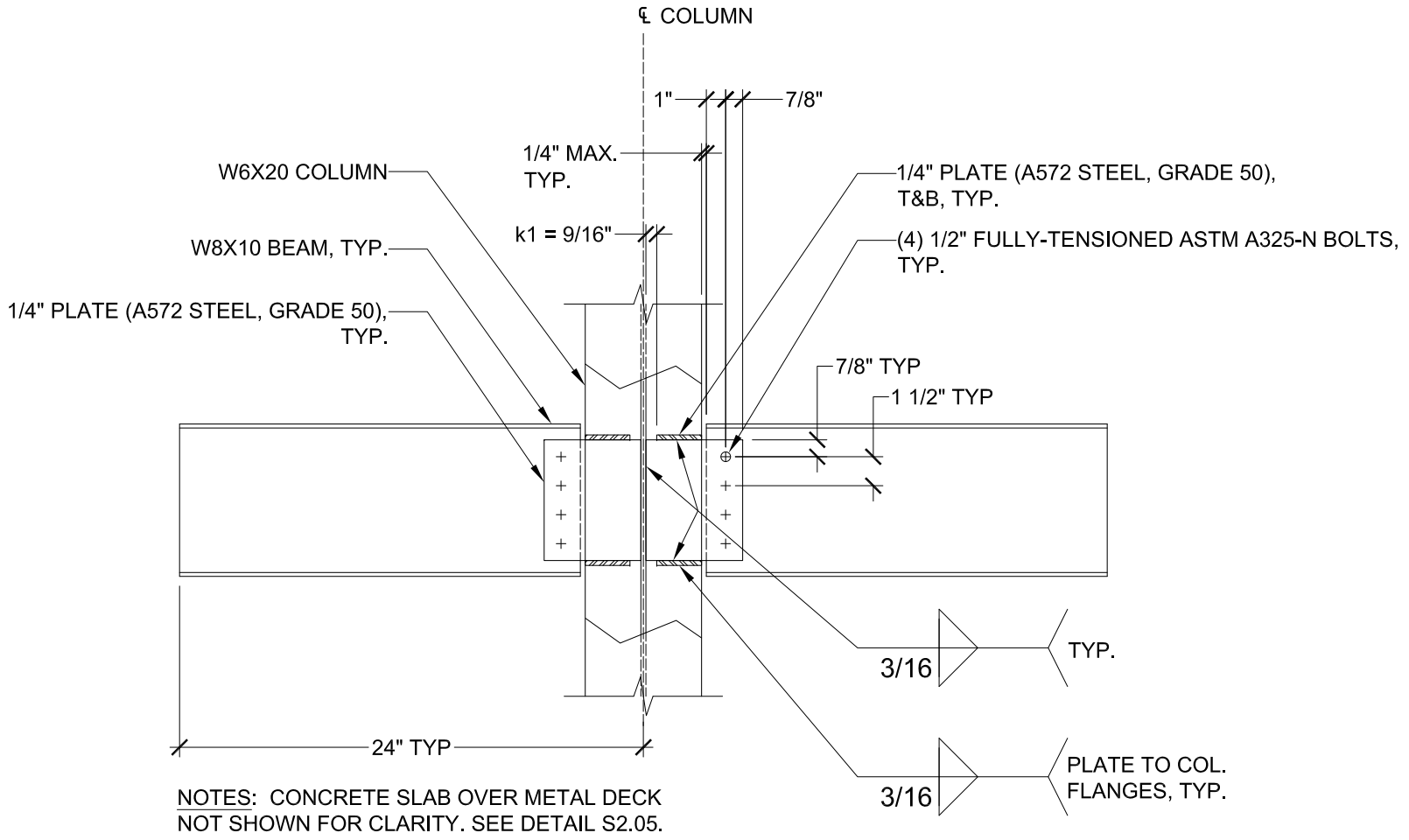


| CONNECTION OF BEAM TO COLUMN | SCALE: 1-1/2" = 1' - 0" | S2.03 |
|---|---|---|

PROJECT: SPECIMEN #2 GRAVITY FRAME
DRAWN: DEL CARPIO RAMOS, MAIKOL
DATE: 08/21/2012

PRODUCED BY AN AUTODESK EDUCATIONAL PRODUCT

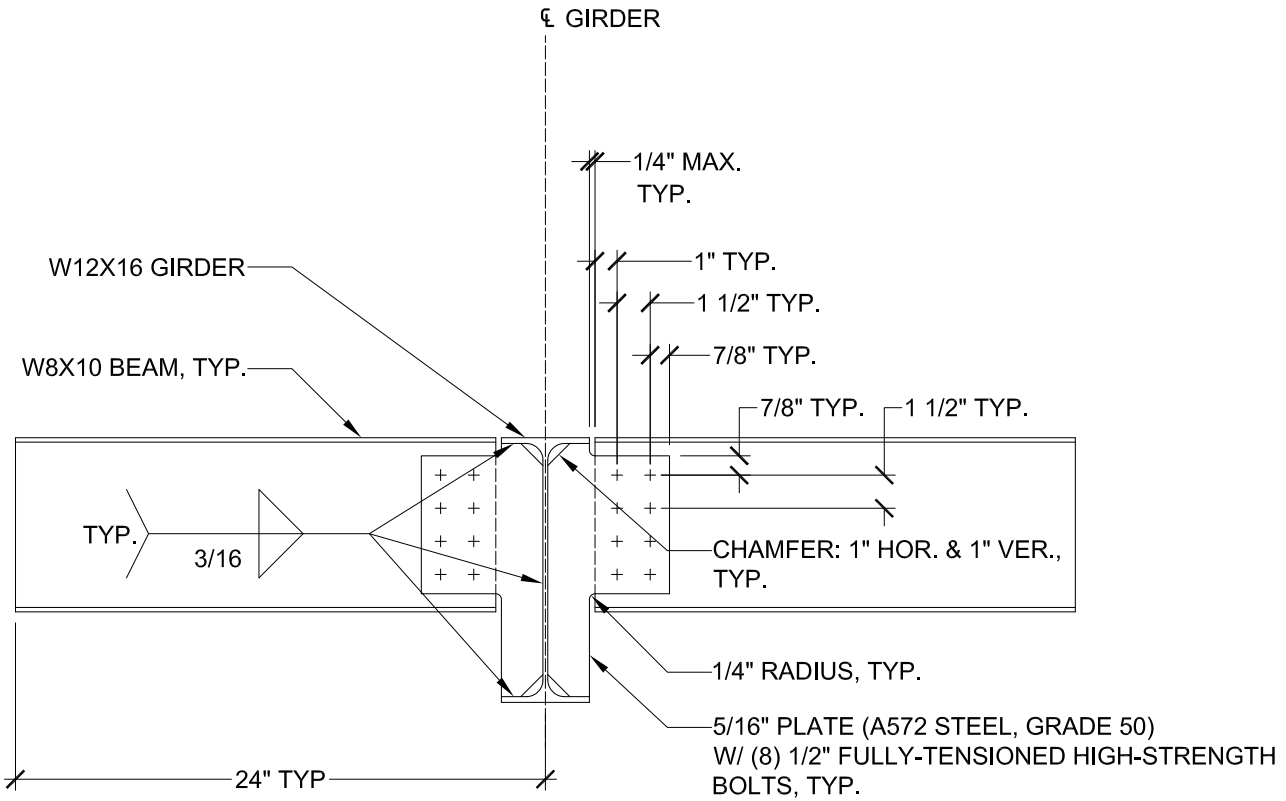


NOTES: CONCRETE SLAB OVER METAL DECK
NOT SHOWN FOR CLARITY. SEE DETAIL S2.05.

| CONNECTION OF BEAM TO GIRDER | SCALE: 1-1/2" = 1' - 0" | S2.04 |
|---|---|---|

PROJECT: SPECIMEN #2 GRAVITY FRAME
DRAWN: DEL CARPIO RAMOS, MAIKOL
DATE: 08/21/2012

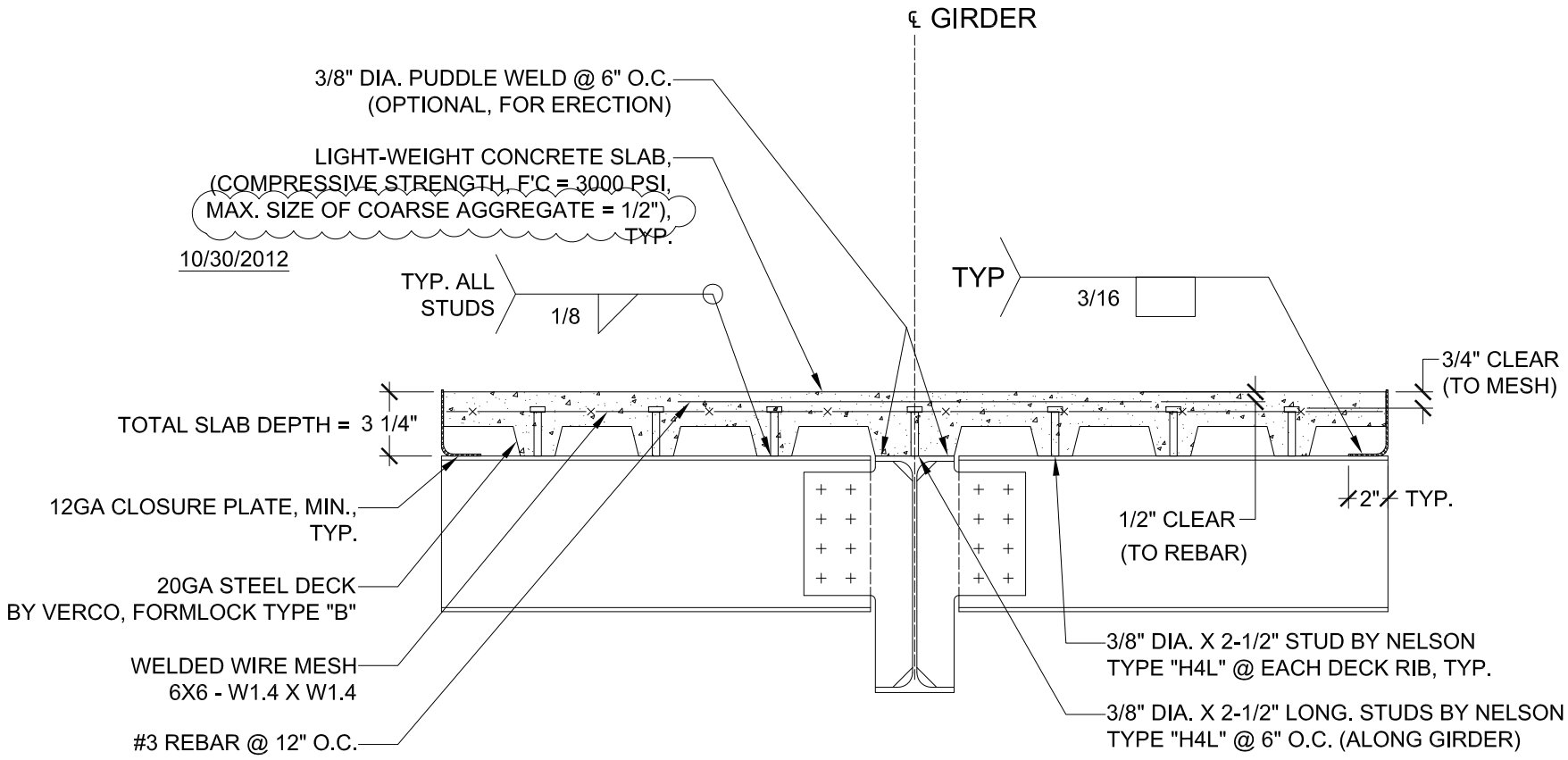


NOTE: SUPPLEMENT INFORMATION WITH DETAIL S2.04

| CONCRETE SLAB OVER METAL DECK DETAIL | SCALE: 1-1/2" = 1' - 0" | S2.05 |
|---|---|---|

PROJECT: SPECIMEN #2 GRAVITY FRAME
DRAWN: DEL CARPIO RAMOS, MAIKOL
DATE: 08/21/2012

PRODUCED BY AN AUTODESK EDUCATIONAL PRODUCT

PRODUCED BY AN AUTODESK EDUCATIONAL PRODUCT

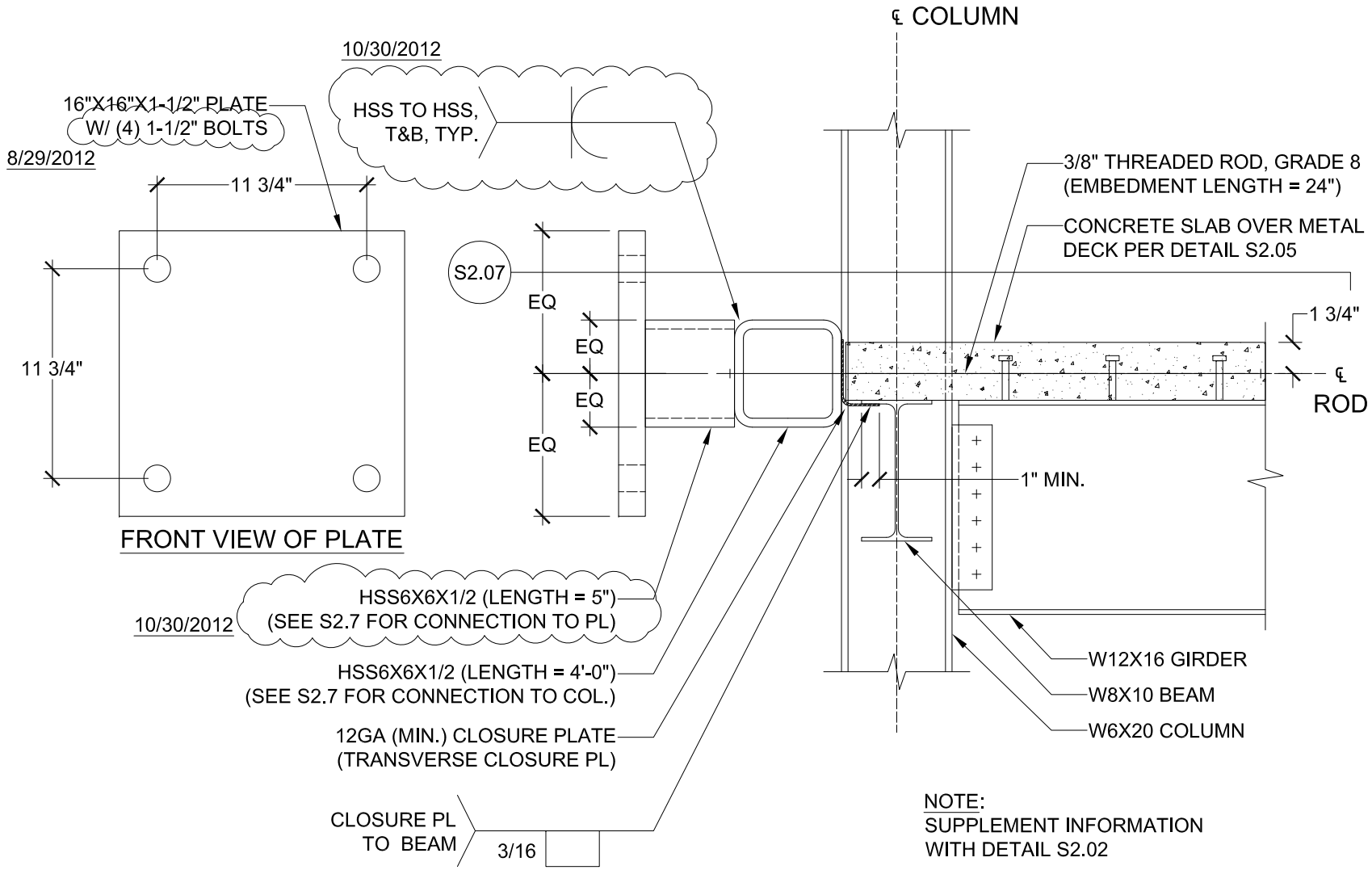


| CONNECTION OF HSS6X6X1/2 TO FRAME - ELEVATION | SCALE: 1-1/2" = 1' - 0" | S2.06 |
|---|---|---|

PROJECT: SPECIMEN #2 GRAVITY FRAME
DRAWN: DEL CARPIO RAMOS, MAIKOL
DATE: 08/21/2012, REVISED 1: 08/29/2012, REVISED 2: 10/30/2012

PRODUCED BY AN AUTODESK EDUCATIONAL PRODUCT

PRODUCED BY AN AUTODESK EDUCATIONAL PRODUCT

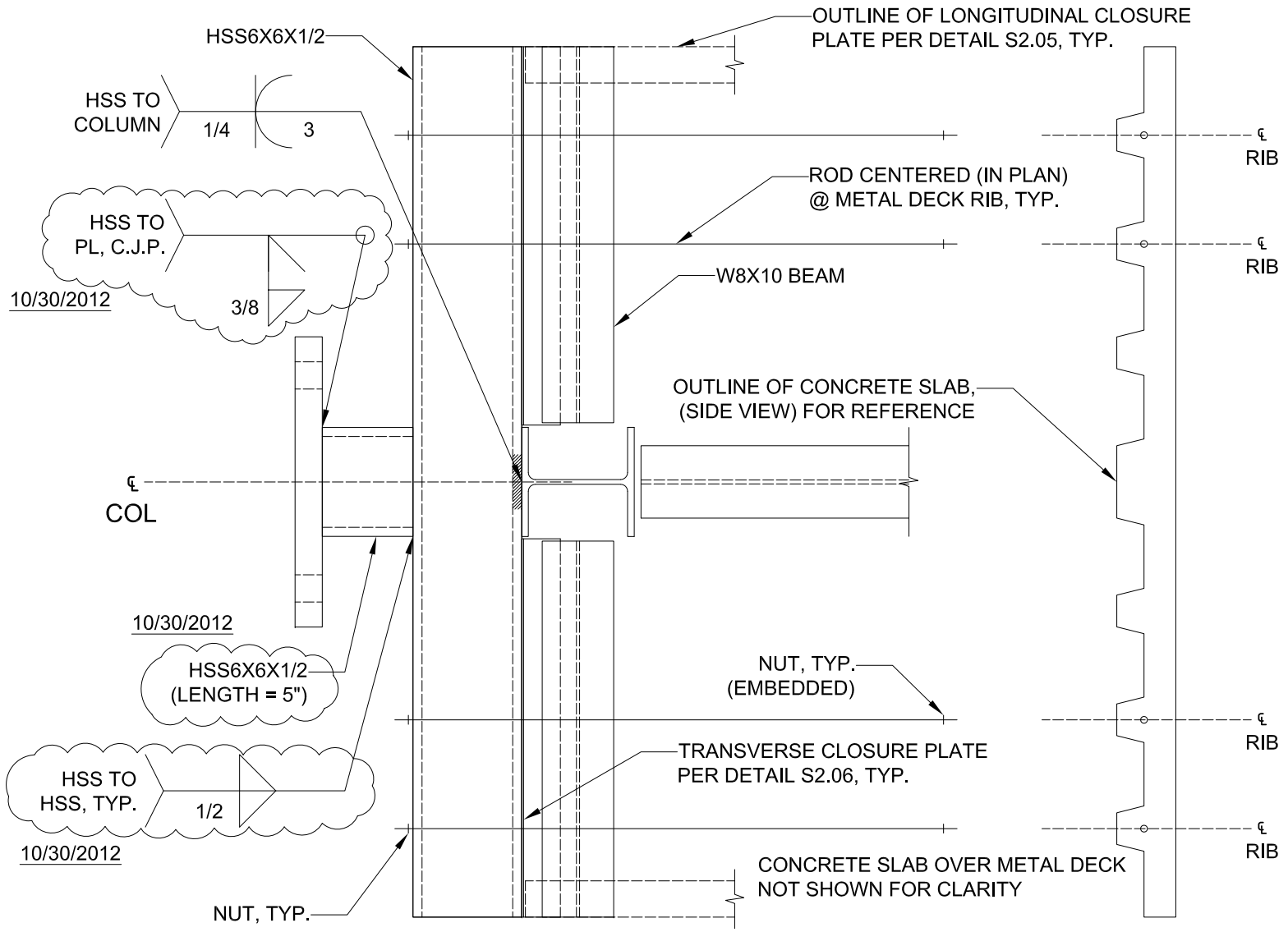


CONNECTION OF HSS6X6X$\frac{1}{2}$ TO FRAME - PLAN VIEW

SCALE: 1-1/2" = 1' - 0"

S2.07

PROJECT: SPECIMEN #2 GRAVITY FRAME
DRAWN: DEL CARPIO RAMOS, MAIKOL
DATE: 08/21/2012

PRODUCED BY AN AUTODESK EDUCATIONAL PRODUCT

PRODUCED BY AN AUTODESK EDUCATIONAL PRODUCT

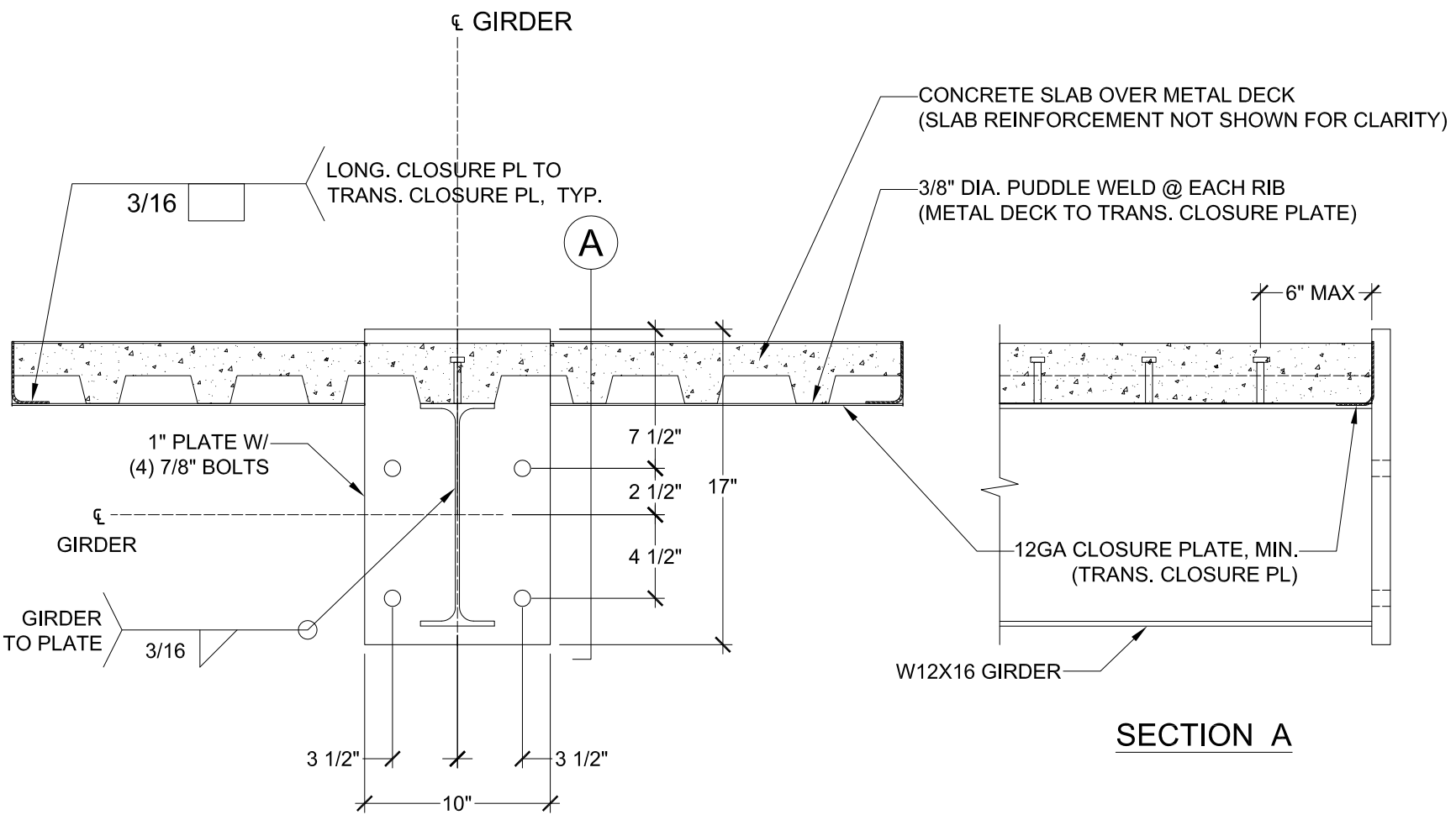


| | | |
|---|---|---|
| END PLATE DETAIL | SCALE: 1-1/2" = 1' - 0" | S2.08 |

PROJECT: SPECIMEN #2 GRAVITY FRAME
DRAWN: DEL CARPIO RAMOS, MAIKOL
DATE: 08/21/2012

PRODUCED BY AN AUTODESK EDUCATIONAL PRODUCT

PRODUCED BY AN AUTODESK EDUCATIONAL PRODUCT

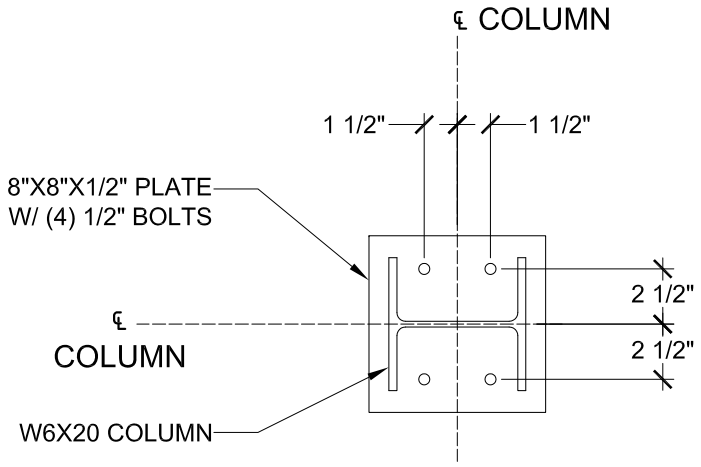


PLAN

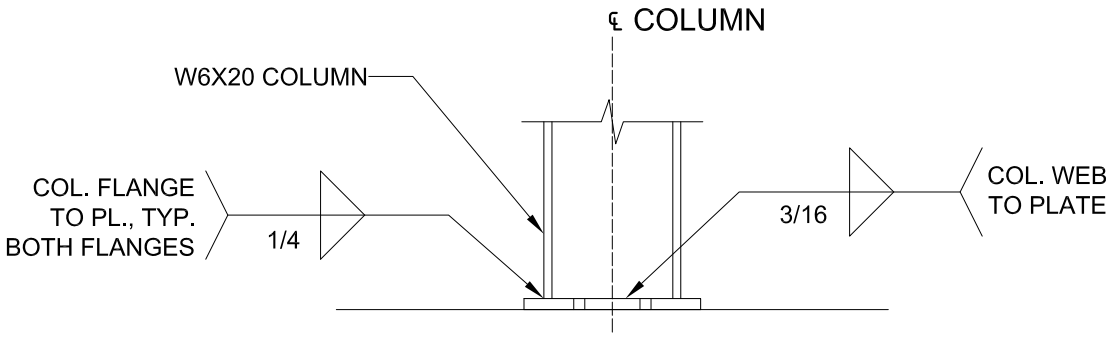


ELEVATION

| | | |
|---|---|---|
| BASE PLATE DETAIL | SCALE: 1-1/2" = 1' - 0" | S2.09 |

PROJECT: SPECIMEN #2 GRAVITY FRAME
DRAWN: DEL CARPIO RAMOS, MAIKOL
DATE: 08/21/2012

PRODUCED BY AN AUTODESK EDUCATIONAL PRODUCT

PRODUCED BY AN AUTODESK EDUCATIONAL PRODUCT

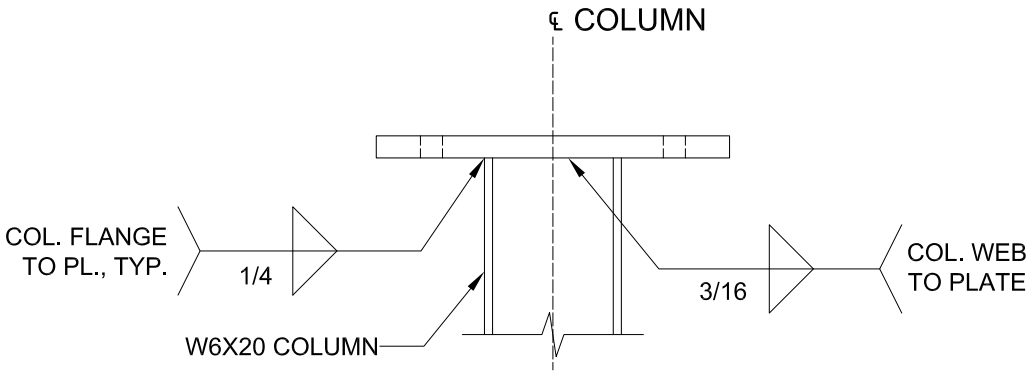


ELEVATION

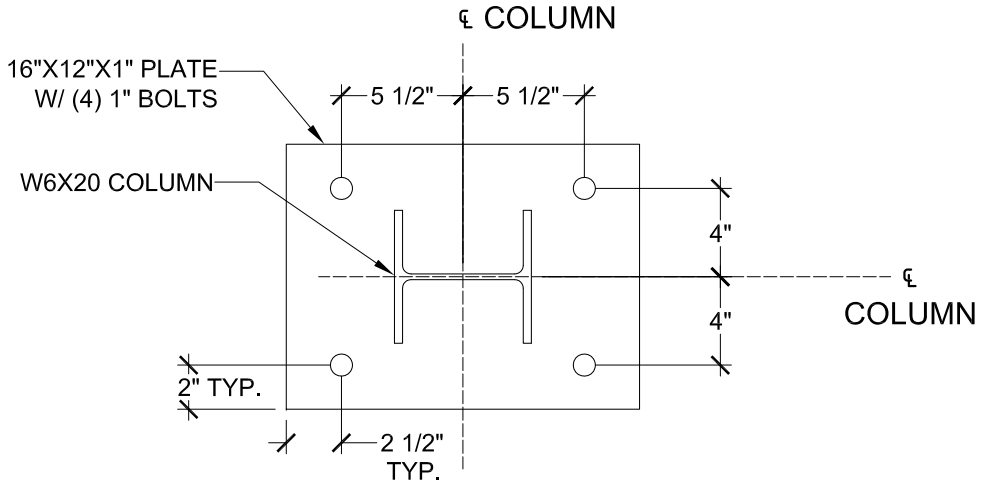


PLAN

| TOP PLATE DETAIL | SCALE: 1-1/2" = 1' - 0" | S2.10 |
|---|---|---|

PROJECT: SPECIMEN #2 GRAVITY FRAME
DRAWN: DEL CARPIO RAMOS, MAIKOL
DATE: 08/21/2012

PRODUCED BY AN AUTODESK EDUCATIONAL PRODUCT

PRODUCED BY AN AUTODESK EDUCATIONAL PRODUCT

## MCEER Technical Reports

MCEER publishes technical reports on a variety of subjects written by authors funded through MCEER. These reports are available from both MCEER Publications and the National Technical Information Service (NTIS). Requests for reports should be directed to MCEER Publications, MCEER, University at Buffalo, State University of New York, 133A Ketter Hall, Buffalo, New York 14260. Reports can also be requested through NTIS, P.O. Box 1425, Springfield, Virginia 22151. NTIS accession numbers are shown in parenthesis, if available.

NCEER-87-0001 "First-Year Program in Research, Education and Technology Transfer," 3/5/87, (PB88-134275, A04, MF-A01).

NCEER-87-0002 "Experimental Evaluation of Instantaneous Optimal Algorithms for Structural Control," by R.C. Lin, T.T. Soong and A.M. Reinhorn, 4/20/87, (PB88-134341, A04, MF-A01).

NCEER-87-0003 "Experimentation Using the Earthquake Simulation Facilities at University at Buffalo," by A.M. Reinhorn and R.L. Ketter, not available.

NCEER-87-0004 "The System Characteristics and Performance of a Shaking Table," by J.S. Hwang, K.C. Chang and G.C. Lee, 6/1/87, (PB88-134259, A03, MF-A01). This report is available only through NTIS (see address given above).

NCEER-87-0005 "A Finite Element Formulation for Nonlinear Viscoplastic Material Using a Q Model," by O. Gyebi and G. Dasgupta, 11/2/87, (PB88-213764, A08, MF-A01).

NCEER-87-0006 "Symbolic Manipulation Program (SMP) - Algebraic Codes for Two and Three Dimensional Finite Element Formulations," by X. Lee and G. Dasgupta, 11/9/87, (PB88-218522, A05, MF-A01).

NCEER-87-0007 "Instantaneous Optimal Control Laws for Tall Buildings Under Seismic Excitations," by J.N. Yang, A. Akbarpour and P. Ghaemmaghami, 6/10/87, (PB88-134333, A06, MF-A01). This report is only available through NTIS (see address given above).

NCEER-87-0008 "IDARC: Inelastic Damage Analysis of Reinforced Concrete Frame - Shear-Wall Structures," by Y.J. Park, A.M. Reinhorn and S.K. Kunnath, 7/20/87, (PB88-134325, A09, MF-A01). This report is only available through NTIS (see address given above).

NCEER-87-0009 "Liquefaction Potential for New York State: A Preliminary Report on Sites in Manhattan and Buffalo," by M. Budhu, V. Vijayakumar, R.F. Giese and L. Baumgras, 8/31/87, (PB88-163704, A03, MF-A01). This report is available only through NTIS (see address given above).

NCEER-87-0010 "Vertical and Torsional Vibration of Foundations in Inhomogeneous Media," by A.S. Veletsos and K.W. Dotson, 6/1/87, (PB88-134291, A03, MF-A01). This report is only available through NTIS (see address given above).

NCEER-87-0011 "Seismic Probabilistic Risk Assessment and Seismic Margins Studies for Nuclear Power Plants," by Howard H.M. Hwang, 6/15/87, (PB88-134267, A03, MF-A01). This report is only available through NTIS (see address given above).

NCEER-87-0012 "Parametric Studies of Frequency Response of Secondary Systems Under Ground-Acceleration Excitations," by Y. Yong and Y.K. Lin, 6/10/87, (PB88-134309, A03, MF-A01). This report is only available through NTIS (see address given above).

NCEER-87-0013 "Frequency Response of Secondary Systems Under Seismic Excitation," by J.A. HoLung, J. Cai and Y.K. Lin, 7/31/87, (PB88-134317, A05, MF-A01). This report is only available through NTIS (see address given above).

NCEER-87-0014 "Modelling Earthquake Ground Motions in Seismically Active Regions Using Parametric Time Series Methods," by G.W. Ellis and A.S. Cakmak, 8/25/87, (PB88-134283, A08, MF-A01). This report is only available through NTIS (see address given above).

NCEER-87-0015 "Detection and Assessment of Seismic Structural Damage," by E. DiPasquale and A.S. Cakmak, 8/25/87, (PB88-163712, A05, MF-A01). This report is only available through NTIS (see address given above).

NCEER-87-0016 "Pipeline Experiment at Parkfield, California," by J. Isenberg and E. Richardson, 9/15/87, (PB88-163720, A03, MF-A01). This report is available only through NTIS (see address given above).

NCEER-87-0017 "Digital Simulation of Seismic Ground Motion," by M. Shinozuka, G. Deodatis and T. Harada, 8/31/87, (PB88-155197, A04, MF-A01). This report is available only through NTIS (see address given above).

NCEER-87-0018 "Practical Considerations for Structural Control: System Uncertainty, System Time Delay and Truncation of Small Control Forces," J.N. Yang and A. Akbarpour, 8/10/87, (PB88-163738, A08, MF-A01). This report is only available through NTIS (see address given above).

NCEER-87-0019 "Modal Analysis of Nonclassically Damped Structural Systems Using Canonical Transformation," by J.N. Yang, S. Sarkani and F.X. Long, 9/27/87, (PB88-187851, A04, MF-A01).

NCEER-87-0020 "A Nonstationary Solution in Random Vibration Theory," by J.R. Red-Horse and P.D. Spanos, 11/3/87, (PB88-163746, A03, MF-A01).

NCEER-87-0021 "Horizontal Impedances for Radially Inhomogeneous Viscoelastic Soil Layers," by A.S. Veletsos and K.W. Dotson, 10/15/87, (PB88-150859, A04, MF-A01).

NCEER-87-0022 "Seismic Damage Assessment of Reinforced Concrete Members," by Y.S. Chung, C. Meyer and M. Shinozuka, 10/9/87, (PB88-150867, A05, MF-A01). This report is available only through NTIS (see address given above).

NCEER-87-0023 "Active Structural Control in Civil Engineering," by T.T. Soong, 11/11/87, (PB88-187778, A03, MF-A01).

NCEER-87-0024 "Vertical and Torsional Impedances for Radially Inhomogeneous Viscoelastic Soil Layers," by K.W. Dotson and A.S. Veletsos, 12/87, (PB88-187786, A03, MF-A01).

NCEER-87-0025 "Proceedings from the Symposium on Seismic Hazards, Ground Motions, Soil-Liquefaction and Engineering Practice in Eastern North America," October 20-22, 1987, edited by K.H. Jacob, 12/87, (PB88-188115, A23, MF-A01). This report is available only through NTIS (see address given above).

NCEER-87-0026 "Report on the Whittier-Narrows, California, Earthquake of October 1, 1987," by J. Pantelic and A. Reinhorn, 11/87, (PB88-187752, A03, MF-A01). This report is available only through NTIS (see address given above).

NCEER-87-0027 "Design of a Modular Program for Transient Nonlinear Analysis of Large 3-D Building Structures," by S. Srivastav and J.F. Abel, 12/30/87, (PB88-187950, A05, MF-A01). This report is only available through NTIS (see address given above).

NCEER-87-0028 "Second-Year Program in Research, Education and Technology Transfer," 3/8/88, (PB88-219480, A04, MF-A01).

NCEER-88-0001 "Workshop on Seismic Computer Analysis and Design of Buildings With Interactive Graphics," by W. McGuire, J.F. Abel and C.H. Conley, 1/18/88, (PB88-187760, A03, MF-A01). This report is only available through NTIS (see address given above).

NCEER-88-0002 "Optimal Control of Nonlinear Flexible Structures," by J.N. Yang, F.X. Long and D. Wong, 1/22/88, (PB88-213772, A06, MF-A01).

NCEER-88-0003 "Substructuring Techniques in the Time Domain for Primary-Secondary Structural Systems," by G.D. Manolis and G. Juhn, 2/10/88, (PB88-213780, A04, MF-A01).

NCEER-88-0004 "Iterative Seismic Analysis of Primary-Secondary Systems," by A. Singhal, L.D. Lutes and P.D. Spanos, 2/23/88, (PB88-213798, A04, MF-A01).

NCEER-88-0005 "Stochastic Finite Element Expansion for Random Media," by P.D. Spanos and R. Ghanem, 3/14/88, (PB88-213806, A03, MF-A01).

NCEER-88-0006 "Combining Structural Optimization and Structural Control," by F.Y. Cheng and C.P. Pantelides, 1/10/88, (PB88-213814, A05, MF-A01).

NCEER-88-0007 "Seismic Performance Assessment of Code-Designed Structures," by H.H-M. Hwang, J-W. Jaw and H-J. Shau, 3/20/88, (PB88-219423, A04, MF-A01). This report is only available through NTIS (see address given above).

NCEER-88-0008 "Reliability Analysis of Code-Designed Structures Under Natural Hazards," by H.H-M. Hwang, H. Ushiba and M. Shinozuka, 2/29/88, (PB88-229471, A07, MF-A01). This report is only available through NTIS (see address given above).

NCEER-88-0009 "Seismic Fragility Analysis of Shear Wall Structures," by J-W Jaw and H.H-M. Hwang, 4/30/88, (PB89-102867, A04, MF-A01).

NCEER-88-0010 "Base Isolation of a Multi-Story Building Under a Harmonic Ground Motion - A Comparison of Performances of Various Systems," by F-G Fan, G. Ahmadi and I.G. Tadjbakhsh, 5/18/88, (PB89-122238, A06, MF-A01). This report is only available through NTIS (see address given above).

NCEER-88-0011 "Seismic Floor Response Spectra for a Combined System by Green's Functions," by F.M. Lavelle, L.A. Bergman and P.D. Spanos, 5/1/88, (PB89-102875, A03, MF-A01).

NCEER-88-0012 "A New Solution Technique for Randomly Excited Hysteretic Structures," by G.Q. Cai and Y.K. Lin, 5/16/88, (PB89-102883, A03, MF-A01).

NCEER-88-0013 "A Study of Radiation Damping and Soil-Structure Interaction Effects in the Centrifuge," by K. Weissman, supervised by J.H. Prevost, 5/24/88, (PB89-144703, A06, MF-A01).

NCEER-88-0014 "Parameter Identification and Implementation of a Kinematic Plasticity Model for Frictional Soils," by J.H. Prevost and D.V. Griffiths, not available.

NCEER-88-0015 "Two- and Three- Dimensional Dynamic Finite Element Analyses of the Long Valley Dam," by D.V. Griffiths and J.H. Prevost, 6/17/88, (PB89-144711, A04, MF-A01).

NCEER-88-0016 "Damage Assessment of Reinforced Concrete Structures in Eastern United States," by A.M. Reinhorn, M.J. Seidel, S.K. Kunnath and Y.J. Park, 6/15/88, (PB89-122220, A04, MF-A01). This report is only available through NTIS (see address given above).

NCEER-88-0017 "Dynamic Compliance of Vertically Loaded Strip Foundations in Multilayered Viscoelastic Soils," by S. Ahmad and A.S.M. Israil, 6/17/88, (PB89-102891, A04, MF-A01).

NCEER-88-0018 "An Experimental Study of Seismic Structural Response With Added Viscoelastic Dampers," by R.C. Lin, Z. Liang, T.T. Soong and R.H. Zhang, 6/30/88, (PB89-122212, A05, MF-A01). This report is available only through NTIS (see address given above).

NCEER-88-0019 "Experimental Investigation of Primary - Secondary System Interaction," by G.D. Manolis, G. Juhn and A.M. Reinhorn, 5/27/88, (PB89-122204, A04, MF-A01).

NCEER-88-0020 "A Response Spectrum Approach For Analysis of Nonclassically Damped Structures," by J.N. Yang, S. Sarkani and F.X. Long, 4/22/88, (PB89-102909, A04, MF-A01).

NCEER-88-0021 "Seismic Interaction of Structures and Soils: Stochastic Approach," by A.S. Veletsos and A.M. Prasad, 7/21/88, (PB89-122196, A04, MF-A01). This report is only available through NTIS (see address given above).

NCEER-88-0022 "Identification of the Serviceability Limit State and Detection of Seismic Structural Damage," by E. DiPasquale and A.S. Cakmak, 6/15/88, (PB89-122188, A05, MF-A01). This report is available only through NTIS (see address given above).

NCEER-88-0023 "Multi-Hazard Risk Analysis: Case of a Simple Offshore Structure," by B.K. Bhartia and E.H. Vanmarcke, 7/21/88, (PB89-145213, A05, MF-A01).

NCEER-88-0024 "Automated Seismic Design of Reinforced Concrete Buildings," by Y.S. Chung, C. Meyer and M. Shinozuka, 7/5/88, (PB89-122170, A06, MF-A01). This report is available only through NTIS (see address given above).

NCEER-88-0025 "Experimental Study of Active Control of MDOF Structures Under Seismic Excitations," by L.L. Chung, R.C. Lin, T.T. Soong and A.M. Reinhorn, 7/10/88, (PB89-122600, A04, MF-A01).

NCEER-88-0026 "Earthquake Simulation Tests of a Low-Rise Metal Structure," by J.S. Hwang, K.C. Chang, G.C. Lee and R.L. Ketter, 8/1/88, (PB89-102917, A04, MF-A01).

NCEER-88-0027 "Systems Study of Urban Response and Reconstruction Due to Catastrophic Earthquakes," by F. Kozin and H.K. Zhou, 9/22/88, (PB90-162348, A04, MF-A01).

NCEER-88-0028 "Seismic Fragility Analysis of Plane Frame Structures," by H.H-M. Hwang and Y.K. Low, 7/31/88, (PB89-131445, A06, MF-A01).

NCEER-88-0029 "Response Analysis of Stochastic Structures," by A. Kardara, C. Bucher and M. Shinozuka, 9/22/88, (PB89-174429, A04, MF-A01).

NCEER-88-0030 "Nonnormal Accelerations Due to Yielding in a Primary Structure," by D.C.K. Chen and L.D. Lutes, 9/19/88, (PB89-131437, A04, MF-A01).

NCEER-88-0031 "Design Approaches for Soil-Structure Interaction," by A.S. Veletsos, A.M. Prasad and Y. Tang, 12/30/88, (PB89-174437, A03, MF-A01). This report is available only through NTIS (see address given above).

NCEER-88-0032 "A Re-evaluation of Design Spectra for Seismic Damage Control," by C.J. Turkstra and A.G. Tallin, 11/7/88, (PB89-145221, A05, MF-A01).

NCEER-88-0033 "The Behavior and Design of Noncontact Lap Splices Subjected to Repeated Inelastic Tensile Loading," by V.E. Sagan, P. Gergely and R.N. White, 12/8/88, (PB89-163737, A08, MF-A01).

NCEER-88-0034 "Seismic Response of Pile Foundations," by S.M. Mamoon, P.K. Banerjee and S. Ahmad, 11/1/88, (PB89-145239, A04, MF-A01).

NCEER-88-0035 "Modeling of R/C Building Structures With Flexible Floor Diaphragms (IDARC2)," by A.M. Reinhorn, S.K. Kunnath and N. Panahshahi, 9/7/88, (PB89-207153, A07, MF-A01).

NCEER-88-0036 "Solution of the Dam-Reservoir Interaction Problem Using a Combination of FEM, BEM with Particular Integrals, Modal Analysis, and Substructuring," by C-S. Tsai, G.C. Lee and R.L. Ketter, 12/31/88, (PB89-207146, A04, MF-A01).

NCEER-88-0037 "Optimal Placement of Actuators for Structural Control," by F.Y. Cheng and C.P. Pantelides, 8/15/88, (PB89-162846, A05, MF-A01).

NCEER-88-0038 "Teflon Bearings in Aseismic Base Isolation: Experimental Studies and Mathematical Modeling," by A. Mokha, M.C. Constantinou and A.M. Reinhorn, 12/5/88, (PB89-218457, A10, MF-A01). This report is available only through NTIS (see address given above).

NCEER-88-0039 "Seismic Behavior of Flat Slab High-Rise Buildings in the New York City Area," by P. Weidlinger and M. Ettouney, 10/15/88, (PB90-145681, A04, MF-A01).

NCEER-88-0040 "Evaluation of the Earthquake Resistance of Existing Buildings in New York City," by P. Weidlinger and M. Ettouney, 10/15/88, not available.

NCEER-88-0041 "Small-Scale Modeling Techniques for Reinforced Concrete Structures Subjected to Seismic Loads," by W. Kim, A. El-Attar and R.N. White, 11/22/88, (PB89-189625, A05, MF-A01).

NCEER-88-0042 "Modeling Strong Ground Motion from Multiple Event Earthquakes," by G.W. Ellis and A.S. Cakmak, 10/15/88, (PB89-174445, A03, MF-A01).

NCEER-88-0043 "Nonstationary Models of Seismic Ground Acceleration," by M. Grigoriu, S.E. Ruiz and E. Rosenblueth, 7/15/88, (PB89-189617, A04, MF-A01).

NCEER-88-0044 "SARCF User's Guide: Seismic Analysis of Reinforced Concrete Frames," by Y.S. Chung, C. Meyer and M. Shinozuka, 11/9/88, (PB89-174452, A08, MF-A01).

NCEER-88-0045 "First Expert Panel Meeting on Disaster Research and Planning," edited by J. Pantelic and J. Stoyle, 9/15/88, (PB89-174460, A05, MF-A01).

NCEER-88-0046 "Preliminary Studies of the Effect of Degrading Infill Walls on the Nonlinear Seismic Response of Steel Frames," by C.Z. Chrysostomou, P. Gergely and J.F. Abel, 12/19/88, (PB89-208383, A05, MF-A01).

NCEER-88-0047 "Reinforced Concrete Frame Component Testing Facility - Design, Construction, Instrumentation and Operation," by S.P. Pessiki, C. Conley, T. Bond, P. Gergely and R.N. White, 12/16/88, (PB89-174478, A04, MF-A01).

NCEER-89-0001 "Effects of Protective Cushion and Soil Compliancy on the Response of Equipment Within a Seismically Excited Building," by J.A. HoLung, 2/16/89, (PB89-207179, A04, MF-A01).

NCEER-89-0002 "Statistical Evaluation of Response Modification Factors for Reinforced Concrete Structures," by H.H-M. Hwang and J-W. Jaw, 2/17/89, (PB89-207187, A05, MF-A01).

NCEER-89-0003 "Hysteretic Columns Under Random Excitation," by G-Q. Cai and Y.K. Lin, 1/9/89, (PB89-196513, A03, MF-A01).

NCEER-89-0004 "Experimental Study of `Elephant Foot Bulge' Instability of Thin-Walled Metal Tanks," by Z-H. Jia and R.L. Ketter, 2/22/89, (PB89-207195, A03, MF-A01).

NCEER-89-0005 "Experiment on Performance of Buried Pipelines Across San Andreas Fault," by J. Isenberg, E. Richardson and T.D. O'Rourke, 3/10/89, (PB89-218440, A04, MF-A01). This report is available only through NTIS (see address given above).

NCEER-89-0006 "A Knowledge-Based Approach to Structural Design of Earthquake-Resistant Buildings," by M. Subramani, P. Gergely, C.H. Conley, J.F. Abel and A.H. Zaghw, 1/15/89, (PB89-218465, A06, MF-A01).

NCEER-89-0007 "Liquefaction Hazards and Their Effects on Buried Pipelines," by T.D. O'Rourke and P.A. Lane, 2/1/89, (PB89-218481, A09, MF-A01).

NCEER-89-0008 "Fundamentals of System Identification in Structural Dynamics," by H. Imai, C-B. Yun, O. Maruyama and M. Shinozuka, 1/26/89, (PB89-207211, A04, MF-A01).

NCEER-89-0009 "Effects of the 1985 Michoacan Earthquake on Water Systems and Other Buried Lifelines in Mexico," by A.G. Ayala and M.J. O'Rourke, 3/8/89, (PB89-207229, A06, MF-A01).

NCEER-89-R010 "NCEER Bibliography of Earthquake Education Materials," by K.E.K. Ross, Second Revision, 9/1/89, (PB90-125352, A05, MF-A01). This report is replaced by NCEER-92-0018.

NCEER-89-0011 "Inelastic Three-Dimensional Response Analysis of Reinforced Concrete Building Structures (IDARC-3D), Part I - Modeling," by S.K. Kunnath and A.M. Reinhorn, 4/17/89, (PB90-114612, A07, MF-A01). This report is available only through NTIS (see address given above).

NCEER-89-0012 "Recommended Modifications to ATC-14," by C.D. Poland and J.O. Malley, 4/12/89, (PB90-108648, A15, MF-A01).

NCEER-89-0013 "Repair and Strengthening of Beam-to-Column Connections Subjected to Earthquake Loading," by M. Corazao and A.J. Durrani, 2/28/89, (PB90-109885, A06, MF-A01).

NCEER-89-0014 "Program EXKAL2 for Identification of Structural Dynamic Systems," by O. Maruyama, C-B. Yun, M. Hoshiya and M. Shinozuka, 5/19/89, (PB90-109877, A09, MF-A01).

NCEER-89-0015 "Response of Frames With Bolted Semi-Rigid Connections, Part I - Experimental Study and Analytical Predictions," by P.J. DiCorso, A.M. Reinhorn, J.R. Dickerson, J.B. Radziminski and W.L. Harper, 6/1/89, not available.

NCEER-89-0016 "ARMA Monte Carlo Simulation in Probabilistic Structural Analysis," by P.D. Spanos and M.P. Mignolet, 7/10/89, (PB90-109893, A03, MF-A01).

NCEER-89-P017 "Preliminary Proceedings from the Conference on Disaster Preparedness - The Place of Earthquake Education in Our Schools," Edited by K.E.K. Ross, 6/23/89, (PB90-108606, A03, MF-A01).

NCEER-89-0017 "Proceedings from the Conference on Disaster Preparedness - The Place of Earthquake Education in Our Schools," Edited by K.E.K. Ross, 12/31/89, (PB90-207895, A012, MF-A02). This report is available only through NTIS (see address given above).

NCEER-89-0018 "Multidimensional Models of Hysteretic Material Behavior for Vibration Analysis of Shape Memory Energy Absorbing Devices, by E.J. Graesser and F.A. Cozzarelli, 6/7/89, (PB90-164146, A04, MF-A01).

NCEER-89-0019 "Nonlinear Dynamic Analysis of Three-Dimensional Base Isolated Structures (3D-BASIS)," by S. Nagarajaiah, A.M. Reinhorn and M.C. Constantinou, 8/3/89, (PB90-161936, A06, MF-A01). This report has been replaced by NCEER-93-0011.

NCEER-89-0020 "Structural Control Considering Time-Rate of Control Forces and Control Rate Constraints," by F.Y. Cheng and C.P. Pantelides, 8/3/89, (PB90-120445, A04, MF-A01).

NCEER-89-0021 "Subsurface Conditions of Memphis and Shelby County," by K.W. Ng, T-S. Chang and H-H.M. Hwang, 7/26/89, (PB90-120437, A03, MF-A01).

NCEER-89-0022 "Seismic Wave Propagation Effects on Straight Jointed Buried Pipelines," by K. Elhmadi and M.J. O'Rourke, 8/24/89, (PB90-162322, A10, MF-A02).

NCEER-89-0023 "Workshop on Serviceability Analysis of Water Delivery Systems," edited by M. Grigoriu, 3/6/89, (PB90-127424, A03, MF-A01).

NCEER-89-0024 "Shaking Table Study of a 1/5 Scale Steel Frame Composed of Tapered Members," by K.C. Chang, J.S. Hwang and G.C. Lee, 9/18/89, (PB90-160169, A04, MF-A01).

NCEER-89-0025 "DYNA1D: A Computer Program for Nonlinear Seismic Site Response Analysis - Technical Documentation," by Jean H. Prevost, 9/14/89, (PB90-161944, A07, MF-A01). This report is available only through NTIS (see address given above).

NCEER-89-0026 "1:4 Scale Model Studies of Active Tendon Systems and Active Mass Dampers for Aseismic Protection," by A.M. Reinhorn, T.T. Soong, R.C. Lin, Y.P. Yang, Y. Fukao, H. Abe and M. Nakai, 9/15/89, (PB90-173246, A10, MF-A02). This report is available only through NTIS (see address given above).

NCEER-89-0027 "Scattering of Waves by Inclusions in a Nonhomogeneous Elastic Half Space Solved by Boundary Element Methods," by P.K. Hadley, A. Askar and A.S. Cakmak, 6/15/89, (PB90-145699, A07, MF-A01).

NCEER-89-0028 "Statistical Evaluation of Deflection Amplification Factors for Reinforced Concrete Structures," by H.H.M. Hwang, J-W. Jaw and A.L. Ch'ng, 8/31/89, (PB90-164633, A05, MF-A01).

NCEER-89-0029 "Bedrock Accelerations in Memphis Area Due to Large New Madrid Earthquakes," by H.H.M. Hwang, C.H.S. Chen and G. Yu, 11/7/89, (PB90-162330, A04, MF-A01).

NCEER-89-0030 "Seismic Behavior and Response Sensitivity of Secondary Structural Systems," by Y.Q. Chen and T.T. Soong, 10/23/89, (PB90-164658, A08, MF-A01).

NCEER-89-0031 "Random Vibration and Reliability Analysis of Primary-Secondary Structural Systems," by Y. Ibrahim, M. Grigoriu and T.T. Soong, 11/10/89, (PB90-161951, A04, MF-A01).

NCEER-89-0032 "Proceedings from the Second U.S. - Japan Workshop on Liquefaction, Large Ground Deformation and Their Effects on Lifelines, September 26-29, 1989," Edited by T.D. O'Rourke and M. Hamada, 12/1/89, (PB90-209388, A22, MF-A03).

NCEER-89-0033 "Deterministic Model for Seismic Damage Evaluation of Reinforced Concrete Structures," by J.M. Bracci, A.M. Reinhorn, J.B. Mander and S.K. Kunnath, 9/27/89, (PB91-108803, A06, MF-A01).

NCEER-89-0034 "On the Relation Between Local and Global Damage Indices," by E. DiPasquale and A.S. Cakmak, 8/15/89, (PB90-173865, A05, MF-A01).

NCEER-89-0035 "Cyclic Undrained Behavior of Nonplastic and Low Plasticity Silts," by A.J. Walker and H.E. Stewart, 7/26/89, (PB90-183518, A10, MF-A01).

NCEER-89-0036 "Liquefaction Potential of Surficial Deposits in the City of Buffalo, New York," by M. Budhu, R. Giese and L. Baumgrass, 1/17/89, (PB90-208455, A04, MF-A01).

NCEER-89-0037 "A Deterministic Assessment of Effects of Ground Motion Incoherence," by A.S. Veletsos and Y. Tang, 7/15/89, (PB90-164294, A03, MF-A01).

NCEER-89-0038 "Workshop on Ground Motion Parameters for Seismic Hazard Mapping," July 17-18, 1989, edited by R.V. Whitman, 12/1/89, (PB90-173923, A04, MF-A01).

NCEER-89-0039 "Seismic Effects on Elevated Transit Lines of the New York City Transit Authority," by C.J. Costantino, C.A. Miller and E. Heymsfield, 12/26/89, (PB90-207887, A06, MF-A01).

NCEER-89-0040 "Centrifugal Modeling of Dynamic Soil-Structure Interaction," by K. Weissman, Supervised by J.H. Prevost, 5/10/89, (PB90-207879, A07, MF-A01).

NCEER-89-0041 "Linearized Identification of Buildings With Cores for Seismic Vulnerability Assessment," by I-K. Ho and A.E. Aktan, 11/1/89, (PB90-251943, A07, MF-A01).

NCEER-90-0001 "Geotechnical and Lifeline Aspects of the October 17, 1989 Loma Prieta Earthquake in San Francisco," by T.D. O'Rourke, H.E. Stewart, F.T. Blackburn and T.S. Dickerman, 1/90, (PB90-208596, A05, MF-A01).

NCEER-90-0002 "Nonnormal Secondary Response Due to Yielding in a Primary Structure," by D.C.K. Chen and L.D. Lutes, 2/28/90, (PB90-251976, A07, MF-A01).

NCEER-90-0003 "Earthquake Education Materials for Grades K-12," by K.E.K. Ross, 4/16/90, (PB91-251984, A05, MF-A05). This report has been replaced by NCEER-92-0018.

NCEER-90-0004 "Catalog of Strong Motion Stations in Eastern North America," by R.W. Busby, 4/3/90, (PB90-251984, A05, MF-A01).

NCEER-90-0005 "NCEER Strong-Motion Data Base: A User Manual for the GeoBase Release (Version 1.0 for the Sun3)," by P. Friberg and K. Jacob, 3/31/90 (PB90-258062, A04, MF-A01).

NCEER-90-0006 "Seismic Hazard Along a Crude Oil Pipeline in the Event of an 1811-1812 Type New Madrid Earthquake," by H.H.M. Hwang and C-H.S. Chen, 4/16/90, (PB90-258054, A04, MF-A01).

NCEER-90-0007 "Site-Specific Response Spectra for Memphis Sheahan Pumping Station," by H.H.M. Hwang and C.S. Lee, 5/15/90, (PB91-108811, A05, MF-A01).

NCEER-90-0008 "Pilot Study on Seismic Vulnerability of Crude Oil Transmission Systems," by T. Ariman, R. Dobry, M. Grigoriu, F. Kozin, M. O'Rourke, T. O'Rourke and M. Shinozuka, 5/25/90, (PB91-108837, A06, MF-A01).

NCEER-90-0009 "A Program to Generate Site Dependent Time Histories: EQGEN," by G.W. Ellis, M. Srinivasan and A.S. Cakmak, 1/30/90, (PB91-108829, A04, MF-A01).

NCEER-90-0010 "Active Isolation for Seismic Protection of Operating Rooms," by M.E. Talbott, Supervised by M. Shinozuka, 6/8/9, (PB91-110205, A05, MF-A01).

NCEER-90-0011 "Program LINEARID for Identification of Linear Structural Dynamic Systems," by C-B. Yun and M. Shinozuka, 6/25/90, (PB91-110312, A08, MF-A01).

NCEER-90-0012 "Two-Dimensional Two-Phase Elasto-Plastic Seismic Response of Earth Dams," by A.N. Yiagos, Supervised by J.H. Prevost, 6/20/90, (PB91-110197, A13, MF-A02).

NCEER-90-0013 "Secondary Systems in Base-Isolated Structures: Experimental Investigation, Stochastic Response and Stochastic Sensitivity," by G.D. Manolis, G. Juhn, M.C. Constantinou and A.M. Reinhorn, 7/1/90, (PB91-110320, A08, MF-A01).

NCEER-90-0014 "Seismic Behavior of Lightly-Reinforced Concrete Column and Beam-Column Joint Details," by S.P. Pessiki, C.H. Conley, P. Gergely and R.N. White, 8/22/90, (PB91-108795, A11, MF-A02).

NCEER-90-0015 "Two Hybrid Control Systems for Building Structures Under Strong Earthquakes," by J.N. Yang and A. Danielians, 6/29/90, (PB91-125393, A04, MF-A01).

NCEER-90-0016 "Instantaneous Optimal Control with Acceleration and Velocity Feedback," by J.N. Yang and Z. Li, 6/29/90, (PB91-125401, A03, MF-A01).

NCEER-90-0017 "Reconnaissance Report on the Northern Iran Earthquake of June 21, 1990," by M. Mehrain, 10/4/90, (PB91-125377, A03, MF-A01).

NCEER-90-0018 "Evaluation of Liquefaction Potential in Memphis and Shelby County," by T.S. Chang, P.S. Tang, C.S. Lee and H. Hwang, 8/10/90, (PB91-125427, A09, MF-A01).

NCEER-90-0019 "Experimental and Analytical Study of a Combined Sliding Disc Bearing and Helical Steel Spring Isolation System," by M.C. Constantinou, A.S. Mokha and A.M. Reinhorn, 10/4/90, (PB91-125385, A06, MF-A01). This report is available only through NTIS (see address given above).

NCEER-90-0020 "Experimental Study and Analytical Prediction of Earthquake Response of a Sliding Isolation System with a Spherical Surface," by A.S. Mokha, M.C. Constantinou and A.M. Reinhorn, 10/11/90, (PB91-125419, A05, MF-A01).

NCEER-90-0021 "Dynamic Interaction Factors for Floating Pile Groups," by G. Gazetas, K. Fan, A. Kaynia and E. Kausel, 9/10/90, (PB91-170381, A05, MF-A01).

NCEER-90-0022 "Evaluation of Seismic Damage Indices for Reinforced Concrete Structures," by S. Rodriguez-Gomez and A.S. Cakmak, 9/30/90, PB91-171322, A06, MF-A01).

NCEER-90-0023 "Study of Site Response at a Selected Memphis Site," by H. Desai, S. Ahmad, E.S. Gazetas and M.R. Oh, 10/11/90, (PB91-196857, A03, MF-A01).

NCEER-90-0024 "A User's Guide to Strongmo: Version 1.0 of NCEER's Strong-Motion Data Access Tool for PCs and Terminals," by P.A. Friberg and C.A.T. Susch, 11/15/90, (PB91-171272, A03, MF-A01).

NCEER-90-0025 "A Three-Dimensional Analytical Study of Spatial Variability of Seismic Ground Motions," by L-L. Hong and A.H.-S. Ang, 10/30/90, (PB91-170399, A09, MF-A01).

NCEER-90-0026 "MUMOID User's Guide - A Program for the Identification of Modal Parameters," by S. Rodriguez-Gomez and E. DiPasquale, 9/30/90, (PB91-171298, A04, MF-A01).

NCEER-90-0027 "SARCF-II User's Guide - Seismic Analysis of Reinforced Concrete Frames," by S. Rodriguez-Gomez, Y.S. Chung and C. Meyer, 9/30/90, (PB91-171280, A05, MF-A01).

NCEER-90-0028 "Viscous Dampers: Testing, Modeling and Application in Vibration and Seismic Isolation," by N. Makris and M.C. Constantinou, 12/20/90 (PB91-190561, A06, MF-A01).

NCEER-90-0029 "Soil Effects on Earthquake Ground Motions in the Memphis Area," by H. Hwang, C.S. Lee, K.W. Ng and T.S. Chang, 8/2/90, (PB91-190751, A05, MF-A01).

NCEER-91-0001 "Proceedings from the Third Japan-U.S. Workshop on Earthquake Resistant Design of Lifeline Facilities and Countermeasures for Soil Liquefaction, December 17-19, 1990," edited by T.D. O'Rourke and M. Hamada, 2/1/91, (PB91-179259, A99, MF-A04).

NCEER-91-0002 "Physical Space Solutions of Non-Proportionally Damped Systems," by M. Tong, Z. Liang and G.C. Lee, 1/15/91, (PB91-179242, A04, MF-A01).

NCEER-91-0003 "Seismic Response of Single Piles and Pile Groups," by K. Fan and G. Gazetas, 1/10/91, (PB92-174994, A04, MF-A01).

NCEER-91-0004 "Damping of Structures: Part 1 - Theory of Complex Damping," by Z. Liang and G. Lee, 10/10/91, (PB92-197235, A12, MF-A03).

NCEER-91-0005 "3D-BASIS - Nonlinear Dynamic Analysis of Three Dimensional Base Isolated Structures: Part II," by S. Nagarajaiah, A.M. Reinhorn and M.C. Constantinou, 2/28/91, (PB91-190553, A07, MF-A01). This report has been replaced by NCEER-93-0011.

NCEER-91-0006 "A Multidimensional Hysteretic Model for Plasticity Deforming Metals in Energy Absorbing Devices," by E.J. Graesser and F.A. Cozzarelli, 4/9/91, (PB92-108364, A04, MF-A01).

NCEER-91-0007 "A Framework for Customizable Knowledge-Based Expert Systems with an Application to a KBES for Evaluating the Seismic Resistance of Existing Buildings," by E.G. Ibarra-Anaya and S.J. Fenves, 4/9/91, (PB91-210930, A08, MF-A01).

NCEER-91-0008 "Nonlinear Analysis of Steel Frames with Semi-Rigid Connections Using the Capacity Spectrum Method," by G.G. Deierlein, S-H. Hsieh, Y-J. Shen and J.F. Abel, 7/2/91, (PB92-113828, A05, MF-A01).

NCEER-91-0009 "Earthquake Education Materials for Grades K-12," by K.E.K. Ross, 4/30/91, (PB91-212142, A06, MF-A01). This report has been replaced by NCEER-92-0018.

NCEER-91-0010 "Phase Wave Velocities and Displacement Phase Differences in a Harmonically Oscillating Pile," by N. Makris and G. Gazetas, 7/8/91, (PB92-108356, A04, MF-A01).

NCEER-91-0011 "Dynamic Characteristics of a Full-Size Five-Story Steel Structure and a 2/5 Scale Model," by K.C. Chang, G.C. Yao, G.C. Lee, D.S. Hao and Y.C. Yeh," 7/2/91, (PB93-116648, A06, MF-A02).

NCEER-91-0012 "Seismic Response of a 2/5 Scale Steel Structure with Added Viscoelastic Dampers," by K.C. Chang, T.T. Soong, S-T. Oh and M.L. Lai, 5/17/91, (PB92-110816, A05, MF-A01).

NCEER-91-0013 "Earthquake Response of Retaining Walls; Full-Scale Testing and Computational Modeling," by S. Alampalli and A-W.M. Elgamal, 6/20/91, not available.

NCEER-91-0014 "3D-BASIS-M: Nonlinear Dynamic Analysis of Multiple Building Base Isolated Structures," by P.C. Tsopelas, S. Nagarajaiah, M.C. Constantinou and A.M. Reinhorn, 5/28/91, (PB92-113885, A09, MF-A02).

NCEER-91-0015 "Evaluation of SEAOC Design Requirements for Sliding Isolated Structures," by D. Theodossiou and M.C. Constantinou, 6/10/91, (PB92-114602, A11, MF-A03).

NCEER-91-0016 "Closed-Loop Modal Testing of a 27-Story Reinforced Concrete Flat Plate-Core Building," by H.R. Somaprasad, T. Toksoy, H. Yoshiyuki and A.E. Aktan, 7/15/91, (PB92-129980, A07, MF-A02).

NCEER-91-0017 "Shake Table Test of a 1/6 Scale Two-Story Lightly Reinforced Concrete Building," by A.G. El-Attar, R.N. White and P. Gergely, 2/28/91, (PB92-222447, A06, MF-A02).

NCEER-91-0018 "Shake Table Test of a 1/8 Scale Three-Story Lightly Reinforced Concrete Building," by A.G. El-Attar, R.N. White and P. Gergely, 2/28/91, (PB93-116630, A08, MF-A02).

NCEER-91-0019 "Transfer Functions for Rigid Rectangular Foundations," by A.S. Veletsos, A.M. Prasad and W.H. Wu, 7/31/91, not available.

NCEER-91-0020 "Hybrid Control of Seismic-Excited Nonlinear and Inelastic Structural Systems," by J.N. Yang, Z. Li and A. Danielians, 8/1/91, (PB92-143171, A06, MF-A02).

NCEER-91-0021 "The NCEER-91 Earthquake Catalog: Improved Intensity-Based Magnitudes and Recurrence Relations for U.S. Earthquakes East of New Madrid," by L. Seeber and J.G. Armbruster, 8/28/91, (PB92-176742, A06, MF-A02).

NCEER-91-0022 "Proceedings from the Implementation of Earthquake Planning and Education in Schools: The Need for Change - The Roles of the Changemakers," by K.E.K. Ross and F. Winslow, 7/23/91, (PB92-129998, A12, MF-A03).

NCEER-91-0023 "A Study of Reliability-Based Criteria for Seismic Design of Reinforced Concrete Frame Buildings," by H.H.M. Hwang and H-M. Hsu, 8/10/91, (PB92-140235, A09, MF-A02).

NCEER-91-0024 "Experimental Verification of a Number of Structural System Identification Algorithms," by R.G. Ghanem, H. Gavin and M. Shinozuka, 9/18/91, (PB92-176577, A18, MF-A04).

NCEER-91-0025 "Probabilistic Evaluation of Liquefaction Potential," by H.H.M. Hwang and C.S. Lee," 11/25/91, (PB92-143429, A05, MF-A01).

NCEER-91-0026 "Instantaneous Optimal Control for Linear, Nonlinear and Hysteretic Structures - Stable Controllers," by J.N. Yang and Z. Li, 11/15/91, (PB92-163807, A04, MF-A01).

NCEER-91-0027 "Experimental and Theoretical Study of a Sliding Isolation System for Bridges," by M.C. Constantinou, A. Kartoum, A.M. Reinhorn and P. Bradford, 11/15/91, (PB92-176973, A10, MF-A03).

NCEER-92-0001 "Case Studies of Liquefaction and Lifeline Performance During Past Earthquakes, Volume 1: Japanese Case Studies," Edited by M. Hamada and T. O'Rourke, 2/17/92, (PB92-197243, A18, MF-A04).

NCEER-92-0002 "Case Studies of Liquefaction and Lifeline Performance During Past Earthquakes, Volume 2: United States Case Studies," Edited by T. O'Rourke and M. Hamada, 2/17/92, (PB92-197250, A20, MF-A04).

NCEER-92-0003 "Issues in Earthquake Education," Edited by K. Ross, 2/3/92, (PB92-222389, A07, MF-A02).

NCEER-92-0004 "Proceedings from the First U.S. - Japan Workshop on Earthquake Protective Systems for Bridges," Edited by I.G. Buckle, 2/4/92, (PB94-142239, A99, MF-A06).

NCEER-92-0005 "Seismic Ground Motion from a Haskell-Type Source in a Multiple-Layered Half-Space," A.P. Theoharis, G. Deodatis and M. Shinozuka, 1/2/92, not available.

NCEER-92-0006 "Proceedings from the Site Effects Workshop," Edited by R. Whitman, 2/29/92, (PB92-197201, A04, MF-A01).

NCEER-92-0007 "Engineering Evaluation of Permanent Ground Deformations Due to Seismically-Induced Liquefaction," by M.H. Baziar, R. Dobry and A-W.M. Elgamal, 3/24/92, (PB92-222421, A13, MF-A03).

NCEER-92-0008 "A Procedure for the Seismic Evaluation of Buildings in the Central and Eastern United States," by C.D. Poland and J.O. Malley, 4/2/92, (PB92-222439, A20, MF-A04).

NCEER-92-0009 "Experimental and Analytical Study of a Hybrid Isolation System Using Friction Controllable Sliding Bearings," by M.Q. Feng, S. Fujii and M. Shinozuka, 5/15/92, (PB93-150282, A06, MF-A02).

NCEER-92-0010 "Seismic Resistance of Slab-Column Connections in Existing Non-Ductile Flat-Plate Buildings," by A.J. Durrani and Y. Du, 5/18/92, (PB93-116812, A06, MF-A02).

NCEER-92-0011 "The Hysteretic and Dynamic Behavior of Brick Masonry Walls Upgraded by Ferrocement Coatings Under Cyclic Loading and Strong Simulated Ground Motion," by H. Lee and S.P. Prawel, 5/11/92, not available.

NCEER-92-0012 "Study of Wire Rope Systems for Seismic Protection of Equipment in Buildings," by G.F. Demetriades, M.C. Constantinou and A.M. Reinhorn, 5/20/92, (PB93-116655, A08, MF-A02).

NCEER-92-0013 "Shape Memory Structural Dampers: Material Properties, Design and Seismic Testing," by P.R. Witting and F.A. Cozzarelli, 5/26/92, (PB93-116663, A05, MF-A01).

NCEER-92-0014 "Longitudinal Permanent Ground Deformation Effects on Buried Continuous Pipelines," by M.J. O'Rourke, and C. Nordberg, 6/15/92, (PB93-116671, A08, MF-A02).

NCEER-92-0015 "A Simulation Method for Stationary Gaussian Random Functions Based on the Sampling Theorem," by M. Grigoriu and S. Balopoulou, 6/11/92, (PB93-127496, A05, MF-A01).

NCEER-92-0016 "Gravity-Load-Designed Reinforced Concrete Buildings: Seismic Evaluation of Existing Construction and Detailing Strategies for Improved Seismic Resistance," by G.W. Hoffmann, S.K. Kunnath, A.M. Reinhorn and J.B. Mander, 7/15/92, (PB94-142007, A08, MF-A02).

NCEER-92-0017 "Observations on Water System and Pipeline Performance in the Limón Area of Costa Rica Due to the April 22, 1991 Earthquake," by M. O'Rourke and D. Ballantyne, 6/30/92, (PB93-126811, A06, MF-A02).

NCEER-92-0018 "Fourth Edition of Earthquake Education Materials for Grades K-12," Edited by K.E.K. Ross, 8/10/92, (PB93-114023, A07, MF-A02).

NCEER-92-0019 "Proceedings from the Fourth Japan-U.S. Workshop on Earthquake Resistant Design of Lifeline Facilities and Countermeasures for Soil Liquefaction," Edited by M. Hamada and T.D. O'Rourke, 8/12/92, (PB93-163939, A99, MF-E11).

NCEER-92-0020 "Active Bracing System: A Full Scale Implementation of Active Control," by A.M. Reinhorn, T.T. Soong, R.C. Lin, M.A. Riley, Y.P. Wang, S. Aizawa and M. Higashino, 8/14/92, (PB93-127512, A06, MF-A02).

NCEER-92-0021 "Empirical Analysis of Horizontal Ground Displacement Generated by Liquefaction-Induced Lateral Spreads," by S.F. Bartlett and T.L. Youd, 8/17/92, (PB93-188241, A06, MF-A02).

NCEER-92-0022 "IDARC Version 3.0: Inelastic Damage Analysis of Reinforced Concrete Structures," by S.K. Kunnath, A.M. Reinhorn and R.F. Lobo, 8/31/92, (PB93-227502, A07, MF-A02).

NCEER-92-0023 "A Semi-Empirical Analysis of Strong-Motion Peaks in Terms of Seismic Source, Propagation Path and Local Site Conditions, by M. Kamiyama, M.J. O'Rourke and R. Flores-Berrones, 9/9/92, (PB93-150266, A08, MF-A02).

NCEER-92-0024 "Seismic Behavior of Reinforced Concrete Frame Structures with Nonductile Details, Part I: Summary of Experimental Findings of Full Scale Beam-Column Joint Tests," by A. Beres, R.N. White and P. Gergely, 9/30/92, (PB93-227783, A05, MF-A01).

NCEER-92-0025 "Experimental Results of Repaired and Retrofitted Beam-Column Joint Tests in Lightly Reinforced Concrete Frame Buildings," by A. Beres, S. El-Borgi, R.N. White and P. Gergely, 10/29/92, (PB93-227791, A05, MF-A01).

NCEER-92-0026 "A Generalization of Optimal Control Theory: Linear and Nonlinear Structures," by J.N. Yang, Z. Li and S. Vongchavalitkul, 11/2/92, (PB93-188621, A05, MF-A01).

NCEER-92-0027 "Seismic Resistance of Reinforced Concrete Frame Structures Designed Only for Gravity Loads: Part I - Design and Properties of a One-Third Scale Model Structure," by J.M. Bracci, A.M. Reinhorn and J.B. Mander, 12/1/92, (PB94-104502, A08, MF-A02).

NCEER-92-0028 "Seismic Resistance of Reinforced Concrete Frame Structures Designed Only for Gravity Loads: Part II - Experimental Performance of Subassemblages," by L.E. Aycardi, J.B. Mander and A.M. Reinhorn, 12/1/92, (PB94-104510, A08, MF-A02).

NCEER-92-0029 "Seismic Resistance of Reinforced Concrete Frame Structures Designed Only for Gravity Loads: Part III - Experimental Performance and Analytical Study of a Structural Model," by J.M. Bracci, A.M. Reinhorn and J.B. Mander, 12/1/92, (PB93-227528, A09, MF-A01).

NCEER-92-0030 "Evaluation of Seismic Retrofit of Reinforced Concrete Frame Structures: Part I - Experimental Performance of Retrofitted Subassemblages," by D. Choudhuri, J.B. Mander and A.M. Reinhorn, 12/8/92, (PB93-198307, A07, MF-A02).

NCEER-92-0031 "Evaluation of Seismic Retrofit of Reinforced Concrete Frame Structures: Part II - Experimental Performance and Analytical Study of a Retrofitted Structural Model," by J.M. Bracci, A.M. Reinhorn and J.B. Mander, 12/8/92, (PB93-198315, A09, MF-A03).

NCEER-92-0032 "Experimental and Analytical Investigation of Seismic Response of Structures with Supplemental Fluid Viscous Dampers," by M.C. Constantinou and M.D. Symans, 12/21/92, (PB93-191435, A10, MF-A03). This report is available only through NTIS (see address given above).

NCEER-92-0033 "Reconnaissance Report on the Cairo, Egypt Earthquake of October 12, 1992," by M. Khater, 12/23/92, (PB93-188621, A03, MF-A01).

NCEER-92-0034 "Low-Level Dynamic Characteristics of Four Tall Flat-Plate Buildings in New York City," by H. Gavin, S. Yuan, J. Grossman, E. Pekelis and K. Jacob, 12/28/92, (PB93-188217, A07, MF-A02).

NCEER-93-0001 "An Experimental Study on the Seismic Performance of Brick-Infilled Steel Frames With and Without Retrofit," by J.B. Mander, B. Nair, K. Wojtkowski and J. Ma, 1/29/93, (PB93-227510, A07, MF-A02).

NCEER-93-0002 "Social Accounting for Disaster Preparedness and Recovery Planning," by S. Cole, E. Pantoja and V. Razak, 2/22/93, (PB94-142114, A12, MF-A03).

NCEER-93-0003 "Assessment of 1991 NEHRP Provisions for Nonstructural Components and Recommended Revisions," by T.T. Soong, G. Chen, Z. Wu, R-H. Zhang and M. Grigoriu, 3/1/93, (PB93-188639, A06, MF-A02).

NCEER-93-0004 "Evaluation of Static and Response Spectrum Analysis Procedures of SEAOC/UBC for Seismic Isolated Structures," by C.W. Winters and M.C. Constantinou, 3/23/93, (PB93-198299, A10, MF-A03).

NCEER-93-0005 "Earthquakes in the Northeast - Are We Ignoring the Hazard? A Workshop on Earthquake Science and Safety for Educators," edited by K.E.K. Ross, 4/2/93, (PB94-103066, A09, MF-A02).

NCEER-93-0006 "Inelastic Response of Reinforced Concrete Structures with Viscoelastic Braces," by R.F. Lobo, J.M. Bracci, K.L. Shen, A.M. Reinhorn and T.T. Soong, 4/5/93, (PB93-227486, A05, MF-A02).

NCEER-93-0007 "Seismic Testing of Installation Methods for Computers and Data Processing Equipment," by K. Kosar, T.T. Soong, K.L. Shen, J.A. HoLung and Y.K. Lin, 4/12/93, (PB93-198299, A07, MF-A02).

NCEER-93-0008 "Retrofit of Reinforced Concrete Frames Using Added Dampers," by A. Reinhorn, M. Constantinou and C. Li, not available.

NCEER-93-0009 "Seismic Behavior and Design Guidelines for Steel Frame Structures with Added Viscoelastic Dampers," by K.C. Chang, M.L. Lai, T.T. Soong, D.S. Hao and Y.C. Yeh, 5/1/93, (PB94-141959, A07, MF-A02).

NCEER-93-0010 "Seismic Performance of Shear-Critical Reinforced Concrete Bridge Piers," by J.B. Mander, S.M. Waheed, M.T.A. Chaudhary and S.S. Chen, 5/12/93, (PB93-227494, A08, MF-A02).

NCEER-93-0011 "3D-BASIS-TABS: Computer Program for Nonlinear Dynamic Analysis of Three Dimensional Base Isolated Structures," by S. Nagarajaiah, C. Li, A.M. Reinhorn and M.C. Constantinou, 8/2/93, (PB94-141819, A09, MF-A02).

NCEER-93-0012 "Effects of Hydrocarbon Spills from an Oil Pipeline Break on Ground Water," by O.J. Helweg and H.H.M. Hwang, 8/3/93, (PB94-141942, A06, MF-A02).

NCEER-93-0013 "Simplified Procedures for Seismic Design of Nonstructural Components and Assessment of Current Code Provisions," by M.P. Singh, L.E. Suarez, E.E. Matheu and G.O. Maldonado, 8/4/93, (PB94-141827, A09, MF-A02).

NCEER-93-0014 "An Energy Approach to Seismic Analysis and Design of Secondary Systems," by G. Chen and T.T. Soong, 8/6/93, (PB94-142767, A11, MF-A03).

NCEER-93-0015 "Proceedings from School Sites: Becoming Prepared for Earthquakes - Commemorating the Third Anniversary of the Loma Prieta Earthquake," Edited by F.E. Winslow and K.E.K. Ross, 8/16/93, (PB94-154275, A16, MF-A02).

NCEER-93-0016 "Reconnaissance Report of Damage to Historic Monuments in Cairo, Egypt Following the October 12, 1992 Dahshur Earthquake," by D. Sykora, D. Look, G. Croci, E. Karaesmen and E. Karaesmen, 8/19/93, (PB94-142221, A08, MF-A02).

NCEER-93-0017 "The Island of Guam Earthquake of August 8, 1993," by S.W. Swan and S.K. Harris, 9/30/93, (PB94-141843, A04, MF-A01).

NCEER-93-0018 "Engineering Aspects of the October 12, 1992 Egyptian Earthquake," by A.W. Elgamal, M. Amer, K. Adalier and A. Abul-Fadl, 10/7/93, (PB94-141983, A05, MF-A01).

NCEER-93-0019 "Development of an Earthquake Motion Simulator and its Application in Dynamic Centrifuge Testing," by I. Krstelj, Supervised by J.H. Prevost, 10/23/93, (PB94-181773, A-10, MF-A03).

NCEER-93-0020 "NCEER-Taisei Corporation Research Program on Sliding Seismic Isolation Systems for Bridges: Experimental and Analytical Study of a Friction Pendulum System (FPS)," by M.C. Constantinou, P. Tsopelas, Y-S. Kim and S. Okamoto, 11/1/93, (PB94-142775, A08, MF-A02).

NCEER-93-0021 "Finite Element Modeling of Elastomeric Seismic Isolation Bearings," by L.J. Billings, Supervised by R. Shepherd, 11/8/93, not available.

NCEER-93-0022 "Seismic Vulnerability of Equipment in Critical Facilities: Life-Safety and Operational Consequences," by K. Porter, G.S. Johnson, M.M. Zadeh, C. Scawthorn and S. Eder, 11/24/93, (PB94-181765, A16, MF-A03).

NCEER-93-0023 "Hokkaido Nansei-oki, Japan Earthquake of July 12, 1993, by P.I. Yanev and C.R. Scawthorn, 12/23/93, (PB94-181500, A07, MF-A01).

NCEER-94-0001 "An Evaluation of Seismic Serviceability of Water Supply Networks with Application to the San Francisco Auxiliary Water Supply System," by I. Markov, Supervised by M. Grigoriu and T. O'Rourke, 1/21/94, (PB94-204013, A07, MF-A02).

NCEER-94-0002 "NCEER-Taisei Corporation Research Program on Sliding Seismic Isolation Systems for Bridges: Experimental and Analytical Study of Systems Consisting of Sliding Bearings, Rubber Restoring Force Devices and Fluid Dampers," Volumes I and II, by P. Tsopelas, S. Okamoto, M.C. Constantinou, D. Ozaki and S. Fujii, 2/4/94, (PB94-181740, A09, MF-A02 and PB94-181757, A12, MF-A03).

NCEER-94-0003 "A Markov Model for Local and Global Damage Indices in Seismic Analysis," by S. Rahman and M. Grigoriu, 2/18/94, (PB94-206000, A12, MF-A03).

NCEER-94-0004 "Proceedings from the NCEER Workshop on Seismic Response of Masonry Infills," edited by D.P. Abrams, 3/1/94, (PB94-180783, A07, MF-A02).

NCEER-94-0005 "The Northridge, California Earthquake of January 17, 1994: General Reconnaissance Report," edited by J.D. Goltz, 3/11/94, (PB94-193943, A10, MF-A03).

NCEER-94-0006 "Seismic Energy Based Fatigue Damage Analysis of Bridge Columns: Part I - Evaluation of Seismic Capacity," by G.A. Chang and J.B. Mander, 3/14/94, (PB94-219185, A11, MF-A03).

NCEER-94-0007 "Seismic Isolation of Multi-Story Frame Structures Using Spherical Sliding Isolation Systems," by T.M. Al-Hussaini, V.A. Zayas and M.C. Constantinou, 3/17/94, (PB94-193745, A09, MF-A02).

NCEER-94-0008 "The Northridge, California Earthquake of January 17, 1994: Performance of Highway Bridges," edited by I.G. Buckle, 3/24/94, (PB94-193851, A06, MF-A02).

NCEER-94-0009 "Proceedings of the Third U.S.-Japan Workshop on Earthquake Protective Systems for Bridges," edited by I.G. Buckle and I. Friedland, 3/31/94, (PB94-195815, A99, MF-A06).

NCEER-94-0010 "3D-BASIS-ME: Computer Program for Nonlinear Dynamic Analysis of Seismically Isolated Single and Multiple Structures and Liquid Storage Tanks," by P.C. Tsopelas, M.C. Constantinou and A.M. Reinhorn, 4/12/94, (PB94-204922, A09, MF-A02).

NCEER-94-0011 "The Northridge, California Earthquake of January 17, 1994: Performance of Gas Transmission Pipelines," by T.D. O'Rourke and M.C. Palmer, 5/16/94, (PB94-204989, A05, MF-A01).

NCEER-94-0012 "Feasibility Study of Replacement Procedures and Earthquake Performance Related to Gas Transmission Pipelines," by T.D. O'Rourke and M.C. Palmer, 5/25/94, (PB94-206638, A09, MF-A02).

NCEER-94-0013 "Seismic Energy Based Fatigue Damage Analysis of Bridge Columns: Part II - Evaluation of Seismic Demand," by G.A. Chang and J.B. Mander, 6/1/94, (PB95-18106, A08, MF-A02).

NCEER-94-0014 "NCEER-Taisei Corporation Research Program on Sliding Seismic Isolation Systems for Bridges: Experimental and Analytical Study of a System Consisting of Sliding Bearings and Fluid Restoring Force/Damping Devices," by P. Tsopelas and M.C. Constantinou, 6/13/94, (PB94-219144, A10, MF-A03).

NCEER-94-0015 "Generation of Hazard-Consistent Fragility Curves for Seismic Loss Estimation Studies," by H. Hwang and J-R. Huo, 6/14/94, (PB95-181996, A09, MF-A02).

NCEER-94-0016 "Seismic Study of Building Frames with Added Energy-Absorbing Devices," by W.S. Pong, C.S. Tsai and G.C. Lee, 6/20/94, (PB94-219136, A10, A03).

NCEER-94-0017 "Sliding Mode Control for Seismic-Excited Linear and Nonlinear Civil Engineering Structures," by J. Yang, J. Wu, A. Agrawal and Z. Li, 6/21/94, (PB95-138483, A06, MF-A02).

NCEER-94-0018 "3D-BASIS-TABS Version 2.0: Computer Program for Nonlinear Dynamic Analysis of Three Dimensional Base Isolated Structures," by A.M. Reinhorn, S. Nagarajaiah, M.C. Constantinou, P. Tsopelas and R. Li, 6/22/94, (PB95-182176, A08, MF-A02).

NCEER-94-0019 "Proceedings of the International Workshop on Civil Infrastructure Systems: Application of Intelligent Systems and Advanced Materials on Bridge Systems," Edited by G.C. Lee and K.C. Chang, 7/18/94, (PB95-252474, A20, MF-A04).

NCEER-94-0020 "Study of Seismic Isolation Systems for Computer Floors," by V. Lambrou and M.C. Constantinou, 7/19/94, (PB95-138533, A10, MF-A03).

NCEER-94-0021 "Proceedings of the U.S.-Italian Workshop on Guidelines for Seismic Evaluation and Rehabilitation of Unreinforced Masonry Buildings," Edited by D.P. Abrams and G.M. Calvi, 7/20/94, (PB95-138749, A13, MF-A03).

NCEER-94-0022 "NCEER-Taisei Corporation Research Program on Sliding Seismic Isolation Systems for Bridges: Experimental and Analytical Study of a System Consisting of Lubricated PTFE Sliding Bearings and Mild Steel Dampers," by P. Tsopelas and M.C. Constantinou, 7/22/94, (PB95-182184, A08, MF-A02).

NCEER-94-0023 “Development of Reliability-Based Design Criteria for Buildings Under Seismic Load,” by Y.K. Wen, H. Hwang and M. Shinozuka, 8/1/94, (PB95-211934, A08, MF-A02).

NCEER-94-0024 “Experimental Verification of Acceleration Feedback Control Strategies for an Active Tendon System,” by S.J. Dyke, B.F. Spencer, Jr., P. Quast, M.K. Sain, D.C. Kaspari, Jr. and T.T. Soong, 8/29/94, (PB95-212320, A05, MF-A01).

NCEER-94-0025 “Seismic Retrofitting Manual for Highway Bridges,” Edited by I.G. Buckle and I.F. Friedland, published by the Federal Highway Administration (PB95-212676, A15, MF-A03).

NCEER-94-0026 “Proceedings from the Fifth U.S.-Japan Workshop on Earthquake Resistant Design of Lifeline Facilities and Countermeasures Against Soil Liquefaction,” Edited by T.D. O’Rourke and M. Hamada, 11/7/94, (PB95-220802, A99, MF-E08).

NCEER-95-0001 "Experimental and Analytical Investigation of Seismic Retrofit of Structures with Supplemental Damping: Part 1 - Fluid Viscous Damping Devices," by A.M. Reinhorn, C. Li and M.C. Constantinou, 1/3/95, (PB95-266599, A09, MF-A02).

NCEER-95-0002 "Experimental and Analytical Study of Low-Cycle Fatigue Behavior of Semi-Rigid Top-And-Seat Angle Connections," by G. Pekcan, J.B. Mander and S.S. Chen, 1/5/95, (PB95-220042, A07, MF-A02).

NCEER-95-0003 "NCEER-ATC Joint Study on Fragility of Buildings," by T. Anagnos, C. Rojahn and A.S. Kiremidjian, 1/20/95, (PB95-220026, A06, MF-A02).

NCEER-95-0004 "Nonlinear Control Algorithms for Peak Response Reduction," by Z. Wu, T.T. Soong, V. Gattulli and R.C. Lin, 2/16/95, (PB95-220349, A05, MF-A01).

NCEER-95-0005 "Pipeline Replacement Feasibility Study: A Methodology for Minimizing Seismic and Corrosion Risks to Underground Natural Gas Pipelines," by R.T. Eguchi, H.A. Seligson and D.G. Honegger, 3/2/95, (PB95-252326, A06, MF-A02).

NCEER-95-0006 "Evaluation of Seismic Performance of an 11-Story Frame Building During the 1994 Northridge Earthquake," by F. Naeim, R. DiSulio, K. Benuska, A. Reinhorn and C. Li, not available.

NCEER-95-0007 "Prioritization of Bridges for Seismic Retrofitting," by N. Basöz and A.S. Kiremidjian, 4/24/95, (PB95-252300, A08, MF-A02).

NCEER-95-0008 "Method for Developing Motion Damage Relationships for Reinforced Concrete Frames," by A. Singhal and A.S. Kiremidjian, 5/11/95, (PB95-266607, A06, MF-A02).

NCEER-95-0009 "Experimental and Analytical Investigation of Seismic Retrofit of Structures with Supplemental Damping: Part II - Friction Devices," by C. Li and A.M. Reinhorn, 7/6/95, (PB96-128087, A11, MF-A03).

NCEER-95-0010 "Experimental Performance and Analytical Study of a Non-Ductile Reinforced Concrete Frame Structure Retrofitted with Elastomeric Spring Dampers," by G. Pekcan, J.B. Mander and S.S. Chen, 7/14/95, (PB96-137161, A08, MF-A02).

NCEER-95-0011 "Development and Experimental Study of Semi-Active Fluid Damping Devices for Seismic Protection of Structures," by M.D. Symans and M.C. Constantinou, 8/3/95, (PB96-136940, A23, MF-A04).

NCEER-95-0012 "Real-Time Structural Parameter Modification (RSPM): Development of Innervated Structures," by Z. Liang, M. Tong and G.C. Lee, 4/11/95, (PB96-137153, A06, MF-A01).

NCEER-95-0013 "Experimental and Analytical Investigation of Seismic Retrofit of Structures with Supplemental Damping: Part III - Viscous Damping Walls," by A.M. Reinhorn and C. Li, 10/1/95, (PB96-176409, A11, MF-A03).

NCEER-95-0014 "Seismic Fragility Analysis of Equipment and Structures in a Memphis Electric Substation," by J-R. Huo and H.H.M. Hwang, 8/10/95, (PB96-128087, A09, MF-A02).

NCEER-95-0015 "The Hanshin-Awaji Earthquake of January 17, 1995: Performance of Lifelines," Edited by M. Shinozuka, 11/3/95, (PB96-176383, A15, MF-A03).

NCEER-95-0016 "Highway Culvert Performance During Earthquakes," by T.L. Youd and C.J. Beckman, available as NCEER-96-0015.

NCEER-95-0017 "The Hanshin-Awaji Earthquake of January 17, 1995: Performance of Highway Bridges," Edited by I.G. Buckle, 12/1/95, not available.

NCEER-95-0018 "Modeling of Masonry Infill Panels for Structural Analysis," by A.M. Reinhorn, A. Madan, R.E. Valles, Y. Reichmann and J.B. Mander, 12/8/95, (PB97-110886, MF-A01, A06).

NCEER-95-0019 "Optimal Polynomial Control for Linear and Nonlinear Structures," by A.K. Agrawal and J.N. Yang, 12/11/95, (PB96-168737, A07, MF-A02).

NCEER-95-0020 "Retrofit of Non-Ductile Reinforced Concrete Frames Using Friction Dampers," by R.S. Rao, P. Gergely and R.N. White, 12/22/95, (PB97-133508, A10, MF-A02).

NCEER-95-0021 "Parametric Results for Seismic Response of Pile-Supported Bridge Bents," by G. Mylonakis, A. Nikolaou and G. Gazetas, 12/22/95, (PB97-100242, A12, MF-A03).

NCEER-95-0022 "Kinematic Bending Moments in Seismically Stressed Piles," by A. Nikolaou, G. Mylonakis and G. Gazetas, 12/23/95, (PB97-113914, MF-A03, A13).

NCEER-96-0001 "Dynamic Response of Unreinforced Masonry Buildings with Flexible Diaphragms," by A.C. Costley and D.P. Abrams," 10/10/96, (PB97-133573, MF-A03, A15).

NCEER-96-0002 "State of the Art Review: Foundations and Retaining Structures," by I. Po Lam, not available.

NCEER-96-0003 "Ductility of Rectangular Reinforced Concrete Bridge Columns with Moderate Confinement," by N. Wehbe, M. Saiidi, D. Sanders and B. Douglas, 11/7/96, (PB97-133557, A06, MF-A02).

NCEER-96-0004 "Proceedings of the Long-Span Bridge Seismic Research Workshop," edited by I.G. Buckle and I.M. Friedland, not available.

NCEER-96-0005 "Establish Representative Pier Types for Comprehensive Study: Eastern United States," by J. Kulicki and Z. Prucz, 5/28/96, (PB98-119217, A07, MF-A02).

NCEER-96-0006 "Establish Representative Pier Types for Comprehensive Study: Western United States," by R. Imbsen, R.A. Schamber and T.A. Osterkamp, 5/28/96, (PB98-118607, A07, MF-A02).

NCEER-96-0007 "Nonlinear Control Techniques for Dynamical Systems with Uncertain Parameters," by R.G. Ghanem and M.I. Bujakov, 5/27/96, (PB97-100259, A17, MF-A03).

NCEER-96-0008 "Seismic Evaluation of a 30-Year Old Non-Ductile Highway Bridge Pier and Its Retrofit," by J.B. Mander, B. Mahmoodzadegan, S. Bhadra and S.S. Chen, 5/31/96, (PB97-110902, MF-A03, A10).

NCEER-96-0009 "Seismic Performance of a Model Reinforced Concrete Bridge Pier Before and After Retrofit," by J.B. Mander, J.H. Kim and C.A. Ligozio, 5/31/96, (PB97-110910, MF-A02, A10).

NCEER-96-0010 "IDARC2D Version 4.0: A Computer Program for the Inelastic Damage Analysis of Buildings," by R.E. Valles, A.M. Reinhorn, S.K. Kunnath, C. Li and A. Madan, 6/3/96, (PB97-100234, A17, MF-A03).

NCEER-96-0011 "Estimation of the Economic Impact of Multiple Lifeline Disruption: Memphis Light, Gas and Water Division Case Study," by S.E. Chang, H.A. Seligson and R.T. Eguchi, 8/16/96, (PB97-133490, A11, MF-A03).

NCEER-96-0012 "Proceedings from the Sixth Japan-U.S. Workshop on Earthquake Resistant Design of Lifeline Facilities and Countermeasures Against Soil Liquefaction, Edited by M. Hamada and T. O'Rourke, 9/11/96, (PB97-133581, A99, MF-A06).

NCEER-96-0013 "Chemical Hazards, Mitigation and Preparedness in Areas of High Seismic Risk: A Methodology for Estimating the Risk of Post-Earthquake Hazardous Materials Release," by H.A. Seligson, R.T. Eguchi, K.J. Tierney and K. Richmond, 11/7/96, (PB97-133565, MF-A02, A08).

NCEER-96-0014 "Response of Steel Bridge Bearings to Reversed Cyclic Loading," by J.B. Mander, D-K. Kim, S.S. Chen and G.J. Premus, 11/13/96, (PB97-140735, A12, MF-A03).

NCEER-96-0015 "Highway Culvert Performance During Past Earthquakes," by T.L. Youd and C.J. Beckman, 11/25/96, (PB97-133532, A06, MF-A01).

NCEER-97-0001 "Evaluation, Prevention and Mitigation of Pounding Effects in Building Structures," by R.E. Valles and A.M. Reinhorn, 2/20/97, (PB97-159552, A14, MF-A03).

NCEER-97-0002 "Seismic Design Criteria for Bridges and Other Highway Structures," by C. Rojahn, R. Mayes, D.G. Anderson, J. Clark, J.H. Hom, R.V. Nutt and M.J. O'Rourke, 4/30/97, (PB97-194658, A06, MF-A03).

NCEER-97-0003 “Proceedings of the U.S.-Italian Workshop on Seismic Evaluation and Retrofit,” Edited by D.P. Abrams and G.M. Calvi, 3/19/97, (PB97-194666, A13, MF-A03).

NCEER-97-0004 "Investigation of Seismic Response of Buildings with Linear and Nonlinear Fluid Viscous Dampers," by A.A. Seleemah and M.C. Constantinou, 5/21/97, (PB98-109002, A15, MF-A03).

NCEER-97-0005 "Proceedings of the Workshop on Earthquake Engineering Frontiers in Transportation Facilities," edited by G.C. Lee and I.M. Friedland, 8/29/97, (PB98-128911, A25, MR-A04).

NCEER-97-0006 "Cumulative Seismic Damage of Reinforced Concrete Bridge Piers," by S.K. Kunnath, A. El-Bahy, A. Taylor and W. Stone, 9/2/97, (PB98-108814, A11, MF-A03).

NCEER-97-0007 "Structural Details to Accommodate Seismic Movements of Highway Bridges and Retaining Walls," by R.A. Imbsen, R.A. Schamber, E. Thorkildsen, A. Kartoum, B.T. Martin, T.N. Rosser and J.M. Kulicki, 9/3/97, (PB98-108996, A09, MF-A02).

NCEER-97-0008 "A Method for Earthquake Motion-Damage Relationships with Application to Reinforced Concrete Frames," by A. Singhal and A.S. Kiremidjian, 9/10/97, (PB98-108988, A13, MF-A03).

NCEER-97-0009 "Seismic Analysis and Design of Bridge Abutments Considering Sliding and Rotation," by K. Fishman and R. Richards, Jr., 9/15/97, (PB98-108897, A06, MF-A02).

NCEER-97-0010 "Proceedings of the FHWA/NCEER Workshop on the National Representation of Seismic Ground Motion for New and Existing Highway Facilities," edited by I.M. Friedland, M.S. Power and R.L. Mayes, 9/22/97, (PB98-128903, A21, MF-A04).

NCEER-97-0011 "Seismic Analysis for Design or Retrofit of Gravity Bridge Abutments," by K.L. Fishman, R. Richards, Jr. and R.C. Divito, 10/2/97, (PB98-128937, A08, MF-A02).

NCEER-97-0012 "Evaluation of Simplified Methods of Analysis for Yielding Structures," by P. Tsopelas, M.C. Constantinou, C.A. Kircher and A.S. Whittaker, 10/31/97, (PB98-128929, A10, MF-A03).

NCEER-97-0013 "Seismic Design of Bridge Columns Based on Control and Repairability of Damage," by C-T. Cheng and J.B. Mander, 12/8/97, (PB98-144249, A11, MF-A03).

NCEER-97-0014 "Seismic Resistance of Bridge Piers Based on Damage Avoidance Design," by J.B. Mander and C-T. Cheng, 12/10/97, (PB98-144223, A09, MF-A02).

NCEER-97-0015 “Seismic Response of Nominally Symmetric Systems with Strength Uncertainty,” by S. Balopoulou and M. Grigoriu, 12/23/97, (PB98-153422, A11, MF-A03).

NCEER-97-0016 “Evaluation of Seismic Retrofit Methods for Reinforced Concrete Bridge Columns,” by T.J. Wipf, F.W. Klaiber and F.M. Russo, 12/28/97, (PB98-144215, A12, MF-A03).

NCEER-97-0017 “Seismic Fragility of Existing Conventional Reinforced Concrete Highway Bridges,” by C.L. Mullen and A.S. Cakmak, 12/30/97, (PB98-153406, A08, MF-A02).

NCEER-97-0018 “Loss Asssessment of Memphis Buildings,” edited by D.P. Abrams and M. Shinozuka, 12/31/97, (PB98-144231, A13, MF-A03).

NCEER-97-0019 “Seismic Evaluation of Frames with Infill Walls Using Quasi-static Experiments,” by K.M. Mosalam, R.N. White and P. Gergely, 12/31/97, (PB98-153455, A07, MF-A02).

NCEER-97-0020 “Seismic Evaluation of Frames with Infill Walls Using Pseudo-dynamic Experiments,” by K.M. Mosalam, R.N. White and P. Gergely, 12/31/97, (PB98-153430, A07, MF-A02).

NCEER-97-0021 “Computational Strategies for Frames with Infill Walls: Discrete and Smeared Crack Analyses and Seismic Fragility,” by K.M. Mosalam, R.N. White and P. Gergely, 12/31/97, (PB98-153414, A10, MF-A02).

NCEER-97-0022 "Proceedings of the NCEER Workshop on Evaluation of Liquefaction Resistance of Soils," edited by T.L. Youd and I.M. Idriss, 12/31/97, (PB98-155617, A15, MF-A03).

MCEER-98-0001 "Extraction of Nonlinear Hysteretic Properties of Seismically Isolated Bridges from Quick-Release Field Tests," by Q. Chen, B.M. Douglas, E.M. Maragakis and I.G. Buckle, 5/26/98, (PB99-118838, A06, MF-A01).

MCEER-98-0002 "Methodologies for Evaluating the Importance of Highway Bridges," by A. Thomas, S. Eshenaur and J. Kulicki, 5/29/98, (PB99-118846, A10, MF-A02).

MCEER-98-0003 "Capacity Design of Bridge Piers and the Analysis of Overstrength," by J.B. Mander, A. Dutta and P. Goel, 6/1/98, (PB99-118853, A09, MF-A02).

MCEER-98-0004 "Evaluation of Bridge Damage Data from the Loma Prieta and Northridge, California Earthquakes," by N. Basoz and A. Kiremidjian, 6/2/98, (PB99-118861, A15, MF-A03).

MCEER-98-0005 "Screening Guide for Rapid Assessment of Liquefaction Hazard at Highway Bridge Sites," by T. L. Youd, 6/16/98, (PB99-118879, A06, not available on microfiche).

MCEER-98-0006 "Structural Steel and Steel/Concrete Interface Details for Bridges," by P. Ritchie, N. Kauhl and J. Kulicki, 7/13/98, (PB99-118945, A06, MF-A01).

MCEER-98-0007 "Capacity Design and Fatigue Analysis of Confined Concrete Columns," by A. Dutta and J.B. Mander, 7/14/98, (PB99-118960, A14, MF-A03).

MCEER-98-0008 "Proceedings of the Workshop on Performance Criteria for Telecommunication Services Under Earthquake Conditions," edited by A.J. Schiff, 7/15/98, (PB99-118952, A08, MF-A02).

MCEER-98-0009 "Fatigue Analysis of Unconfined Concrete Columns," by J.B. Mander, A. Dutta and J.H. Kim, 9/12/98, (PB99-123655, A10, MF-A02).

MCEER-98-0010 "Centrifuge Modeling of Cyclic Lateral Response of Pile-Cap Systems and Seat-Type Abutments in Dry Sands," by A.D. Gadre and R. Dobry, 10/2/98, (PB99-123606, A13, MF-A03).

MCEER-98-0011 "IDARC-BRIDGE: A Computational Platform for Seismic Damage Assessment of Bridge Structures," by A.M. Reinhorn, V. Simeonov, G. Mylonakis and Y. Reichman, 10/2/98, (PB99-162919, A15, MF-A03).

MCEER-98-0012 "Experimental Investigation of the Dynamic Response of Two Bridges Before and After Retrofitting with Elastomeric Bearings," by D.A. Wendichansky, S.S. Chen and J.B. Mander, 10/2/98, (PB99-162927, A15, MF-A03).

MCEER-98-0013 "Design Procedures for Hinge Restrainers and Hinge Sear Width for Multiple-Frame Bridges," by R. Des Roches and G.L. Fenves, 11/3/98, (PB99-140477, A13, MF-A03).

MCEER-98-0014 "Response Modification Factors for Seismically Isolated Bridges," by M.C. Constantinou and J.K. Quarshie, 11/3/98, (PB99-140485, A14, MF-A03).

MCEER-98-0015 "Proceedings of the U.S.-Italy Workshop on Seismic Protective Systems for Bridges," edited by I.M. Friedland and M.C. Constantinou, 11/3/98, (PB2000-101711, A22, MF-A04).

MCEER-98-0016 "Appropriate Seismic Reliability for Critical Equipment Systems: Recommendations Based on Regional Analysis of Financial and Life Loss," by K. Porter, C. Scawthorn, C. Taylor and N. Blais, 11/10/98, (PB99-157265, A08, MF-A02).

MCEER-98-0017 "Proceedings of the U.S. Japan Joint Seminar on Civil Infrastructure Systems Research," edited by M. Shinozuka and A. Rose, 11/12/98, (PB99-156713, A16, MF-A03).

MCEER-98-0018 "Modeling of Pile Footings and Drilled Shafts for Seismic Design," by I. PoLam, M. Kapuskar and D. Chaudhuri, 12/21/98, (PB99-157257, A09, MF-A02).

MCEER-99-0001 "Seismic Evaluation of a Masonry Infilled Reinforced Concrete Frame by Pseudodynamic Testing," by S.G. Buonopane and R.N. White, 2/16/99, (PB99-162851, A09, MF-A02).

MCEER-99-0002 "Response History Analysis of Structures with Seismic Isolation and Energy Dissipation Systems: Verification Examples for Program SAP2000," by J. Scheller and M.C. Constantinou, 2/22/99, (PB99-162869, A08, MF-A02).

MCEER-99-0003 "Experimental Study on the Seismic Design and Retrofit of Bridge Columns Including Axial Load Effects," by A. Dutta, T. Kokorina and J.B. Mander, 2/22/99, (PB99-162877, A09, MF-A02).

MCEER-99-0004 "Experimental Study of Bridge Elastomeric and Other Isolation and Energy Dissipation Systems with Emphasis on Uplift Prevention and High Velocity Near-source Seismic Excitation," by A. Kasalanati and M. C. Constantinou, 2/26/99, (PB99-162885, A12, MF-A03).

MCEER-99-0005 "Truss Modeling of Reinforced Concrete Shear-flexure Behavior," by J.H. Kim and J.B. Mander, 3/8/99, (PB99-163693, A12, MF-A03).

MCEER-99-0006 "Experimental Investigation and Computational Modeling of Seismic Response of a 1:4 Scale Model Steel Structure with a Load Balancing Supplemental Damping System," by G. Pekcan, J.B. Mander and S.S. Chen, 4/2/99, (PB99-162893, A11, MF-A03).

MCEER-99-0007 "Effect of Vertical Ground Motions on the Structural Response of Highway Bridges," by M.R. Button, C.J. Cronin and R.L. Mayes, 4/10/99, (PB2000-101411, A10, MF-A03).

MCEER-99-0008 "Seismic Reliability Assessment of Critical Facilities: A Handbook, Supporting Documentation, and Model Code Provisions," by G.S. Johnson, R.E. Sheppard, M.D. Quilici, S.J. Eder and C.R. Scawthorn, 4/12/99, (PB2000-101701, A18, MF-A04).

MCEER-99-0009 "Impact Assessment of Selected MCEER Highway Project Research on the Seismic Design of Highway Structures," by C. Rojahn, R. Mayes, D.G. Anderson, J.H. Clark, D'Appolonia Engineering, S. Gloyd and R.V. Nutt, 4/14/99, (PB99-162901, A10, MF-A02).

MCEER-99-0010 "Site Factors and Site Categories in Seismic Codes," by R. Dobry, R. Ramos and M.S. Power, 7/19/99, (PB2000-101705, A08, MF-A02).

MCEER-99-0011 "Restrainer Design Procedures for Multi-Span Simply-Supported Bridges," by M.J. Randall, M. Saiidi, E. Maragakis and T. Isakovic, 7/20/99, (PB2000-101702, A10, MF-A02).

MCEER-99-0012 "Property Modification Factors for Seismic Isolation Bearings," by M.C. Constantinou, P. Tsopelas, A. Kasalanati and E. Wolff, 7/20/99, (PB2000-103387, A11, MF-A03).

MCEER-99-0013 "Critical Seismic Issues for Existing Steel Bridges," by P. Ritchie, N. Kauhl and J. Kulicki, 7/20/99, (PB2000-101697, A09, MF-A02).

MCEER-99-0014 "Nonstructural Damage Database," by A. Kao, T.T. Soong and A. Vender, 7/24/99, (PB2000-101407, A06, MF-A01).

MCEER-99-0015 "Guide to Remedial Measures for Liquefaction Mitigation at Existing Highway Bridge Sites," by H.G. Cooke and J. K. Mitchell, 7/26/99, (PB2000-101703, A11, MF-A03).

MCEER-99-0016 "Proceedings of the MCEER Workshop on Ground Motion Methodologies for the Eastern United States," edited by N. Abrahamson and A. Becker, 8/11/99, (PB2000-103385, A07, MF-A02).

MCEER-99-0017 "Quindío, Colombia Earthquake of January 25, 1999: Reconnaissance Report," by A.P. Asfura and P.J. Flores, 10/4/99, (PB2000-106893, A06, MF-A01).

MCEER-99-0018 "Hysteretic Models for Cyclic Behavior of Deteriorating Inelastic Structures," by M.V. Sivaselvan and A.M. Reinhorn, 11/5/99, (PB2000-103386, A08, MF-A02).

MCEER-99-0019 "Proceedings of the 7th U.S.- Japan Workshop on Earthquake Resistant Design of Lifeline Facilities and Countermeasures Against Soil Liquefaction," edited by T.D. O'Rourke, J.P. Bardet and M. Hamada, 11/19/99, (PB2000-103354, A99, MF-A06).

MCEER-99-0020 "Development of Measurement Capability for Micro-Vibration Evaluations with Application to Chip Fabrication Facilities," by G.C. Lee, Z. Liang, J.W. Song, J.D. Shen and W.C. Liu, 12/1/99, (PB2000-105993, A08, MF-A02).

MCEER-99-0021 "Design and Retrofit Methodology for Building Structures with Supplemental Energy Dissipating Systems," by G. Pekcan, J.B. Mander and S.S. Chen, 12/31/99, (PB2000-105994, A11, MF-A03).

MCEER-00-0001 "The Marmara, Turkey Earthquake of August 17, 1999: Reconnaissance Report," edited by C. Scawthorn; with major contributions by M. Bruneau, R. Eguchi, T. Holzer, G. Johnson, J. Mander, J. Mitchell, W. Mitchell, A. Papageorgiou, C. Scaethorn, and G. Webb, 3/23/00, (PB2000-106200, A11, MF-A03).

MCEER-00-0002 "Proceedings of the MCEER Workshop for Seismic Hazard Mitigation of Health Care Facilities," edited by G.C. Lee, M. Ettouney, M. Grigoriu, J. Hauer and J. Nigg, 3/29/00, (PB2000-106892, A08, MF-A02).

MCEER-00-0003 "The Chi-Chi, Taiwan Earthquake of September 21, 1999: Reconnaissance Report," edited by G.C. Lee and C.H. Loh, with major contributions by G.C. Lee, M. Bruneau, I.G. Buckle, S.E. Chang, P.J. Flores, T.D. O'Rourke, M. Shinozuka, T.T. Soong, C-H. Loh, K-C. Chang, Z-J. Chen, J-S. Hwang, M-L. Lin, G-Y. Liu, K-C. Tsai, G.C. Yao and C-L. Yen, 4/30/00, (PB2001-100980, A10, MF-A02).

MCEER-00-0004 "Seismic Retrofit of End-Sway Frames of Steel Deck-Truss Bridges with a Supplemental Tendon System: Experimental and Analytical Investigation," by G. Pekcan, J.B. Mander and S.S. Chen, 7/1/00, (PB2001-100982, A10, MF-A02).

MCEER-00-0005 "Sliding Fragility of Unrestrained Equipment in Critical Facilities," by W.H. Chong and T.T. Soong, 7/5/00, (PB2001-100983, A08, MF-A02).

MCEER-00-0006 "Seismic Response of Reinforced Concrete Bridge Pier Walls in the Weak Direction," by N. Abo-Shadi, M. Saiidi and D. Sanders, 7/17/00, (PB2001-100981, A17, MF-A03).

MCEER-00-0007 "Low-Cycle Fatigue Behavior of Longitudinal Reinforcement in Reinforced Concrete Bridge Columns," by J. Brown and S.K. Kunnath, 7/23/00, (PB2001-104392, A08, MF-A02).

MCEER-00-0008 "Soil Structure Interaction of Bridges for Seismic Analysis," I. PoLam and H. Law, 9/25/00, (PB2001-105397, A08, MF-A02).

MCEER-00-0009 "Proceedings of the First MCEER Workshop on Mitigation of Earthquake Disaster by Advanced Technologies (MEDAT-1), edited by M. Shinozuka, D.J. Inman and T.D. O'Rourke, 11/10/00, (PB2001-105399, A14, MF-A03).

MCEER-00-0010 "Development and Evaluation of Simplified Procedures for Analysis and Design of Buildings with Passive Energy Dissipation Systems, Revision 01," by O.M. Ramirez, M.C. Constantinou, C.A. Kircher, A.S. Whittaker, M.W. Johnson, J.D. Gomez and C. Chrysostomou, 11/16/01, (PB2001-105523, A23, MF-A04).

MCEER-00-0011 "Dynamic Soil-Foundation-Structure Interaction Analyses of Large Caissons," by C-Y. Chang, C-M. Mok, Z-L. Wang, R. Settgast, F. Waggoner, M.A. Ketchum, H.M. Gonnermann and C-C. Chin, 12/30/00, (PB2001-104373, A07, MF-A02).

MCEER-00-0012 "Experimental Evaluation of Seismic Performance of Bridge Restrainers," by A.G. Vlassis, E.M. Maragakis and M. Saiid Saiidi, 12/30/00, (PB2001-104354, A09, MF-A02).

MCEER-00-0013 "Effect of Spatial Variation of Ground Motion on Highway Structures," by M. Shinozuka, V. Saxena and G. Deodatis, 12/31/00, (PB2001-108755, A13, MF-A03).

MCEER-00-0014 "A Risk-Based Methodology for Assessing the Seismic Performance of Highway Systems," by S.D. Werner, C.E. Taylor, J.E. Moore, II, J.S. Walton and S. Cho, 12/31/00, (PB2001-108756, A14, MF-A03).

MCEER-01-0001 "Experimental Investigation of P-Delta Effects to Collapse During Earthquakes," by D. Vian and M. Bruneau, 6/25/01, (PB2002-100534, A17, MF-A03).

MCEER-01-0002 "Proceedings of the Second MCEER Workshop on Mitigation of Earthquake Disaster by Advanced Technologies (MEDAT-2)," edited by M. Bruneau and D.J. Inman, 7/23/01, (PB2002-100434, A16, MF-A03).

MCEER-01-0003 "Sensitivity Analysis of Dynamic Systems Subjected to Seismic Loads," by C. Roth and M. Grigoriu, 9/18/01, (PB2003-100884, A12, MF-A03).

MCEER-01-0004 "Overcoming Obstacles to Implementing Earthquake Hazard Mitigation Policies: Stage 1 Report," by D.J. Alesch and W.J. Petak, 12/17/01, (PB2002-107949, A07, MF-A02).

MCEER-01-0005 "Updating Real-Time Earthquake Loss Estimates: Methods, Problems and Insights," by C.E. Taylor, S.E. Chang and R.T. Eguchi, 12/17/01, (PB2002-107948, A05, MF-A01).

MCEER-01-0006 "Experimental Investigation and Retrofit of Steel Pile Foundations and Pile Bents Under Cyclic Lateral Loadings," by A. Shama, J. Mander, B. Blabac and S. Chen, 12/31/01, (PB2002-107950, A13, MF-A03).

MCEER-02-0001 "Assessment of Performance of Bolu Viaduct in the 1999 Duzce Earthquake in Turkey" by P.C. Roussis, M.C. Constantinou, M. Erdik, E. Durukal and M. Dicleli, 5/8/02, (PB2003-100883, A08, MF-A02).

MCEER-02-0002 "Seismic Behavior of Rail Counterweight Systems of Elevators in Buildings," by M.P. Singh, Rildova and L.E. Suarez, 5/27/02. (PB2003-100882, A11, MF-A03).

MCEER-02-0003 "Development of Analysis and Design Procedures for Spread Footings," by G. Mylonakis, G. Gazetas, S. Nikolaou and A. Chauncey, 10/02/02, (PB2004-101636, A13, MF-A03, CD-A13).

MCEER-02-0004 "Bare-Earth Algorithms for Use with SAR and LIDAR Digital Elevation Models," by C.K. Huyck, R.T. Eguchi and B. Houshmand, 10/16/02, (PB2004-101637, A07, CD-A07).

MCEER-02-0005 "Review of Energy Dissipation of Compression Members in Concentrically Braced Frames," by K.Lee and M. Bruneau, 10/18/02, (PB2004-101638, A10, CD-A10).

MCEER-03-0001 "Experimental Investigation of Light-Gauge Steel Plate Shear Walls for the Seismic Retrofit of Buildings" by J. Berman and M. Bruneau, 5/2/03, (PB2004-101622, A10, MF-A03, CD-A10).

MCEER-03-0002 "Statistical Analysis of Fragility Curves," by M. Shinozuka, M.Q. Feng, H. Kim, T. Uzawa and T. Ueda, 6/16/03, (PB2004-101849, A09, CD-A09).

MCEER-03-0003 "Proceedings of the Eighth U.S.-Japan Workshop on Earthquake Resistant Design f Lifeline Facilities and Countermeasures Against Liquefaction," edited by M. Hamada, J.P. Bardet and T.D. O'Rourke, 6/30/03, (PB2004-104386, A99, CD-A99).

MCEER-03-0004 "Proceedings of the PRC-US Workshop on Seismic Analysis and Design of Special Bridges," edited by L.C. Fan and G.C. Lee, 7/15/03, (PB2004-104387, A14, CD-A14).

MCEER-03-0005 "Urban Disaster Recovery: A Framework and Simulation Model," by S.B. Miles and S.E. Chang, 7/25/03, (PB2004-104388, A07, CD-A07).

MCEER-03-0006 "Behavior of Underground Piping Joints Due to Static and Dynamic Loading," by R.D. Meis, M. Maragakis and R. Siddharthan, 11/17/03, (PB2005-102194, A13, MF-A03, CD-A00).

MCEER-04-0001 "Experimental Study of Seismic Isolation Systems with Emphasis on Secondary System Response and Verification of Accuracy of Dynamic Response History Analysis Methods," by E. Wolff and M. Constantinou, 1/16/04 (PB2005-102195, A99, MF-E08, CD-A00).

MCEER-04-0002 "Tension, Compression and Cyclic Testing of Engineered Cementitious Composite Materials," by K. Kesner and S.L. Billington, 3/1/04, (PB2005-102196, A08, CD-A08).

MCEER-04-0003 "Cyclic Testing of Braces Laterally Restrained by Steel Studs to Enhance Performance During Earthquakes," by O.C. Celik, J.W. Berman and M. Bruneau, 3/16/04, (PB2005-102197, A13, MF-A03, CD-A00).

MCEER-04-0004 "Methodologies for Post Earthquake Building Damage Detection Using SAR and Optical Remote Sensing: Application to the August 17, 1999 Marmara, Turkey Earthquake," by C.K. Huyck, B.J. Adams, S. Cho, R.T. Eguchi, B. Mansouri and B. Houshmand, 6/15/04, (PB2005-104888, A10, CD-A00).

MCEER-04-0005 "Nonlinear Structural Analysis Towards Collapse Simulation: A Dynamical Systems Approach," by M.V. Sivaselvan and A.M. Reinhorn, 6/16/04, (PB2005-104889, A11, MF-A03, CD-A00).

MCEER-04-0006 "Proceedings of the Second PRC-US Workshop on Seismic Analysis and Design of Special Bridges," edited by G.C. Lee and L.C. Fan, 6/25/04, (PB2005-104890, A16, CD-A00).

MCEER-04-0007 "Seismic Vulnerability Evaluation of Axially Loaded Steel Built-up Laced Members," by K. Lee and M. Bruneau, 6/30/04, (PB2005-104891, A16, CD-A00).

MCEER-04-0008 "Evaluation of Accuracy of Simplified Methods of Analysis and Design of Buildings with Damping Systems for Near-Fault and for Soft-Soil Seismic Motions," by E.A. Pavlou and M.C. Constantinou, 8/16/04, (PB2005-104892, A08, MF-A02, CD-A00).

MCEER-04-0009 "Assessment of Geotechnical Issues in Acute Care Facilities in California," by M. Lew, T.D. O'Rourke, R. Dobry and M. Koch, 9/15/04, (PB2005-104893, A08, CD-A00).

MCEER-04-0010 "Scissor-Jack-Damper Energy Dissipation System," by A.N. Sigaher-Boyle and M.C. Constantinou, 12/1/04 (PB2005-108221).

MCEER-04-0011 "Seismic Retrofit of Bridge Steel Truss Piers Using a Controlled Rocking Approach," by M. Pollino and M. Bruneau, 12/20/04 (PB2006-105795).

MCEER-05-0001 "Experimental and Analytical Studies of Structures Seismically Isolated with an Uplift-Restraint Isolation System," by P.C. Roussis and M.C. Constantinou, 1/10/05 (PB2005-108222).

MCEER-05-0002 "A Versatile Experimentation Model for Study of Structures Near Collapse Applied to Seismic Evaluation of Irregular Structures," by D. Kusumastuti, A.M. Reinhorn and A. Rutenberg, 3/31/05 (PB2006-101523).

MCEER-05-0003 "Proceedings of the Third PRC-US Workshop on Seismic Analysis and Design of Special Bridges," edited by L.C. Fan and G.C. Lee, 4/20/05, (PB2006-105796).

MCEER-05-0004 "Approaches for the Seismic Retrofit of Braced Steel Bridge Piers and Proof-of-Concept Testing of an Eccentrically Braced Frame with Tubular Link," by J.W. Berman and M. Bruneau, 4/21/05 (PB2006-101524).

MCEER-05-0005 "Simulation of Strong Ground Motions for Seismic Fragility Evaluation of Nonstructural Components in Hospitals," by A. Wanitkorkul and A. Filiatrault, 5/26/05 (PB2006-500027).

MCEER-05-0006 "Seismic Safety in California Hospitals: Assessing an Attempt to Accelerate the Replacement or Seismic Retrofit of Older Hospital Facilities," by D.J. Alesch, L.A. Arendt and W.J. Petak, 6/6/05 (PB2006-105794).

MCEER-05-0007 "Development of Seismic Strengthening and Retrofit Strategies for Critical Facilities Using Engineered Cementitious Composite Materials," by K. Kesner and S.L. Billington, 8/29/05 (PB2006-111701).

MCEER-05-0008 "Experimental and Analytical Studies of Base Isolation Systems for Seismic Protection of Power Transformers," by N. Murota, M.Q. Feng and G-Y. Liu, 9/30/05 (PB2006-111702).

MCEER-05-0009 "3D-BASIS-ME-MB: Computer Program for Nonlinear Dynamic Analysis of Seismically Isolated Structures," by P.C. Tsopelas, P.C. Roussis, M.C. Constantinou, R. Buchanan and A.M. Reinhorn, 10/3/05 (PB2006-111703).

MCEER-05-0010 "Steel Plate Shear Walls for Seismic Design and Retrofit of Building Structures," by D. Vian and M. Bruneau, 12/15/05 (PB2006-111704).

MCEER-05-0011 "The Performance-Based Design Paradigm," by M.J. Astrella and A. Whittaker, 12/15/05 (PB2006-111705).

MCEER-06-0001 "Seismic Fragility of Suspended Ceiling Systems," H. Badillo-Almaraz, A.S. Whittaker, A.M. Reinhorn and G.P. Cimellaro, 2/4/06 (PB2006-111706).

MCEER-06-0002 "Multi-Dimensional Fragility of Structures," by G.P. Cimellaro, A.M. Reinhorn and M. Bruneau, 3/1/06 (PB2007-106974, A09, MF-A02, CD A00).

MCEER-06-0003 "Built-Up Shear Links as Energy Dissipators for Seismic Protection of Bridges," by P. Dusicka, A.M. Itani and I.G. Buckle, 3/15/06 (PB2006-111708).

MCEER-06-0004 "Analytical Investigation of the Structural Fuse Concept," by R.E. Vargas and M. Bruneau, 3/16/06 (PB2006-111709).

MCEER-06-0005 "Experimental Investigation of the Structural Fuse Concept," by R.E. Vargas and M. Bruneau, 3/17/06 (PB2006-111710).

MCEER-06-0006 "Further Development of Tubular Eccentrically Braced Frame Links for the Seismic Retrofit of Braced Steel Truss Bridge Piers," by J.W. Berman and M. Bruneau, 3/27/06 (PB2007-105147).

MCEER-06-0007 "REDARS Validation Report," by S. Cho, C.K. Huyck, S. Ghosh and R.T. Eguchi, 8/8/06 (PB2007-106983).

MCEER-06-0008 "Review of Current NDE Technologies for Post-Earthquake Assessment of Retrofitted Bridge Columns," by J.W. Song, Z. Liang and G.C. Lee, 8/21/06 (PB2007-106984).

MCEER-06-0009 "Liquefaction Remediation in Silty Soils Using Dynamic Compaction and Stone Columns," by S. Thevanayagam, G.R. Martin, R. Nashed, T. Shenthan, T. Kanagalingam and N. Ecemis, 8/28/06 (PB2007-106985).

MCEER-06-0010 "Conceptual Design and Experimental Investigation of Polymer Matrix Composite Infill Panels for Seismic Retrofitting," by W. Jung, M. Chiewanichakorn and A.J. Aref, 9/21/06 (PB2007-106986).

MCEER-06-0011 "A Study of the Coupled Horizontal-Vertical Behavior of Elastomeric and Lead-Rubber Seismic Isolation Bearings," by G.P. Warn and A.S. Whittaker, 9/22/06 (PB2007-108679).

MCEER-06-0012 "Proceedings of the Fourth PRC-US Workshop on Seismic Analysis and Design of Special Bridges: Advancing Bridge Technologies in Research, Design, Construction and Preservation," Edited by L.C. Fan, G.C. Lee and L. Ziang, 10/12/06 (PB2007-109042).

MCEER-06-0013 "Cyclic Response and Low Cycle Fatigue Characteristics of Plate Steels," by P. Dusicka, A.M. Itani and I.G. Buckle, 11/1/06 06 (PB2007-106987).

MCEER-06-0014 "Proceedings of the Second US-Taiwan Bridge Engineering Workshop," edited by W.P. Yen, J. Shen, J-Y. Chen and M. Wang, 11/15/06 (PB2008-500041).

MCEER-06-0015 "User Manual and Technical Documentation for the REDARS$^{TM}$ Import Wizard," by S. Cho, S. Ghosh, C.K. Huyck and S.D. Werner, 11/30/06 (PB2007-114766).

MCEER-06-0016 "Hazard Mitigation Strategy and Monitoring Technologies for Urban and Infrastructure Public Buildings: Proceedings of the China-US Workshops," edited by X.Y. Zhou, A.L. Zhang, G.C. Lee and M. Tong, 12/12/06 (PB2008-500018).

MCEER-07-0001 "Static and Kinetic Coefficients of Friction for Rigid Blocks," by C. Kafali, S. Fathali, M. Grigoriu and A.S. Whittaker, 3/20/07 (PB2007-114767).

MCEER-07-0002 "Hazard Mitigation Investment Decision Making: Organizational Response to Legislative Mandate," by L.A. Arendt, D.J. Alesch and W.J. Petak, 4/9/07 (PB2007-114768).

MCEER-07-0003 "Seismic Behavior of Bidirectional-Resistant Ductile End Diaphragms with Unbonded Braces in Straight or Skewed Steel Bridges," by O. Celik and M. Bruneau, 4/11/07 (PB2008-105141).

MCEER-07-0004 "Modeling Pile Behavior in Large Pile Groups Under Lateral Loading," by A.M. Dodds and G.R. Martin, 4/16/07(PB2008-105142).

MCEER-07-0005 "Experimental Investigation of Blast Performance of Seismically Resistant Concrete-Filled Steel Tube Bridge Piers," by S. Fujikura, M. Bruneau and D. Lopez-Garcia, 4/20/07 (PB2008-105143).

MCEER-07-0006 "Seismic Analysis of Conventional and Isolated Liquefied Natural Gas Tanks Using Mechanical Analogs," by I.P. Christovasilis and A.S. Whittaker, 5/1/07, not available.

MCEER-07-0007 "Experimental Seismic Performance Evaluation of Isolation/Restraint Systems for Mechanical Equipment – Part 1: Heavy Equipment Study," by S. Fathali and A. Filiatrault, 6/6/07 (PB2008-105144).

MCEER-07-0008 "Seismic Vulnerability of Timber Bridges and Timber Substructures," by A.A. Sharma, J.B. Mander, I.M. Friedland and D.R. Allicock, 6/7/07 (PB2008-105145).

MCEER-07-0009 "Experimental and Analytical Study of the XY-Friction Pendulum (XY-FP) Bearing for Bridge Applications," by C.C. Marin-Artieda, A.S. Whittaker and M.C. Constantinou, 6/7/07 (PB2008-105191).

MCEER-07-0010 "Proceedings of the PRC-US Earthquake Engineering Forum for Young Researchers," Edited by G.C. Lee and X.Z. Qi, 6/8/07 (PB2008-500058).

MCEER-07-0011 "Design Recommendations for Perforated Steel Plate Shear Walls," by R. Purba and M. Bruneau, 6/18/07, (PB2008-105192).

MCEER-07-0012 "Performance of Seismic Isolation Hardware Under Service and Seismic Loading," by M.C. Constantinou, A.S. Whittaker, Y. Kalpakidis, D.M. Fenz and G.P. Warn, 8/27/07, (PB2008-105193).

MCEER-07-0013 "Experimental Evaluation of the Seismic Performance of Hospital Piping Subassemblies," by E.R. Goodwin, E. Maragakis and A.M. Itani, 9/4/07, (PB2008-105194).

MCEER-07-0014 "A Simulation Model of Urban Disaster Recovery and Resilience: Implementation for the 1994 Northridge Earthquake," by S. Miles and S.E. Chang, 9/7/07, (PB2008-106426).

MCEER-07-0015 "Statistical and Mechanistic Fragility Analysis of Concrete Bridges," by M. Shinozuka, S. Banerjee and S-H. Kim, 9/10/07, (PB2008-106427).

MCEER-07-0016 "Three-Dimensional Modeling of Inelastic Buckling in Frame Structures," by M. Schachter and AM. Reinhorn, 9/13/07, (PB2008-108125).

MCEER-07-0017 "Modeling of Seismic Wave Scattering on Pile Groups and Caissons," by I. Po Lam, H. Law and C.T. Yang, 9/17/07 (PB2008-108150).

MCEER-07-0018 "Bridge Foundations: Modeling Large Pile Groups and Caissons for Seismic Design," by I. Po Lam, H. Law and G.R. Martin (Coordinating Author), 12/1/07 (PB2008-111190).

MCEER-07-0019 "Principles and Performance of Roller Seismic Isolation Bearings for Highway Bridges," by G.C. Lee, Y.C. Ou, Z. Liang, T.C. Niu and J. Song, 12/10/07 (PB2009-110466).

MCEER-07-0020 "Centrifuge Modeling of Permeability and Pinning Reinforcement Effects on Pile Response to Lateral Spreading," by L.L Gonzalez-Lagos, T. Abdoun and R. Dobry, 12/10/07 (PB2008-111191).

MCEER-07-0021 "Damage to the Highway System from the Pisco, Perú Earthquake of August 15, 2007," by J.S. O'Connor, L. Mesa and M. Nykamp, 12/10/07, (PB2008-108126).

MCEER-07-0022 "Experimental Seismic Performance Evaluation of Isolation/Restraint Systems for Mechanical Equipment – Part 2: Light Equipment Study," by S. Fathali and A. Filiatrault, 12/13/07 (PB2008-111192).

MCEER-07-0023 "Fragility Considerations in Highway Bridge Design," by M. Shinozuka, S. Banerjee and S.H. Kim, 12/14/07 (PB2008-111193).

MCEER-07-0024 "Performance Estimates for Seismically Isolated Bridges," by G.P. Warn and A.S. Whittaker, 12/30/07 (PB2008-112230).

MCEER-08-0001 "Seismic Performance of Steel Girder Bridge Superstructures with Conventional Cross Frames," by L.P. Carden, A.M. Itani and I.G. Buckle, 1/7/08, (PB2008-112231).

MCEER-08-0002 "Seismic Performance of Steel Girder Bridge Superstructures with Ductile End Cross Frames with Seismic Isolators," by L.P. Carden, A.M. Itani and I.G. Buckle, 1/7/08 (PB2008-112232).

MCEER-08-0003 "Analytical and Experimental Investigation of a Controlled Rocking Approach for Seismic Protection of Bridge Steel Truss Piers," by M. Pollino and M. Bruneau, 1/21/08 (PB2008-112233).

MCEER-08-0004 "Linking Lifeline Infrastructure Performance and Community Disaster Resilience: Models and Multi-Stakeholder Processes," by S.E. Chang, C. Pasion, K. Tatebe and R. Ahmad, 3/3/08 (PB2008-112234).

MCEER-08-0005 "Modal Analysis of Generally Damped Linear Structures Subjected to Seismic Excitations," by J. Song, Y-L. Chu, Z. Liang and G.C. Lee, 3/4/08 (PB2009-102311).

MCEER-08-0006 "System Performance Under Multi-Hazard Environments," by C. Kafali and M. Grigoriu, 3/4/08 (PB2008-112235).

MCEER-08-0007 "Mechanical Behavior of Multi-Spherical Sliding Bearings," by D.M. Fenz and M.C. Constantinou, 3/6/08 (PB2008-112236).

MCEER-08-0008 "Post-Earthquake Restoration of the Los Angeles Water Supply System," by T.H.P. Tabucchi and R.A. Davidson, 3/7/08 (PB2008-112237).

MCEER-08-0009 "Fragility Analysis of Water Supply Systems," by A. Jacobson and M. Grigoriu, 3/10/08 (PB2009-105545).

MCEER-08-0010 "Experimental Investigation of Full-Scale Two-Story Steel Plate Shear Walls with Reduced Beam Section Connections," by B. Qu, M. Bruneau, C-H. Lin and K-C. Tsai, 3/17/08 (PB2009-106368).

MCEER-08-0011 "Seismic Evaluation and Rehabilitation of Critical Components of Electrical Power Systems," S. Ersoy, B. Feizi, A. Ashrafi and M. Ala Saadeghvaziri, 3/17/08 (PB2009-105546).

MCEER-08-0012 "Seismic Behavior and Design of Boundary Frame Members of Steel Plate Shear Walls," by B. Qu and M. Bruneau, 4/26/08 . (PB2009-106744).

MCEER-08-0013 "Development and Appraisal of a Numerical Cyclic Loading Protocol for Quantifying Building System Performance," by A. Filiatrault, A. Wanitkorkul and M. Constantinou, 4/27/08 (PB2009-107906).

MCEER-08-0014 "Structural and Nonstructural Earthquake Design: The Challenge of Integrating Specialty Areas in Designing Complex, Critical Facilities," by W.J. Petak and D.J. Alesch, 4/30/08 (PB2009-107907).

MCEER-08-0015 "Seismic Performance Evaluation of Water Systems," by Y. Wang and T.D. O'Rourke, 5/5/08 (PB2009-107908).

MCEER-08-0016 "Seismic Response Modeling of Water Supply Systems," by P. Shi and T.D. O'Rourke, 5/5/08 (PB2009-107910).

MCEER-08-0017 "Numerical and Experimental Studies of Self-Centering Post-Tensioned Steel Frames," by D. Wang and A. Filiatrault, 5/12/08 (PB2009-110479).

MCEER-08-0018 "Development, Implementation and Verification of Dynamic Analysis Models for Multi-Spherical Sliding Bearings," by D.M. Fenz and M.C. Constantinou, 8/15/08 (PB2009-107911).

MCEER-08-0019 "Performance Assessment of Conventional and Base Isolated Nuclear Power Plants for Earthquake Blast Loadings," by Y.N. Huang, A.S. Whittaker and N. Luco, 10/28/08 (PB2009-107912).

MCEER-08-0020 "Remote Sensing for Resilient Multi-Hazard Disaster Response – Volume I: Introduction to Damage Assessment Methodologies," by B.J. Adams and R.T. Eguchi, 11/17/08 (PB2010-102695).

MCEER-08-0021 "Remote Sensing for Resilient Multi-Hazard Disaster Response – Volume II: Counting the Number of Collapsed Buildings Using an Object-Oriented Analysis: Case Study of the 2003 Bam Earthquake," by L. Gusella, C.K. Huyck and B.J. Adams, 11/17/08 (PB2010-100925).

MCEER-08-0022 "Remote Sensing for Resilient Multi-Hazard Disaster Response – Volume III: Multi-Sensor Image Fusion Techniques for Robust Neighborhood-Scale Urban Damage Assessment," by B.J. Adams and A. McMillan, 11/17/08 (PB2010-100926).

MCEER-08-0023 "Remote Sensing for Resilient Multi-Hazard Disaster Response – Volume IV: A Study of Multi-Temporal and Multi-Resolution SAR Imagery for Post-Katrina Flood Monitoring in New Orleans," by A. McMillan, J.G. Morley, B.J. Adams and S. Chesworth, 11/17/08 (PB2010-100927).

MCEER-08-0024 "Remote Sensing for Resilient Multi-Hazard Disaster Response – Volume V: Integration of Remote Sensing Imagery and VIEWS$^{TM}$ Field Data for Post-Hurricane Charley Building Damage Assessment," by J.A. Womble, K. Mehta and B.J. Adams, 11/17/08 (PB2009-115532).

MCEER-08-0025 "Building Inventory Compilation for Disaster Management: Application of Remote Sensing and Statistical Modeling," by P. Sarabandi, A.S. Kiremidjian, R.T. Eguchi and B. J. Adams, 11/20/08 (PB2009-110484).

MCEER-08-0026 "New Experimental Capabilities and Loading Protocols for Seismic Qualification and Fragility Assessment of Nonstructural Systems," by R. Retamales, G. Mosqueda, A. Filiatrault and A. Reinhorn, 11/24/08 (PB2009-110485).

MCEER-08-0027 "Effects of Heating and Load History on the Behavior of Lead-Rubber Bearings," by I.V. Kalpakidis and M.C. Constantinou, 12/1/08 (PB2009-115533).

MCEER-08-0028 "Experimental and Analytical Investigation of Blast Performance of Seismically Resistant Bridge Piers," by S.Fujikura and M. Bruneau, 12/8/08 (PB2009-115534).

MCEER-08-0029 "Evolutionary Methodology for Aseismic Decision Support," by Y. Hu and G. Dargush, 12/15/08.

MCEER-08-0030 "Development of a Steel Plate Shear Wall Bridge Pier System Conceived from a Multi-Hazard Perspective," by D. Keller and M. Bruneau, 12/19/08 (PB2010-102696).

MCEER-09-0001 "Modal Analysis of Arbitrarily Damped Three-Dimensional Linear Structures Subjected to Seismic Excitations," by Y.L. Chu, J. Song and G.C. Lee, 1/31/09 (PB2010-100922).

MCEER-09-0002 "Air-Blast Effects on Structural Shapes," by G. Ballantyne, A.S. Whittaker, A.J. Aref and G.F. Dargush, 2/2/09 (PB2010-102697).

MCEER-09-0003 "Water Supply Performance During Earthquakes and Extreme Events," by A.L. Bonneau and T.D. O'Rourke, 2/16/09 (PB2010-100923).

MCEER-09-0004 "Generalized Linear (Mixed) Models of Post-Earthquake Ignitions," by R.A. Davidson, 7/20/09 (PB2010-102698).

MCEER-09-0005 "Seismic Testing of a Full-Scale Two-Story Light-Frame Wood Building: NEESWood Benchmark Test," by I.P. Christovasilis, A. Filiatrault and A. Wanitkorkul, 7/22/09 (PB2012-102401).

MCEER-09-0006 "IDARC2D Version 7.0: A Program for the Inelastic Damage Analysis of Structures," by A.M. Reinhorn, H. Roh, M. Sivaselvan, S.K. Kunnath, R.E. Valles, A. Madan, C. Li, R. Lobo and Y.J. Park, 7/28/09 (PB2010-103199).

MCEER-09-0007 "Enhancements to Hospital Resiliency: Improving Emergency Planning for and Response to Hurricanes," by D.B. Hess and L.A. Arendt, 7/30/09 (PB2010-100924).

MCEER-09-0008 "Assessment of Base-Isolated Nuclear Structures for Design and Beyond-Design Basis Earthquake Shaking," by Y.N. Huang, A.S. Whittaker, R.P. Kennedy and R.L. Mayes, 8/20/09 (PB2010-102699).

MCEER-09-0009 "Quantification of Disaster Resilience of Health Care Facilities," by G.P. Cimellaro, C. Fumo, A.M Reinhorn and M. Bruneau, 9/14/09 (PB2010-105384).

MCEER-09-0010 "Performance-Based Assessment and Design of Squat Reinforced Concrete Shear Walls," by C.K. Gulec and A.S. Whittaker, 9/15/09 (PB2010-102700).

MCEER-09-0011 "Proceedings of the Fourth US-Taiwan Bridge Engineering Workshop," edited by W.P. Yen, J.J. Shen, T.M. Lee and R.B. Zheng, 10/27/09 (PB2010-500009).

MCEER-09-0012 "Proceedings of the Special International Workshop on Seismic Connection Details for Segmental Bridge Construction," edited by W. Phillip Yen and George C. Lee, 12/21/09 (PB2012-102402).

MCEER-10-0001 "Direct Displacement Procedure for Performance-Based Seismic Design of Multistory Woodframe Structures," by W. Pang and D. Rosowsky, 4/26/10 (PB2012-102403).

MCEER-10-0002 "Simplified Direct Displacement Design of Six-Story NEESWood Capstone Building and Pre-Test Seismic Performance Assessment," by W. Pang, D. Rosowsky, J. van de Lindt and S. Pei, 5/28/10 (PB2012-102404).

MCEER-10-0003 "Integration of Seismic Protection Systems in Performance-Based Seismic Design of Woodframed Structures," by J.K. Shinde and M.D. Symans, 6/18/10 (PB2012-102405).

MCEER-10-0004 "Modeling and Seismic Evaluation of Nonstructural Components: Testing Frame for Experimental Evaluation of Suspended Ceiling Systems," by A.M. Reinhorn, K.P. Ryu and G. Maddaloni, 6/30/10 (PB2012-102406).

MCEER-10-0005 "Analytical Development and Experimental Validation of a Structural-Fuse Bridge Pier Concept," by S. El-Bahey and M. Bruneau, 10/1/10 (PB2012-102407).

MCEER-10-0006 "A Framework for Defining and Measuring Resilience at the Community Scale: The PEOPLES Resilience Framework," by C.S. Renschler, A.E. Frazier, L.A. Arendt, G.P. Cimellaro, A.M. Reinhorn and M. Bruneau, 10/8/10 (PB2012-102408).

MCEER-10-0007 "Impact of Horizontal Boundary Elements Design on Seismic Behavior of Steel Plate Shear Walls," by R. Purba and M. Bruneau, 11/14/10 (PB2012-102409).

MCEER-10-0008 "Seismic Testing of a Full-Scale Mid-Rise Building: The NEESWood Capstone Test," by S. Pei, J.W. van de Lindt, S.E. Pryor, H. Shimizu, H. Isoda and D.R. Rammer, 12/1/10 (PB2012-102410).

MCEER-10-0009 "Modeling the Effects of Detonations of High Explosives to Inform Blast-Resistant Design," by P. Sherkar, A.S. Whittaker and A.J. Aref, 12/1/10 (PB2012-102411).

MCEER-10-0010 "L'Aquila Earthquake of April 6, 2009 in Italy: Rebuilding a Resilient City to Withstand Multiple Hazards," by G.P. Cimellaro, I.P. Christovasilis, A.M. Reinhorn, A. De Stefano and T. Kirova, 12/29/10.

MCEER-11-0001 "Numerical and Experimental Investigation of the Seismic Response of Light-Frame Wood Structures," by I.P. Christovasilis and A. Filiatrault, 8/8/11 (PB2012-102412).

MCEER-11-0002 "Seismic Design and Analysis of a Precast Segmental Concrete Bridge Model," by M. Anagnostopoulou, A. Filiatrault and A. Aref, 9/15/11.

MCEER-11-0003 'Proceedings of the Workshop on Improving Earthquake Response of Substation Equipment," Edited by A.M. Reinhorn, 9/19/11 (PB2012-102413).

MCEER-11-0004 "LRFD-Based Analysis and Design Procedures for Bridge Bearings and Seismic Isolators," by M.C. Constantinou, I. Kalpakidis, A. Filiatrault and R.A. Ecker Lay, 9/26/11.

MCEER-11-0005 "Experimental Seismic Evaluation, Model Parameterization, and Effects of Cold-Formed Steel-Framed Gypsum Partition Walls on the Seismic Performance of an Essential Facility," by R. Davies, R. Retamales, G. Mosqueda and A. Filiatrault, 10/12/11.

MCEER-11-0006 "Modeling and Seismic Performance Evaluation of High Voltage Transformers and Bushings," by A.M. Reinhorn, K. Oikonomou, H. Roh, A. Schiff and L. Kempner, Jr., 10/3/11.

MCEER-11-0007 "Extreme Load Combinations: A Survey of State Bridge Engineers," by G.C. Lee, Z. Liang, J.J. Shen and J.S. O'Connor, 10/14/11.

MCEER-12-0001 "Simplified Analysis Procedures in Support of Performance Based Seismic Design," by Y.N. Huang and A.S. Whittaker.

MCEER-12-0002 "Seismic Protection of Electrical Transformer Bushing Systems by Stiffening Techniques," by M. Koliou, A. Filiatrault, A.M. Reinhorn and N. Oliveto, 6/1/12.

MCEER-12-0003 "Post-Earthquake Bridge Inspection Guidelines," by J.S. O'Connor and S. Alampalli, 6/8/12.

MCEER-12-0004 "Integrated Design Methodology for Isolated Floor Systems in Single-Degree-of-Freedom Structural Fuse Systems," by S. Cui, M. Bruneau and M.C. Constantinou, 6/13/12.

MCEER-12-0005 "Characterizing the Rotational Components of Earthquake Ground Motion," by D. Basu, A.S. Whittaker and M.C. Constantinou, 6/15/12.

MCEER-12-0006 "Bayesian Fragility for Nonstructural Systems," by C.H. Lee and M.D. Grigoriu, 9/12/12.

MCEER-12-0007 "A Numerical Model for Capturing the In-Plane Seismic Response of Interior Metal Stud Partition Walls," by R.L. Wood and T.C. Hutchinson, 9/12/12.

MCEER-12-0008 "Assessment of Floor Accelerations in Yielding Buildings," by J.D. Wieser, G. Pekcan, A.E. Zaghi, A.M. Itani and E. Maragakis, 10/5/12.

MCEER-13-0001 "Experimental Seismic Study of Pressurized Fire Sprinkler Piping Systems," by Y. Tian, A. Filiatrault and G. Mosqueda, 4/8/13.

MCEER-13-0002 "Enhancing Resource Coordination for Multi-Modal Evacuation Planning," by D.B. Hess, B.W. Conley and C.M. Farrell, 2/8/13.

MCEER-13-0003 "Seismic Response of Base Isolated Buildings Considering Pounding to Moat Walls," by A. Masroor and G. Mosqueda, 2/26/13.

MCEER-13-0004 "Seismic Response Control of Structures Using a Novel Adaptive Passive Negative Stiffness Device," by D.T.R. Pasala, A.A. Sarlis, S. Nagarajaiah, A.M. Reinhorn, M.C. Constantinou and D.P. Taylor, 6/10/13.

MCEER-13-0005 "Negative Stiffness Device for Seismic Protection of Structures," by A.A. Sarlis, D.T.R. Pasala, M.C. Constantinou, A.M. Reinhorn, S. Nagarajaiah and D.P. Taylor, 6/12/13.

MCEER-13-0006 "Emilia Earthquake of May 20, 2012 in Northern Italy: Rebuilding a Resilient Community to Withstand Multiple Hazards," by G.P. Cimellaro, M. Chiriatti, A.M. Reinhorn and L. Tirca, June 30, 2013.

MCEER-13-0007 "Precast Concrete Segmental Components and Systems for Accelerated Bridge Construction in Seismic Regions," by A.J. Aref, G.C. Lee, Y.C. Ou and P. Sideris, with contributions from K.C. Chang, S. Chen, A. Filiatrault and Y. Zhou, June 13, 2013.

MCEER-13-0008 "A Study of U.S. Bridge Failures (1980-2012)," by G.C. Lee, S.B. Mohan, C. Huang and B.N. Fard, June 15, 2013.

MCEER-13-0009 "Development of a Database Framework for Modeling Damaged Bridges," by G.C. Lee, J.C. Qi and C. Huang, June 16, 2013.

MCEER-13-0010 "Model of Triple Friction Pendulum Bearing for General Geometric and Frictional Parameters and for Uplift Conditions," by A.A. Sarlis and M.C. Constantinou, July 1, 2013.

MCEER-13-0011 "Shake Table Testing of Triple Friction Pendulum Isolators under Extreme Conditions," by A.A. Sarlis, M.C. Constantinou and A.M. Reinhorn, July 2, 2013.

MCEER-13-0012 "Theoretical Framework for the Development of MH-LRFD," by G.C. Lee (coordinating author), H.A Capers, Jr., C. Huang, J.M. Kulicki, Z. Liang, T. Murphy, J.J.D. Shen, M. Shinozuka and P.W.H. Yen, July 31, 2013.

MCEER-13-0013 "Seismic Protection of Highway Bridges with Negative Stiffness Devices," by N.K.A. Attary, M.D. Symans, S. Nagarajaiah, A.M. Reinhorn, M.C. Constantinou, A.A. Sarlis, D.T.R. Pasala, and D.P. Taylor, September 3, 2014.

MCEER-14-0001 "Simplified Seismic Collapse Capacity-Based Evaluation and Design of Frame Buildings with and without Supplemental Damping Systems," by M. Hamidia, A. Filiatrault, and A. Aref, May 19, 2014.

MCEER-14-0002 "Comprehensive Analytical Seismic Fragility of Fire Sprinkler Piping Systems," by Siavash Soroushian, Emmanuel "Manos" Maragakis, Arash E. Zaghi, Alicia Echevarria, Yuan Tian and Andre Filiatrault, August 26, 2014.

MCEER-14-0003 "Hybrid Simulation of the Seismic Response of a Steel Moment Frame Building Structure through Collapse," by M. Del Carpio Ramos, G. Mosqueda and D.G. Lignos, October 30, 2014.

MCEER-14-0005 "Seismic Performance of Steel Plate Shear Walls Considering Various Design Approaches," by R. Purba and M. Bruneau, October 31, 2014.

MCEER-14-0006 "Air-Blast Effects on Civil Structures," by Jinwon Shin, Andrew S. Whittaker, Amjad J. Aref and David Cormie, October 30, 2014.

MCEER-14-0007 "Seismic Performance Evaluation of Precast Girders with Field-Cast Ultra High Performance Concrete (UHPC) Connections," by G.C. Lee, C. Huang, J. Song, and J. S. O'Connor, July 31, 2014.


ISSN 1520-295X